ANALYSIS PROCEDURES FOR CAISSON-RETAINED ISLAND TYPE STRUCTURES

by

FRANCISCO MANUEL GONÇALVES ALVES SALGADO

B.Sc., Technical University of Lisbon, Portugal, 1972

M.A.Sc., University of British Columbia, Vancouver, Canada, 1981

A THESIS SUBMITTED IN PARTIAL FULFILLMENT OF

THE REQUIREMENTS FOR THE DEGREE OF

DOCTOR OF PHILOSOPHY

in

THE FACULTY OF GRADUATE STUDIES

Department of Civil Engineering

We accept this thesis as conforming

to the required standard

THE UNIVERSITY OF BRITISH COLUMBIA

May, 1990

In presenting this thesis in partial fulfilment of the requirements for an advanced degree at the University of British Columbia, I agree that the Library shall make it freely available for reference and study. I further agree that permission for extensive copying of this thesis for scholarly purposes may be granted by the head of my department or by his or her representatives. It is understood that copying or publication of this thesis for financial gain shall not be allowed without my written permission.

Department of CIVIL ENGINEERING

The University of British Columbia
Vancouver, Canada

Date May 16, 1990

ABSTRACT

This thesis is concerned with the analysis of large offshore gravity structures used for oil exploration and recovery in the Beaufort Sea. Because of the high ice loads and the water depths involved, these structures comprise a large steel box infilled with a sand core for stability. One such structure was subjected to severe ice loading in April 1986 causing portions of the sand core to liquefy and bring the structure to a near failure condition. This structure was heavily monitored and thus serves as a case study against which the proposed analysis procedure can be checked.

The behaviour of these soil-structure systems is highly complex depending upon the characteristics of the soil, the structural elements and the soil-structure interface. In this thesis a three-dimensional Finite Element computer program with soil, interface and structural elements is developed.

Emphasis is placed on the three-dimensional stress-strain constitutive law both in terms of its ability to model observed laboratory response as well as the determination of the constitutive law parameters from in situ testing.

The results obtained in terms of displacement, acceleration and zones of liquefaction by the analysis were then compared with the field measurements obtained during the April 1986 ice load event. The good agreement obtained between predicted and observed response is a validation of the proposed procedure.

TABLE OF CONTENTS

TABLE OF CONTENTS (Continued)

TABLE OF CONTENTS (Continued)

TABLE OF CONTENTS (Continued)

TABLE OF CONTENTS (Continued)

TABLE OF CONTENTS (Cont'd)

TABLE OF CONTENTS (Cont'd)

TABLE OF CONTENTS (Cont'd)

TABLE OF CONTENTS (Cont'd)

TABLE OF CONTENTS (Continued)

LIST OF TABLES

LIST OF FIGURES

LIST OF FIGURES (Continued)...

LIST OF FIGURES (Continued)

LIST OF FIGURES (Continued)

LIST OF FIGURES (Continued)

LIST OF FIGURES (Continued)

LIST OF FIGURES (Continued)

LIST OF FIGURES (Continued)

LIST OF FIGURES (Continued)...

LIST OF FIGURES (Continued)...

NOMENCLATURE

A = area

Acc = accelerometer

$A(t)$ = peak acceleration at time t

a_i = direction cosines of the normal stress, σ_{SMP}, in relation to principal direction i, (i = 1,2,3)

a = $(\sigma_1-\sigma_3)/(\sigma_1+\sigma_3) = \sin(\phi_{13})$

b_i = $(bi)_{\sigma i}$ = direction cosines of the shear stress τ_{SMP} in relation to principal direction i, (i = 1,2,3)

$(b_i)_{\Delta\epsilon_i^p}$ = direction cosines of the increment of plastic shear strain, $\Delta\gamma^p_{SMP}$, in relation to direction i, (i = 1,2,3)

b = b - value = $(\sigma_2-\sigma_3)/(\sigma_1-\sigma_3)$

B = bulk modulus

B_e = B_{ur} = elastic or unload/reload bulk modulus

B_t = tangent bulk modulus

C = cohesion

Ca = cohesion (interface)

$[C^e]$ = elastic constitutive matrix

$[C^{ep}]$ = elasto-plastic constitutive matrix

$[C^p]$ = plastic constitutive matrix

CMP = compounded mobilized planes

CPT = cone penetration test

C_u = uniformity coefficient

d = displacement

D_r = relative density

D_{10} = effective grain size

D_{50} = medium grain size

E = Young's modulus

E_{max} = maximum Young's modulus

E_N = normal modulus (interface)

e = void ratio

e_c = consolidated void ratio (in situ)

$(e_c)_{av}$ = average consolidated void ratio (in situ)

e_o = consolidated void ratio (laboratory)

e_{ss} = void ratio at steady state

e_{ss_1} = void ratio at steady state (defined at 1 kPa)

$\{f\}_{LS}$ = nodal load vector for load shedding

f_o = frequency

FS = factor of safety

G = shear modulus

G_{CH} = maximum shear modulus obtained from cross hole seismic tests

G_{DH} = maximum shear modulus obtained from down hole seismic tests

G_{HH} = maximum shear modulus in the horizontal plane

G_i = initial shear modulus (interface element)

G_o = the initial slope of the hyperbolic relationship between (τ_{zx}/σ_x) and γ_{zx}

G_p = plastic shear modulus parameter

G_{pt} = tangent plastic shear modulus parameter

G_{pi} = initial slope of the hyperbolic relationship between $(\tau_{SMP}/\sigma_{SMP})$ and γ^p_{SMP}

G_{max} = G_e = elastic or maximum shear modulus

$G_{max,o}$ = maximum in situ shear modulus

G_{rc} = maximum shear modulus from resonant column tests

G_s = secant shear modulus (also used as specific gravity)

G_t = tangent shear modulus

G_{VH} = maximum shear modulus in the vertical plane

G^* = equivalent elastic shear modulus evaluated from unload/reload pressuremeter tests data

H = height

I_i = principal stress invariants (i = 1,2,3)

I_x, I_y = moments of inertia

k = earth pressure coefficient

k_o = earth pressure coefficient 'at-rest'

[K] = stiffness matrix

K = modulus number

KB (or K_b) = bulk modulus number

KB_e = KB_{ur} = elastic or unload/reload bulk modulus number

K_c = σ_1'/σ_3'

KE (or K_e) = Young's modulus number

KE_{max} = maximum Young's modulus number

KG = shear modulus number

KG_e = KG_{max} = elastic or maximum shear modulus number

$(KG_{max})_{av}$ = average maximum shear modulus number

KG_p = plastic shear modulus parameter number

K_I = stiffness number (interface element)

K_N = normal modulus number

K_{si} = initial tangent stiffness (interface element)

K_{st} = tangent stiffness (interface element)

K_{UR} = unload/reload modulus number

$(K_2)_{max}$ = parameter to define G_{max} (Chapter 6)

L = length

ℓ_i = direction cosine of x-axis in relation to principal direction i(i = 1,2,3)

mi = direction cosine of y-axis in relation to principal direction i(i = 1,2,3)

m = bulk shear modulus exponent

MP = mobilized plane (2-D)

MSL = mobilized stress level

$(MSL)_{max}$ = maximum mobilized stress level

ni = direction cosine of z-axis in relation to principal direction i(i = 1,2,3)

n = shear and Young's modulus exponent; also normal direction to interface.

np = plastic shear modulus parameter exponent

N = standard penetration resistance; also number of cycles; also yield stress ratio (σ_1/σ_3)

$(N)_{60}$ = standard penetration resistance (hammer energy = 60%)

$(N_1)_{60}$ = normalized standard penetration resistance

N_ℓ = number of cycles to liquefaction

P = earth pressure

P_o = initial earth pressure 'at-rest'

P_a = atmospheric pressure

Q_c (or q_c) = cone penetration test end bearing

$(q_c)_1$ = normalized (or modified) cone end bearing

R (or) r = radial distance

r = interface shear direction

R_{face} = current pressuremeter radius

R_o = initial pressuremeter radius

R_p = plastic radius

R_F = failure ratio

s = $(\sigma_1+\sigma_3)/2$; also interface shear direction

SBP = self-boring pressuremeter

SMP = Spatial Mobilized Plane

SL = stress level

SRL = stress ratio level

s_u = residual shear strength

t = $(\sigma_1-\sigma_3)/2$; also interface thickness

U = displacement; also static pore pressure

U_g = generated porewater pressure

U_p = displacement at the boundary between plastic and elastic zones

U_r = relative displacement

$X(t)$ = the amplitude of the static displacement at time t correspondent to one-half cycle of load/unload

α = angle between the σ_3 direction and the horizontal direction

α_A = anisotropic factor

α_D = disturbancy factor

α_P = G^*/G_{max}

β = angle between the σ_1 direction and the horizontal direction

γ = $\epsilon_1-\epsilon_3$ = maximum shear strain

γ_{MP} = shear strain on the Mobilized Plane (2-D)

γ_o^p = plastic shear strain at which ϵ_{MP}^p is a minimum

γ_{oct} = octahedral shear strain

γ_{SMP} = shear strain on the Spatial Mobilized Plane (3-D)

γ = unit weight of soil

γ' = unit weight of submerged soil

γ_d = unit weight of dry soil

γ_{sat} = unit weight of saturated soil

γ_w = unit weight of water

δ = interface friction angle

Δ = increment

Δb_i = $(bi)_{\sigma_i} - (bi)_{\Delta\epsilon_i^p}$

$\Delta(i,x)$ = increment of the angle of rotation of the principal axes, i, (i = 1,2,3) with x-axis

$\Delta(i,y)$ = increment of the angle of rotation of the principal axes, i, (i = 1,2,3) with y-axis

$\Delta(i,z)$ = increment of the angle of rotation of the principal axes, i, (i = 1,2,3) with z-axis

ΔU_{cy} = cyclic developed porewater pressure

$\Delta\gamma_{MP}^p$ = increment of plastic shear strain on the Mobilized Plane (2-D)

$\Delta\gamma_{SMP}^p$ = increment of plastic shear strain on the Spatial Mobilized Plane

$\Delta\epsilon_{MP}^p$ = increment of plastic normal strain on the Mobilized Plane (2-D)

$\Delta\epsilon_{SMP}^p$ = increment of plastic normal strain on the Spatial Mobilized Plane (3-D)

$\{\Delta\sigma\}_{LS}$ = load shedding stress vector

$\Delta\sigma_{mcy}$ = cyclic variation in total mean normal stress

$\Delta\tau_{LS}$ = over-shear stresses to be shed

$\Delta(\tau_{SMP}/\sigma_{SMP})$ = decrease in failure stress ratio for a 10 fold increase in $(\sigma_{SMP})_F$

$\Delta\phi$ = decrease in friction angle for a 10 fold increase in σ_m

ϵ = strain

ϵ_i = principal strain in direction i, (i = 1,2,3)

ϵ_i^e = elastic principal strain in direction i, (i = 1,2,3)

ϵ_i^p = plastic principal strain in direction i, (i = 1,2,3)

$\{\epsilon\}$ = strain vector

$\{\epsilon^e\}$ = elastic strain vector

$\{\epsilon^p\}$ = plastic strain vector

ϵ_{MP} = normal strain on the Mobilized Plane (2-D)

ϵ_{SMP} = normal strain on the Spatial Mobilized Plane (3-D)

ϵ_r = radial strain

$(\epsilon_r)_{face}$ = radial strain at the face of the pressuremeter

ϵ_θ = circumferential strain

$(\epsilon_\theta)_{face}$ = circumferential strain at the face of the pressuremeter

ϵ_v = volumetric strain

$\epsilon_{v_{400}}$ = volumetric strain associated with 400 cycles of load

ξ = angle defined by the vertical direction and the direction of the major principal strain increment, $\Delta\epsilon_1$

λ = slope of Matsuoka's flow rule, and 1st hardening rule

λ_{ss} = slope of steady state line

μ = intercept of Matsuoka's flow rule

μ' = intercept of Matsuoka's 1st hardening rule

ν = poisson's ratio; also used as dilation angle

ν_{max} = maximum dilation angle

(NOTE: All σ stresses below are considered to be effective)

σ' = stress

σ'_i = principal stress in direction i, (i = 1,2,3)

$\{\sigma'\}$ = stress vector

σ'_a = normal stress in direction of wave propagation

σ'_{ar} = $(\sigma'_a + \sigma'_p)/2$

σ_b = boundary radial chamber stress

σ'_c = confining stress

σ_d = $\sigma_1 - \sigma_3$

σ'_m = mean normal stress

$\sigma'm_i$ = initial mean normal stress

σ'_{MP} = normal stress on the Mobilized Plane (2-D)

σ'_N = normal stress to interface

σ'_o = initial pressuremeter radial stress

σ'_p = normal stress in direction of particle vibration

σ'_r = radial stress

$(\sigma'_r)_{face}$ = radial stress at the face of the pressuremeter

σ'_{RP} = radial stress at the outer radius of the plastic zone

σ'_{SMP} = normal stress on the spatial mobilized plane (3-D)

$(\sigma'_{SMP})_F$ = normal stress on the spatial mobilized plane at failure

σ'_{xo} = initial cartesian stress in the x-direction (simple shear test)

σ'_v = vertical stress

σ'_{vo} = in situ vertical stress

$(\sigma'_1/\sigma'_3)_{max}$ = failure stress ratio

τ = maximum shear stress = $(\sigma_1 - \sigma_3)/2$

(τ_{av}/σ'_{vo}) or (τ_{cy}/σ'_{vo}) or (τ_{eq}/σ'_{vo}) = cyclic stress ratio causing liquefaction

τ_f = failure shear stress

τ_L = shear stress prior to unloading

τ_m = mobilized shear stress

τ_{MP} = shear stress on the Mobilized Plane (2-D)

(τ_{MP}/σ_{MP}) = stress ratio on the Mobilized Plane (2-D)

$(\tau_{MP}/\sigma_{MP})_{ult}$ = asymptotic value of the stress ratio on the Mobilized Plane (2-D)

$(\tau_{MP}/\sigma_{MP})_F$ = failure stress ratio on the Mobilized Plane (2-D)

τ_N = shear stress to cause liquefaction in N cycles

τ_{oct} = octahedral shear stress

τ_{SMP} = shear stress on the Spatial Mobilized Plane (3-D)

$(\tau_{SMP}/\sigma_{SMP})$ = stress ratio on the Spatial Mobilized Plane (3-D)

$(\tau_{SMP}/\sigma_{SMP})_{ult}$ = asymptotic value of the stress ratio on the Spatial Mobilized Plane

$(\tau_{SMP}/\sigma_{SMP})_F$ = failure stress ration on the Spatial Mobilized Plane (3-D)

$(\tau_{SMP}/\sigma_{SMP})_1$ = failure stress ratio on the Spatial Mobilized Plane at $(\sigma_{SMP})_F$ = 1 atmosphere

τ_{ult} = asymptotic shear stress

τ_{15} = shear stress to cause liquefaction in 15 cycles

ϕ = angle of internal friction

ϕ_{cv} = angle of internal friction at constant volume

ϕ_F = failure friction angle

ϕ_F^{ps} = failure friction angle (plane strain)

ϕ_F^{tx} = failure friction angle (triaxial conditions)

$\phi^*_{F_{13}}$ = failure friction angle (for $\sigma_2 \neq \sigma_3$ and $\sigma_2 \neq \sigma_1$)

$\phi_{F_{13}}$ = failure friction angle (defined by principal stresses σ_1 and σ_3)

$\phi_{F_{23}}$ = failure friction angle (defined by principal stresses σ_2 and σ_3)

$\phi_{F_{12}}$ = failure friction angle (defined by principal stresses σ_1 and σ_2)

ϕ_m = mobilized friction angle

$\phi_{m_{13}}$ = mobilized friction angle (defined by principal stresses σ_1 and σ_3)

$\phi_{m_{23}}$ = mobilized friction angle (defined by principal stresses σ_2 and σ_3)

$\phi_{m_{12}}$ = mobilized friction angle (defined by principal stresses σ_1 and σ_2)

ϕ_P = peak friction angle

ϕ_R = residual friction angle

ϕ_1 = peak friction angle at the effective mean normal stress of 1 atmosphere

χ = angle defined by the vertical direction and the direction of the major principal stress increment, $\Delta\sigma_1$

ψ = angle defined by the vertical direction and the direction of the major principal stress, σ_1

ψ = state parameter (chapter 6)

$\omega(t)$ = angular frequency at time t

ACKNOWLEDGEMENTS

I am extremely thankful to my supervisor, Professor P.M. Byrne, for his guidance, ideas, encouragement and enthusiastic interest throughout my research. Despite an overflown timetable Professor Byrne has always been 100% available to clarify my ideas and strengthen my arguments.

I would also like to express my grateful appreciation to Professors Y.P. Vaid, W.D.L. Finn, D.L. Anderson and K.W. Savigny for their critical comments and for being flexible in their schedule in meeting my deadlines. The valuable suggestions received from Professor Vaid are much appreciated. In addition, I extend my thanks to: Professor P.K. Robertson and J.A. Howie for many stimulating discussions on the pressuremeter tests; as well as Mr. M.G. Jefferies for the valuable discussions and the data on the Molikpaq study; Dr. M.K. Lee for his assistance in implementing the hyperbolic stress-strain law into 3-D F.E. formulation; my friends and colleagues Dawit Negussey, Mustapha Zergoun, Afzal Sulleman, Upul Atukorala, Li Yan, Blair Gohl, (Yoge) M. Yogendrakumar, Alberto Sayao and (Wije) W. Wijewickreme, whose cheerfulness and comments have carried me through moments of factor of safety ≈ 1.0; Mrs. Kelly Lamb for typing my thesis with such ability and speed and for being flexible in her time table to meet my deadlines.

I am grateful for the financial support provided by the University of British Columbia, the National Science and Engineering Research Council, the Graduate Research Engineering and Technology (G.R.E.A.T.) award sponsored by the Science Council of British Columbia and Golder Associates (Vancouver, British Columbia).

Finally I would like to thank my daughter Marta, my parents Luciano and Etelvina and brother Zé whose encouragement, faith and support made this thesis a reality.

CHAPTER 1

INTRODUCTION

1.1 Purpose

This thesis is concerned with the development and evaluation of analysis procedures for caisson-retained island type structures deployed in the Beaufort Sea for oil exploration and recovery.

Offshore exploratory oil drilling has been carried out through the years from either piled platforms or gravity platforms, the type being dependent essentially on the depth of water, the characteristics of the foundation soil and the loading, wave or ice. In the Beaufort Sea one of the governing factors for the type of platform to be used is the presence of ice, which covers the sea for at least 3/4 of the year. Loads developed on stationary structures by movements of the ice can be very high and have a dynamic as well as static component. Because of the high ice loads, gravity platforms comprised of artificial sand islands have been used in shallow waters. In deeper waters, however, such an approach is not viable due to the very large volume of fill required. To overcome this problem, two of the major oil companies (Esso Resources Canada and Gulf Canada Resources Inc.) have investigated the concept of an artificial caisson-retained island. The first monolithic caisson-retained island deployed in the Beaufort Sea was a mobile arctic caisson called Molikpaq, shown in Fig. 1.1, and owned by Gulf Canada Resources Inc. The Molikpaq has been described in several publications including: Bruce and Harrington, 1982; McCreath et al., 1982; Fitzpatrick and Stenning, 1983; Jefferies et al., 1985; Stewart and Brakel, 1986; Jefferies and Wright, 1988; and Jefferies et al., 1988.

The platform consists of a steel caisson containing ballast water tanks, with a simply supported steel deck. In plan the caisson is almost a square as shown in Fig. 1.1 with an outside dimension of 111 metres. The central void, which is approximately 72 by 72 metres in plan is filled with sand to provide sufficient mass to resist the large horizontal ice loads. The overall height of the structure is 33.5 metres and the height of the sand fill core is approximately 21.0 metres. As shown in Fig. 1.2 the steel caisson with its sand core rests on a submerged sand berm, which in turn rests on a prepared area of the sea floor. The thickness of the sand

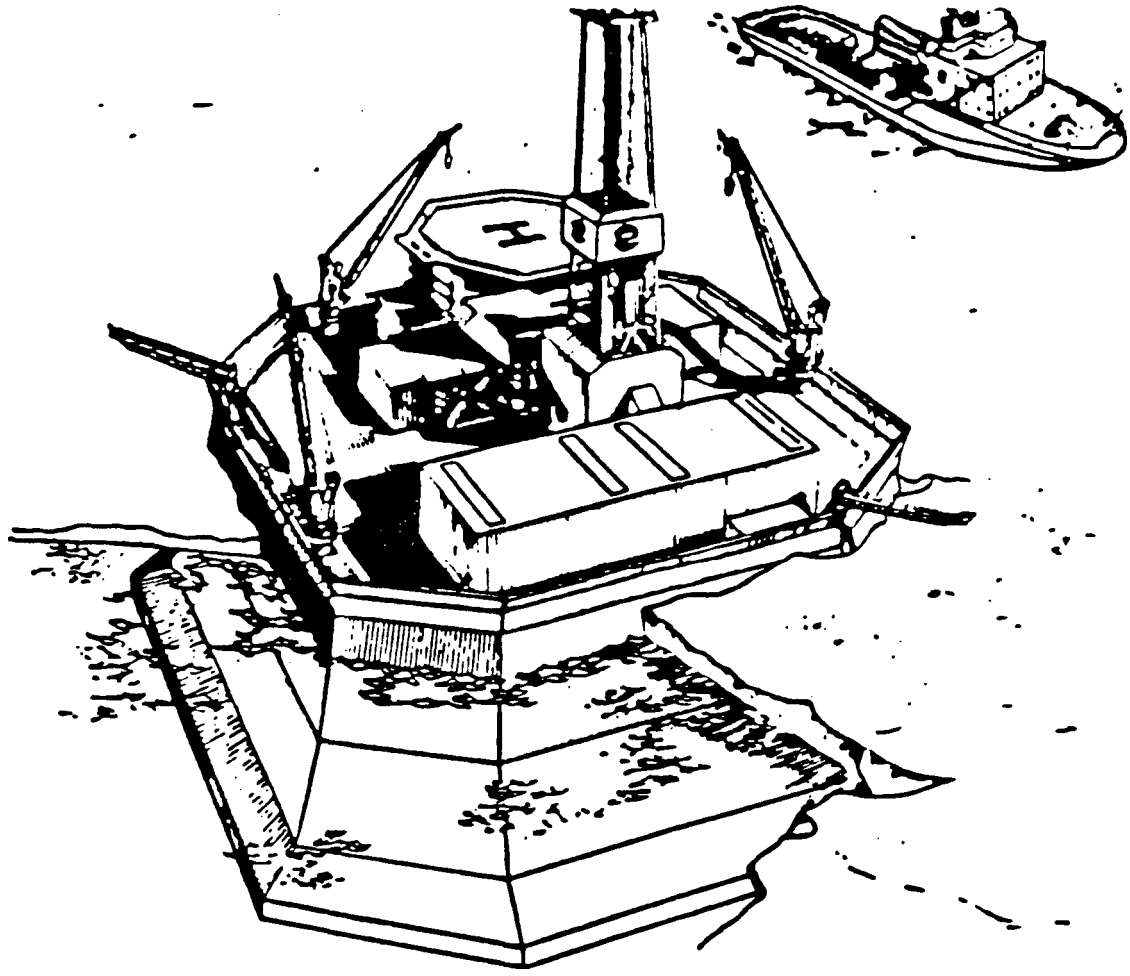

Figure 1.1 Beaudril Mobile Artic Caisson "Molikpaq" (after Jefferies et al., 1988)

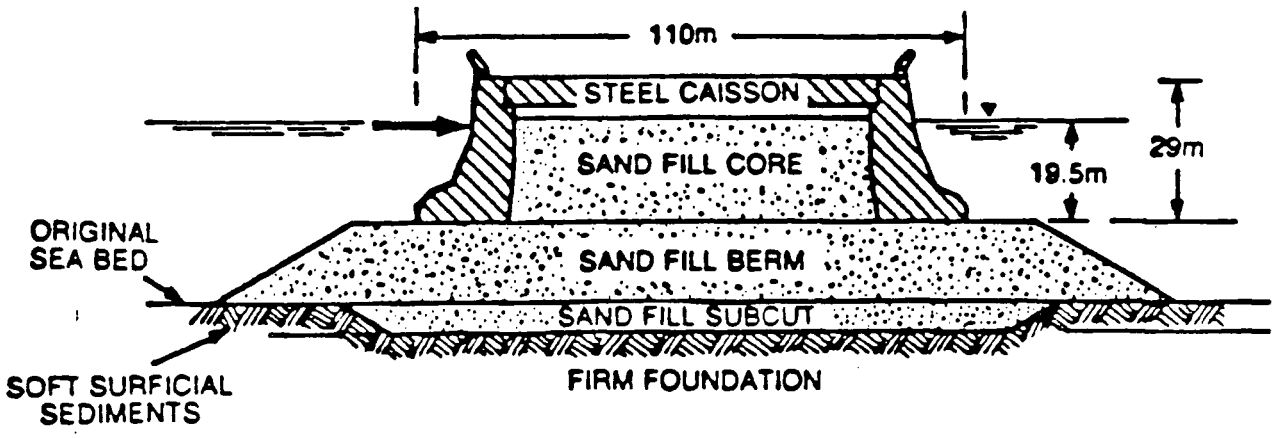

Figure 1.2 Schematic Cross-Section of Molikpaq and Berm (after Jefferies et al., 1988)

berm at a particular site depends on the water depth and on the strength characteristics of the sea floor deposits. Soft sea floor sediments are removed and replaced by a sand fill subcut prior to constructing the berm. The caisson is then placed on the berm and filled with sand to provide a stable drilling platform. After completion of exploratory drilling at a site the core sand fill is removed, the ballast water pumped out, making the caisson reusable for another site.

The Molikpaq was first deployed in October 1984 at Tarsiut P-45, see Fig. 1.3 for location, where the ice-loads mobilized were considered to be quite modest (Jefferies and Wright, 1988). In September 1985, the Molikpaq was moved to Amauligak I-65. At this site during the Winter 1985/86 the ice loads, which were dynamic in nature, were quite large and caused part of the sand core fill to liquefy and the platform to come close to limiting stability (Jefferies and Wright, 1988; and Jefferies et al., 1988).

The behaviour of these soil-structure systems is highly complex depending upon the characteristics of the soil and structural elements as

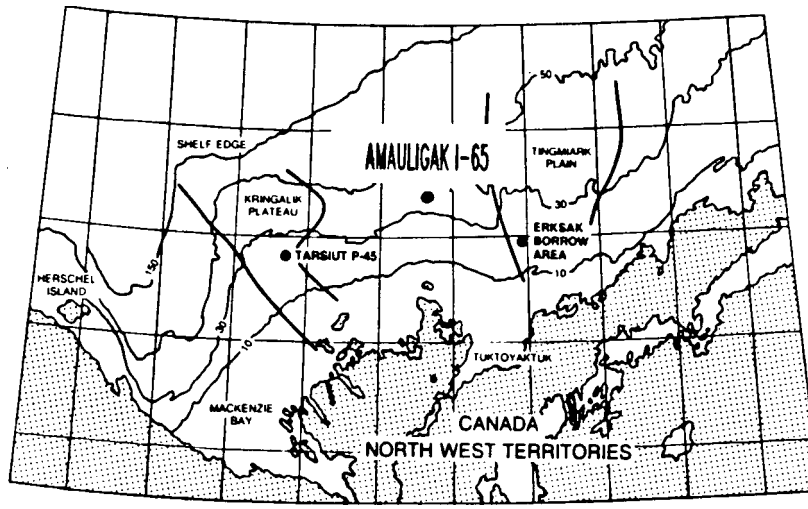

Figure 1.3 Molikpaq Site Locations (after Jefferies et al., 1988)

well as the construction sequence and the type of loading. Important aspects of their behaviour can be obtained from field observation as well as laboratory centrifuge tests. In addition, much can be learned from analytical modelling of these structures, particularly when such models can be calibrated with known field behaviour. This thesis is concerned with the development of such a model and in comparing its predictions with field measurements.

1.2 Scope

A sophisticated modelling of Molikpaq type structures require a three dimensional (3-D) computer program for non-linear analysis of soil-structure interaction problems. Besides structural elements, the following is required:

- Soil elements with an appropriate 3-D constitutive law for soil.

- Assessment of stress-strain parameters of the soils from laboratory and field tests.
- Interface elements.
- Analysis procedure to assess the static response of the Molikpaq during the fill construction phase and moderate ice loading phases.
- Analysis procedure to assess the dynamic response of the Molikpaq during high ice loading phase.

The above topics are briefly discussed next.

a) 3-D Constitutive Law for Sands

Due to the 3-D nature of the problem, not only in geometric terms but also in the terms of the loading, the stress paths mobilized in the core and berm sand fills during the construction phase and the ice loading phases, a 3-D constitutive law for sands that can model its shear, dilation and principal stress axis rotation characteristics is required. The three parameter dilatant elastic plastic stress-strain model for sands developed by Byrne and Eldridge (1982) was used in preliminary analysis after extending it to 3-dimensions. It was soon found, however, that although this formulation is able to model adequately the shear and dilation characteristics of the sand when subject to the triaxial stress path, it could not model the shear, dilation and deformation under principal stress rotation characteristics of the sand when subject to the simple shear stress path, a path which is considered to be more representative of the stress change induced by the horizontal ice load movement on the Molikpaq structure.

To satisfy the above requirements, a 3-D model for sands following the concept of the Spatial Mobilized Plane (SMP) (Matsuoka, 1974,1983) was developed and implemented into Finite Element (F.E.) form.

The performance of this model is evaluated by comparison with laboratory measurements obtained from triaxial tests, true triaxial tests, simple shear tests and pressuremeter chamber tests, and also by comparison with in-situ measurements obtained from field tests.

b) Evaluation of Stress-Strain Parameters of Soil from Laboratory and In Situ Testing

Extensive in situ testing is carried out in the core, berm and foundation of the Molikpaq, any time this structure is deployed at a new site in order to assess the quality and strength characteristics of the foundation soil and of the sand fills used (Jefferies et al., 1985). The in situ testing consists mainly of cone penetration tests (CPT), self-boring pressuremeter tests (SBP) and shear wave measurements by downhole and crosshole methods. In addition, laboratory testing is also carried out on samples obtained from those fills to complement the in situ testing.

A special effort was made in this thesis for the development of procedures to evaluate soil parameters for use in the two analytical models described earlier. It will be shown that soil parameters can be obtained from the following three sources:

i) Laboratory tests

ii) Pressuremeter tests

iii) Laboratory and cone penetration tests.

Particular attention in this thesis is paid to the pressuremeter test. This test can yield useful information about the in situ stress-strain behaviour of soil during loading and unloading. However, because the stress field induced by the SBP is not homogeneous, a rational analysis and

interpretation of the SBP test data requires that it be analyzed using selected stress-strain relations. In addition, it is important that such analysis and interpretation be checked against experimental data under controlled conditions before application to in situ field conditions. A review of the existing methods to infer soil parameters from the unloading, and the first time loading pressuremeter test data indicate that:

- A detailed analysis method, that considers both the stress and void ratio changes induced by pressuremeter loading and the nonlinear stress-strain response upon unloading, to infer the maximum in situ shear modulus, $G_{max,o}$ from the unload pressuremeter shear modulus, G*, had not been developed. Herein such a procedure is developed and checked against both laboratory and field data.

- The evaluation of soil parameters from the first time loading part of the pressuremeter tests in sand has been restricted for many years to the evaluation of the peak friction angle, ϕ_p, and the dilation angle, ν. Only recently, Manassero (1989) proposed a method that allows the complete plane strain nonlinear stress and volume change response of sand to be obtained from pressuremeter pressure-expansion data. This method was analytically verified herein against Finite Element generated pressuremeter data which was computed using the 3-D SMP model developed in this thesis. Procedures to evaluate soil parameters for use in this 3-D model from the pressuremeter test data were also developed. These procedures used Manassero's method after expanding it to take into account the intermediate principal stress, σ_2.

Particular attention was also focussed on the evaluation of soil parameters from the data obtained from both cone penetration and laboratory

tests. The in situ void ratio, e_c, was the key parameters used to link the laboratory test data with the CPT data. Soil moduli such as the Young's modulus, E, the shear modulus, G, and the bulk modulus, B, are highly dependent on the consolidated void ratio, e_c. The in situ void ratio, e_c was evaluated from the in situ state parameter, ψ, which was pre-obtained from the CPT cone bearing, q_c, following the procedures developed by Been et al. (1986). Once e_c was known, the in situ moduli were estimated from existing laboratory data.

c) Interface Elements

Interface elements were considered necessary to model the contact between the Molikpaq steel structure and the sand fill. A 3-D interface element following the concept of Desai's 'Thin' element (Desai et al., 1984), was developed and implemented into the finite element formulation. Procedures for the evaluation of soil parameters for this interface element were also developed. Its performance was evaluated by comparisons with available closed form solutions. In addition, both the 'Thin' element and the SMP model predictions were compared with earth pressure measurements on a 10 m retaining wall field test. These F.E. studies were considered necessary to check the procedures followed in the construction analysis of the Molikpaq, since there were no earth pressure measurements during the core construction phase of this structure.

d) Static Assessment

To assess the static response of the Molikpaq upon gravity loading (construction phase) and moderate ice loading the following procedures were followed in the analysis:

• Construction Phase:

The construction of the berm and core was simulated in the 3-D analysis by placing the above fills in one single layer. Although the ideal approach is to "analytically construct" these fills in layers, that procedure was not followed due to the large band width of the system of equations. However, the stresses so obtained from the 3-D analysis (along the cross-section oriented in the direction of the ice load) were compared with the stresses obtained from 2-D analysis in which construction in layers was simulated. It was found that the stresses obtained from both 2-D and 3-D analyses were in reasonable agreement.

• Moderate Ice Loading Phase

On March 25, 1986 the Molikpaq structure was subject to moderate ice loads of about 110 MN. Based on data reported by Jefferies and Wright (1988), this event was considered to be a static ice load event. Therefore 3-D static analysis simulating the ice load conditions of March 25, 1986 were carried out and the model used in the analysis was calibrated against the reported field behaviour.

e) Dynamic Assessment

On April 12, 1986 the Molikpaq structure was subject to severe dynamic ice loads. To analyse this event a 3-D finite element dynamic program with an appropriate stress-strain law is required. To date, however, such a program does not exist.

Adequate 2-D finite element dynamic programs do exist, such as the program RICEL developed by Yogendrakumar and Finn (1987). This program was used in 2-D dynamic and pseudo-dynamic analysis of the Molikpaq's response

to the above ice load event by Finn et al. (1988), who showed that the Molikpaq's system damping was very large and consequently no significant dynamic amplification occurred. Hence the response of the structure can be estimated from pseudo-dynamic or pseudo-static analysis which do not consider inertia forces.

The 3-D dynamic assessment was carried out using 3-D pseudo-static analysis, following an approach in which the response of the Molikpaq structure to a number of ice load cycles was inferred from the displacements and stresses computed from a single static loading cycle. The proposed procedure is outlined later in Chapter 7.

The stress cycles obtained from the pseudo-static analysis were used to compute the potential for liquefaction by comparing these stresses with the liquefaction resistance of the sand fills. This liquefaction resistance was developed based on the cone penetration resistance, q_c, of the fills and on the chart proposed by Seed and DeAlba (1986). However, because this chart is valid for earthquakes of magnitude 7.5 or 15 significant load cycles and because the Molikpaq was subject to a substantially larger number of cycles than 15 (Jefferies and Wright, 1988), an extrapolation of this chart for a larger number of cycles was required and this was considered herein, as is described later in Chapter 6.

CHAPTER 2

3-D CONSTITUTIVE MODEL FOR SANDS FOLLOWING THE CONCEPT OF THE SPATIAL MOBILIZED PLANE

2.1 Introduction

The Molikpaq caisson retained island represents a good example of a 3-D geotechnical problem. The 3-D aspects are evident not only from the 3-D geometry of the structure but also from the 3-D aspects of the ice movement which can strike the structure from any horizontal direction. For these reasons soil elements within the core and berm fills can be subjected to many different stress paths. Constant stress ratio conditions ($\sigma_1/\sigma_3 = 1/K_0$) are likely to develop during the construction phase in the soil elements located on the centreline of the fills (K_0 is the earth pressure coefficient at rest). Simple shear conditions are likely to develop in the sand fills during the ice loading phase. A rigorous solution of the problem requires an adequate constitutive law that can model the shear, dilation and principal stress axis rotation characteristics of sand in a 3-D stress space.

The hyperbolic model which was developed by Duncan and Chang (1970) and Duncan et al. (1980) was used in preliminary analysis after extending it to 3 dimensions and implementing it in the 3-D F.E. code 'NONSAP' (Bathe et al., 1974). In this model the stress-strain curves are assumed to be hyperbolic as first proposed by Kondner (1963) and Kondner and Zelasko (1963) and are characterized by a tangent Young's and tangent bulk moduli that vary with both stress level and relative density.

This model was later modified and expanded by Byrne and Eldridge (1982) with an additional dilatant parameter based on Rowe's (1962, 1971) stress-dilatancy theory to account for the dilation characteristics of the

sand material when subject to a triaxial stress path as shown in Fig. 2.1 (a). However, this model can not predict adequately the shear, dilation and principal stress axis rotation characteristics of sand when subject to the simple shear stress path. Predictions using the hyperbolic model (with and without dilation parameters) of the simple shear results in Ottawa sand (Vaid, Byrne and Hughes, 1981) are presented in Fig. 2.1(b). It may be seen that the dilation effects of the test correspondent to D_r = 72.3% were reasonably modelled (with dilation parameters), however, the predicted shear stresses are too low. This is due to the Mohr-Coulomb failure criterion used in the hyperbolic model. This criterion assumes that the friction angle, ϕ, at failure is constant regardless of the stress path to failure, i.e. the influence of the intermediate principal stress, σ_2, is not considered.

Since the simple shear stress path is most likely to occur in the Molikpaq sand fill during the ice loading phase it was decided to review the existing 3-D constitutive models for sand to select the most appropriate one. A brief review is presented below.

The yield criterion used in the existing plasticity based constitutive models is considered here to be one of the key issues for the selection. The other important issue is the capability of the constitutive law to model adequately the stress-strain dilatancy behaviour of sand in a 3-dimensional space. These issues are briefly discussed next.

Wroth (1984), Matsuoka and Nakai (1985) presented good reviews of the 3-dimensional failure criteria for sands most used in practice. These consist of the following:

i) Extended Mohr-Coulomb, defined by ϕ = constant

ii) Lade (1972), Lade and Duncan (1975) defined by I_1^3/I_3 = constant

iii) Matsuoka-Nakai (1974,1985), defined by $I_1 I_2/I_3$ = constant

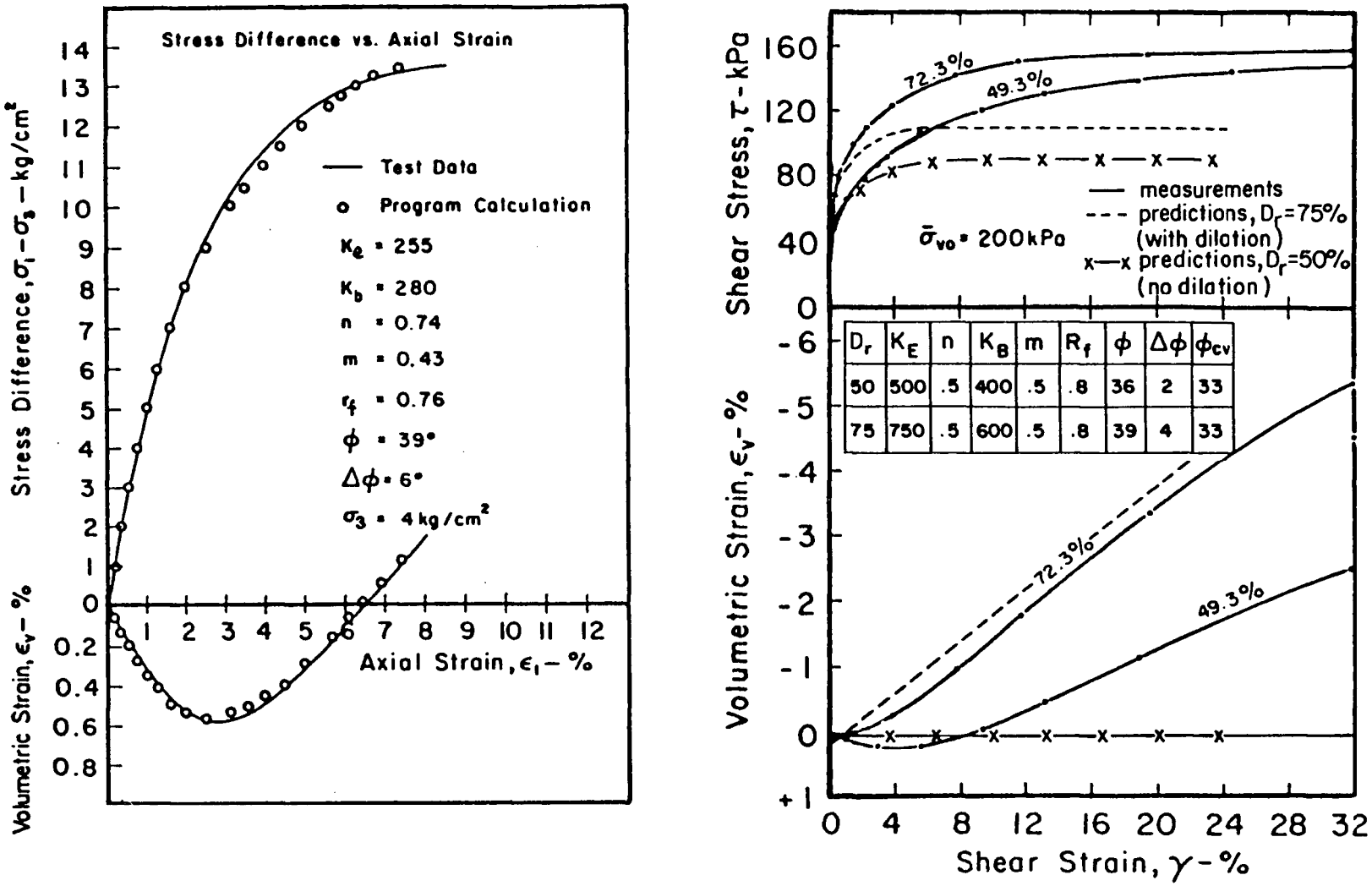

D_r	K_E	n	K_B	m	R_f	ϕ	$\Delta\phi$	ϕ_{cv}
50	500	.5	400	.5	.8	36	2	33
75	750	.5	600	.5	.8	39	4	33

Figure 2.1 Analysis of Laboratory Tests on Sand Carried out With the Hyperbolic Model: (a) Standard Triaxial Test (Byrne and Eldridge, 1982); (b) Simple Shear Test (present study)

where I_1, I_2 and I_3 are the known three principal stress invariants.

A sketch showing these criteria projected on the octahedral plane is presented in Fig. 2.2. It may be seen that both Lade and Matsuoka-Nakai failure surfaces coincide with the Mohr-Coulomb criterion for triaxial compression tests. The Matsuoka-Nakai and Mohr-Coulomb criteria also coincide for triaxial extension tests, whereas the Lade curve does not. Nevertheless Lade's and Matsuoka-Nakai failure criteria are very similar.

Of the three criteria, Matsuoka-Nakai's was chosen here for two reasons: (a) it was initially developed from theory and not from curve fitting of experimental data (Wroth, 1984); and (b) it appears to predict experimental data best (based on the proceedings of the Cleveland workshop on constitutive equations for granular non-cohesive soils (Saada and Bianchani, 1987)).

Based on the above discussion and because Matsuoka's 3-D flow rule following the concept of the Spatial Mobilized Plane (SMP) considers the stress-strain dilatancy behaviour of sand in a 3-Dimensional stress space (Matsuoka, 1983) his SMP model was selected here with some modifications to make it more practical and, take into account the rotation of the principal stress axis of sand when subject to the simple shear stress path. A detailed description of this model and its implementation to 3-D, 2-D and axisymmetric F.E. codes is presented in this chapter. Before describing this model, however, it was felt that a brief description of Matsuoka's 2-D constitutive model which is based upon the Mobilized Plane (MP) concept should be presented first because its development served as a basis for the more complex 3-D SMP model.

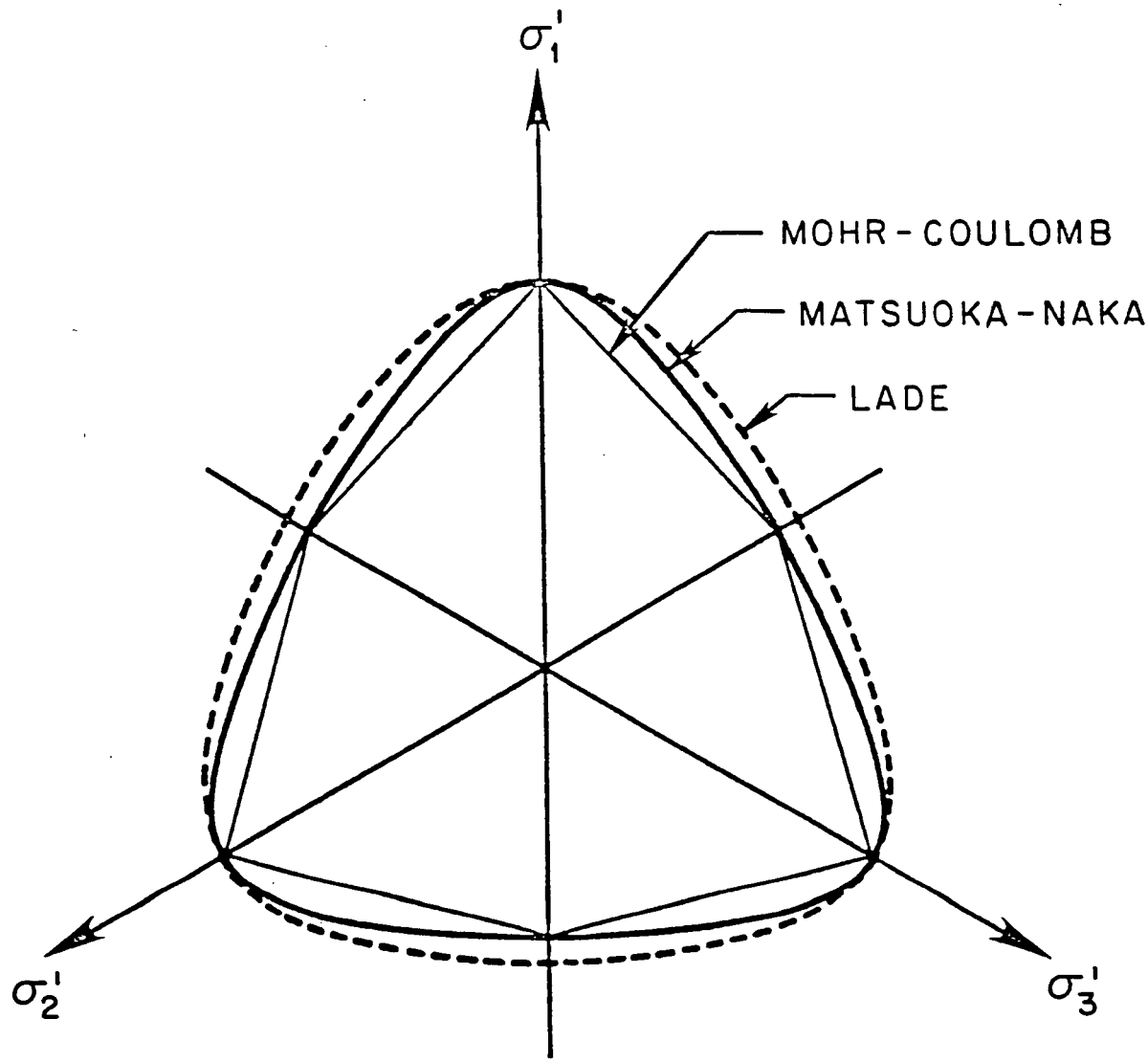

Figure 2.2 Mohr-Coulomb, Lade and Matsuoka-Nakai Failure Criteria

2.2 2-D Constitutive Model for Sand Following the Concept of the Mobilized Plane

The concept of a single mobilized plane for 2-D constitutive models was first developed by Murayama (1964). The term "Mobilized Plane" (MP) refers to the plane where the mobilized stress ratio between the shear stress and normal stress on the plane, τ_{MP}/σ_{MP}, is a maximum. The 2-D representation of this plane is shown in Fig. 2.3(a). The plane forms an angle of $45° + (\phi_m/2)$ with the major principal stress plane, where ϕ_m is the maximum angle of friction that is mobilized. This ϕ_m angle can be easily obtained by constructing the Mohr's circle for the current principal stresses σ_1 and σ_3 as shown in Fig. 2.3(b).

Based on the above "Mobilized Plane" concept Matsuoka developed 2-D and 3-D constitutive models. A brief description of the 2-D constitutive model is presented below.

2.2.1 Brief Description of the 2-D Constitutive Model

The 2-D model for sand following the Mobilized Plane concept is an elasto-plastic model. As in any model of this type its constitutive matrix, $\{C^{ep}\}$, which relates the increments of strain $\{\Delta\epsilon\}$ with the stresses $\{\sigma\}$, is elasto-plastic and is composed of two components, an elastic component $\{C^e\}$ and a plastic component $\{C^p\}$ related by the following equation:

$$\{C^{ep}\} = \{C^e\} + \{C^p\} \tag{2.1}$$

The elastic component is defined by Hooke's constitutive law and the plastic component is based on a yield criterion, a flow rule, and a hardening rule. What makes this model different from other elasto-plastic

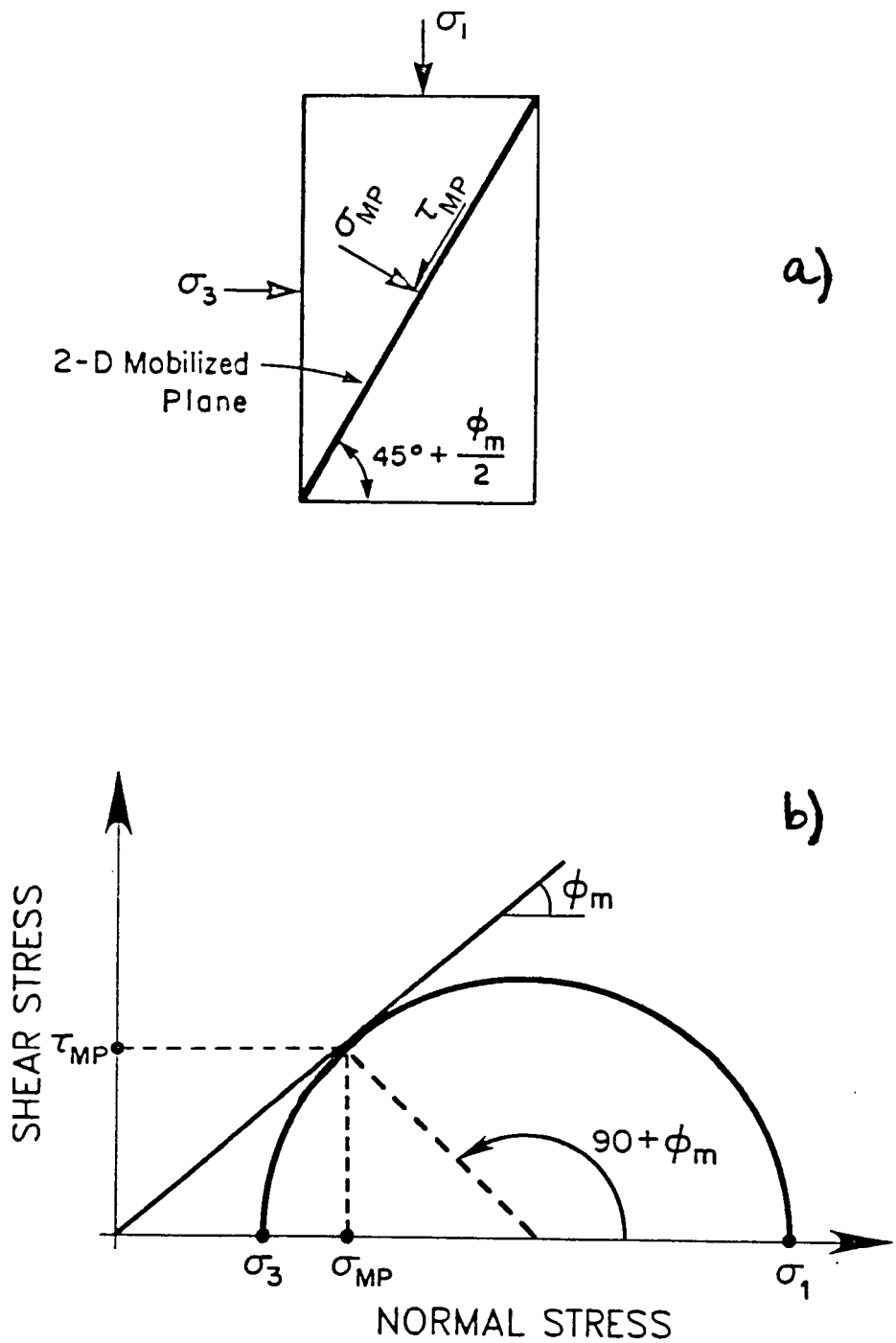

Figure 2.3 (a) 2-Dimensional Mobilized Plane; (b) Evaluation of ϕ_m, σ_{MP}, and τ_{MP}

models existing in the literature is the way these three components are defined.

2.2.1.1 Yield Criterion

The yield criterion of the model describes the stress conditions causing elastic or plastic strains and is composed of the yield and failure surfaces described below.

A family of yield surfaces in the (τ_{MP}, σ_{MP}) stress space is schematically shown in Fig. 2.4. These yield surfaces are given by the following equation developed by Matsuoka and Nakai (1974,1985)

$$\tau_{MP}/\sigma_{MP} = \tan(\phi_m) = K \qquad (2.2)$$

The "current" yield surface corresponding to the stress state at a point in a mass of soil, is defined by the maximum stress ratio mobilized at the point during its history of loading. Assuming that at a given time of loading the "current" yield surface is yield surface A ($K = K_A$) (see Fig. 2.4), than inside this yield surface ($K \leq K_A$) only reversible (elastic) strains occur. This corresponds to an unloading condition. Outside the yield surface A ($K_B > K_A$) both reversible and irreversible (plastic) strains occur and when this happens the yield surface moves from line A to line B. This corresponds to a loading condition. The limit or bound of the yield surfaces is called failure surface and no further loading is possible outside this surface. The failure surface is defined by the following equation:

$$(\tau_{MP}/\sigma_{MP})_F = \tan(\phi_F) = K_F \qquad (2.3)$$

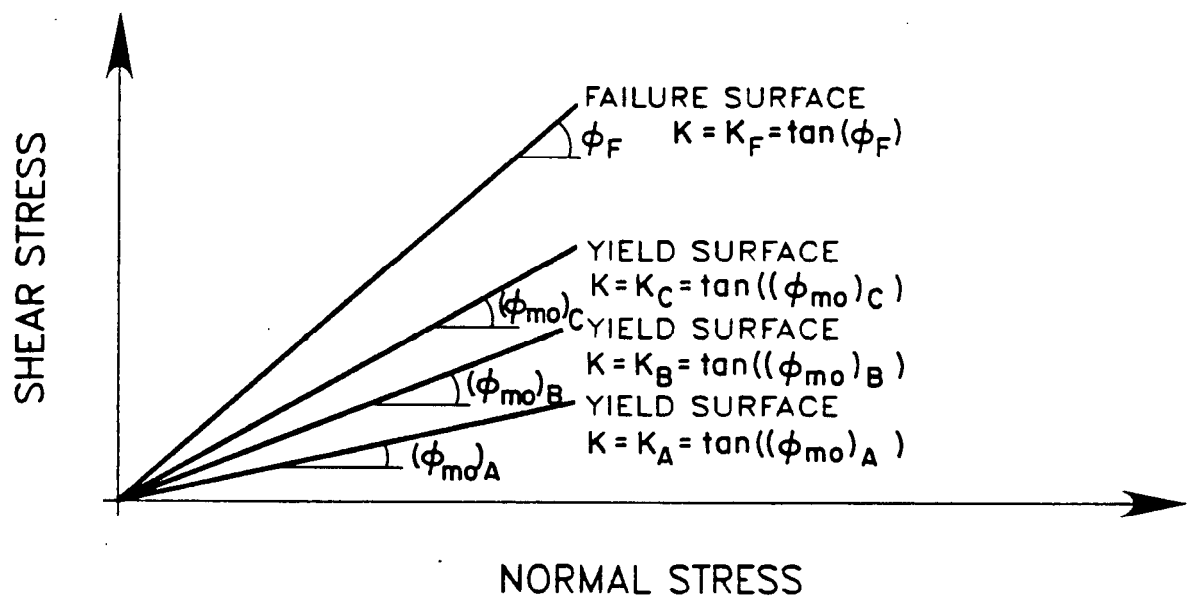

Figure 2.4 Matsuoka-Nakai 2-D Failure Criterion

where:

ϕ_F = the failure friction angle of the sand

$(\tau_{MP}/\sigma_{MP})_F$ = the failure stress ratio

2.2.1.2 Flow Rule

The flow rule of the model relates the plastic strain increment ratio, defined on the current mobilized plane (or yield surface) with the stress state at the point.

Murayama and Matsuoka (1973), Matsuoka (1974) developed the following relationship between the shear-normal stress ratio (τ_{MP}/σ_{MP}) on the Mobilized Plane and the increment ratio $(\Delta\epsilon_{MP}/\Delta\gamma_{MP})$

$$\frac{\tau_{MP}}{\sigma_{MP}} = \lambda \left(- \frac{\Delta\epsilon_{MP}}{\Delta\gamma_{MP}}\right) + \mu \qquad (2.4)$$

where λ,μ are soil parameters evaluated as is shown in Fig. 2.5(a) (pg. 23) and the stresses τ_{MP} and σ_{MP}, and the increments of strain $\Delta\gamma_{MP}$ and $\Delta\epsilon_{MP}$ are evaluated as is described later in section 2.2.2 (pg. 29).

This relationship was verified by data derived from triaxial tests (compression and extension), under constant mean principal stress, σ_m, and a plane strain test under constant σ_3, on Toyoura sand as shown in pg. 23, Fig. 2.5(a). It may be seen that the data points plot in a straight line despite the initial void ratio, e_i, which ranged from .64 to .89 and the mean normal stress, σ_m, which ranged from 100 kPa to 396 kPa.

It should be noted that the above increments of strain, $\Delta\epsilon_{MP}$ and $\Delta\gamma_{MP}$ were treated initially as increments of total strain, however in later

publications Matsuoka (1987) refers to these quantities as increments of plastic strain and therefore, these are designated from now on as $\Delta\epsilon^p_{MP}$ and $\Delta\gamma^p_{MP}$.

From eq. (2.4), $\Delta\epsilon^p_{MP}$ can be obtained as follows:

$$\boxed{\Delta\epsilon^p_{MP} = (\mu - \tau_{MP}/\sigma_{MP}) \frac{1}{\lambda} \Delta\gamma^p_{MP}} \qquad (2.5)$$

To develop an incremental stress strain law it is necessary to relate the term $\Delta\gamma^p_{MP}$ with the increment of the stress ratio $\Delta(\tau_{MP}/\sigma_{MP})$ on the current Mobilized Plane (or yield surface), and that is done by combining the above flow rule with the hardening rule described below.

2.2.1.3 Hardening Rule

Two different types of hardening rules were developed by Matsuoka which resulted in two different 2-D stress strain laws.

- 1st Hardening Rule

Matsuoka (1974) developed the following relationship between the stress ratio (τ_{MP}/σ_{MP}) and the normal-shear plastic strain ratio $(\epsilon^p_{MP}/\gamma^p_{MP})$ on the Mobilized Plane:

$$\frac{\tau_{MP}}{\sigma_{MP}} = \lambda \left(-\frac{\epsilon^p_{MP}}{\gamma^p_{MP}}\right) + \mu' \qquad (2.6)$$

where:

λ = same soil parameter used in eq. (2.4)

μ' = soil parameter

This relationship was also verified by data derived from triaxial tests (compression and extension), under constant mean principal stress, σ_m, on Toyoura sand as shown in Fig. 2.5(b). The initial void ratios, e_i, of these tests varied from .68 to .89 and the mean normal stress, σ_m, from 100 kPa to 398 kPa. Again the fit with the laboratory data is seen to be good.

Combining the flow rule given by eq. (2.4) with the hardening rule given by eq. (2.6) the following equation was obtained by Matsuoka (1983)

$$\frac{\tau_{MP}}{\sigma_{MP}} = (\mu' - \mu) \ln \frac{\gamma^p_{MP}}{\gamma^p_o} + \mu \tag{2.7}$$

where:

γ^p_o = plastic shear strain at which ϵ^p_{MP} is a minimum

Differentiating eq. (2.7) with respect to the stress ratio (τ_{MP}/σ_{MP}) the following incremental stress-strain law is obtained:

$$\boxed{\Delta\gamma^p_{MP} = \frac{\gamma^p_o}{\mu'-\mu} \exp\left(\frac{(\tau_{MP}/\sigma_{MP})-\mu}{\mu'-\mu}\right) \Delta(\tau_{MP}/\sigma_{MP})} \tag{2.8}$$

Designating $G_p = \gamma_o/(\mu-\mu')\exp\left(\frac{(\tau_{MP}/\sigma_{MP})-u}{\mu'-\mu}\right)$, the above equation can be rewritten as follows:

$$\boxed{\Delta\gamma^p_{MP} = \frac{1}{G_p} \Delta(\tau_{MP}/\sigma_{MP})} \tag{2.9}$$

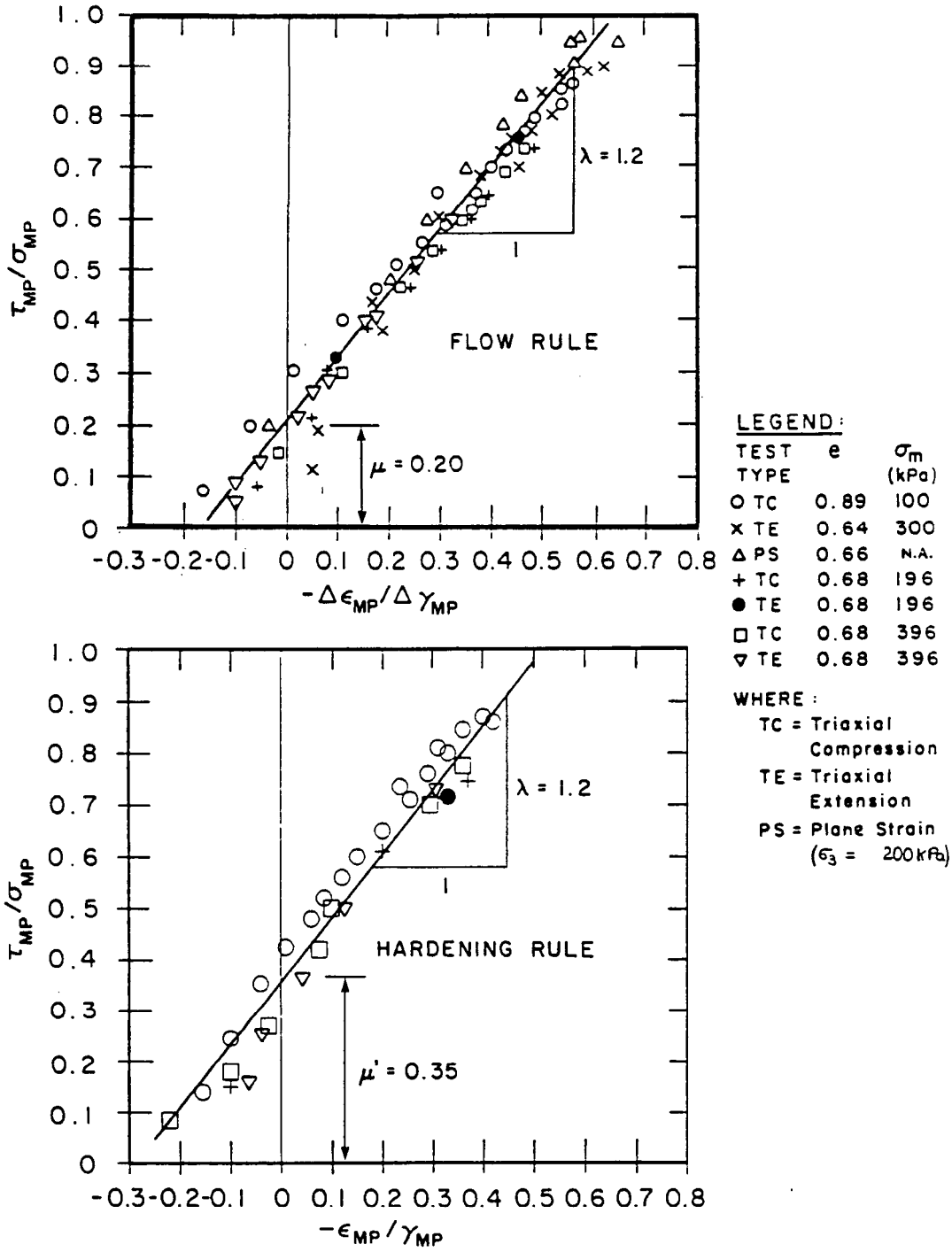

Figure 2.5 (a) Relationship Between (τ_{MP}/σ_{MP}) and $-(\Delta\epsilon_{MP}/\Delta\gamma_{MP})$. Toyoura Sand (after Matsuoka, 1974,1983)

(b) Relationship Between (τ_{MP}/σ_{MP}) and $-\epsilon_{MP}/\gamma_{MP}$. Toyoura Sand (after Matsuoka, 1983)

where G_p is designated here as the plastic shear modulus parameter which relates the increment of plastic shear strain with the stress ratio increment on the current mobilized plane (or yield surface).

Equation (2.9) represents Matsuoka's first incremental stress strain law.

- 2nd Hardening Rule

Matsuoka (1987) developed a model for soil where the rotation of principal stresses is taken into account. The flow rule of the model is the same as that described by eq. (2.4). However, the hardening rule was developed based on the assumption that the relationship between the ratio of the shear stress and vertical stress, τ_{xz}/σ_z, with the shear strain, γ_{xz}, is hyperbolic and given by the following equation:

$$\gamma_{xz} = \frac{1}{G_o} \frac{(\tau_{xz}/\sigma_z)_F \, (\tau_{xz}/\sigma_z)}{(\tau_{xz}/\sigma_z)_F - (\tau_{xz}/\sigma_z)} \tag{2.10}$$

where:

G_o = the initial slope of the relation between (τ_{xz}/σ_z) and γ_{xz}.

$(\tau_{xz}/\sigma_z)_F$ = the failure stress ratio

After some manipulations, Matsuoka shows that eq. (2.10) can be rewritten as:

$$\gamma_{xy} = \frac{1}{G_o} \frac{\sin(\phi_F) \sin(\phi_m) \sin(2\alpha)}{\sin(\phi_F) - \sin(\phi_m)} \tag{2.10a}$$

where:

ϕ_F = the failure friction angle

ϕ_m = the mobilized friction angle

α = the angle between the σ_3 direction and the σ_x direction.

To account for the "shear" on the Mobilized Plane and the "rotation" of the principal stress axis, eq. (2.10a) is differentiated with respect to ϕ_m and α, respectively. The details are given by Matsuoka (1987). When α = 45°, eq. (2.10a) becomes

$$\gamma = \frac{1}{G_o} \frac{\sin(\phi_F)\ \sin(\phi_m)}{\sin(\phi_F)-\sin(\phi_m)} \qquad (2.10b)$$

where:

γ = the maximum shear strain = $\epsilon_1-\epsilon_3$.

Based on the above, Matsuoka (1987) concludes that G_o can be obtained from either the simple shear test (eq. 2.10a) or the triaxial test (eq. 2.10b). This approach, however, was not followed here as is explained below.

Matsuoka (1983) has also shown that the relationship between the stress ratio (τ_{MP}/σ_{MP}) and the plastic shear strain γ^p_{MP} on the Mobilized plane is hyperbolic as is shown in Fig. 2.6, which is based on data obtained from triaxial tests (compression and extension) on Toyoura sand. Because this relationship is considered to be more fundamental and easier to implement in a 3-D space than the relationships given by eqs. (2.10), it was decided to develop the plastic hardening of the model as is described below.

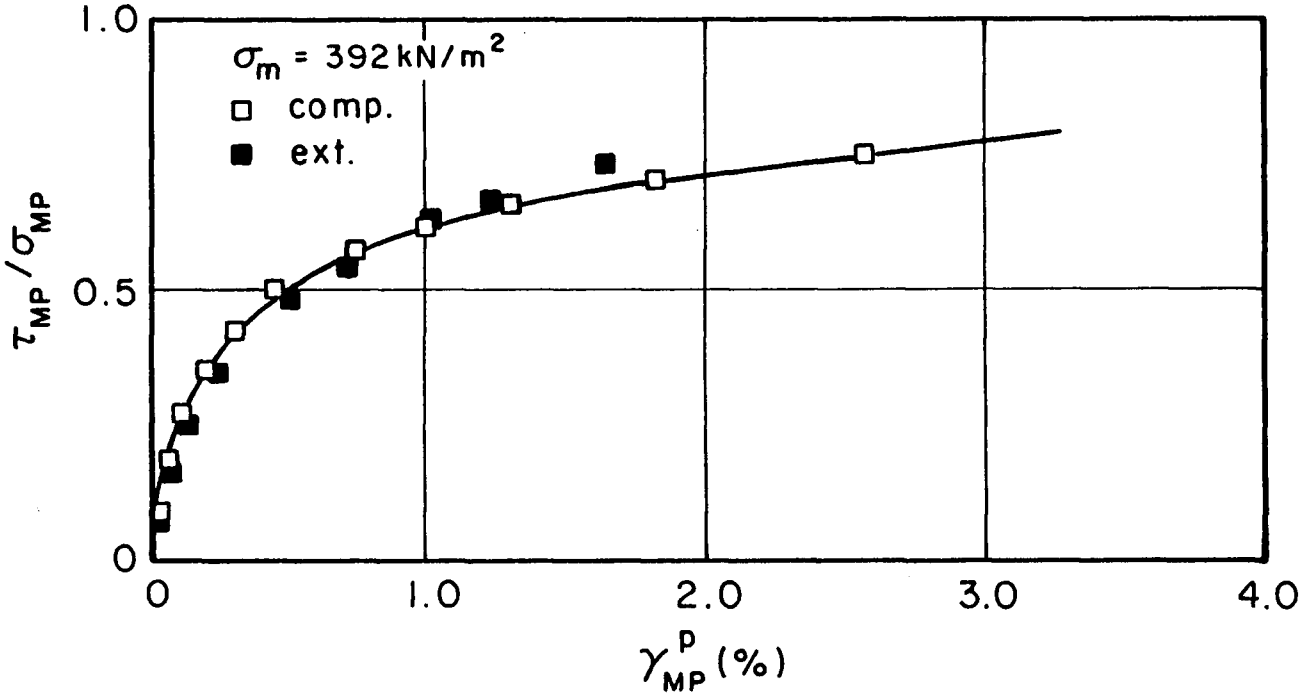

Figure 2.6 Hyperbolic Relationship Between (τ_{MP}/σ_{MP}) and γ^p_{MP}. Toyoura Sand (after Matsuoka, 1983).

Following similar procedures as outlined by Kondner (1963) and Kondner and Zelasko (1963) the following equation representative of the hyperbolic relationship on the Mobilized Plane is obtained:

$$\frac{\tau_{MP}}{\sigma_{MP}} = \frac{\gamma^p_{MP}}{\frac{1}{G_{pi}} + \frac{\gamma^p_{MP}}{(\tau_{MP}/\sigma_{MP})_{ult}}} \qquad (2.11)$$

where:

G_{pi} = the initial slope of the stress ratio - strain curve

and

$(\tau_{MP}/\sigma_{MP})_{ult}$ = the asymptotic value of the stress ratio which is related closely to the failure stress ratio $(\tau_{MP}/\sigma_{MP})_F$.

The plastic shear strain increment, $\Delta\gamma^p_{MP}$ is obtained from eq. (2.11) and is given by:

$$\boxed{\Delta\gamma^p_{MP} = \frac{1}{G_{pt}} \Delta\left(\frac{\tau_{MP}}{\sigma_{MP}}\right)} \qquad (2.11a)$$

This equation represents the hardening rule of the proposed model and is the substitute for Matsuoka's 1st and 2nd hardening rules which were given earlier by eqs. (2.9) and (2.10), respectively.

Since the proposed hardening relationship is assumed to be hyperbolic the procedures developed by Duncan et al. (1980) to evaluate the tangent Young's modulus, E_t, for the hyperbolic model were followed here and by

analogy give the tangent shear plastic parameter G_{pt}. This parameter is considered to be dependent on both the normal stress, σ_{MP}, and stress ratio level, SRL, and given by the following equation:

$$G_{pt} = G_{pi} (1 - R_F \, SRL)^2 \tag{2.12}$$

where:

G_{pi} = $KG_p \, (\sigma_{MP}/Pa)^{np}$

KG_p = the plastic shear number

np = the plastic shear exponent

Pa = the atmospheric pressure

R_F = a parameter that relates the asymptotic value of the stress ratio, $(\tau_{MP}/\sigma_{MP})_{ult}$, with the failure stress ratio, $(\tau_{MP}/\sigma_{MP})_F$, by the equation:

$$(\tau_{MP}/\sigma_{MP})_F = R_F(\tau_{MP}/\sigma_{MP})_{ult} \tag{2.13}$$

and the stress ratio level, SRL, is given by the equation:

$$SRL = (\tau_{MP}/\sigma_{MP})/(\tau_{MP}/\sigma_{MP})_F$$

or

$$SRL = \tan(\phi_m)/\tan(\phi_F) \tag{2.14}$$

i.e., SRL relates the "current" yield surface defined by $\tan(\phi_m)$ with the failure surface defined by $\tan(\phi_F)$. At failure SRL = 1.

2.2.2 Brief Development of the 2-D model in the Cartesian System of Coordinates

A brief development of the 2-D stress-strain constitutive law is presented here since its development will give an insight into the more complex development of the 3-D stress-strain constitutive law which will be described later.

The development of the 2-D model consists briefly of the following:

Relationships between the shear stress, τ_{MP}, normal stress, σ_{MP}, on the Mobilized Plane and the principal stresses σ_1 and σ_3 can be obtained from the Mohr circle plot shown in Fig. 2.7(a). From this figure the following relationships are obtained:

$$\tau_{MP} = (\sigma_1-\sigma_3)/2 \cos\phi_m$$

$$\sigma_{MP} = (\sigma_1+\sigma_3)/2 - (\sigma_1-\sigma_3)/2 \sin\phi_m \qquad (2.15)$$

Assuming that the direction of the increments of plastic principal strain coincide with the direction of the principal stresses Matsuoka (1983) obtains the increments of plastic strain as is shown in Fig. 2.7(b). From this figure the following relationships are obtained,

$$\Delta\gamma^p_{MP} = (\Delta\epsilon^p_1 - \Delta\epsilon^p_3) \cos\phi_m$$

$$\Delta\epsilon^p_{MP} = (\Delta\epsilon^p_1 + \Delta\epsilon^p_3)/2 - (\Delta\epsilon^p_1 - \Delta\epsilon^p_3)/2 \sin\phi_m \qquad (2.16)$$

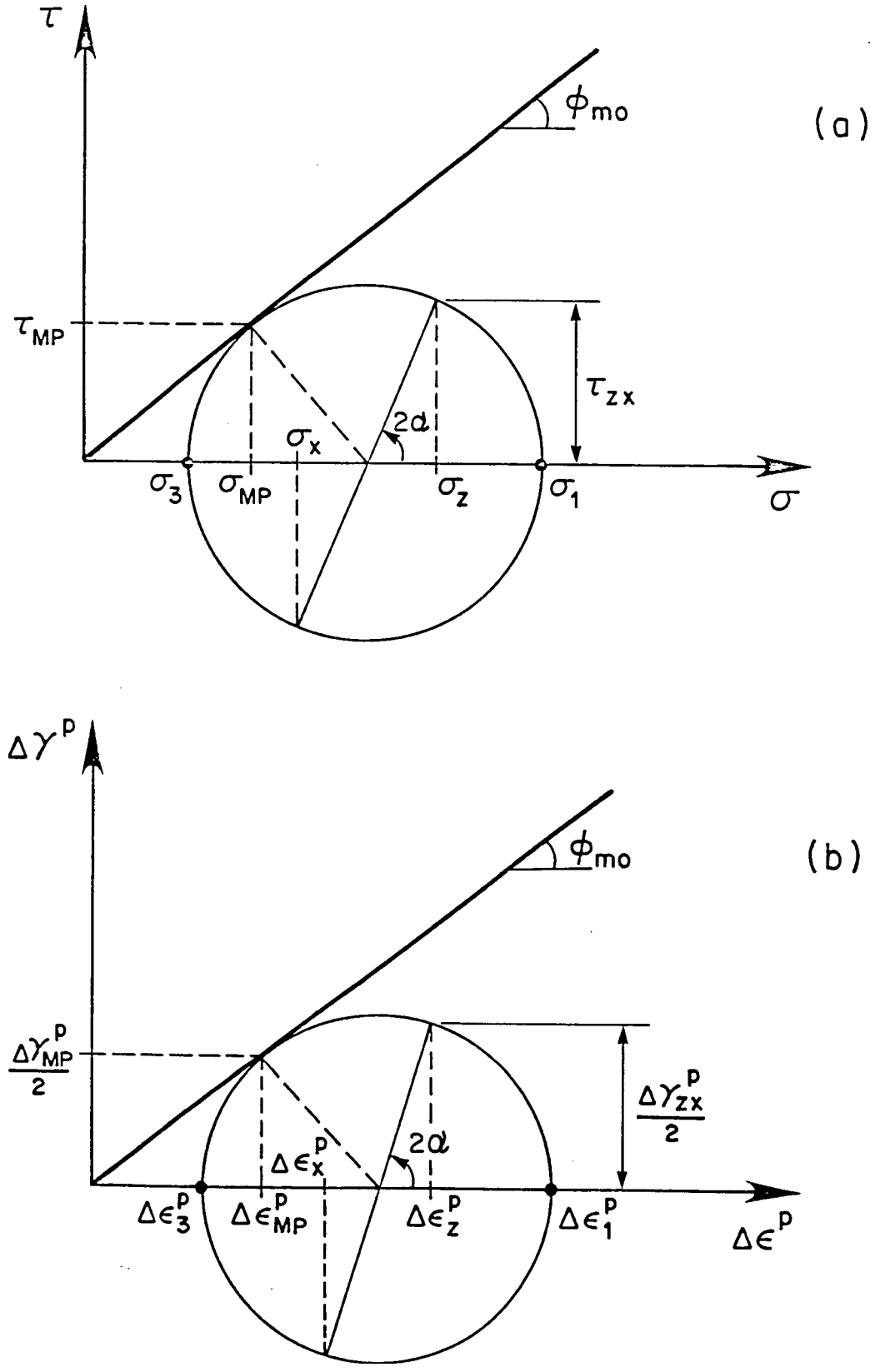

Figure 2.7 (a) Mohr Circle of Stresses; (b) Mohr Circle of Increments of Plastic Strain

Substituting the values of $\sin\phi_m = (\sigma_1-\sigma_3)/(\sigma_1+\sigma_3)$ and $\cos\phi_m = 2\sqrt{\sigma_1\sigma_3}/(\sigma_1+\sigma_3)$ in the above equations and solving for $\Delta\epsilon_1^p$ and $\Delta\epsilon_3^p$ the following equations are obtained:

$$\Delta\epsilon_1^p = \Delta\epsilon_{MP}^p + (\sigma_1/\sigma_3)^{1/2}\,\Delta\gamma_{MP}^p/2$$
$$\Delta\epsilon_3^p = \Delta\epsilon_{MP}^p - (\sigma_3/\sigma_1)^{1/2}\,\Delta\gamma_{MP}^p/2 \qquad (2.17)$$

From Fig. 2.7(b) the following relationship between increments of plastic strain, $\{\Delta\epsilon^p\}$ and increments of plastic principal strain are obtained:

$$\Delta\epsilon_x^p = (\Delta\epsilon_1^p + \Delta\epsilon_3^p)/2 - (\Delta\epsilon_1^p - \Delta\epsilon_3^p)/2\,\cos2\alpha$$
$$\Delta\epsilon_z^p = (\Delta\epsilon_1^p + \Delta\epsilon_3^p)/2 + (\Delta\epsilon_1 - \Delta\epsilon_3)/2\,\cos2\alpha \qquad (2.18)$$
$$\Delta\gamma_{zx}^p = (\Delta\epsilon_1^p - \Delta\epsilon_3^p)\sin2\alpha$$

Since $\Delta\epsilon_{MP}^p = (\mu - \tau_{MP}/\sigma_{MP})\,\Delta\gamma_{MP}^p/\lambda$ (see eq. (2.5)), and $\Delta\gamma_{MP}^p = 1/G_{pt}\,\Delta(\tau_{MP}/\sigma_{MP})$ (see eq. (2.11)), then, manipulating the above equation, relationships between increments of plastic strain, $\{\Delta\epsilon^p\}$, and the increment of stress ratio on the Mobilized Plane can be obtained. The manipulation of these equations is not presented here since only a brief insight to the model is intended at this stage. Nevertheless the increments of plastic strain would be given by equations of the following form:

$$\Delta\epsilon_x^p = \frac{1}{G_{pt}} (f_x)\ \Delta(\tau_{MP}/\sigma_{MP})$$

$$\Delta\epsilon_z^p = \frac{1}{G_{pt}} (f_z)\ \Delta(\tau_{MP}/\sigma_{MP}) \qquad (2.19)$$

$$\Delta\gamma_{zx}^p = \frac{1}{G_{pt}} (f_{zx})\ \Delta(\tau_{MP}/\sigma_{MP})$$

where the terms f_x, f_z, f_{zx} can be obtained as described above.

To completely define the stress-plastic strain relation it is necessary to develop a relationship between the increment of the stress ratio on the Mobilized Plane, $\Delta(\tau_{MP}/\sigma_{MP})$, and the increments of stress, $\Delta\sigma_x$, $\Delta\sigma_z$ and $\Delta\tau_{zx}$.

Such development will not be carried out here because it will be carried out later for the 3-D Spatial Mobilized Plane. Nevertheless that relationship would be given by an equation such as the following:

$$\Delta(\tau_{MP}/\sigma_{MP}) = (TMX)\Delta\sigma_x + (TMZ)\Delta\sigma_z + (TMZX)\Delta\tau_{zx} \qquad (2.20)$$

where TMX, TMZ and TMZX are terms that will be defined later in Section 2.4.3.5.

Substituting this equation into eqs. (2.19), the plastic strain-stress relation shown below can be obtained:

$$\{\Delta\epsilon^p\} = [C^p]\ \{\Delta\sigma\} \qquad (2.21)$$

The above equation completes the development of the plastic constitutive matrix of the model. As described earlier the elastic strain-stress relation is given by:

$$\{\Delta\epsilon^e\} = [C^e]\ \{\Delta\sigma\} \qquad (2.22)$$

where $[C^e]$ is Hooke's constitutive law.

Therefore, to obtain the complete strain-stress relation, designated also as elasto-plastic strain-stress relation, eqs. (2.21) and (2.22) are added to give

$$\{\Delta\epsilon\} = \{\Delta\epsilon^e + \Delta\epsilon^p\} = [C^e]\{\Delta\sigma\} + [C^p]\{\Delta\sigma\} = [C^{ep}]\{\Delta\sigma\} \qquad (2.23)$$

The extension of the 2-D Mobilized Plane concept to 3-D is discussed next.

2.3 Discussion on the Theories of the 'Compounded Mobilized Planes' (CMP) and the 'Spatial Mobilized Plane' (SMP)

The concept of the 2-D Mobilized Plane was later expanded to 3-D by Matsuoka and Nakai (1974). From their work, two theories were developed. The theory of the 'Compounded Mobilized Planes' (CMP) and the theory of the 'Spatial Mobilized Plane' (SMP). These two theories are well described by Matsuoka (1983) and only a brief discussion is presented here.

In the CMP theory the 3-D stress-strain constitutive model is developed based on three 2-D mobilized planes which are defined based on the three pairs of principal stresses (σ_1,σ_2), (σ_2,σ_3) and (σ_1,σ_3) as shown in pg 35, Fig. 2.8(a), and, the correspondent mobilized friction angles, $\phi_{m_{12}}$, $\phi_{m_{23}}$ and $\phi_{m_{13}}$ are obtained as shown in Fig. 2.8(b).

To evaluate the deformations at a point representative of a mass of soil, the same 2-D stress-strain constitutive law is used independently for each of the three mobilized planes, and the principal strain ϵ_i in the direction i (i = 1,2,3) is obtained by a linear summation.

In the SMP theory the 3-D stress-strain constitutive law is based upon a single 3-D mobilized plane as shown in Fig. 2.8(c), and the deformations are obtained directly from stress-strain relationships developed for this plane.

The first theory, CMP, was favoured by Matsuoka and in 1987 he introduced the hyperbolic hardening rule (described earlier in section 2.2.1.3) in order that the rotation of principal axis is taken into account. The constitutive law is 2-D and is expanded to 3-D following the CMP concept described above.

The second theory, SMP, was favoured here because this concept is considered to be more fundamental, since the stress-strain relations are obtained directly for a 3-D stress space and the 2-D constitutive relations can be obtained from the 3-D constitutive relations by imposing the necessary boundary conditions as will be described later.

A detailed description of the SMP model is presented next.

2.4 3-D Constitutive Model for Sand Following the Concept of the Spatial Mobilized Plane

A constitutive model based on one 2-D mobilized plane, defined by the major and minor principal stresses (σ_1 and σ_3), has been presented in section 2.2.

In this section a 3-D model based on the Spatial Mobilized Plane (SMP) (Matsuoka, 1983) is presented. This model is also based on a single plane, however, this time the plane is defined in a 3-D space by the three principal stresses (σ_1, σ_2 and σ_3).

The concept of the 2-D model described earlier will be closely followed for the development of the 3-D model and includes several devia-

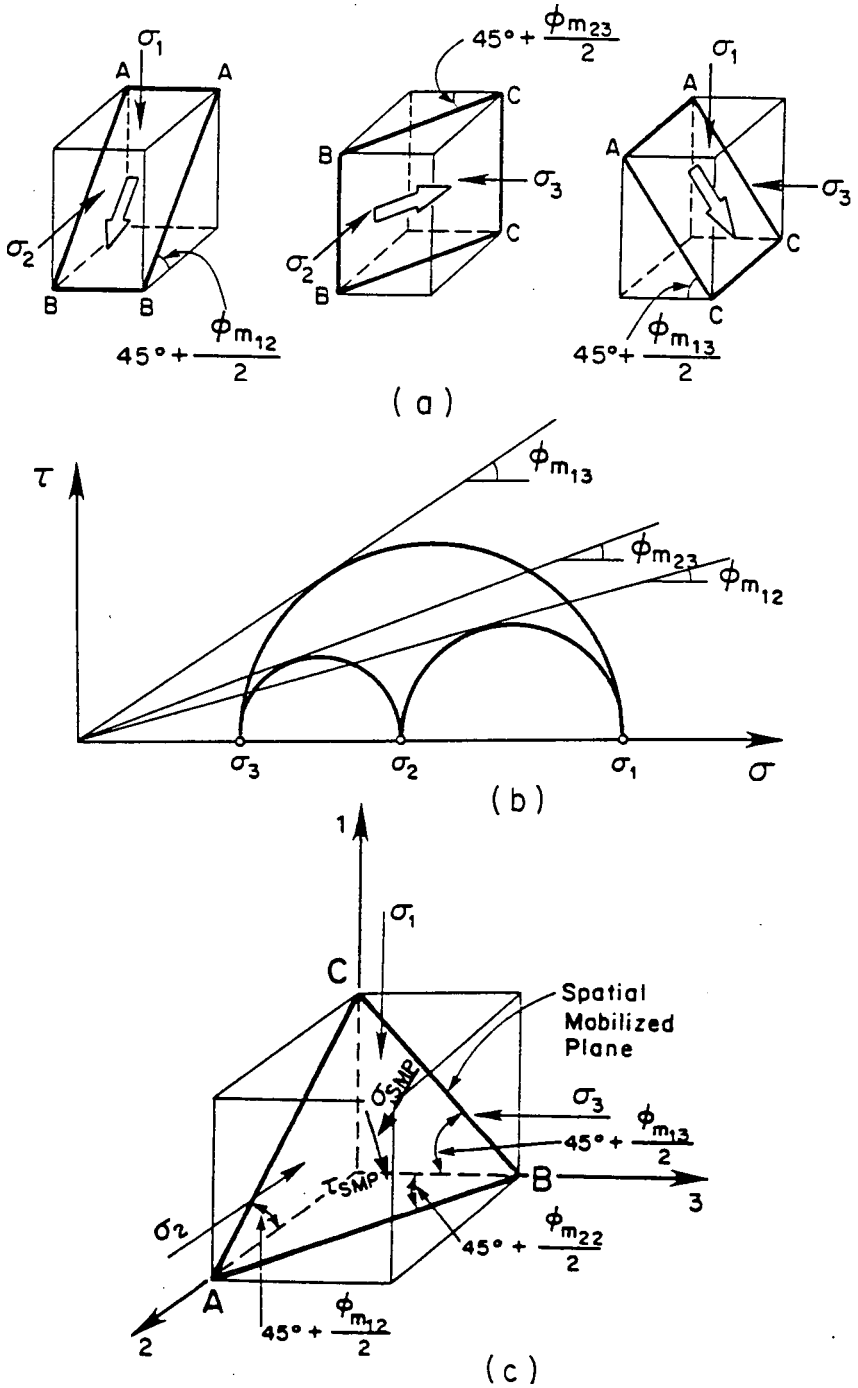

Figure 2.8 (a) Three 2-Dimensional Mobilized Planes; (b) Development of Three Mobilized Friction Angles in the τ, σ Stress Space; (c) Spatial Mobilized Plane

tions from Matsuoka's 3-D SMP model. As will be shown, these deviations allow adequate modelling of the 3-D shear, dilation and rotation characteristics of sand when subject to several stress paths including simple shear.

A detailed description of the 3-D formulation will be presented first, and the 2-D and axisymmetric formulations which are obtained from the 3-D formulation by imposing boundary conditions will be presented after.

2.4.1 Description of the SMP (After Matsuoka, 1983)

The state of stress on a soil element can be characterized by its three principal stresses σ_1, σ_2, and σ_3. Based on these stresses three Mohr circles can be constructed as shown earlier in Fig. 2.8(b) and three mobilized friction angles $\phi_{m_{13}}$, $\phi_{m_{12}}$ and $\phi_{m_{23}}$ obtained. Based on these mobilized friction angles a 3-D plane is geometrically developed in principal stress space and intercepts the principal stress axes 1, 2, and 3 at the points A, B and C as shown earlier in Fig. 2.8(c). This plane (ABC), which is defined by Matsuoka as "the plane on which the soil particles are most mobilized on average in the 3-D stress space", is designated as Spatial Mobilized Plane (SMP).

The SMP is characterized by a normal direction, n, normal stress, σ_{SMP}, and shear stress, τ_{SMP}. The direction cosines of the normal to the SMP are given by the following equation:

$$a_i = \left(\frac{\sigma_1 \sigma_2 \sigma_3}{\sigma_i(\sigma_1\sigma_2 + \sigma_2\sigma_3 + \sigma_3\sigma_1)}\right)^{1/2} \qquad (2.24)$$

where:

σ_i = principal stress in direction i (i = 1,2,3)

a_i = cos(n,i), direction cosine in relation to principal direction i

and the normal stress, σ_{SMP} and the shear stress τ_{SMP} on the SMP are given by the following equations:

$$\sigma_{SMP} = \sigma_1 a_1^2 + \sigma_2 a_2^2 + \sigma_3 a_3^2 \tag{2.25}$$

and

$$\tau_{SMP} = ((\sigma_1-\sigma_2)^2 a_1^2 a_2^2 + (\sigma_2-\sigma_3)^2 a_2^2 a_3^2 + (\sigma_3-\sigma_1)^2 a_3^2 a_1^2)^{1/2} \tag{2.26}$$

where:

a_i (i = 1,2,3) are given by eq. (2.24).

Assuming that the principal plastic strain increments, $\Delta\epsilon_i^p$, have the same direction as the principal stresses σ_i, it follows that the increment of the plastic normal strain, $\Delta\epsilon_{SMP}^p$, and the increment of the plastic shear strain, $\Delta\gamma_{SMP}^p$, on the SMP are given by the following equations:

$$\Delta\epsilon_{SMP}^p = \Delta\epsilon_1^p a_1^2 + \Delta\epsilon_2^p a_2^2 \quad \Delta\epsilon_3^p a_3^2 \tag{2.27}$$

and

$$\Delta\gamma_{SMP}^p/2 = ((\Delta\epsilon_1^p-\Delta\epsilon_2^p)^2 a_1^2 a_2^2+(\Delta\epsilon_2^p-\Delta\epsilon_3^p)^2 a_2^2 a_3^2+(\Delta\epsilon_3^p-\Delta\epsilon_1^p)^2 a_3^2 a_1^2)^{1/2} \tag{2.28}$$

Because the above assumption is one of the key assumptions of the model, it will be discussed in detail in section 2.5 of this chapter.

2.4.2 Development of the Plastic Constitutive Matrix $[C^p]$

The plastic component of the 3-D constitutive matrix is based on the yield criterion, flow rule and hardening rule described below.

2.4.2.1 Yield Criterion

The 3-D failure criterion of the SMP model is the same as the 2-D failure criterion described earlier except that this time the yield and failure surfaces are defined based upon the three principal stresses σ_1, σ_2 and σ_3.

The yield and failure surfaces are given by the following equations developed by Matsuoka and Nakai (1974,1985).

- Yield Surfaces

$$\tau_{SMP}/\sigma_{SMP} = 2/3\ (\tan\phi_{mo_{12}} + \tan\phi_{mo_{23}} + \tan\phi_{mo_{13}})^{1/2} = K \qquad (2.29)$$

- Failure Surface

$$(\tau_{SMP}/\sigma_{SMP})_F = 2/3\ (\tan\phi_{F_{12}} + \tan\phi_{F_{23}} + \tan\phi_{F_{13}})^{1/2} = K_F \qquad (2.30)$$

where:

$\phi_{m_{12}}$, $\phi_{m_{23}}$ and $\phi_{m_{13}}$ are the mobilized friction angles

and

$\phi_{F_{12}}$, $\phi_{F_{23}}$ and $\phi_{F_{13}}$ are the failure friction angles.

Earlier attempts made by the writer to predict measurements obtained from simple shear tests on Leighton-Buzzard sand (Stroud, 1971) and from true-triaxial tests on Ottawa sand (Yong and Ko, 1980) (Workshop soil modelling, McGill University) indicate however that the peak failure stress ratio, $(\tau_{SMP}/\sigma_{SMP})_F$, is dependent on the normal stress on the SMP at failure, $(\sigma_{SMP})_F$, and that a better agreement with the laboratory data was obtained if the failure stress ratio was expressed by the following equation:

$$\left(\frac{\tau_{SMP}}{\sigma_{SMP}}\right)_F = \left(\frac{\tau_{SMP}}{\sigma_{SMP}}\right)_1 - \Delta\left(\frac{\tau_{SMP}}{\sigma_{SMP}}\right) \log_{10}\left(\frac{(\sigma_{SMP})_F}{p_a}\right) \qquad (2.31)$$

where

$\left(\frac{\tau_{SMP}}{\sigma_{SMP}}\right)_1$ = failure stress ratio at $(\sigma_{SMP})_F$ = 1 atmosphere.

and

$\Delta\left(\frac{\tau_{SMP}}{\sigma_{SMP}}\right)$ = decrease in failure stress ratio for a 10 fold increase in $(\sigma_{SMP})_F$.

A sketch of the failure surface, projected on the octahedral plane and in the 3-D stress space is presented in Fig. 2.9(a) and (b) respectively. The 3-D Mohr-Coulomb failure surface is also shown in the figures and it may be seen that the Mohr-Coulomb and Matsuoka-Nakai failure surfaces coincide whenever the triaxial stress path is followed (compression or extension) but differ for any other stress path.

To show the influence of the intermediate principal, σ_2, on the failure friction angle $\phi_{13} = \sin^{-1}((\sigma_1-\sigma_3)/(\sigma_1-\sigma_3))$, better known as ϕ, a relationship was developed between ϕ_{13} and b-value which is a parameter that was developed by Bishop (1966). The relationship is given by the following equation, which was obtained from eq. (2.30) (see Appendix 2.1)

$$\tan\phi^*_{F_{13}} = K_F \frac{3}{2} \left(\frac{b(1+a)+(1-a)(1-b)}{(1+a)(b+b^2)+(1-a)(2-3b+b^2)}\right)^{1/2} \qquad (2.32)$$

where:

$b = (\sigma_2-\sigma_3)/(\sigma_1-\sigma_3)$

$a = (\sigma_1-\sigma_3)/(\sigma_1+\sigma_3) = \sin\phi_{F_{13}}$

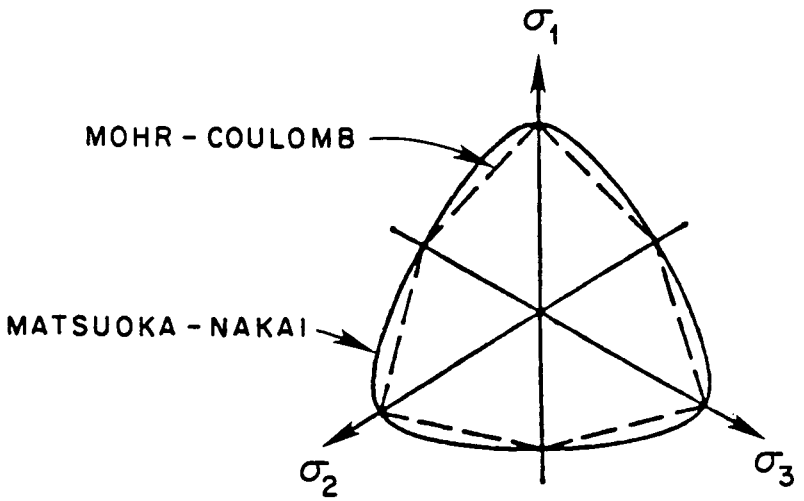

(a)

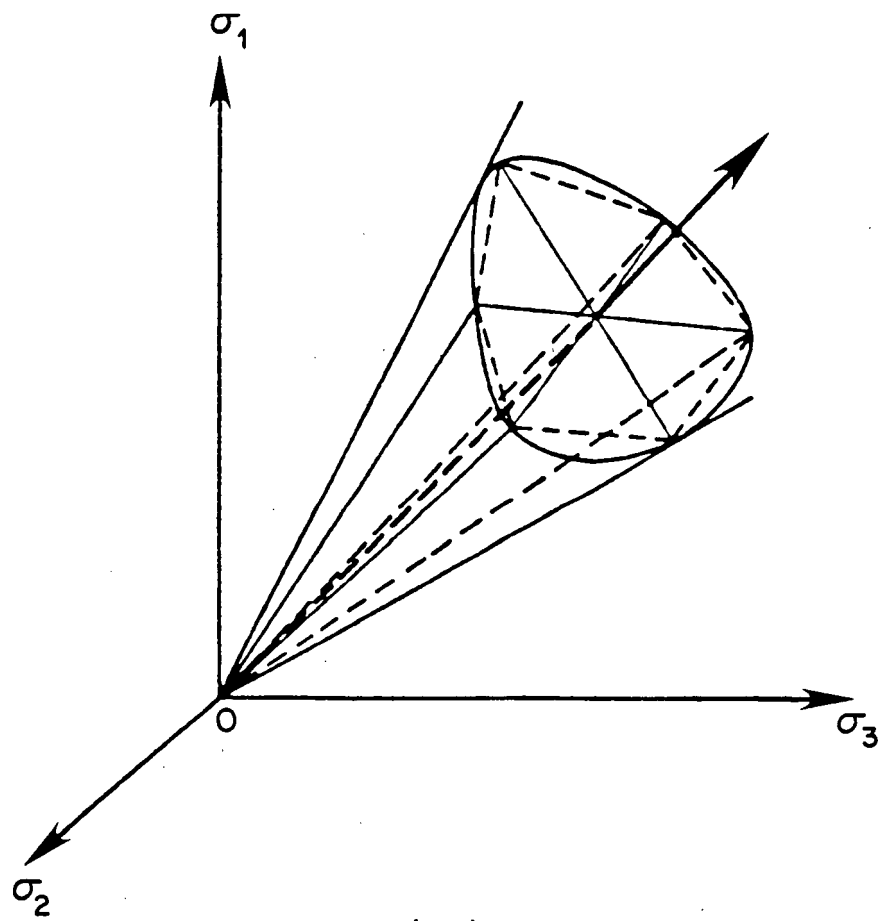

(b)

Figure 2.9 Matsuoka-Nakai and Mohr-Coulomb Failure Criteria: (a) Projection on the Octahedral Plane; (b) 3-Dimensional Stress Space

K_F = constant = $2\sqrt{2}/3 \tan \phi_{F_{13}}$ (obtained from eq. (2.30)

Designating $\phi_{F_{13}}$ by ϕ_F^{tx} i.e. the failure friction angle corresponding to triaxial conditions, then:

$$\phi^*_{F_{13}} = \phi_F^{tx} \qquad \text{for} \quad b = 0 \quad \text{or} \quad b = 1$$

$$\phi^*_{F_{13}} \neq \phi_F^{tx} \qquad \text{for} \quad 0 < b < 1$$

i.e., $\phi^*_{F_{13}}$ is the failure friction angle, defined by σ_1 and σ_3, for $\sigma_2 \neq \sigma_1$ and $\sigma_2 \neq \sigma_3$.

Values of $\phi^*_{F_{13}}$ were computed for different values of ϕ_F^{tx} and for different values of the b-value using eq. (2.32), and the differences between $\phi^*_{F_{13}}$ and ϕ_F^{tx} evaluated. The results are presented in Fig. 2.10. It may be seen that the value $(\phi^*_{F_{13}} - \phi_F^{tx})$ is equal to zero when b = 0 or b = 1 (triaxial compression or triaxial extension) and has values > 0, when 0 < b < 1. The highest difference occurs when $\phi_F^{tx} = 50°$ and b is about .25. This behaviour has been observed by many researchers based on laboratory measurements from tests on sand using true-triaxial, plane strain (triaxial and simple shear), hollow cylinder and other devices.

2.4.2.2 Flow Rule

The 2-D flow rule described earlier by eq. (2.4) has been extended to the SMP by Matsuoka and Nakai (1974) and Matsuoka (1983) who show that eq. (2.4) can be re-written as:

$$\tau_{SMP}/\sigma_{SMP} = \lambda(-\Delta\epsilon^p_{SMP}/\Delta\gamma^p_{SMP}) + \mu \qquad (2.33)$$

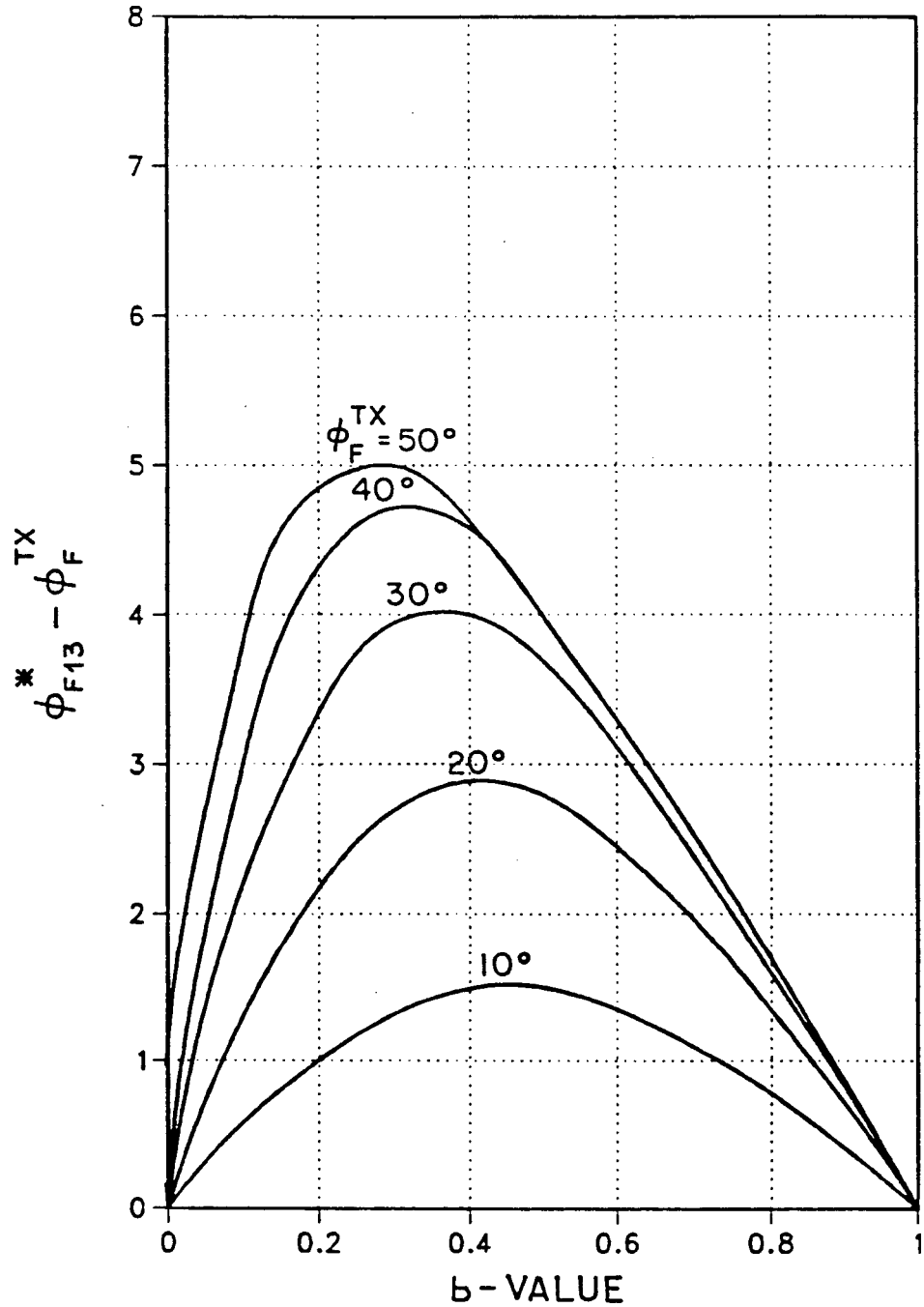

Figure 2.10 Variation of $(\phi^{*}_{F_{13}} - \phi^{tx}_{F})$ with b-Value.

where:

λ,μ are the same soil parameters earlier defined for the 2-D model.

This relationship was verified by data derived from triaxial tests (compression and extension) on Toyoura sand as shown in Fig. 2.11(a) It may be seen that the same intercept (μ = .20) and about the same slope (λ = 1.12) is obtained from the 3-D flow rule as compared with the 2-D flow rule, (μ = .20 and λ = 1.20), shown earlier in Fig. 2.5(a).

2.4.2.3 Hardening Rule

The 2-D hyperbolic hardening rule described earlier by eqs. (2.11) is extended here to the SMP by re-writing this equation as follows:

$$\Delta\gamma^{p}_{SMP} = \frac{1}{G_{pt}} \Delta\left(\frac{\tau_{SMP}}{\sigma_{SMP}}\right) \tag{2.34}$$

This relationship is shown to be verified by the triaxial test data (compression and extension) on Toyoura sand, presented in Fig. 2.11(b).

To evaluate the tangent plastic shear parameter, G_{pt}, eq. 2.12, which was derived earlier for the 2-D model is used here, i.e. $G_{pt} = G_{pi}(1-R_F\ SRL)^2$, however in the 3-D model, G_{pi}, R_F and SRL are defined on the SMP by the following equations:

$$G_{pi} = KG_p\ (\sigma_{SMP}/Pa)^{np} \tag{2.35}$$

$$R_F = (\tau_{SMP}/\sigma_{SMP})_F/(\tau_{SMP}/\sigma_{SMP})_{ult} \tag{2.36}$$

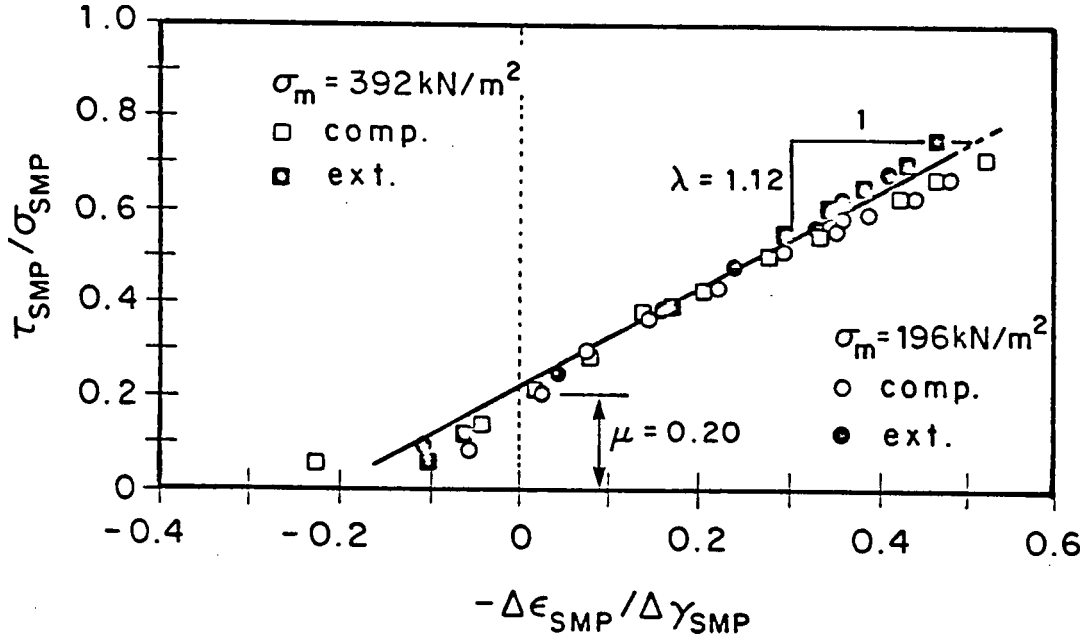

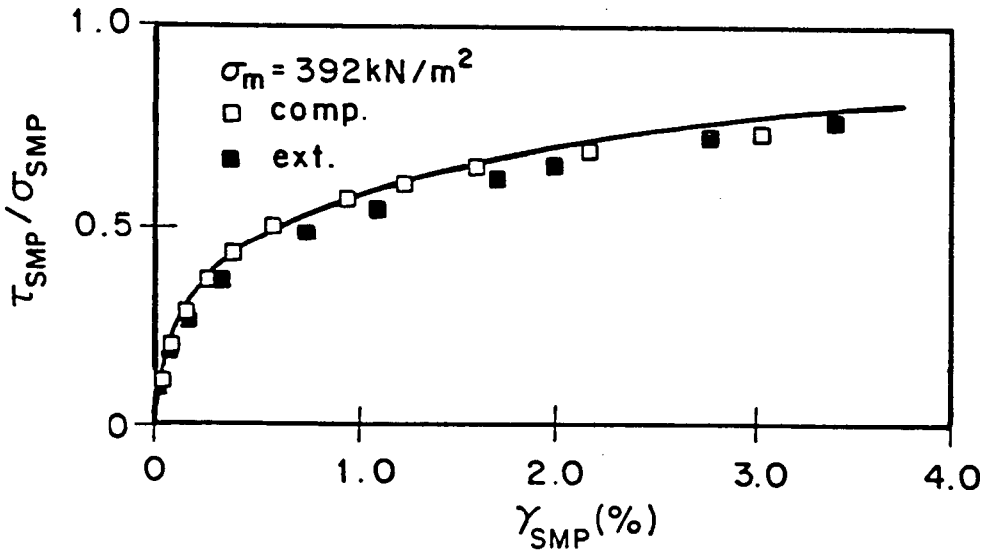

Figure 2.11 (a) Relationship Between (τ_{SMP}/σ_{SMP}) and $-(\Delta\epsilon_{SMP}/\Delta\gamma_{SMP})$. Toyoura sand (after Matsuoka, 1983).
(b) Relationship Between (τ_{SMP}/σ_{SMP}) and γ_{SMP}. Toyoura Sand (after Matsuoka, 1983).

and

$$SRL = (\tau_{SMP}/\sigma_{SMP})/(\tau_{SMP}/\sigma_{SMP})_F \tag{2.37}$$

2.4.2.4 Summary of the Basic Equations of the SMP Model

The basic equations of the SMP model are presented below.

- Yield Criterion

$$(\tau_{SMP}/\sigma_{SMP})_F = (\tau_{SMP}/\sigma_{SMP})_1 - \Delta(\tau_{SMP}/\sigma_{SMP}) \log_{10}(\sigma_{SMP}/p_a) \tag{2.38}$$

- Hyperbolic Hardening Rule

$$\Delta\gamma^p_{SMP} = \frac{1}{G_{pt}} \Delta(\tau_{SMP}/\sigma_{SMP}) \tag{2.39}$$

- Flow Rule

$$\Delta\, \epsilon^p_{SMP} = 1/\lambda(\mu - (\tau_{SMP}/\sigma_{SMP}))\ \Delta\gamma^p_{SMP} \tag{2.40}$$

2.4.3 Development of the SMP's Plastic Constitutive Matrix in the Cartesian System of Coordinates

A brief development of the plastic constitutive matrix $\{C^p\}$ is presented below. Details will be given after.

The following relationships will be developed:

- $\Delta\epsilon^p_i = f_a\ (\Delta\epsilon^p_{SMP},\ \Delta\gamma^p_{SMP})$ (2.41a)

The relationship f_a is developed in section 2.4.3.1 (pg. 47)

$$\bullet \quad \Delta\epsilon_i^p = f_b \left(\Delta(\tau_{SMP}/\sigma_{SMP})\right) \tag{2.41b}$$

The relationship f_b is obtained by substituting eqs. (2.39) and (2.40) into eq. (2.41a). This is described in section 2.4.3.2 (pg. 51).

$$\bullet \quad \{\Delta\epsilon^p\} = f_c \left(\Delta\epsilon_i^p\right) \tag{2.41c}$$

where $\{\Delta\epsilon^p\}$ = increments of plastic strain.

The relationship f_c is developed in section 2.4.3.3 (pg. 51)..

$$\bullet \quad \{\Delta\epsilon^p\} = f_d \left(\Delta(\tau_{SMP}/\sigma_{SMP})\right) \tag{2.41d}$$

The relationship f_d is obtained by substituting eq. (2.41b) into eq. (2.41c). This is described in section 2.4.3.4 (pg. 53).

$$\bullet \quad \Delta(\tau_{SMP}/\sigma_{SMP}) = f_e \left(\{\Delta\sigma\}\right) \tag{2.41e}$$

where $\{\Delta\sigma\}$ = increments of stress.

The relationship f_e is developed in section 2.4.3.5 (pg. 53).

$$\bullet \quad \{\Delta\epsilon^p\} = [C^p]\{\Delta\sigma\} \tag{2.41f}$$

where the plastic constitutive matrix, $[C^p]$, is obtained by substituting eq. (2.41e) into eq. (2.41d). This is described in section 2.4.4 (pg. 56).

To develop the above relationships the procedures described by Matsuoka (1983) will be followed here except for a few deviations that will be outlined.

2.4.3.1 Relationship Between Increments of Plastic Principal Strain, $\Delta\epsilon_i^p$ and $\Delta\epsilon_{SMP}^p$ and $\Delta\gamma_{SMP}^p$

Matsuoka (1983) showed that the relationship between $\Delta\epsilon_i^p$ and, $\Delta\epsilon_{SMP}^p$ and $\Delta\gamma_{SMP}^p$ is given by the following equation (see Appendix 2.2):

$$\Delta\epsilon_i^p = \Delta\epsilon_{SMP}^p + \frac{b_i}{a_i}\frac{\Delta\gamma_{SMP}^p}{2} \tag{2.42}$$

where:

a_i = the direction cosines of the normal stress σ_{SMP} (see eq. 2.24)

$b_i = \frac{\sigma_i - \sigma_{SMP}}{\tau_{SMP}} a_i$ = the direction cosines of the shear stress τ_{SMP} (see Appendix 2.2) (2.43)

To establish the above eq. (2.42) the following two assumptions were considered by Matsuoka:

a) That the direction cosines of $\Delta\epsilon_{SMP}^p$ are the same as the direction cosines a_i

b) that the direction cosines of $\Delta\gamma_{SMP}^p$ are the same as the direction cosines b_i

Earlier attempts made by the writer to predict laboratory measurements obtained from simple shear tests (data published by Stroud, 1971, on Leighton-Buzzard sand), and from true-triaxial tests (data used in the

workshop soil modelling competition, McGill University, on Ottawa sand, Yong and Ko, 1980), indicate, however, that the assumption regarding the direction cosines b_i was not in agreement with the published laboratory data. Deviations between the b_i values obtained from the stresses, σ_i, and the b_i values obtained from the increments of plastic strain, $\Delta\epsilon_i^p$, were observed to be stress path dependent and a function of the 'b-value' = $(\sigma_2-\sigma_3)/(\sigma_1-\sigma_3)$. These deviations of b_i are given by the following equation:

$$\Delta b_i = (b_i)_{\sigma_i} - (b_i)_{\Delta\epsilon_i^p} \tag{2.44}$$

where:

$(b_i)_{\sigma_i}$ = direction cosines of the shear stress direction

$(b_i)_{\Delta\epsilon_i^p}$ = direction cosines of the increment of plastic shear direction

The variation of Δb_i with the 'b-value' are shown in Fig. 2.12. Based on this figure eq. (2.41) is re-written in a different form as follows:

$$\Delta\epsilon_i^p = \Delta\epsilon_{SMP}^p + \frac{(b_i-\Delta b_i)}{a_i}\,\frac{\Delta\gamma_{SMP}^p}{2} \tag{2.45}$$

Predictions of the simple shear test data reported by Stroud, using $\Delta b_i = 0$, and $\Delta b_i \neq 0$ (obtained from Fig. 2.12) are shown in Fig. 2.13. It

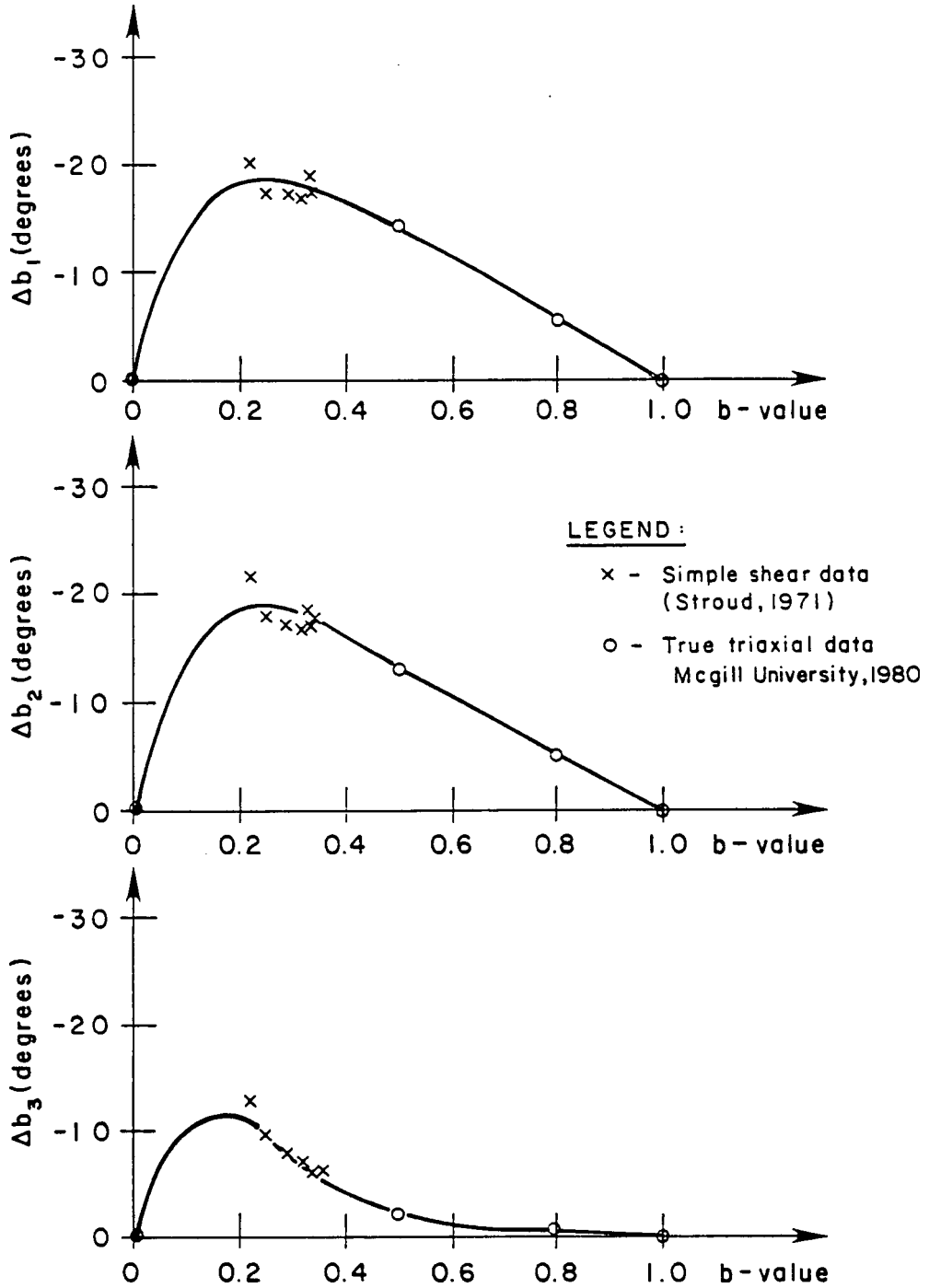

Figure 2.12 Variations of Δb_i (i = 1,2,3) with 'b-Value'. (a) i=1; (b) i=2; (c) i=3

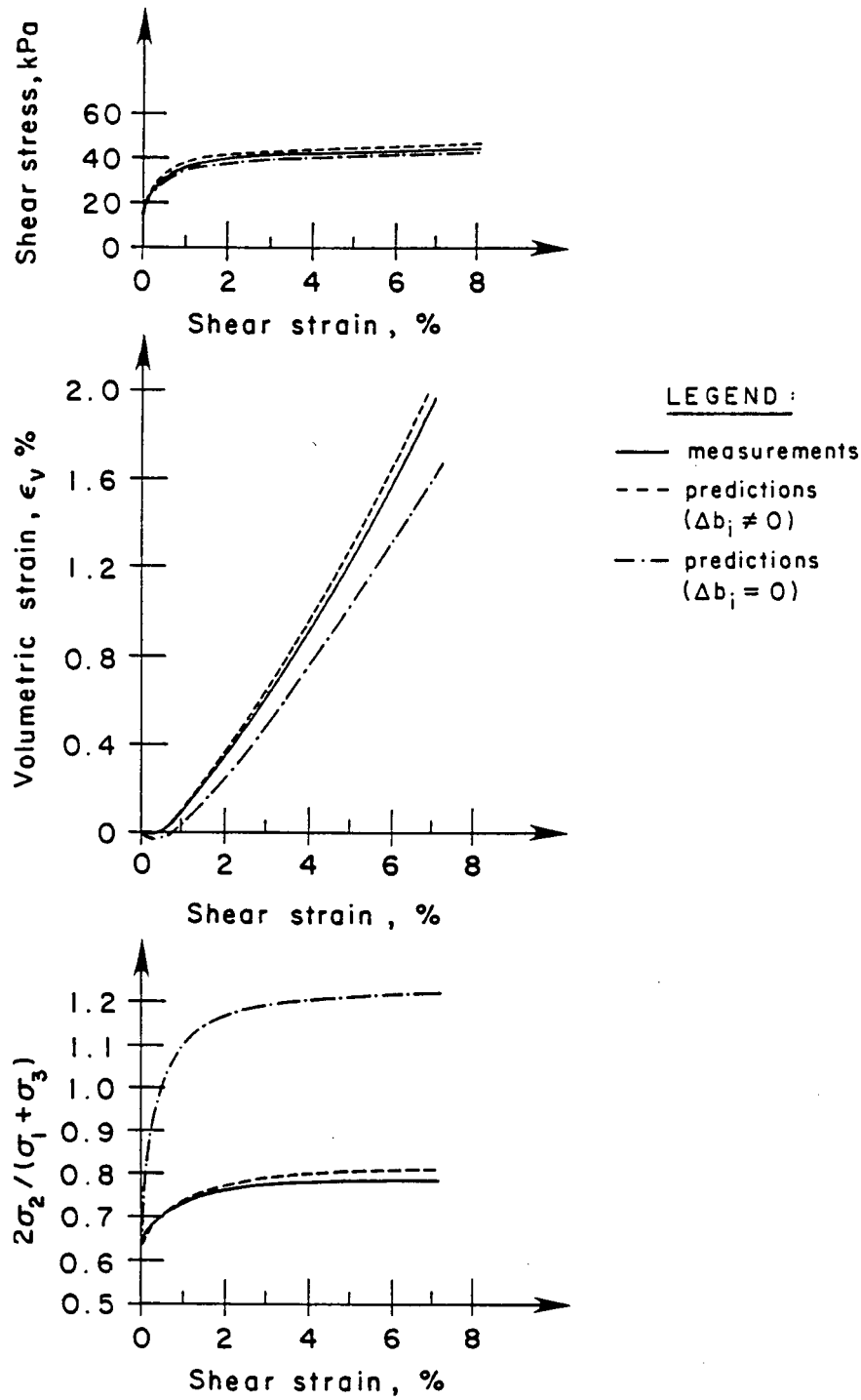

Figure 2.13 Predicted and Measured Simple Shear Data. (a) τ_{zx} versus γ_{zx}; (b) ϵ_v versus γ_{zx}; (c) $(2\sigma_2/\sigma_1+\sigma_3)$ versus γ

may be seen that good agreement with the measured data is obtained when $\Delta b_i \neq 0$. When $\Delta b_i = 0$ the predictions of the shear stress, and volumetric strain, versus shear strain are in fair agreement with the measured data, however, the prediction of $2\sigma_2/(\sigma_1+\sigma_3)$ versus shear strain is extremely high, and inadequate. Therefore the use of eq. (2.45) instead of eq. (2.42) in the SMP formulation is considered to be justified.

2.4.3.2 Relationship Between Increments of Plastic Principal Strain, $\Delta\epsilon_i^p$ and Increment of the Stress Ratio on the SMP, $\Delta(\tau_{SMP}/\sigma_{SMP})$

Substituting the values of $\Delta\gamma^p_{SMP}$ from eq. (2.39) and $\Delta\epsilon^p_{SMP}$ from eq. (2.40) into eq. (2.45) the following equation is obtained:

$$\Delta\epsilon_i^p = \left[\left(\frac{\mu - (\tau_{SMP}/\sigma_{SMP})}{\lambda}\right) + \left(\frac{b_i - \Delta b_i}{2a_i}\right)\right] \frac{1}{G_p} \Delta\left(\frac{\tau_{SMP}}{\sigma_{SMP}}\right) \qquad (2.46)$$

where i = 1,2,3.

Designating the term in square brackets by M_i then eq. (2.46) can be rewritten as:

$$\Delta\epsilon_i^p = [M_i] \frac{1}{G_p} \Delta\left(\frac{\tau_{SMP}}{\sigma_{SMP}}\right) \qquad (2.47)$$

2.4.3.3 Relationship Between Increments of Plastic Cartesian Strain $\{\Delta\epsilon^p\}$ and Increments of Plastic Principal Strain $\{\Delta\epsilon_i^p\}$

Now that a relationship between $\Delta\epsilon_i^p$ and, $\Delta\epsilon^p_{SMP}$ and $\Delta\gamma^p_{SMP}$ has been established a relationship between the cartesian components of plastic strain $\{\Delta\epsilon^p\}$ and $\Delta\epsilon_i^p$ is needed.

Matsuoka (1983) assumes that the direction cosines ℓ_i, m_i and n_i (i = 1,2,3) which relate cartesian stresses with principal stresses, are the

same direction cosines that relate increments of plastic cartesian strain with increments of plastic principal strain. Based on the above assumption, the following equations are obtained (see Appendix 2.3):

$$\Delta\epsilon_x^p = \sum_{i=1,3} \Delta\epsilon_i^p \, \ell_i^2 \qquad \frac{\Delta\gamma_{xy}^p}{2} = \sum_{i=1,3} \Delta\epsilon_i^p \, \ell_i m_i$$

$$\Delta\epsilon_y^p = \sum_{i=1,3} \Delta\epsilon_i^p \, m_i^2 \qquad \frac{\Delta\gamma_{yz}^p}{2} = \sum_{i=1,3} \Delta\epsilon_i^p \, m_i n_i \qquad (2.48)$$

$$\Delta\epsilon_z^p = \sum_{i=1,3} \Delta\epsilon_i^p \, n_i^2 \qquad \frac{\Delta\gamma_{zx}^p}{2} = \sum_{i=1,3} \Delta\epsilon_i^p \, n_i \ell_i$$

The above assumption is considered to be correct for stress paths such as the triaxial or other paths where there is no rotation of principal stress axes. However simple shear test data reported by Roscoe (1970), Stroud (1971) and Wood et al. (1979) on Leighton-Buzzard sand show that the above assumption is not strictly correct. A review of these is carried out later in section 2.5. From this review it is concluded that during the initial stages of all tests the angle ψ (defined by the vertical direction and the direction of the major principal stress, σ_1), and the angle ξ (defined by the vertical direction and the direction of the major principal strain increment, $\Delta\epsilon_1$, can diverge considerably but when failure is approached these angles start converging and at failure the deviation between the angles ψ and ξ is not significant.

Based on the above it is concluded that the assumption considered by Matsuoka (1983) is reasonable and can be used here to relate the increments of plastic cartesian strain with the increments of plastic principal strain as presented by eqs. (2.48) above.

2.4.3.4 Relationship Between Increments of Plastic Strain, $\{\Delta\epsilon^p\}$, and Increment of Stress Ratio on the SMP

The relationship between the increments of plastic strain, $\{\Delta\epsilon^p\}$ and the increments of the stress ratio on the SMP, $\Delta(\tau_{SMP}/\sigma_{SMP})$ are given by the following equations which were obtained by substituting eq. (2.47) into eq. (2.48):

$$\Delta\epsilon_x^p = \left(\sum_{i=1,3} M_i \ell_i^2\right) \frac{1}{G_p} \Delta\left(\frac{\tau_{SMP}}{\sigma_{SMP}}\right) \qquad \frac{\Delta\gamma_{xy}^p}{2} = \left(\sum_{i=1,3} M_i \ell_i m_i\right) \frac{1}{G_p} \Delta\left(\frac{\tau_{SMP}}{\sigma_{SMP}}\right)$$

$$\Delta\epsilon_y^p = \left(\sum_{i=1,3} M_i m_i^2\right) \frac{1}{G_p} \Delta\left(\frac{\tau_{SMP}}{\sigma_{SMP}}\right) \qquad \frac{\Delta\gamma_{yz}^p}{2} = \left(\sum_{i=1,3} M_i m_i n_i\right) \frac{1}{G_p} \Delta\left(\frac{\tau_{SMP}}{\sigma_{SMP}}\right)$$

$$\Delta\epsilon_z^p = \left(\sum_{i=1,3} M_i n_i^2\right) \frac{1}{G_p} \Delta\left(\frac{\tau_{SMP}}{\sigma_{SMP}}\right) \qquad \frac{\Delta\gamma_{zx}^p}{2} = \left(\sum_{i=1,3} M_i n_i \ell_i\right) \frac{1}{G_p} \Delta\left(\frac{\tau_{SMP}}{\sigma_{SMP}}\right)$$

(2.49)

2.4.3.5 Evaluation of the Increment of the Stress Ratio on the SMP as a Function of the Increments of Stress, $\{\Delta\sigma\}$

The last step required to develop $\{C^p\}$ consists of developing a relationship between $\Delta(\tau_{SMP}/\sigma_{SMP})$ and the increments of stress, $\{\Delta\sigma\}$. The approach described by Matsuoka (1987) to account for the "shear" on the 2-D Mobilized Plane, MP, and the "rotation" of the principal stress axis is followed below after adapting it to the 3-D Spatial Mobilized Plane, SMP.

The stress ratio on the SMP is given by the following equation which is obtained from eq. (2.25) and eq. (2.26):

$$\frac{\tau_{SMP}}{\sigma_{SMP}} = \frac{[(\sigma_1-\sigma_2)^2 a_1^2 a_2^2+(\sigma_2-\sigma_3)^2 a_2^2 a_3^2+(\sigma_3-\sigma_1)^2 a_3^2 a_1^2]^{1/2}}{\sigma_1 a_1^2+\sigma_2 a_2^2+\sigma_3 a_3^2} \qquad (2.50)$$

To account for the "shear" on the SMP, the following steps were taken:

- Differentiating Eq. (2.50) with respect to the principal stresses, σ_i ($i = 1,2,3$), and the direction cosines, a_i, of the normal to the SMP the following equation is obtained (see Appendix 2.4):

$$\Delta(\tau_{smp}/\sigma_{smp}) = f_1(\Delta\sigma_i, \Delta a_i) \tag{2.51}$$

- Eq. (2.24), which relates a_i with σ_i is differentiated with respect to σ_i, and relationships between Δa_i and $\Delta\sigma_i$ are obtained. Substituting these in eq. (2.51) the following equation is obtained (see Appendix 2.4)

$$\Delta\left(\frac{\tau_{smp}}{\sigma_{smp}}\right) = (TSMOB1)\Delta\sigma_1 + (TSMOB2)\Delta\sigma_2 + (TSMOB3)\Delta\sigma_3 \tag{2.52}$$

where the terms TSMOB1, TSMOB2 and TSMOB3 are as described in the Appendix.

To account for the "rotation" of the principal stress axis the following relationships were considered:

$$\begin{aligned}
&(\sigma_x-\sigma_i)\cos(i,x) + \tau_{xy}\cos(i,y) + \tau_{zx}\cos(i,z) = 0 \\
&\tau_{yx}\cos(i,x) + (\sigma_y-\sigma_i)\cos(i,y) + \tau_{yz}\cos(i,z) = 0 \\
&\tau_{zx}\cos(i,x) + \tau_{zy}\cos(i,y) + (\sigma_z-\sigma_i)\cos(i,z) = 0 \\
&\cos^2(i,x) + \cos^2(i,x) + \cos^2(i,z) = 1
\end{aligned} \tag{2.53}$$

where $\cos(i,x)$, $\cos(i,y)$ and $\cos(i,z)$ are the direction cosines of direction i (i=1,2,3) with respect to directions x,y and z, respectively.

In the above, the first three equations were obtained from the fundamental relationships between cartesian stresses and principal stresses and the fourth equation from the known relation for direction cosines (see Appendix 2.5).

By differentiating the above equations, equations for the increments of principal stress, $\Delta\sigma_i$ and for the increments of the angle of rotation of principal stress axis, $\Delta(i,x)$, $\Delta(i,y)$ and $\Delta(i,z)$ are obtained as functions of the increments of the stresses, $\{\Delta\sigma\}$ (see Appendix 2.5). Since "i" above has values of 1, 2 and 3, then three systems of 4 equations with 4 unknowns, are obtained. Solving these equations yields values of $\Delta\sigma_i$, which take into account the rotation of the principal stress axis, in terms of the increments of the stresses, $\{\Delta\sigma\}$.

The above procedures are presented in detail in Appendix 2.5. The final results are as follows:

$$\Delta\sigma_i = (Q_{xi})\Delta\sigma_x + (Q_{yi})\Delta\sigma_y + (Q_{zi})\Delta\sigma_z + (Q_{xyi})\Delta\tau_{xy} + (Q_{yzi})\Delta\tau_{yz} + (Q_{zxi})\Delta\tau_{zx} \tag{2.54}$$

where: Q_{xi}, Q_{yi}, Q_{zi}, Q_{xyi}, Q_{yzi} and Q_{zxi} are terms described in Appendix 2.5.

Substituting the values of $\Delta\sigma_i$ from eq. (2.54) into eq. (2.52) a relationship between $\Delta(\tau_{SMP}/\sigma_{SMP})$ and $\{\Delta\sigma\}$ is obtained and given by:

$$\Delta(\tau_{SMP}/\sigma_{SMP}) = (TMX)\Delta\sigma_x + (TMY)\Delta\sigma_y + (TMZ)\Delta\sigma_z + (TMXY)\Delta\tau_{xy} + (TMYZ)\,\Delta\tau_{yz} + (TMZX)\,\Delta\tau_{zx} \tag{2.55}$$

where:

$$TMX = \sum_{i=1,3} (TSMOBi)(Q_{xi}) \qquad TMXY = \sum_{i=1,3} (TSMOBi)(Q_{xyi})$$

$$TMY = \sum_{i=1,3} (TSMOBi)(Q_{yi}) \qquad TMYZ = \sum_{i=1,3} (TSMOBi)(Q_{yzi}) \qquad (2.56)$$

$$TMZ = \sum_{i=1,3} (TSMOBi)(Q_{zi}) \qquad TMZX = \sum_{i=1,3} (TSMOBi)(Q_{zxi})$$

2.4.3.6 Evaluation of the Plastic Constitutive Matrix

Substituting eq. (2.55) into eq. (2.49) a relationship between increments of plastic strain $\{\Delta\epsilon^p\}$ and increments of stress $\{\Delta\sigma\}$ is obtained and given by the following equation:

$$\{\Delta\epsilon^p\} = [C^p]\{\Delta\sigma\} \qquad (2.57)$$

where $\{C^p\}$ is the plastic constitutive matrix of the SMP model. This matrix is given in detail in Appendix 2.6.

2.4.4 Evaluation of the Elasto-Plastic Constitutive Matrix $[C^{ep}]$

As described earlier the strains in the SMP model are composed of two components. The plastic strains are given by the above eq. (2.57) and the elastic strains by the following equation:

$$\Delta\epsilon^e = [C^e]\{\Delta\sigma\} \qquad (2.58)$$

$[C^e]$ is defined using an incremental linear elastic and isotropic law. Isotropy is a convenient assumption since it lowers the number of elastic parameters to two. The two parameters selected here are the shear modulus, G, and the bulk modulus, B. Both moduli are considered to be dependent on the mean normal stress and evaluated in the formulation by the following equations:

$$G = KG\ P_a\ (\sigma_m/P_a)^n \tag{2.59}$$

$$B = KB\ P_a\ (\sigma_m/P_a)^m \tag{2.60}$$

where: KG and KB are the shear modulus and bulk modulus number, and
n and m are the shear modulus and bulk modulus exponent.

To obtain the complete strain-stress relation, eq. 2.57 and 2.58 are added to give

$$\{\Delta\epsilon\} = [C^{ep}]\{\Delta\sigma\} \tag{2.61}$$

Procedures for the evaluation of both the elastic and plastic parameters for use in the modified SMP model will be given later, in Chapter 3 (from laboratory test data), in Chapter 5 (from pressuremeter test data), and Chapter 6 (from laboratory and cone penetration test data).

2.4.4.1 Loading and Unloading Constitutive Matrix

One of the major advantages of using an elasto-plastic constitutive matrix $[C^{ep}]$ is that it is very easy to model the loading and unloading characteristics of the sand material in a F.E. formulation.

A soil element is considered to be in a loading stress path whenever the stress ratio level (SRL) of the element, in the current load step, is higher than the SRL of the previous load step, and for this condition the full $[C^{ep}]$ matrix in eq. (2.61) will be used in the analysis. However, if the current SRL is smaller or equal to a previous SRL then the soil element is considered to be on an unloading stress path. The plastic component $[C^{p}]$ of the total constitutive matrix $[C^{ep}]$ will be dropped and only the elastic component $[C^{e}]$ given by eq. (2.58) will be used in the analysis.

2.4.4.2 Implementation of the Modified SMP Model into Finite Element Form

To analyze the response of the Molikpaq structure to ice loading, the modified SMP model was implemented in the 3-D computer code '3DSLB'. Unfortunately because the required computer memory to analyze the Molikpaq exceeds the existing UBC computer (Amdahl) capacity of 1 megaword, this model could not be used in the 3-D analysis. However, the modified SMP model was implemented in the 2-D computer code '2DSLB' and 2-D plane strain analysis of the Molikpaq were carried out.

The modified SMP model was also implemeted in axisymmetric form in the computer code '2DSLB' to analyse pressuremeter test data obtained in the fills of the Molikpaq. Both the 2-D plane strain and axisymmetric formulations were obtained from the 3-D formulation by imposing the corresponding boundary conditions. The details are presented in Appendix 2.6.

Formulation for "load shedding" was also included in the above two computer codes and this is briefly discussed next.

2.4.4.3 Load Shedding Formulation

During the ice loading on the Molikpaq structure the soil elements adjacent to the loaded wall can undergo shear failure due to loading (see Fig. 2.14(a)) and the soil elements underneath the base of the structure on the side of the loaded wall can undergo shear and/or tension failure due to unloading (see Figs. 2.14(b) and 2.14(c)).

In the F.E. formulations (3-D and 2-D) earlier described, whenever a soil element reaches failure the G_p shear parameter is defaulted to a prescribed low value so that the element does not absorb any additional significant shear stresses during subsequent load steps.

This approach will work provided the soil element is being subject to increasing normal stresses. Its effectiveness depends on the magnitude of the load increment to failure, see Fig. 2.14(a), on how low the G_p parameter is defaulted to and on how small the subsequent load increments will be.

This approach, however, will not work if the normal stresses on the element decreases during the load step, because the element stresses will stay practically the same violating the failure criteria.

To solve the problem, Zienkiewicz et al. (1968), Byrne and Janzen (1984) proposed a stress redistribution technique called "stress transfer" or "load shedding" by which the element overstresses are redistributed to the adjacent stiffer soil or structural elements.

Briefly this "load shedding" technique consists of the following:

(a) Evaluation of the over-shear stress, $\Delta\tau_{LS}$ to be shed in terms of increments of cartesian stress, $\{\Delta\sigma\}_{LS}$ (i.e. $\Delta\sigma_{x_{LS}}$, $\Delta\sigma_{y_{LS}}$.., $\Delta\tau_{zx_{LS}}$).

(b) Correct the current stresses $\{\sigma\}$ of the element overriding the failure criterion by $-\{\Delta\sigma\}_{LS}$.

(c) Default the shear modulus of this element to a low value.

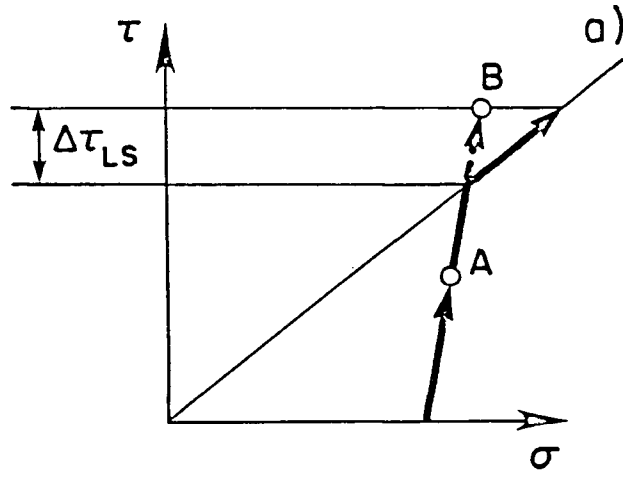

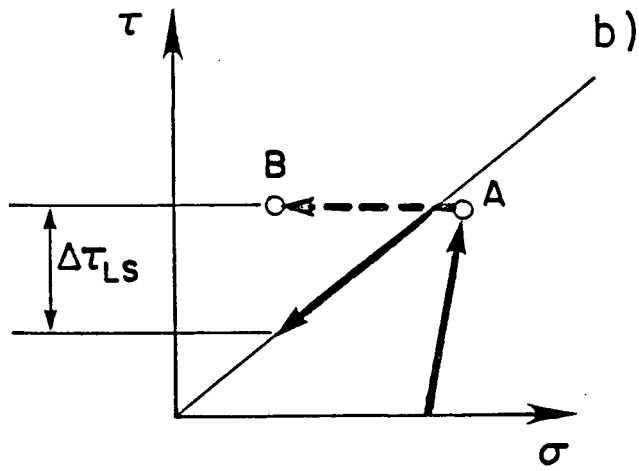

LEGEND :

A = stress point at load increment (K)

B = stress point at load increment (K + 1)

$\Delta\tau_{LS}$ = amount of shear stress to be shedded

$\Delta\sigma_{LS}$ = amount of normal stress to be shedded

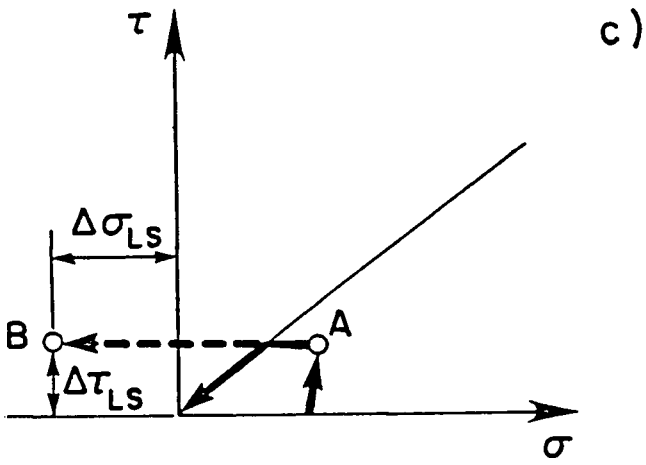

Figure 2.14 (a) Shear Failure During Loading; (b) Shear Failure During Unloading; (c) Shear and Tension Failure During Unloading.

(d) Compute nodal loads $(f)_{LS}$ that are equivalent to the overstress. Perform an additional load step of analysis with the load vector $(f)_{LS}$. This will redistribute the load to the adjacent elements.

By doing the above, the quantity $\{\Delta\sigma\}_{LS}$ which is in violation is taken from the element and is redistributed to the adjacent elements in such a way as to satisfy both equilibrium, compatibility and the failure criterion.

The implementation of the above procedures in the modified SMP formulation is presented in Appendix 2.7.

2.5 Review of the Assumptions Considered in the Modified SMP Model

The assumptions considered in the formulation of the modified SMP model were described while the model was presented. A summary of these assumptions is presented below.

2.5.1 Summary of the Assumptions Used in the Modified SMP Model

1st Assumption: The elastoplastic constitutive matrix $[C^{ep}]$ is composed of two components, an elastic component $[C^{e}]$ and a plastic component $[C^{p}]$.

2nd Assumption: The elastic constitutive matrix $[C^{e}]$ is assumed to be isotropic.

3rd Assumption: The increments of elastic principal strain are assumed to have the same direction as the increments of principal stress.

4th Assumption: The increments of plastic principal strains are assumed to have the same direction as the principal stresses.

5th Assumption: The Spatial Mobilized Plane is assumed to be the plane in which the soil particles are most mobilized on average in the 3-D stress space.

6th Assumption: The relationship between the stress ratio τ_{SMP}/σ_{SMP} and the ratio of the increments of plastic strain $\Delta\epsilon^p_{SMP}/\Delta\gamma^p_{SMP}$ is assumed to be given by the following equation,

$$\tau_{SMP}/\sigma_{SMP} = \lambda(-\Delta\epsilon^p_{SMP}/\Delta\gamma^p_{SMP}) + \mu$$

The above relationship, which is designated as flow rule, is assumed to be independent of both the initial void ratio e_i and the initial confining, σ_{mi}.

7th Assumption: The relationship between the stress ratio τ_{SMP}/σ_{SMP} and the plastic shear strain γ^p_{SMP} is assumed to be hyperbolic and given by the following equation:

$$\Delta\gamma^p_{SMP} = \frac{1}{G_p}\,\Delta(\tau_{SMP}/\sigma_{SMP})$$

This equation represents the hardening rule and it assumes that the shear parameter, G_p, is dependent on both the normal stress, σ_{SMP}, and stress ratio level, SRL.

8th Assumption: The sand material fails when the stress ratio τ_{SMP}/σ_{SMP} reaches a limiting value, which is given by the equation

$$\left(\frac{\tau_{SMP}}{\sigma_{SMP}}\right)_F = \frac{2}{3}\sqrt{\tan^2\phi_{12F} + \tan^2\phi_{23F} + \tan^2\phi_{13F}} = K_F$$

and it is assumed that the above equation is valid for any stress path.

From the above assumptions the ones regarding the direction of the increments of principal strain (Assumptions #3 and #4) and the assumption regarding the SMP failure criterion (Assumption #8) are considered to be the most pertinent and are discussed below.

2.5.2 Discussion of the Assumptions Regarding the Direction of the Increments of Principal Strain

As described, simple shear conditions are likely to develop in the sand fills of the Molikpaq structure during ice loading. Therefore the simple shear data on Leighton-Buzzard sand reported by Roscoe (1970) will be briefly discussed below.

The rotation of principal axes with shear strain during a typical simple shear test is presented in Fig. 2.15. The directions of the principal axes of stress, increments of strain and increments of stress are defined as is shown in Fig. 2.15(a) in which ψ, ξ and χ are the angles with the vertical made by the directions of the major principal stress σ_1, major principal strain increment $\Delta\epsilon_1$, and major principal stress increment $\Delta\sigma_1$, respectively. Virgin loading test data is shown in Fig. 2.15(b) and, virgin loading, unloading and reloading test data is shown in Fig. 2.15(c). Based on these test results, Roscoe (1970) concluded the following:

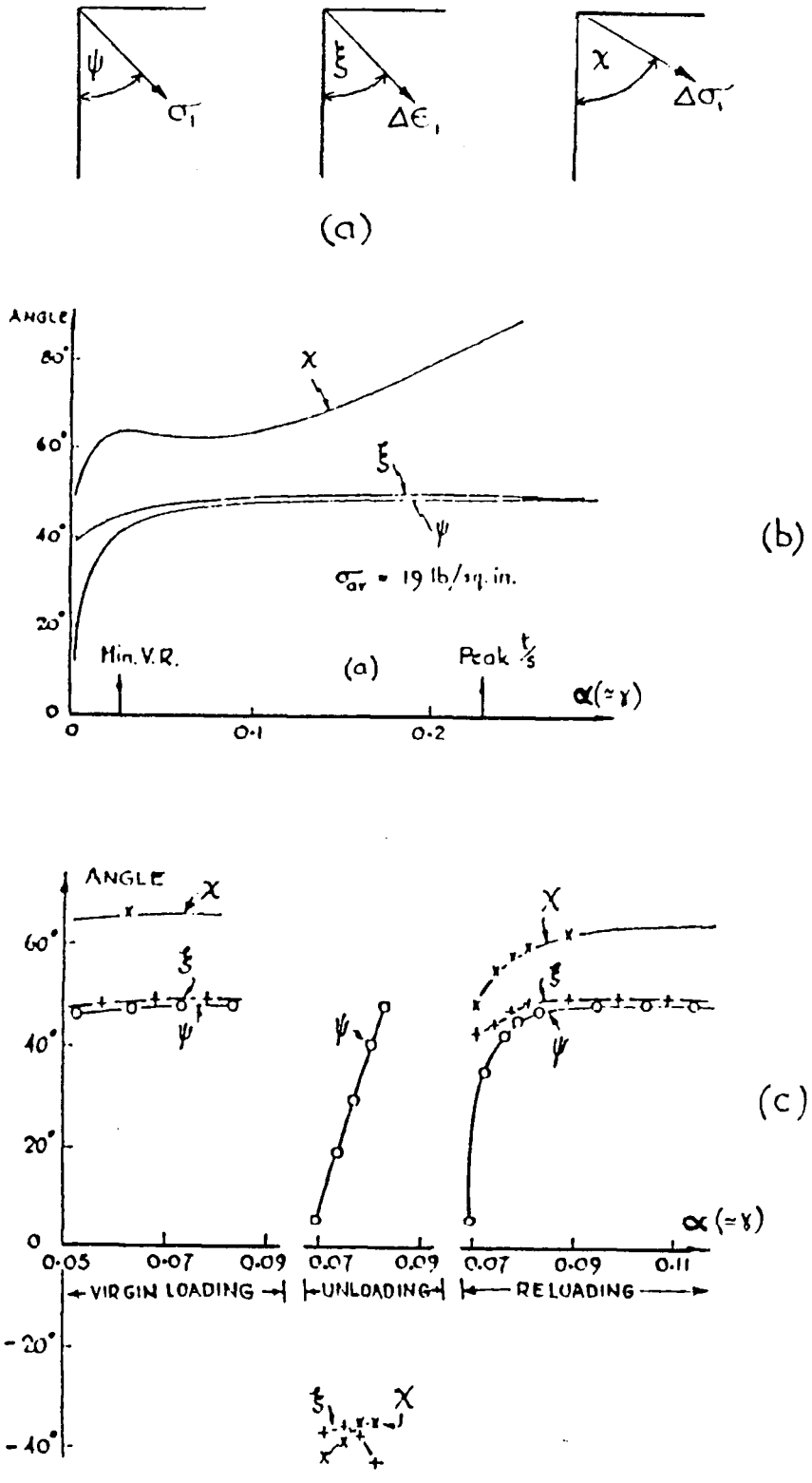

Figure 2.15 Rotation of Principal Axes During Simple Shear Tests on Leighton-Buzzard Sand (e_o = .64). Data reported by Roscoe (1970). (a) Definition of Angles ψ, ξ and χ; (b) Virgin Loading Test Data, and (c) Virgin Loading, Unloading and Reloading Test Data.

a) For monotonically increasing stresses the principal axes of increments of strain (ξ) and of stresses (ψ) coincide as the sand was sheared, except for the earliest stages of the test before the sample developed its minimum void ratio (Min.V.R.) (see Fig. 2.15(b)). This fact reinforces Assumption #4 because after Min.V.R. the deformations are essentially plastic.

b) At no stage of a virgin loading test did the axes of increment of strain (ξ) and increment of stresses (χ) coincide. However, if after monotonic increase of the shear stress this stress was reduced and then increased again the angles ξ and χ coincide (see Fig. 2.15(c)) indicating elastic behaviour. This fact reinforces Assumption #3.

However, to fully validate the above assumptions, other stress paths with rotation of principal axis should be addressed. For that the research work carried out by Symes et al. (1982,1984,1988) on Ham river sand and Sayao (1989) on Ottawa sand using the hollow cylinder torsional apparatus are briefly discussed in Appendix 2.8. The main conclusions are as follows:

For the "continuous rotation tests" carried out by Symes et al. and Sayao, with increasing or decreasing values of ψ but with constant values of stress ratio σ_1/σ_3, b-value and, mean normal stress σ_m it is concluded that the deviations between the angle ψ (stresses) and the angle ξ (increments of strain) can be quite significant. The same conclusions apply for the "continuous variation in b-value tests" carried out, by Sayao, with increasing or decreasing b-value but with constant values of ψ, σ_1/σ_3 and σ_m. This indicates that Assumption #4 is not valid for these two types of tests. However Assumption #4 is shown to be valid for the hollow cylinder tests where a stress path to failure was followed (except for the

early stages of the tests) such as the "initial anisotropic tests" carried out, by Symes et al. and Sayao, with increasing σ_1/σ_3 but with constant values of ψ, b-value and σ_m. The same conclusions apply for the "proportional loading tests" carried out by Sayao with increasing σ_m but constant σ_1/σ_3, ψ and b-value.

Since for the case of the Molikpaq the stress path that matters is a failure stress path, it is concluded therefore that Assumption #4 is considered to be adequate enough for the Molikpaq analysis.

2.5.3 Discussion of the Assumption Regarding the SMP Yield Criterion

As discussed the SMP yield criterion developed by Matsuoka and Nakai (1974,1985) assume that at failure, the stress ratio τ_{SMP}/σ_{SMP} is constant regardless of the stress path followed up to failure. The above also implies that the failure friction angle ϕ_{13} defined by the principal directions σ_1 and σ_3 is the same for the triaxial stress path in compression or extension. Based on experimental data reported by some reseachers, however, the above have not been verified. As an example, the variation of ϕ_{13} with b-value obtained from the data reported by Arthur et al. (1977) ispresented in Fig. 2.16. This data was obtained from true-triaxial tests on Leighton-Buzzard sand (e_0 = .52). In the figure the ϕ_{13} obtained from the simple shear results on the same sand (e_0 = .53) reported by Stroud (1971) is also presented.

Applying Matsuoka-Nakai failure criterion equation with the ϕ_{13} obtained from the triaxial compression test (b-value = 0) the dashed line No. 1 is obtained. Following the same procedure with the ϕ_{13}, values obtained from the simple shear test (b-value = .33) and triaxial extension test (b-value = 1) than the dashed lines No. 2 and 3 are obtained, respectively.

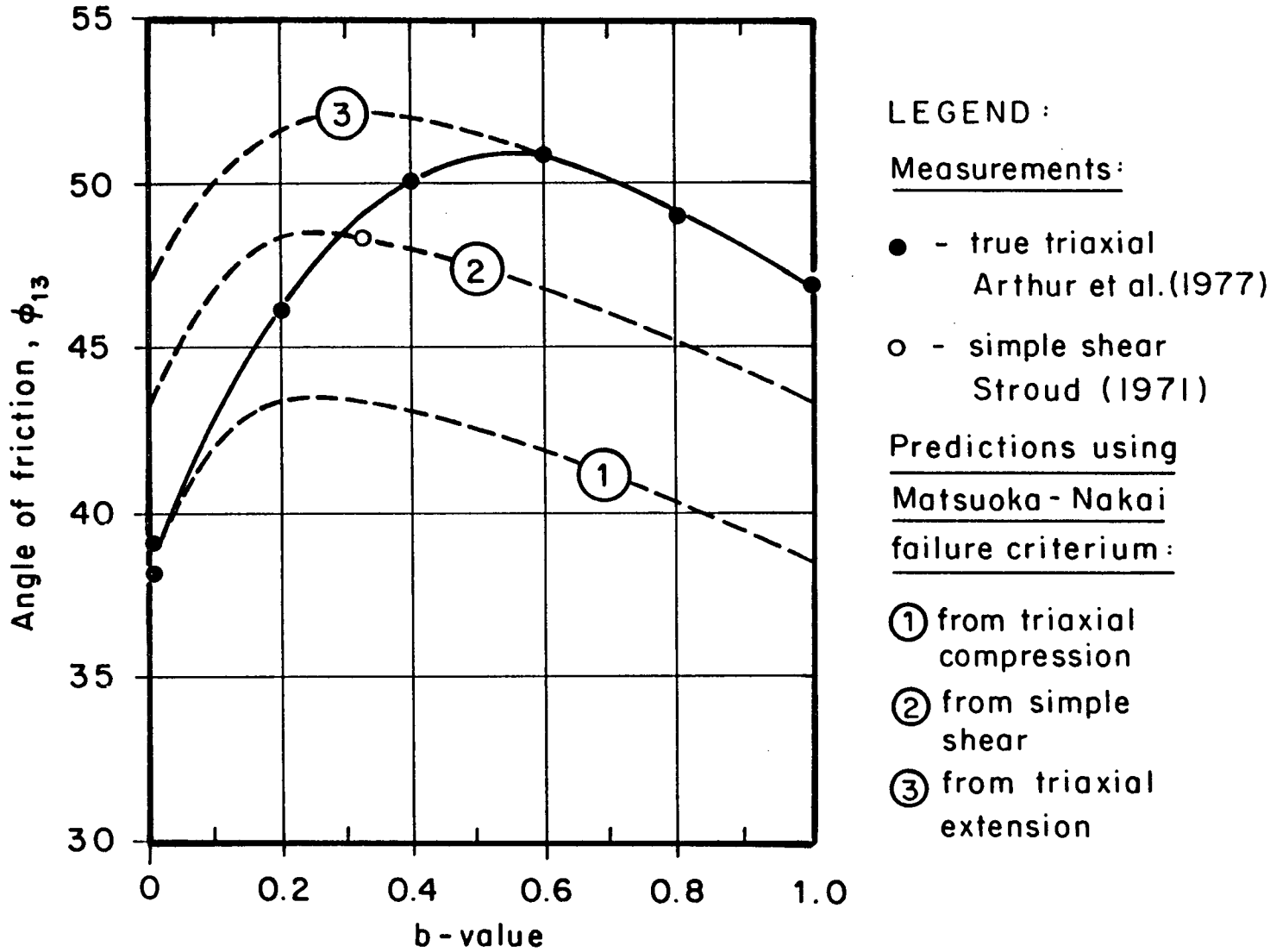

Figure 2.16 Variation of Friction Angle ϕ With 'b-Value' for Leighton-Buzzard Sand.

It may be seen from the figure, that for this set of data, the Matsuoka-Nakai failure criterion underestimates the ϕ_{13} for b > 0 if the triaxial compression data point is used.

From the above it is concluded that although the Matsuoka- Nakai failure criterion represents an improvement as compared with the Mohr-Coulomb failure criterion, which does not show any increase of ϕ_{13} with the b-value, it can not account for the different values of ϕ_{13} for the cases of triaxial compression and extension.

2.6 Disadvantages of the SMP Modified Model

The main disadvantage of the proposed formulation is that it involves a non-symmetric stiffness matrix [K] and therefore it requires a solver routine for non-symmetric system of equations. This fact in itself is not a problem because routines to solve this type of systems are available. However, the required computer memory is considerably larger than that required for the standard symmetric banded system of equations. This disadvantage became relevant for the case of the 3-D FE mesh used in the analysis of the Molikpaq (Chapter 7) because a 2.5 megaword memory capacity was required and this is larger than the existing 1 megaword memory capacity of the current UBC computer (Amdahl). Therefore the modified SMP model could not be used in the 3-D FE analysis of the Molikpaq and only 2-D FE analysis could be carried out with this model. For the 3-D FE analysis the hyperbolic model (Duncan et al., 1980) which uses a symmetric stiffness matrix was used instead. This disadvantage however is considered to be a temporary one since computers with larger memory capacity than the UBC Amdahl are used in other other technological fields and hopefully soon will be available to solve special geotechnical problems such as the Molikpaq study.

CHAPTER 3

PROCEDURES FOR THE EVALUATION OF SOIL PARAMETERS FOR USE IN THE MODIFIED SMP MODEL. VERIFICATION OF THE MODIFIED SMP MODEL

3.1 Introduction

This chapter is concerned with the following aspects which are important to any constitutive model:

a) Development of procedures for the evaluation of soil parameters for use in the model.

b) Verification of the model against observed laboratory test results. The laboratory data selected here was obtained from the following three sources:

- Data reported by Stroud (1971) for Leighton-Buzzard sand using the Cambridge Simple-Shear Apparatus Mark 7.
- Data reported by Vaid, Byrne and Hughes (1981) for Ottawa sand using the UBC Simple-Shear Apparatus.
- Data provided for the workshop on "Limit Equilibrium Plasticity and Generalized Stress-Strain in Geotechnical Engineering", McGill University, and published by Yong and Ko (1980). The data consists of true triaxial test results on Ottawa sand.

The simple shear test receives particular attention here because the shear, dilation and deformation under the principal stress rotation of sand when subject to the simple shear stress path is considered to be representative of the stress change induced by the horizontal ice loading on the Molikpaq sand fills.

3.2 Evaluation of Soil Parameters for Use in the Modified SMP Model from the Standard Triaxial Test

The soil parameters required for the modified SMP model can be divided into two main groups:

i) Elastic parameters

ii) Plastic parameters

In all, 11 parameters are used in the modified SMP model. These parameters are summarized below in Table 3.1.

Table 3.1

Summary of Soil Parameters for Use in the Modified SMP Model

Type		Parameter	Description
Elastic		KG_e	Elastic shear modulus number
		n	Elastic shear modulus exponent
		KB_e	Elastic bulk modulus number
		m	Elastic bulk modulus exponent
Plastic	Hardening Rule	KG_p	Plastic shear number
		np	Plastic shear exponent
	Flow Rule	μ	Flow rule intercept
		λ	Flow rule slope
	Failure	$(\tau_{SMP}/\sigma_{SMP})_i$	Failure stress ratio at 1 atmosphere
		$\Delta(\tau_{SMP}/\sigma_{SMP})$	Decrease in one log cycle of $(\tau_{SMP}/\sigma_{SMP})_F$
		R_F	Failure ratio

The above soil parameters can be evaluated from: (a) laboratory test results, (b) pressuremeter test results, and (c) laboratory and cone penetration test (CPT) results.

The procedures to evaluate the soil parameters from the standard triaxial test are presented in Appendix 3.1. Procedures to evaluate soil parameters from pressuremeter test results are presented in Chapter 5 and from laboratory and CPT results are presented in Chapter 6 where the soil parameters for use in the Molikpaq analysis are obtained.

3.3 Verification of the Modified SMP Model Against Observed Laboratory Test Data

To check the modified SMP model's formulation and capabilities the following two levels of verification were carried out:

1° Level of Verification (Calibration)

This consists of an evaluation of soil parameters from the results of a particular laboratory test on sand and calibration with the measured results obtained from the same test. This will allow a check of the following:

a) that the procedures described earlier to evaluate soil parameters are correct; and

b) that the formulation used in the model is also correct.

2° Level of Verification

Evaluation of soil parameters from the results of a compression triaxial test (b-value = 0) and/or extension triaxial test (b-value = 1) on a particular sand and prediction of the observed laboratory data obtained from other tests (simple shear, true-triaxial) on the same sand consolidated to the same void ratio. This will allow a check of the capability of the model to predict the response of sand when subject to various stress paths, using soil parameters that were determined from the standard triaxial test.

3.3.1 First Level of Verification of the Modified SMP Model. Calibration with the Simple Shear Test Data Reported by Stroud on Leighton-Buzzard Sand

The data reported by Stroud (1971) for Leighton-Buzzard sand using the Cambridge simple-shear apparatus Mark 7 (SSAM7) was selected here to calibrate and verify the 3-dimensional formulation of the modified SMP model because:

- The SSAM7, which was developed by Stroud, gives information on all three principal stresses, σ_1, σ_2 and σ_3 during the simple shear test.
- A gradual rotation of the axes of principal stress and strain occur during this test.
- Simple shear conditions are likely to develop in the fills of the Molikpaq structure during ice loading.

3.3.1.1 Soil Parameters for Leighton-Buzzard Sand (e_0=.53) for Use in the Modified SMP Model

The Leighton-Buzzard sand tested by Stroud (1971) is a coarse rounded quartz sand graded between No. 14 and No. 25 BS sieves with 60-65% passing no. 18 BS sieve. The sand samples were prepared with a void ratio e_0=.53 (Dr = 87%).

The soil parameters for Leighton-Buzzard sand for use in the modified SMP model are summarized in Table 3.2 and were obtained as described in Appendix 3.2.

3.3.1.2 Calibration with the Simple Shear Data Reported by Stroud

From the data reported by Stroud (1971) the tests carried out with constant vertical stress, σ_z = 48 kPa, σ_z = 76 kPa and σ_z = 172 kPa were selected here to be predicted. In the numerical analysis the initial values for the horizontal stresses, σ_x, (the direction of shear) and σ_y, (the direction of the intermediate stress) were taken equal to .44 σ_z which were the values reported by Stroud.

Table 3.2

Soil Parameters for Leighton-Buzzard Sand (e_0=.53) for use in the Modified SMP Model

Elastic Parameters		KG_e = 620
		n = 0.63
		KB_e = 580
		m = 0.60
Plastic Parameters	Plastic Shear Modulus Parameters	KG_p = 335
		np = -.48
	Flow Rule Parameters	μ = .20
		λ = 1.20
	Failure Parameters	$(\frac{\tau_{SMP}}{\sigma_{SMP}})_{1 \text{ atm.}}$ = .862
		$\Delta(\frac{\tau_{SMP}}{\sigma_{SMP}})$ = .08
		$(R_F)_{av}$ = .957

Using the soil parameters shown in Table 3.2 the following predictions were carried out:

(a) t/s versus γ (presented in Fig. 3.1)

where:

$t = (\sigma_1 - \sigma_3)/2$ = shear stress

$s = (\sigma_1 + \sigma_3)/2$ = mean normal stress

and $\gamma = (\epsilon_1 - \epsilon_3)$ = shear strain

(b) τ_{zx} versus γ_{zx} (presented in Fig. 3.2(a))

where:

τ_{zx} = cartesian shear stress

γ_{zx} = cartesian shear strain

(c) ϵ_v versus γ_{zx} (presented in Fig. 3.2(b))

where:

ϵ_v = volumetric strain

(d) σ_x/σ_{xo} versus γ (presented in Fig. 3.3)

where:

σ_{xo} = the initial horizontal stress in the x-direction

σ_x = the mobilized stress, due to shear, in the x-direction (see Appendix 3.3 for the evaluation of σ_x from the reported laboratory data)

(e) σ_3/s versus γ (presented in Fig. 3.4).

The above predictions were carried out using both the 3-D and 2-D plane strain formulations of the modified SMP model, both gave exactly the same predictions.

The overall agreement between the predictions and the measured data is seen to be good except for the σ_x/σ_{xo} versus γ predictions. These differences are attributed to deviations of the measured vertical stress, σ_v', from the assumed constant vertical stress boundary conditions of the tests. Based on the above, it is concluded that the procedures described in Appendix 3.1 to evaluate soil parameters and both the 3-D and 2-D formulations of the model have been verified.

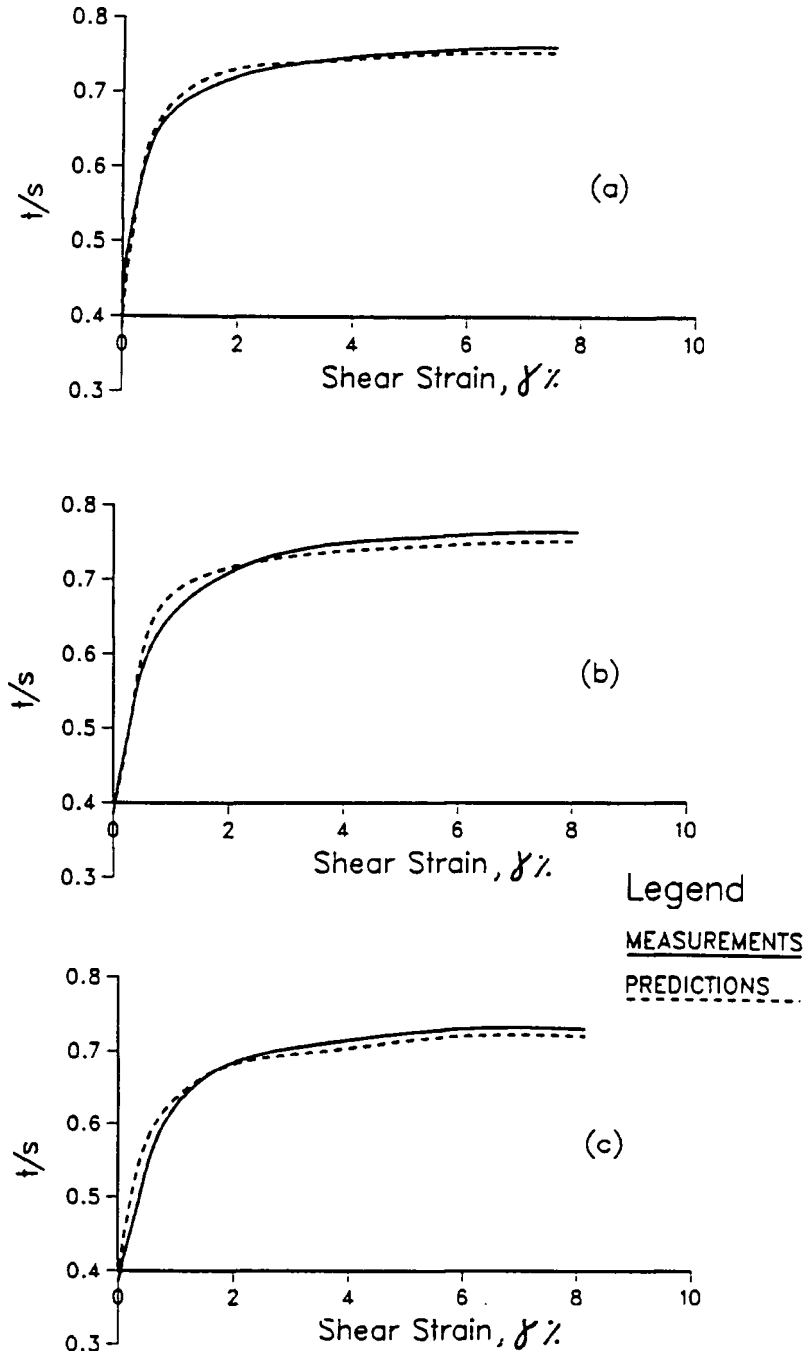

Figure 3.1 Predicted and Measured Simple Shear Data on Leighton-Buzzard Sand (t/s versus γ). (a) σ_v = 48 kPa; (b) σ_v = 72 kPa; and (c) σ_v = 172 kPa

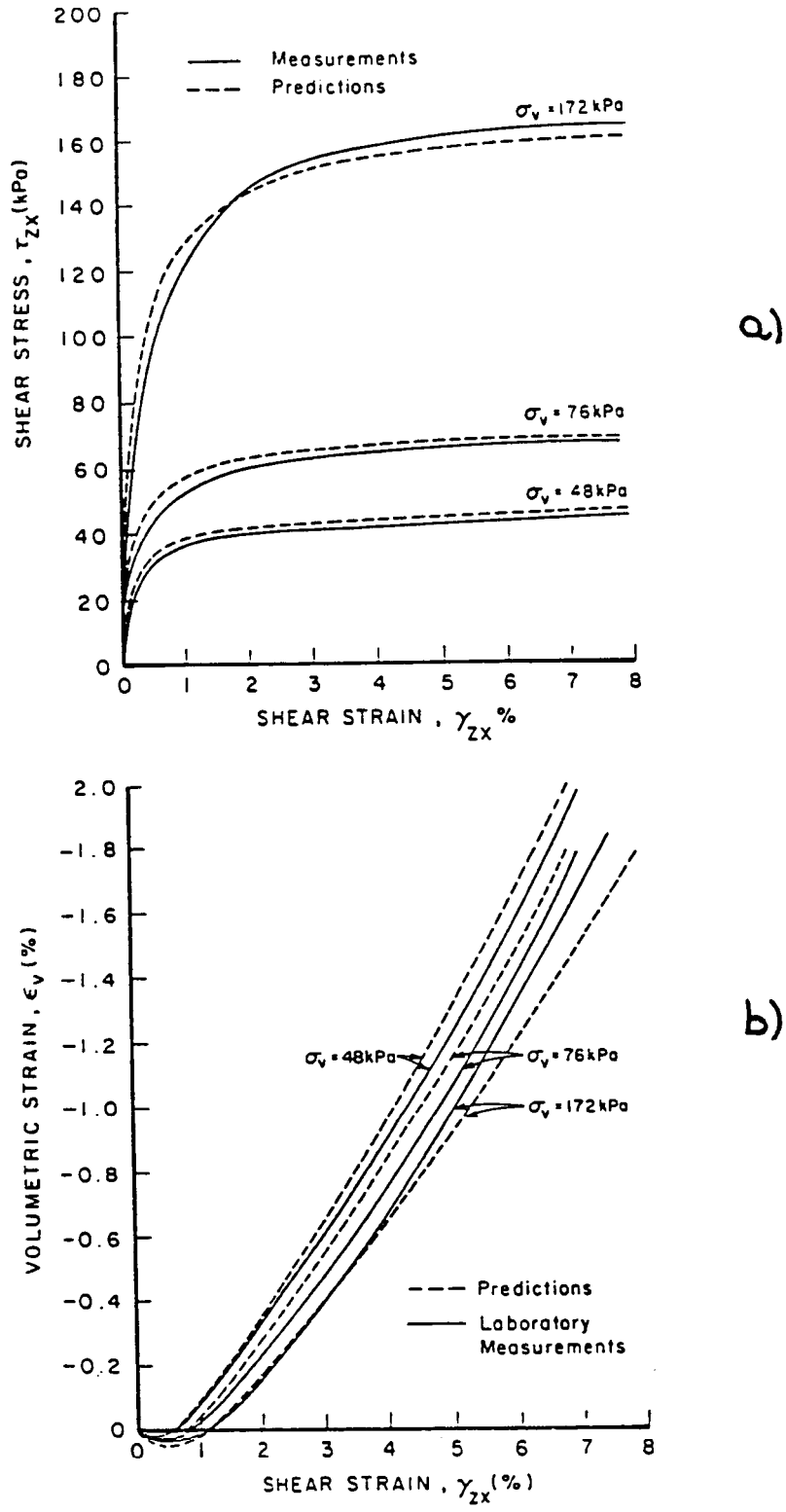

Figure 3.2 Predicted and Measured Simple Shear Data on Leighton-Buzzard Sand. (a) τ_{zx} versus γ_{zx}; (b) ϵ_v versus γ_{zx}

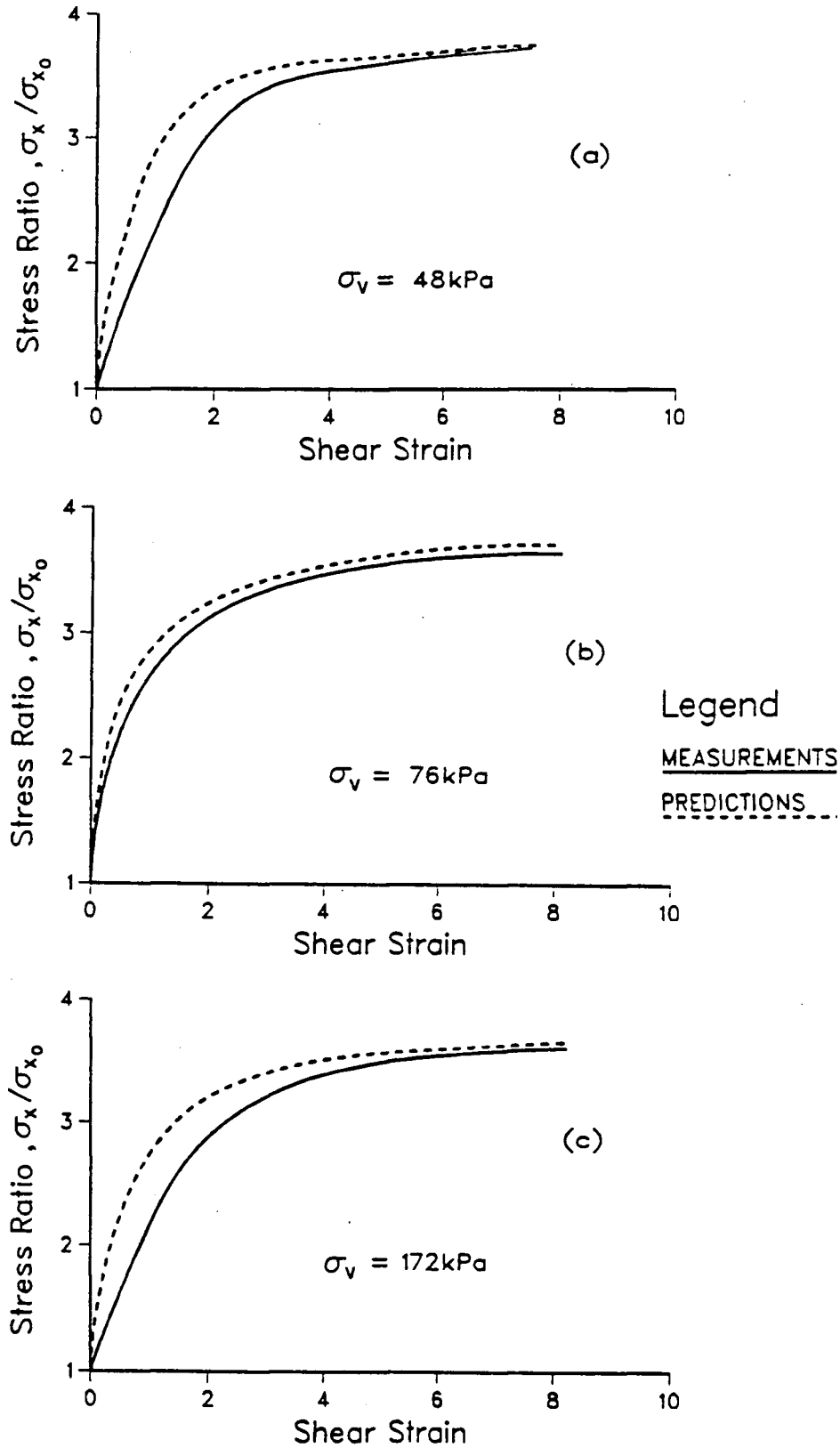

Figure 3.3 Predicted and Measured Simple Shear Data on Leighton-Buzzard Sand (σ_x/σ_{xo} versus γ). (a) σ_v = 48 kPa; (b) σ_v = 72 kPa; and (c) σ_v = 172 kPa

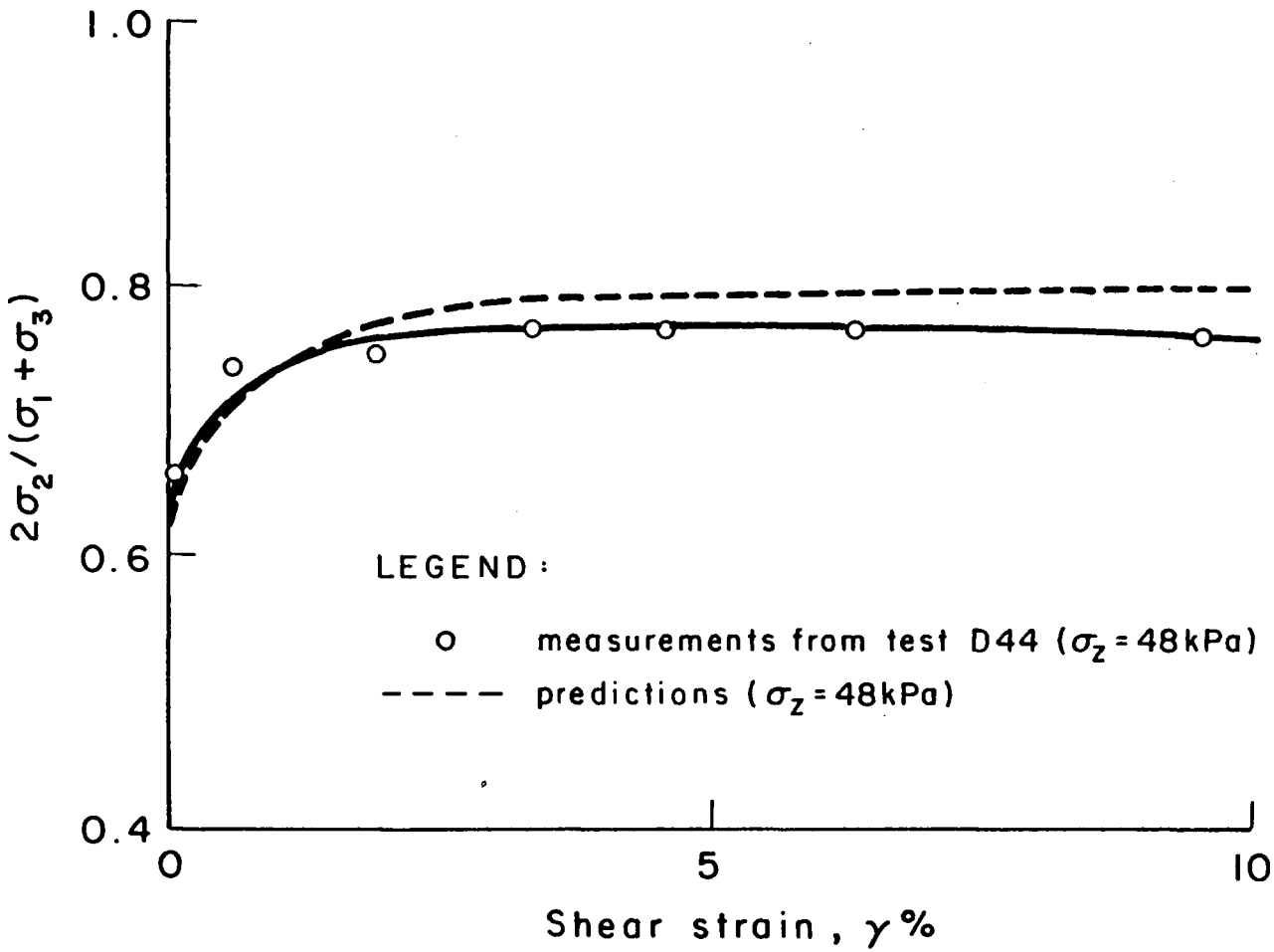

Figure 3.4 Predicted and Measured Simple Shear Data on Leighton-Buzzard Sand (σ_2/s versus γ). σ_v = 48 kPa

3.3.2 Second Level of Verification of the Modified SMP Model. Predictions of Simple Shear and True-Triaxial Test Data on Ottawa Sand

The true triaxial test data on Ottawa sand (D_r = 87%) used in the 1980 workshop on McGill University (data reported by Yong and Ko) is used here, as is described below, together with the simple shear test data reported by Vaid, Byrne and Hughes (1981) on the same sand (D_r = 72.3% and 92.7%) to further verify the modified SMP model.

The above test data was subdivided here into two sets of data:

- Data Base from which the soil parameters for use in the model were obtained. The stress paths used to generate the data base are presented in Fig. 3.5(a) and the grain size distribution of the Ottawa sand used in the tests is shown in Fig. 3.5(b). It may be seen that the tests consisted of conventional triaxial tests (compression (CTC) and extension (CTE)), constant mean stress triaxial tests (compression (TC) and extension (TE)) and hydrostatic compression test (HC). This data is the same data base (or pre-workshop data) used in the 1980 workshop at McGill University.
- Data Used for Predictions. The stress paths considered for the predictions were subdivided into the following five groups:
  - Simple shear test which can be characterized by a b-value = .30 (see Fig. 3.6(a)),
  - Constant mean stress triaxial tests with b-values of .2, .5 and .8 (see Fig. 3.6(a)),
  - Proportional loading tests, PL1 and PL2 (see Fig. 3.6(b)),
  - Reduced triaxial tests, RTC and RTE (see Fig. 3.6(b)), and
  - Circular path test (see Fig. 3.6(c)).

  A detailed description of these tests is given later in the predictions section.

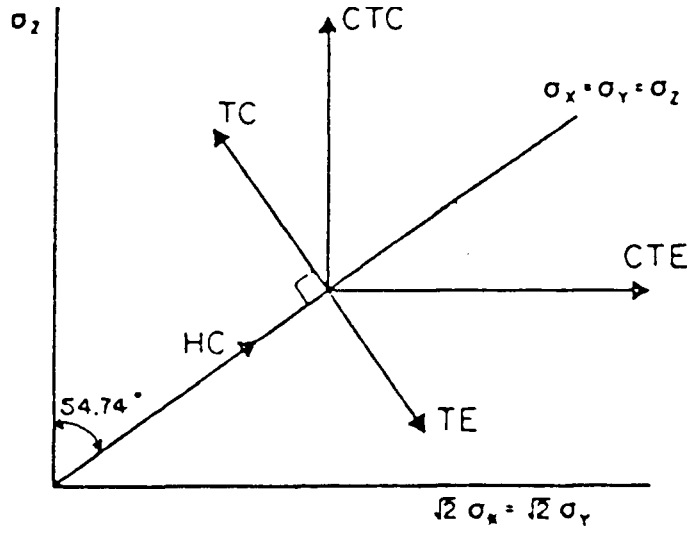

a)

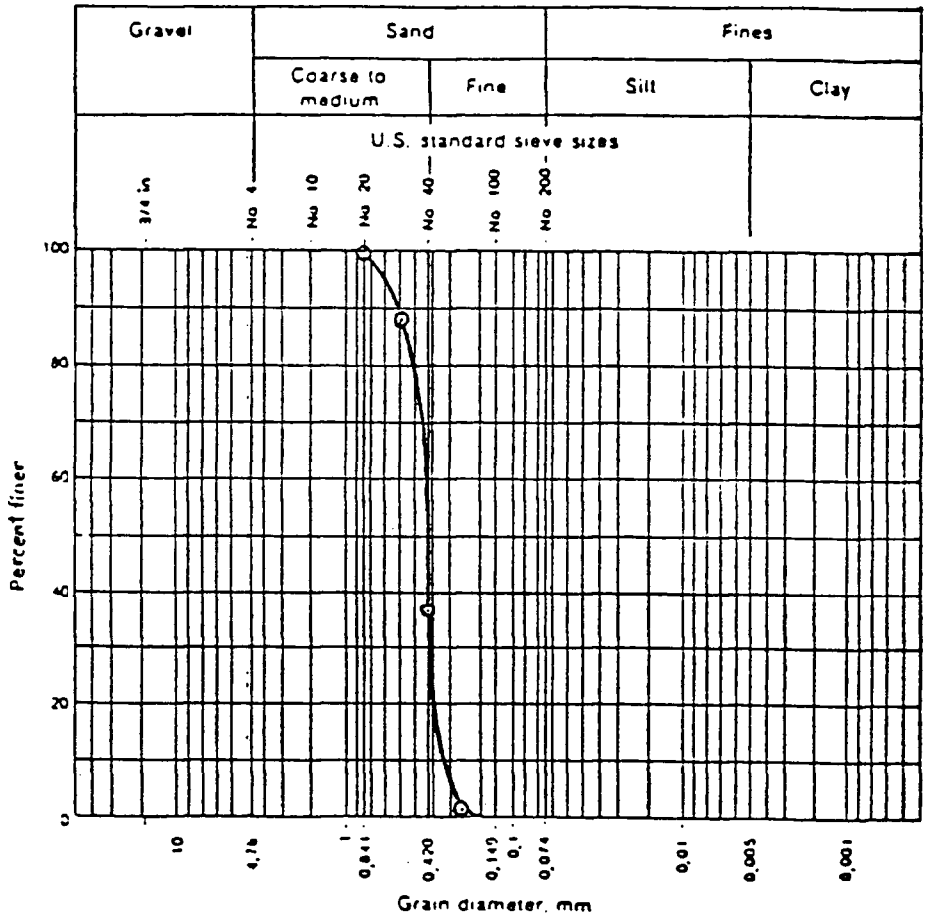

b)

Figure 3.5 (a) Stress Paths Used to Generate Data Base for Modelling; (b) Grain Size Distribution of Ottawa Sand.

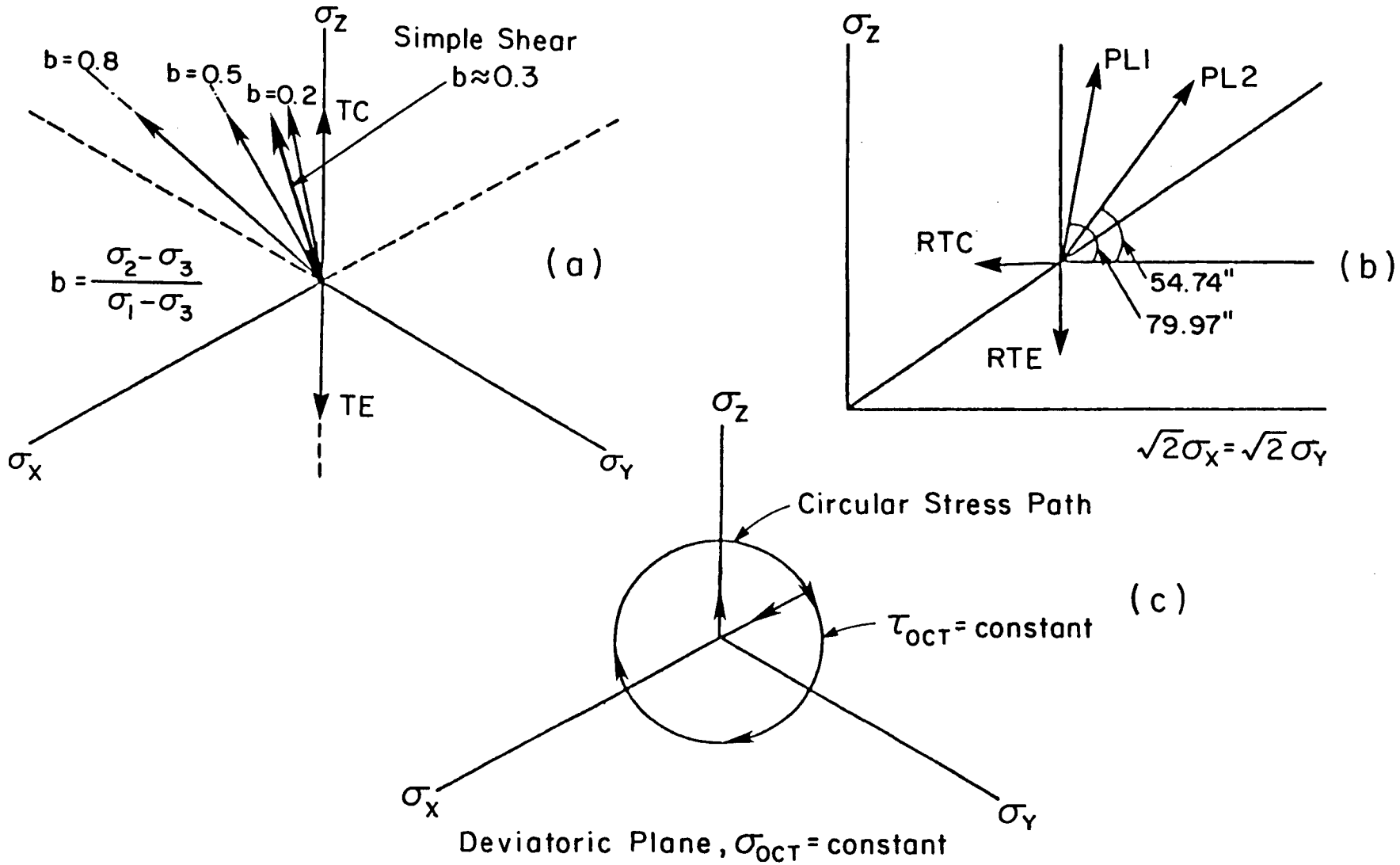

Figure 3.6(a,b,c) Stress Paths Used for Predictions

For comparison purposes, predictions of the above tests using the hyperbolic model (Duncan et al. (1980)) are also included here because the hyperbolic model was used in the 3-Dimensional analysis of the Molikpaq.

3.3.2.1 Soil Parameters for Ottawa Sand (D_r=87%) for Use in the Modified SMP Model and the Hyperbolic Model

The soil parameters for use in the modified SMP model were evaluated from the Data base as described in Appendix 3.3. A summary of the soil parameters is given in Table 3.3.

The soil parameters for Ottawa sand (D_r = 87%) for use in the hyperbolic model are presented in Table 3.4 and were evaluated by Duncan and published by Yong and Ko (1980).

Table 3.3

Soil Parameters for Ottawa Sand (D_r = 87%) for Use in the Modified SMP Model

KG_e = 1640 n = 0.49 KB_e = 2578 m = 0.25	Elastic Parameters	
KG_p = 190 np = -.50	Plastic Shear Modulus Parameters	Plastic Parameters
μ = .25 λ = 1.10	Flow Rule Parameters	
$(\frac{\tau_{SMP}}{\sigma_{SMP}})_1$ = .935 $\Delta(\frac{\tau_{SMP}}{\sigma_{SMP}})$ = .62 $(R_F)_{av}$ = .97	Failure Parameters	

Table 3.4

Soil Parameters for Ottawa Sand (D_r = 87%) (Evaluated by Duncan (1980) and Used in the Hyperbolic Model)

Parameter	Average Value	Range
K	400	± 120
K_{UR}	2000	-
n	0.85	-
Cohesion, c	0.5 psi	
K_b	700	-
m	0.50	-
ϕ	43°	± 3°
R_f	.86	-

3.3.2.2 Predictions of the Simple Shear Test Data Reported by Vaid, Byrne and Hughes (1980)

The simple shear tests on Ottawa sand were carried out using the UBC simple shear apparatus described by Finn and Vaid (1977), which is a Cambridge type of apparatus similar to that developed by Roscoe (1953). The tests were carried out under drained conditions at a constant vertical confining stress, σ_z = 200 kPa. The test results are shown in Fig. 3.7 for a range of relative densities. The tests were strain controlled and one test (D_r = 92.7%) exhibited strain softening.

In order to take into account the strain softening behaviour of Ottawa sand the modified SMP formulation was expanded with two additional soil parameters. The details are given in Appendix 3.5 and follow similar procedures as outlined by Carter and Yeung (1985) after some adaptations to the SMP formulation.

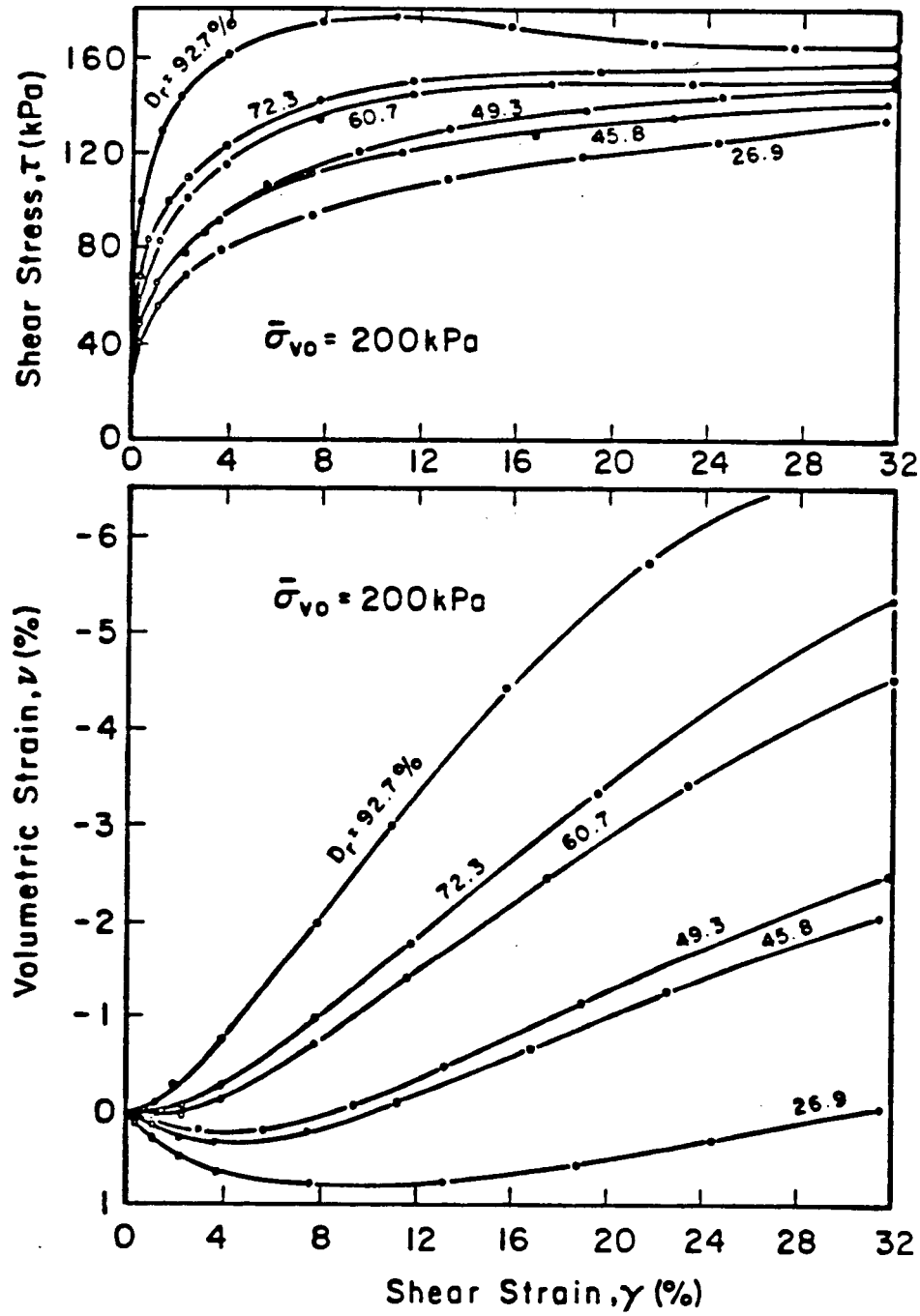

Figure 3.7 Stress-Strain Behaviour of Ottawa Sand in Drained Simple Shear (after Vaid, Byrne and Hughes, 1980)

Predictions of the simple shear test results were carried out using both the modified SMP model (with and without strain softening parameters) and the hyperbolic model. Because the relative density corresponding to the Data base was 87%, only the measured simple shear test data for D_r = 72.3% and 92.7% will be considered here to bound the predictions.

The initial stresses used in the analysis consisted of: vertical stress, σ_z = 200 kPa, which remained constant; and $\sigma_x = \sigma_y$ = 86.5 kPa which assumes a K_0 = .43. This K_0 value represents the average value of that reported by Stroud (1971) (K_0 = .440) and, Wood, Drescher and Budhu (1979) (K_0 = .425) which were obtained from the experimental values recorded in the elaborately instrumented Cambridge simple shear apparatus.

The laboratory results together with the predictions obtained with the two models are presented in Fig. 3.8. It may be seen that up to peak shear stress the predictions obtained with the modified SMP model for D_r = 87% lie very close to the laboratory measurements (shear and volume measurement) corresponding to D_r = 92.7%. After peak, the predictions taking into account the strain softening effects are in good agreement with the laboratory measurements. On the other hand, if strain softening is not considered, the mobilized shear stresses τ_{zx} maintains a constant value after the peak shear stress is reached.

The predictions evaluated here using the soil parameters developed by Duncan with the hyperbolic model are also presented in Fig. 3.8 and show that this model underestimates the failure strength of the Ottawa sand when it follows the simple shear stress path. This is related with the Mohr-Coulomb failure criteria that is used in the hyperbolic model. Regarding the volumetric predictions, the hyperbolic model does not predict any

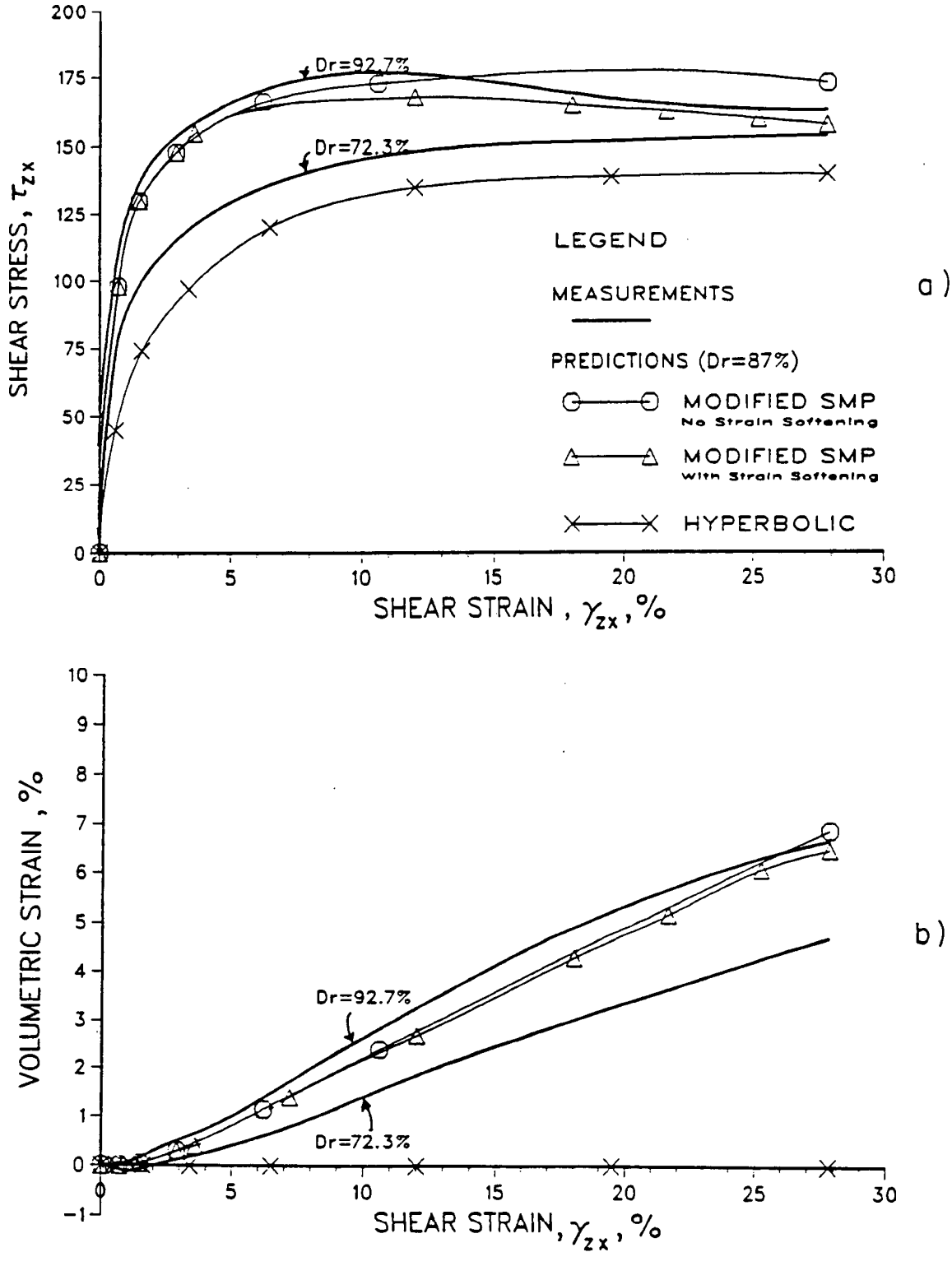

Figure 3.8 Predicted and Measured Simple Shear Data on Ottawa Sand. (a) τ_{zx} versus γ_{zx}. (b) ϵ_v versus γ_{zx}

volume changes since its formulation does not take into account volume changes mobilized by the shear component. As described in the beginning of this chapter even using the version of the hyperbolic model developed by Byrne and Eldridge (1982) which takes into account the volume changes due to dilation, the failure strength of the Ottawa sand for this particular stress path was well underestimated. This was one of the reasons why the modified SMP model was developed.

3.3.2.3 Predictions of the Post-Workshop Test Data of the 1980 Workshop of McGill University

The test equipment used is a flexible, fluid cushion cubical device with stress control, which is known as cube or true-triaxial device. The vertical axis, z, and the horizontal axes x and y are principal stress axes, which means that shear stresses cannot be applied with this device.

The stress paths of the tests the investigators were asked to predict in the 1980 workshop of McGill University were given earlier in Figs. 3.5(b), (c) and (d). These tests can be divided into four groups:

a) constant mean stress tests

b) proportional loading tests

c) reduced triaxial tests

d) circular path test

The predictions of the test results will be presented following the above order together with a brief description of each test and comments on the quality of the predictions by the two constitutive models.

a) Constant Mean Stress Tests

Four tests where the σ_m and the b-value were kept constant were performed:

a_1) b = .2 and σ_m = 10 psi. During this test $\Delta\sigma_x = 1/3\ \Delta\sigma_z$, and $\Delta\sigma_y = 2/3\ \Delta\sigma_z$.

a_2) b = .5 and σ_m = 5 psi. During this test $\Delta\sigma_x = \Delta\sigma_z$.

a_3) b = .5 and σ_m = 20 psi. During this test $\Delta\sigma_x = \Delta\sigma_z$.

a_4) b = .8 and σ_m = 10 psi. During this test $\Delta\sigma_x = .5\ \Delta\sigma_z$ and $\Delta\sigma_y = 1.5\ \Delta\sigma_z$.

The test results and the predictions from the two models are presented in Fig. 3.9 to Fig. 3.12.

The predictions obtained with the modified SMP model are in good agreement with the measured results for both the initial phase and the failure phase of the tests. Test with b=.5 and σ_m=20 psi was the only exception where 1 psi difference of τ_{oct} at failure is noted.

The predictions obtained by Duncan with the hyperbolic model show that the higher bound of the predicted range is in good agreement with the tests with b=.2 and b=.8, but that the predictions for the tests b=.5 (σ_m=5 and 20 psi) reach failure conditions much sooner than the laboratory measurements indicate. The reasons for this are most likely related with the Mohr-Coulomb failure criteria used in the hyperbolic model, which underestimates the failure friction angle for stress paths with b values different than 0 (triaxial compression) or 1 (triaxial extension).

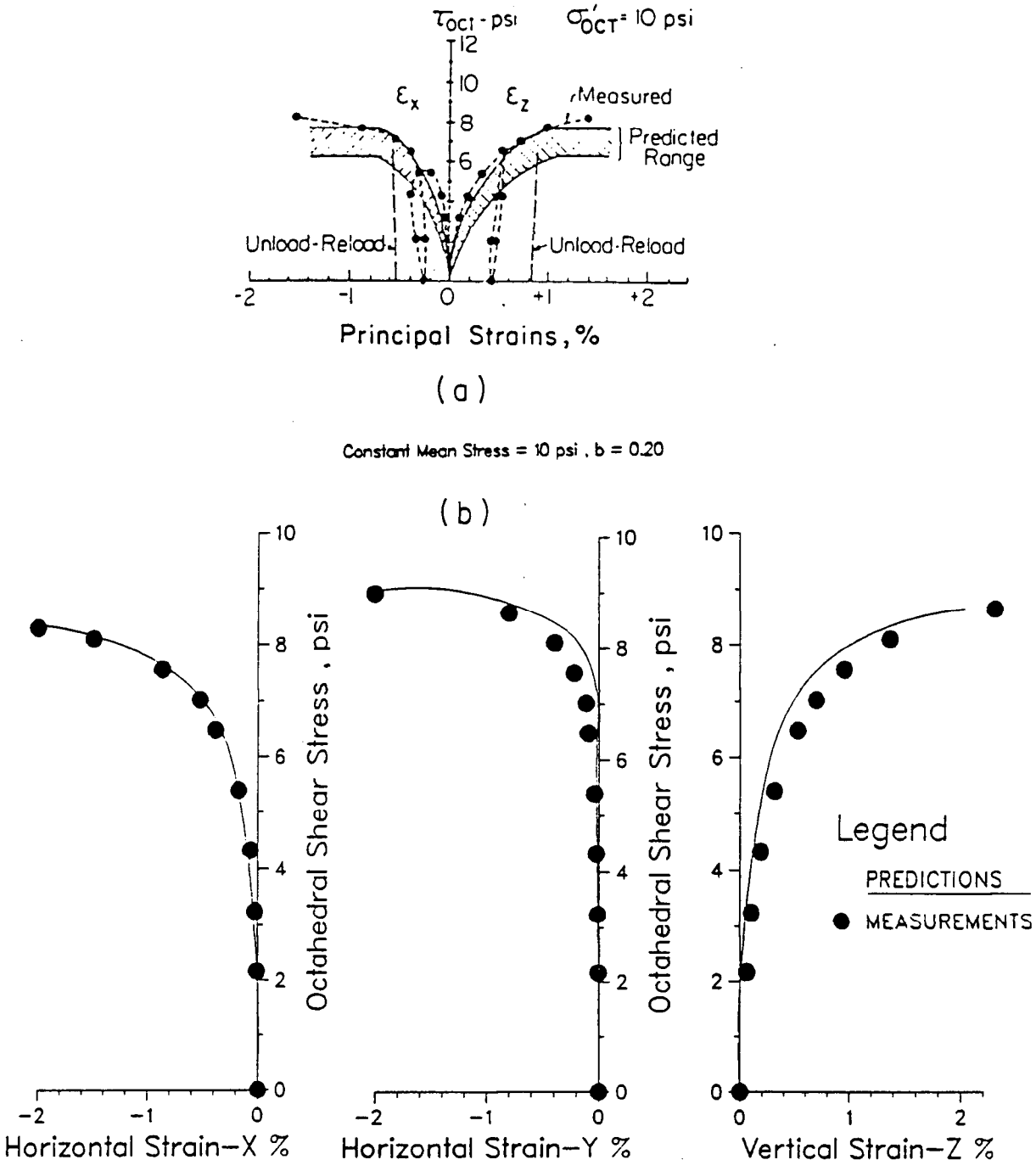

Figure 3.9 Predicted and Measured Constant Mean Stress Test Data on Ottawa Sand. b = 0.2, σ_m = 10 psi. (a) Predictions with the Hyperbolic Model. (b) Predictions with the Modified SMP Model

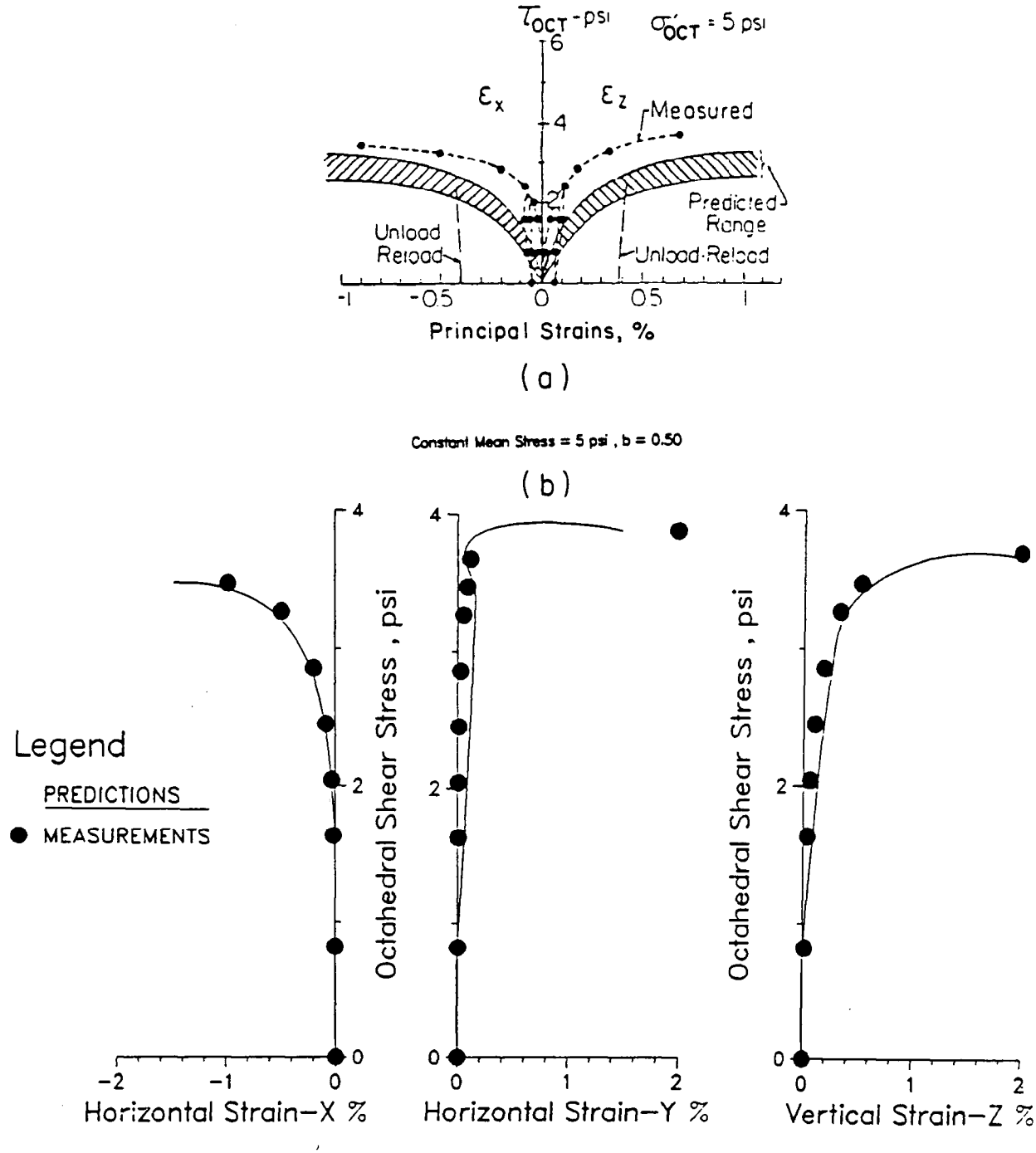

Figure 3.10 Predicted and Measured Constant Mean Stress Test Data on Ottawa Sand: b = 0.5, σ_m = 5 psi. (a) Predictions with the Hyperbolic Model. (b) Predictions with the Modified SMP Model

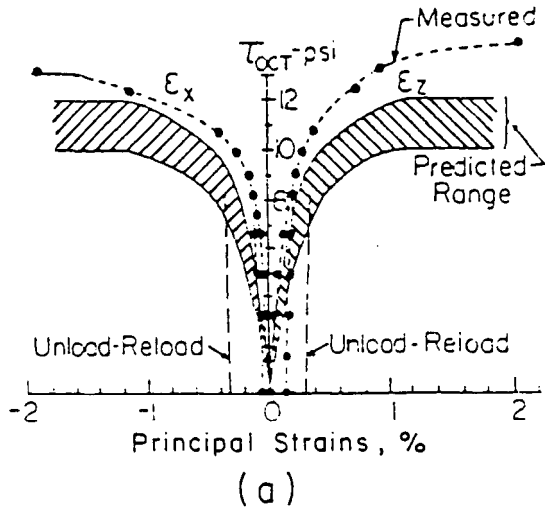

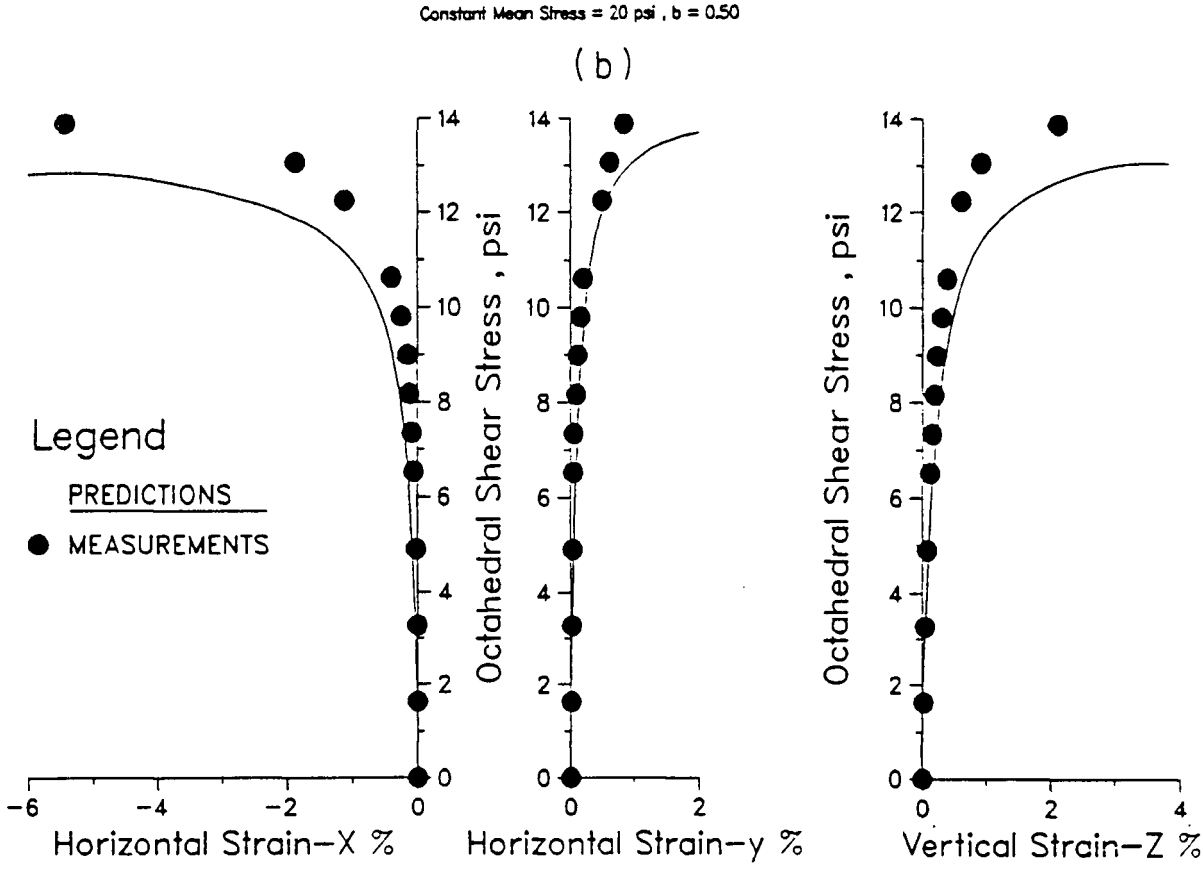

Figure 3.11 Predicted and Measured Constant Mean Stress Test Data on Ottawa Sand. b = 0.5, σ_m = 20 psi. (a) Predictions with the Hyperbolic Model. (b) Predictions with the Modified SMP Model

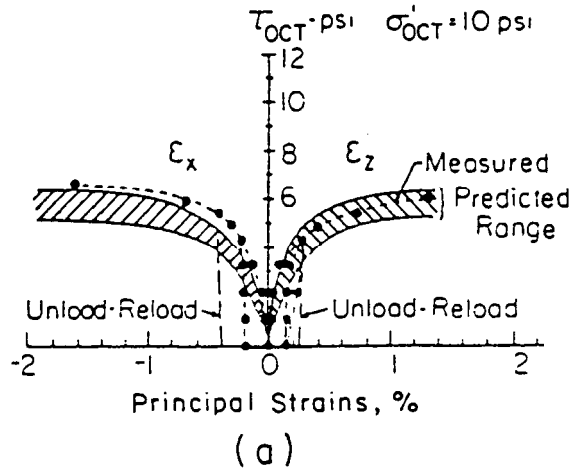

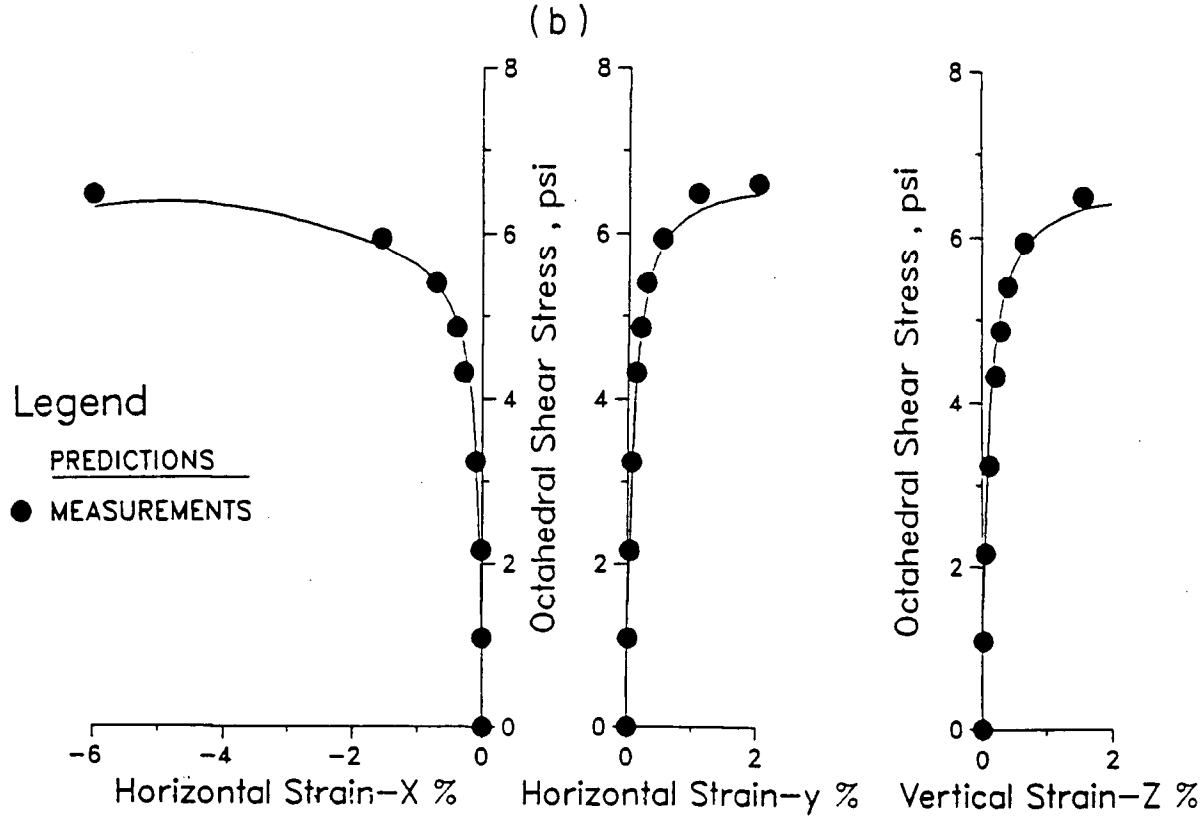

Figure 3.12 Predicted and Measured Constant Mean Stress Test Data on Ottawa Sand. b = 0.8, σ_m = 10 psi. (a) Predictions with the Hyperbolic Model. (b) Predictions with the Modified SMP Model

b) Proportional Loading Tests

Two proportional loading tests with $(\sigma_m)_i$ = 10 psi were carried out. In the first $\Delta\sigma_x = \Delta\sigma_y = 1/8\ \Delta\sigma_z$ and was designated PL_1. In the second $\Delta\sigma_x = \Delta\sigma_y = 1/2\ \Delta\sigma_z$ and was designated PL_2. The test results together with the predictions are presented in Fig. 3.13.

The predictions by the two models of the PL_1 test underestimate considerably the failure phase of the test, and no apparent reasons can be offered since the b value = 0.

The predictions of the PL_2 test indicate that the predictions of ϵ_z strain by the modified SMP model and the high bound of the hyperbolic model are in very good agreement up to a ϵ_z = .3% and after that the laboratory data seems to deviate from its initial trend. Regarding the ϵ_x and ϵ_y strains, both models predict strains with the wrong sign as compared with the laboratory measurements and again no apparent reason can be offered to justify that deviation.

c) Reduced Triaxial tests

Two reduced triaxial tests with $(\sigma_m)_i$ = 20 psi were carried out. One was a reduced triaxial compression test, RTC, with b=0, $\Delta\sigma_z$=0 and decreasing $\Delta\sigma_x = \Delta\sigma_y$, and the other a reduced triaxial extension test RTE with b=1, $\Delta\sigma_x = \Delta\sigma_y = 0$ and decreasing $\Delta\sigma_z$. The test results and predictions are shown in Fig. 3.14.

The predictions of the RTC and RTE tests carried out by the two models are in good agreement with the laboratory measurments.

d) Circular Path Test

This test, which was performed with a constant σ_m = 10 psi, is composed of 3 phases. In the first phase the sand is loaded in shear until

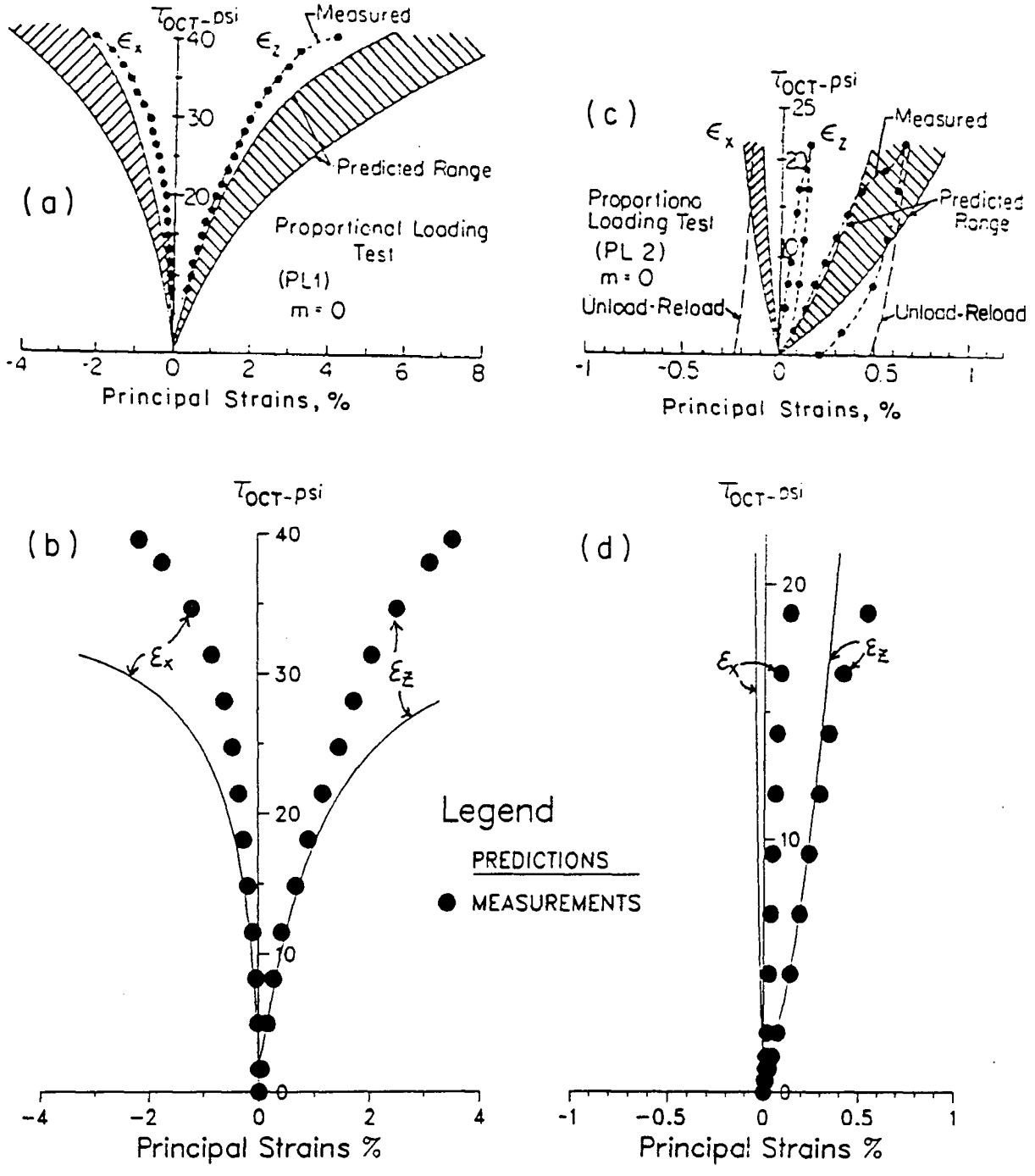

Figure 3.13 Predicted and Measured Proportional Loading Test Data on Ottawa Sand, σ_{mi} = 10 psi: (a) PL1 Test, Predictions with the Hyperbolic Model, (b) LL1 Test, Predictions with the Modified SMP Model, (c) PL2 Test, Predictions with the Hyperbolic Model, (d) PL2 Test, Predictions with the Modified SMP Model

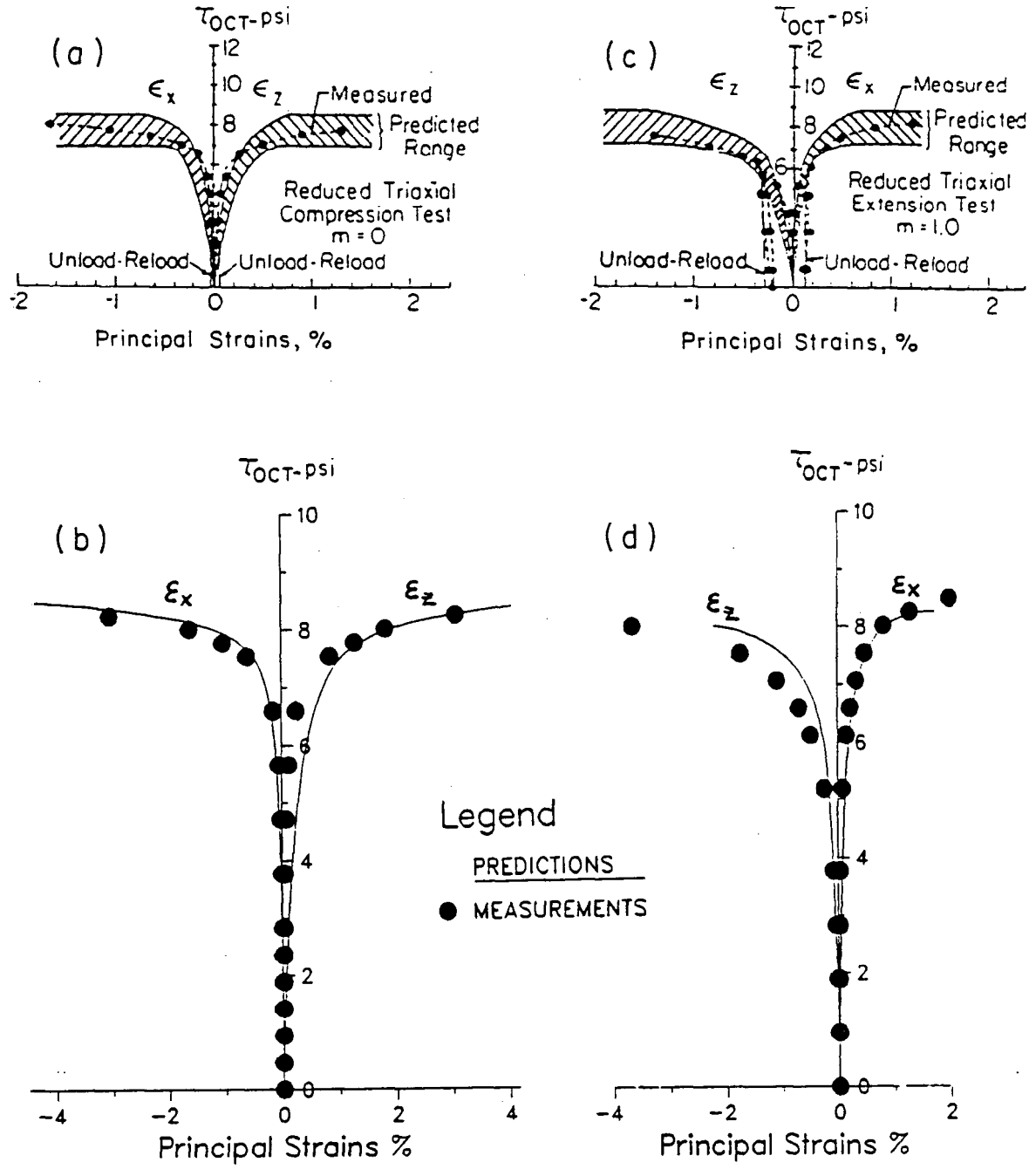

Figure 3.14 Predicted and Measured Reduced Triaxial Test Data on Ottawa Sand, σ_{mi} = 20 psi. Reduced Triaxial Compression Test (RTC): (a) Predictions with the Hyperbolic Model, (b) Predictions with the Modified SMP Model. Reduced Triaxial Compression Test (RTE): (c) Predictions with the Hyperbolic Model; (d) Predictions with the Modified SMP Model.

a τ_{oct}= 4.2 psi is developed. The second phase is characterized by maintaining a constant τ_{oct} = 4.2 psi while the three stresses σ_x, σ_y and σ_z vary in magnitude, and share at different times the directions of the principal stresses σ_1, σ_2 and σ_3. Although the name of the test (circular path) seems to imply that a gradual rotation of the principal stress axis is taking place, in reality that is not the case, and what takes place is an instant flip of the principal directions at different times during the test. This phase is terminated when the "apparent" angle of rotation θ reaches a value of 420°. During the last phase of the test the sand is unloaded from τ_{oct} = 4.2 psi to τ_{oct} = 0. The results and the predictions corresponding to the 2nd phase of the test are shown in Fig. 3.15.

The predictions obtained by Duncan using the hyperbolic model are in fair agreement with the laboratory measurements. On the other hand the predictions carried out with the modified SMP model, which are in fair agreement with the laboratory measurements during the first (1/3) of the second phase of the test, show a poor agreement for the rest of the test. However, because this circular path test is not representative of the stress paths that occur in the sand fills of the Molikpaq structure during either the construction or ice loading phases, explanations for the above differences were not investigated at this time, but will deserve consideration in the future by the writer.

3.4 Summary and Conclusions

Procedures for the evaluation of soil parameters from laboratory test results for use in the modified SMP model has been presented in this chapter. This was followed by a verification of the proposed model against

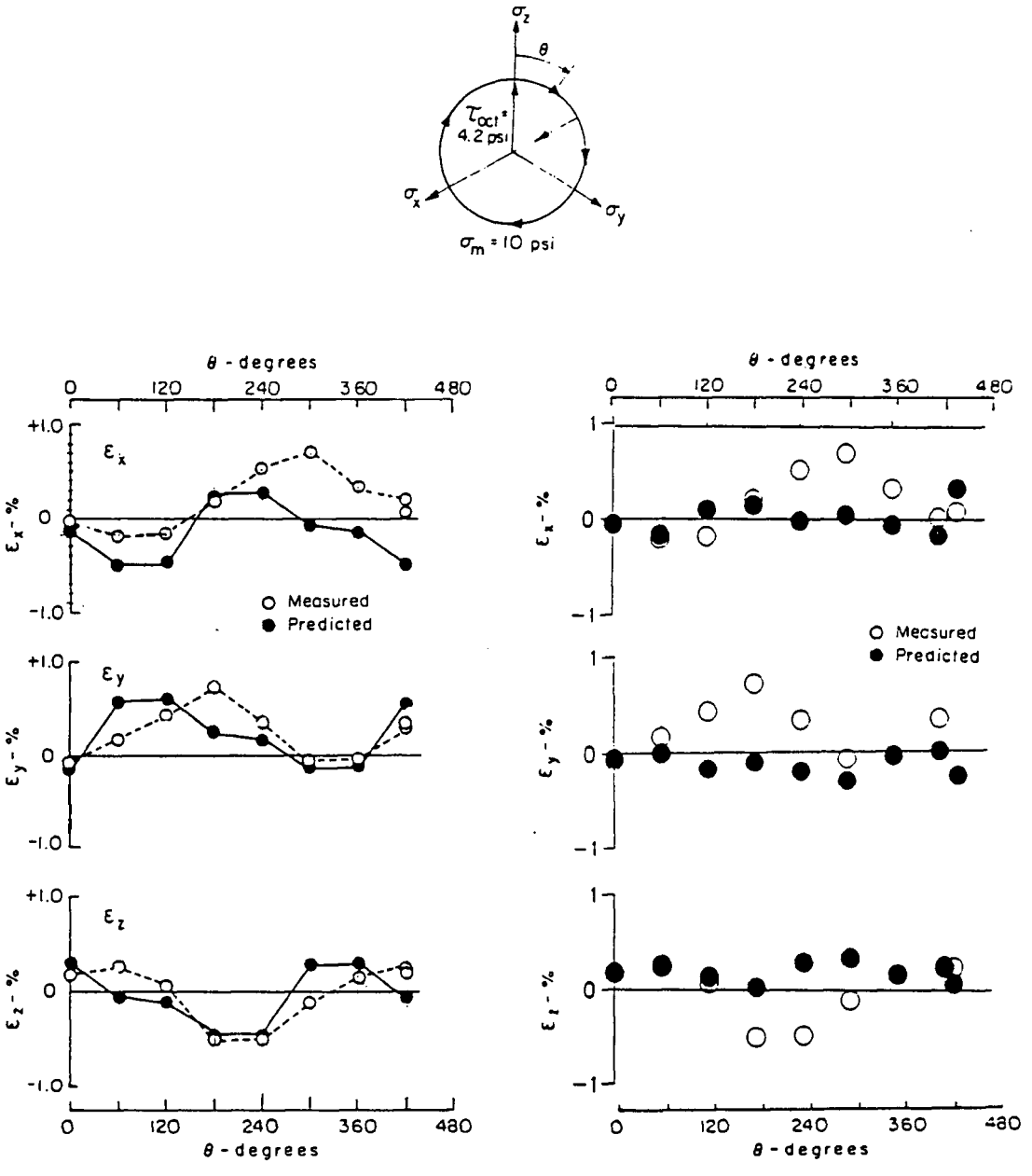

Figure 3.15 Predicted and Measured Circular Stress Path Test Data on Ottawa Sand. σ_m = 10 psi; τ_{oct} = 4.2 psi. (a) Predictions with the Hyperbolic Model. (b) Predictions with the Modified SMP Model

observed laboratory test results. Based on the overall good agreement between the predictions and the reported data the following is concluded:

(1) The procedures described in this chapter are adequate to evaluate soil parameters for use in the modified SMP model.

(2) Both the 3-D and 2-D plane strain formulations of the proposed model can reproduce well the reported simple shear test data on Leighton-Buzzard sand.

This indicates the following:

(a) The model takes into account the gradual rotation of the axes of principal stresses and strains that occur during that test.

(b) The 2-D formulation which is derived from the 3-D formulation by applying the appropriate boundary conditions give a good prediction of the intermediate principal stress σ_2.

(3) The overall good predictions of the simple shear and true-triaxial tests on Ottawa sand, with the exception of the circular path test, further indicate that the proposed model is able to predict the behaviour of that sand with reasonable accuracy for the stress-paths of practical importance.

(4) Because the circular path test is not representative of the stress paths that occur in the sand fills of the Molikpaq structure during either the construction or ice loading phases, the reasons for the poor predictions of this test by the modified SMP model were not investigated herein.

CHAPTER 4

INTERFACE ELEMENTS

4.1 Introduction

The behaviour of the interface between the sand fills used in the core and berm and the Molikpaq steel structure are important aspects that will effect the behaviour of the soil-structure system under load.

In this chapter a brief review of the existing interfaces elements available in the literature is presented. From this review an interface element designated as "thin" element is selected due its simplicity, concept and performance. Next this "thin" element is described together with methods for the evaluation of the soil parameters used in the constitutive laws for the element. Procedures for the implementation of the thin element to 2-D and 3-D F.E. codes, are also described and include the implementation of load shedding techniques for elements that failed in tension or shear. Finally, the performance of the "thin" interface element is assessed by comparing F.E. results with the closed form solutions of a pipe-soil system and with earth pressures measured on a 10 meter retaining wall field study.

4.2 Brief Review of the Existing Interface Elements

A good review on this topic is given by Desai (1981) and Desai et al. (1984) and a brief summary is presented here.

The first interface elements described in the literature are the pin-ended element (Anderson and Dodd, 1966), the spring element (Ngo and Scordelis, 1967) and the zero thickness joint element (Goodman et al., 1968). From these, the one that received most attention and has been

used in F.E. analysis, (Clough and Duncan, 1971) and others, is the interface element proposed by Goodman. This element's formulation is derived on the basis of relative nodal displacements of the solid or structural elements surrounding the interface. Because there is a lack of physical basis for this zero thickness interface element and because it requires a formulation with a special element stiffness matrix, other types of interface elements have been developed since then. Of these elements, the one derived by Desai et al. (1984) was found most desirable due to its simplicity and excellent performance. This element with a finite but thin thickness was designated as a "thin" interface element. This element is described next.

4.3 Description of the "Thin" Interface Element

The "Thin" element is treated essentially like any other solid isoparametric F.E. element, except for a few differences described below. Its behaviour involves a finite thin zone as shown in Fig. 4.1(a) (2-D element) and Fig. 4.1(b) (3-D element).

The two basic differences between the "thin" element and the standard isoparametric solid element are:

(1) The "Thin" element uses an anisotropic constitutive law, where the two moduli used to described its behaviour, normal modulus, E_N, and shear modulus, G, are independent of each other.

The E_N modulus is used to characterize the normal response of the element when subject to compressive loads (bonding mode, i.e. normal stress, $\sigma_N > 0$) or tensile loads (debonding mode, $\sigma_N \leq 0$) as shown in Fig. 4.2. When $\sigma_N > 0$ the E_N modulus is equal to a value that characterizes its

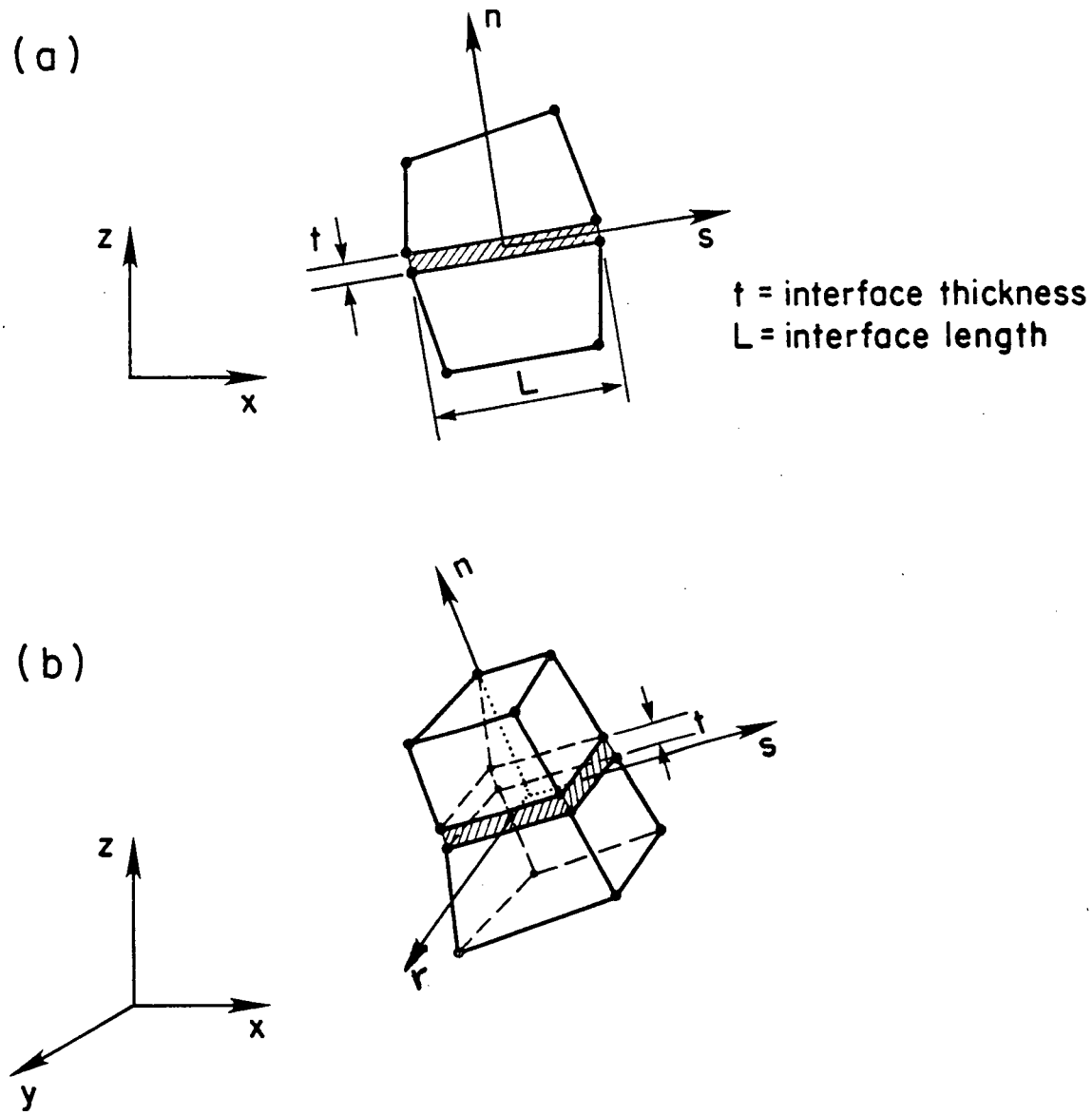

Figure 4.1 "Thin" Interface Element: (a) 2-Dimensional; (b) 3-Dimensional

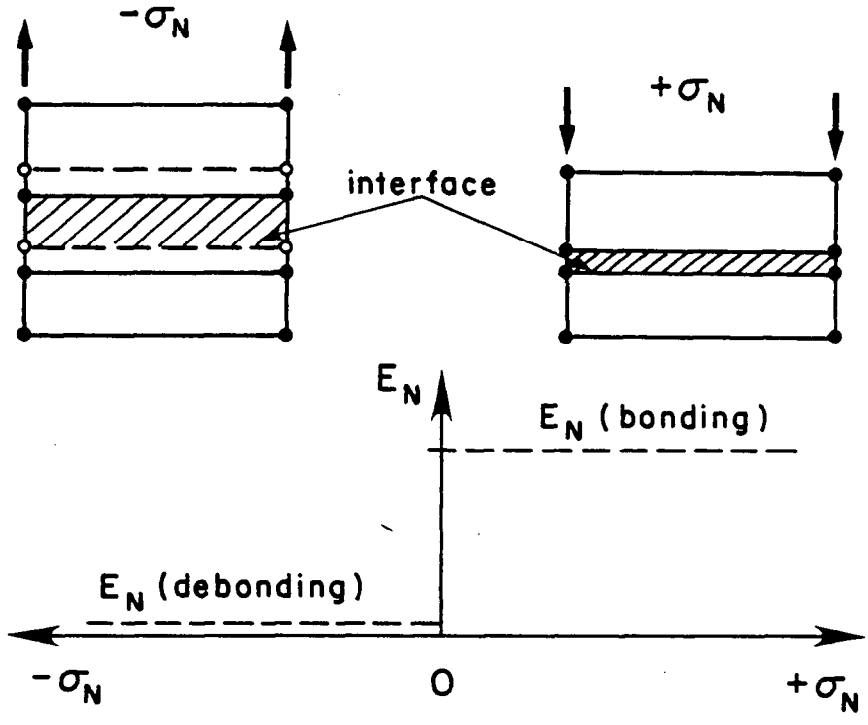

Figure 4.2 Bonding and Debonding Modes

compressive behaviour, and when $\sigma_N \leq 0$ the E_N modulus is equal to a small value in order that the element does not absorb any more tensile stresses during the subsequent load increments.

The G modulus is used to characterize the shear response of the element when subject to shear loads as shown in Fig. 4.3. When the absolute value of the mobilized shear stress, $|\tau_m|$, is smaller than the resistant shear stress, τ_R the element is in a "no slip" mode and the G modulus is equal to a value that characterizes its shear behaviour, and when $|\tau_m| \geq \tau_R$ the element is in slip mode and the G modulus is defaulted to a small value in order that the element does not absorb any more shear stresses during the subsequent load increments. Recommendations concerning the values of the moduli E_N and G and the interface failure parameters angle of friction, δ, and cohesion, C_a, are given later in Section 4.5 of this chapter together with the constitutive models that are generally used in practice.

The advantage of using an uncoupled pair of moduli is that in the case where the interface element fails in shear (slips) the low shear modulus does not also imply a low E_N inferring a tension failure, i.e. the element behaves as cross-anisotropic. If a coupled pair of moduli was used instead the element will behave isotropically, which means that when it fails in shear the element will soften in both shear and axial directions since the moduli E and G are linked this time by the Poisson's ratio, ν.

(2) The other difference from the standard isoparametric solid elements is that the constitutive matrix [D] that relates the strains and stresses of each element, is defined in the local coordinate system (n, r, s) of the

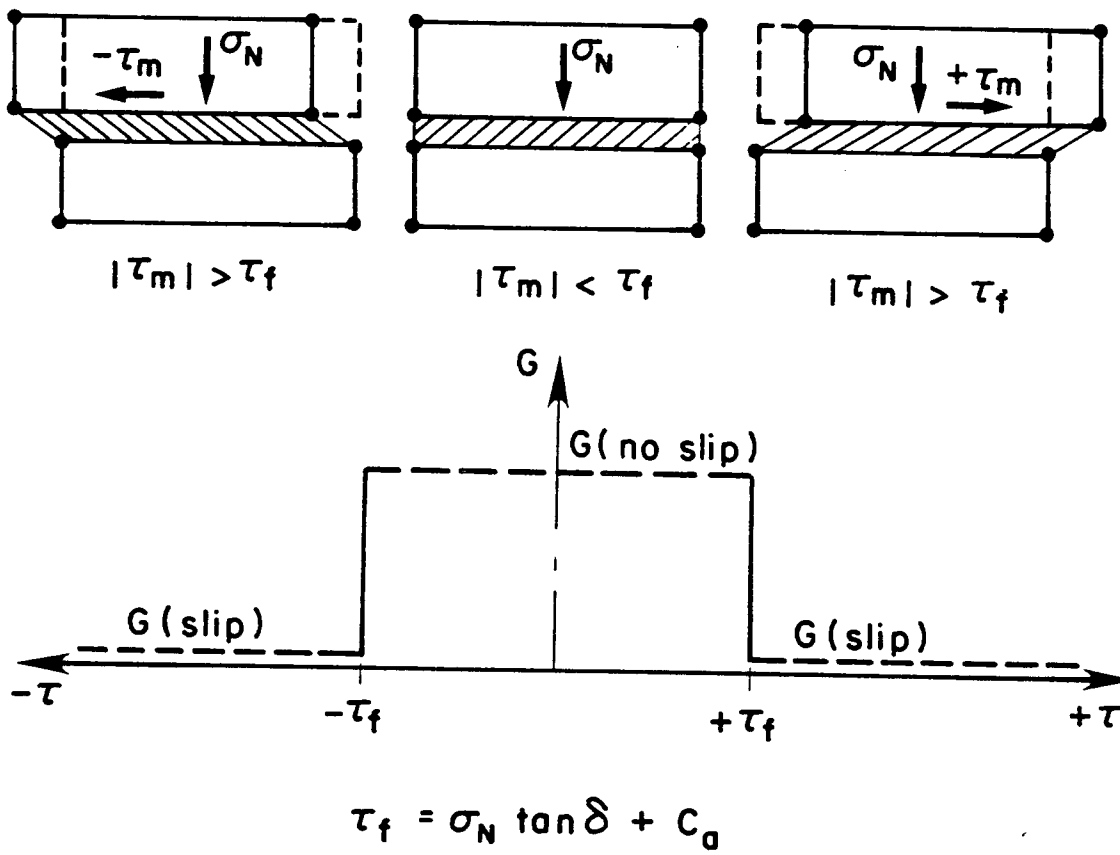

$$\tau_f = \sigma_N \tan\delta + C_a$$

Figure 4.3 Slip and No Slip Modes

element rather than the global coordinate system (x,y,z) used in the standard solid element's formulation (see Fig. 4.1).

4.4 Determination of Soil Parameters: Constitutive Modelling

The soil parameters required to define the characteristic behaviour of the interfaces can be divided into two groups: shear parameters and normal parameters.

• Evaluation of Shear Parameters

For the evaluation of the shear modulus, G, the interface friction angle, δ, and cohesion, C_a, the test most recommended in the literature is the direct shear test. These tests are performed using a standard direct shear machine, where the soil is compacted in the upper half of the shear box and the lower half consists of a specimen of the structure under consideration (steel, concrete, wood, etc.). Several tests are generally carried out at different normal stresses, σ_N, to simulate the expected range of stresses in situ. The measured relative displacements between the upper and lower halves of the shear box are assumed to characterize the shear interface response upon the applied stresses. Other devices also used are the torsion ring shear and the not so common multi-degree-of-freedom shear device (Desai, 1981), where translational and rotational modes can be mobilized.

From the results obtained from the direct shear test the following relationships can be obtained:

a) Shear stress, τ, versus relative displacement, u_r.

b) Failure shear stress τ_f versus normal stress, σ_N.

From relationship (a) the shear modulus, G, can be obtained, and from relationship (b) the strength parameters δ and C_a will be evaluated as described next.

• Evaluation of the Shear Modulus, G

To evaluate the shear modulus, G, the procedures recommended by Clough and Duncan (1971) combined with the procedures recommended by Desai (1984) will be followed.

Clough and Duncan assume that the relationship between the shear stress, τ, and the relative displacement, u_r, is hyperbolic as shown in Fig. 4.4(a) and that the initial tangent stiffness, K_{si}, is given by the following equation:

$$K_{si} = K_I \gamma_w \left(\frac{\sigma_N}{Pa}\right)^n \qquad (4.1)$$

where:

K_I = dimensionless stiffness number

n = stiffness exponent

γ_w = unit weight of water

Pa = atmospheric pressure

To obtain the above terms, several direct shear tests are carried out at different normal stresses and plots of (u_r/τ) versus u_r are developed as shown in Fig. 4.4(b). From these transformed plots, and following steps that are very similar to the steps followed to evaluate the parameters K_E and n used for the standard hyperbolic model (Duncan and Chang, 1970; Duncan et al., 1980), the parameters K_I and n are evaluated.

As for the case of the standard hyperbolic model, the shear behaviour of the interfaces is assumed to be dependent on the stress level, and the tangent stiffness, K_{st}, is given by the following equation:

$$K_{st} = K_{si} \left(1 - \frac{R_f \tau_m}{\tau_f}\right)^2 \qquad (4.2)$$

where:

R_f = failure ratio = τ_f/τ_{ult}

τ_f = failure shear stress = $C_a + \sigma_N \tan \delta$

τ_{ult} = the asymptotic shear stress = inverse of the slope of the transformed plot

τ_m = mobilized shear stress

To evaluate the value of the initial shear modulus G_i the equation proposed by Desai (1984) will be followed:

$$G_i = K_{si} \cdot t \qquad (4.3)$$

where:

t = interface thickness

and the tangent shear modulus, G_t of the interface is given by:

$$G_t = K_{st} \cdot t$$

or

$$G_t = G_i \left(1 - R_f \frac{\tau_m}{\tau_f}\right)^2 \qquad (4.4)$$

Substituting the values of eqs. (4.1) and (4.3) into (4.4)

$$G_t = K_I \gamma_w \cdot t \cdot \left(\frac{\sigma_N}{Pa}\right)^n \left(1 - R_f \frac{\tau_m}{\tau_f}\right)^2$$

and to be consistent with the formulation used in Chapter 2, the tangent shear modulus G_t is given by

$$\boxed{G_t = K_G \, Pa \left(\frac{\sigma_N}{Pa}\right)^n \left(1 - R_f \frac{\tau_m}{\tau_f}\right)^2} \qquad (4.5)$$

where the shear modulus number, K_G is given by the following equation:

$$K_G = K_I(\gamma_w/Pa) \cdot t \qquad (4.6)$$

• Evaluation of Interface Thickness, t

As described by Desai (1984) the quality of simulation of the interface behaviour will depend on a number of factors such as physical and geometric properties of the surrounding media, nonlinear material behaviour and the thickness, t, of the "thin" interace element. If the thickness is too large in comparison with the length, L, of the interface (see Fig. 4.1), the "thin" element will behave essentially as a standard solid element. If it is too small, computational difficulties may arise. The choice of the element thickness, t, is therefore an important issue. Based on parametric studies in which the predictions from various thickness, t,

were compared with direct shear test observations, Desai (1984) concluded that if the ratio t/L is within the range 0.01 to 0.1 than satisfactory agreement between the predicted results and the laboratory measurements was obtained.

• Evaluation of δ and Ca

The values of the interface friction angle, δ, and cohesive, Ca, are easily evaluated from the plot of the failure shear stress, τ_f versus the normal stress σ_N as it is illustrated in Fig. 4.4(c).

• Evaluation of Normal Parameters

Regarding the normal modulus, E_N, the literature is not to clear how to evaluate it. Based on the assumption that the structural and geological media do not overlap at interfaces, generally a high value has been assigned for this modulus. Desai believes, however, that there is no physical ground for such an assumption, which can create numerical instability problems. In reality, the normal properties of the interface must be dependent upon the characteristics of the thin interface zone as well as the state of stress and properties of the surrounding elements. Based on Desai's experience he concludes that satisfactory results can be obtained by assigning the interface normal component the same properties as those of the adjacent soil elements. This concept was followed in this thesis with satisfactory results as will be shown later when the predictions are carried out. Therefore in the formulation, E_N, is considered to be dependent on the normal stress, σ_N, and given by the following equation:

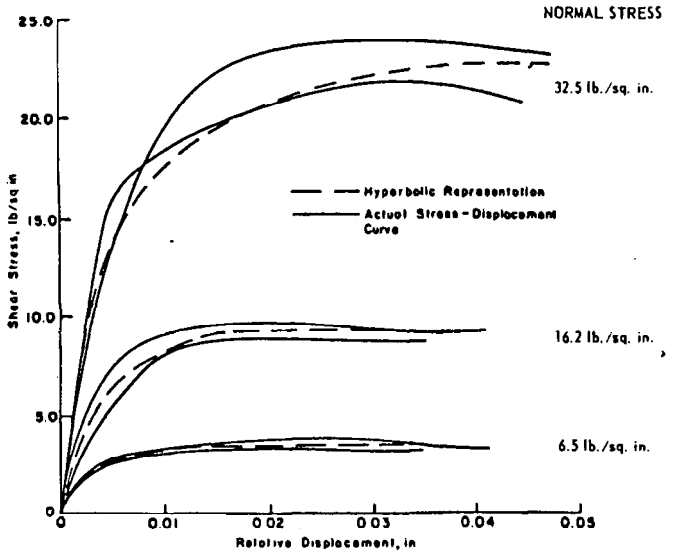

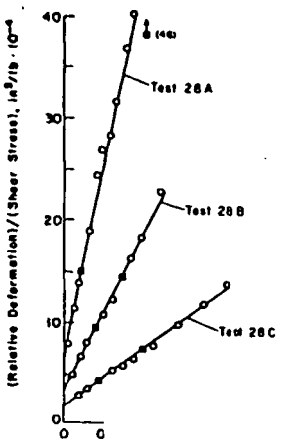

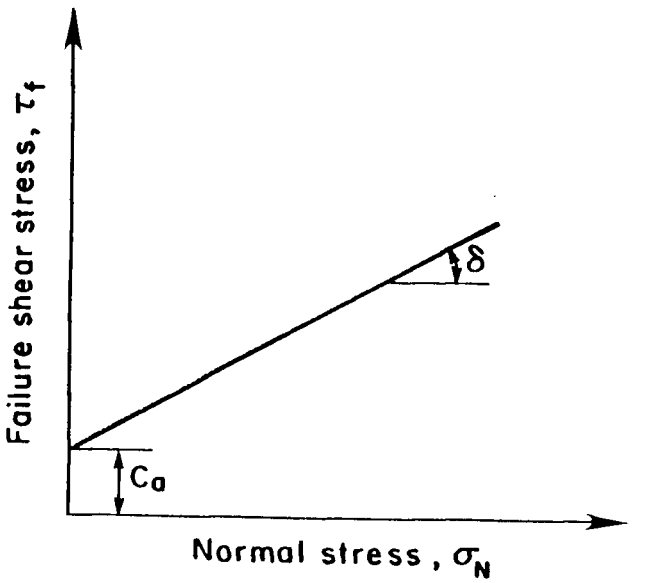

Figure 4.4 (a) Comparison of Hyperbolic and Actual Stress-Displacement data (after Clough and Duncan, 1971); (b) Transformed Linear Hyperbolic Plots for Interface Tests (after Clough and Duncan, 1971); (c) Evaluation of δ and C_a from Direct Shear Tests

$$E_N = K_N \, Pa \, (\frac{\sigma_N}{Pa})^n \qquad (4.7)$$

where:

K_N = normal modulus number, generally taken = K_E (Young's modulus number) of the adjacent material

n = normal modulus exponent, generally equal to the Young's modulus exponent of the adjacent material

4.5 Implementation of the "Thin" Interface Element into the Finite Element Formulation

The "Thin" interface element was implemented in the 3-D and 2-D F.E. formulation codes '3DSLB' and '2DSLB'. The required F.E. formulation is rather simple and is described in detail in Appendix 4.1. A load shedding formulation for the "Thin" element was also developed and implemented into the above two computer codes. The details are presented in Apendix 4.2.

4.6 Performance Studies of the "Thin" Interface Element

4.6.1 Closed Form Solution of a Soil-Pipe System

In order to gain confidence with these formulations, predictions of a closed form solution were made. A closed form solution of a soil-pipe system was developed by Burns and Richards (1964) in their study of "Attenuation of Stresses for Buried Cylinders". A schematic view of the idealized soil-pipe system is shown in Fig. 4.5. The pipe, which is treated as a linear elastic material has a radius of .84 m and is encased in a homogeneous soil which is also linear elastic. The external boundaries are located four radii from the pipe centre as shown. The boundary and loading conditions are also shown in Fig. 4.5. For this soil-pipe

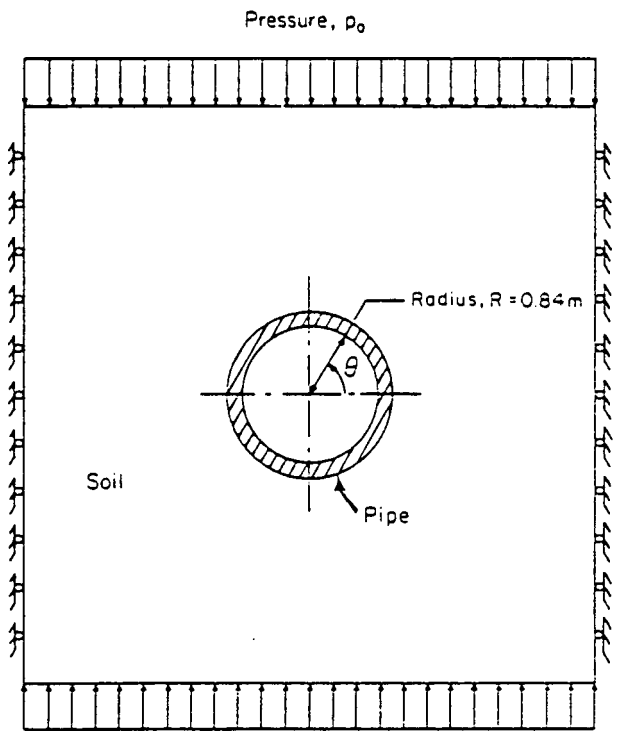

Figure 4.5 Soil Pipe System

system, Burns and Richards developed two closed form solutions correspondent to the two extreme frictional cases: (a) completely bonded; and (b) completely frictionless. The results from these two extreme frictional cases were predicted. Because these two extreme cases are not representative of sandy soils an additional frictional case was also considered: (c) interface friction angle $\delta = 14°$. For this case no closed form solution is available.

Since the problem is plane strain, the 2-D F.E. code 2DSLB was used in the analysis. In addition, and to test the capability of the 3-D interface element, 3-D F.E. analyses were also carried out using the computer code 3DSLB.

The F.E. meshes for both the 2-D and 3-D analysis are shown in Fig. 4.6 together with the soil, interface and pipe properties. To insure that the 3-D analyses were carried out under plane strain conditions the width, b, of the 3-D F.E. mesh was assigned a value b=1 unit length. In addition, movement was restricted in the width direction (see Fig. 4.6(b)). The interface thickness, t, was assumed to be L/10, where L = side length of the interface elements.

The closed form solutions together with the F.E. predictions for both 2-D and 3-D analysis are shown in Fig. 4.7. It may be seen that the predictions obtained are in very good agreement with the closed form solutions for both the bonded and frictionless cases. The 3rd solution where a intermediate friction $\delta = 14°$ was used appear reasonable since both normal and shear pressures are in between the two extreme cases. To note that the 2-D and 3-D results were exactly the same and therefore a degree of confidence is established for the implementation of the "thin" interface element in both the 2-D and 3-D F.E. computer codes.

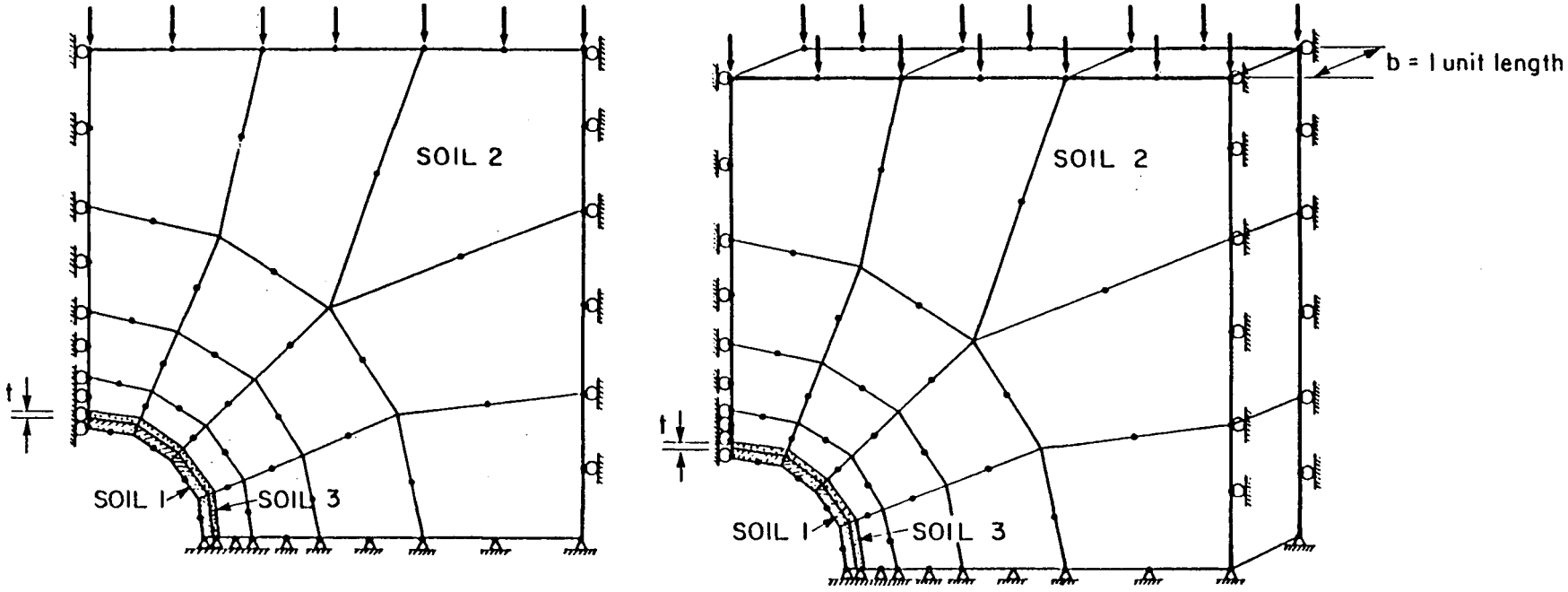

PROPERTIES

SOIL TYPE	MATERIAL	E (kPa)	ν	tanδ
1	Pipe	20.7×10^7	.30	10.0
2	Soil	18×10^3	.33	10.0
3	Interface •Bonded •Frictionless •Friction	18×10^3	.33	10.0 0.0 .25

Figure 4.6 F.E. Meshes and Soil Properties Used for the Soil Pipe Closed Form Solution

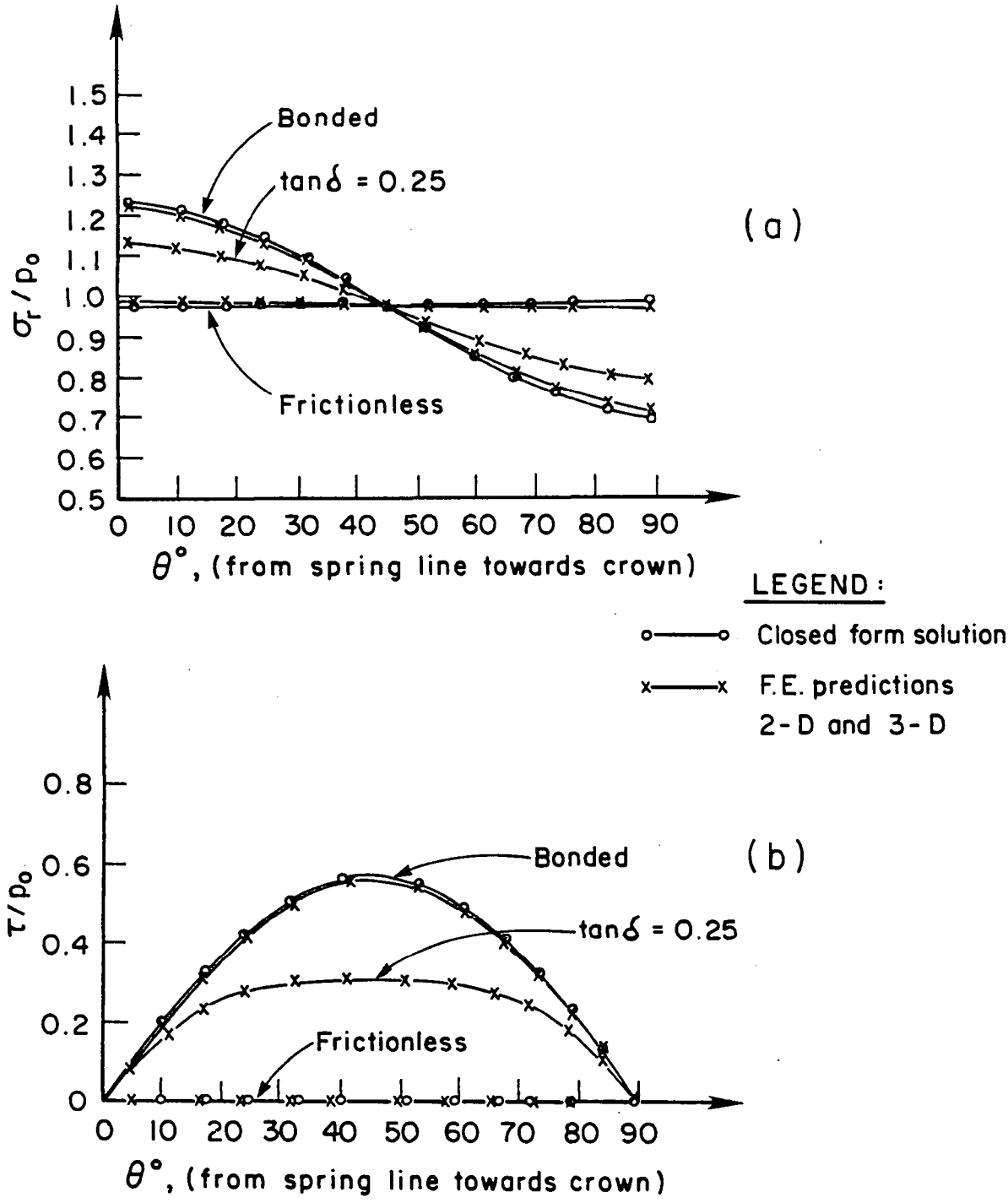

Figure 4.7 Soil Pipe System. Closed Form Solutions and F.E. Predictions 2-D and 3-D: (a) σ_r/po; (b) τ/po

4.6.2 Retaining Wall Study

Introduction

The analyses presented above are of interest because they allowed a check on the performance of the "Thin" element against a closed form solution situation. However that example does not represent the conditions at the interface between the Molikpaq steel structure and its sand fills. Since no measurements of earth pressures were carried out in the structure fill interface during the core placement phase at the Molikpaq's two sites (Tarsiut and Amauligak), the writer looked elsewhere for a case study that could resemble such a situation. The experimental study of earth pressures developed in a 10 m retaining wall carried out by Matsuo et al. (1978) represents a good field case to further test the described "thin" element and at the same time test the performance of the two nonlinear stress-strain models, the hyperbolic (Duncan et al., 1980) and the modified SMP model.

From the results obtained in the field and in the F.E. analysis, discussions will be made regarding the following points: (a) the importance or not of using the "thin" interface element instead of using the standard solid element for this given situation; (b) comparisons between the two nonlinear stress strain models and a third point, (c) assessment of the coefficient of earth pressure K_0, which as will be shown later (Chapter 7) will play an important role in the F.E. predictions of the Molikpaq upon ice loading.

- Description of the Retaining Wall Field Test

A detailed description of the problem is given by Matsuo et al. (1978). herein a brief description is presented.

A schematic section of the retaining wall is shown in Fig. 4.8(a). This wall which is 10 m high and made of concrete is laterally supported by three oil jacks which are installed between the retaining wall and the wall of an adjacent building, and, is bottom supported by a hinge which allows the wall to stay in a state of rest position (vertical position) or to rotate to an active state position (inclined position) as shown in Fig. 4.8(b). To measure the earth pressures mobilized during the above two positions, twenty load cells were employed which were located between the retaining wall and five pressure receiving plates as shown in Fig. 4.8(a). This way the earth pressure was evaluated in detail at five locations.

Three different field tests were carried out using three different types of backfill materials. One using a silty sand backfill and the other two using slags produced from iron manufacture plants. From these three field tests only the first will be analyzed here since in the Molikpaq the fill material used is sand.

• Characteristics of the Silty Sand Fill

The silty sand fill was placed in lifts until a height of 10 m was achieved. The average unit weight of this fill was about 19 kN/m^3 and the water contents ranged between 5% and 8%.

The parameters describing the silty sand fill are given by Matsuo et al. (1978) and are reproduced in Fig. 4.9. It is understood that the strength parameters Ca and δ given in that figure represent the mean values of many data obtained by direct shear tests in which soil samples of 10 cm in diameter with 5.5% to 6.7% in water content and a unit weight of $\approx$ 19 kN/m^3 were used. Unfortunately, laboratory data curves of shear stress versus shear strain were not published by Matsuo and therefore values for

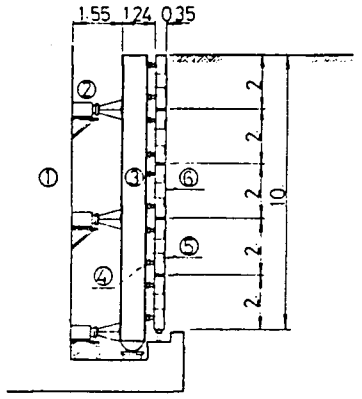

a)

① WALL OF THE EXISTING BUILDING
② OIL JACK
③ RETAINING WALL
④ LOAD CELL
⑤ EARTH PRESSURE CELL
⑥ PRESSURE RECEIVING PLATE

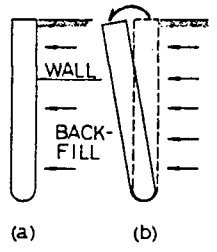

b)

(a) STATE AT REST
(b) ACTIVE STATE

Figure 4.8 Retaining Wall Field Story: (a) Retaining Wall Instrumentation; (b) Wall Positions

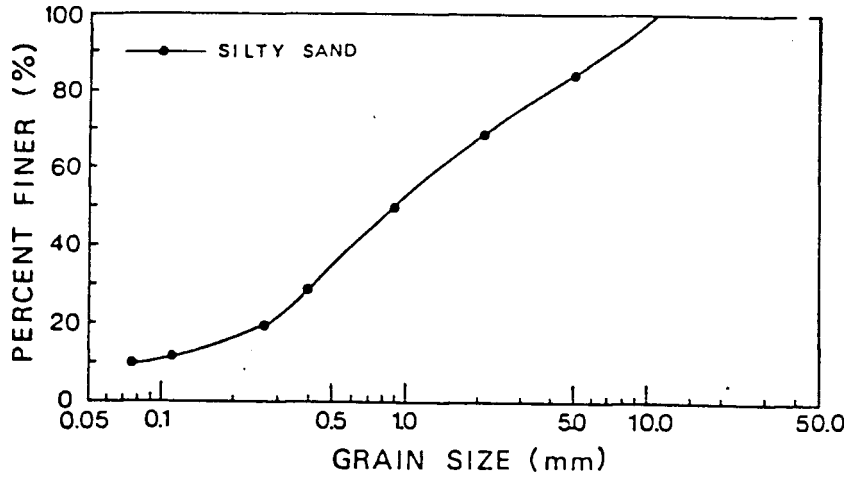

BACKFILL PROPERTIES

	Silty Sand	
G_s	2.69	
$\omega_{opt}(\%)$	11.9	
γ_{dmax} (t/m³)	1.94	
Strength Parameters	C	2.3 (t/m²)
	ϕ	27°

Figure 4.9 (a) Grain Size Distribution of Silty Sand; (b) Index Properties and Strength Parameters of Silty Sand

the moduli used in the F.E. analysis were based on the published work by Byrne et al. (1987) and on the writer's experience on sands with similar characteristics of strength.

• Assessment of the Quality of the Field Measurements

The field measurements of the earth pressures mobilized at the "at-rest" or K_o position and at several inclined positions of the wall are shown in Fig. 4.10(a), where d is the displacement at the top of the wall. The inferred earth pressure coefficients, K, for d = 0, d = 1.6 cm, and d = 8.4 cm, are shown in Fig. 4.10(b). As shown, highest values for K were computed as expected for the "at-rest" position, d=0, and ranged from .74 at a depth of 1.0 m to .28 at a depth of 5.0 m with an average value $(K)_{av}$ = .47. On the other hand, when the wall is rotated and d = 1.6 cm, the K values ranged from .09 at 5.0 m depth to .4 at 9.0 m depth with an average value $(K)_{av}$ = .25. If the wall is further rotated to d = 8.4 cm, the K values further decreased to a $(K)_{av}$ = .11.

The data presented above in Figs. 4.10(a) and (b) show that as the displacement, d, increases the K values decrease as expected. To further assess the quality of the field measurements in Fig. 4.10(c), the plot developed by Matsuo et al. (1978) is shown where the ratio between the earth pressure for different wall rotated positions, p, and the initial earth pressure at rest, p_0, for different depths, is plotted against the displacements inferred for these depths. It may be seen that the active state for the whole backfill was reached for values of d ranging from .3 to .8 cm (or d/H ranging from .003 to .008, where H = 10 m is the wall height). This is in good agreement with the results of tests performed by Terzaghi (1934) which showed that the active conditions on a rough wall was

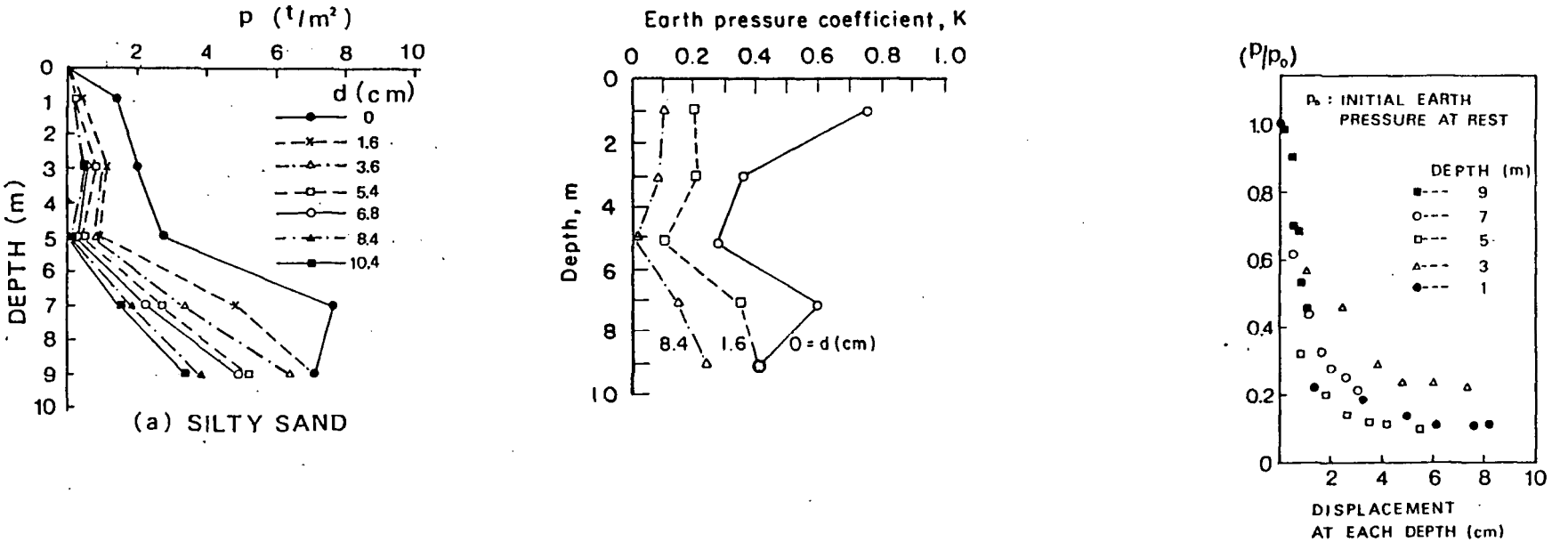

Figure 4.10 (a) Earth Pressure Measurements Versus Depth; (b) Inferred Earth Pressure Coefficient, K versus Depth; (c) Relationship Between P/po and Displacement at Each Depth

reached for a value of d/H = .0014 for dense sand, and a value d/H = .0084 for loose sand.

Now that the measured earth pressures carried out by Matsuo et al. (1978) are considered to be reliable, then F.E. analysis were carried out to assess the reliability of the different F.E. element types and constitutive model types.

• F.E. Analysis

A cross-section showing the geometric conditions at the site is given in Fig. 4.11(a) and the F.E. mesh together with the soil parameters used in the analysis is shown in Fig. 4.11(b).

Three field conditions were analyzed: (a) at rest condition (d/H = 0) and, active conditions (d/H = .0016) and (d/H = .0084).

To analyze these conditions, a simulation of the in situ sequence of construction was carried out by placing the different soil layers shown in Fig. 4.11 in 10 layers and following the analytical procedures described by Byrne and Duncan (1979). During the construction sequence the nodes located on the wall were not allowed to move in the horizontal direction. At the end of the construction phase the stresses obtained were stored and used as initial streses for the active phase were this time those nodes were allowed to move in both horizontal and vertical directions being only constrained by the movements of the stiffer beam member used to represent the wall.

Each of the above conditions was analyzed with different sets of element types and constitutive law types. In all, three F.E. studies were carried out. These are described below:

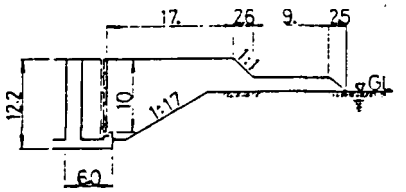

a)

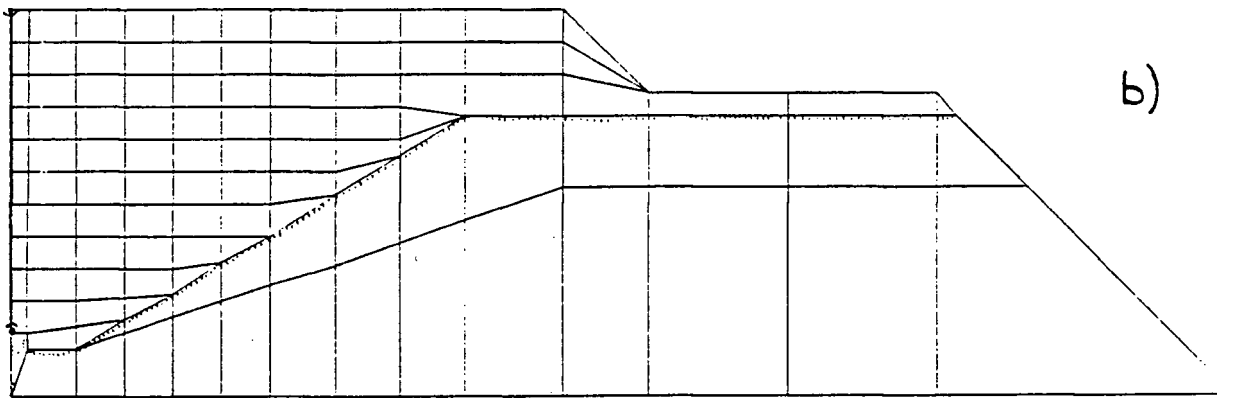

b)

HYPERBOLIC MODEL			MODIFIED SMP MODEL			INTERFACE MODEL	
SOIL PARAMETER	BACKFILL	FOUNDATION	SOIL PARAMETER	BACKFILL	FOUNDATION	SOIL PARAMETER	INTERFACE MATERIAL
K_E; n	400; .5	1500 ; .5	K_{Ge}; n	410; .5	1540; .50	K_N; n	400; .50
K_B; m	240; .25	900; .25	K_{Be}; m	600; .25	2250; .25	K_G; n	165; .50
--	--	--	K_{Gp}; np	270; .5	1030; -.50	--	--
R_F	.8	.7	R_F	.9	.9	R_F	0.0
ϕ_1	27°	40°	$(\tau_{SMP}/\sigma_{SMP})_1$	.48	.79	δ	27°
$\Delta\phi$	0	0	$\Delta(\tau_{SMP}/\sigma_{SMP})$	0.0	.0	--	--
c (kPa)	22.6	.0	c (kPa)	21.3	.0	C_a (kPa)	22.6
K_o	1.0	.4	K_o	1.0	.4	K_o	1.0
--	--	--	μ	.25	.25	--	--
--	--	--	λ	1.0	1.0	--	--

Figure 4.11 (a) Cross Section Illustrating Retaining Wall and Backfill; (b) Finite Element Mesh and Soil Properties Used in the Analysis

In the first study, the wall soil interface was represented by the "thin" interface element using an elastic perfect plastic model and the backfill soil represented by standard solid elements using the hyperbolic model. In the second analysis both interface and backfill were represented by standard solid elements using the modified SMP model and in the third analysis both interface and backfill were represented by standard solid elements, this time using the hyperbolic model.

It should be noted that the modified SMP model's formulation was expanded with an additional parameter, the cohesion, c, in order that the strength of the backfill material was properly characterized in the analysis using this model. The details are given in Appendix 4.3.

• F.E. Results

The results obtained in the F.E. analyses are given in Figs. 4.12 to 4.14 together with the field measurements observed by Matsuo and his co-workers. From the comparisons between the field measurements and the F.E. predictions the following conclusions are made:

(1) All the combination of element types and constitutive model types give an almost identical earth pressure distribution for the "at-rest" condition (see Fig. 4.12). These results are considered to be in agreement with the field measurements with the exception of the "at-rest" earth pressures computed at the depths of 5 and 7 m where the field measurements are overestimated and underestimated respectively by approximately 15 kPa.

(2) The F.E. results obtained for the active conditions (see fig. 4.13 and 4.14) are shown to be in agreement with the field measurements, especially the earth pressures computed by the modified SMP model.

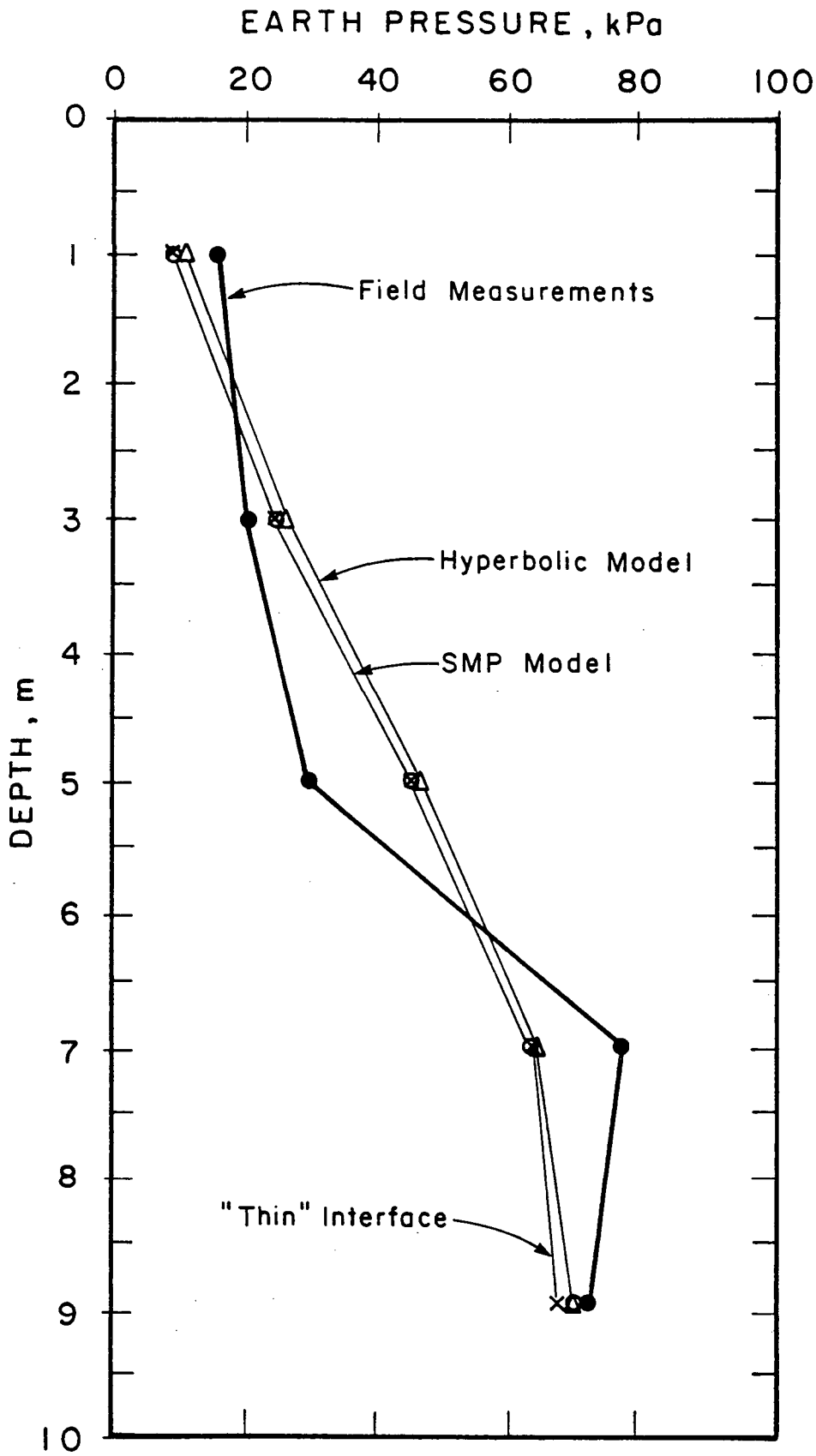

Figure 4.12 Comparison Between Earth Pressure Measurements and F.E. Predictions: At Rest Condition, d = 0.0 cm.

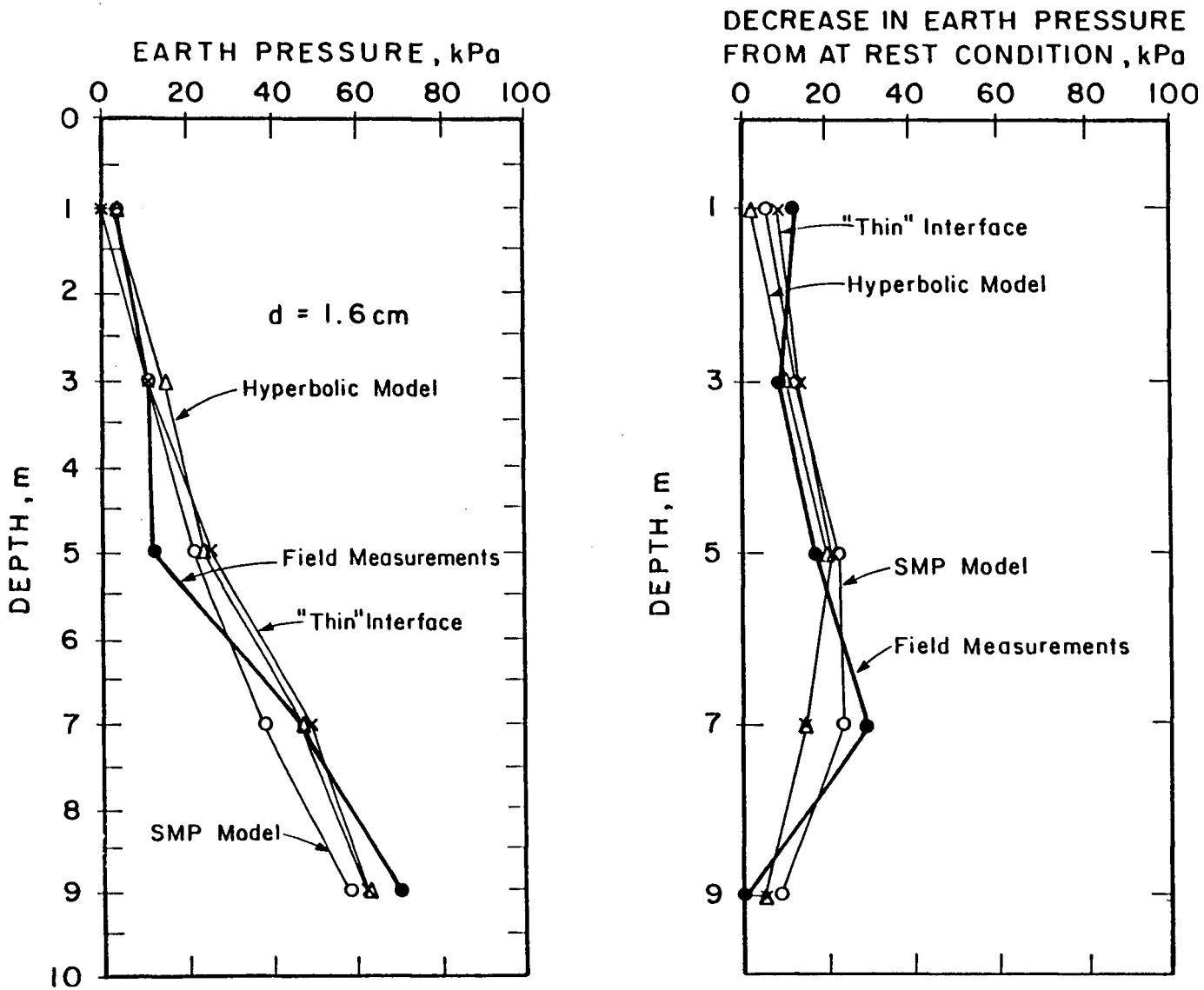

Figure 4.13 Comparison Between Earth Pressure Measurements and F.E. Predictions: Active Condition, d = 1.6 cm.

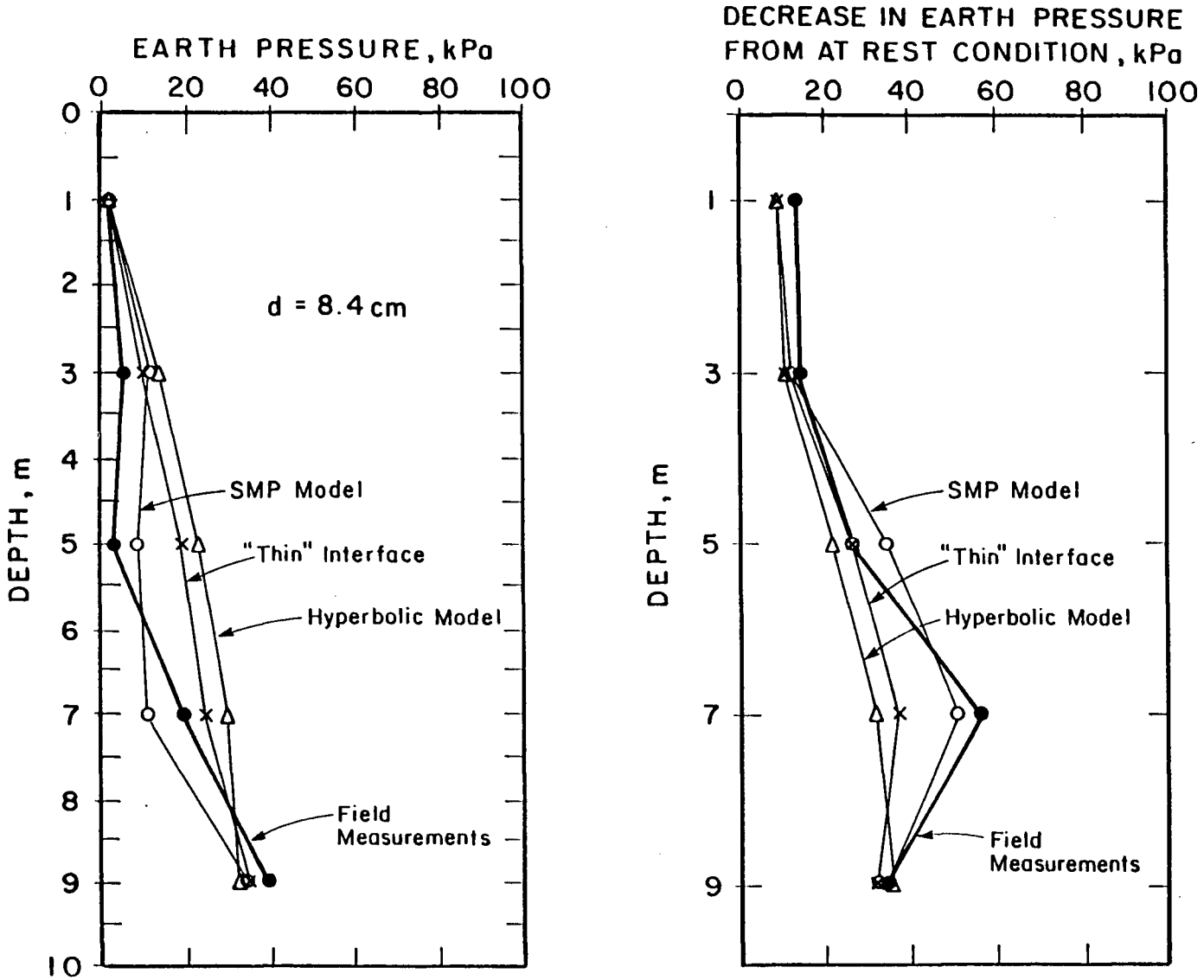

Figure 4.14 Comparison Between Earth Pressure Measurements and F.E. Predictions: Active Condition, d = 8.4 cm

(3) From this particular case study it seems that standard solid elements when used with adequate stress-strain constitutive laws are adequate to model interface behaviour and there is no the need for a "thin" interface type of element.

• F.E. Parametric Studies Carried Out by Others (Influence of δ)

It was the intention of the writer to carry out F.E. analysis where the angle δ would vary from $\delta=0$ (smooth wall) to $\delta=\phi$ (rough wall) to show its importance, but such study has been done by Clough and Duncan (1971) and herein only a brief description of their study together with their main conclusions is presented instead. Their analytical study comprised a 10 foot retaining wall. The interface between the wall and the soil backfill was represented by the zero thickness element proposed by Goodman, following the hyperbolic model described in section 4.4. The soil properties used in the analysis together with the results obtained are reproduced in Fig. 4.15. It may be seen that the variation of δ from a smooth wall condition ($\delta = 0$) to a rough wall condition ($\delta = \phi$) makes little difference in the results. The results obtained by Clough and Duncan (1971) show that the active condition was reached over the entire height of the backfill when the outward movement at the top, d, has become equal to .0023 H which is also in good agreement with the results of tests performed by Terzaghi (1934) for a medium dense sand. Their results also show that the initial assumed value of the coefficient of earth pressure K_o = .43 decreases considerably as the wall moves away from the backfill. Average K values of .25 to .28 can be inferred, using the equation presented below, from their results when d/H = .0023.

Backfill (1)	Parameter (2)	Symbol (3)	Value (4)
Medium-dense sand backfill	Unit weight, in pounds per cubic foot	γ	100
	Coefficient of earth pressure at rest	K_o	0.43
	Cohesion intercept, in pounds per square foot	c	0
	Friction angle in degrees	ϕ	35
	Primary loading modulus number	K	720
	Unloading-reloading modulus number	K_{ur}	900
	Modulus exponent	n	0.5
	Failure ratio	R_f	0.8
	Poisson's ratio	ν	0.3
Wall-backfill interface	Friction angle in degrees	δ	Varies
	Stiffness number	K_I	Varies
	Stiffness exponent	n	Varies
	Failure ratio	R_f	Varies
Base-backfill interface	Friction angle in degrees	δ	24
	Stiffness number	K_I	75,000
	Stiffness exponent	n	0.5
	Failure ratio	R_f	0.9

Properties Used by Clough and Duncan (1971)

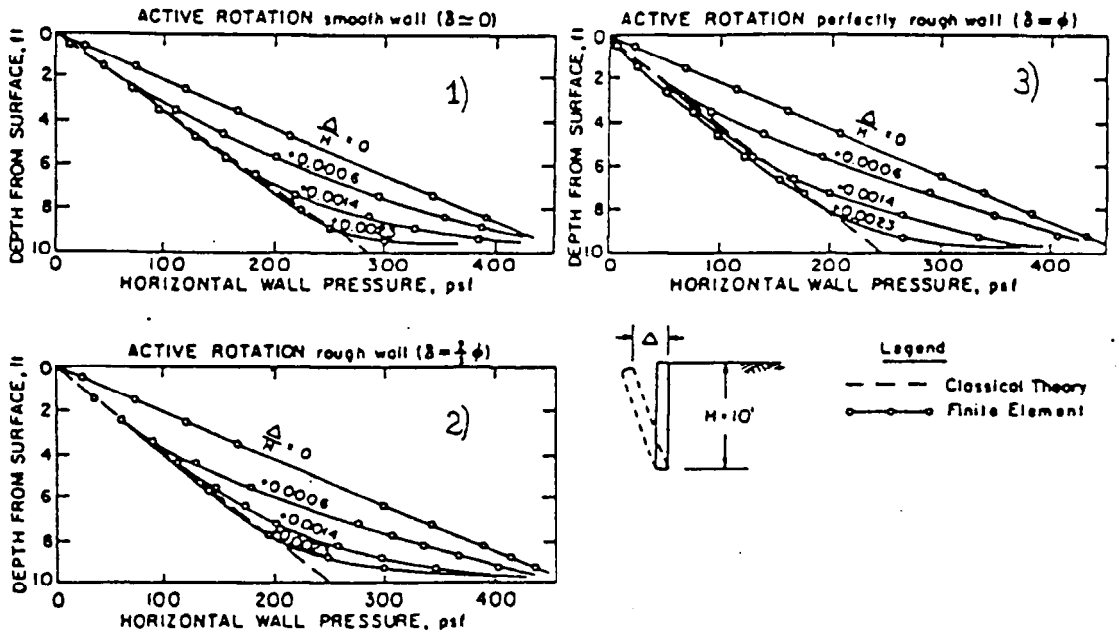

1) That the interface was smooth. For this analysis δ=0.1°, K_I=1.0, n=0.0, and R_f=1.0
2) That the wall-friction angle was 2/3 of ϕ. For this analysis δ=24°, K_I=40,000, n=1.0, and R_f=0.9
3) That the wall-friction angle was equal to ϕ. For this analysis δ=35°, K_I=75,000, n=1.0, and R_f=0.9

Figure 4.15 Variation of Horizontal Wall Pressure Distribution with Wall Movement and Interface Friction Angle, δ (after Clough and Duncan, 1971)

$$K = \frac{\sigma_H}{\sigma_{H_0}} K_0 \qquad (4.22)$$

where:

K_0 = earth pressure coefficient at rest (= .43)

σ_{H_0} = horizontal wall pressure for d = 0

σ_H = horizontal wall pressure for d > 0

Similar K values were recorded by Matsuo et al. as was described previously.

4.7 Conclusions

From the material presented in this Chapter, the following can be concluded:

(1) The F.E. results show that an excellent agreement with the closed form solutions of a soil-pipe system developed by Burns and Richards (1964) is obtained when the "thin" element is used in both the 2-D and 3-D F.E. analysis (plane strain conditions).

(2) The field measurements carried out by Matsuo et al. (1978) and the F.E. predictions carried out by the writer, are in good agreement with the results of tests performed by Terzaghi (1934) and with the analytical work carried out by Clough and Duncan (1971). The field measurements show that the coefficient of earth pressure at rest, K_0 varies from a maximum K_0 = .74 at 1.0 m depth to a minimum K_0 = .28 at 5.0 m depth. If the wall is allowed to rotate away from the backfill then the coefficient of earth pressure, K, decreases considerably to

an average $(K)_{av}$ = .11 which corresponds to a movement of the top of the wall of 8.4 cm or .84% of the wall height.

(3) F.E. studies carried out by Clough and Duncan (1971) show that the predicted earth pressures on a 10 ft. retaining wall are only slightly affected by the interference friction angle δ when it varies from a smooth wall conditions (δ=0) to a rough wall condition (δ=ϕ).

(4) F.E. predictions of the earth pressures measured on a 10 m retaining wall by Matsuo et al. (1978) show that adequate results are obtained using standard solid elements with an appropriate stress-strain models, such as the hyperbolic model (Duncan et al., 1980) or the modified SMP model both expanded with load shedding capabilities. There is no need for a special interface element.

CHAPTER 5

EVALUATION OF SOIL PARAMETERS FROM THE PRESSUREMETER TEST IN SAND

5.1 Introduction

Analytical predictions of the response of sand masses to applied loads requires a suitable stress-strain law whose parameters are adequately defined. While these parameters can be determined from laboratory tests on sand samples it is very difficult to recover and test undisturbed samples and determine meaningful parameters for in situ conditions. Due to the above, any time the Molikpaq structure is deployed at a new site, extensive in situ testing is carried out in the hydraulically placed core and berm fills.

The Self-Boring Pressuremeter (SBP) Test is one of the in situ tests that was performed at the Amaulikpaq I-65 site to evaluate soil parameters representative of the sand fill. However, because the stress field induced by the SBP is not homogeneous, a rational analysis and interpretation of the SBP test requires that it be analyzed using selected stress-strain relations. In addition, it is important that such analysis and interpretation be checked against experimental data under controlled conditions before application to in situ field conditions.

This chapter is concerned with the evaluation of soil parameters from the SBP test in sand, and is subdivided in the following two sections:

a) Evaluation of the maximum shear modulus, G_{max} from the unload-reload loop of the pressuremeter test.

b) Evaluation of soil parameters from the first time loading part of the pressuremeter test.

These two topics are briefly discussed below.

- Evaluation of G_{max}

One of the soil parameters that can be derived from the SBP is the equivalent elastic unload shear modulus, G*, which is obtained from the slope of the unload-reload pressuremeter loop as shown in Figure 5.1. G*, however, is not equal to the maximum shear modulus, $G_{max,o}$ at the original stress due to expansion of the pressuremeter as well as high shear strains close to the face of the pressuremeter. $G_{max,o}$ is a fundamental soil parameter that is essential for dynamic analysis of soil structures and is also one of the elastic parameters used in the modified SMP model. Previous researchers (Robertson (1982); Robertson and Hughes (1986); and Belloti et al. (1989)) have proposed methods for correcting the measured G* to obtain $G_{max,o}$ based upon an average stress and strain in the plastic zone. In the first part of this chapter a more detailed analysis considering the complete variation in the stress and strain state is presented. The method considers both the stress and void ratio changes induced by pressuremeter loading and the nonlinear stress-strain response upon unloading. The results are presented in the form of a chart that allow $G_{max,o}$ to be determined from the equivalent elastic unload modulus, G*, for a wide range of loading and unloading conditions. The analysis procedure is checked with laboratory and field data and the results are found to be in good agreement provided factors to account for disturbance and anisotropy are considered.

- Evaluation of Soil Parameters from the First Time Loading Part of the Pressuremeter Test

The evaluation of soil parameters from the first time loading part of the pressuremeter tests in sand have been restricted for many years to the

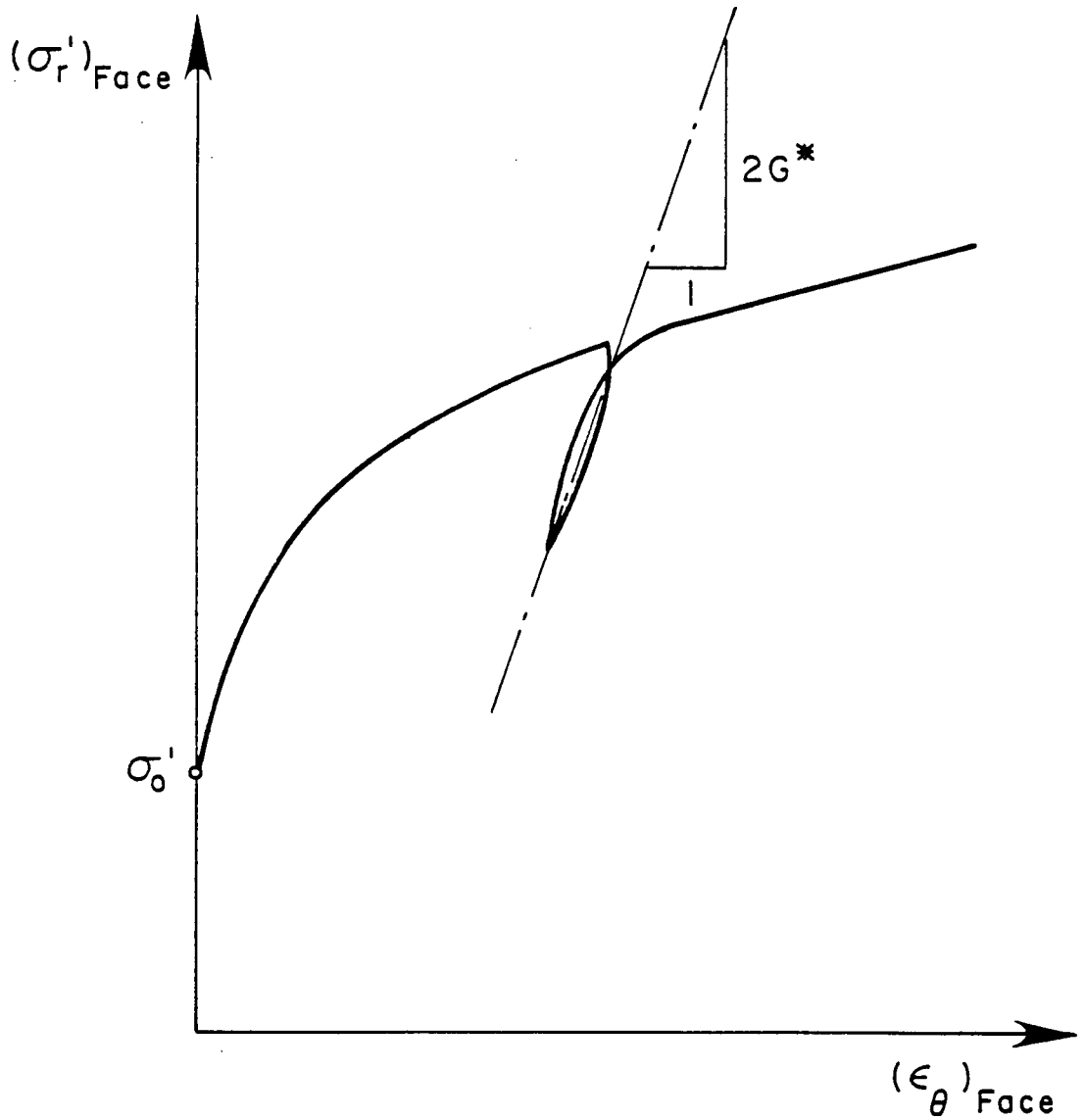

Figure 5.1 Pressuremeter Unload Modulus, G*.

evaluation of the peak friction angle ϕ_p and the dilation angle ν. Ladanyi (1963), Vesic (1972), Wroth and Windle (1975), Hughes et al. (1977), Robertson (1982), and Robertson and Hughes (1986), proposed procedures to determine ϕ_p by assuming that the sand around the pressuremeter behaves as a plane strain linear elastic-perfect plastic material. The main differences between these methods is the way that volume changes due to shear are taken into account. Only recently, Manassero (1989) proposed a method that allows the complete plane strain nonlinear stress and volume change response of sand to be obtained from pressuremeter pressure-expansion data. This method can be used to determine parameters for the proposed stress-strain model as will be discussed later in this chapter.

5.2 Evaluation of the Maximum Shear Modulus for Sand From the Unload Shear Modulus Obtained from Pressuremeter Tests

The shear modulus G* obtained from the pressuremeter test is unlikely to be equal to the maximum shear modulus G_{max} because of the stress and strain changes caused by the pressuremeter. An analysis procedure for correcting the measured G* to G_{max} is presented herein. The method is based upon an elastic-plastic analysis of the pressuremeter domain to determine the stresses in the domain prior to unloading, and a nonlinear elastic analysis to determine the displacement at the pressuremeter face upon unloading, which in turn is used to compute the equivalent pressuremeter shear modulus, G*. By comparing the computed G* with G_{max} for various levels of applied radial stress prior to unloading, and for various amounts of unload, a chart is generated from which G^*/G_{max} can be obtained depending on the applied pressuremeter loading conditions.

Because the stress-strain relations used to model the behaviour of sand during unloading are an important factor in the analysis these are described prior to presenting the analysis and results.

5.2.1 Assumed Stress-Strain Relations for Sand Upon Unloading

Upon unloading it is assumed that the initial shear modulus is the maximum shear modulus, G_{max}, and that the unloading curve is nonlinear and hyperbolic. Justification for these assumptions is presented in Fig. 5.2 and 5.3 from Byrne et al. (1987) based on triaxial tests by Negussey (1984). Figure 5.2 shows that the Young's modulus upon unloading is nonlinear with strain, and Fig. 5.3 shows that the initial unload modulus is equal to the maximum modulus obtained from resonant column tests. Since the Young modulus, E and the shear modulus, G are related through the Poisson's ratio, ν, it is reasonable to assume the same behaviour for the shear modulus.

The above indicates that the observed unload response of the pressuremeter can yield the in situ $G_{max,o}$ value if appropriate modifications for stress and strain levels are applied as discussed below.

- G_{max} and Stress Level

Hardin (1978) proposed that G_{max} for sand can be expressed as follows:

$$G_{max} = A \cdot F(e) \cdot Pa \cdot (\sigma'_m/Pa)^{0.5} \qquad (5.1)$$

where:

σ'_m = $1/3(\sigma'_1+\sigma'_2+\sigma'_3)$ = the mean effective stress

Pa = atmostpheric pressure

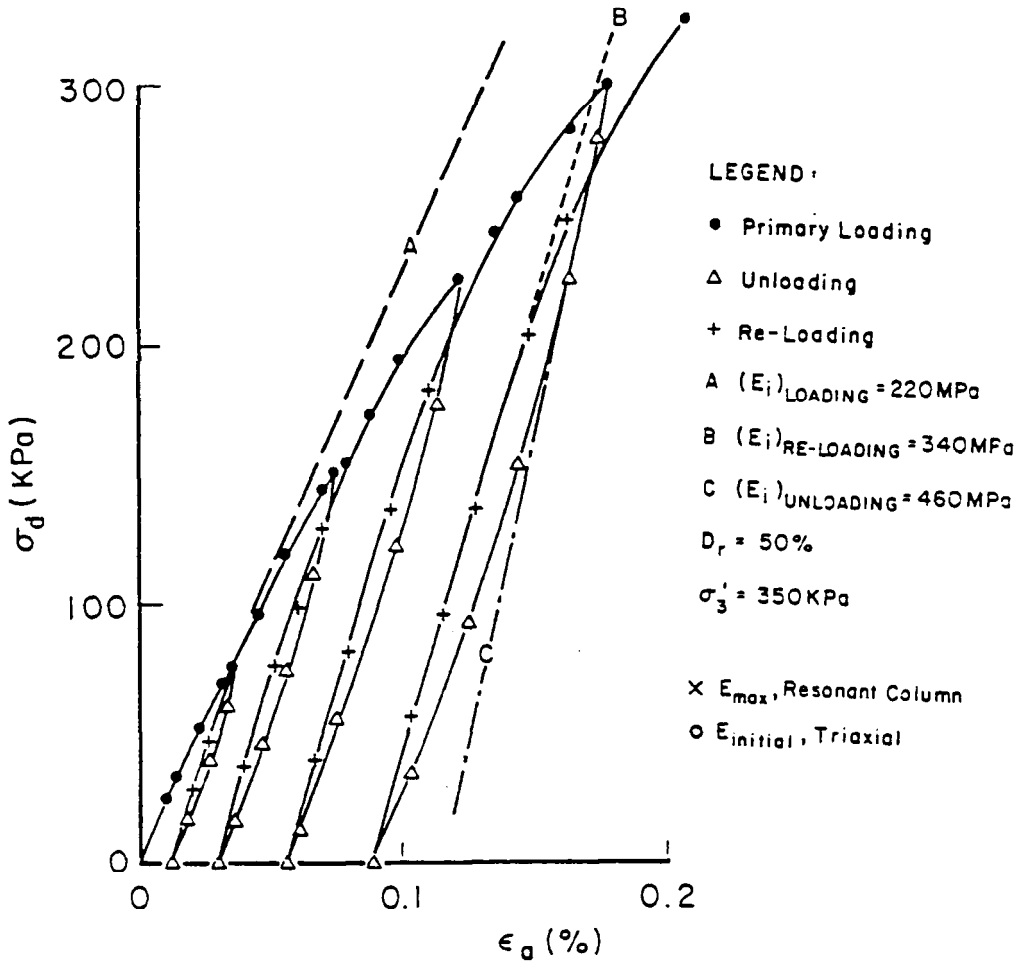

Figure 5.2 Loading and Unloading in a Conventional Triaxial Path (After Negussey, 1984)

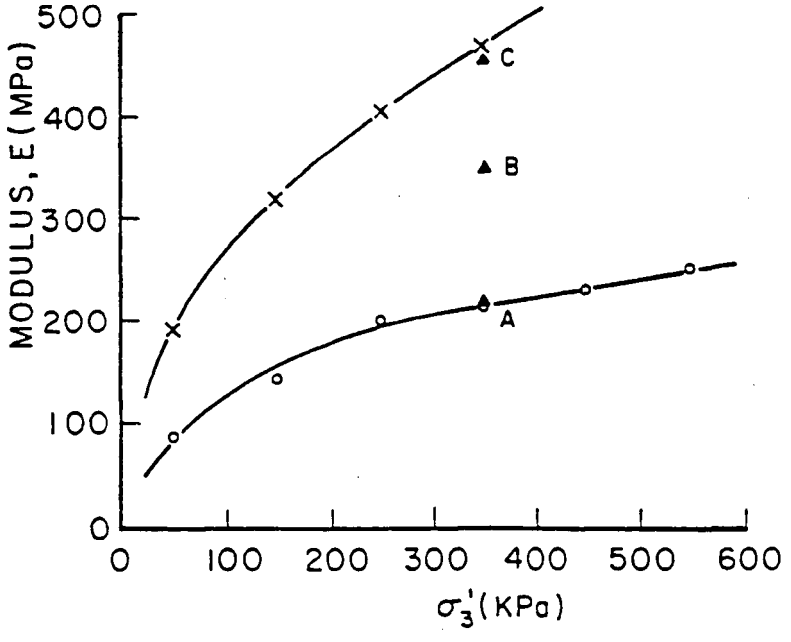

Figure 5.3 Comparison Between E_{max} and Various Initial Modulis E_i (After Negussey, 1984)

and the parameters A and F(e) depend on particle shape and void ratio, e, as follows:

$$\left.\begin{aligned} F(e) &= (2.17-e)^2/(1+e) \\ A &= 700 \end{aligned}\right\} \text{Rounded sand} \qquad (5.2)$$

$$\left.\begin{aligned} F(e) &= (2.97-e)^2/(1+e) \\ A &= 326 \end{aligned}\right\} \text{Angular sand} \qquad (5.3)$$

Hardin and Black (1966) and Hardin (1978) concluded that G_{max} was independent of deviator stress or stress ratio level depending only on σ'_m. However, more recent test data presented by Yu and Richart (1984) indicates that G_{max} depends on an average effective stress, σ'_{av} that is somewhat different to σ'_m. In addition, G_{max}, also depends on the stress ratio, σ'_1/σ'_3. Their proposed equation is:

$$G_{max} = A \cdot F(e) \cdot Pa \cdot (\sigma'_{av}/Pa)^{0.5} \ (1-0.3k_n^{1.5}) \qquad (5.4)$$

where:

$\sigma'_{av} = (\sigma'_a + \sigma'_p)/2$

σ'_a = the normal effective stress in direction of wave propagation

σ'_p = the normal effective stress in direction of particle vibration

and

$$k_n = (\sigma'_1/\sigma'_3-1)/((\sigma_1/\sigma_3)_{max}-1) \qquad (5.5)$$

where:

$(\sigma'_1/\sigma'_3)_{max}$ is the failure stress ratio.

In the above eq. (5.4) σ'_{av} may also be considered as the average effective stress in the plane in which the strains are induced and therefore in the pressuremeter analysis carried out herein $\sigma'_{av} = (\sigma'_r+\sigma'_\theta)/2$ in which σ'_r and σ'_θ are the effective radial and circumferential stresses.

Equation (5.4) is in good agreement with the results of resonant column tests as shown in Fig. 5.4. It indicates that for a given sand at a given void ratio, e, the maximum shear modulus, G_{max} will increase with increased average effective stress, σ'_{av}, but will decrease with increased stress ratio, σ'_1/σ'_3. There will be a 30 percent reduction in G_{max} in zones where the stress ratio is a maximum, i.e. where the strength of the sand is fully mobilized.

Upon unloading, the sand is assumed to respond in a nonlinear elastic manner as shown in Fig. (5.5). In the analysis the unload stress-strain curve is assumed to be hyperbolic with the secant and tangent shear modulus given by:

$$G_s = G_{max} (1 - SL) \tag{5.6}$$

$$G_t = G_{max} (1 - SL)^2 \tag{5.7}$$

where:

G_{max} = the maximum shear modulus, obtained from eq. (5.4)

SL = the stress level, which is given by:

$$SL = (\tau_L - \tau)/(\tau_L + \tau_f) \tag{5.8}$$

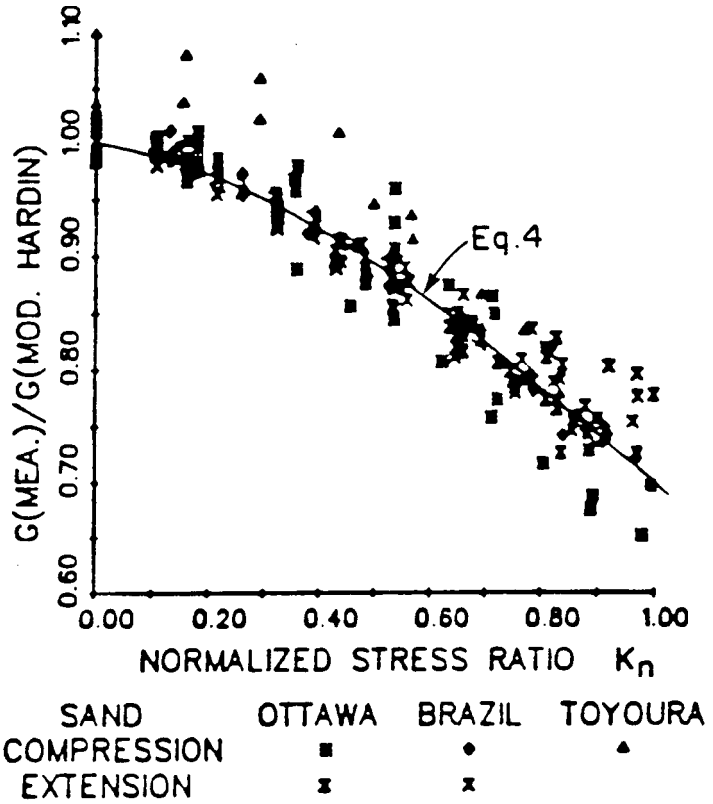

Figure 5.4 Measured and Computed G_{max} Values. (After Yu and Richart, 1984).

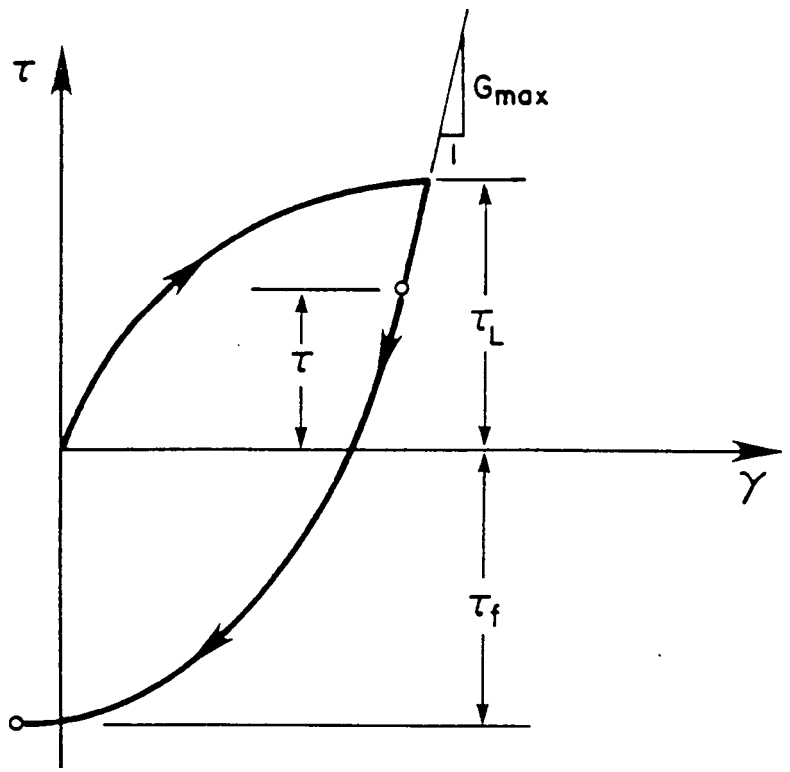

Figure 5.5 Assumed Unload Stress-Strain Behaviour.

where:

τ_L = the shear stress prior to unloading

τ = the current shear stress

τ_f = the shear stress at failure

These shear stresses are shown in Fig. 5.5.

The secant shear modulus, G_s as defined by eq. (5.6) implies a modulus reduction with stress or strain level as shown in Fig. 5.6. The computed values of modulus reduction from the stress-strain unload-reload loops of Fig. 5.2 are also shown in Fig. 5.6 and are in reasonable agreement with eq. (5.6). Also shown in the figure are the average upper and lower bounds described by Seed et al. (1986). It may be seen that the equation chosen lies within the bounds specified by Seed et al.

5.2.2 Analysis Procedure

A brief description of the procedures followed in the analysis is presented below.

A sketch of the pressuremeter loading and unloading phases is shown in Fig. 5.7. These two different phases are treated in the analysis as two separate cases as is described next.

From point A to point C the pressuremeter is loading and at point C the stresses mobilized in the sand domain prior to unloading are computed herein using available closed form solutions.

From point C to point D the pressuremeter is unloading. A finite element axisymmetric plain strain analysis was used herein to evaluate the inward movement, u, of the pressuremeter face at point D.

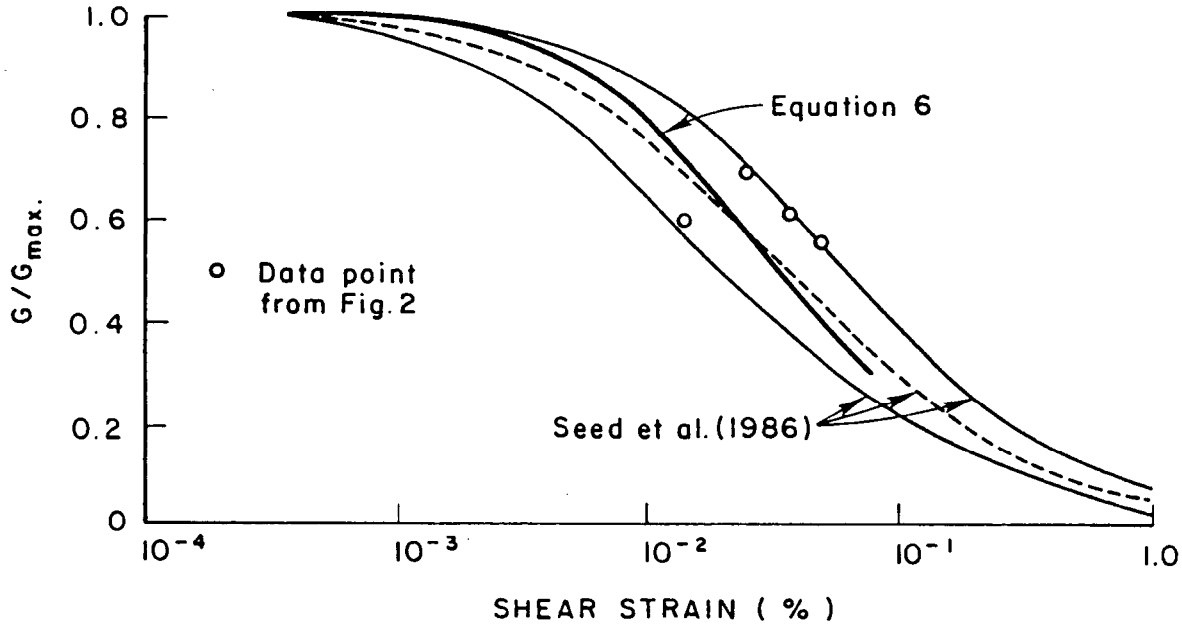

Figure 5.6 G/G_{max} Versus Shear Strain.

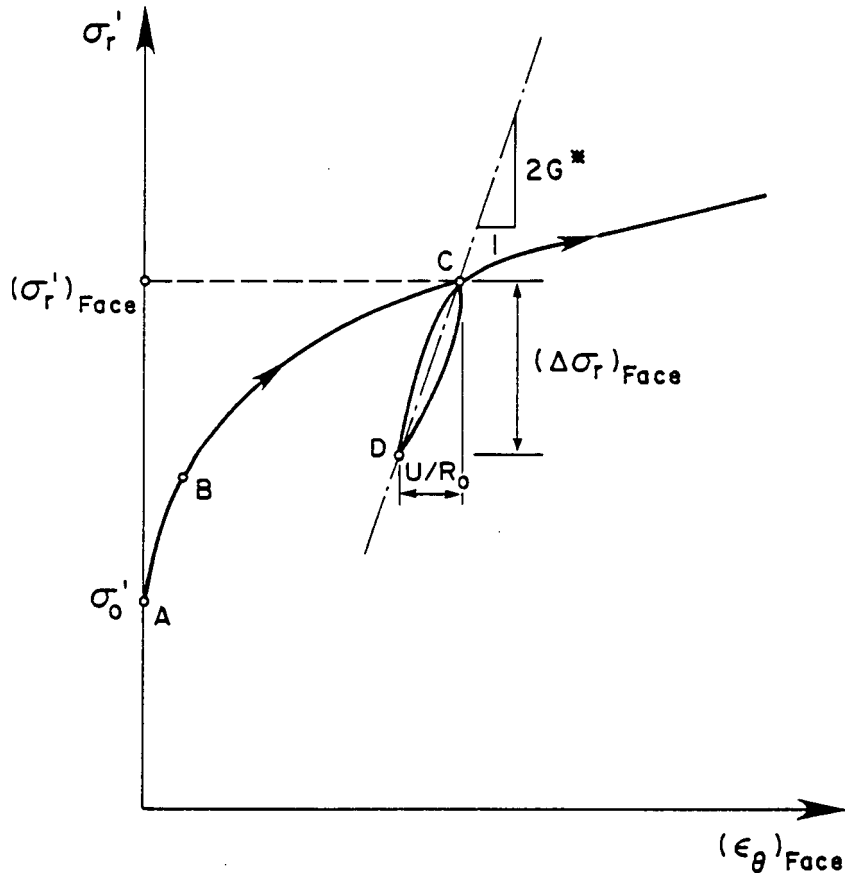

Figure 5.7 Sketch of the Loading and Unloading Response of the Pressuremeter.

Assuming that the soil behaves elastically during unloading, the pressuremeter unload shear modulus, G*, is evaluated using the following equation:

$$G^* = (\Delta\sigma_r)_{face}/((2 \cdot u)/R_o) \qquad (5.9)$$

where:

$(\Delta\sigma_r)_{face}$ = the decrease in pressure at the pressuremeter face from point C to point D.

R_o = the initial pressuremeter radius

By comparing the computed G* with the in situ maximum shear modulus, $G_{max,o}$, for various levels of applied radial stress prior to unloading and for various amounts of unload, a chart is generated from which $G^*/G_{max,o}$ can be obtained depending on the applied pressuremeter loading conditions.

A detailed description of the procedures followed in the analysis for the loading and unloading phases is presented next.

5.2.2.1 Loading Phase

Prior to loading, at point A (see Fig. 5.7) the in situ maximum shear modulus $G_{max,o}$ is evaluated using eq. (5.4). Since $\sigma_r' = \sigma_\theta' = \sigma_o'$, i.e., $\sigma_1'/\sigma_3' = 1$ (in the horizontal plane), it follows that:

$$G_{max,o} = A \cdot F(e) \cdot Pa\ (\sigma_o'/Pa)^{0.5} \qquad (5.10)$$

During loading the stresses in the sand domain change as shown in Fig. 5.8. Initially the radial stress σ_r' increases while the circumferential

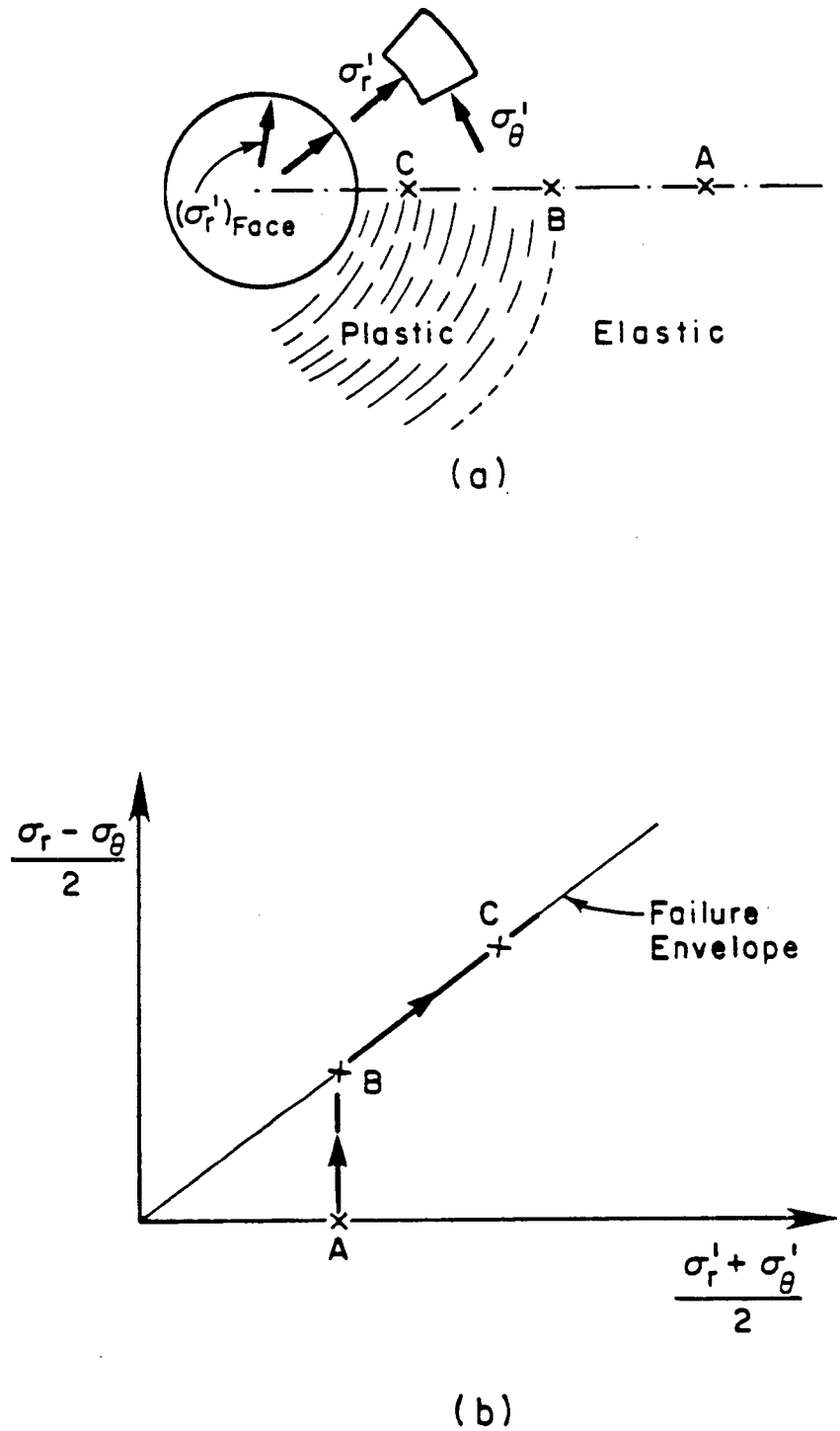

Figure 5.8 Stress State After Pressuremeter Loading (Elastic-Plastic Model).

stress, σ'_θ decreases. However, once the failure envelope is reached (at point B) and a plastic zone develops, σ'_θ commences to increase in the plastic zone and the average effective stress $\sigma'_{av} = (\sigma'_r+\sigma'_\theta)/2$ increases as shown in the figure.

As described, the stresses prior to unloading, at point C (see Figs. 5.7 and 5.8) were computed using a closed form solution. The deformations were assumed to occur under plane strain and follow an elastic-plastic stress-strain law. The closed form solutions followed in the analysis has been described by Gibson ad Anderson (1961), Ladanyi (1963), Vesic (1972) and Hughes et al. (1977), and herein only the selected equations will be presented.

In the plastic zone, which is defined by Mohr-Coulomb failure criterion, the radial and circumferential effective stresses σ'_r and σ'_θ are linked by

$$\sigma'_r/\sigma'_\theta = \sigma'_1/\sigma'_3 = \tan^2(45 + \phi/2) = N \qquad (5.11)$$

where:

ϕ = the angle of internal friction (assumed to be constant in the analysis)

N = the failure stress ratio

The outer radius of the plastic zone, R_p, (see Fig. 5.8) is given by:

$$R_p = R_{face}\,((\sigma'_r)_{face}/(\sigma'_0(1+\sin\phi)))^{(1+\sin\phi)/(2\sin\phi)} \qquad (5.12)$$

where:

R_{face} = the current pressuremeter radius

$(\sigma'_r)_{face}$ = the current effective radial stress at the pressuremeter face

The stresses in the plastic zone, ($r \leq R_p$), are given by:

$$\sigma'_r = \sigma'_{R_p} \cdot (R_p/r)^{1-N} \tag{5.13}$$

$$\sigma'_\theta = \sigma'_r/N \tag{5.14}$$

where the radial stress at the outer radius of the plastic zone, σ'_{R_p} is given by:

$$\sigma'_{R_p} = \sigma'_o (1+\sin\phi) \tag{5.15}$$

Outside the plastic zone or within the elastic zone ($r > R_p$), the stresses are given by:

$$\sigma'_r = \sigma'_o (1 + (R_p^2/r^2)\sin\phi) \tag{5.16}$$

$$\sigma'_\theta = \sigma'_o (1 - (R_p^2/r^2)\sin\phi) \tag{5.17}$$

The above equations describe the stresses induced by expansion of the pressuremeter and these will be used in eq. (5.4) to compute G_{max} prior to unloading. In addition, there may be additional changes in G_{max} due to shear induced volume changes and this will be addressed next.

Based upon Hughes et al. (1977), the shear strain distribution γ as a function of r in the plastic region is given by:

$$\gamma = (R_p/r)^{(n+1)} \ (U_p/R_p)^{(n+1)} \tag{5.18}$$

where:

U_p = the displacement that takes place at the interface between the plastic and elastic zones and is given by:

$$U_p = (R_p/2G) \cdot \sigma_o' \cdot \sin\phi \tag{5.19}$$

$$n = (1-\sin\upsilon)/(1+\sin\upsilon) \tag{5.20}$$

and

υ = the dilation angle

Assuming that the dilation angle is constant with shear strain, the volumetric strain is given by:

$$\epsilon_v = -\gamma \sin\upsilon \tag{5.21}$$

and the change in void ratio is given by:

$$\Delta e = (1 + e_o)\epsilon_v \tag{5.22}$$

This change in void ratio was included in eq. (5.4) when computing the value of G_{max} prior to unloading.

5.2.2.2 Unloading Phase

Upon unloading the whole domain is assumed to behave in a nonlinear elastic manner. However, because the average stress, $(\sigma_r'+\sigma_\theta')/2$, the stress

ratio, σ'_r/σ'_θ, and the shear strain, γ, prior to unloading are different at every point within the domain, G_{max} will be different throughout the domain. In addition the appropriate shear modulus will reduce with the level of unloading in accordance with eqs. (5.6) or (5.7). Consequently, although the material is assumed to be elastic upon unloading the state of stress is not homogeneous in the elastic zone and hence it is not appropriate to use closed form elastic equations to compute stress changes upon unloading. Herein a finite element analysis using a plane strain axisymmetric domain as shown in Fig. 5.9 was used, following the procedures described next:

- The initial stresses σ'_r and σ'_θ in the soil elements were computed for a given pressuremeter stress, $(\sigma'_r)_{face}$ using the closed form solutions described above.
- The shear strains and consequent changes in void ratio were computed from eqs. (5.18) and (5.22), using $G = 1/2\ G_{max,o}$.
- From these stresses and void ratio changes, G_{max} values were evaluated for each element based upon eq. (5.4).
- The stress at the face of the pressuremeter was then unloaded in a series of small steps and a tangent shear modulus corresponding to the average shear stress in each element was computed in accordance to eq. (5.7).
- The inward displacement at the face of the pressuremeter $(\Delta u)_{face}$ was computed for each step of unloading $(\Delta\sigma_r)_{face}$ and summed to allow the complete unloading response to be determined.
- The equivalent modulus G* was computed at various stages of unloading using eq. (5.9) and compared with $G_{max,o}$ which was computed from the initial stress and void ratio state, using eq. (5.10). The ratio $G^*/G_{max,o}$ was then determined for a range of $(\Delta\sigma_r)_{face}/(\sigma'_r)_{face}$ ratios.

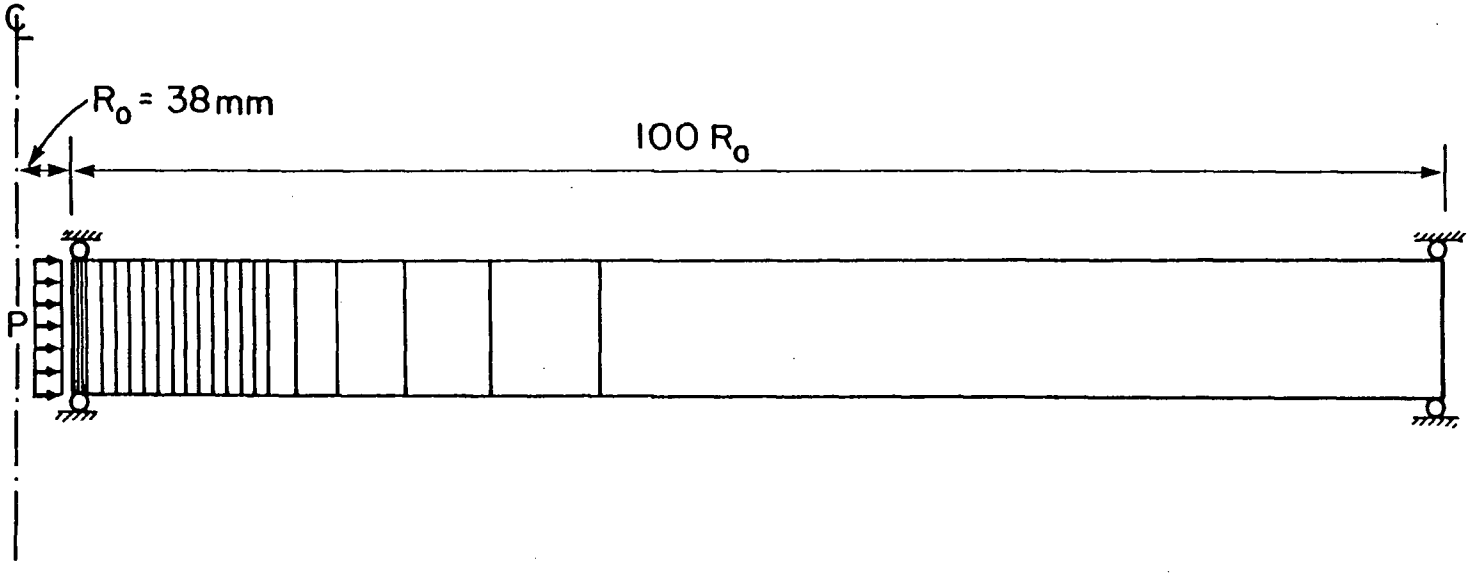

Figure 5.9 Plain Strain Axisymmetric Finite Element Mesh.

- The process was then repeated using a range of $(\sigma_r')_{face}$ values. This allowed $G^*/G_{max,o}$ to be computed as functions of both $(\sigma_r')_{face}/\sigma_o'$ and $(\Delta\sigma_r)_{face}/(\sigma_r')_{face}$ as described next.

5.2.3 Results

Based on the Self-Boring Pressuremeter field tests carried out at the Amaulikpaq I-65 site the following range of stress ratios was considered appropriate and was used in the analysis:

$$3 \leq ((\sigma_r')_{face}/\sigma_o') \leq 12$$

and

$$0.0 \leq ((\Delta\sigma_r)_{face}/(\sigma_r')_{face}) \leq 0.60$$

The results obtained from the analysis for the different loading-unloading conditions are presented in a form of a chart in Fig. 5.10 where the factor $\alpha_p = G^*/G_{max,o}$ is plotted against the stress ratio $(\sigma_r')_{face}/\sigma_o'$ for the different stress ratios $(\Delta\sigma_r)_{face}/(\sigma_r')_{face}$.

The analyses were carried out over a range of σ_o' values as well as a range of void ratio values ($.4 < e_o < .7$) and the results were found to be insensitive to these variables. It was also found that shear induced void ratio effects on G_{max} were less than 5% for all loading conditions shown in Fig. 5.10. Dilation angles ranging between 0° for loose sands and 16° for dense sands were considered.

5.2.4 Validation of the Proposed $G^*/G_{max,o}$ Chart

The proposed analysis presents a method of determining the in situ $G_{max,o}$ value from the secant modulus G^* from the unload-reload

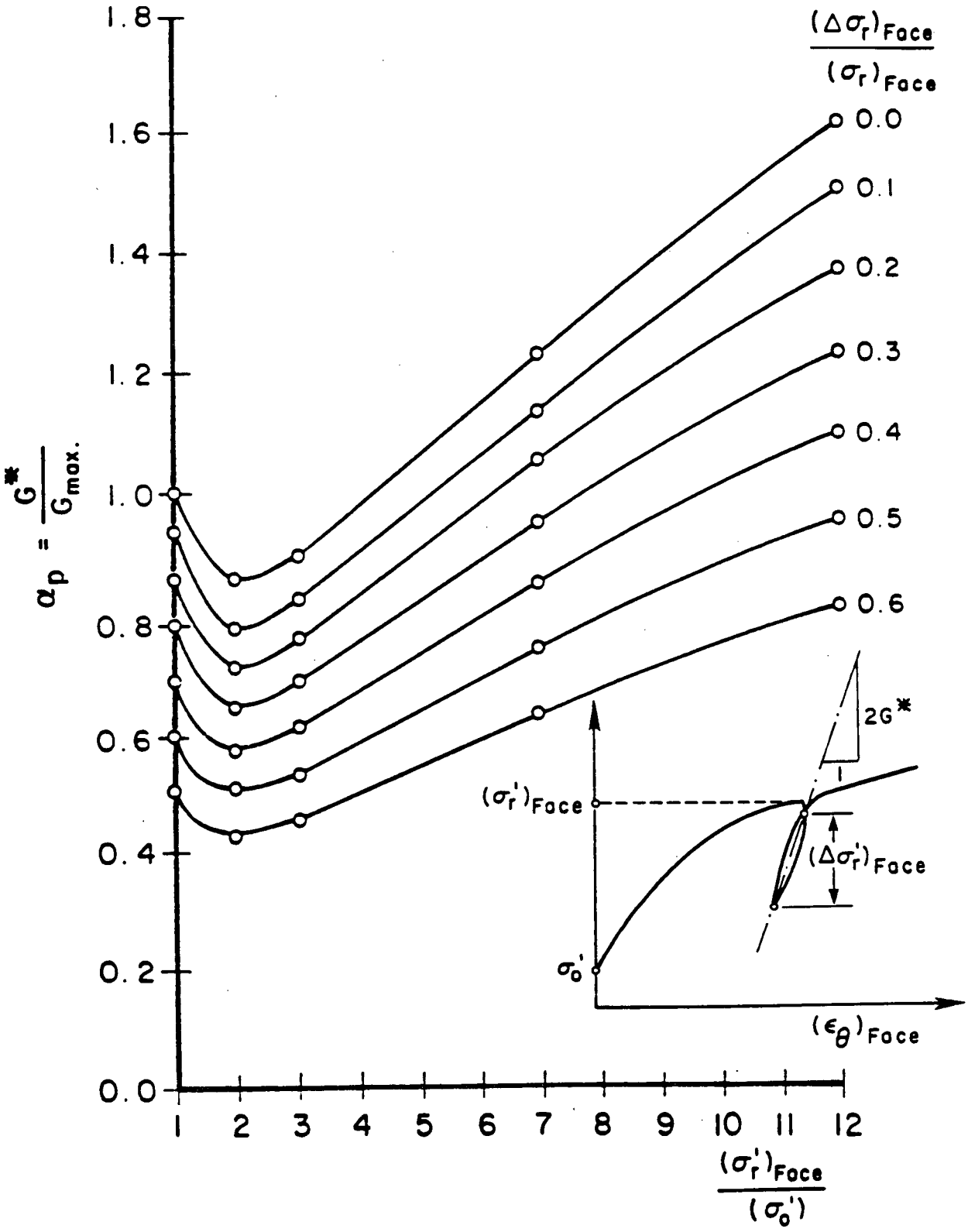

Figure 5.10 Chart for Determination of $G_{max,o}$ from the Measured G* Value (after Byrne, Salgado and Howie, 1990)

pressuremeter loops which considers the variation in stress-strain and void state imposed by the pressuremeter. The results are expressed in terms of a single parameter α_p which is obtained from the chart of Fig. 5.10 and allows $G_{max,o}$ to be determined as follows:

$$G_{max,o} = \frac{G^*}{\alpha_p} \tag{5.23}$$

The method is based upon analytical concepts and idealized soil behaviour and its validation requires comparison with measured data under controlled conditions before application to in situ field conditions.

Belloti et al. (1989) present both pressuremeter and resonant column and shear wave velocity tests for both laboratory and field conditions which allow an evaluation of the proposed chart. Their data is used in the evaluation that follows.

G_{max} values were computed from the pressuremeter data using the chart of Fig. 5.10 and compared with G_{max} from the resonant column or shear wave velocity tests. The comparison from the "ideal" pressuremeter chamber tests in which the pressuremeter was inserted prior to placing the sand is shown in Fig. 5.11(a) where it may be seen that G_{max} values from the resonant column tests, G_{rc}, are on average higher than those from the pressuremeter test by a factor of 1.25. Pressuremeter tests involve strains in the horizontal plane whereas resonant column tests involve strain in the vertical plane. Bellotti et al. (1989) based on tests (Knox, 1982; Stokie and Ni, 1985; Lee, 1986) indicate that the anisotropic factor $\alpha_A = G_{VH}/G_{HH} \approx 1.2$ in which G_{VH} = the maximum shear modulus in the vertical plane and G_{HH} = the maximum shear modulus in the horizontal plane. Thus

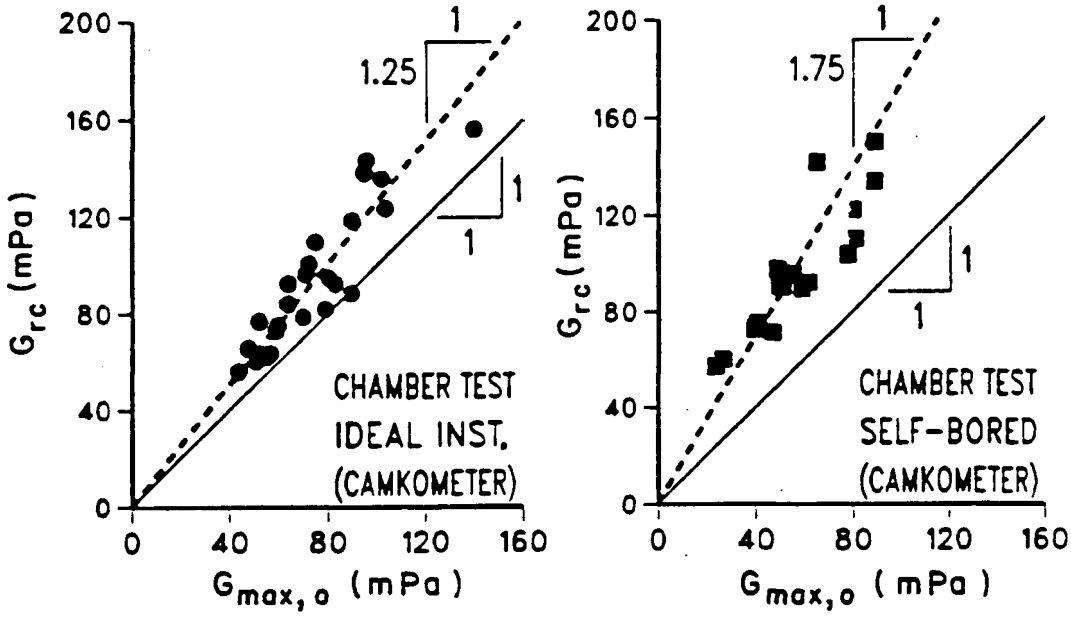

Figure 5.11 Relationship Between $G_{max,o}$ and G_{rc}.

(a) Chamber Test, Ideal Installation (Camkometer)
(b) Chamber Test, Self-Bored (Camkometer)

(After Byrne, Salgado, and Howie, 1990)

the predicted G_{max} values from the pressuremeter are in good agreement with the expected G_{max} values for strains in the horizontal plane.

A similar comparison for "self-bored" pressuremeter chamber tests is shown in Fig. 5.11(b). It may be seen that the G_{max} values from the resonant column test, G_{rc}, are on average 1.75 times higher than those from the pressuremeter test. This indicates that the process of self-boring introduces a disturbance factor, $\alpha_D = 1.75/1.25 = 1.4$.

Comparisons of G_{max} values computed from self-boring pressuremeter and crosshole (CH) seismic tests for field conditions are shown in Fig. 5.12(a) and (b). It may be seen that the G_{CH} values exceed those computed from the pressuremeter by a factor of 1.58 for the Camkometer and 1.43 for the PAF-79 probe. If the disturbance factor α_D for Camkometer is taken as 1.4, then $\alpha_A = 1.58/1.4 = 1.13$.

The comparison with laboratory and field data indicates that the proposed method can be used to predict the in situ $G_{max,o}$ value provided corrections are made for disturbance and anisotropy. The maximum shear modulus for horizontal loading G_{HH} can be obtained from pressuremeter tests as follows:

$$G_{HH} = \frac{G^*}{\alpha_P} \alpha_D \tag{5.24}$$

in which G* is the secant modulus from the pressuremeter unloading loop, α_P is the factor from the proposed chart shown in Fig. 5.10 and α_D is the disturbance factor = 1.4 for the Camkometer.

The G_{max} value for vertical loading, G_{VH}, which corresponds with seismic crosshole (CH) or downhole (DH) can be expressed as follows:

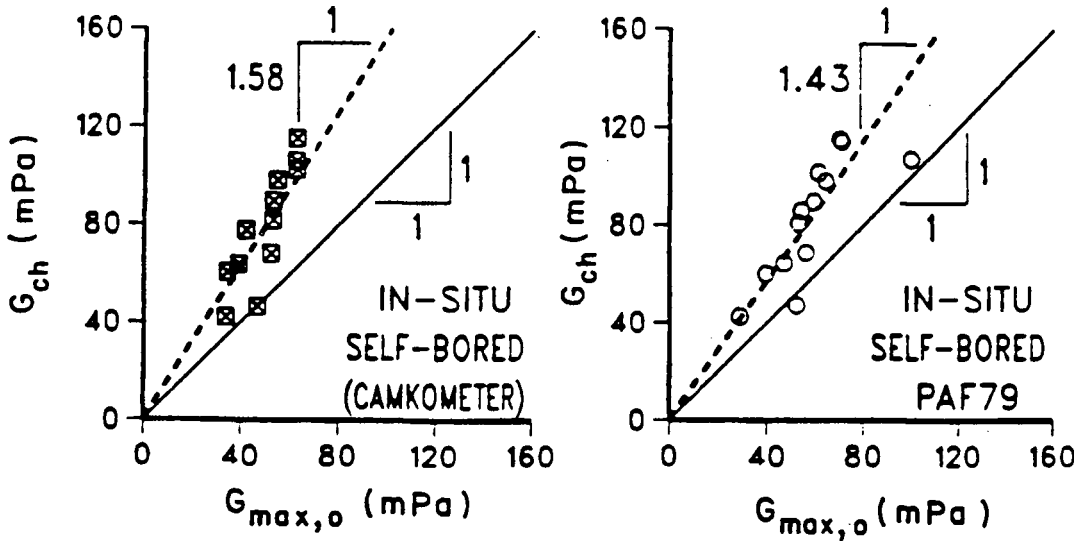

Figure 5.12 Relationship Between $G_{max,o}$ and G_{ch}.

(a) In Situ, Self-Bored (Camkometer).
(b) In Situ, Self-Bored (PAF-79).

(After Byrne, Salgado and Howie, 1990)

$$G_{VH} = G_{CH} = G_{DH} = G_{HH}\alpha_A = \frac{G^*}{\alpha_P}\alpha_D\alpha_A \qquad (5.25)$$

in which α_A is an anisotropic factor. Belloti et al. (1989) suggest α_A = 1.2. Yan and Byrne (1989) based upon hydraulic gradient model tests and shear wave velocity measurements found $\alpha_A \approx 1.1$, and the test data analyzed herein shows that: $\alpha_A = 1.25$ (Chamber tests, 'ideal' installation) and α_A = 1.13 (in situ tests, 'self-bored'). Based on the above four α_A values an average value $(\alpha_A)_{av} = 1.17$ is obtained. This value together with the proposed chart will be used later (Chapter 6) to evaluate values of G_{VH} from the SBP tests carried out at the Amauligak I-65 site. It will be shown that G_{max} values obtained as described here are in good agreement with G_{VH} values obtained from the cone penetration test (CPT) using empirical correlations.

5.3 Evaluation of Soil Parameters from the First Time Loading Part of the Pressuremeter Tests in Sand

The evaluation of soil parameters for use in stress-strain models for sand from the first time loading part of the pressuremeter tests have been restricted for many years to the evaluation of the peak friction angle ϕ_p and the dilation angle, ν. However, Manassero (1989) proposed a method that allows the complete plane strain nonlinear stress and volume change response the sand to be obtained from pressuremeter pressure-expansion data.

To verify numerically Manassero's method, F.E. pressuremeter test analyses under plane strain and infinite outer boundary conditions were carried out using the modified SMP model. Manassero's method was then applied to the F.E. generated pressuremeter response and the stress-strain

and volume change response for an element at the face of the pressuremeter obtained by his method was compared with the F.E. predictions at the face using the modified SMP model.

First, however, before the above analysis were carried out, the modified SMP model was validated against known and controlled pressuremeter chamber test data. This is presented next.

5.3.1 Finite Element Predictions of Pressuremeter Chamber Tests

Leighton-Buzzard sand has been tested under controlled laboratory conditions by many researchers. Simple shear tests on this sand were reported by Stroud (1971) and pressuremeter chamber tests on the same sand are reported by Jewell et al. (1980).

Stroud's data was used earlier to evaluate soil parameters for the modified SMP model and predictions by this model of Stroud's data were shown to be in very good agreement (see Chapter 3). To further validate the modified SMP model, F.E. predictions of the pressuremeter chamber tests reported by Jewell et al. were carried out herein using the SMP model. The soil parameters used in the analysis are presented in Table 5.1 below.

Table 5.1

Soil Parameters for Leighton-Buzzard Sand (e_o = .53) for Use in the Modified SMP Model

Elastic Parameters	KG_e = 620, n = .63
	KB_e = 580, m = .60
Plastic Parameters:	
• Hardening parameters	KG_p = 330, np = -.48
• Flow rule parameters	μ = .20, λ = 1.20
• Failure parameters	$(\tau_{SMP}/\sigma_{SMP})_i$ = .862
	$\Delta(\tau_{SMP}/\sigma_{SMP})$ = .08
	R_F = .957

A description of the pressuremeter chamber conditions and the results are presented next.

Pressuremeter Chamber Tests

A detailed description of the pressuremeter chamber tests is given by Jewell et al. (1980). The test apparatus is shown in Fig. 5.13. The main features of the chamber are that independent horizontal and vertical boundary stresses can be applied to the sides and base of the sand domain using the membranes (1) and (2), and that the lateral movements of the sides were monitored. Nine pressuremeter tests were reported by Jewell et al. An initial radial stress of 90 kPa was used for all tests. The vertical stress was controlled by a pressure applied at the base. Tests were conducted using vertical pressures of 200, 90 and 45 kPa and a constant radial outer boundary stress, σ_r, of 90 kPa.

Finite Element analyses of the pressuremeter chamber tests were carried out using the axisymmetric mesh shown in Fig. 5.14 which simulates the geometry and boundary conditions used in the laboratory tests.

To study the influence of different boundary conditions, analyses were also carried out using a plane strain axisymmetric domain with an outer boundary at a distance R = .467 m which corresponds with the chamber test as well as an outer boundary which simulates an infinite radius. The finite element mesh used for this analysis is shown in Fig. 5.9

For all the analyses the radial pressure at the inner boundary was increased in small increments and the stresses and deformations examined in the domain.

The predicted and observed pressuremeter response in terms of radial stress at the face $(\sigma_r)_{face}$, and circumferential strain at the face,

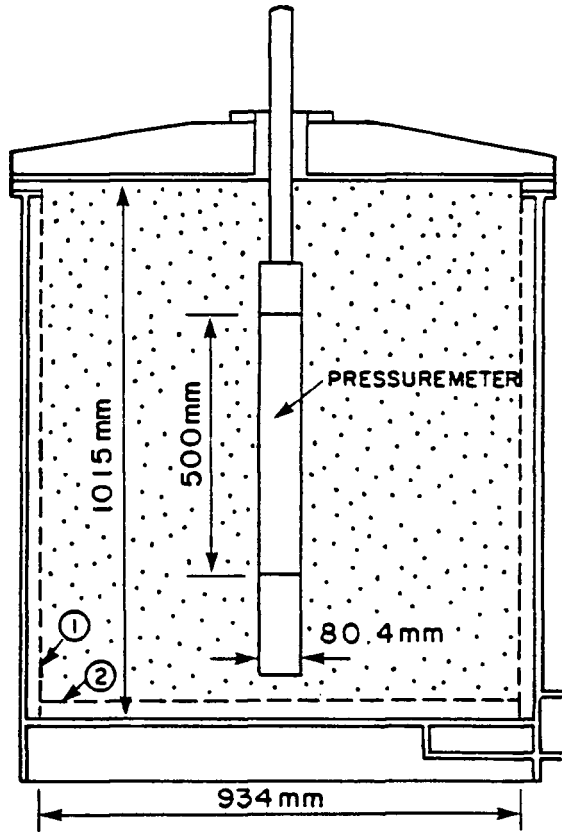

Figure 5.13 Pressuremeter Chamber Test Set Up.

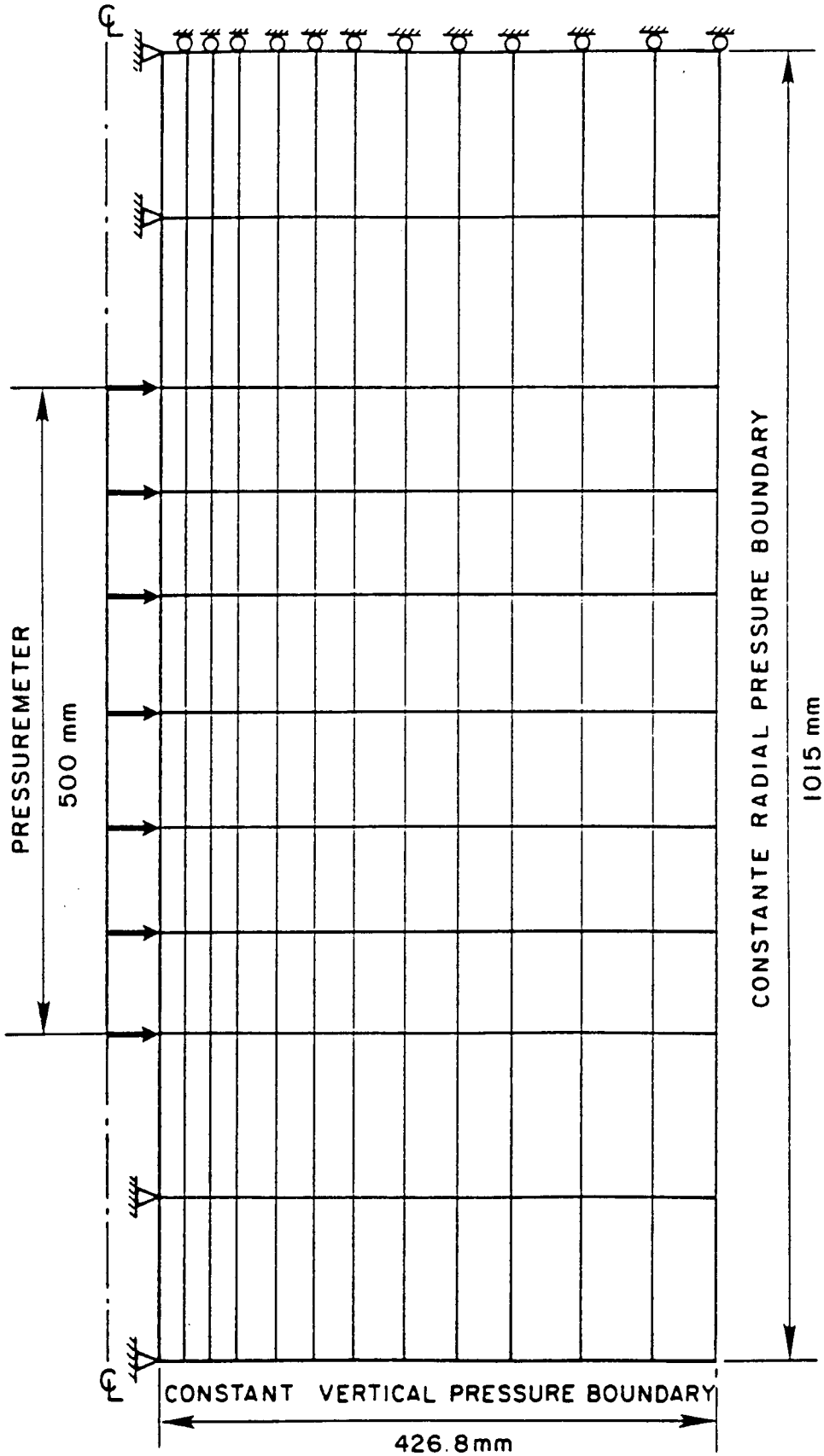

Figure 5.14 Axi-Symmetric Domain Used in F.E. Analyses.

$(\epsilon_\theta)_{face}$ is shown in Fig. 5.15. It may be seen that there is generally good agreement between the predicted and observed response, provided the actual boundary conditions of the chamber test are used in the analysis. The observed response is somewhat softer than computed during the initial loading stage for σ_z = 200 kPa (Fig. 5.15(a)), but is in good agreement with the compute response for σ_z = 90 kPa (Fig. 5.15(b)). The observed response for σ_z = 45 kPa was not published by Jewell et al. and therefore comparisons with the computed results are not presented.

The computed responses for a plane strain condition corresponding with the outer boundary at: (i) the chamber test location; and, (ii) at infinity are also shown in Fig. 5.15(a) and are seen to be significantly softer and stiffer, respectively in the high stress range than the computed using the actual boundary conditions.

Computed and observed displacements of the inner and outer boundary movements are shown in Fig. 5.16. It may be seen that for any selected level of inner boundary movement the computed displacement at the outer boundary are significantly higher than the observed values for the test carried out at σ_z = 200 kPa. However at higher stress levels the computed ratio between the inner and outer boundary movements, i.e. the slope of the line, is in good agreement with the measured values. It may be also seen that the computed values of displacement at the outer boundary are highly dependent on σ_z, being much lower for the lower σ_z values. Jewell et al. do not show outer boundary movements for these lower σ_z stresses but they can be inferred to be much lower from their computation regarding dilation.

The strong influences of the vertical boundary stresses, σ_z, on the displacements can be understood from the computed displacement patterns shown in Fig. 5.17. It may be seen that for σ_z = 200 kPa, upward

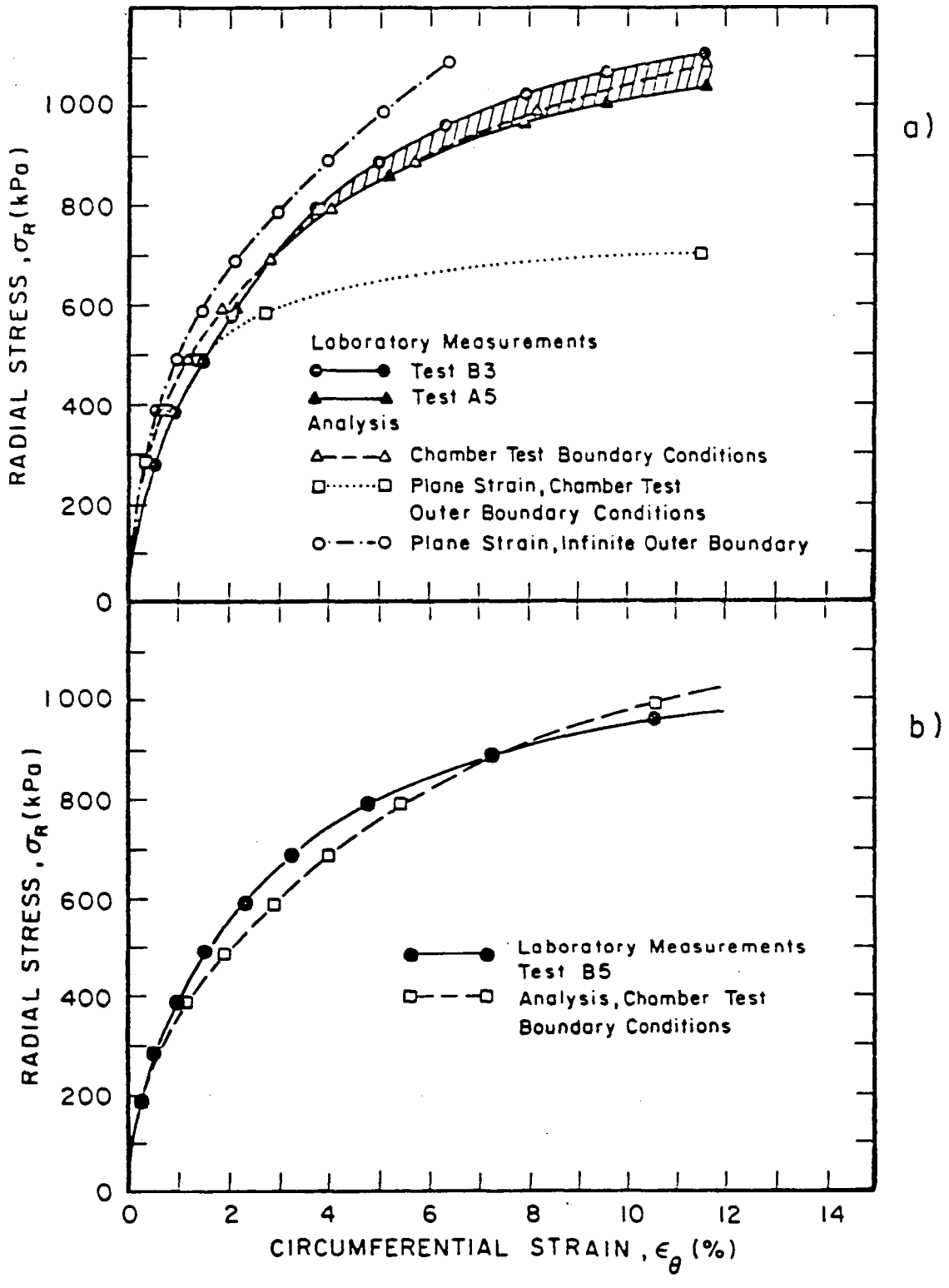

Figure 5.15 Predicted and Observed Response at Face of Pressuremeter. (a) σ_z = 200 kPa. (b) σ_z = 90 kPa.

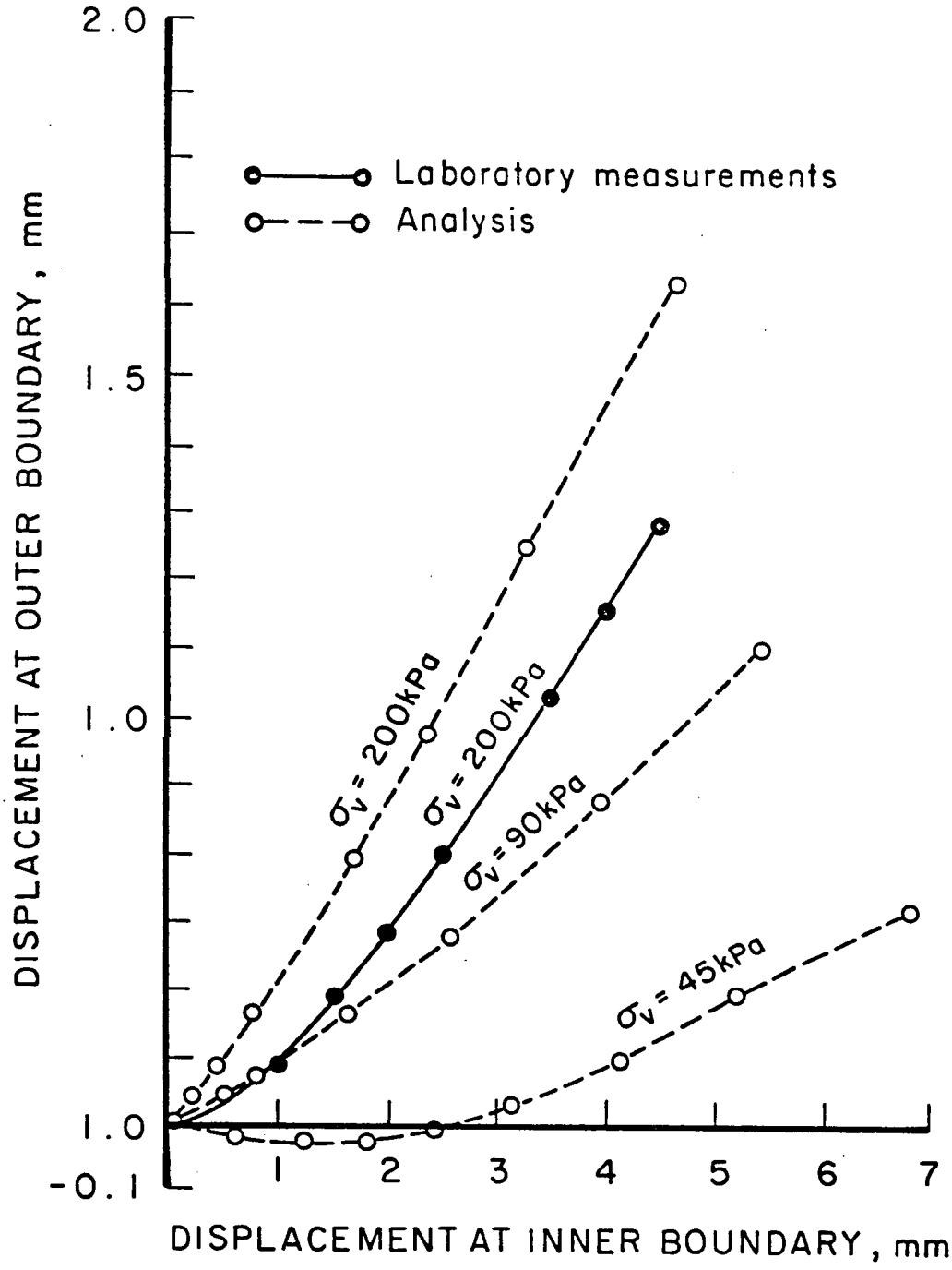

Figure 5.16 Displacement at Inner and Outer Boundary.

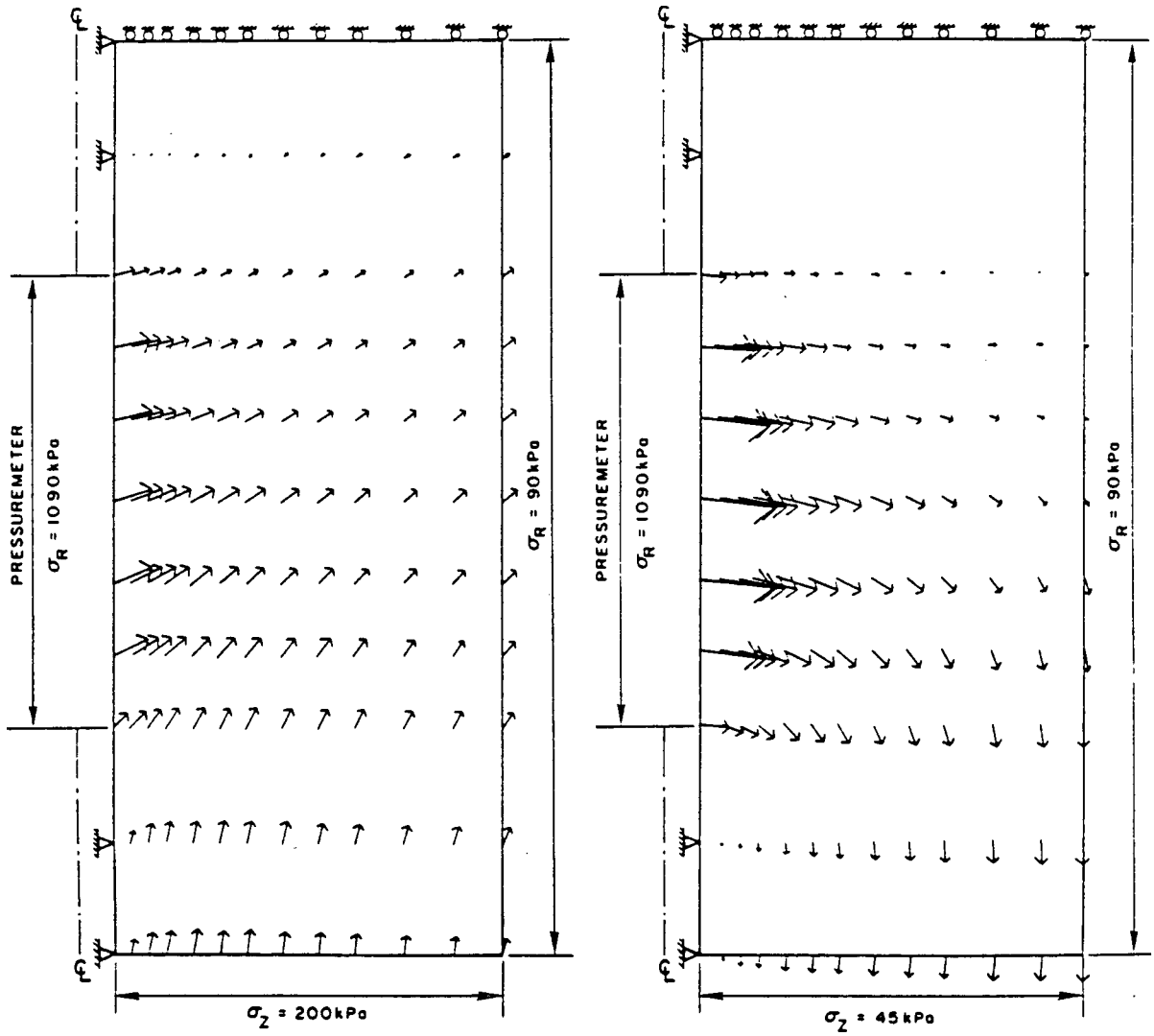

Figure 5.17 Predicted Displacement Patterns.
(a) σ_z = 200 kPa; (b) σ_z = 45 kPa

displacement at the bottom boundary is predicted while for σ_z = 45 kPa downward displacement is predicted. These vertical movements greatly affect the predicted horizontal movements, particularly at the outer boundary and suggest that there could be considerable error in applying a plane strain analysis to these tests as was done by Jewell et al. to compute dilation effects.

The analysis indicates that the chosen stress-strain model can accurately predict the pressuremeter response under controlled chamber test conditions. In this case the parameters for the model were first obtained from simple shear tests. In practice, what is needed is the reverse, i.e., given the pressuremeter response, what are the appropriate stress-strain model parameters for the in situ sand. One could vary the model parameters in a finite element analysis of the pressuremeter and by trial and error determine a set of parameters that gives a best fit to the observed pressuremeter response. However, Manassero (1989) has presented a method of obtaining plane strain stress-strain response from pressuremeter tests. A numerical verification of this method using the F.E. data presented in Fig. 5.15(a) for plane strain infinite outer boundary conditions is presented next.

5.3.2 Evaluation of Soil Parameters from the Pressuremeter Test

This section is concerned with the evaluation of soil parameters from pressuremeter test data and is subdivided into the following parts:

(a) A numerical verification of the method proposed by Manassero (1989) is carried out first.

(b) Procedures for the evaluation of soil parameters for use in the modified SMP model from pressuremeter test data are presented last.

5.3.2.1 Numerical Verification of the Method Proposed by Manassero

Manassero's method is briefly described in Appendices 5.1 and 5.2. This method was applied to the finite element generated pressuremeter response for plane strain conditions with the outer boundary at infinity. As described, Manassero's method yields the stress-strain and volume change response for an element at the face of the pressuremeter and this is compared in Fig. 5.18(a) and (b) with the finite element prediction at the face using the modified SMP model. It may be seen that Manassero's method predicts a stress-strain and volume change response that is in amazing agreement with the modified SMP model. His model predicts values of ϕ_p^{ps} = 45.5° and ν = 13° while the computed values by the modified SMP model are ϕ_p^{ps} = 45.5° and ν = 14°. An assessment of the actual values for ϕ_p^{ps} and ν based on laboratory data is presented in Appendix 5.3. From this assessment values of ϕ_p^{ps}= 46° and ν = 15° were obtained and are considered to be representative of the failure strength and dilation characteristics of Leighton-Buzzard sand for the pressuremeter test stress conditions analyzed herein. It may be seen that the set of values computed by both the modified SMP model and Manassero's method agree extremely well with the expected values.

The stress-strain and volume change obtained from simple shear test data and predictions of these using the modified SMP model are also shown in Fig. 5.18(a) and (b). It may be seen that the predictions are in very good agreement with the measured data, however, the stress-strain and volume change response computed by the modified SMP model for the pressuremeter and simple shear stress paths is not quite the same. The difference is due to the greater increases in mean stress during the pressuremeter test as shown in Fig. 5.18(c). The higher confining stresses in the

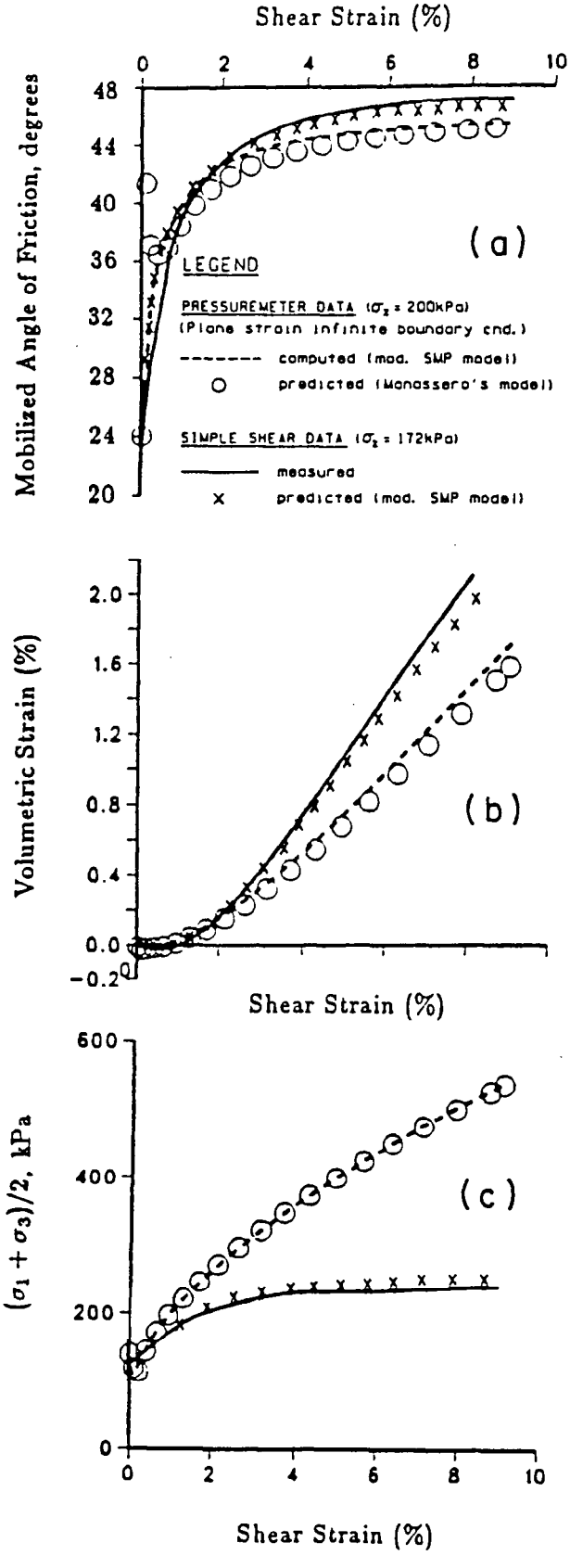

Figure 5.18 Pressuremeter and Simple Shear Data Versus Shear Strain, γ.

pressuremeter leads to lower dilation and hence lower mobilized friction in agreement with the data.

The excellent agreement between the Manassero and modified SMP predictions indicates that parameters for the proposed SMP model can be determined from the pressuremeter test data using Manassero's method. This is described in detail in the next section.

5.3.2.2 Procedures for the Evaluation of Soil Parameters for Use in the Modified SMP Model from Pressuremeter Test Data

The modified SMP model is a 3-D stress-strain model that requires two different types of soil parameters: (a) elastic; and (b) plastic.

- Evaluation of Elastic Soil Parameters From Unload-Reload Pressuremeter Test Data

The elastic components are specified in the modified SMP model by tangent shear and bulk moduli, G_t and B_t defined as follows:

$$G_t = KG_e \, Pa \, (\sigma_m/Pa)^n \qquad (5.27)$$

and

$$B_t = KB_e \, Pa \, (\sigma_m/Pa)^m$$

where $\sigma_m = (\sigma_1+\sigma_2+\sigma_3)/3$, and KG_e, n, KB_e and m have been described earlier (Chapters 2 and 3).

To evaluate KG_e, the $G^*/G_{max,o}$ (or G^*/G_{HH}) chart developed in section 5.2 will be used here as follows.

The maximum shear modulus for horizontal loading, G_{HH}, is evaluated first from the unload reload shear modulus, G*, using the chart presented in Fig. 5.10 together with eq. (5.24), which is repeated below:

$$G_{HH} = \frac{G^*}{\alpha_P} \alpha_D \tag{5.28}$$

Manipulating the above equations (see Appendix 5.4), the following equation is obtained:

$$KG_e = (Pa/(K_o \sigma_{v_o}))^{0.5} G_{HH} \tag{5.29}$$

where σ_{vo} = the in situ vertical stress.

To evaluate KB_e the following relationship is obtained (assuming that the exponent m = 0.5):

$$KB_e = (2KG_e(1+\upsilon))/(3(1-2\upsilon)) \tag{5.30}$$

Assuming that a Poisson'e ratio value of $\upsilon \approx 0.1$ is representative of the elastic behaviour of sand, it follows from Eq. (5.30) that

$$KB_e \approx KG_e \tag{5.31}$$

- Evaluation of Plastic Soil Parameters from First Time Loading Pressuremeter Test Data

Before the method proposed by Manassero is used herein to evaluate plastic soil parameters, it is necessary to develop an additional relationship to estimate the changes of the intermediate principal stress, σ_2 during the pressuremeter cavity expansion for the following reasons:

(a) The modified SMP model is a 3-D stress-strain model, i.e. considers the three principal stresses σ_1, σ_2 and σ_3.

(b) The method proposed by Manassero is a 2-D plane strain model, i.e. σ_2 is not considered.

Such a relationship was developed earlier in Appendix 5.3 and is presented in Fig. 5.19 where the variation of b-value = $(\sigma_2-\sigma_3)/(\sigma_1-\sigma_3)$ with shear strain, $\gamma = \epsilon_1-\epsilon_3$ is presented. Because the above relationship is hyperbolic a relationship between (γ/b-value) and γ was developed and is presented in Fig. 5.19(b). It may be seen that a straight line is obtained for $\gamma \geq 0.5\%$. From this figure, the following equation is obtained

$$\text{b-value} = \gamma/(1.2 + 2.83\gamma) \tag{5.32}$$

From the above equation the value of the intermediate principal stress $\sigma_2 = \sigma_v$ is easily obtained and given by:

$$\sigma_2 = \sigma_v = (\sigma_r-\sigma_\theta)((\epsilon_r-\epsilon_\theta)/(1.2+2.83(\epsilon_r-\epsilon_\theta)) + \sigma_\theta \tag{5.33}$$

The above equation is valid for the case when $\sigma_r=\sigma_1$, otherwise $\sigma_2=\sigma_r$ which is the measured stress.

Since Manassero's method computes values of ϵ_r and σ_θ from the measured σ_r and ϵ_θ pressuremeter data (see Appendix 5.1) substituting these values in eq. (5.33) the value for σ_2 can be evaluated.

To validate the above, Manassero's method was applied together with eq. (5.33) to the finite element generated pressuremeter response for plane strain conditions with the outer boundary at infinity for the case of K_o = .45. The computed values of $(\sigma_r)_{face}$, $(\sigma_v)_{face}$ and $(\sigma)_{\theta face}$, by the modified SMP model, versus shear strain $(\gamma)_{face}$ for an element at the face

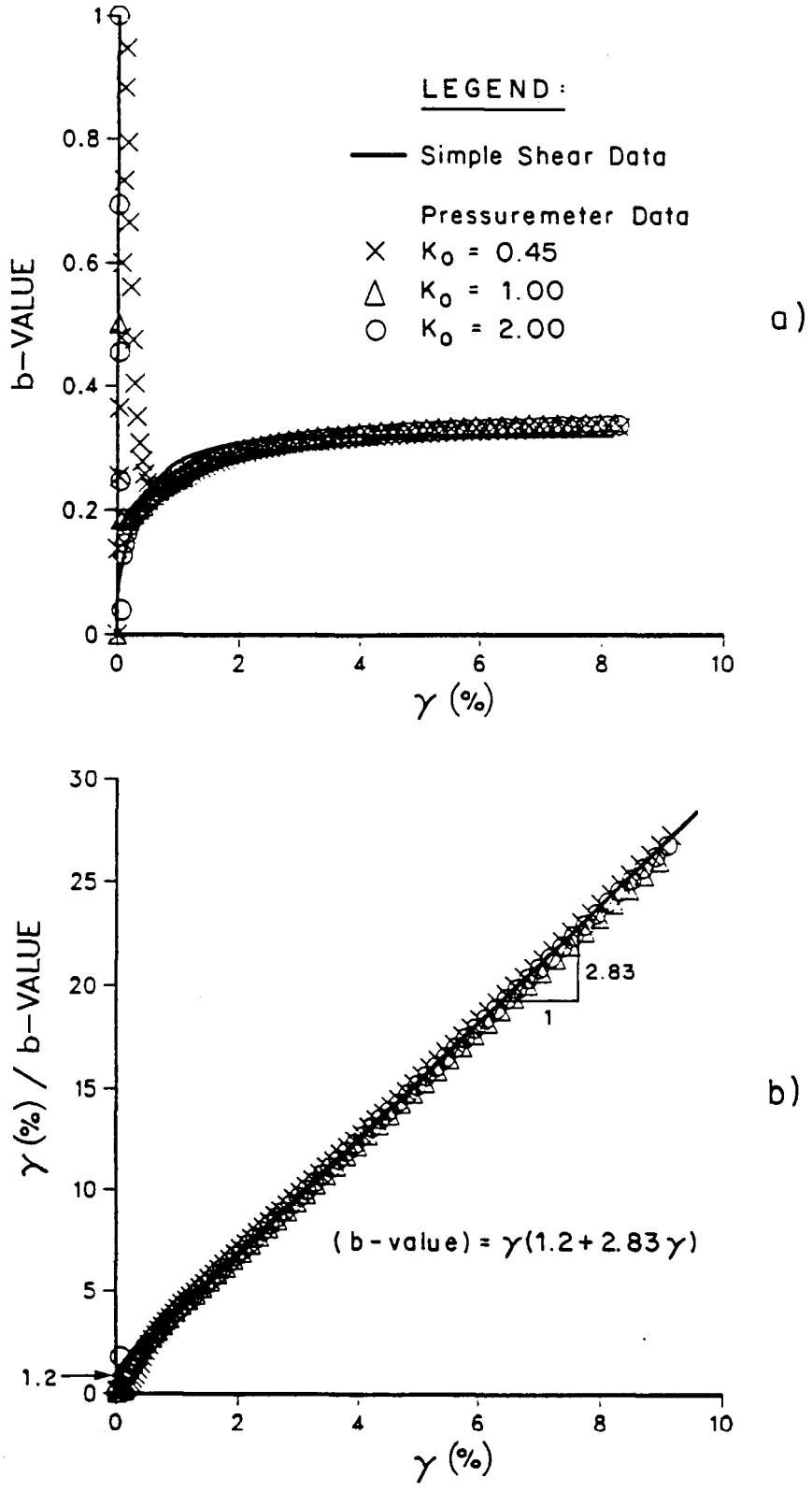

Figure 5.19 (a) Variation of b-Value with Shear Strain, γ.
(b) Variation of (γ/b-value) with γ.

of the pressuremeter is presented in Fig. 5.20(a) together with the corresponding values predicted by Manassero model and eq. (5.33). It may be seen that an excellent agreement is obtained.

A comparison between the computed values of $(\epsilon_r)_{face}$ and $(\epsilon_\theta)_{face}$ versus shear strain $(\gamma)_{face}$ is presented in Fig. 5.20(b) together with the values predicted by Manassero's model. As expected the agreement is very good.

Since the soil parameters used in the F.E. analysis are known the data shown in Fig. 5.20 was used to back predict these same soil parameters. This was carried out in Appendix 5.5, and a comparison between the soil parameters used in the F.E. analysis and the backpredicted from the data generated by Manassero's model and eq. (5.33) are presented in Table 5.2.

Table 5.2

Comparison Between Plastic Soil Parameters

		Used in the F.E. analysis	Back-Predicted	Deviation (%)
Hardening Parameters	KG_p	335.0	325.0	-2.98
	np	-.480	-.500*	not applicable
Flow Rule Parameters	μ	0.200	.195	-2.50
	λ	1.20	1.220	+1.67
Failure Parameters	$(\frac{\tau_{smp}}{\sigma_{smp}})_i$	0.862	0.854	-.93
	$\Delta(\frac{\tau_{smp}}{\sigma_{smp}})$	0.080	0.076	-5.00
	R_F	0.957	0.976	+1.95

*Assumed value

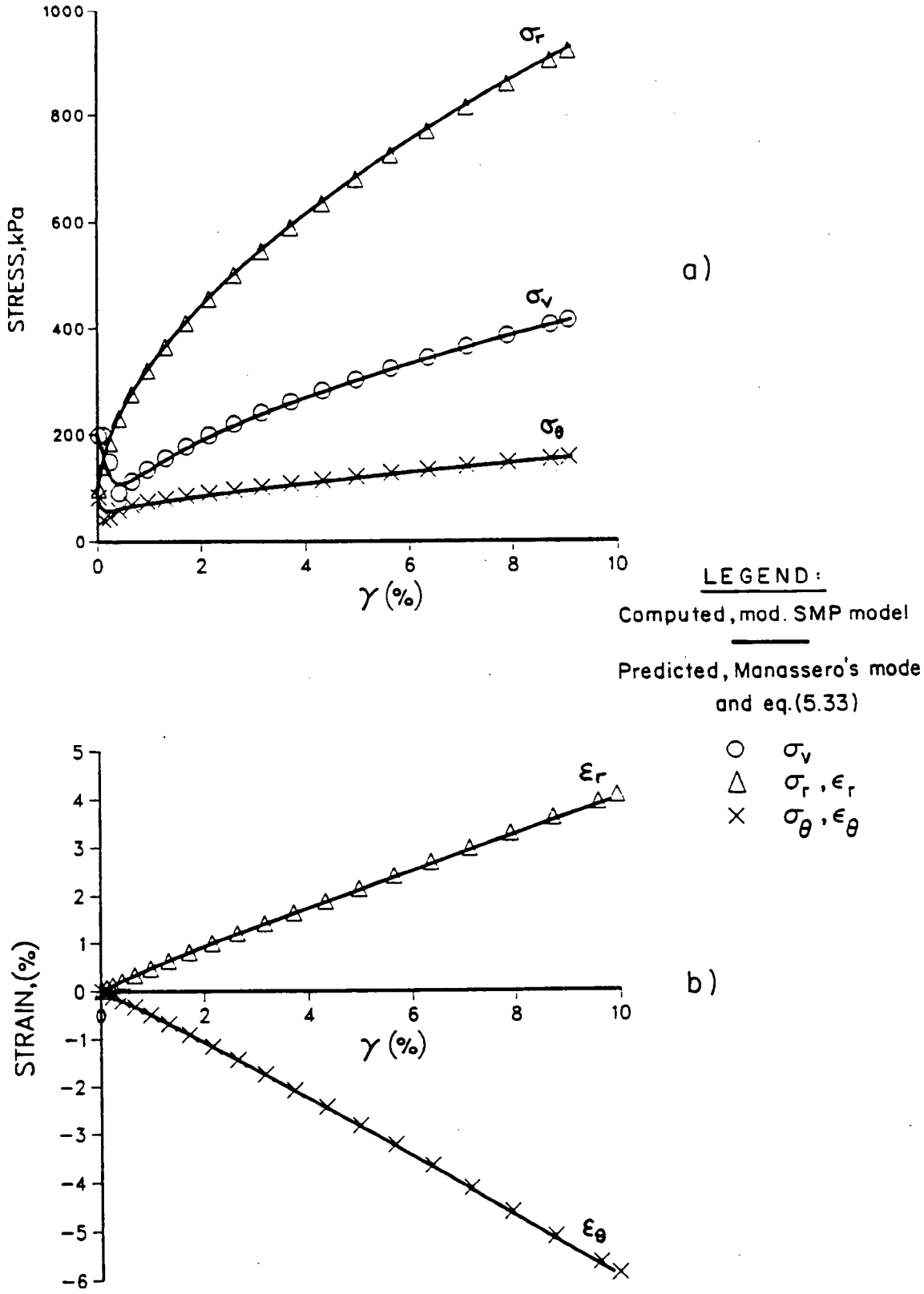

Figure 5.20 (a) Variation of $(\sigma_r)_{face}$, $(\sigma_v)_{face}$ and $(\sigma_\theta)_{face}$ with γ.

(b) Variation of $(\epsilon_r)_{face}$ and $(\epsilon_\theta)_{face}$ with γ.

It may be seen that very good agreement is obtained.

Based on the above comparisons, it is concluded that, theoretically, soil parameters for use in the modified SMP model can be obtained using the method proposed by Manassero. However, from a practical point of view, the proposed method needs further validation to assess the influence of initial disturbance that might occur at the beginning of in situ SBP tests.

Because the method proposed by Manassero (1989) is a recent method and because the SBP tests at the Amauligak I-65 site were carried out under partially drained conditions (Jefferies, 1988) the first time loading data obtained from these tests was not analyzed herein to infer first time loading soil parameters for use in F.E. analysis of the Molikpaq. These soil parameters will be estimated on the basis of both cone penetration test (CPT) data and laboratory data as will be described in the next chapter.

5.4 Summary

(a) A procedure for analyzing the unloading response of the pressuremeter has been presented. The analysis considers the effects of change in the average stress $(\sigma'_r+\sigma'_\theta)/2$, the stress ratio σ'_r/σ'_θ, and shear induced volume change on the maximum modulus. Results of the analysis are presented in a chart which allows the in situ, $G_{max,o}$ to be computed from the equivalent elastic shear modulus G* taking into account both the level of pressuremeter loading and unloading.

The predicted G_{max} values from pressuremeter chamber and field tests using the proposed chart are compared with values obtained from resonant column and crosshole seismic test and are found to be in good

agreement provided factors are included to account for disturbance and anisotropic effects.

(b) Finite element predictions of the pressuremeter chamber tests reported by Jewell et al. (1980) were carried out to further validate the modified SMP model. The soil parameters were obtained from simple shear test data reported by Stroud (1971) on Leighton-Buzzard sand the same sand used in the pressuremeter chamber tests.

The results indicate generally good agreement between computed and observed pressure-deflection relations at the face of the pressuremeter provided the actual boundary conditions of the chamber tests are modelled. The measured response is a little softer at the initial stages of loading. This may be due to disturbance.

The computed displacement patterns in the chamber tests are sensitive to the vertical stress σ_z applied at the base of the chamber and indicate that plane strain conditions did not prevail in the chamber tests.

(c) A procedure for analyzing the first time loading response of the pressuremeter has been developed by Manassero (1989). His method was applied to the finite element generated pressuremeter response for plane strain conditions with the outer boundary at infinity. An excellent agreement was obtained between the stress-strain and volume changes, predicted by Manassero's method, and computed by the modified SMP model.

(d) Soil parameters for use in the modified SMP model can be determined from poressuremeter test data using Manassero's method provided that: (i) elastic parameters for the model are estimated first from the unloading response of the pressuremeter using the proposed $G^*/G_{max,o}$

chart; and (ii) that Manassero's method is expanded to take into account the intermediate principal stress, σ_2.

(e) From a practical point of view (i.e. to interpret in situ self boring pressuremeter tests) the method proposed by Manassero needs further validation to assess the influence of initial disturbance that might occur at the beginning of these tests.

CHAPTER 6

EVALUATION OF SOIL PROPERTIES FOR USE IN THE ANALYSIS OF THE MOLIKPAQ STRUCTURE AT THE AMAULIGAK I-65 SITE

6.1 Introduction

The soil types and their stress-strain parameters used in the analysis of the Molikpaq structure at the Amauligak I-65 site are described in this chapter. Two different stress-strain models were used in the Finite Element (F.E.) analysis of the response of the structure during both the construction and ice loading phases. The hyperbolic model was used in 3-D and 2-D F.E. analysis and the modified SMP model was used only in 2-D F.E. analyses.

As will be described later in Chapter 7 these analyses included: (a) a static assessment of the response of the Molikpaq structure during the construction and moderate ice loading phases; and (b) a dynamic assessment of the response of the Molikpaq structure during high ice loading phases.

The soil parameters were estimated on the basis of both in situ test and laboratory data. The in situ test data at the Amauligak I-65 site consisted of cone penetration test (CPT) data (Gulf Canada Resources Inc., 1986) and self-boring pressuremeter (SBP) data (Thurber Consultants, 1986). In situ test data obtained at the Tarsiut I-45 site were also used in the assessment of soil parameters because the in situ conditions at Tarsiut are considered to be reasonably similar to those at Amauligak.

The laboratory data used in the assessment consisted of monotonic drained and cyclic undrained triaxial tests (Golder Associates, 1986 and 1987).

This chapter is divided into three main sections:

In the first section, a brief description of the on site investigation and construction sequence of the berm and core fills is presented together with a description of the sand used.

In the second section, the procedures followed to obtain the appropriate soil parameters for use in the two stress-strain models are presented.

Finally, in the third section the procedures followed to obtain the liquefaction resistance curves of the core and berm fills for use in the dynamic assessment are presented.

6.2 Brief Description of the On Site Investigation and Construction Sequence. Type of Sand Used in the Berm and Core of the Molikpaq

A good description of Island construction in the Canadian Beaufort Sea (including the Molikpaq) is given by Jefferies et al. (1988). Herein only a brief summary of the investigation and construction sequence at the Amauligak I-65 site is presented and consists of the following (see Fig. 6.1(a)):

1) A detailed geotechnical investigation program including sampling, in situ testing and laboratory testing was carried out in order to provide parameters for foundation design (Jefferies and Livinstone, 1985). This investigation showed that the foundation soil conditions at the site consist of the following (see Fig. 6.1(b)):

   - very soft to soft silty clay 9 m thick, followed by
   - compact silty sand 5 m thick, followed by
   - compact to very dense fine sand 35 m thick, followed by

- stiff to very stiff clayey silt 10 m thick, followed by
- very hard, frozen sand (permafrost).

Based on MacKay (1972) permafrost as much as 300 to 400 m thick should exist in the southern Beaufort Sea. Herein considerations of time-dependent deformations of the permafrost foundation are not considered because the Molikpaq is a temporary structure for oil exploration purposes. However, if this structure becomes a permanent structure for oil recovery purposes, then time-dependent deformations (creep) of the permafrost should be accounted for in the long term stability of the structure.

2) The weak superficial sediments (silty clay) were removed;

3) The excavation was backfilled and the berm was constructed in several "lifts" by both the "pump-out" and the "bottom discharge" methods. These two methods are well described by Jefferies et al. (1988). Verification of adequate berm density was carried out and consisted of nine CPT's. Then the berm was levelled prior to set down of the Molikpaq;

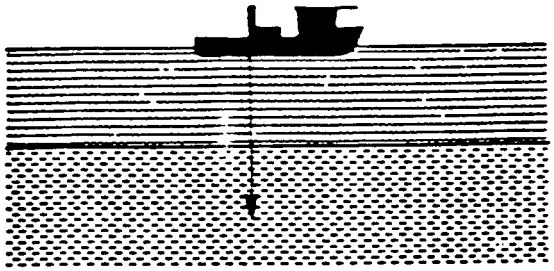

1. SITE INVESTIGATION

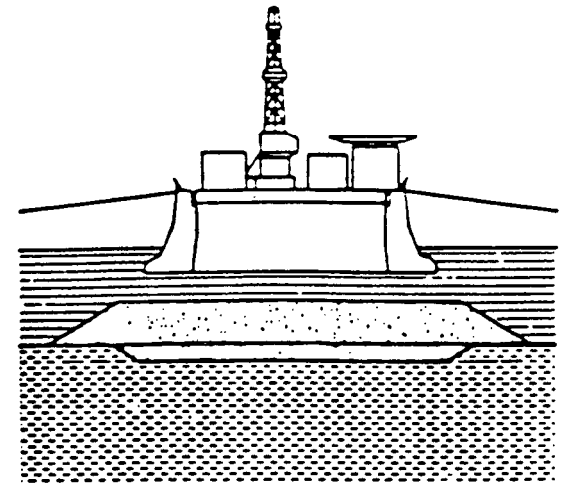

4. SET-DOWN

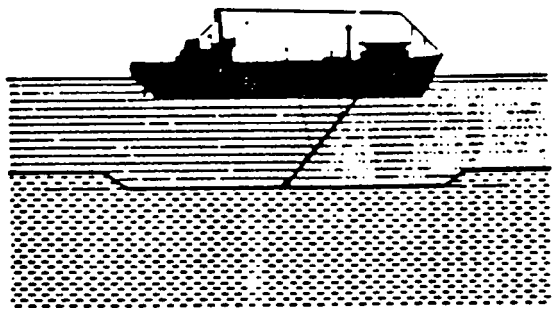

2. EXCAVATE SOFT SURFICIAL SEDIMENT (SUBCUTTING

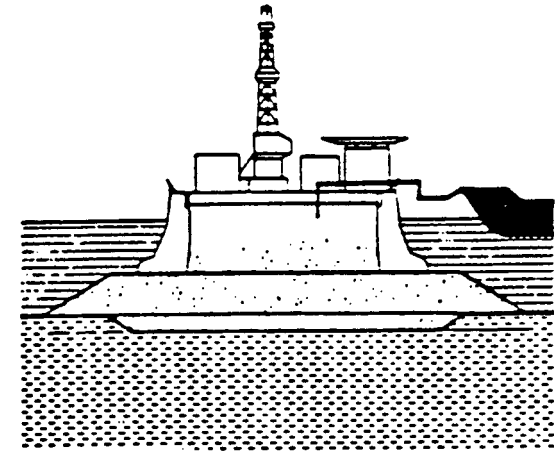

5. CORE FILLING

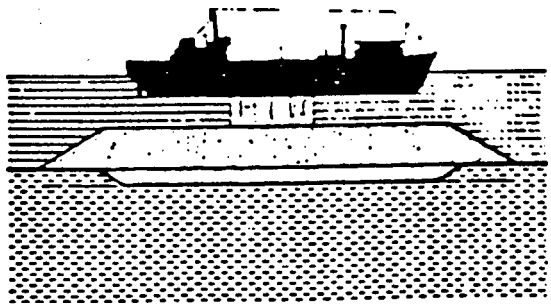

3. CONSTRUCT BERM

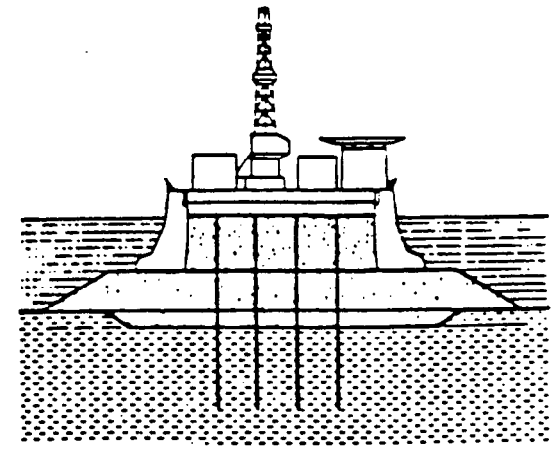

6. VERIFICATION

Figure 6.1 (a) On site investigation and construction sequence (after Jefferies et al., 1985)

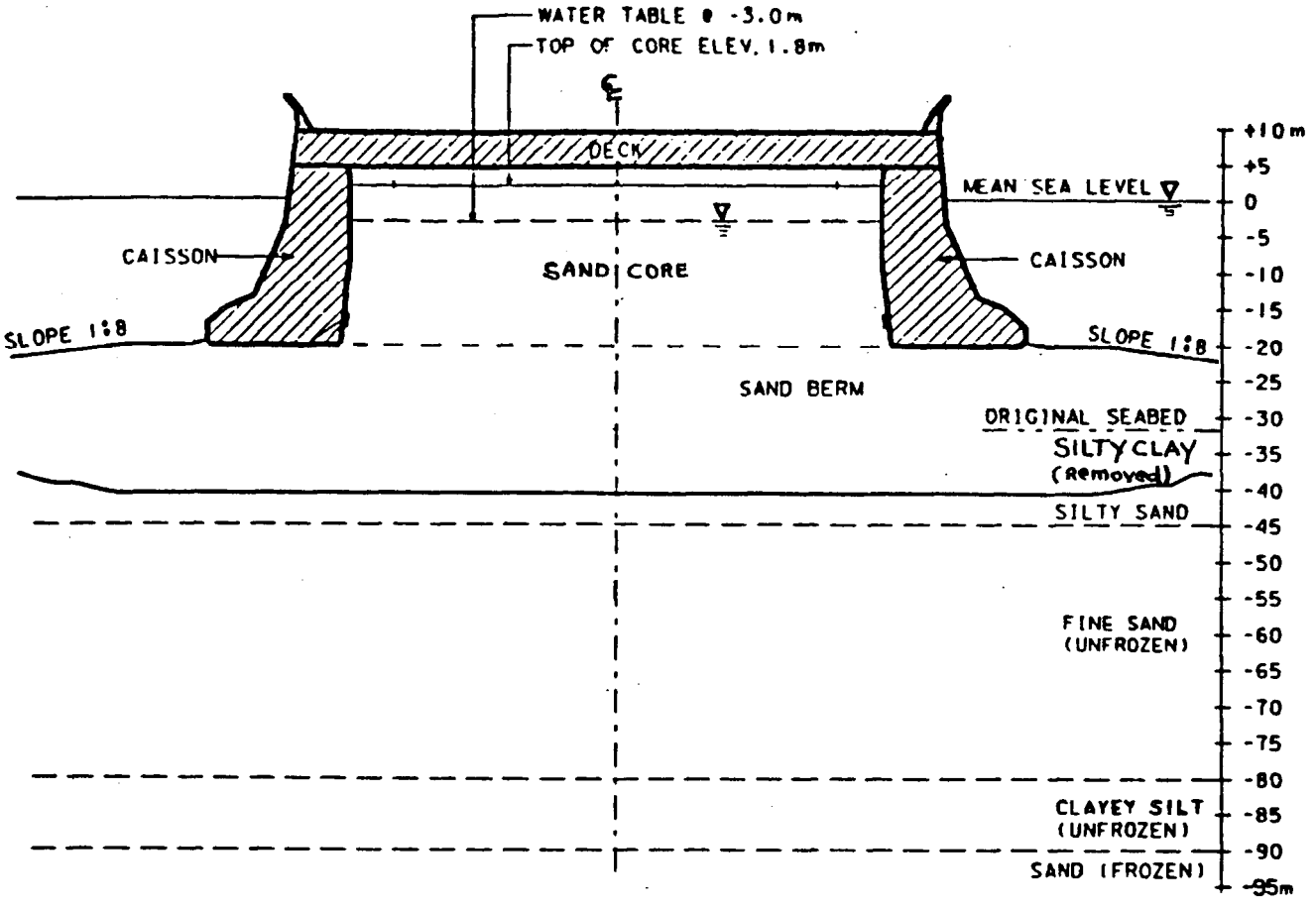

Fig. 6.1(b) Soil conditions at the Amauligak I-65 Site (after Jefferies and Livinstone, 1985).

4) The Molikpaq was positioned over the berm and setdown by filling its ballast water tanks;

5) The caisson core was hydraulically filled with sand using a moveable (horizontally and vertically) discharge pipe;

6) A verification program was carried out from the surface of the sand core. 20 CPT's together with 3 SBP holes (20 tests) were carried out to verify that the core and the berm had adequate densities.

Determination of the fill quality used in the berm and core was obtained from grain size testing on representative samples of sand.

Based on available information the Erksak 320/1 sand is considered to be the type of sand representative of the berm and core fills used at the Amaulikpaq I-65 site. It is a uniform, brown fine to medium sand and its grain size distribtuion is shown in Fig. 6.2. Index properties of the Erksak 320/1 sand were reported by Golder Associates (1986) and are presented in Table 6.1.

6.3 Evaluation of the Soil Parameters for Erksak 320/1 Sand

This section is subdivided into two subsections. In the first, the procedures for the assessment of the different moduli used in the hyperbolic and the modified SMP models are presented. In the second, the procedures for the evaluation of the failure angle of internal friction used in the hyperbolic model and of the failure stress ratio on the SMP used in the modified SMP model are presented.

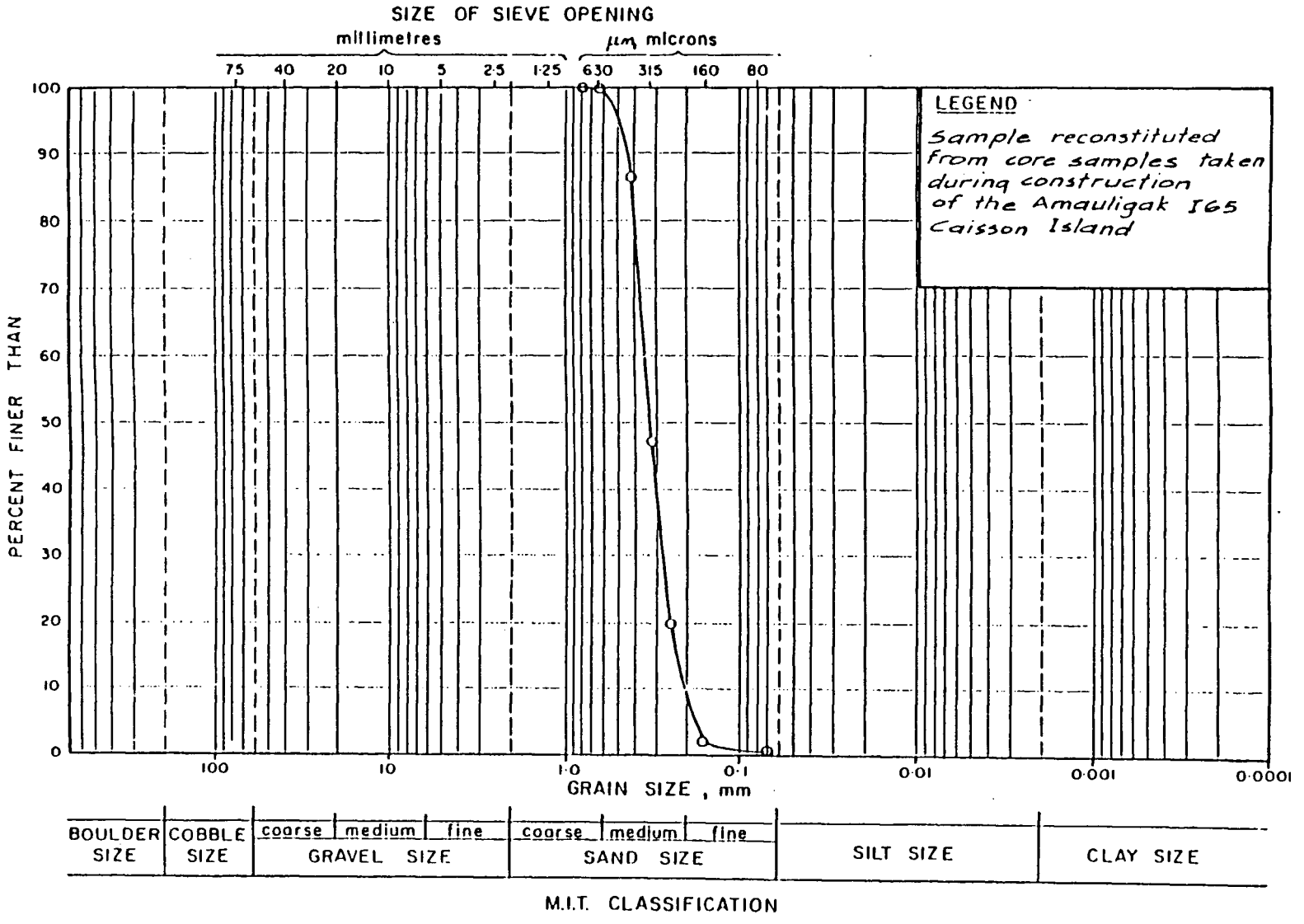

Figure 6.2 Grain size distribution of Erksak 320/1 sand
(after Golder Associates, 1986)

Table 6.1

Index Properties of Erksak 320/1 Sand
Reported by Golder Associates (1986)

PROPERTY	DESCRIPTION (or) VALUE
Mineralogical composition (visual inspection)	Quartz, calcite, feldspar and mica
Medium grain size, D_{50} (μm)	320
Effective grain size, D_{10} (μm)	200
Uniformity coefficient, $C_u = D_{60}/D_{10}$	1.6
% passing #200 sieve	0.8
Specific gravity, G_s	2.67
Average sphericity	0.67
Average roundness	0.47
Particle shape	Subrounded

6.3.1 Evaluation of the Moduli Used in the Analysis

The void ratio is a fundamental soil parameter. Soil moduli such as the Young's modulus, E, shear modulus, G, and bulk modulus, B, are highly dependent on the consolidated void ratio, e_c, and therefore in situ moduli may be estimated once the in situ void ratio is known by combining it with data from laboratory testing or using it with empirical correlations.

The procedure followed for estimating the in situ void ratio is presented below.

6.3.1.1 Evaluation of the In Situ Void Ratio Versus Depth

The in situ void ratio was evaluated from the in situ state parameter, ψ, which was obtained from the CPT cone bearing, q_c, as it will be described. The state parameter concept was developed by Been and Jefferies (1985), and is a quantitative measure of the state of the sand that combines both the effects of void ratio and effective mean normal stress in a unique way for each sand.

As shown in Fig. 6.3, the state parameter, ψ, is a measure of the distance of the consolidated void ratio, e_c, from the steady state line. The steady state line represents a condition of zero dilation during shear (Castro, 1969). Once the in situ state parameter, ψ, and in situ effective mean normal stress, σ'_m, are known, the in situ void ratio e_c can be evaluated.

To evaluate the in situ state parameter the procedures outlined by Been et al. (1986) were followed. Based on chamber test data Been et al. conclude that ψ can be estimated from CPT data using the following equation:

$$\psi = -\frac{1}{m} \ln \left[\left(\frac{q_c - \sigma_m}{\sigma'_m}\right)/K\right] \qquad (6.1)$$

where:

m = $(8.1 - \ln \lambda_{ss}) = 11.2$

q_c = CPT cone bearing ("mean" q_c value was considered)

σ'_m = effective mean normal stress = $\sigma'_v (1+2K_o)/3$

K_o = .40 (based on K_o study presented in Appendix 6.1)

σ'_v = effective vertical stress (based upon γ_b = 9.5 kN/m³)

u = static pore pressure (based upon water level = 3.0 m below top of core, estimated from CPT soundings)

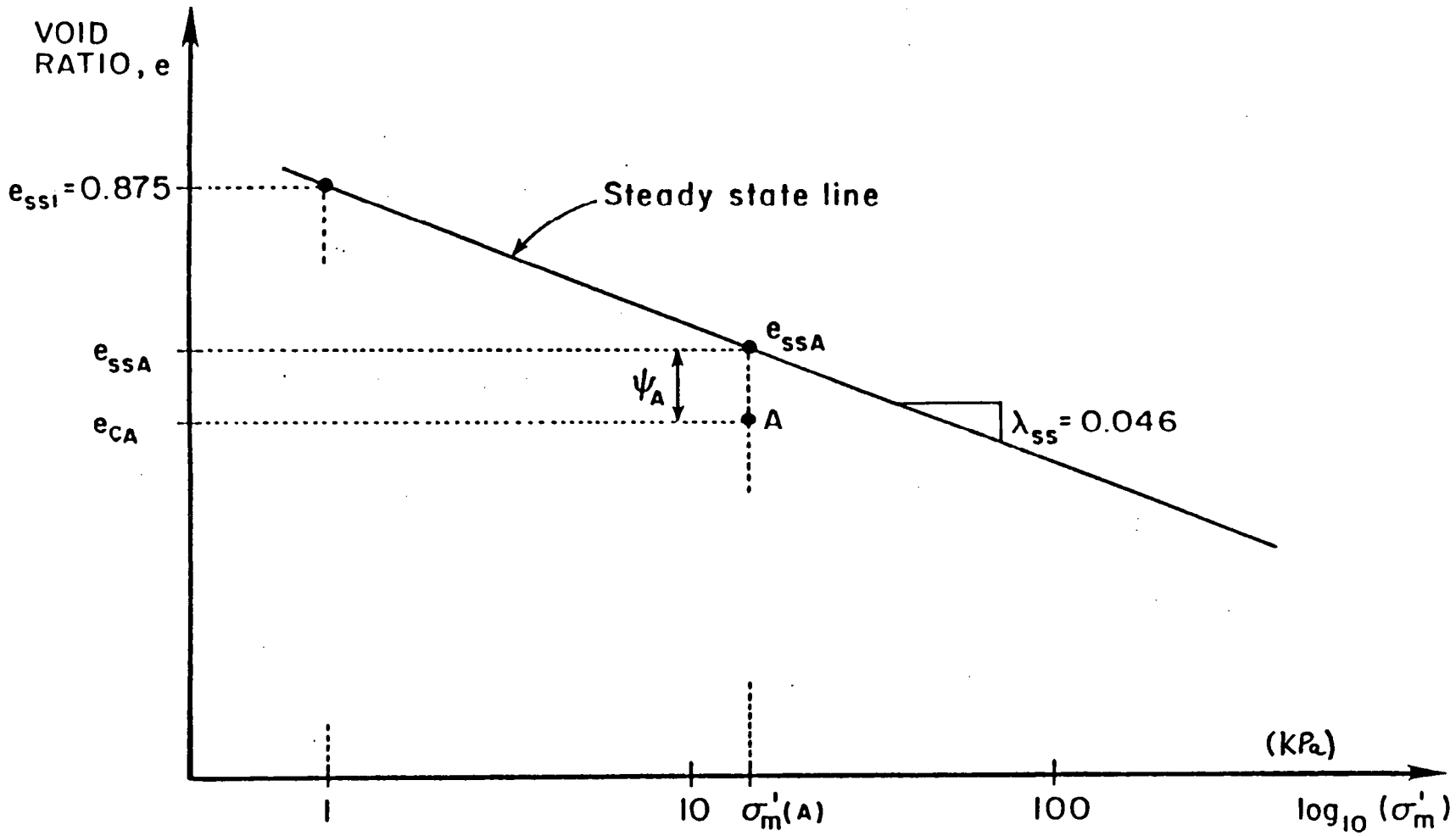

Figure 6.3 State parameter and steady state line

σ_m = Total mean normal stress = $\sigma'_m + u$

$K = (8 + \frac{.55}{\lambda_{ss} - 0.01}) = 23.3$

and

λ_{ss} = slope of steady state line = 0.046 for the Erksak 320/1 sand (Golder Associates, 1986)

Using the "mean" q_c value for the core and berm fills shown in Fig. 6.4, which is based upon 20 CPT's carried out in the fills of the Molikpaq (see Fig. 6.5 for CPT location), a profile of the state parameter versus depth was evaluated and is presented in Fig. 6.6. Based on the ψ values shown in this figure the in situ void ratio was then obtained following the steps described below:

1) The in situ void ratio on the steady state line, e_{ss} is evaluated using the following equation (see Fig. 6.3)

$$e_{ss} = e_{ss_1} - \lambda_{ss} \log_{10} (\sigma'_m) \qquad (6.2)$$

where: e_{ss_1} = 0.875 (Golder Associates, 1986) is the void ratio on the steady state line correspondent to σ'_m = 1 kPa, and the effective mean normal stress, σ'_m was computed as described in equation (6.1).

2) The in situ void ratio, e_c, is then evaluated from the equation:

$$e_c = e_{ss} + \psi \qquad (6.3)$$

The resulting values of the in situ void ratio versus depth are shown in Fig. 6.7. In order to define different soil types to be used in the analysis, the profile shown was divided into four depth segments each of

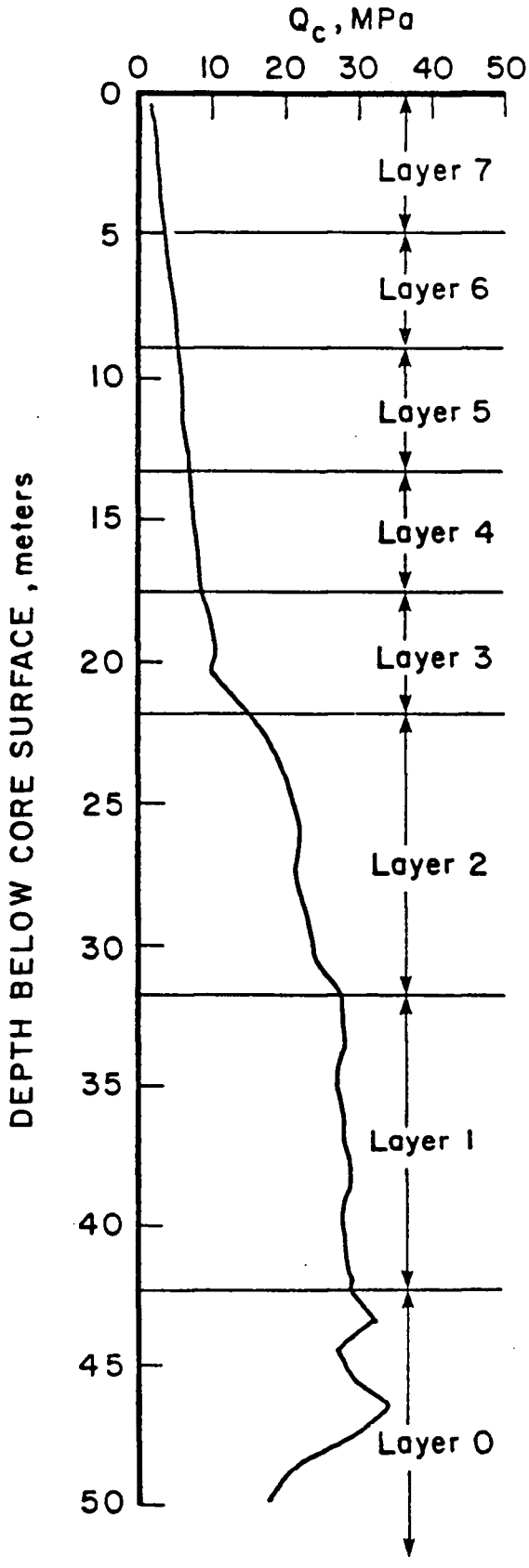

NOTE:

LAYERS SHOWN ARE THE LAYERS USED IN THE FINITE ELEMENT ANALYSIS.

Figure 6.4 "Mean" values of q_c in the core, berm and foundation (after Jefferies and Livingstone, 1985)

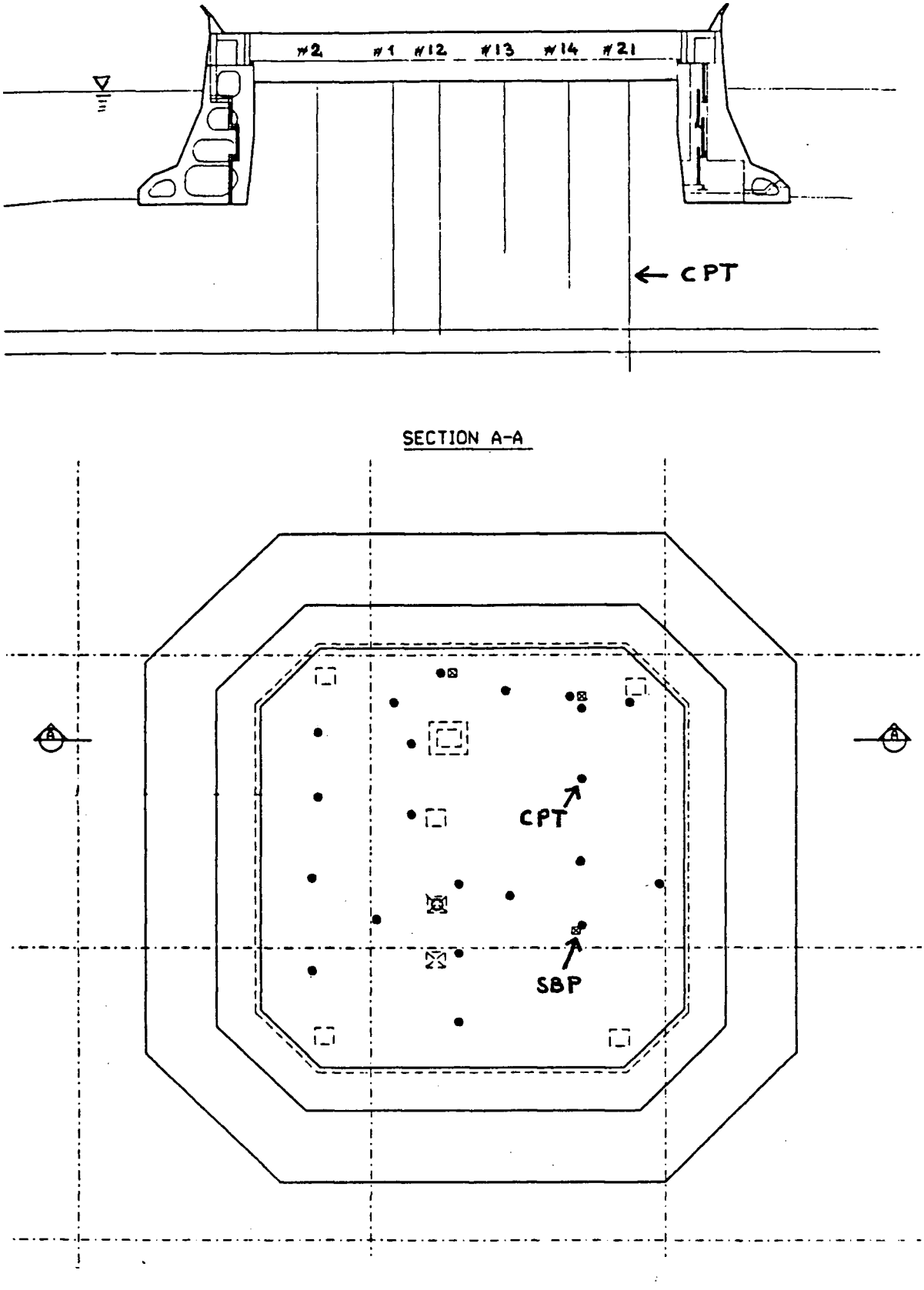

Figure 6.5 Location of cone penetration tests carried out in the Molikpaq core

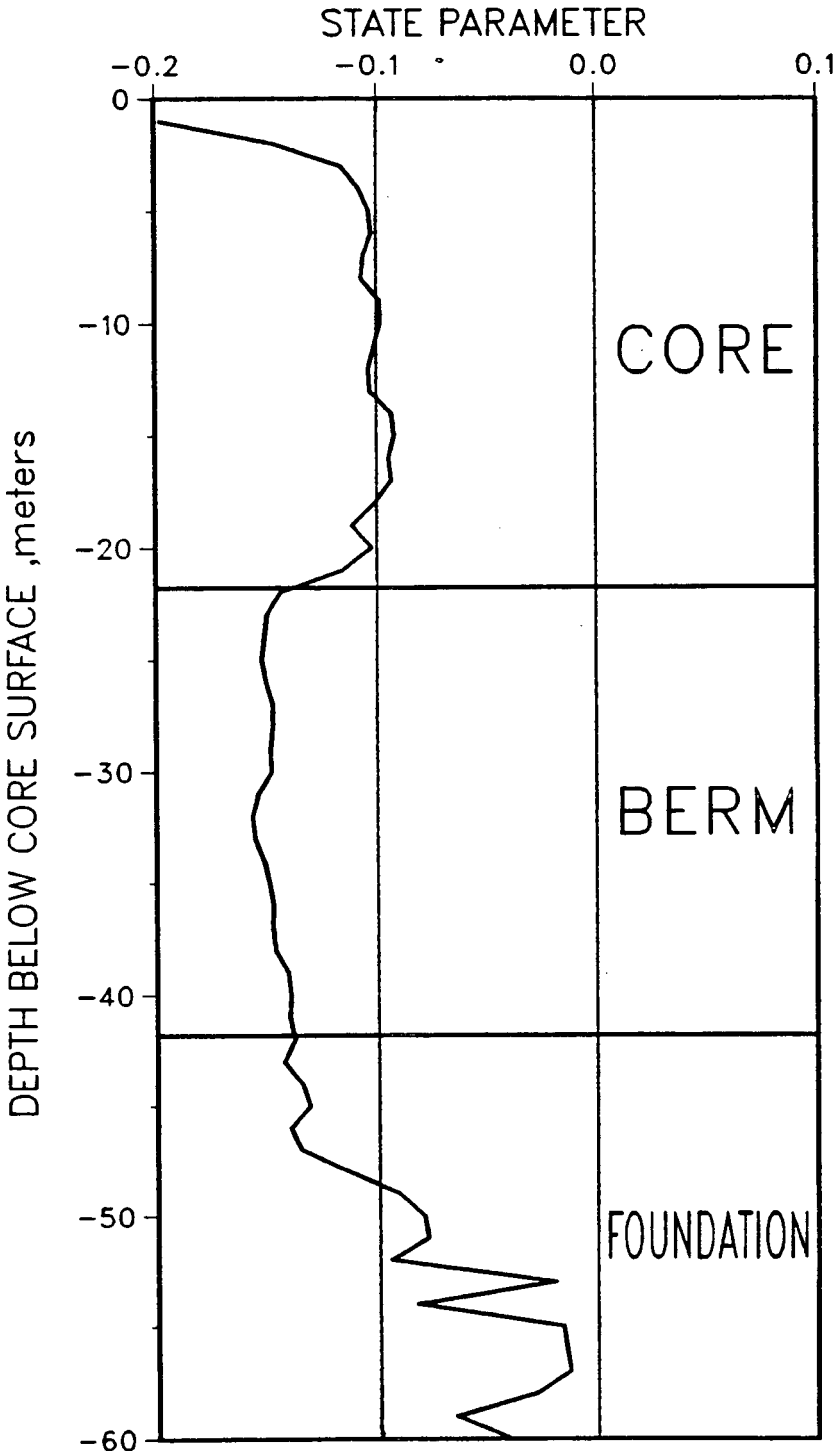

Figure 6.6 In situ state parameter, ψ, versus depth

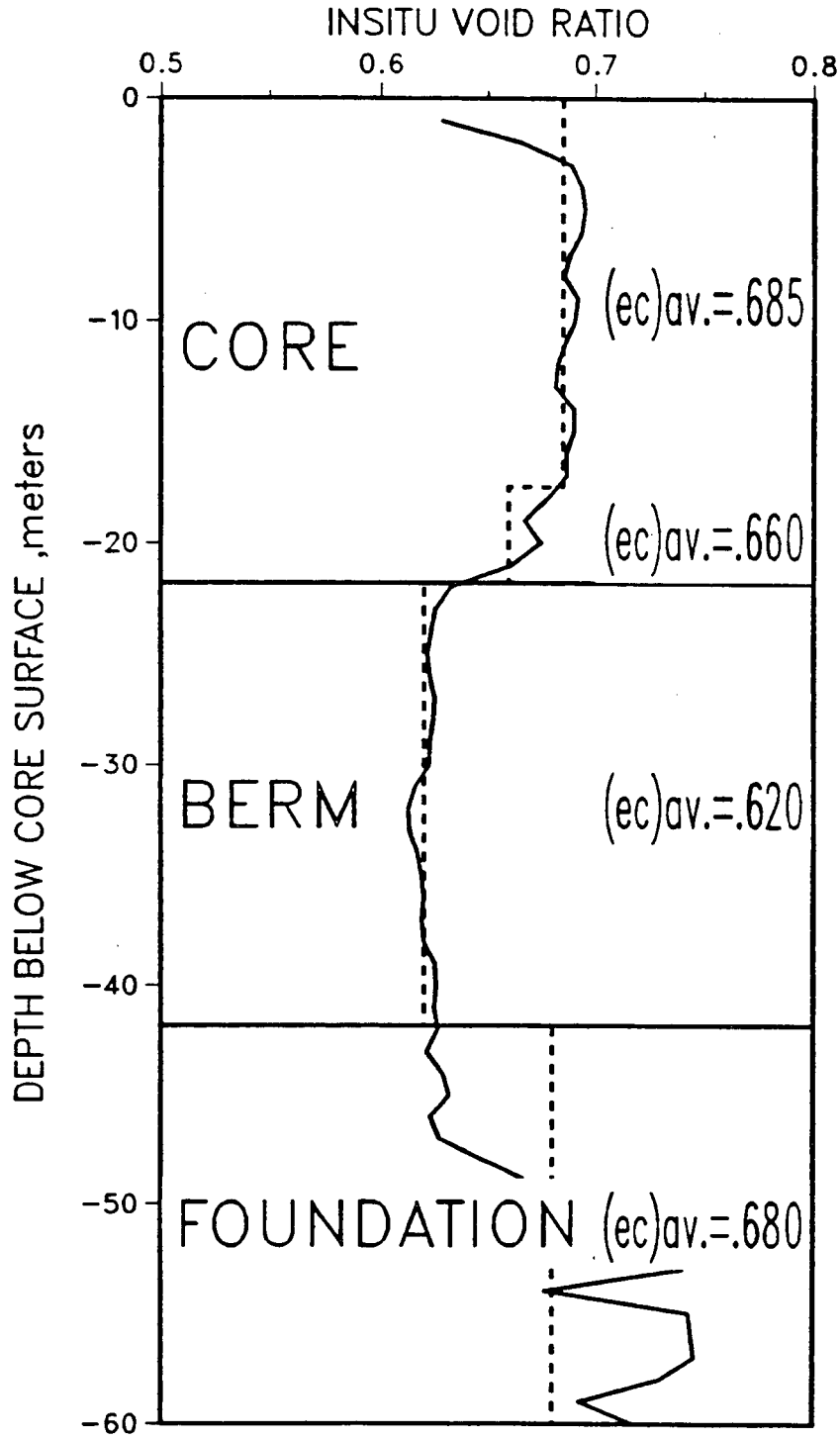

Figure 6.7 In situ void ratio, e_c versus depth

which was assigned an average in situ void ratio, $(e_c)_{av}$, as shown in the figure. It may be seen that $(e_c)_{av}$ range from .620 in the berm to .685 in the upper 17.5 m of the core. In the transition zone of the core and berm $(e_c)_{av}$ = .660 and for the foundation soil $(e_c)_{av}$ = .680.

6.3.1.2 Evaluation of the In Situ Maximum Shear Modulus Versus Depth

The in situ maximum (low strain) shear modulus, G_{max}, was determined from empirical correlations between void ratio, CPT data, pressuremeter tests, and from direct in situ measurements of shear wave velocity.

The values of G_{max} as a function of depth obtained from the various methods described below are shown in Fig. 6.8.

• Hardin and Drnevich (1972): The shear modulus G_{max} is a function of the in situ void ratio and effective mean normal stress and is given by the following equation:

$$G_{max} = 320 \frac{(2.973 - e_c)^2}{1 + e_c} p_a \left(\frac{\sigma'_m}{p_a}\right)^{1/2} \qquad (6.4)$$

where p_a is the atmospheric pressure.

This equation together with the in situ void ratios from Fig. 6.7 were used to estimate the Hardin and Drnevich values.

• Robertson and Campanella (1984): The G_{max} values were obtained from the "mean" cone bearing resistance q_c values of Fig. 6.4 following the relationship proposed by Robertson and Campanella (1984) which is shown in Fig. 6.9.

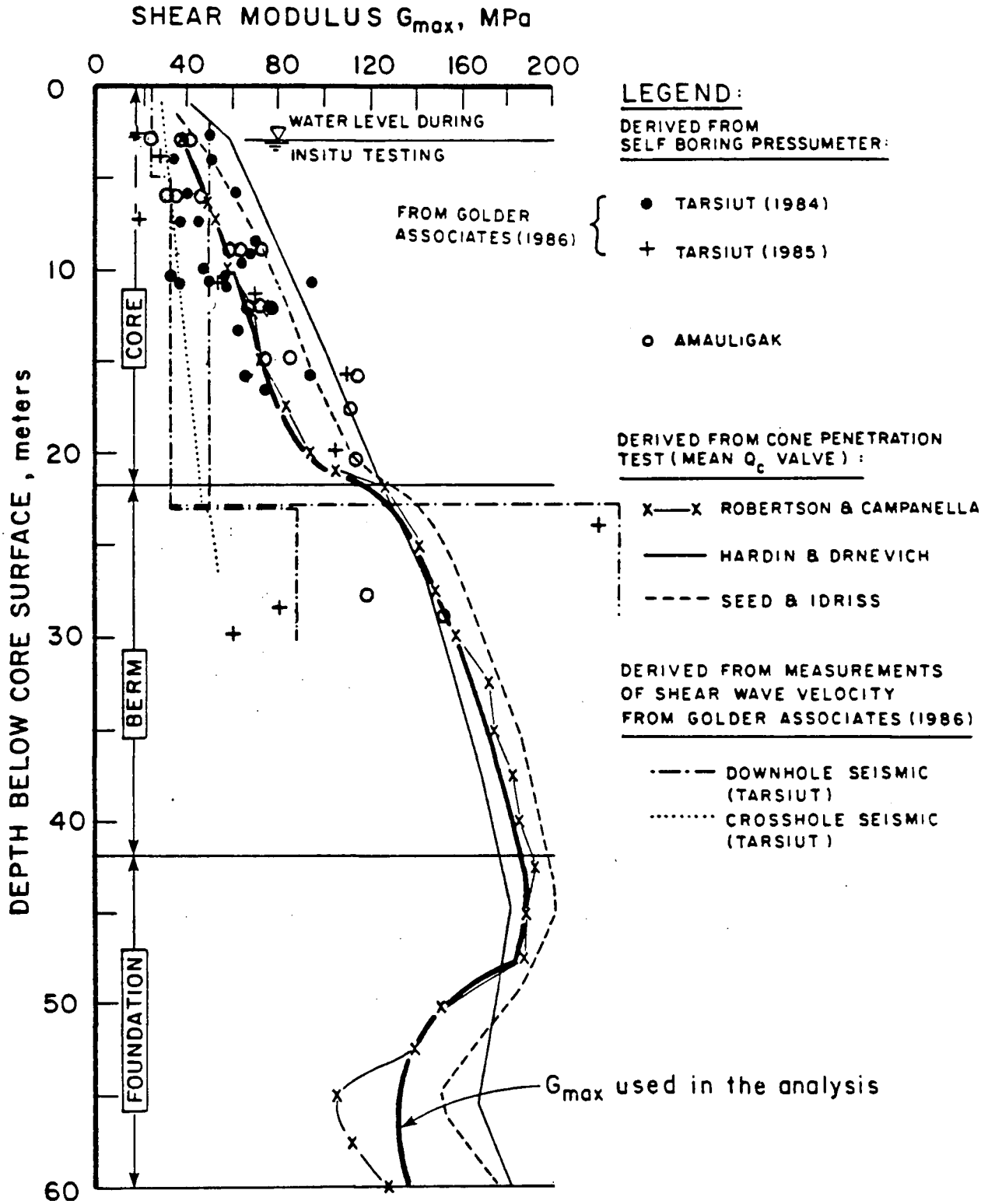

Figure 6.8 Variation of maximum shear modulus, G_{max} with depth

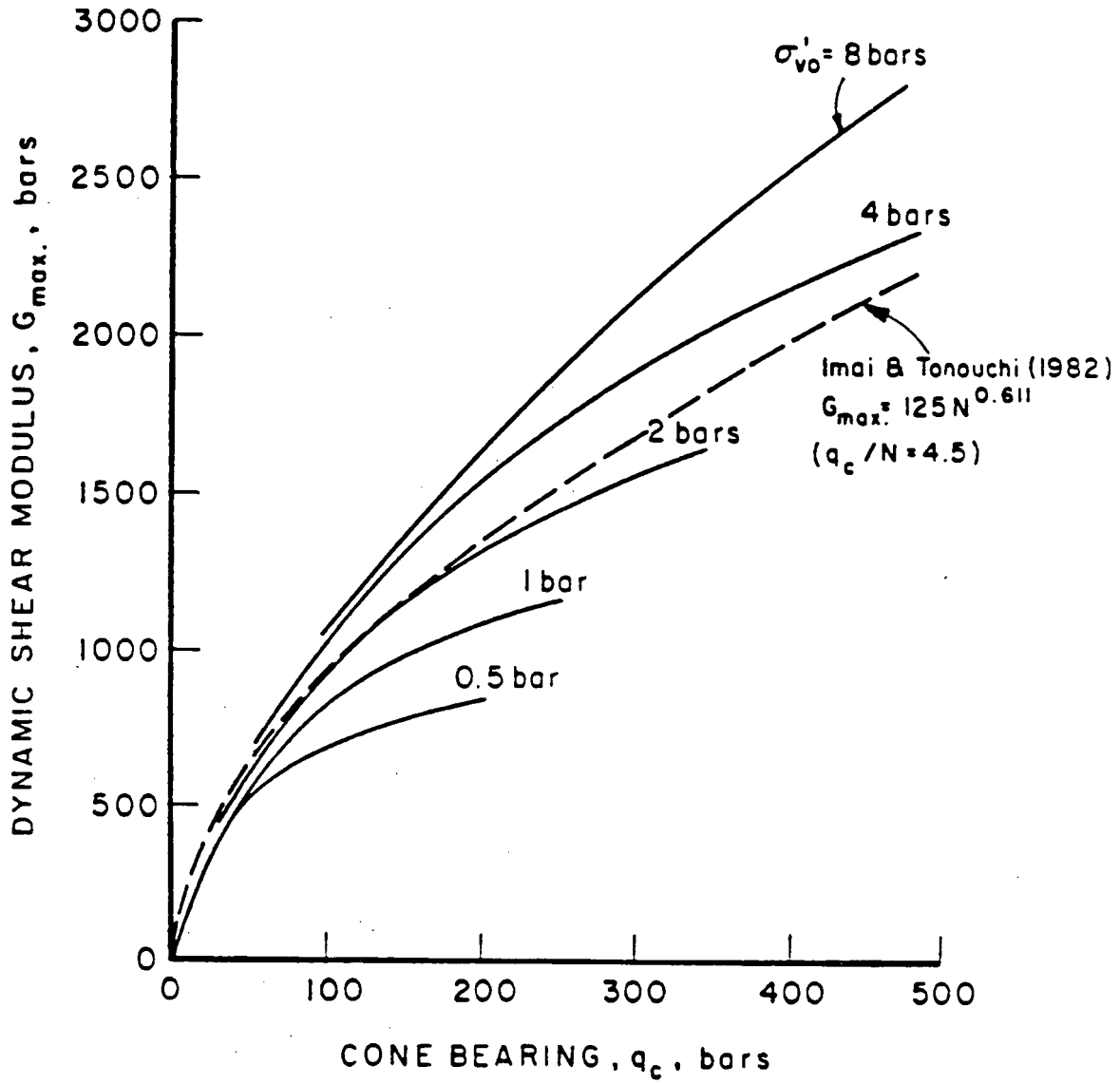

Figure 6.9 Relationship between cone bearing, q_c and maximum shear modulus, G_{max} (after Robertson and Campanella, 1984)

• Seed and Idriss (1970): The shear modulus, G_{max} is given by the equation:

$$G_{max} = 21.7\ (K_2)_{max}\ p_a\ (\frac{\sigma'_m}{p_a})^{1/2} \qquad (6.5)$$

where $(K_2)_{max}$ depends upon the density or normalized standard penetration resistance of the sand, $(N_1)60$. Tokimatsu and Seed (1987) suggest the following relationship:

$$(K_2)_{max} = 20[(N_1)_{60}]^{1/3} \qquad (6.6)$$

The $(N_1)_{60}$ values were obtained as follows. First the $(N)_{60}$ values were computed using the chart proposed by Seed and DeAlba (1986) that correlates the penetration ratio $q_c/(N)_{60}$ with the mean grain size D_{50}. This chart is shown in Fig. 6.10. For the Erksak 320/1 sand with D_{50} = .32 mm, $q_c/(N)_{60}$ = 4.6. The q_c values of Fig. 6.4 were used to obtain $(N)_{60}$ values as a function of depth and these were modified to $(N_1)_{60}$ values using the following equation proposed by Liao and Whitman (1986):

$$(N_1)_{60} = (\frac{p_a}{\sigma'_v})^{1/2} \cdot (N)_{60} \qquad (6.7)$$

The computed values of G_{max} vs depth using these $(N_1)_{60}$ values and Eqs. (6.5) and (6.6) are shown in Fig. (6.8).

• G_{max} from Self-Boring Pressuremeter Data: The self-boring pressuremeter data obtained at the Amauligak I-65 site were analyzed using the method described in Chapter 5 and are shown in Fig. 6.8. The shear

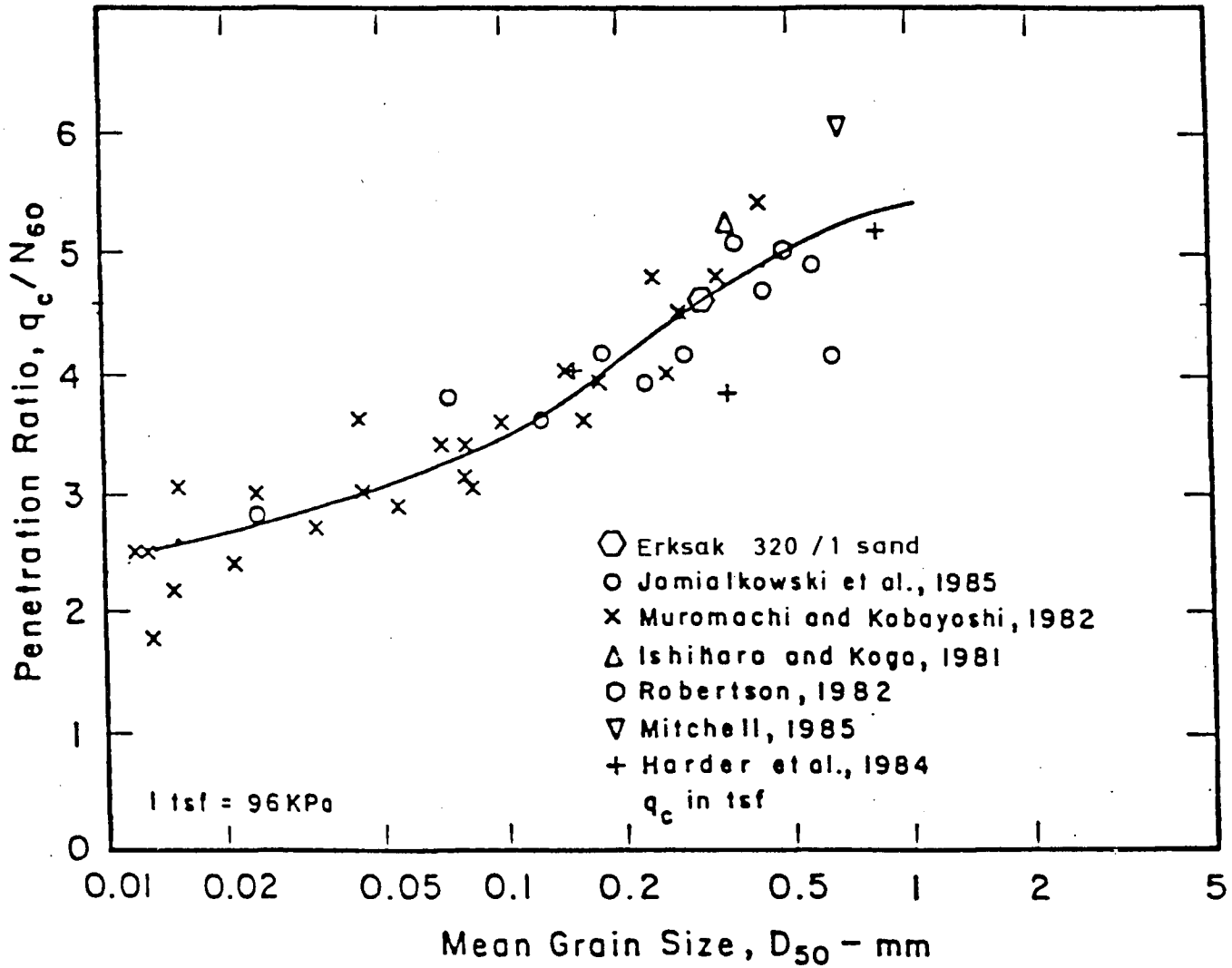

Figure 6.10 Variation of (q_c/N_{60}) with mean grain size (after Seed and DeAlba, 1986)

modulus G_{max} was determined from the secant unloading modulus G* using the chart developed in Chapter 5 and shown earlier in Fig. 5.10.

G_{max} values determined by Golder Associates (1987) from analysis of SBP data from TARSIUT I-45 are also shown in Fig. 6.8.

• Seismic Determination of G_{max}: The shear moduli deduced from down-hole and crosshole measurements of shear wave velocities at the TARSIUT I-45 site reported by Golder Associates (1986) are shown in Fig. 6.8.

It may be seen from the G_{max} data shown in Fig. 6.8 that there is considerable scatter. The solid line, which closely follows the Robertson and Campanella prediction represents the average G_{max} of all the data shown in the figure and was used in the analysis.

• KG_{max} Versus Void Ratio

In the analysis carried out with the modified SMP model the maximum shear modulus was obtained using the following equation which has been already described in Chapter 2:

$$G_{max} = KG_{max}\ Pa\ (\frac{\sigma'_m}{Pa})^n$$

From this equation KG_{max} is obtained as follows:

$$KG_{max} = G_{max}/(Pa(\frac{\sigma'_m}{Pa})^n \qquad (6.8)$$

Assuming that n = .5 (common value for sands), and using eq. (6.8) and the G_{max} values shown in Fig. 6.8 by the solid line, KG_{max} values versus depth were obtained. From these values, average $(KG_{max})_{av}$ values were obtained and are presented in Fig. 6.11. Combining the values of $(e_c)_{av}$ and

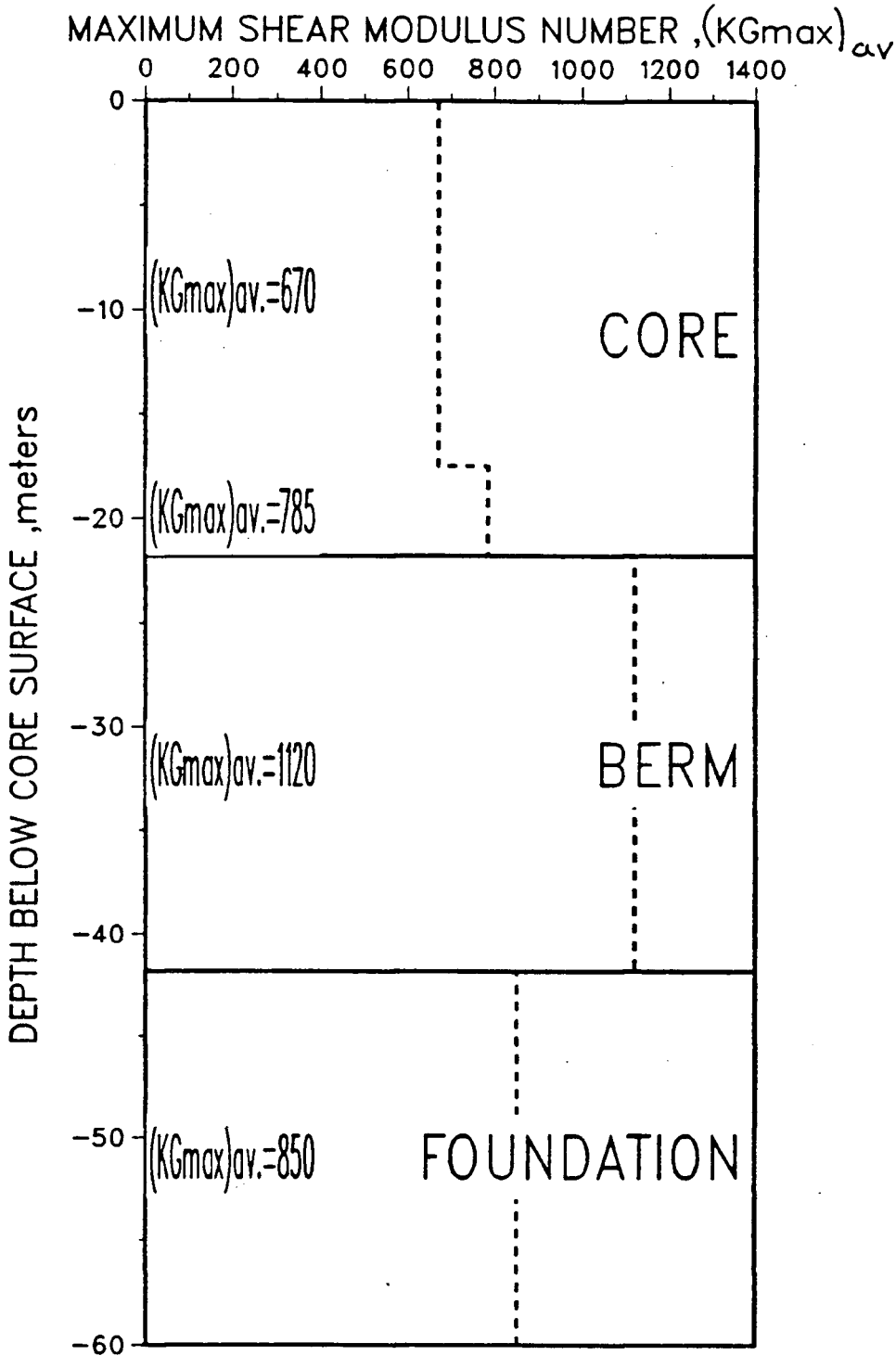

Figure 6.11 Variation of maximum shear modulus number, $(KG_{max})_{av}$ with depth

$(KG_{max})_{av}$ a relationship between KG_{max} and e_c is obtained and shown in Fig. 6.12. In this figure the points representative of the core and berm (points A, B, C) define a curve that is thought to be representative of KG_{max} vs e_c for the Erksak 320/1 sand. It may be seen that point D, which is representative of the foundation soil was not taken into account to define that relationship, since the data available for the foundation soil is based on 1 single CPT test and also it is thought that the foundation soil is located too far away from the ice loading location for its importance to be relevant in the analysis.

6.3.1.3 Evaluation of the Young's Modulus

Two Young's moduli were used in the analysis carried out with the hyperbolic model. One is the tangent Young's modulus on first loading, E_t, and the other the unloading/reloading or maximum Young's modulus, E_{max}.

The Young's modulus, E_t was evaluated in the analysis using the following equation developed by Duncan et al. (1980):

$$E_t = KE\ Pa\ (\sigma'_m/Pa)^n\ (1 - SL\ R_F)^2 \qquad (6.9)$$

where:

KE = Young's modulus number

n = Young's modulus exponent

R_F = failure ratio, the ratio of the strength from the Mohr-Coulomb criterion to the strength from the hyperbola

SL = stress level, the ratio of the mobilized deviator stress $(\sigma_1-\sigma_3)_m$ to the deviator stress at failure $(\sigma_1-\sigma_3)_f$.

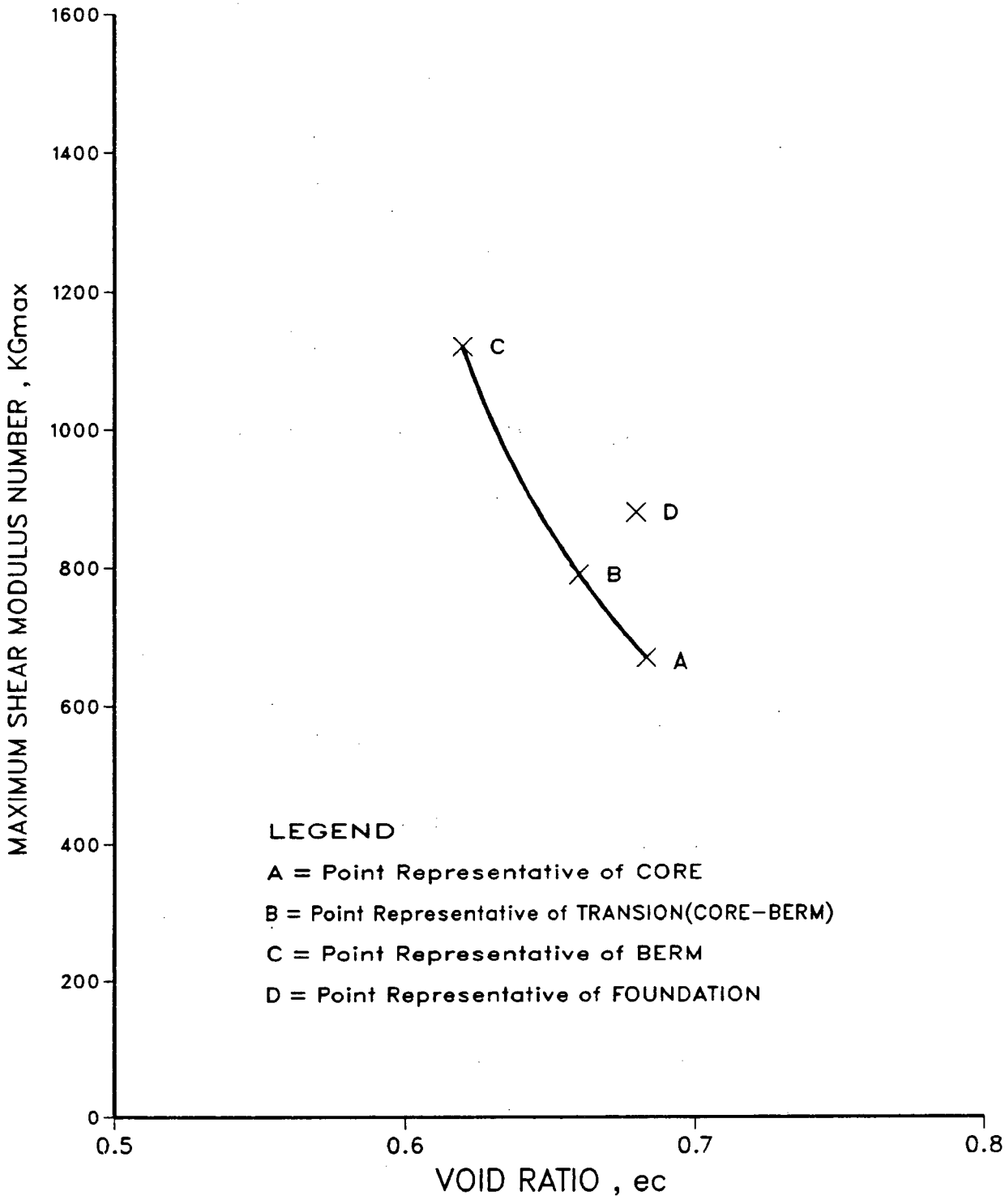

Figure 6.12 Maximum shear modulus number, KG_{max} versus void ratio, e_c

The soil parameters KE, n and R_F as a function of void ratio, e_c are shown in Fig. 6.13 and were obtained using the drained triaxial test data on Erksak 320/1 sand reported by Golder Associates (1986). The relevant data for that evaluation is presented in Appendix 6.2.

The maximum Young's modulus, E_{max} was evaluated in the analysis using the following equation:

$$E_{max} = KE_{max}\ Pa\ (\sigma'_m/Pa)^n \qquad (6.10)$$

To evaluate the maximum Young's modulus number, KE_{max}, the equation that relates the Young's modulus with the shear modulus was adapted to the parameters KE_{max} and KG_{max}, i.e.

$$KE_{max} = 2(1+\upsilon)KG_{max} \qquad (6.11)$$

The relationship between KE_{max} and e_c is shown in Fig. 6.13 and was obtained using equation (6.11), assuming a Poisson's ratio value of $\upsilon = .2$ and using the values of KG_{max} versus e_c shown in Fig. 6.12.

6.3.1.4 Evaluation of the Bulk Modulus

As for the case of the Young's modulus, two bulk moduli were used in the analysis. One is the tangent bulk modulus on first loading, B_t, and the other the unloading/reloading bulk modulus, B_{ur}. Both B_t and B_{ur} depend on void ratio and effective mean normal stress and were evaluated in the analysis using the following equation:

$$B_t(\text{or } B_{ur}) = KB\ (\text{or } KB_{ur})\ Pa\ \left(\frac{\sigma'_m}{Pa}\right)^m \qquad (6.12)$$

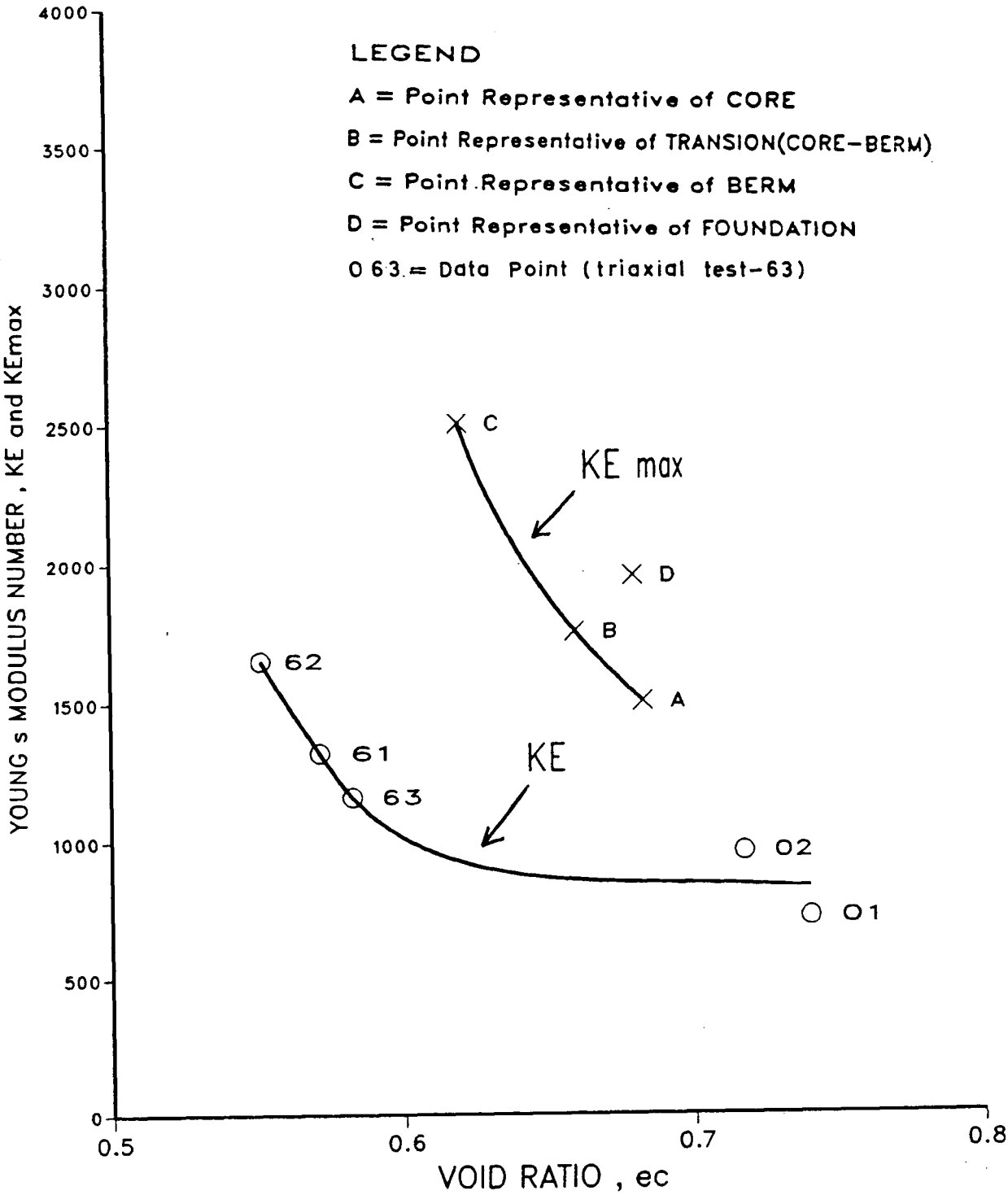

Figure 6.13 Young's modulus numbers, KE_{max} and KE versus void ratio

where:

KB = bulk modulus number (first loading)

KB_{ur} = bulk modulus number (unloading/reloading)

σ'_m = effective mean normal stress

m = bulk modulus exponent

The tangent bulk modulus parameters, KB and m for Erksak 320/1 sand are shown in Fig. 6.14 and were determined from the triaxial isotropic compression test data reported by Golder Associates (1986), following the procedures outlined by Byrne and Eldridge (1982). The relevant data for this evaluation is presented in Appendix 6.2.

The unloading/reloading bulk modulus number, KB_{ur} was evaluated from B_t/B_{ur} relationships which were obtained from test data on Ottawa sand provided by Negussey (1987). The relationship between KB_{ur} and e_c for the Erksak 320/1 sand is also shown in Fig. 6.14.

6.3.1.5 Evaluation of the Plastic Shear Parameter G_p and the Flow Rule Parameters for Use With the Modified SMP Model

As described in Chapter 2 the plastic shear parameter, G_p, is evaluated in the analysis by the following equation:

$$G_p = KG_p(\sigma'_m/Pa)^{np} (1 - R_F\ SL)^2 \qquad (6.13)$$

The soil parameters KG_p, np and R_F as a function of void ratio, e_c, are shown in Fig. 6.15 and were obtained from the drained triaxial test data reported by Golder Associates (1986), following the procedures outlined earlier in Chapter 3.

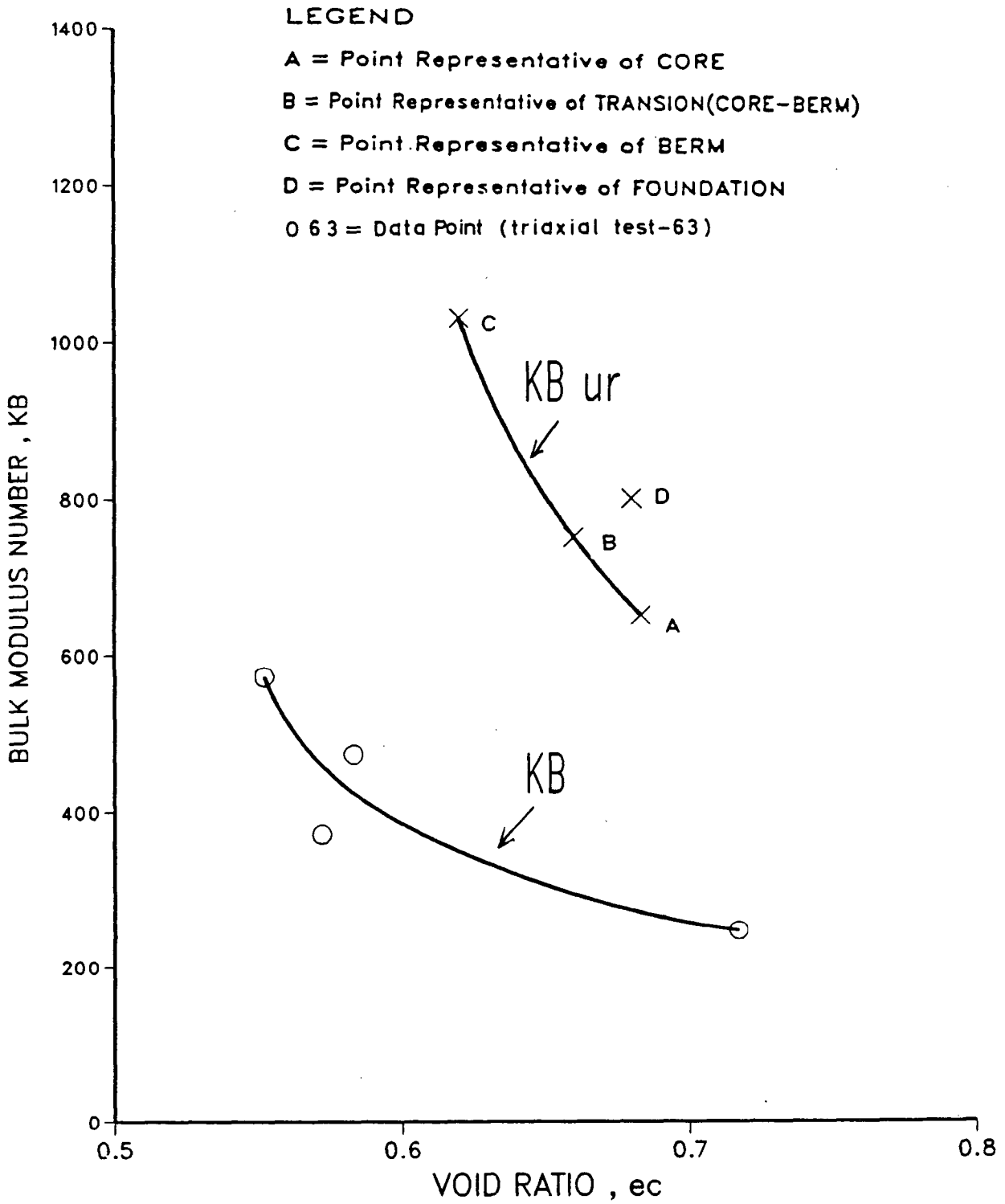

Figure 6.14 Bulk modulus numbers, KB_{ur} and KB versus void ratio

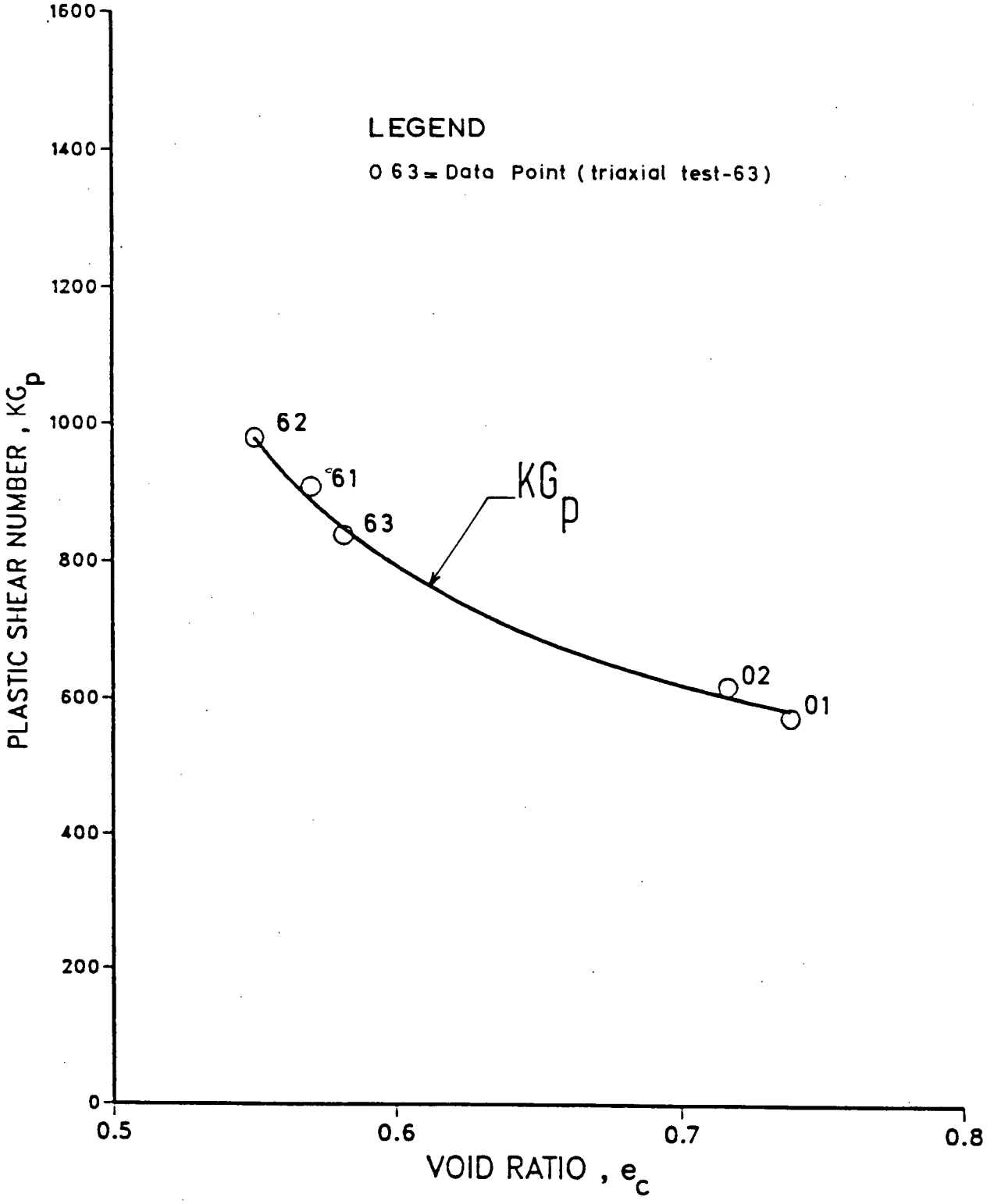

Figure 6.15 Plastic shear number, KG_p versus void ratio, e_c

The Flow Rule relationship for Erksak 320/1 sand is shown in Fig. 6.16. From this figure values of λ = .97 and μ = .25 were obtained. The relevant data used to obtain the above quantities is given in Appendix 6.2.

6.3.2 Evaluation of the Failure Friction Angle and the Failure Stress Ratio on the SMP

Relationships between the moduli and void ratio have been established in the previous section. The two additional soil parameters needed are the failure friction angle, ϕ_F, to use with the hyperbolic model, and the failure stress ratio on the SMP $(\tau_{SMP}/\sigma_{SMP})_F$, to use with the modified SMP model. The procedures followed to evaluate these two soil parameters are described below.

6.3.2.1 Evaluation of the Failure Friction Angle

In the analysis carried out, the failure friction angle was defined using the following equation:

$$\phi_F = \phi_1 - \Delta\phi \log_{10}(\sigma'_m/Pa) \qquad (6.14)$$

where:

ϕ_1 = peak friction angle at the effective mean normal stress of 1 atmosphere

$\Delta\phi$ = decrease in ϕ_F for a ten-fold increase in effective mean normal stress

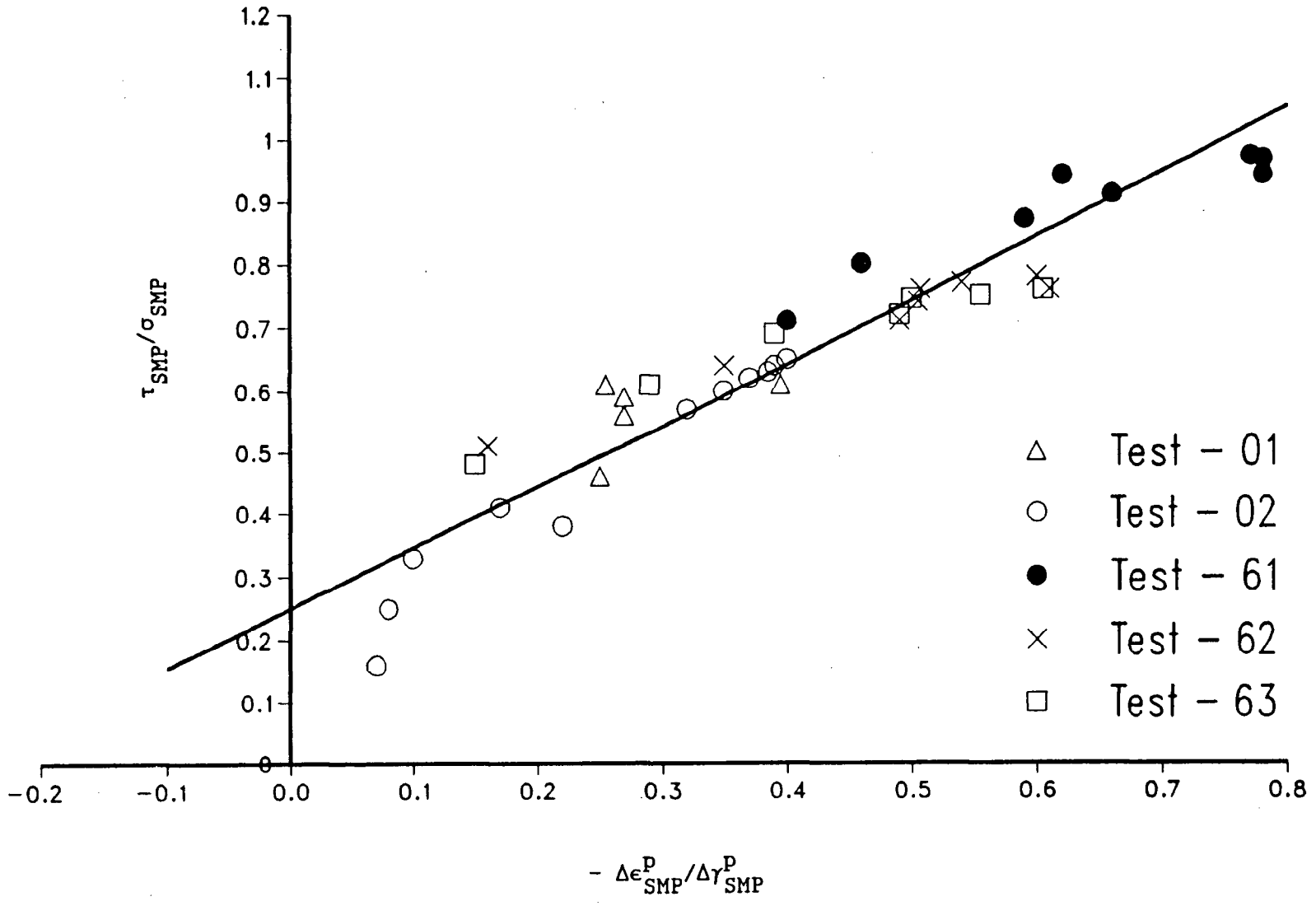

Figure 6.16 Flow rule relationship for Erksak 320/1 sand

The above equation is based on the equation developed by Duncan et al. (1980), to define ϕ_F. The only difference is that, herein, σ'_m is used to define the term $\Delta\phi$ rather than σ'_3 which is used by Duncan et al.

The two soil parameters ϕ_1 and $\Delta\phi$ were evaluated as follows.

A relationship between failure friction angle, ϕ_F and state parameter, ψ, for several sands including the Erksak 320/1 sand, was developed by Golder Associates (1986) and is presented in Fig. 6.17. Using the in situ state parameter values shown in Fig. 6.6 together with the corresponding in situ effective mean normal stress, σ'_m, a plot of ϕ_F versus $\log_{10}(\sigma'_m/Pa)$ was developed and is shown in Fig. 6.18.

Data points evaluated from the drained triaxial test data reported by Golder Associated (1986), together with data points representative of the berm fills prior to placement of the core are also included in Fig. 6.18. These berm values were obtained using the "mean" q_c data shown in Fig. 6.19.

Void ratio values, e_c, correspondent to the triaxial test and the berm and core fills are also shown in Fig. 6.18. It may be seen that the field and laboratory data plot in agreement with each other and the data points representative of the berm fills before and after the placement of the core show that the failure friction angle decreases with σ'_m, as would be expected, and converge towards a residual friction angle $\phi_R = 33°$. A similar trend is also observed for the core material and for the three triaxial tests carried out at the lower void ratios.

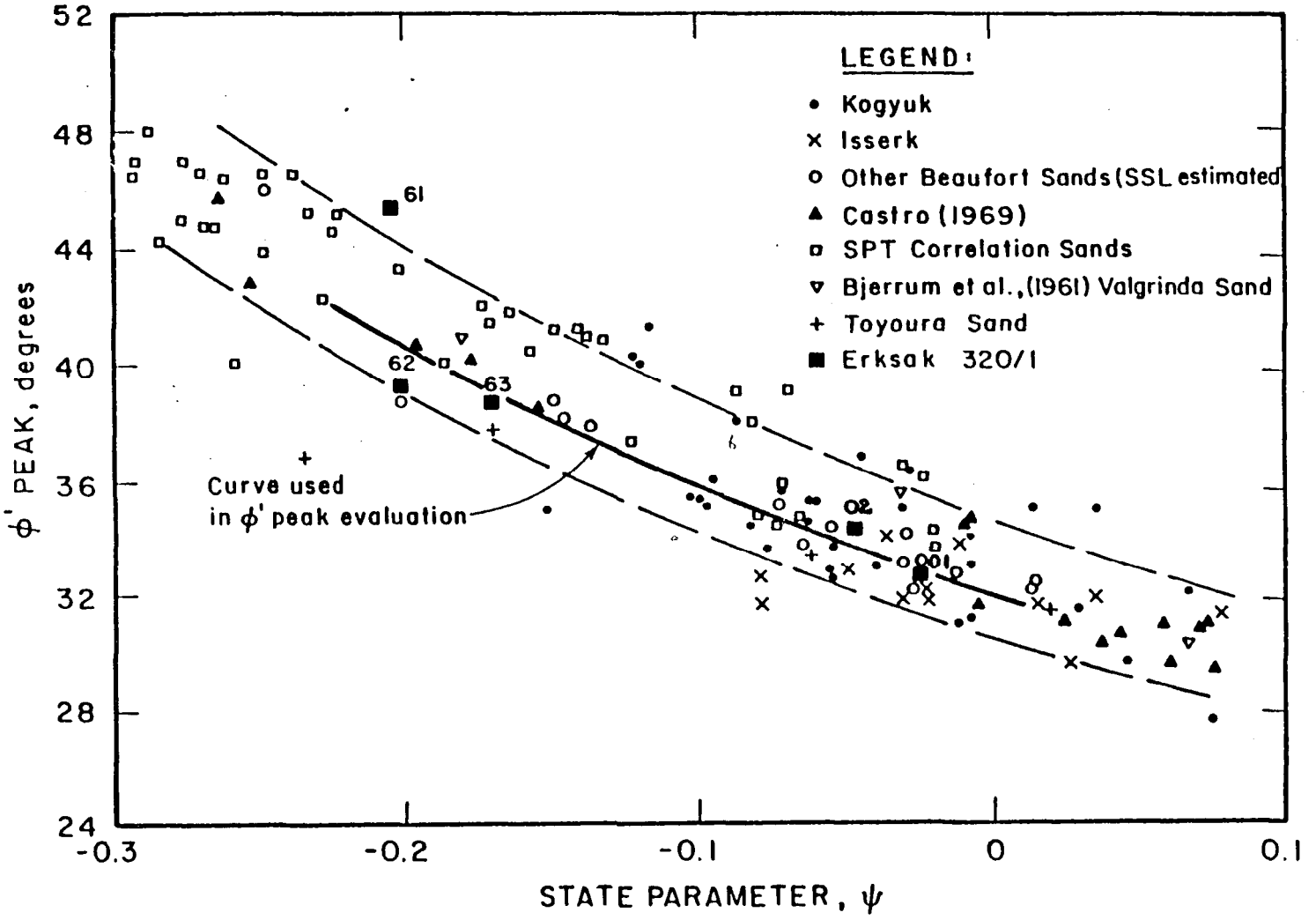

Figure 6.17 Relationship between state parameter, ψ and peak friction angle, ϕ_p (after Golder Associates, 1986)

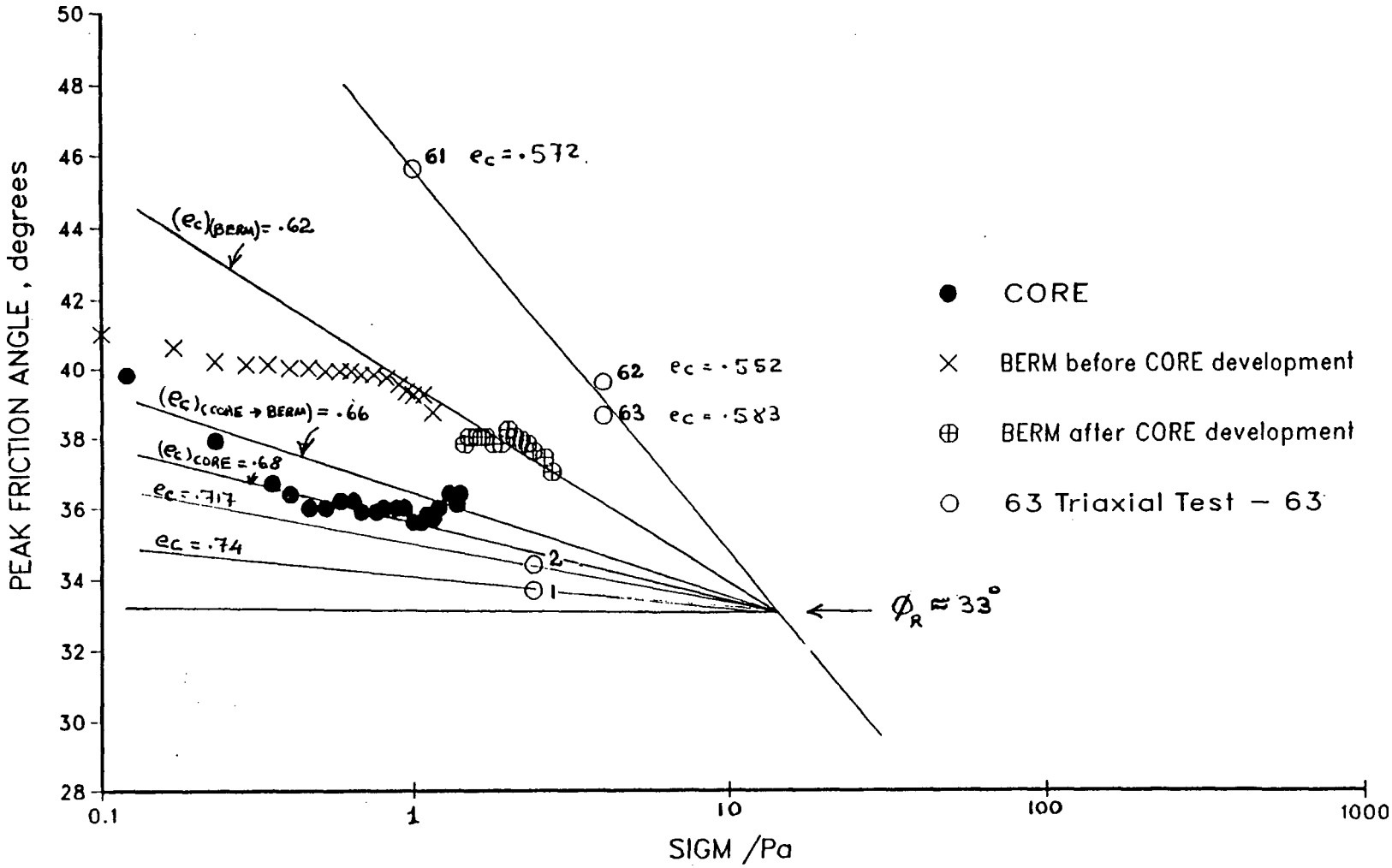

Figure 6.18 Relationship between failure friction angle, ϕ_F and $\log_{10}((\sigma'_m)_i/Pa)$ for Erksak 320/1 sand

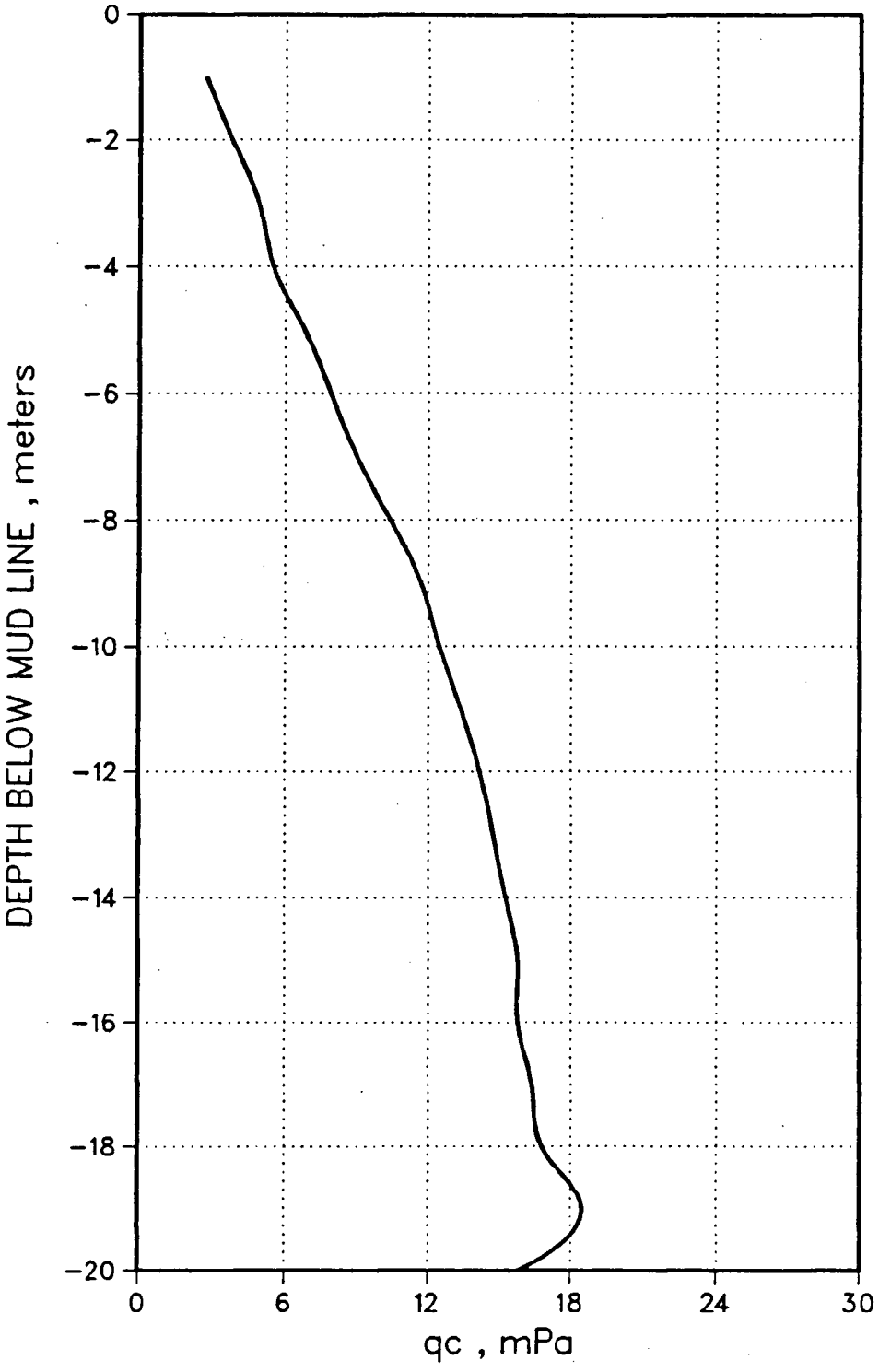

Figure 6.19 "Mean" values of q_c in the berm before placement of the core (after Jefferies and Livingstone, 1985)

Based on the results shown in Fig. 6.18 values of ϕ_1 and $\Delta\phi$ were evaluated for each data point and in turn a relationship of ϕ_1 and $\Delta\phi$ versus depth was developed. Based on these values, average $(\phi_1)_{av}$ and $(\Delta\phi)_{av}$ values, corresponding to the same depth intervals used to evaluate the average in situ void ratios $(e_c)_{av}$, were evaluated and are shown in Fig. 6.20. It may be seen that $(\phi_1)_{av}$ range from 35.7° for the upper 17.5 m of the core to 39.7° for the berm, while the corresponding $(\Delta\phi)_{av}$ range from 2.8° to 6.1° for the same sand zones.

6.3.2.2 Evaluation of the Peak Stress Ratio on the SMP

In the analysis carried out with the modified SMP model the peak stress ratio on the SMP was defined using the following equation developed earlier in Chapter 2.

$$(\tau_{SMP}/\sigma_{SMP})_F = (\tau_{SMP}/\sigma_{SMP})_1 - \Delta(\tau_{SMP}/\sigma_{SMP})\log_{10}((\sigma'_{SMP})_F/Pa) \qquad (6.15)$$

where:

$(\tau_{SMP}/\sigma_{SMP})_1$ = the failure stress ratio on the SMP at $(\sigma'_{SMP})_F$ = 1 atmosphere.

$\Delta(\tau_{SMP}/\sigma_{SMP})$ = the decrease in $(\tau_{SMP}/\sigma_{SMP})$ for a ten-fold increase in $(\sigma'_{SMP})_F$

$(\sigma'_{SMP})_F$ = the effective normal stress on the SMP at failure.

The two soil parameters $(\tau_{SMP}/\sigma_{SMP})_1$ and $\Delta(\tau_{SMP}/\sigma_{SMP})$ were evaluated as follows:

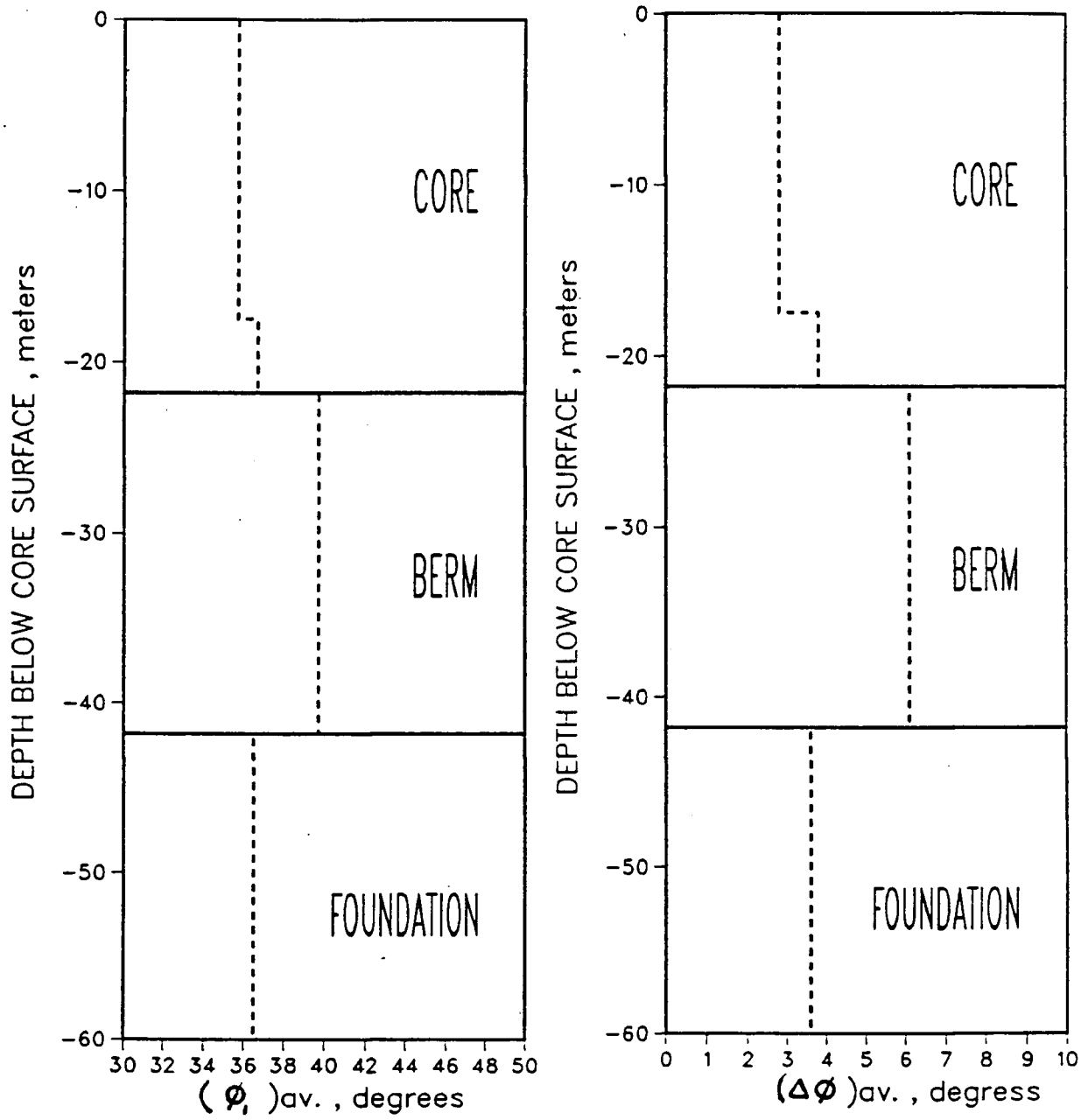

Figure 6.20 Variation of $(\phi_1)_{av}$ and $(\Delta\phi)_{av}$ with depth

Using the drained triaxial test data on Erksak 320/1 sand reported by Golder Associates (1986), the relationships shown in Fig. 6.21 between $(\tau_{SMP}/\sigma_{SMP})_F$ and $\log_{10}((\sigma'_{SMP})_F/Pa)$ were obtained, and from it, values of $(\tau_{SMP}/\sigma_{SMP})_i$ and $\Delta(\tau_{SMP}/\sigma_{SMP})$ were evaluated for each test. Using these values and the values of ϕ_i and $\Delta\phi$, earlier obtained for the same tests, linear relationships were obtained between $(\tau_{SMP}/\sigma_{SMP})_i$ and ϕ_i, and between $\Delta(\tau_{SMP}/\sigma_{SMP})$ and $\Delta\phi$. These two relationships are shown in Fig. 6.22. Finally using the $(\phi_i)_{av}$ and $(\Delta\phi)_{av}$ values shown in Fig. 6.20 together with the relationships shown in Fig. 6.22 the values of $((\tau_{SMP}/\sigma_{SMP})_i)_{av}$ and $\Delta(\tau_{SMP}/\sigma_{SMP})_{av}$ shown in Fig. 6.23 were obtained.

6.3.3 Predictions of the Drained Triaxial Tests on Erksak 320/1 Sand

In the previous two sections (6.3.1 and 6.3.2) the following relationships were established: (a) void ratio versus depth; (b) moduli versus void ratio; (c) ϕ_i and $\Delta\phi$ versus depth; and (d) $(\tau_{SMP}/\sigma_{SMP})_i$ and $\Delta(\tau_{SMP}/\sigma_{SMP})$ versus depth.

To validate the soil parameters obtained from these relationships, predictions of the drained triaxial tests on Erksak 320/1 sand were carried out using the hyperbolic model with the soil parameters shown in Table 6.2 and the modified SMP model with the soil parameters shown in Table 6.3.

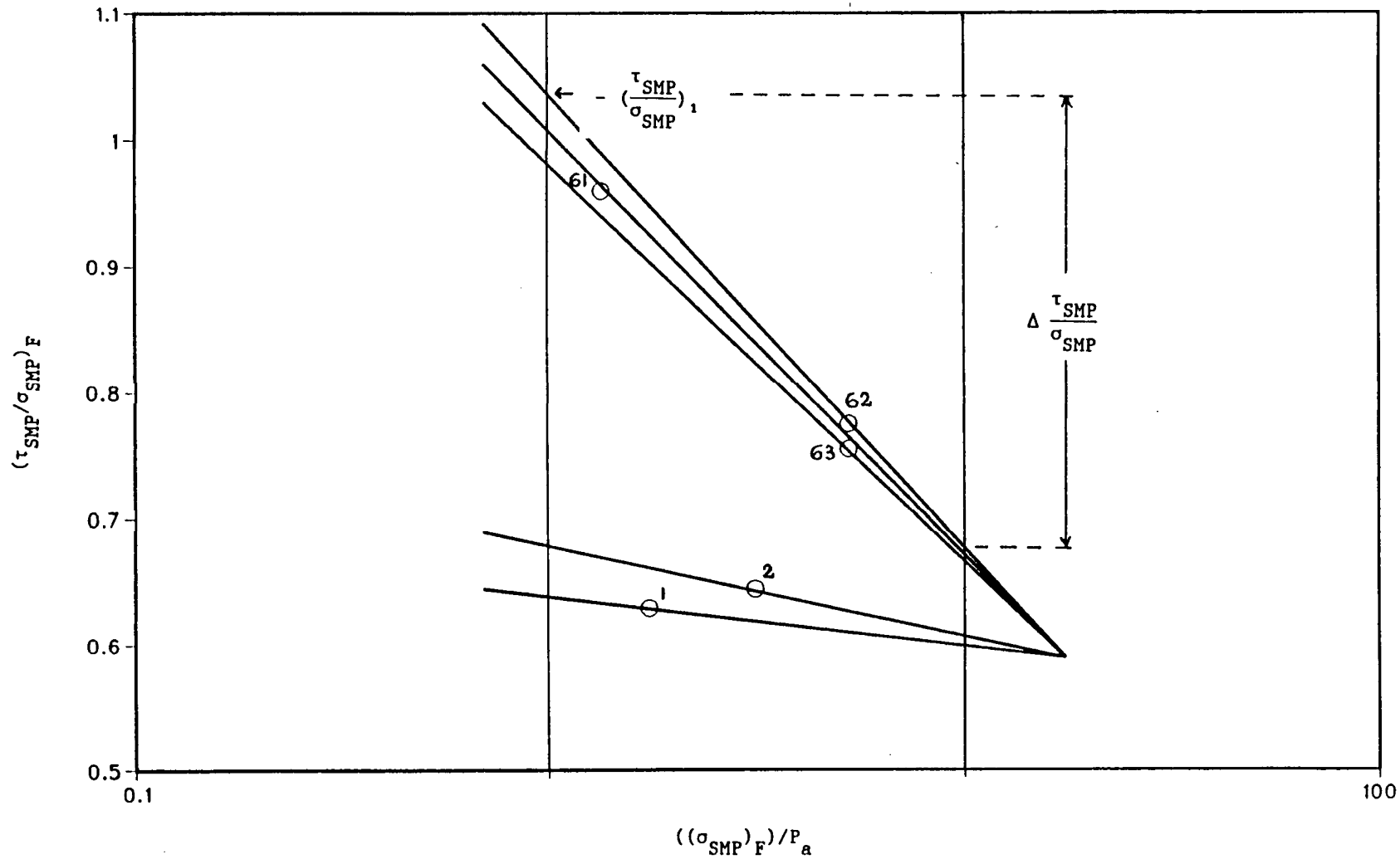

Figure 6.21 Relationship between $(\tau_{SMP}/\sigma_{SMP})_F$ and $\log_{10}((\sigma_{SMP})_F/Pa)$ for Erksak 320/1 sand

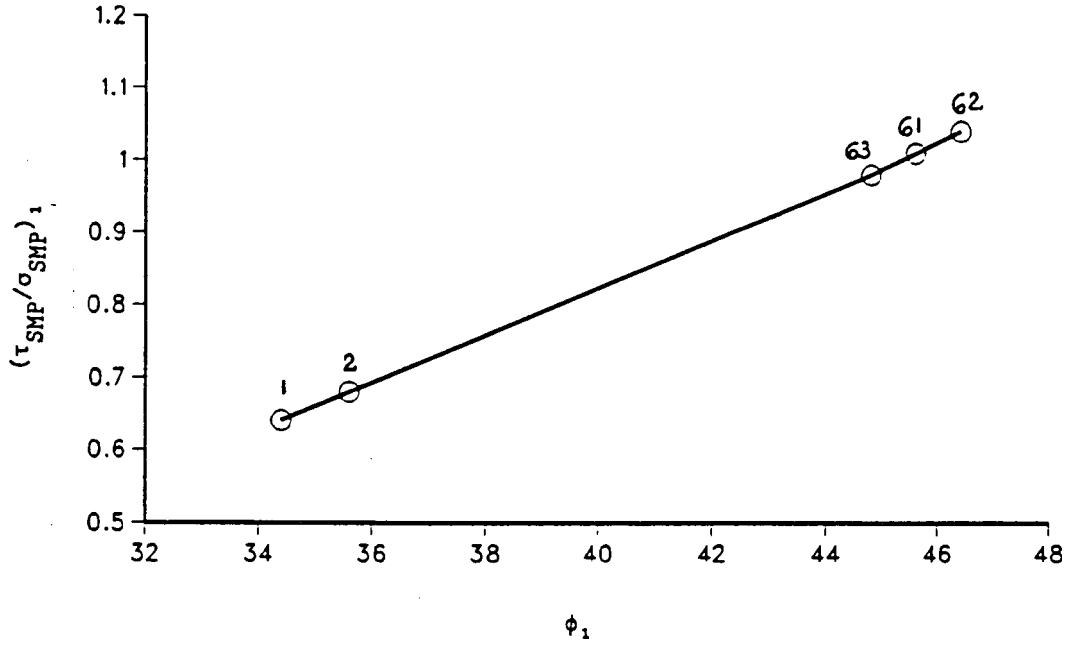

Figure 6.22(a) Relationship between $(\tau_{SMP}/\sigma_{SMP})_1$ and ϕ_1 for Erksak 320/1 sand

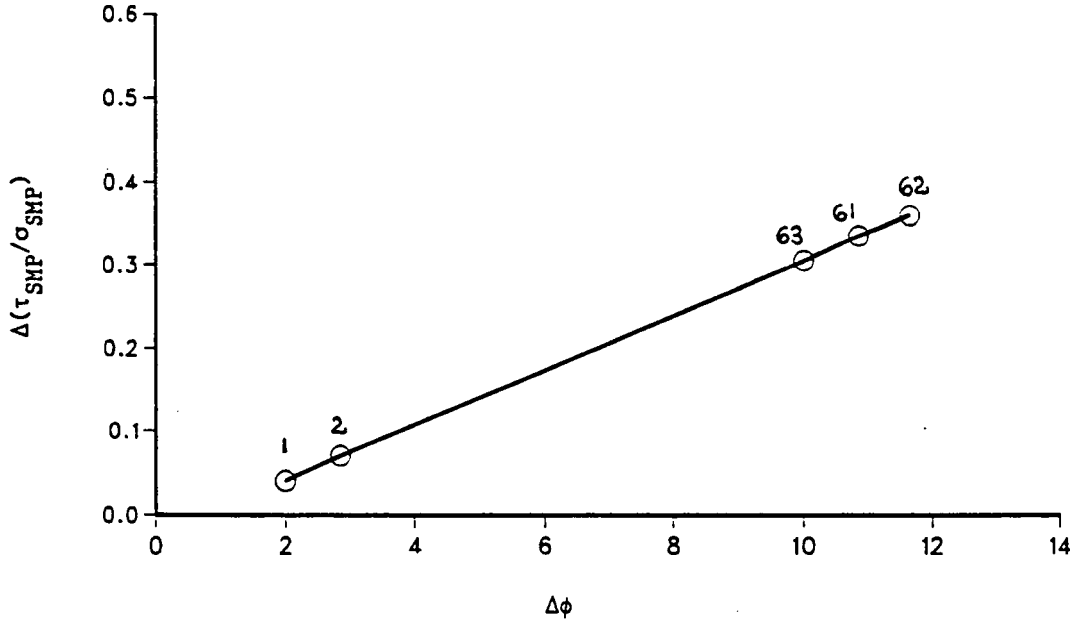

Figure 6.22(b) Relationship between $\Delta(\tau_{SMP}/\sigma_{SMP})$ and $\Delta\phi$ for Erksak 320/1 sand

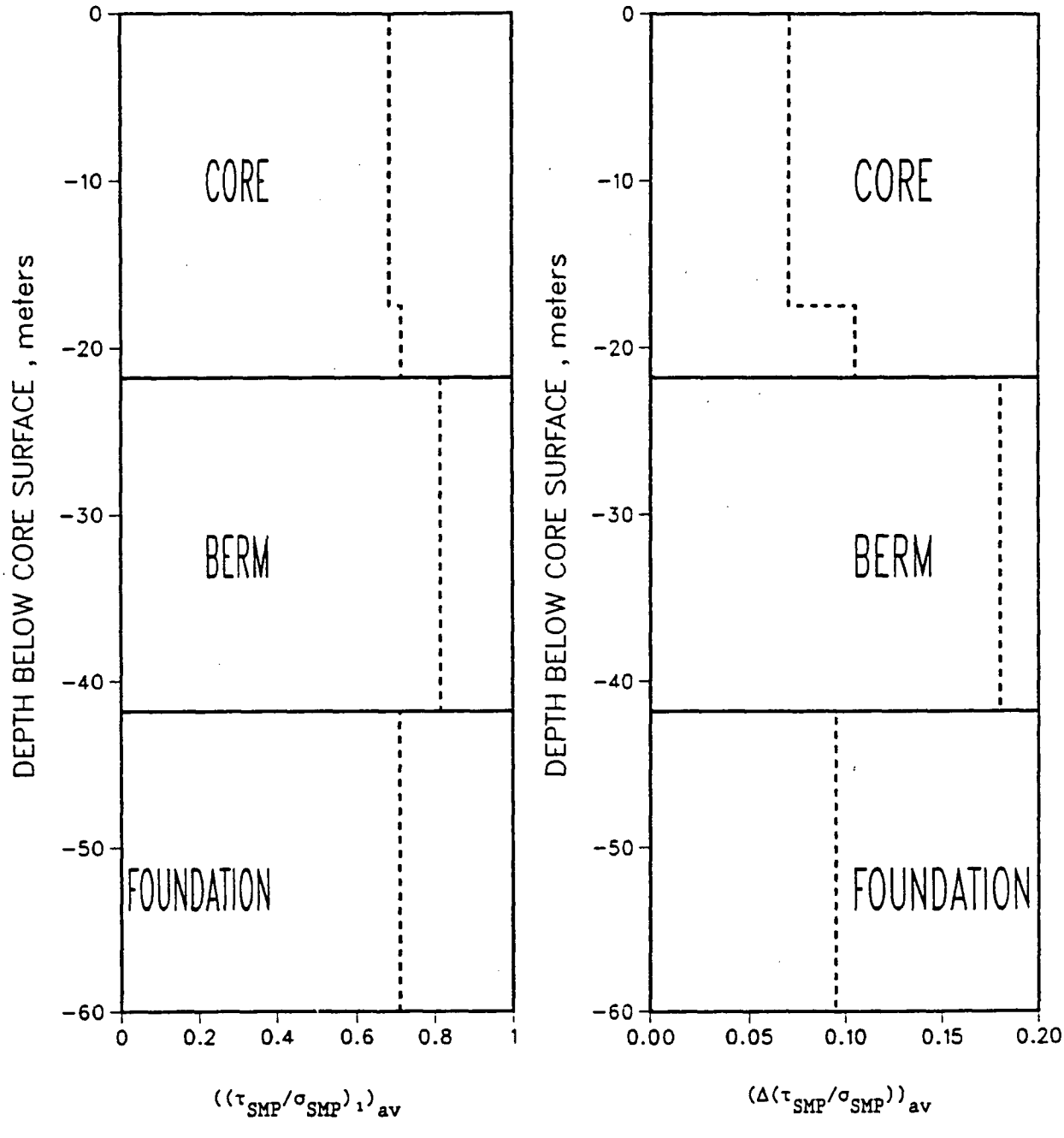

Figure 6.23 Variation of $((\tau_{SMP}/\sigma_{SMP})_1)_{av}$ and $(\Delta(\tau_{SMP}/\sigma_{SMP}))_{av}$ with depth

Table 6.2

Hyperbolic Soil Parameters - Erksak 320/1 Sand

Test #	e_c	KE	KE_{max}	n	KB	KB_{ur}	m	R_F	ϕ_1	$\Delta\phi$	ϕ_p
01	.740	720	1260	.50	230	550	.38	.80	34.4	2.0	33.8
02	.717	960	1710	.50	250	610	.38	.80	35.5	2.8	34.4
61	.572	1320	4000	.50	378	1130	.36	.90	45.6	10.8	45.6
62	.552	1648	4600	.50	573	1750	.40	.87	46.4	11.6	39.5
63	.583	1160	3600	.50	474	1420	.38	.83	44.8	10.0	38.6

Table 6.3

Modified SMP: Soil Parameters - Erksak 320/1 Sand

Test #	e_c	KG_{max}	n	KB_{ur}	m	KG_p	np	RF	$(\frac{\tau_{SMP}}{\sigma_{SMP}})_1$	$\Delta(\frac{\tau_{SMP}}{\sigma_{SMP}})$	u	λ
01	.740	525	.5	550	.38	575	-.56	.95	.64	.04	.25	.97
02	.717	710	.5	610	.38	620	-.56	.94	.68	.072	.25	.97
61	.572	1670	.5	1130	.36	910	-.56	1.00	1.01	.340	.25	.97
62	.552	1920	.5	1750	.40	980	-.56	.94	1.04	.362	.25	.97
63	.583	1500	.5	1420	.38	840	-.56	.94	.98	.313	.25	.97

The predictions obtained with the hyperbolic model are presented in Fig. 6.24. It may be seen that the shear behaviour up to peak stress ratio is very well predicted by this model. However, as may be seen the volumetric dilative strains were not predicted. This is because the hyperbolic model used in the analysis does not consider dilatant effects.

The predictions obtained with the modified SMP model are presented in Fig. 6.25. It may be seen there is very good agreement between the measured and computed values of both shear and volume change responses up to the peak stress ratio. However, since strain softening parameters were not considered for the predictions, past the peak the predictions are not in good agreement with the measurements of those tests that do show strain softening.

6.3.4 Selection of Soil Types and Soil Parameters to Use in the Molikpaq Analysis

The soil types and parameters for use in the Molikpaq analysis for both the hyperbolic and the modified SMP models are tabulated in Fig. 6.26(a) and (b) respectively and were obtained following the procedures described below.

Based on the profile of the in situ void ratio versus depth evaluated earlier, and the existing water level at the time of the April 1987 ice loading event (4.8 m below core surface), five soil types were identified as shown in Fig. 6.27. Also shown in the figure are the locations of the different soil layers used in the F.E. analysis.

To obtain the different soil parameters shown in Fig. 6.26(a) and 6.26(b), the $(e_c)_{av}$ value of each soil type obtained from Fig. 6.27 was used together with the following figures:

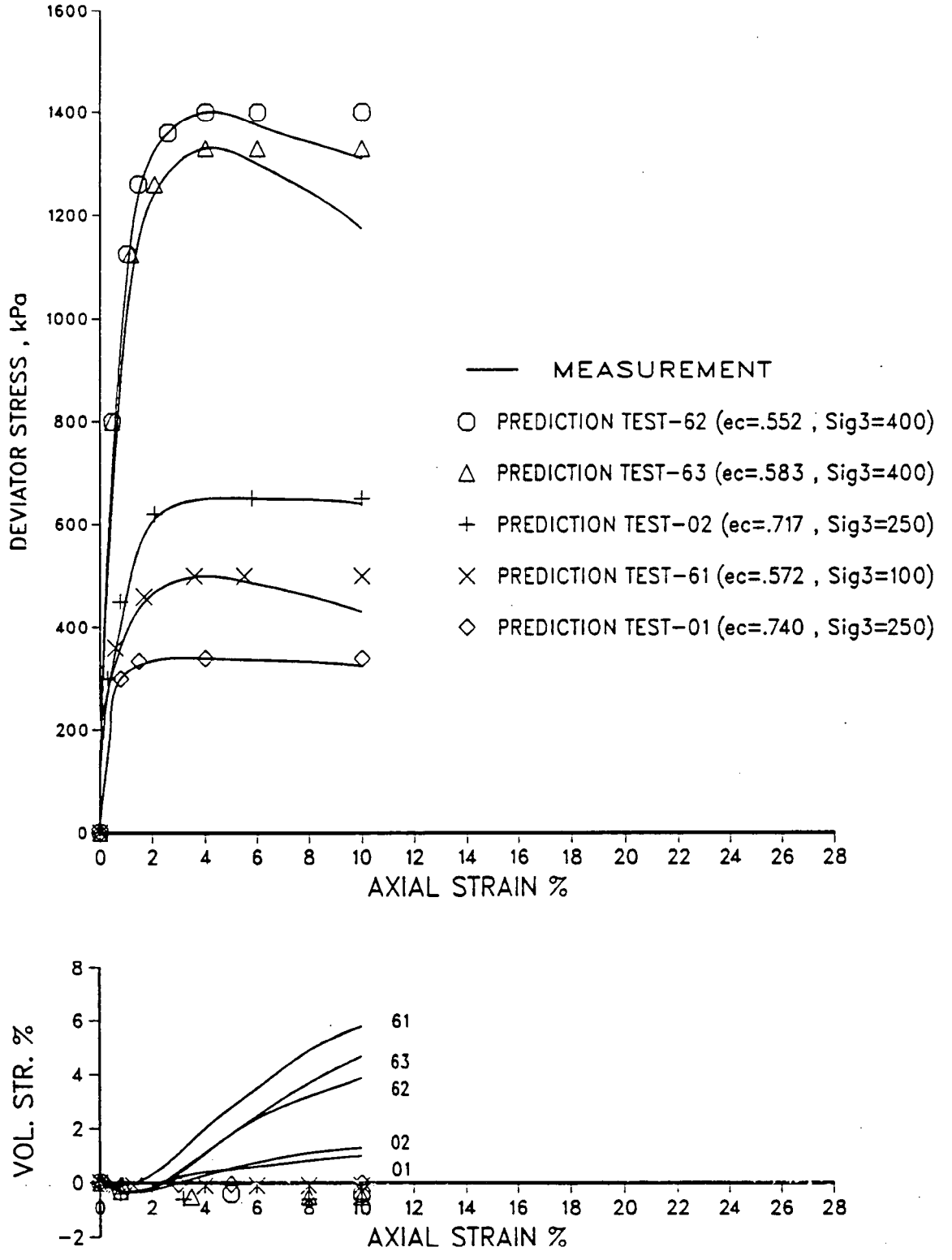

Figure 6.24 Predictions of drained triaxial tests on Erksak 320/1 sand using the hyperbolic model

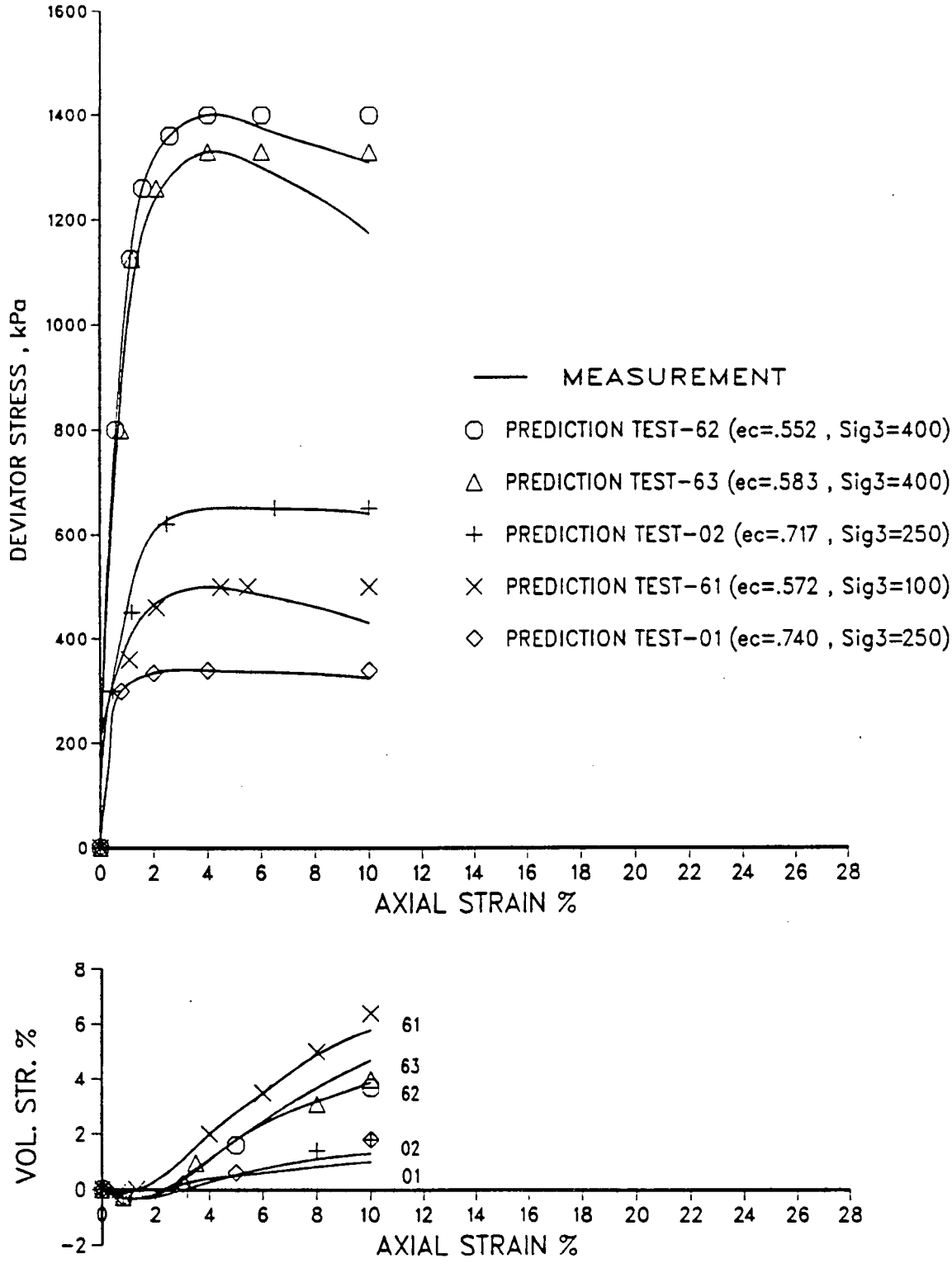

Figure 6.25 Predictions of drained triaxial tests on Erksak 320/1 sand using the modified SMP model

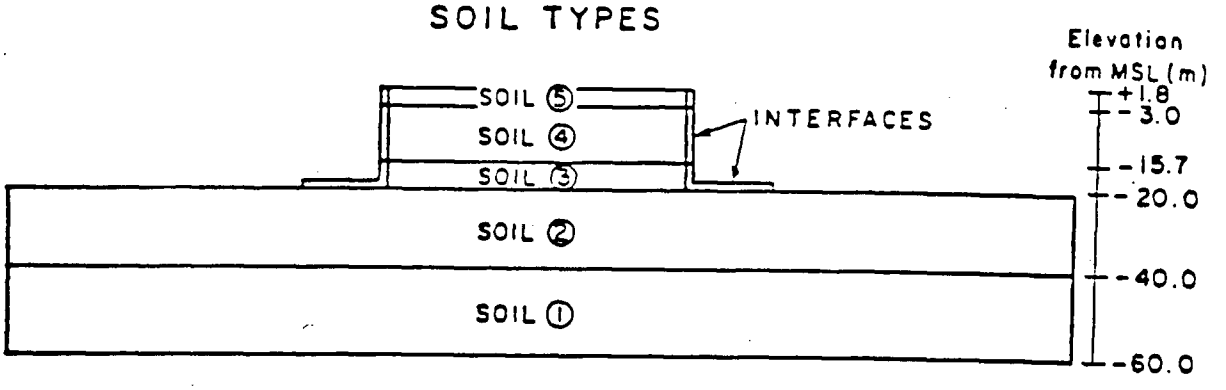

Soil Type No.	Avg. Void Ratio $(e_c)_{av}$	γ kN/m³	K_o	ϕ_1 Degrees	$\Delta\phi$ Degrees	First Loading Parameters KE	n	R_F	K_B	m	Repeated Loading Parameters KE_{max}	n	R_F	KB_{ur}	m
5	.685	15.6	0.4	35.7	2.8	900	.50	.80	290	.38	1600	.50	0.0	750	.38
4	.685	9.7	0.4	35.7	2.8	900	.50	.80	290	.38	1600	.50	0.0	750	.38
3	.660	9.7	0.4	36.7	3.8	920	.50	.80	295	.38	1880	.50	0.0	850	.38
2	.620	9.7	0.4	39.7	6.1	1000	.50	.80	370	.38	2690	.50	0.0	1030	.38
1	.680	9.7	0.4	36.5	3.6	900	.50	.80	295	.38	2100	.50	0.0	750	.38

Figure 6.26(a) Soil types and parameters for use in the Molikpaq analysis with the hyperbolic model

Soil Type No.	Avg. Void Ratio $(e_c)_{av}$	γ kN/m	K_o	Elastic Parameters KG_{max}	n	KB_{ur}	m	Plastic Parameters: Hardening Parameter KG_p	np	Flow Rule Param. μ	λ	Yield Parameters $(\frac{\tau_{SMP}}{\sigma_{SMP}})_1$	$\Delta(\frac{\tau_{SMP}}{\sigma_{SMP}})$	R_F
5	.685	15.6	.40	670	.50	750	.38	645	-.56	.25	.97	.685	.070	.94
4	.685	9.7	.40	670	.50	750	.38	645	-.56	.25	.97	.685	.070	.94
3	.660	9.7	.40	790	.50	850	.38	685	-.56	.25	.97	.715	.105	.94
2	.620	9.7	.40	1120	.50	1030	.38	760	-.56	.25	.97	.815	.180	.94
1	.680	9.7	.40	880	.50	750	.38	650	-.56	.25	.97	.710	.095	.94

Figure 6.26(b) Soil types and parameters for use in the Molikpaq analysis with the modified smp model.

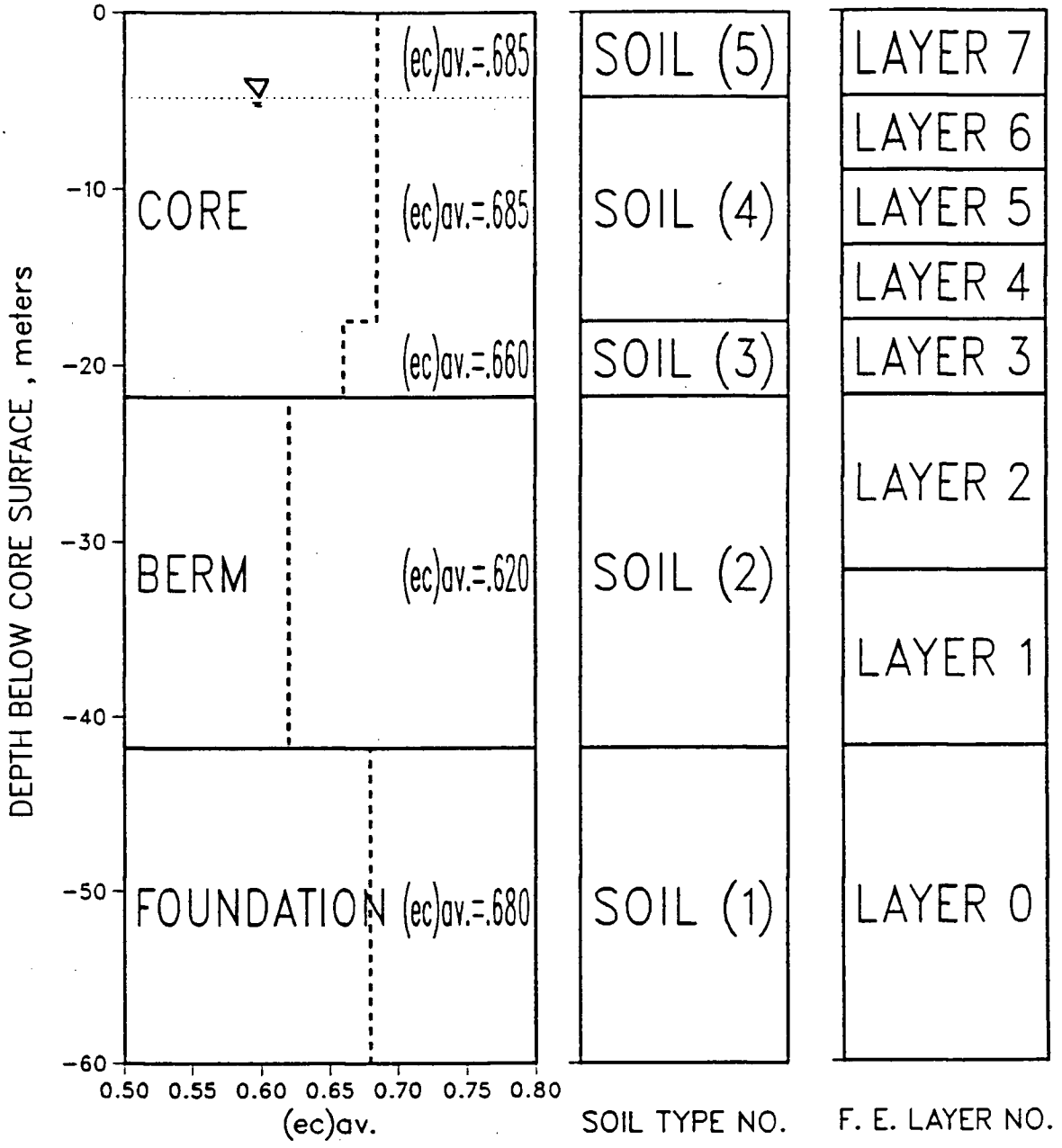

Figure 6.27 Soil types and finite element layers used in the Molikpaq analysis

- Fig. 6.12 to obtain KG_{max}
- Fig. 6.13 to obtain KE_{max} and KE
- Fig. 6.14 to obtain KB_{ur} and KB
- Fig. 6.15 to obtain KG_{p}
- Fig. 6.21 to obtain ϕ_1 and $\Delta\phi$
- Fig. 6.23 to obtain $(\tau_{SMP}/\sigma_{SMP})_1$ and $\Delta(\tau_{SMP}/\sigma_{SMP})$

6.4 Evaluation of Liquefaction Resistance Curves for Erksak 320/1 Sand

Most of the geotechnical engineering experience with cyclic loading has been developed over the past 30 years based on field data obtained from both earthquake and wave storm events as well as from laboratory tests simulating these events. This experience has shown that the liquefaction resistance of sandy soils depends essentially on the following major factors:

- Density and grain size characteristics of the soil.
- Static stress conditions prior to cyclic event.
- Amplitude and number of cycles of loading.
- Past history of cyclic loading.
- Drainage conditions.

These factors will be discussed next together with a review of the available cyclic loading laboratory tests on Erksak 320 sand.

6.4.1 Review of Available Cyclic Loading Triaxial Tests on Erksak Sand

A series of repeated loading triaxial tests were carried out by Golder Associates (1987) on samples of sand obtained from the Molikpaq core after

the dynamic ice load event of April 1986. A review of the above data indicates the following.

The data available for predicting liquefaction resistance were from tests carried out with a static shear stress bias corresonding to consolidation ratios $K_c = \sigma_1'/\sigma_3'$ in the range 2 to 3. Based on the static bias developed by the ice loads, which will be discussed in detail later in Chapter 7, these high K_c values seemed, at first, to be appropriate. However, liquefaction occurred in none of the tests. This fact is contrary to what happened in the field where liquefation was triggered in the soil elements adjacent to the loaded wall. The above contradiction is discussed below.

The soil elements adjacent to the loaded wall would initially have a static bias. However in contrast to the triaxial test conditions where the shear stress bias is imposed, the elements of the core that experience a significant increase in porewater pressure will gradually lose their bias during subsequent cyclic loading because the shear stresses initially carried out by these elements will be transferred to other parts of the structure. This stress transfer (or reduction in static bias) will ultimately allow a soil element adjacent to the loaded wall to achieve 100% porewater pressure rise and liquefy.

It is understood that additional testing was carried out by Golder Associates where no static bias was considered. Unfortunately that data was not available for this study.

Based on the above, the liquefaction resistance curves for Erksak 320/1 sand were evaluated based on curves available in the literature for no static bias rather than the available laboratory data reported by Golder Associates.

The procedures followed for that evaluation are described below.

6.4.2 Evaluation of Liquefaction Resistance Curves for Erksak 320/1 Sand Based on no Static Bias

The liquefaction assessment chart proposed by Seed and DeAlba (1986) and shown in Fig. 6.28 was used to evaluate the liquefaction resistance of Erksak 320/1 sand. This chart shows the relationship between the modified cone tip resistance $(q_c)_1$ and the cyclic stress ratio τ_{eq}/σ'_{vo} causing liquefaction in 15 cycles and is appropriate for sands and silty sands. The correlations are based on a large body of field data on liquefaction due to earthquake shaking. It may be seen that the resistance is strongly dependent on the mean grain size D_{50} of the sand and the % of fines. For Erksak 320/1 sand D_{50} = .32 mm and % fines ≤ 5%. The shear stress, τ_{eq}, is the uniform shear stress that would have the same effect in 15 cycles of shaking as the actual irregular shear stress, and σ'_{vo} is the effective overburden pressure.

The April 1986 ice event involved a much larger number of cycles than 15 and therefore it was necessary to develop a relationship between the shear stress τ_N to cause liquefaction in N cycles and τ_{15} which caused liquefaction in 15 cycles. Such a correlation was developed by Been (1988) based on both published data and data obtained by Golder Associates (1984) as shown in Fig. 6.29.

Based on the charts shown in Fig. 6.28 and 6.29 the liquefaction resistance curve for the different soil layers used in the analysis were obtained as follows:

1) The relationship between stress ratio causing liquefaction and $(q_c)_1$ for 15 cycles and D_{50} = .32 and % fines ≤ 5 was obtained from Fig. 6.28.

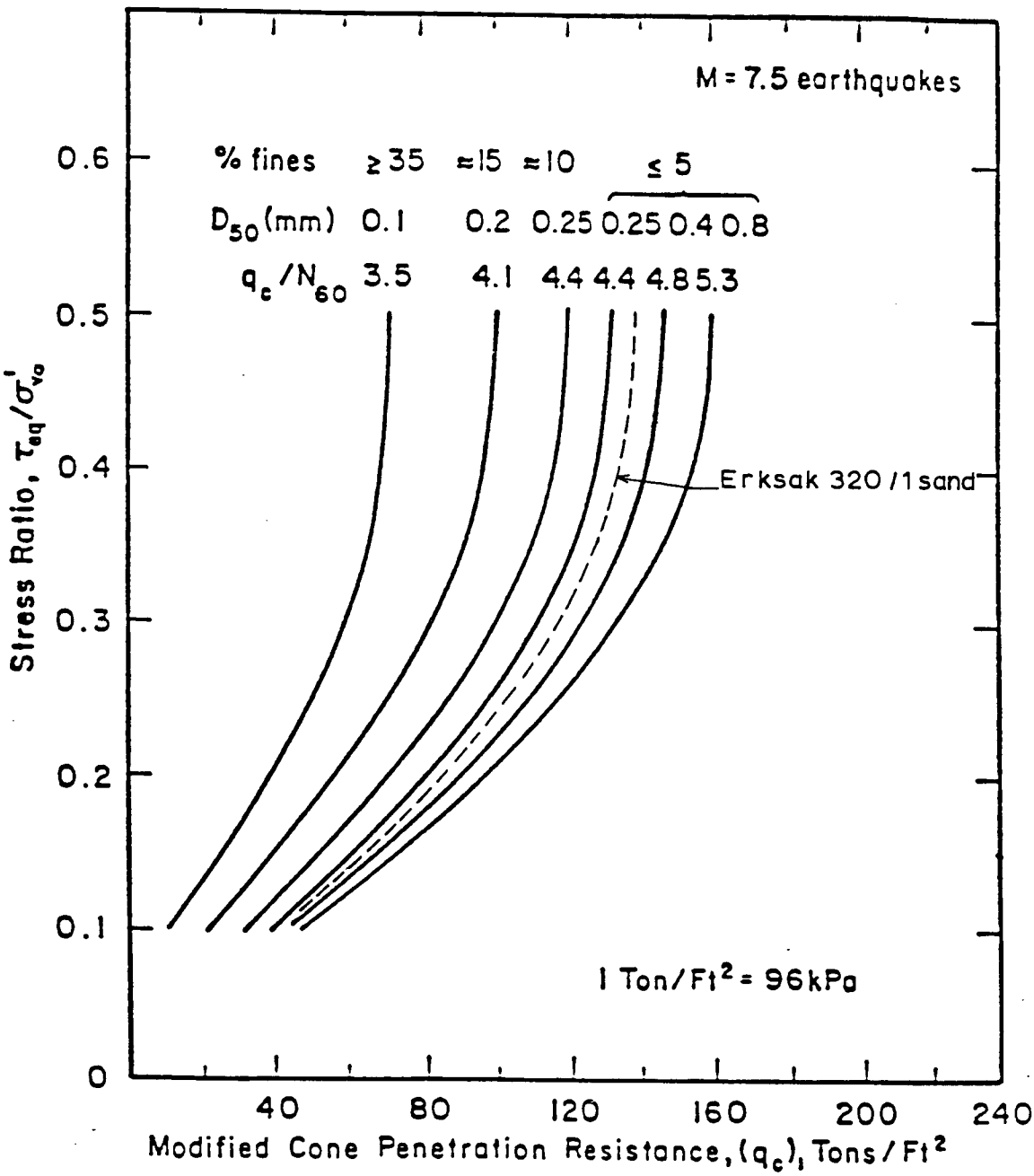

Figure 6.28 Relationship between stress ratio causing liquefction in 15 cycles and modified cone tip resistance for sands and silty sands (after Seed and DeAlba, 1986)

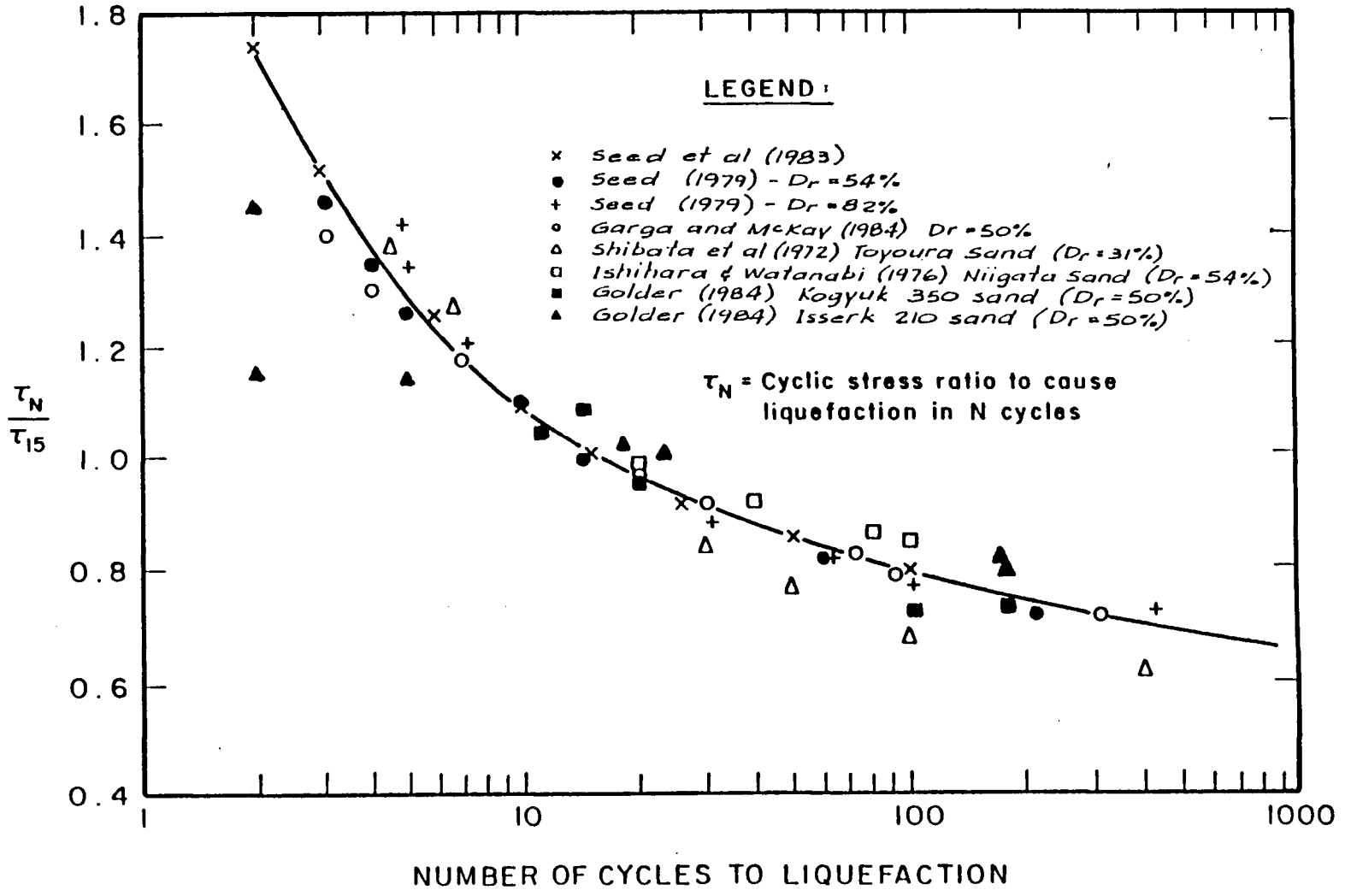

Figure 6.29. Relationship between cyclic stress level and the number of cycles to cause liquefaction (after Been, 1988)

2) Cyclic shear stress ratios, τ_N/τ_{15} for N = 5, 15, 100, 500 and 1000 cycles were obtained using Fig. 6.29.

3) The relationship, obtained in (1), for N = 15 cycles was scaled by the shear stress ratio τ_N/τ_{15} obtained in (2) using the following equation:

$$(q_{c_1})_{Ni} = (q_{c_1})_{15}/(\tau_{Ni}/\tau_{15}) \qquad (6.16)$$

where:

Ni = 5, 100, 500, 1000 cycles

These relationships are presented in Fig. 6.30.

4) The appropriate $(q_c)_1$ for each layer was obtained from the "mean" q_c profile shown earlier in Fig. 6.4 and the normalizing equation proposed by Liao and Whitman (1986):

$$q_{c_1} = q_c \ (Pa/\sigma'_{vo})^{1/2} \qquad (6.17)$$

A plot of of the average $(q_c)_1$, $((q_c)_1)_{av}$ for each layer is presented in Fig. 6.31.

5) Using the $((q_c)_1)_{av}$ values corresponding to each soil layer, and using Fig. 6.30 relationships between the stress ratio, τ_{eq}/σ'_{vo}, and the number of cycles causing liquefaction was obtained for all the soil layers used in the analysis as is shown in Fig. 6.32.

These relationships represent the liquefaction resistance curves for Erksak 320/1 sand.

In the above evaluation the effects of both the past-history of cyclic loading and drainage conditions at the Amauligak I-65 site were not taken into account due to unavailability of data. Nevertheless its possible influence on the liquefaction resistance curves is briefly discussed next.

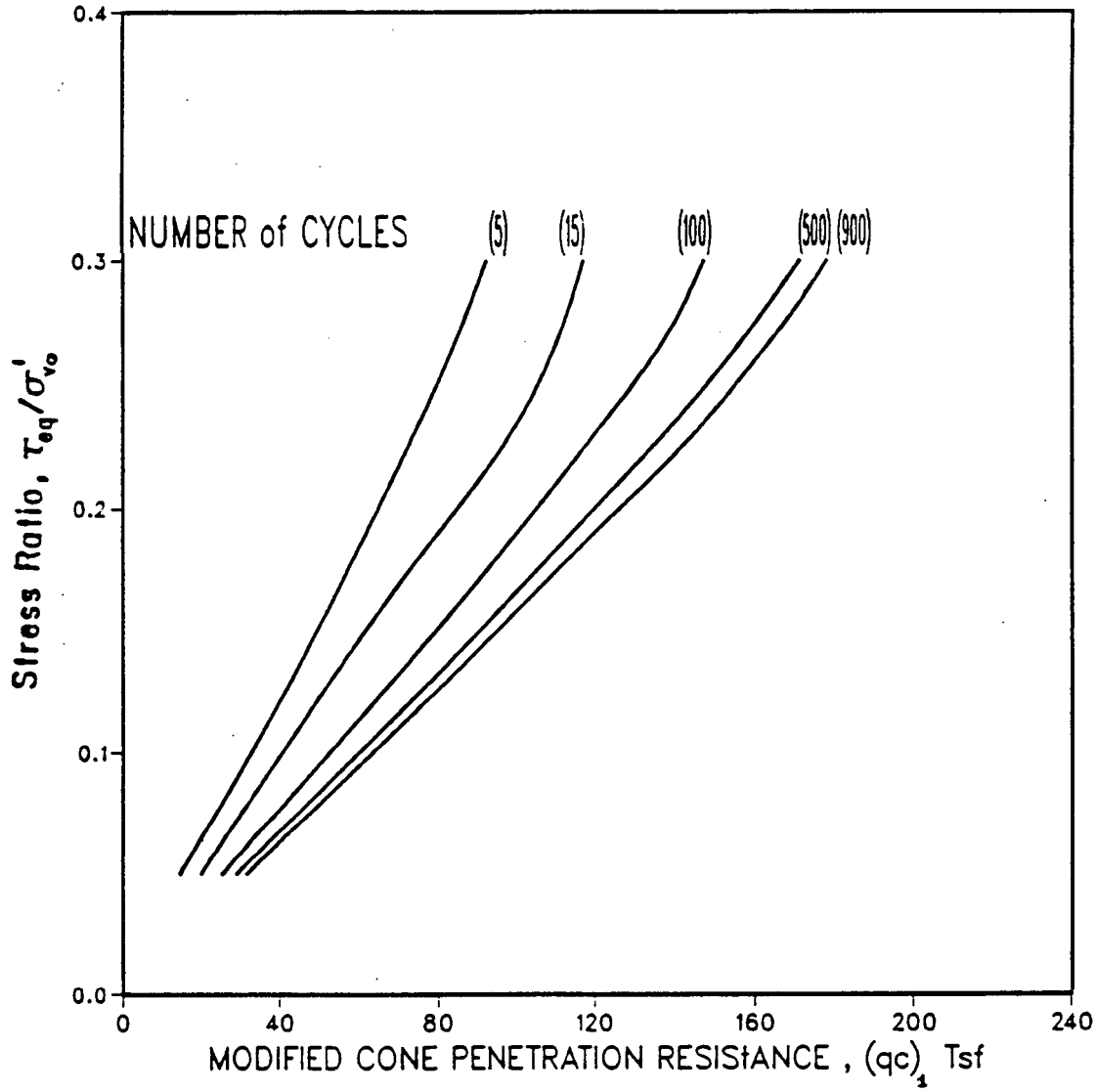

Figure 6.30 Relationship between stress ratio causing liquefaction in 5 to 1000 cycles and modified cone tip resistance for Erksak 320/1 sand

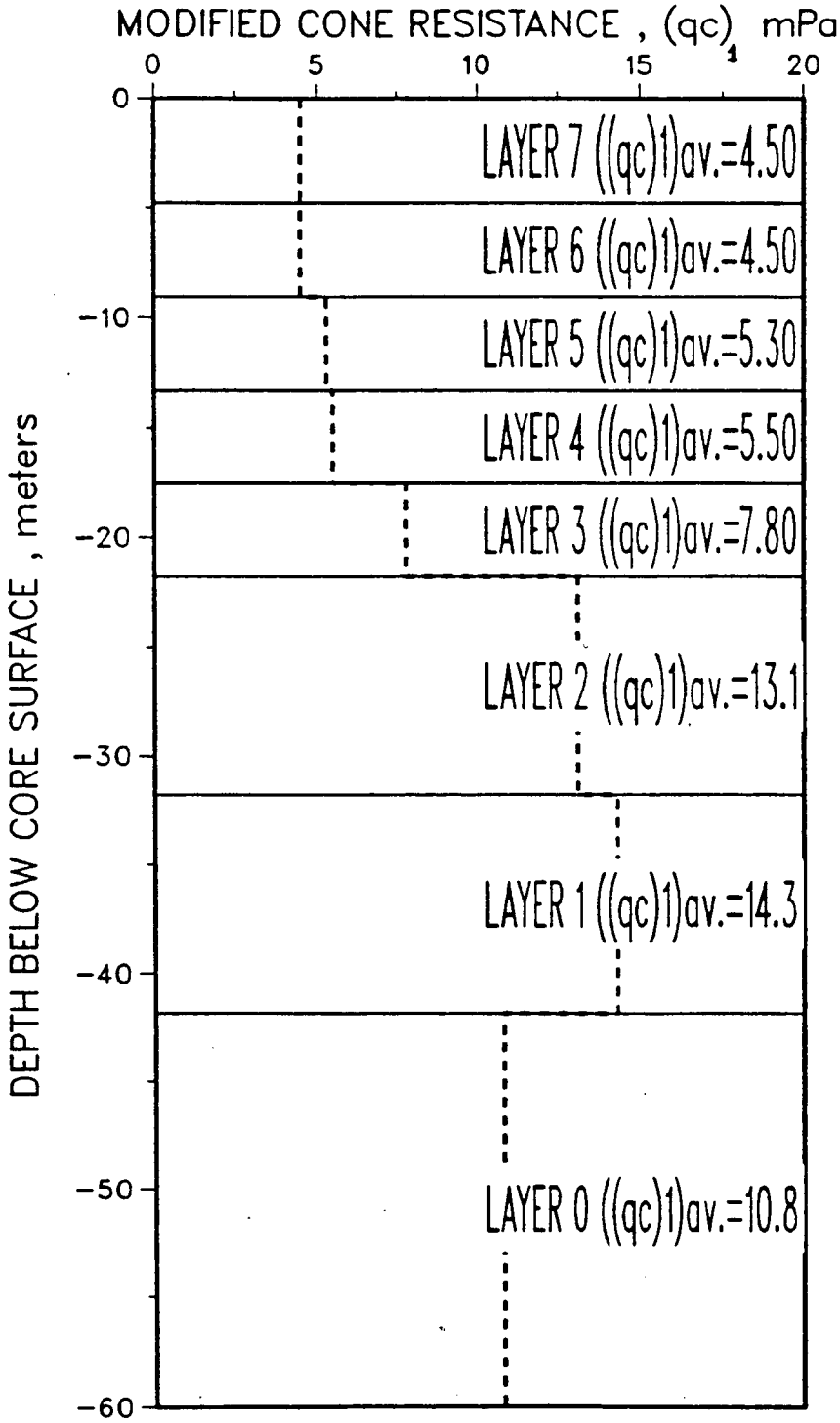

Figure 6.31 Variation of average $(q_c)_1$ with depth.

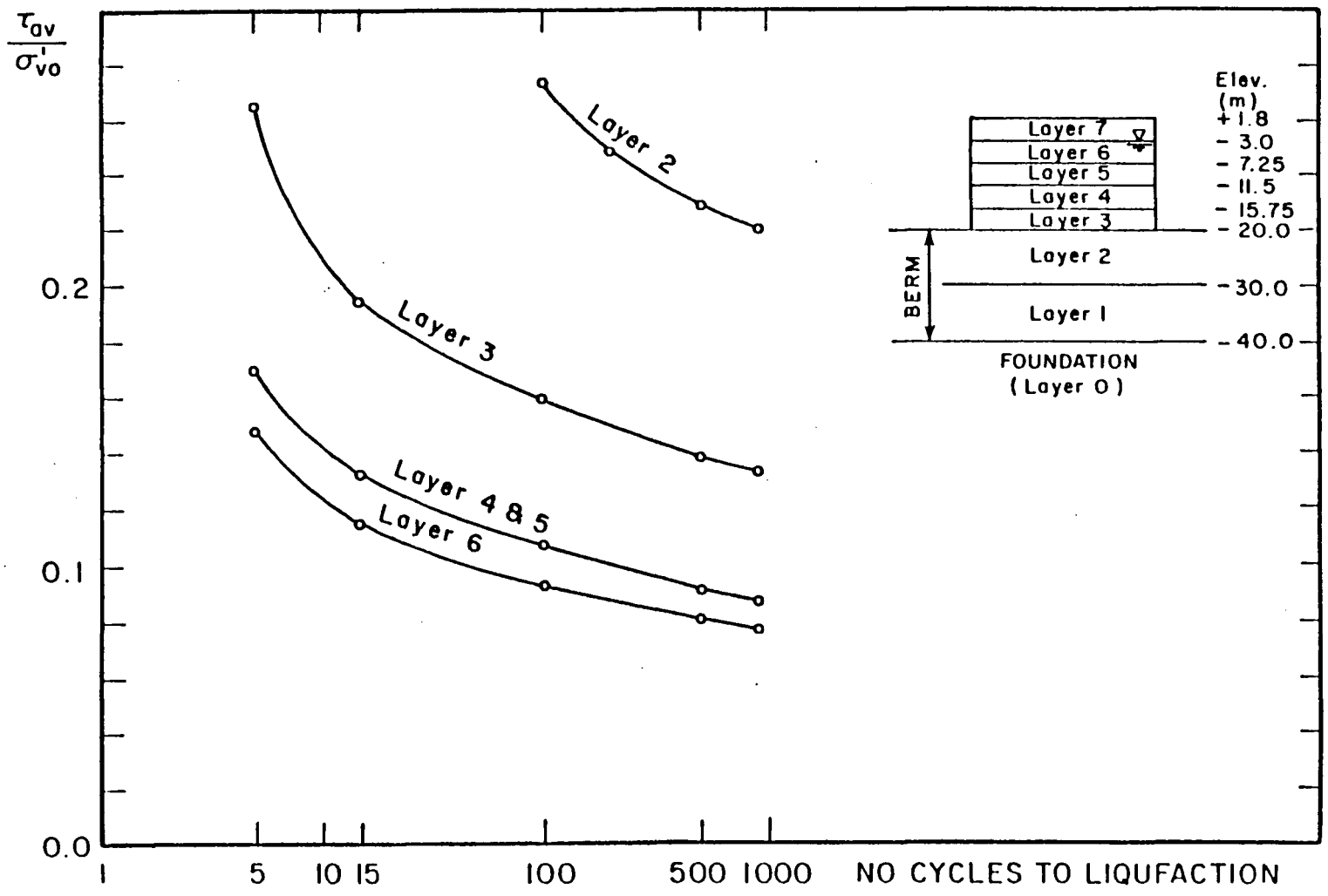

Figure 6.32 Liquefaction resistance curves for Erksak 320/1 sand

6.4.3 Discussion on the Past History of Cyclic Loading and Drainage Conditions at the Amauligak I-65 Site

- Past-History of Cyclic Loading

The Molikpaq structure while stationed at the Amauligak I-65 site was subject to several ice loading events as described by Jefferies and Wright (1988). A summary of these is presented in Table 6.4. It may be seen that

Table 6.4

Summary of Multi-Year Ice Loading Events (Spring, 1986)

(after Jefferies and Wright, 1988)

Date/Time	Peak Ice Load (MN)	Failure Mode* and Direction	Normalized** Dynamic Amplitude	Comments
March 7 15:30-17:43	230	Crushing at north west (N.W.) faces	16%	-
March 8 17:32-18:37	320	crushing at north west (N.W.) faces same flow	26%	-
March 25 13:00-16:00	110	viscous flow/ buckling at at north face	0%	-
April 12A 08:00-08:45	>500***	crushing followed by ridge break out at east face	45%	Liquefaction in the core adjacent to east face
April 12B 13:02-13:51	210	crushing at south east (S.E.) face	0%	-
May 12 03:01-03:26	250	crushing at north face	20 to 45%	-
June 25 05:31-05:44	130	crushing at west face	25%	-

Notes:

* for failure mode definition see Jefferies and Wright (1988)

** 0% indicates static ice loading conditions; 45% indicates dynamic ice loading conditions with an amplitude of ±45% of the average ice load

*** Maximum ice load greater than this value (not recorded due to instrumentation failure)

prior to the event under study herein (April 12) the Molikpaq structure was subject to two major dynamic ice loading events. Peak loads of 230 and 320 MN were applied to the N.W. faces of the structure on March 7 and 8 respectively. The possible significance of these two events was discussed by Finn et al (1988), their main points are summarized below.

Based on simple shear tests Finn et al. (1971) showed that previous cyclic loading had a significant effect on the rate of porewater pressure generation and liquefaction resistance. Generally, cyclic loading which generates small shear strains and does not disrupt the structure of the soil, results in greatly increased resistance to liquefaction and a slower rate of porewater pressure development in subsequent loading.

Typical effects of previous cyclic loading are illustrated in Fig. 6.33(a) for a medium dense sand and in Fig. 6.33(b) for a loose sand. In each case a virgin sample was subjected to undrained cyclic loading in a simple shear test until the porewater pressure reached 50% of the effective confining pressure. The samples were then drained and again subjected to cycles of undrained loading of the same amplitude as previously. Although the void ratio had changed by only a very small amount, there was a marked increase in liquefaction resistance and a much slower rate of porewater pressure development than previously. The liquefaction resistance of the dense sand increased from about 17 to 145 cycles and the resistance of the loose sand from about 25 to 65 cycles. Recent investigations by Seed and Lee (1988) have confirmed these earlier conclusions. They found increases in liquefaction resistance between 25-35% due to previous loading (see fig. 6.34).

This phenomenon is routinely taken into account in the determination of the resistance of North Sea sands to wave loading. Generally, in

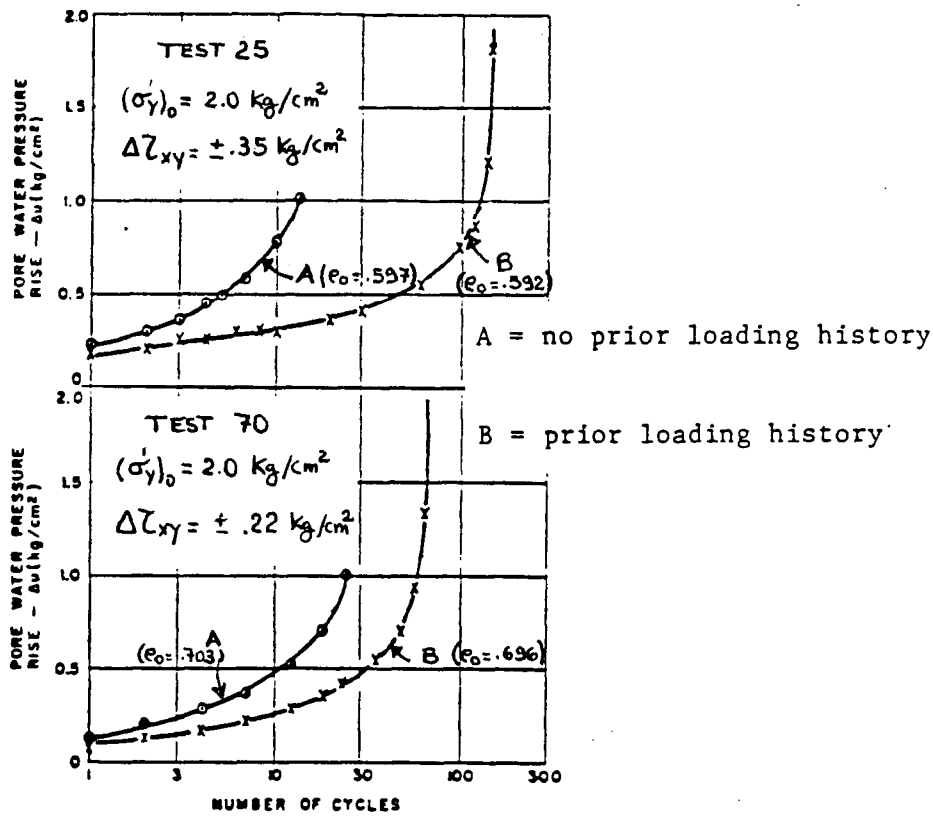

Figure 6.33 Effect of Previous Cyclic Loading on Porewater Pressure Development in (a) Medium Dense, and (b) Loose Sand (after Finn et al., 1970).

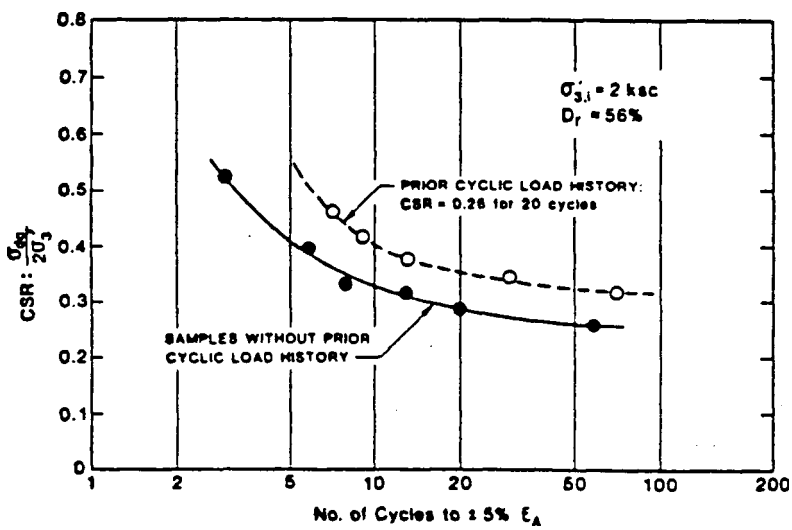

Figure 6.34 Effect of Previous Loading History on Liquefaction Resistance (after Seed et al., 1988)

testing these materials, samples are first subjected to a considerable number of small strain cycles to simulate the effect of the milder summer storms before the samples are subjected to the large amplitude stresses and strains considered typical of the winter storms (Bjerrum, 1973).

Because test data was not available to determine the possible increase in liquefaction resistance of the sand core of the Molikpaq due to past load events of March 7 and 8, 1986, the curves shown in Fig. 6.32 were not modified.

- Drainage Conditions

For stability reasons the water level inside the core of the Molikpaq was maintained at an elevation of -3.0 m below mean sea level (msl). This lowering of the water table was developed by a series of water pumps located around the inside perimeter of the structure near the core berm interface.

In order to assess correctly the liquefaction resistance and (or) the porewater pressures rise developed in the fills during the dynamic ice loading event of April 12, 1986, the drainage effects developed by those water pumps should be taken into account. A rigorous solution of the problem would require a 3-D consolidation analysis in which both generation and dissipation are considered to occur simultaneously. That was not considered in the present study. Nevertheless it is considered that the liquefaction resistance for the soil located near the core berm interface and adjacent to the perimeter of the structure should be higher than that shown in Fig. 6.32.

To summarize the liquefaction resistance curves presented in Fig. 6.32 do not take into account the following factors:

a) initial effects of the static bias developed by the ice loading,

b) past history of cyclic loading, and

c) drainage conditions.

In addition, the possibility of seasonal frost at the top of the core sand fill was also not considered herein.

Based on the above it is considered that the curves shown in Fig. 6.32 represent a lower bound to liquefaction resistance. This will be taken into account, later in Chapter 7, when assessing the results obtained from the analysis.

6.4.4 Pore Pressure Rise

The liquefaction resistance curves evaluated in the previous section were used to assess the soil elements that liquefy, i.e. the soil elements in which the ratio between the generated porewater pressure and the effective overburden pressure, $u_g/\sigma'_{vo} = 1$.

To evaluate the porewater pressure rise within the sand fill material during the dynamic ice load event of April 1986, two different models were considered. One to estimate the increase of the residual porewater pressure and the other to estimate the cyclic porewater pressure.

• Residual Porewater Pressure Model: The following equation proposed by Seed et al. (1976) was used in the analysis to predict the residual pore pressure,

$$u_g/\sigma'_{vo} = 2/\pi \sin^{-1} (N/N_\ell)^{1/2\alpha} \qquad (6.18)$$

where:

u_g = the generated porewater pressure

σ'_{vo} = the effective overburden pressure

N = the number of cycles

N_ℓ = the number of cycles to cause liquefaction

α = an exponent taken to be 0.7

This equation which is valid for cases where there is no static bias such as horizontal ground, is plotted in Fig. 6.35.

As discussed earlier the static bias will be initially present during ice loading and could perhaps cause a significantly different initial rise in porewater pressure than assumed by the use of Eq. 6.18. This was considered by examining the pore pressure rise data from the Golder tests with K_c values in the range 2 to 3 which corresponds to a high static bias. The data from these tests are also shown on Fig. 6.35 and indicate that the initial porewater pressure rise at low values of N/N_ℓ would be a little faster than predicted by Seed's curve. However this is compensated for in the analyses herein, by using an N_ℓ value corresponding to zero static bias which is lower.

At higher ratios of N/N_ℓ, the forced static bias of the Golder tests curtails the rise of porewater pressure. However, in the Molikpaq as discussed earlier the static bias drops as the soil softens and hence the porewater pressure will continue to rise. It was therefore considered that Seed's model, used in conjunction with N_ℓ based upon zero static bias, would give a reasonable estimate of the residual porewater pressure rise in the Molikpaq.

• Cyclic Pore Pressures: Data from the Golder cyclic triaxial tests described above, indicated that the transient or cyclic component pore pressure could be approximated by the following equation:

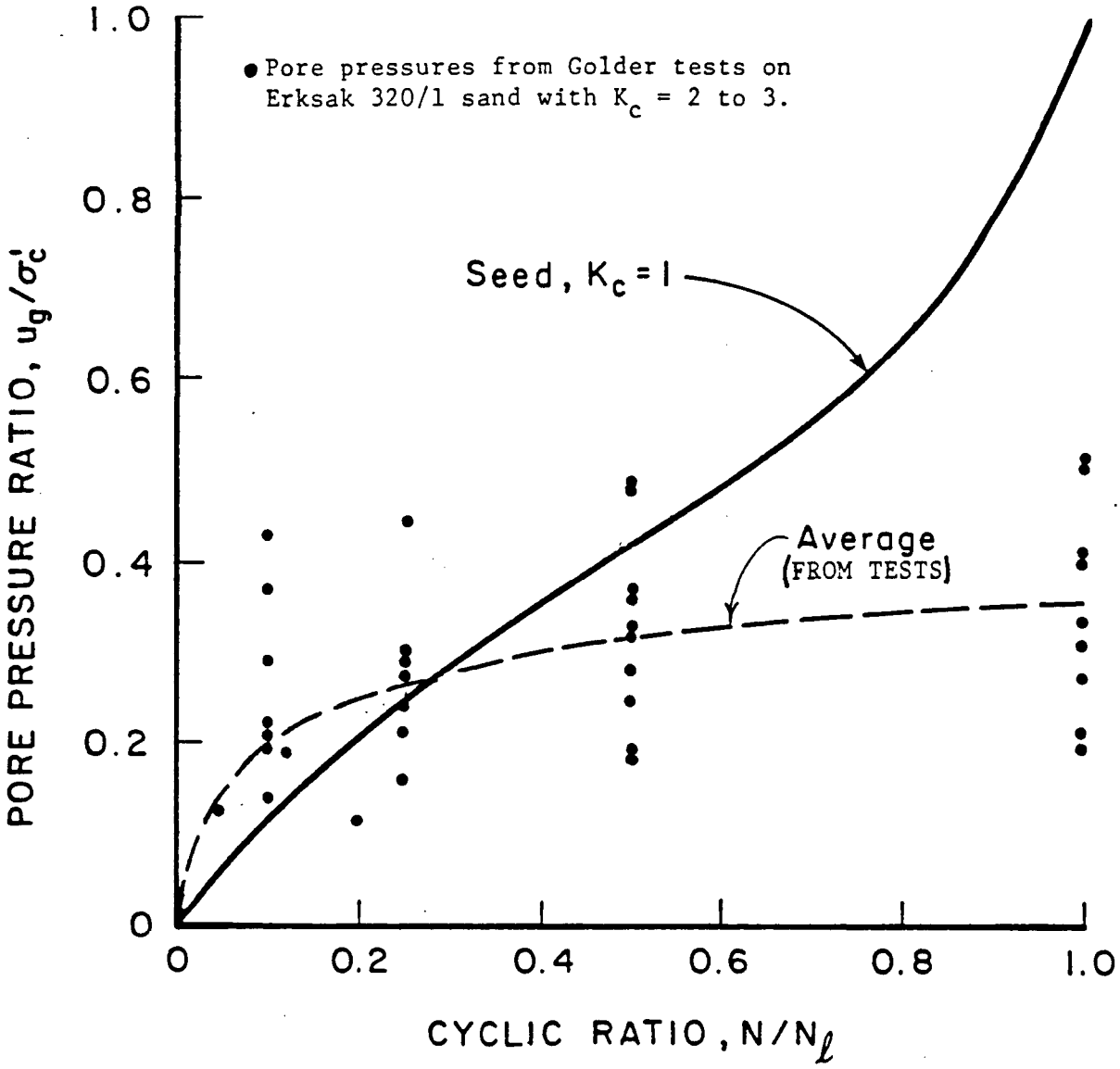

Figure 6.35 Residual porewater pressure rise as a function of the number of cycles to liquefaction

$$\Delta u_{cy} = \Delta\sigma_m - 0.7\ \Delta\tau_{oct} \qquad (6.19)$$

where:

Δu_{cy} = cyclic developed pore pressure

$\Delta\sigma_{m_{cy}}$ = cyclic variation in total mean normal stress

$\Delta\tau_{oct}$ = $2/3\ [((\Delta\sigma_1-\Delta\sigma_2)/2)^2 + ((\Delta\sigma_2-\Delta\sigma_3)/2)^2 + ((\Delta\sigma_3-\Delta\sigma_1)/2^2]^{1/2}$

= cyclic variation in octahedral shear stress

CHAPTER 7

3-DIMENSIONAL FINITE ELEMENT ANALYSIS OF THE MARCH 25 AND APRIL 12, 1986 ICE LOAD EVENTS

7.1 Introduction

On April 12, 1986 the Molikpaq structure, while stationed at the Amauligak I-65 site in the Beaufort Sea, was subject to high ice loading (maximum ice load > 500 MN), dynamic in nature, causing vibrations which were sufficiently severe to induce partial liquefaction of the sand core. Since this is the principal element by which the Molikpaq resists the driving forces of the ice, the ability of the platform to withstand such load conditions was almost compromised (Jefferies and Wright, 1988).

To study this complex soil-structure geotechnical problem, five research groups, three in Canada (Golder Associates, Calgary; EBA Engineering Consultants Ltd.; and the University of British Columbia (UBC)), and two in the United States (University of Southern California (USC); and Wooward-Clyde) were commissioned in 1987, by Supply and Services Canada, to predict the geotechnical response of the Molikpaq to this ice loading event. The predictions included the assessment of porewater pressures, accelerations, horizontal displacements and settlement.

The writer, due to the topic of his Ph.D. research programme, was part of the UBC research team, which was led by W.D. Finn. The final UBC report was based on the work of several investigators and comprised the different studies listed below.

a) 3-Dimensional and 2-Dimensional Structural Model of the Molikpaq. Work carried out by D.L. Anderson, P.M. Byrne and F.M. Salgado.

b) Assessment of Soil Properties to be used in the Static and Pseudo-Static Analysis. Work carried out by P.M. Byrne and F.M. Salgado and presented earlier in Chapter 6.

c) Assessment of Liquefaction Resistance Curves to be used in the Analysis. Work carried out by P.M. Byrne, F.M. Salgado and B. Stuckert.

d) Assessment of soil properties to be used in the dynamic and pseudo-dynamic analysis. Work carried out by W.D. Finn and M. Yogendrakumar.

e) 3-Dimensional and 2-Dimensional Static and Pseudo-Static, Finite Element Analysis of the Molikpaq. Work carried out by P.M. Byrne and F.M. Salgado.

f) 2-Dimensional, Dynamic and Pseudo-Dynamic, Finite Element Analysis of the Molikpaq. Work carried out by W.D. Finn and M. Yogendrakumar.

This chapter is divided into three sections and references to the UBC report are made, when necessary, by referring to the appropriate investigators.

An assessment of the ice loading function used in the analysis is presented in the first section.

The structural model, finite element mesh and stress-strain law used in the 3-Dimensional analysis are described in the second section.

The procedures followed in the 3-Dimensional analysis are presented in the third section together with both the results obtained and the available field measurements.

To study the influence on the results of some key parameters, including the stress-strain law used in the analysis, several 2-Dimensional analysis were also carried out.

7.2 Ice Loading Function Used in the Analysis

Ice cover is a major environmental feature in the Beaufort Sea. Ice loads used for design are influenced by two major factors: risk of exposure to thick ice and type of the artificial island (Jefferies et al., 1988). During the ice event of April 12, 1986 the ice was approximately 1.5 m thick (Jefferies, 1987). The failure pressure of thin ice against a stationary structure whose width is 100 m (such as the Molikpaq) is about 1 MPa. For this type of structure (vertical ice/island interface) the ice failure consists of pure crushing whereby intact ice is fractured to a granular material which is then extruded from the failure zone. This type of crushing of ice produces systematic load cycling with an amplitude in the order of 50% of the peak load and frequencies in the order of 1 Hz (Jefferies and Wright, 1988).

The given ice loading function for use in the analysis is presented in Fig. 7.1. It should be noted that this is an idealized version of the actual ice load which is shown (part of it) in Fig. 7.2. Because the actual load was made available after the analysis had been carried out, the following assessment applies only to the idealized load version. It may be seen that from time 8:10:00 to 8:17:51 the ice load increased slowly reaching a peak value of about 59 MN and a trough value of 22 MN. From 8:17:51 to 8:21:45 the ice load increased very rapidly to a peak value of 397 MN and a trough value of 161 MN. Between 8:21:45 to 8:26:00 the peak and trough load remained constant at 397 MN and 161 MN respectively. Subsequently, the load increased rapidly to a maximum load of 500 MN, however, between 8:27:00 and 8:29:10 a data gap is observed. After 8:29:10 the ice load decreased rapidly.

In the analysis the above ice loading function was treated as follows:

a) 8:10:00 to 8:17:51 loading: this low cyclic load level was ignored; and

b) 8:17:51 to 8:21:45 loading: This phase of the ice loading with its variable dynamic amplitude which lasted for 290 cycles was scaled to 60 equivalent cycles of a uniform dynamic amplitude of 118 MN which is the amplitude of the steady cyclic phase from 8:21:45 to 8:26:00. This greatly simplifies the analysis while preserving the effects of the more complicated load. The scaling technique used is presented in Appendix 7.1 and follows the procedures described by Seed and Idriss (1982).

c) 8:21:45 to 8:26:00 loading: The ice loading function was kept the same and 250 cycles of amplitude = 118 MN are inferred for this interval.

d) 8:26:00 to 8:27:00 loading: The 40 cycles of amplitude = 127.5 MN were scaled to 90 cycles of amplitude 118 MN as discussed in Appendix 7.1

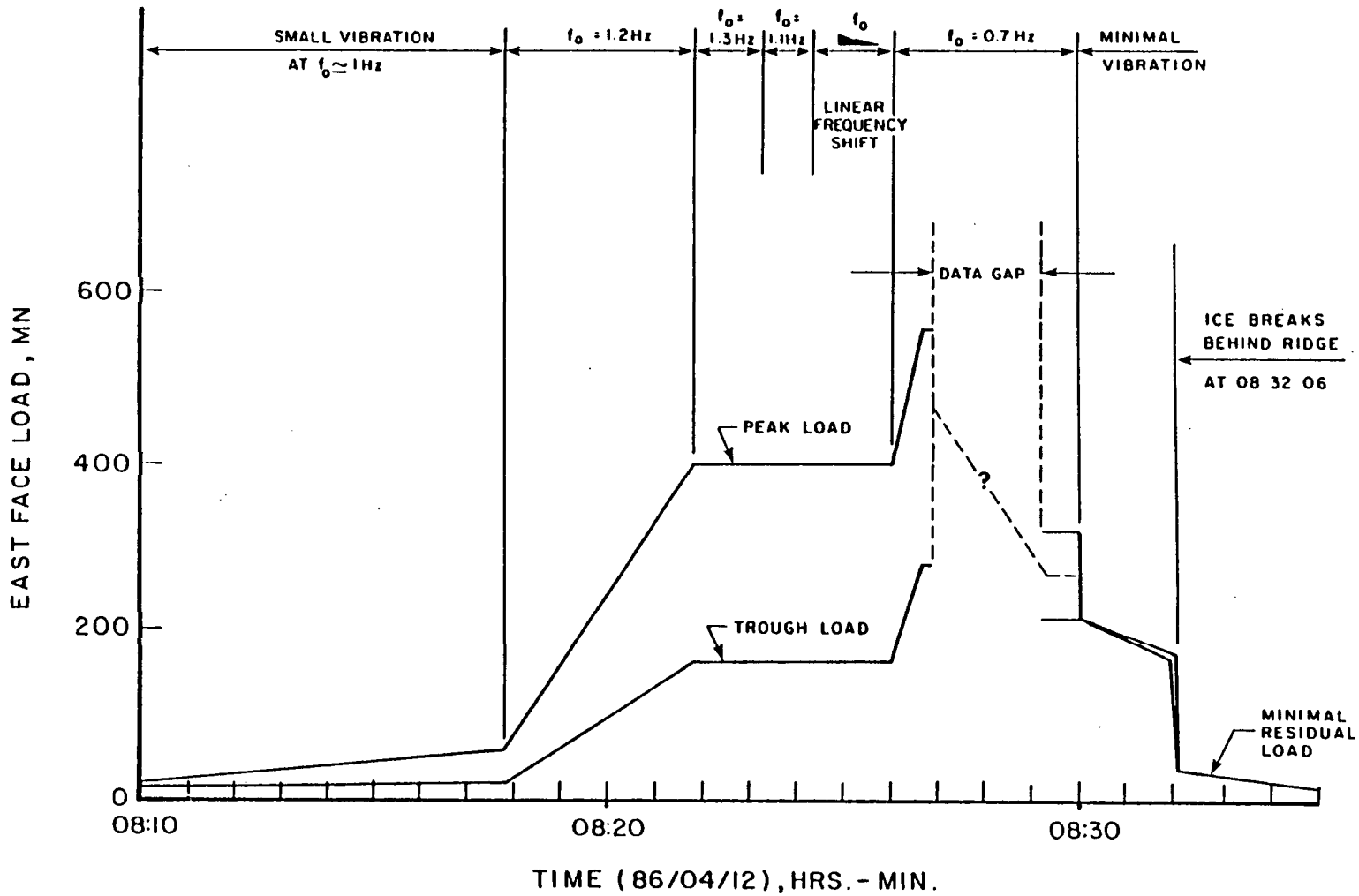

Figure 7.1 Idealized ice loading function used in the analysis

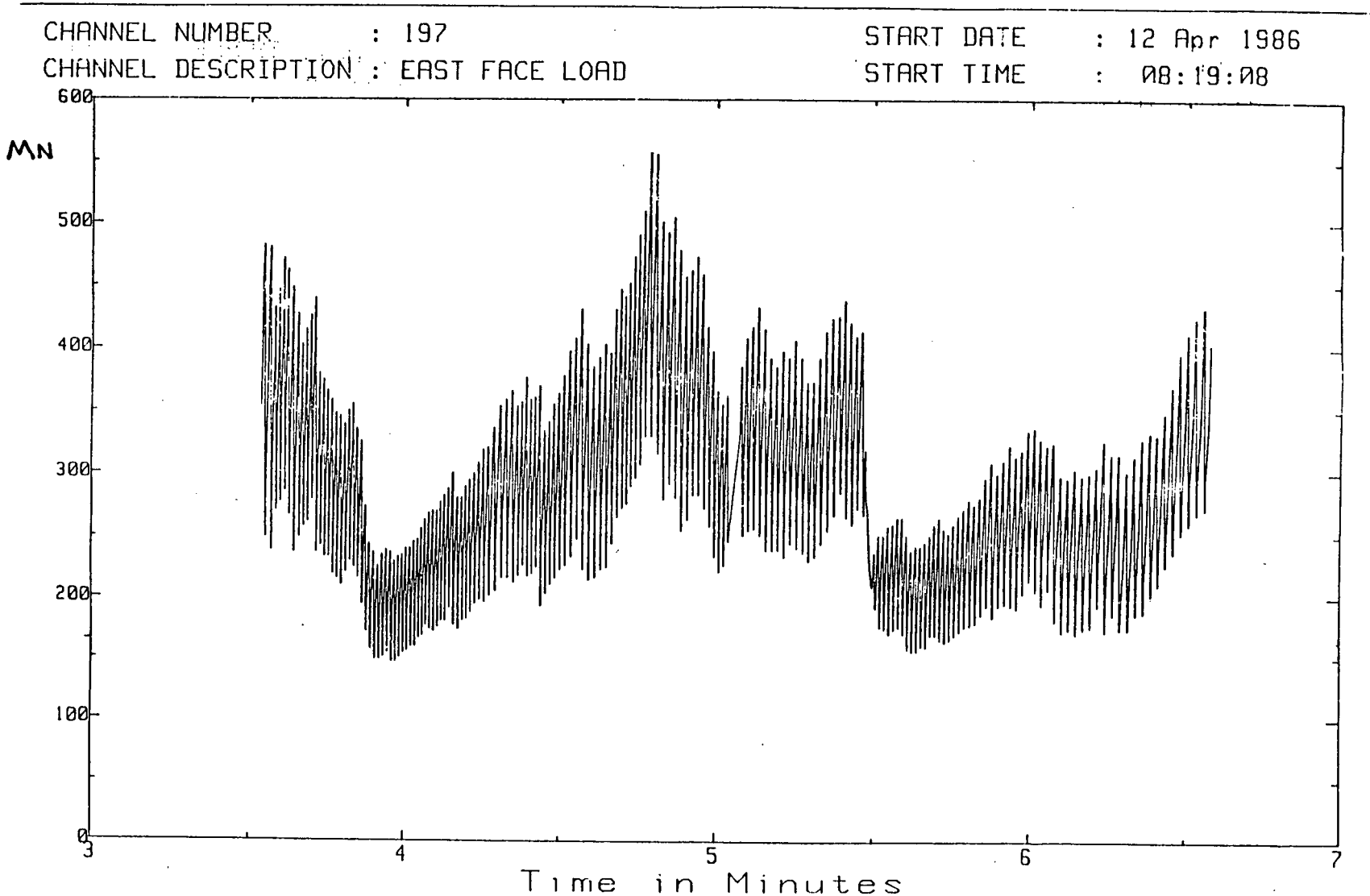

Figure 7.2 Actual ice loading function.

Based on the above, the given loading function was treated in the analysis as a load with a static component = 280 MN and a dynamic component comprising 400 uniform cycles with amplitude = 118 MN.

7.3 3-Dimensional Modelling of the Molikpaq

Descriptions of the structural model, finite element (F.E.) mesh and stress-strain law used in the 3-Dimensional (3-D) F.E. analysis are presented below.

7.3.1 3-Dimensional Structural Model of the Molikpaq

The (3-D) structural model of the Molikpaq's steel caisson was developed by D.L. Anderson (see Section 7.1 of this chapter) and is described below.

A 2-Dimensional sketch of the Molikpaq's steel caisson is shown in Fig. 7.3. The caisson acts as a large beam-column and the overall section member properties are also presented in Fig. 7.3. In order to take into account both the torsional response and the differing "hoop" forces between the top and bottom of the caisson, Anderson proposed the 3-D structural model as shown in Fig. 7.4. It may be seen that the 3-D structural model of the caisson comprises two ring beams connected by truss members. The properties of the members of the 3-D structural model are also given in Fig. 7.4 and were chosen so as to match the lateral, torsional and axial stiffnesses of the caisson section shown in the previous Fig. 7.3.

7.3.2 3-Dimensional Finite Element Mesh Used in the Analysis

The ice loading was treated in the analysis as being perpendicular to its eastern face and therefore because of symmetry only half of the domain was modelled in the analysis. The ice loading and the 3-D F.E. mesh, which

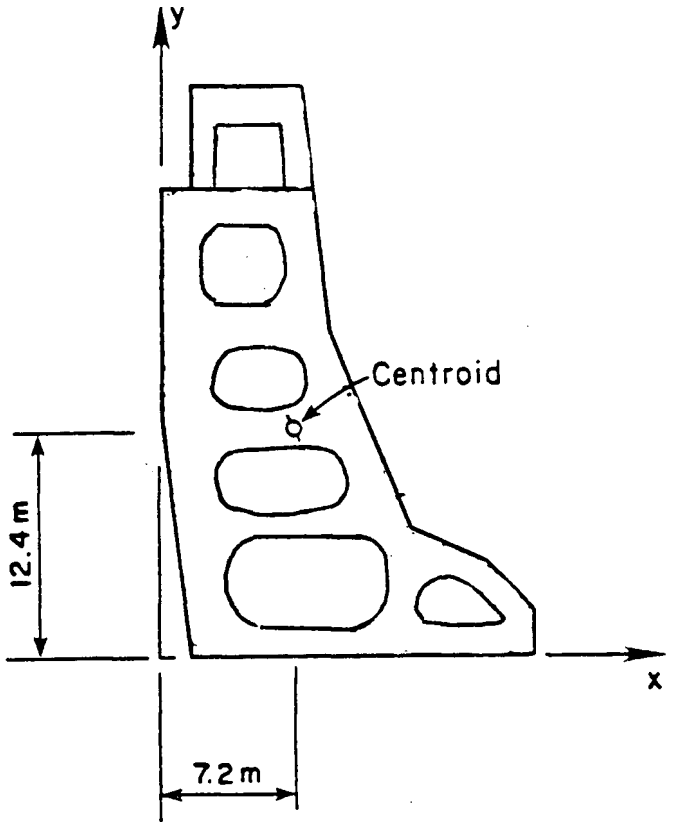

Caisson Properties

I_x	= 375 m⁴	$\bar{y}$	= 12.4 m
I_y	= 132 m⁴	Shear areas:	
J'	= 134.5 m⁴	A_x	= 1.0 m²
A	= 3.81 m²	A_y	= 1.8 m²
$\bar{x}$	= 7.2 m	E	= 200,000 MPa

Figure 7.3 2-Dimensional sketch and properties of the Molikpaq's steel caisson

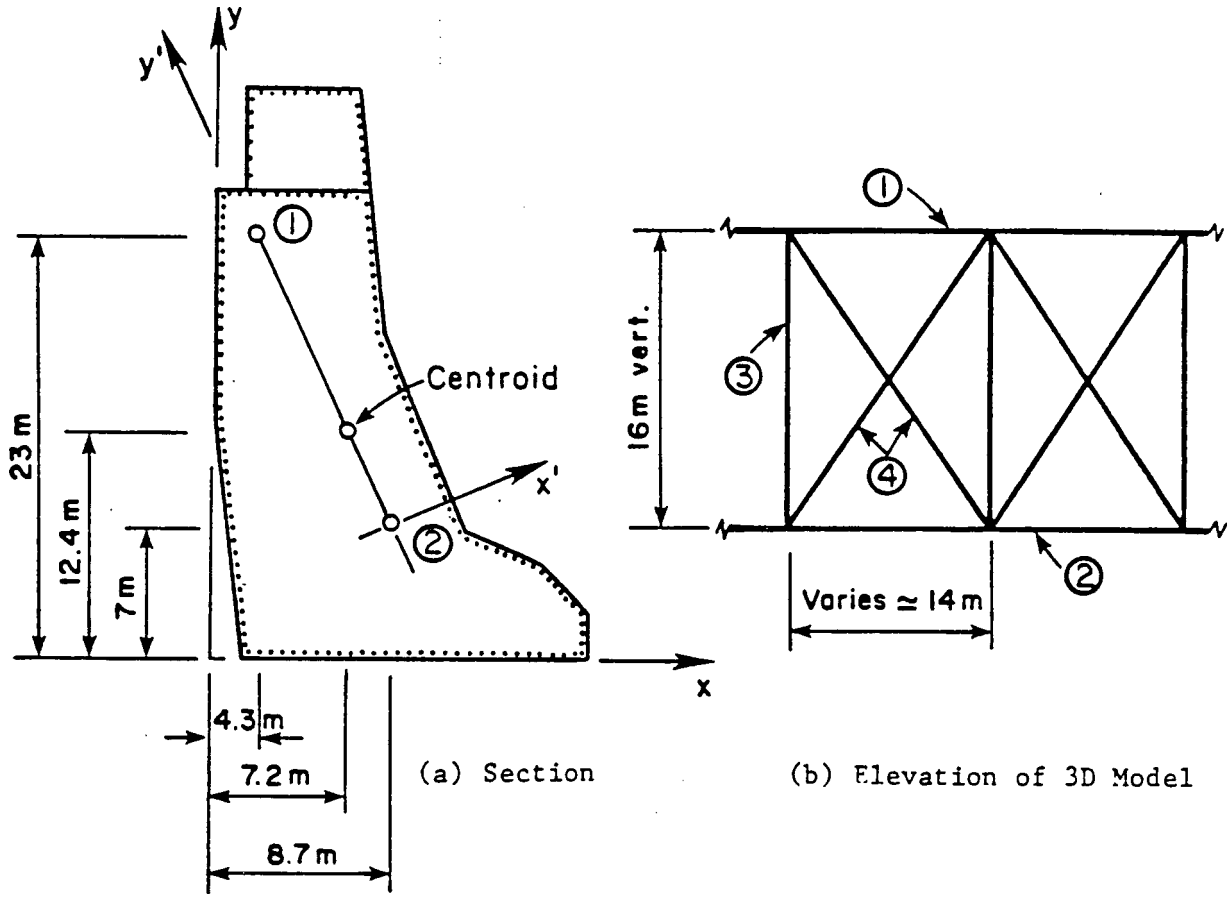

(a) Section

(b) Elevation of 3D Model

3D Structural Model Properties

Member	Area	Shear Area		J	$I_{x'}$	$I_{y'}$
	A m^2	$A_{x'}$ m^2	$A_{y'}$ m^2	m^4	m^4	m^4
1	1.31	0.33	0.60	46	54	38
2	2.50	0.67	1.20	88	104	74
3	4.0	0*	0	0	200	200
4	4.0	0	0	0	0	0

*A zero shear area indicates shear deformation is neglected

E = 200,000 MPa

G = 80,000 MPa

Figure 7.4 3-Dimensional structural model of the Molikpaq's steel caisson and properties used in the analysis

comprises 675 soil elements and 204 beam elements, are shown in Fig. 7.5(a). The soil elements were modelled by 3-D brick isoparametric finite elements. The total number of degrees of freedom is 2448. The mesh is 250 meters long in the x direction, 100 m long in the y direction (direction perpendicular to the ice load direction) and 63.5 m in the vertical or z direction. Nodes located on the vertical boundary planes were not allowed to move in the direction perpendicular to those planes, but were free to move in the other two directions. Nodes on the foundation base were assumed fixed. The interface between the steel caisson and the sand fills was considered in the analysis as shown in Fig. 7.5(b) where part of the cross-section of the 3-D finite element mesh along the core center line is shown. The interface elements which were treated as standard 3-D soil brick elements were assigned a thickness, t = 5 cm and an angle of internal friction, $\delta = 20°$ (Broms, 1966).

7.3.3 3-Dimensional Soil Model Used in the Analysis

The stress-strain law used in the analysis is presented in this section which includes a description of the different types of moduli and failure criteria used in the analysis.

The complex nonlinear stress-strain relations of the soil elements shown in Fig. 7.5 were modelled in the 3-D analysis, using the hyperbolic model (Duncan et al., 1980) by a 2 parameter incremental elastic and isotropic law using a tangent Young's modulus, E, and a tangent bulk modulus, B, described in Chapter 6. The tangent Young's modulus depends upon the initial consolidated void ratio, e_c, the mean effective stress, σ'_m, and the mobilized shear stress level, MSL. The tangent bulk modulus, B, depends upon e_c and σ'_m. In addition, both moduli were considered to be

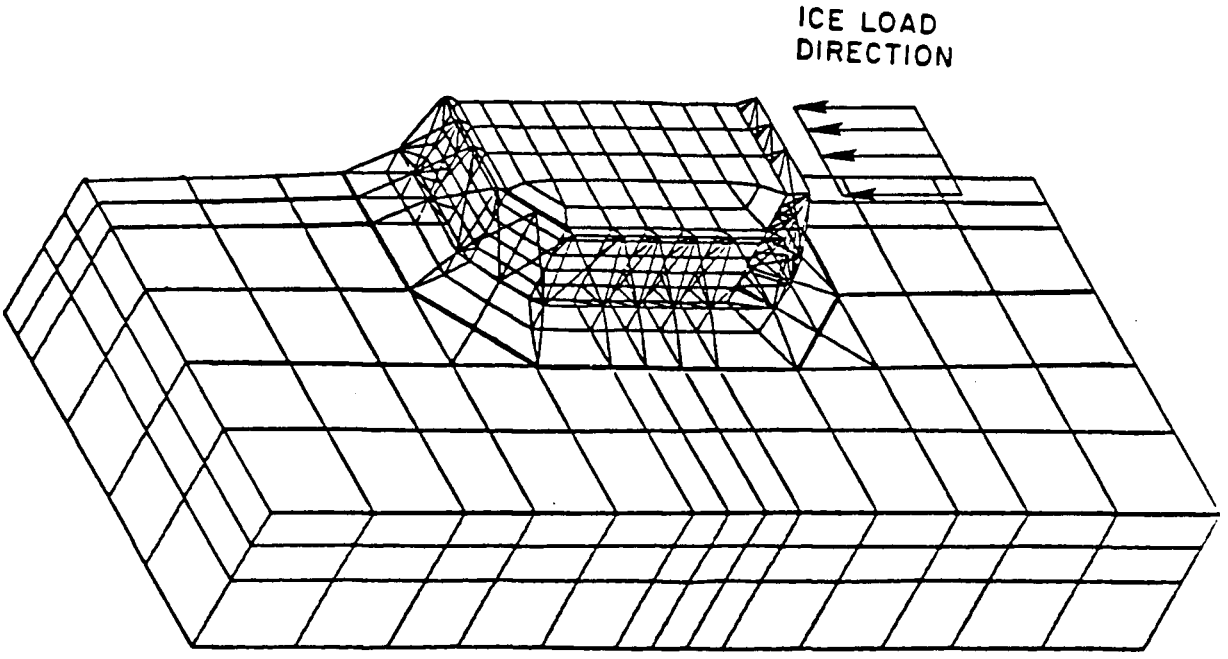

Figure 7.5(a) 3-Dimensional F.E. mesh used in the analysis

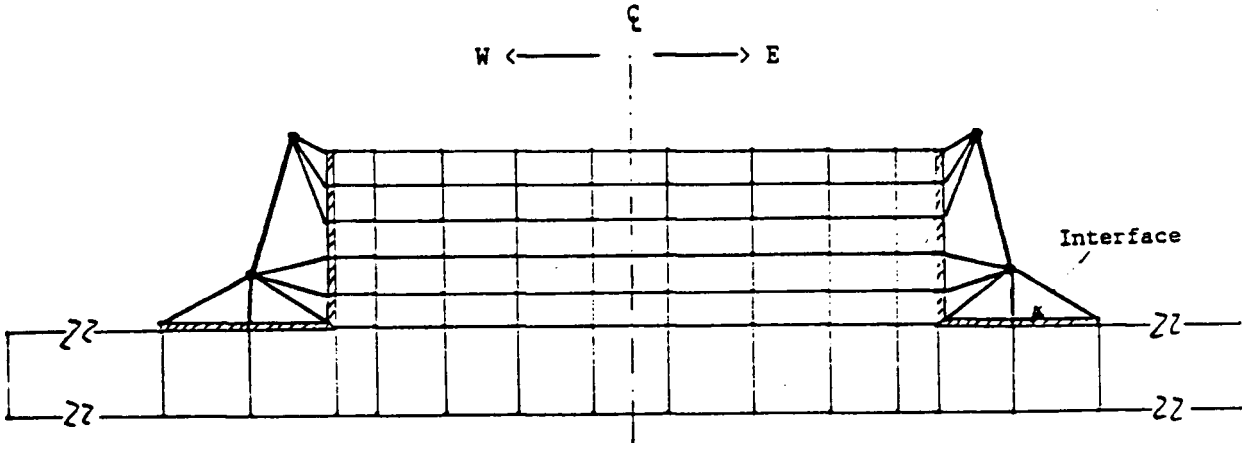

Figure 7.5(b) Cross-section of the 3-Dimensional F.E. mesh along the core center line

dependent upon the loading condition, i.e. whether it is a first time loading or an unloading/reloading condition. The soil parameters used in the analysis for the two different loading conditions are presented in Fig. 7.6 and were evaluated as described earlier in Chapter 6.

In order to trigger the appropriate moduli for the different loading conditions, an additional soil parameter was included in the stress-strain model used in the analysis. This parameter, designated as $(MSL)_{max}$ is defined as the maximum mobilized stress level during the loading history of the soil elements. The mobilized stress level, MSL, is defined in the analysis as follows:

$$MSL = \frac{(\sigma_1-\sigma_3)_{mobilized}}{(\sigma_1-\sigma_3)_{failure}} \qquad (7.1)$$

When $MSL < (MSL)_{max}$ the soil elements will respond with the unload/reload or repeated loading parameters shown in Fig. 7.6. Otherwise the first loading parameters shown in Fig. 7.6 will be used and the soil elements will follow a hyperbolic stress-strain law.

The first time loading parameters were used in the analysis of the construction of the berm and core, and at the end of this loading phase an average value of $(MSL)_{max} = .7$ was computed and subsequently used for all soil elements.

Upon ice loading, MSL first drops in value due to the increase in horizontal normal stress and therefore, in this ice loading phase, the repeated loading soil parameters were used in the analysis. At higher levels of loading, MSL increases again and for $MSL > (MSL)_{max}$ a hyperbolic stress-strain law was used in the analysis.

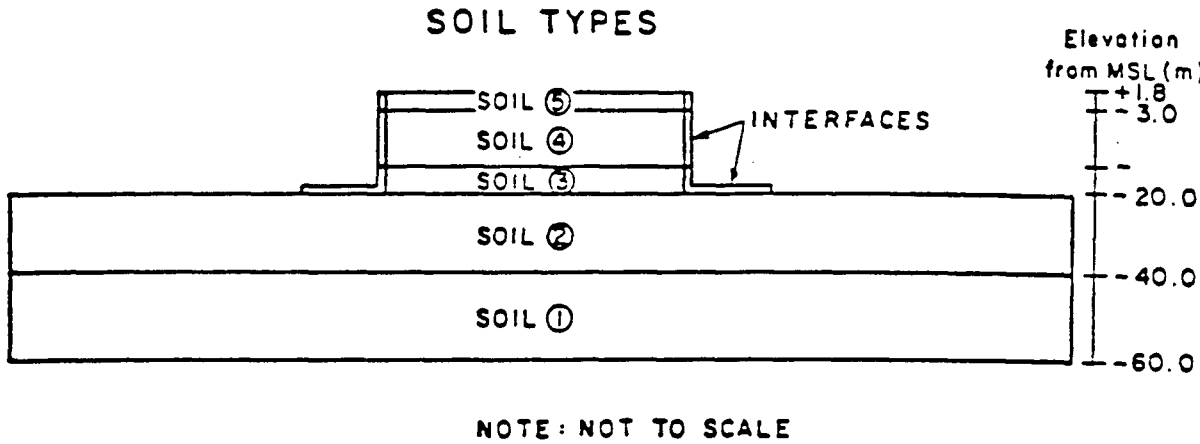

Soil Type No.	Avg. Void Ratio $(e_c)_{av}$	γ kN/m³	K_o	ϕ_1 Degrees	$\Delta\phi$ Degrees	First Loading Parameters KE	n	R_F	KB	m	Repeated Loading Parameters KE_{max}	n	R_F	KB_{ur}	m
5	.685	15.6	0.4	35.7	2.8	900	.50	.80	290	.38	1600	.50	0.0	750	.38
4	.685	9.7	0.4	35.7	2.8	900	.50	.80	290	.38	1600	.50	0.0	750	.38
3	.660	9.7	0.4	36.7	3.8	920	.50	.80	295	.38	1880	.50	0.0	850	.38
2	.620	9.7	0.4	39.7	6.1	1000	.50	.80	370	.38	2690	.50	0.0	1030	.38
1	.680	9.7	0.4	36.5	3.6	900	.50	.80	295	.38	2100	.50	0.0	750	.38

Figure 7.6 Soil types and properties used in the analysis

During analysis of the construction phase, the 3-D Mohr-Coulomb failure criterion was used. However, during the ice loading phase, a 2-D failure criterion was used. The 2-D Mohr-Coulomb failure criterion was selected because the shear τ_{zx} in the direction of ice loading was considered to be most effective in controlling strains and displacements and in generating pore pressure.

When a soil element fails in shear according to the Mohr-Coulomb failure criterion (MSL = 1) a low value of the tangent Young's modulus given by $E_t^* = 0.03\ B_t$ was used. This corresponds to a Poisson's ratio, $\nu = 0.495$.

The soil may also fail in tension. A soil element is considered to be failing in tension whenever σ_3' is less than or equal to zero. Low values of the tangent Young's modulus, E_t^*, and tangent Bulk modulus, B_t^*, given by $B_t^* = B_t/10$ and $E_t^* = 0.03\ B_t^*$ were used.

A soil element is considered to have liquefied whenever the cyclic stress ratio $(\Delta\tau_{zx}/\sigma_{vo}')_e$ is greater than or equal to the cyclic resistance ratio $(\tau_{eq}/\sigma_o')_\ell$. Once an element liquefies, its shear stiffness is considered to be very small.

7.4 3-Dimensional Analysis

The following 3-D assessments of the Molikpaq response to different load conditions were carried out:

- static assessment during the construction phase of the berm and core;
- static assessment during the moderate ice loading phase of the event of March 25, 1986;
- pseudo-static assessment during the high ice loading phases of the event of April 12, 1986;

- static assessment of the settlement phase after the ice loading event of April 12, 1986.

The procedures followed in the analysis are described next.

7.4.1 Construction Phase Analysis

The ideal approach to simulate the construction of the berm and core fills is to "analytically construct" these fills by layers as recommended by Kulhawy et al. (1969). To do that, the nodes of the F.E. mesh shown earlier in Fig. 7.5 need to be numbered along horizontal planes, starting from the bottom. However, such a numbering procedure leads to a system of equations with a large band width which in turn requires a large computer time for its solution.

To overcome the problem, the nodes were numbered along vertical planes, which led to an acceptable band width. However, this restricts the modelling of the sand fills to a gravity "turn-on" type of construction, which simulates deployment in 1 single placement.

To minimize the differences between the results that would be obtained by the gravity "turn-on" approach and the ideal approach described above, the following procedures were followed in the analysis.

a) All soil elements were initialized, prior to applying the gravity loads, with moduli based on the following effective stresses: vertical stress, $\sigma'_z = 1/2\ (\gamma' h)$ and horizontal stresses $\sigma'_x = \sigma'_y = 1/2\ (K_0\ \sigma'_z)$, where h is the distance from the centroid of each element to the top of the sand fill. The unit weight, γ', and K_0 values used are shown in Fig. 7.6.

b) During the gravity loading the moduli of the soil elements were reformulated at mid-step following the procedures described by Duncan et al. (1980).

Since field observations of the stresses mobilized at the end of construction were not carried out, it was considered important to compare the results obtained from the gravity approach against 2-D plane strain construction analysis where the sand fills were built in 7 layers.

The 2-D analyses were carried out using the finite element mesh and the structural model shown in Fig. 7.7. This mesh is an exact replica of the cross-section, along the E-W core centre line, of the 3-D finite element mesh presented earlier in Fig. 7.5.

The results of the horizontal and vertical displacements of the structure obtained from the construction analysis are presented in Fig. 7.8(a). It may be seen that the computed vertical displacement of the structure by the "gravity method" is 182 mm (3-D analysis) and 193 mm (2-D analysis), and by the "layer method" (2-D analysis) is 71 mm. This is because higher shear stresses, τ_{zx}, are computed by the "gravity method" at the fill-structure interface than the "layer method". Nevertheless the horizontal displacements of the structure, and the vertical displacement of its base relative to the structure inside corner, computed by all analyses are in good agreement as is shown in the figure.

The results of the stresses σ'_z, σ'_x and τ_{zx} versus depth obtained from all the above construction analyses (3-D and 2-D following the gravity method and 2-D following the layer method) are presented in Fig. 7.8 (b,c,d). It may be seen that the results obtained by the two, 2-D

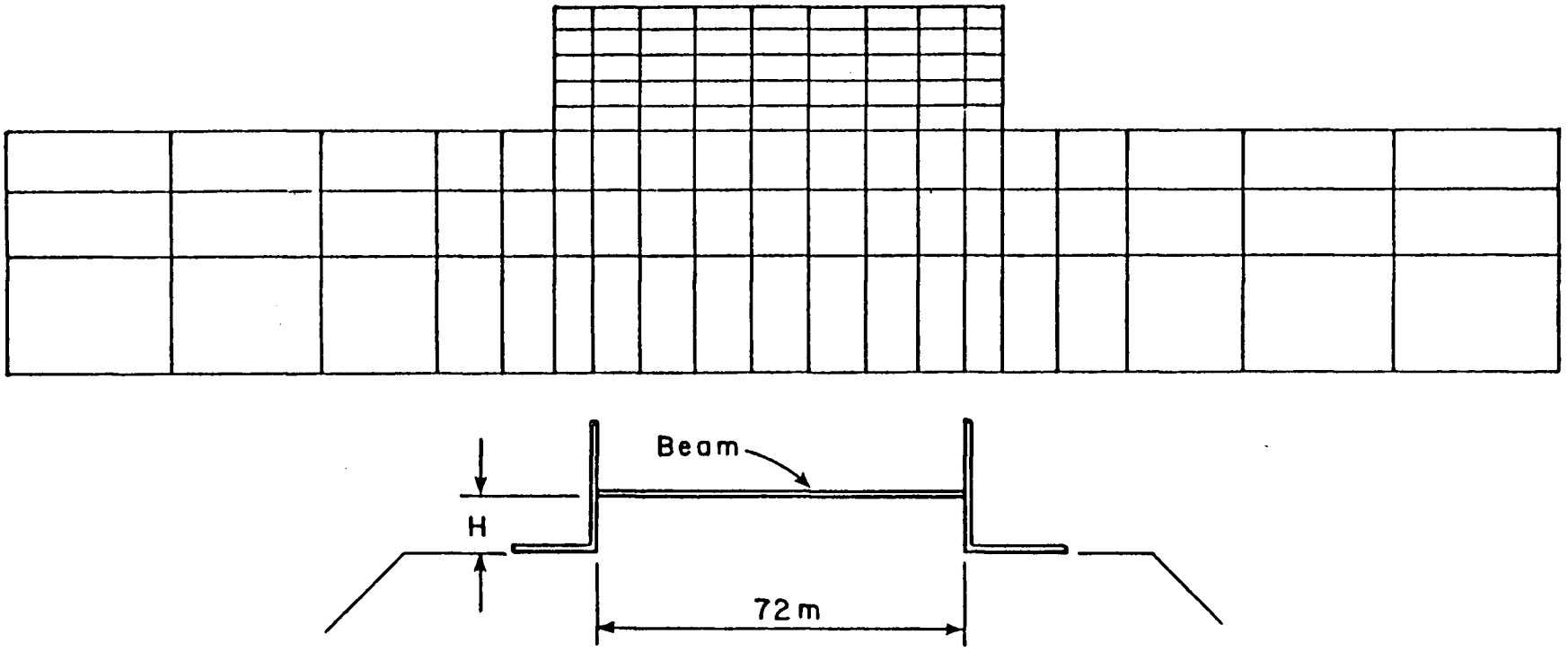

PROPERTIES FOR 2-D STRUCTURAL MODEL CONSTRUCTION PHASE (See Appendix 7.2)		
A = 0.042 m^2/m	I = 82 m^4/m	E = 200,000 MPa
Location, H = 13.5 m		

Figure 7.7 2-Dimensional finite element mesh and structural model used in the construction analysis

construction methods and the 3-D gravity method agree quite well (except for the τ_{zx} stresses at the fill-structure interface). Based on the above, the computed 3-D construction stresses were considered appropriate for use as the initial stress condition in the ice loading phase analysis that are considered in the next section.

7.4.2 3-D Analysis of the Static Ice Load Event of March 25, 1986

Prior to the dynamic ice load event of April 12, 1986, the Molikpaq structure was subject to several other ice load events as described earlier in Chapter 6. Because the event of March 25, 1987 was the best documented ice event, several 3-D analyses were carried out to compare with the available field measurements and therefore calibrate the soil-structure para-

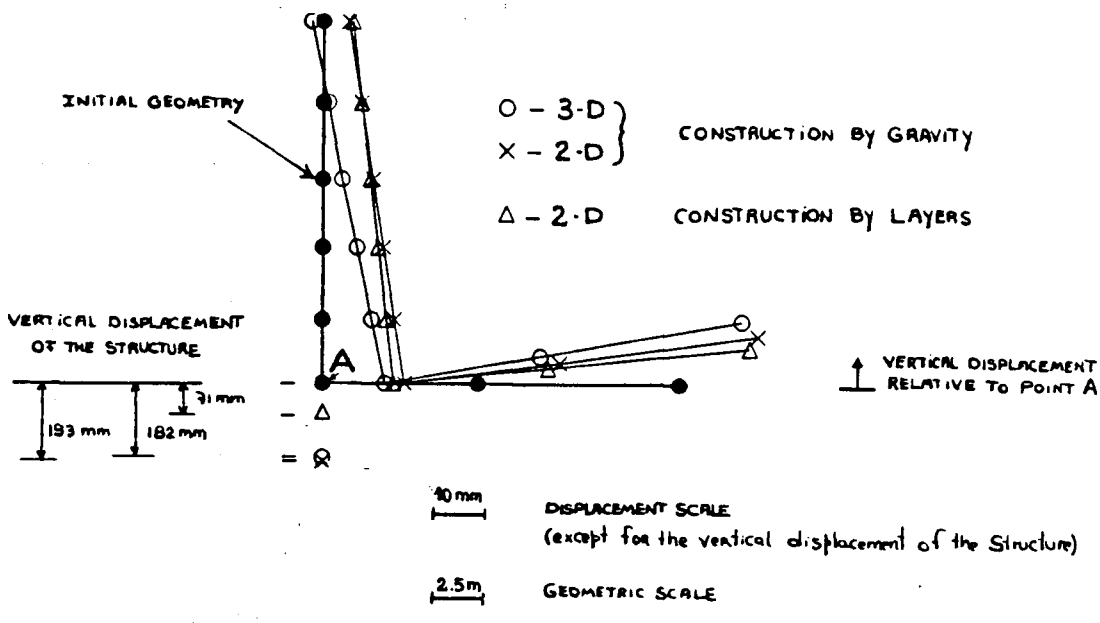

Fig. 7.8(a) Displacements of the structure after construction.

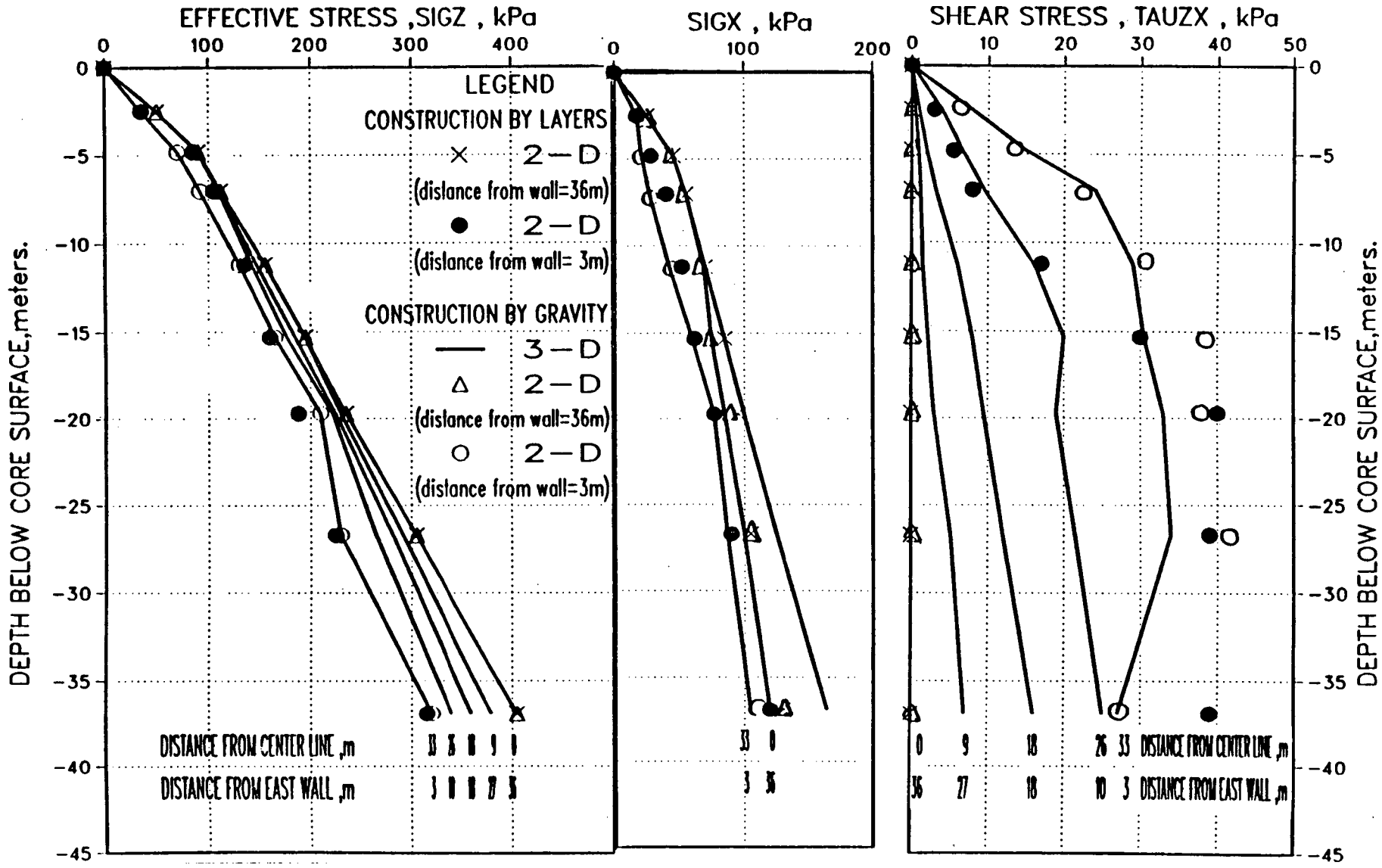

Figure 7.8(b,c,d) Distributions of stress with depth, computed from 3-D and 2-D finite element analysis of the construction phase: (b) σ_z versus depth; (c) σ_x versus depth; and (d) τ_{zx} versus depth

parameters for use subsequently in the 3-D analysis of the dynamic ice load event of April 12, 1986.

The procedures followed in the analysis are described below.

It is understood that the ice load event of March 25, 1986 was characterized by a static ice load of approximately 110 MN (see Chapter 6, Table 6.4) applied to the north face of the Molikpaq structure. The load center line was at 18.5 m above the base of the structure or 1 m below mean sea level. To simulate this ice load, the two 3-D ice pressure distributions shown in Fig. 7.9 were considered in the analysis because of the uncertainties about the actual ice pressure distribution. The 3-D load vector associated with these two pressures was computed as is described in Appendix 7.3.

Prior to applying the above load vector, all soil elements were initialized with the stresses that were computed at the end of the construction analysis.

Based on preliminary 3-D results the mobilized stress level, (MSL), (see eq. (7.1)), computed at the end of loading (ice load = 110 MN), decreased in value from the MSL evaluated at the end of construction. Therefore the unload/reload soil parameters shown in Figure 7.6 were used in the analysis which were carried out using one single increment of load = 110 MN.

The results obtained using the two different pressure ice load distributions are presented and compared below with the field observations which consisted of displacement measurements carried out, during and after the loading, with the inclinometer and extensometers shown in Fig. 7.10.

The measured 3-D caisson deformations due to the 110 MN ice load are shown in Fig. 7.11 together with the results obtained. From the two sets

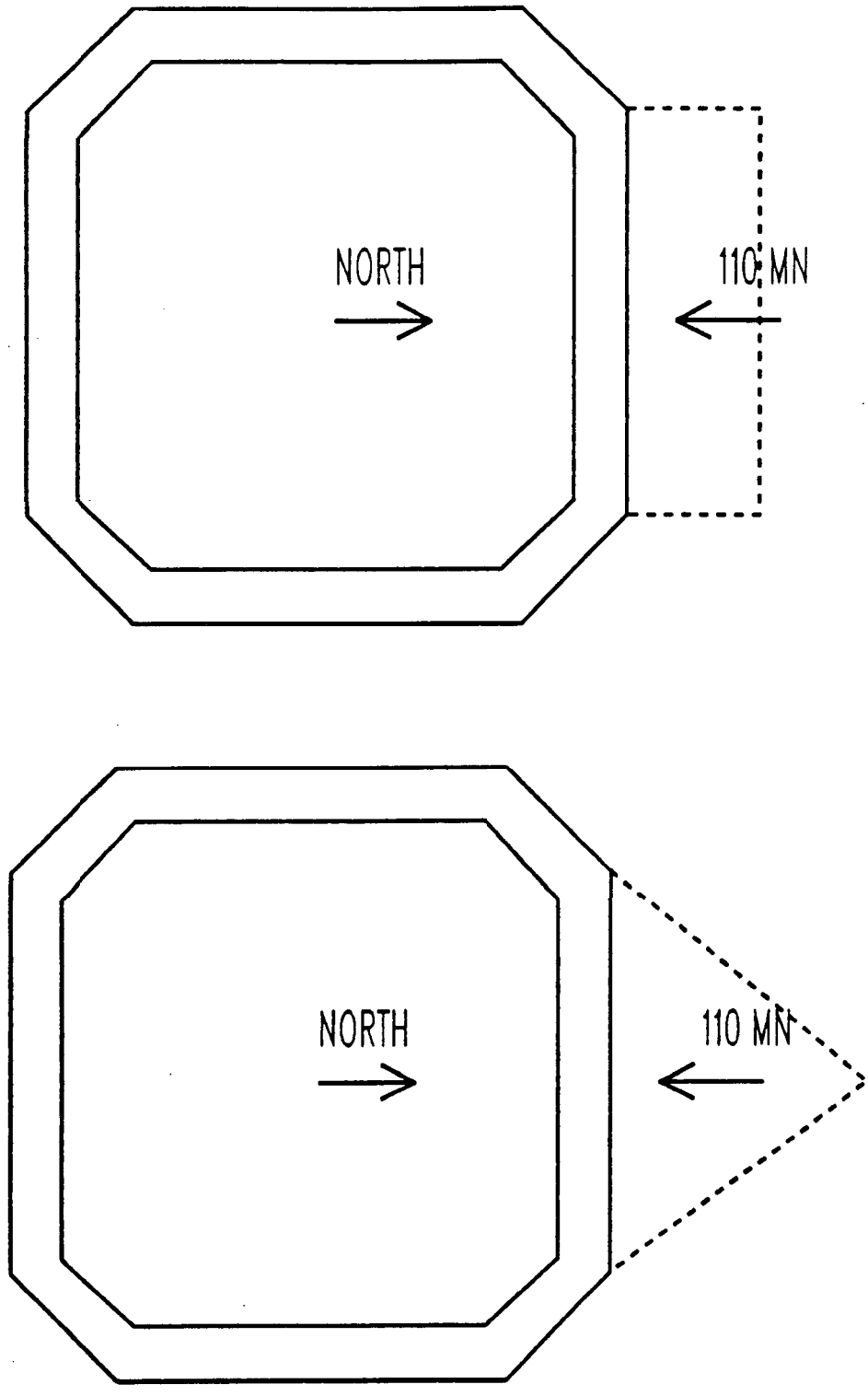

Figure 7.9 Possible ice pressure distributions during the ice load event of March 25, 1986

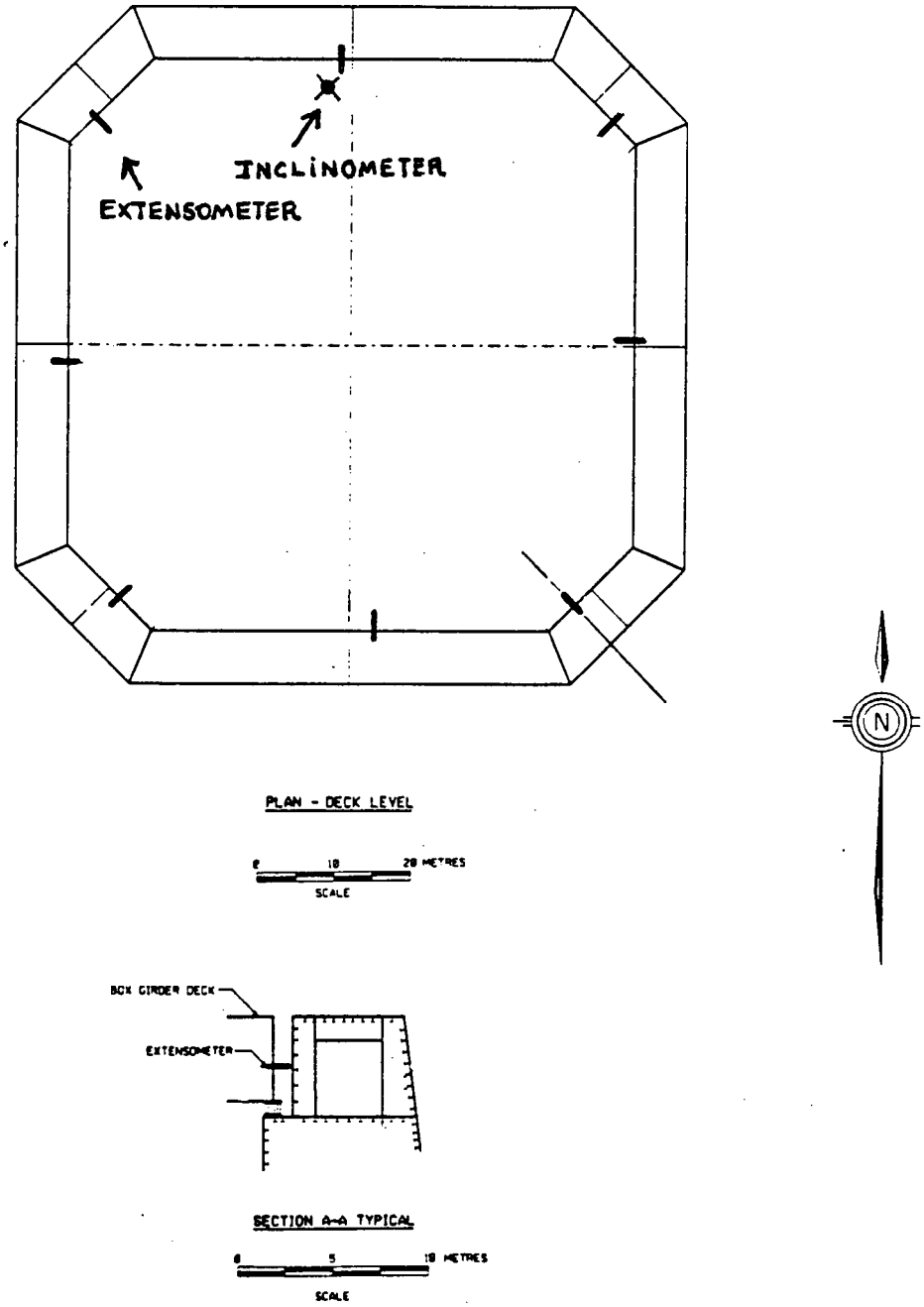

Figure 7.10 Location of the instruments used to monitor the ice load event of 25 March, 1986

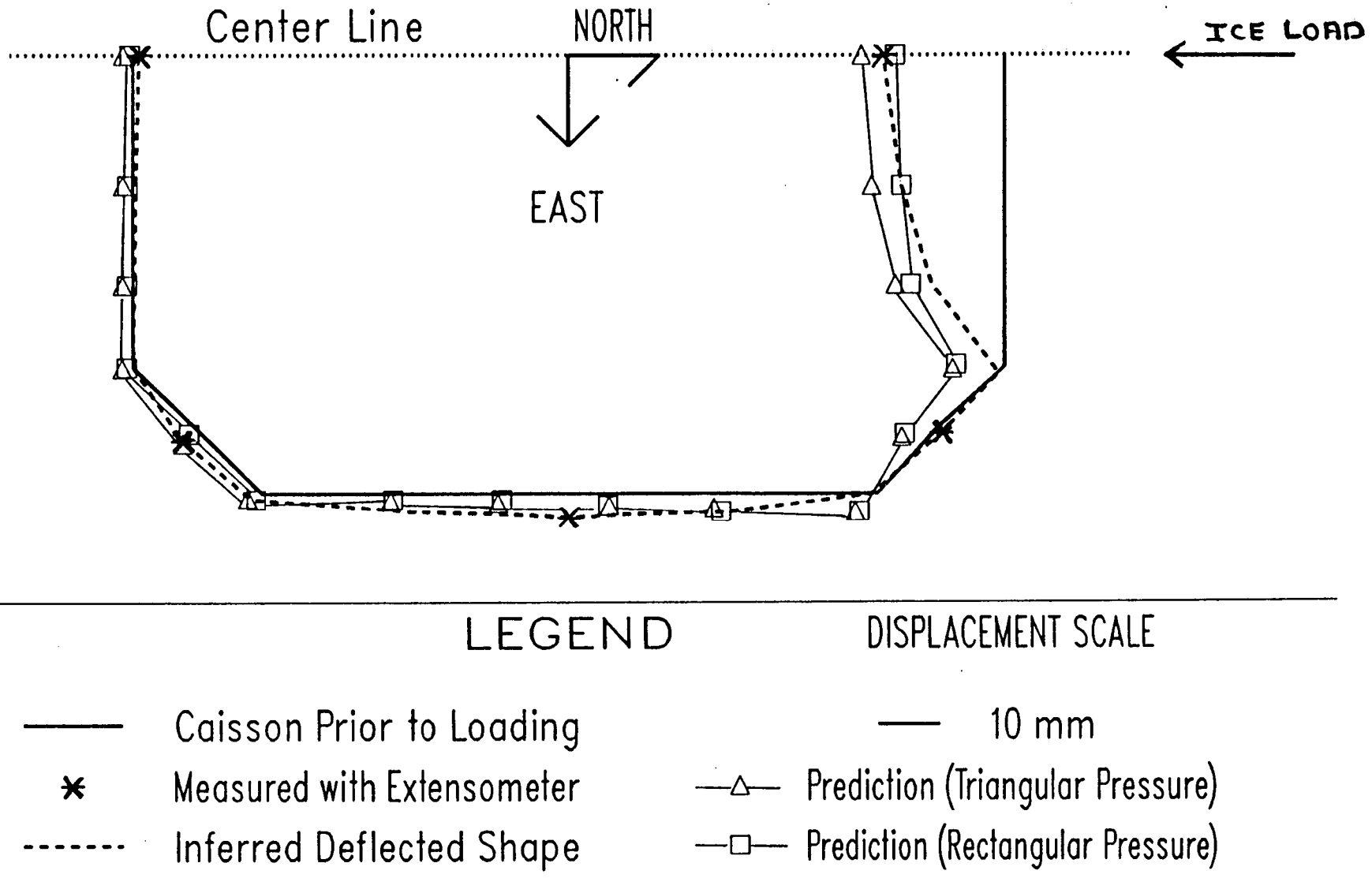

Figure 7.11 3-Dimensional caisson deformations due to the ice load event of 25 March, 1986. Comparisons between field observations and predictions.

of predictions shown in the Figure, the results obtained using the triangular pressure distribution are considered to be the ones that best model the inferred deflected caisson shape (see Fig. 7.11). It may be seen that the 3-D deflected shape of the caisson is adequately modelled by the analysis except for the NE corner, where the results obtained indicate movements in the opposite direction from the measurements.

The measured deformation profile in the core and berm due to the 110 MN ice load is shown in Fig. 7.12. These deformations were measured by the in-place inclinometer located at the centre line and approximately 3 m from the loaded face (see Fig. 7.10).

The results obtained from the analysis using the triangular pressure distribution of the ice load are also shown in Fig. 7.12. Because there were no nodes at the inclinometer location, displacements were computed at 0 and 6 m from the face and an average value was obtained to assess the displacements at the inclinometer location (see Fig. 7.12).

It may be seen that the average of the computed results agree extremely well with the field measurements and both show a remarkable difference between the shear behaviour of the core and the shear behaviour of the berm. This is in agreement with the maximum shear modulus profile selected for use in the analysis and presented earlier in Chapter 6.

Based on Jefferis, M.G. (1987), the in-place inclinometer returned to its pre-ice loading position after unloading. This indicates that the core and berm sand fills responded elastically during the ice load event of 25 March, 1986. This is in agreement with the unload/reload set of parameters used in the analysis.

Based on the quality of the predictions shown above, it is concluded therefore that the soil parameters shown earlier in Fig. 7.6 are adequate

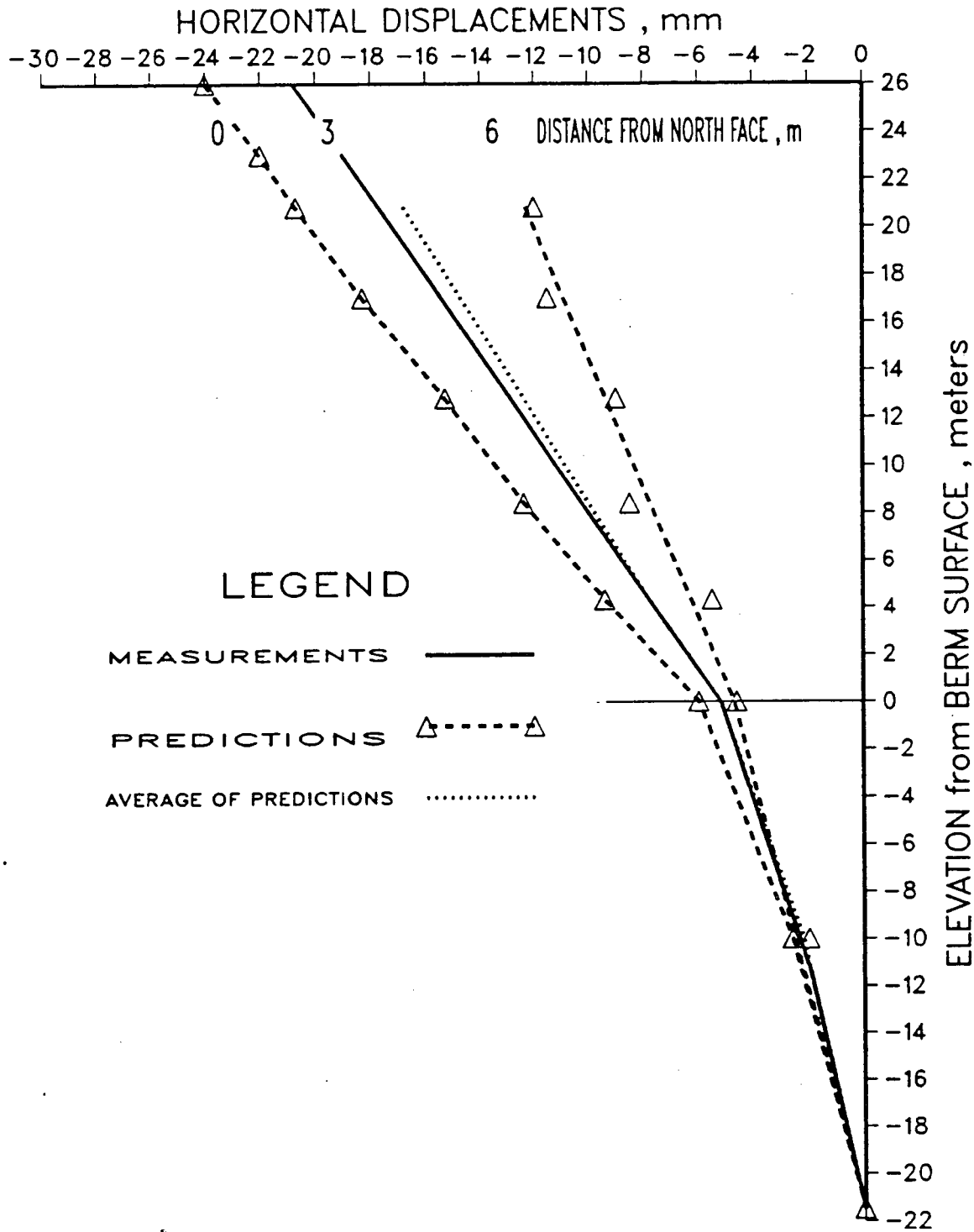

Figure 7.12 Deformation profile in the core and berm due to the ice load event of 25 March, 1986. Comparisons between field observations and predictions.

for use in the subsequent analysis of the dynamic ice load event of 12 April 1986.

7.4.3 3-D Analysis of the Dynamic Ice Load Event of April 12, 1986

The procedures followed in the 3-D analysis of the above ice load event are described below.

Prior to applying the ice loads, all soil elements were initialized with the stresses mobilized due to the gravity loads.

The ice load shown earlier in Fig. 7.1, was treated in the analysis as a rectangular pressure on the east face of the caisson. A triangular pressure was not considered because during the ice event of April 12, 1986 the full lateral perimeter of the caisson was surrounded by ice which moved from an eastern direction.

The 3-D dynamic assessment of the response of the Molikpaq to the ice loading was subdivided herein into three separate assessments: (a) liquefaction assessment; (b) porewater pressure rise assessment; and (c) acceleration assessment.

7.4.3.1 Liquefaction Assessment

The 3-D response of the caisson to series of cyclic ice loading pulses was determined by computing the static response to one-half cycle of load/unload. The cyclic stress ratios so computed were assumed to be the dynamic values corresponding to a dynamic amplification factor of 1. This is in close agreement with the findings of the 2-D dynamic analysis carried out by Finn and Yogendrakumar (see section 7.1 of this chapter).

Once these cyclic stress ratios were obtained the potential for liquefaction was assesed by comparing these stresses with the liquefaction

resistance stress ratios of the Molikpaq sand fills. These resistance stresses are shown in Fig. 7.13 and were developed earlier in Chapter 6 based on the cone penetration resistance of the fills, q_c, and an extrapolation of the chart developed by Seed and DeAlba (1986).

These procedures are described in detail in Appendix 7.4 (section 7.4.1). A brief summary is presented below.

(1) The east face of the caisson was loaded to 397 MN (see Fig. 7.1). During this phase the soil elements were considered to be drained.

(2) Next the east face of the caisson was unloaded back to 297 MN (i.e. one-half cycle of load/unload) and the cyclic stress ratio, $\Delta\tau_{zx}/\sigma'_{vo}$, evaluated for each soil element by the following equation:

$$\frac{\Delta\tau_{zx}}{\sigma'_{vo}} = \frac{\tau_{zx_{397}} - \tau_{zx_{279}}}{\sigma'_{z_{279}}} \qquad (7.2)$$

The numbers 279 and 397 indicate the ice load levels in MN.

(3) The soil elements that would liquefy were determined by comparing the above cyclic stress ratio, $\Delta\tau_{zx}/\sigma'_{vo}$, with the cyclic resistance ratio, τ_{av}/σ'_{vo}, obtained from Fig. 7.13.

(4) The Young's modulus and bulk modulus of the liquefied elements were now assigned their default values. The east face of the caisson was loaded again from 0 to 397 MN and the static analysis repeated.

(5) Steps (2) to (4) were repeated for different stages of loading (i.e. different number of cycles), as is described in Appendix 7.4, and the liquefaction assessment updated.

The 3-D liquefaction assessment at the end of the given ice loading is presented in Figs. 7.14(a) to 7.14(d). It may be seen that the 3-D

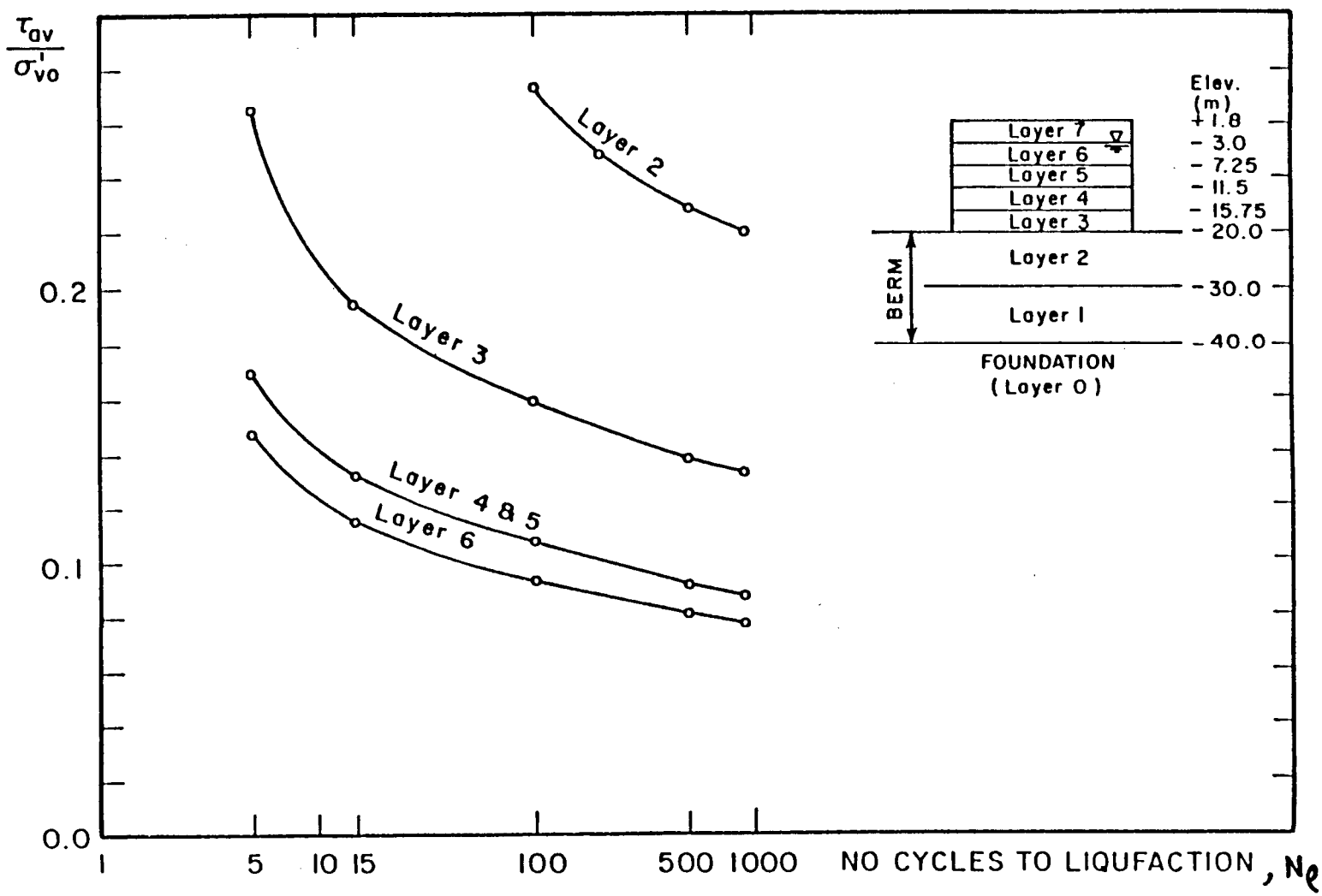

Figure 7.13 Liquefaction resistance curves used in the analyses

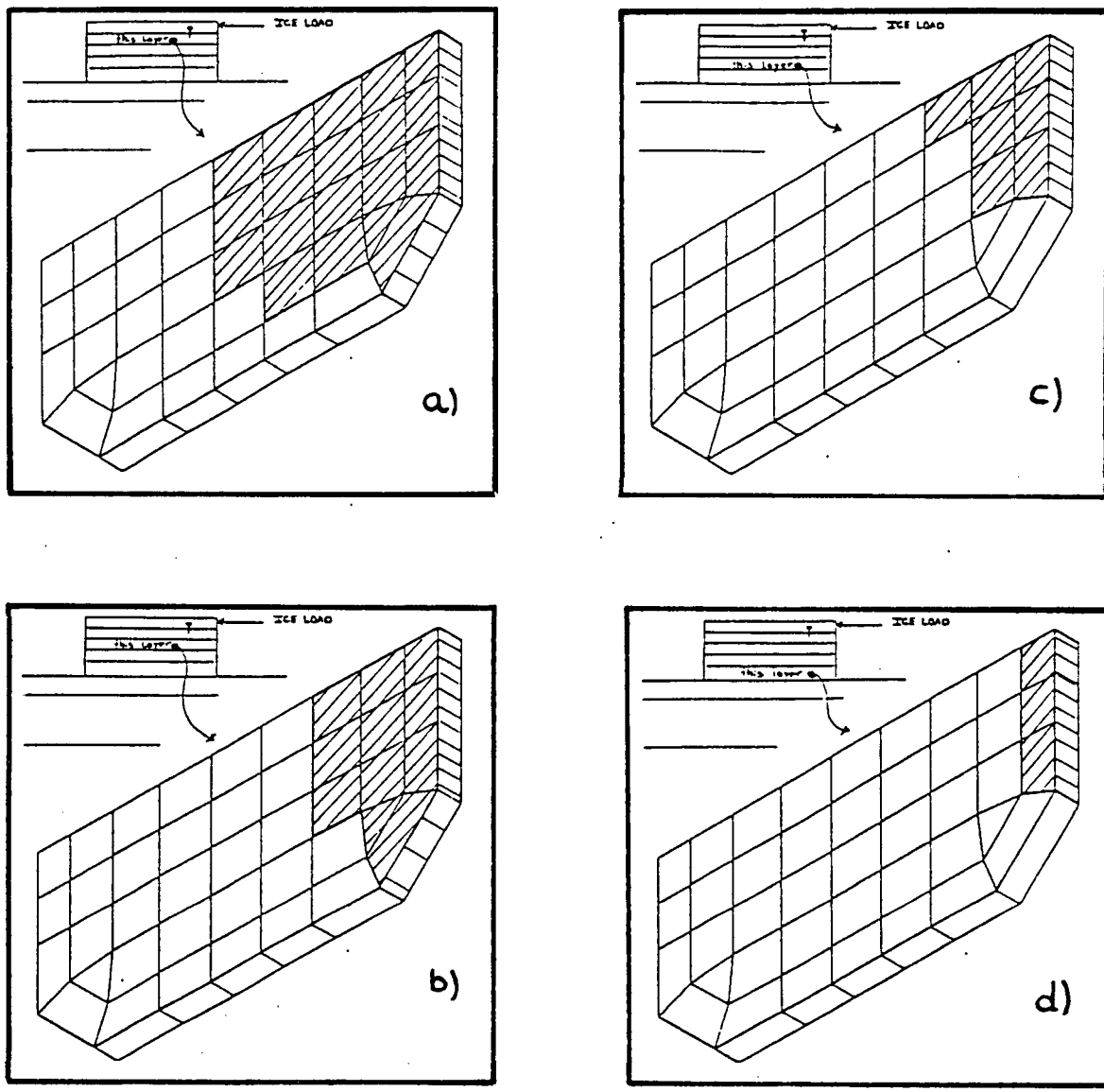

Figure 7.14 3-Dimensional liquefaction assessment: (a) layer no. 6; (b) layer no. 5; (c) layer no. 4; and (d) layer no. 3.

liquefied zone is concentrated around the loaded face and has its greatest horizontal extent near the top where the load was applied. This is in agreement with the actual liquefaction areal extent as is shown in Fig. 7.15 where is plotted the observed settlement of the core surface (along the E-W cross-section of the 3-D F.E. mesh) and the computed liquefiable soil for the same location Since the observed settlement was due to the dissipation of the porewater pressure from the liquefied soil zone it is concluded that a good liquefaction prediction was obtained by the analysis.

7.4.3.2 Pore Pressure Rise Assessment

During cyclic loading two kinds of porewater pressure are generated in saturated sands. One is cyclic in nature and the other is residual.

The procedures followed to assess the soil elements that liquefy (i.e. the soil elements in which the ratio between the generated residual porewater pressure and effective overburden pressure, $U_g/\sigma'_{vo} = 1$), were described in the previous section.

The porewater pressure model developed by Seed et al. (1976) was used to evaluate the residual porewater pressure rise (i.e. to evaluate the ratios $U_g/\sigma'_{vo} < 1$). The procedures followed are described in detail in Appendix 7.4 (section 7.4.2) where are also described the procedures followed to evaluate the cyclic porewater pressure, ΔU_{cy}.

A comparison between the results obtained and the field porewater pressures developed during the ice load event of April 12, 1986 is presented next.

The location of the piezometers used to monitor the porewater pressures is shown in Fig. 7.16. It may be seen that the piezometers E1,

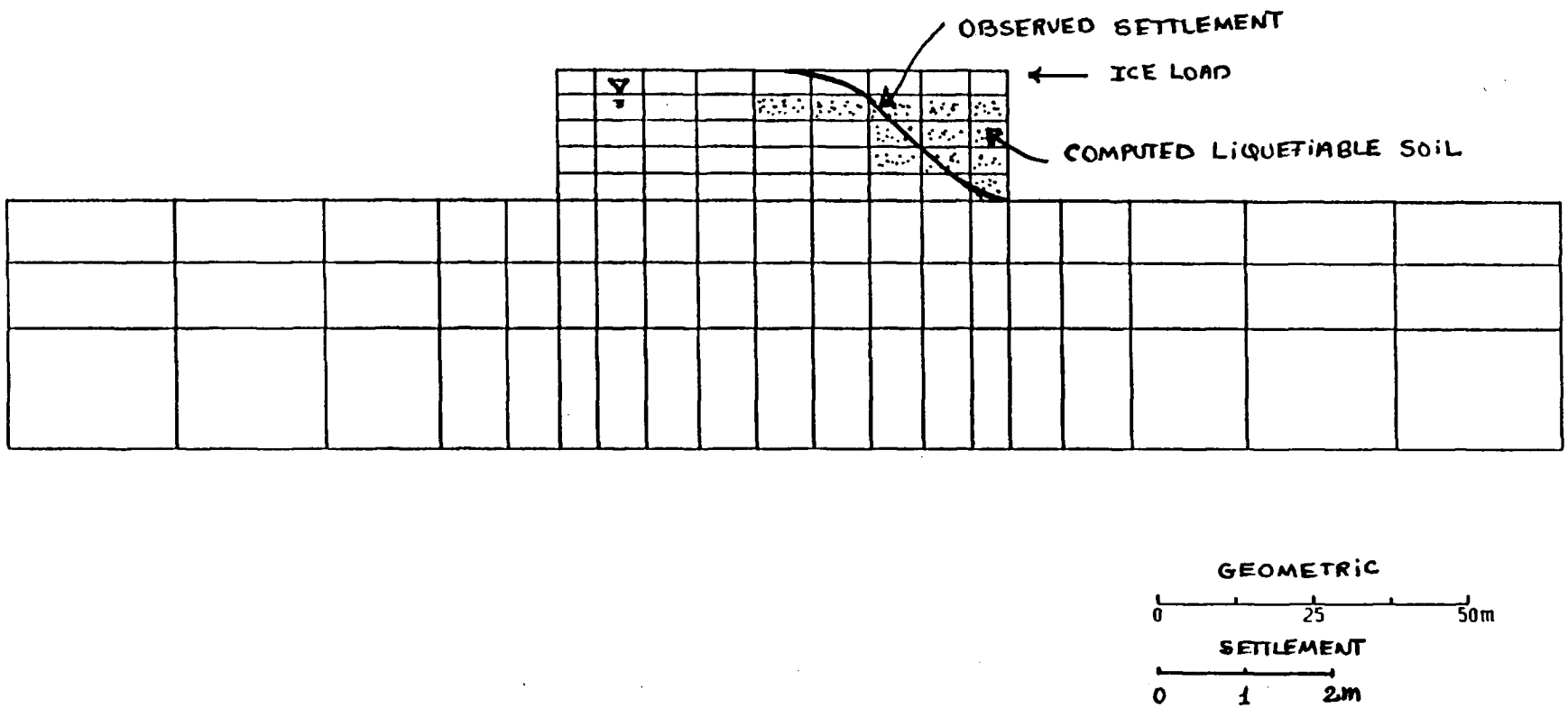

Figure 7.15 Plots of the Observed Settlement and the Computed Liquefiable Soil.

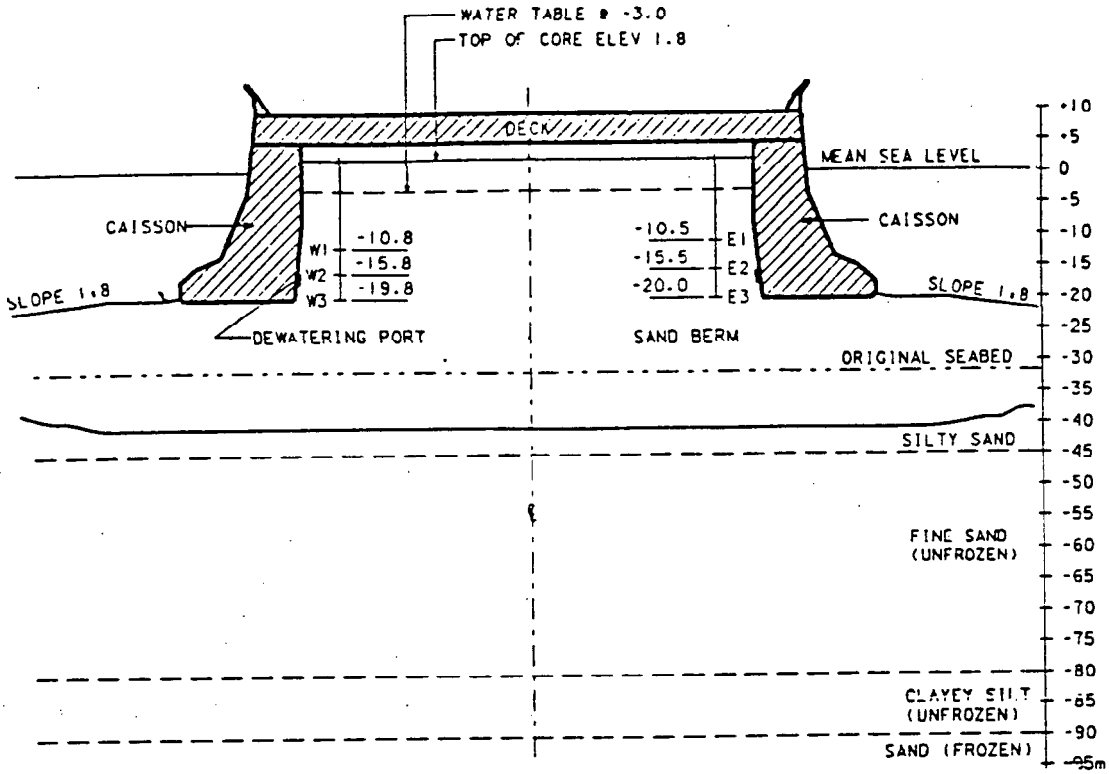

SECTION A-A

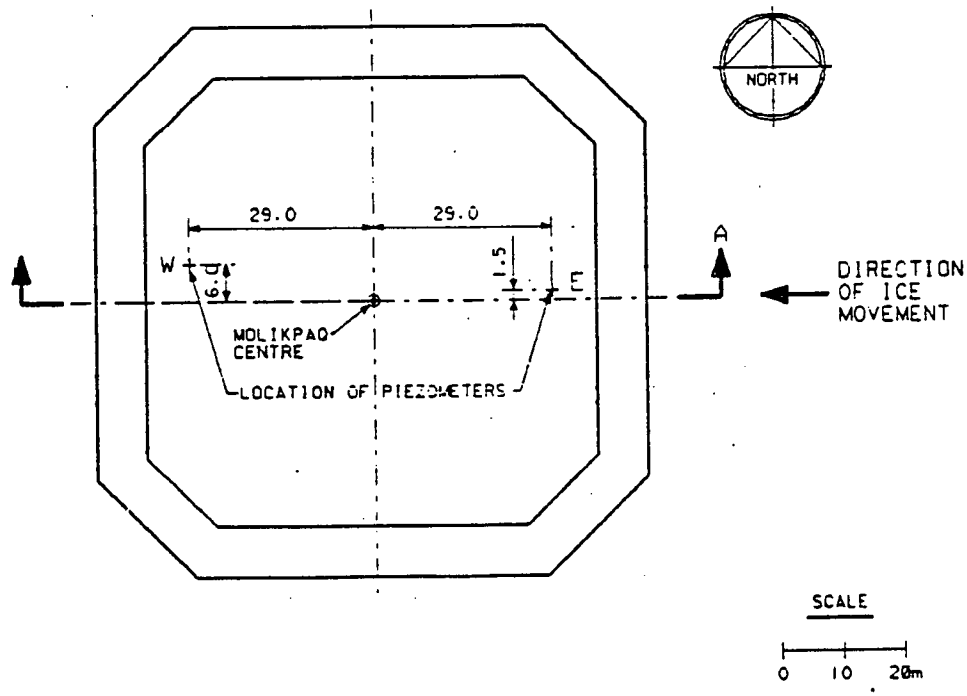

PLAN

Figure 7.16 Location of Piezometers

E2 and E3 are located near the loaded face and the piezometers W1, W2 and W3 are located near the trailing face.

Before a comparison between the measurements and the computed values is made, a description of the drainage conditions in the core is briefly described below because of its importance in the interpretation of the results.

For stability reasons the water level inside the core was maintained at an elevation of -3.0 m below mean sea water level. This lowering of the water table was developed by a series of water pumps located around the inside perimeter of the structure near the base of the caisson (see Fig. 7.16).

In order to assess correctly the porewater pressures developed during the dynamic ice loading event, the drainage effects developed by those water pumps should be taken into account. However, as described earlier, drainage was not considered in the analysis, but its possible effects should be kept in mind in the interpretation of the results presented below.

The maximum residual excess porewater pressures recorded, and predicted by the 3-D analysis following the procedures described earlier are presented in Table 7.1.

Table 7.1

Maximum Residual Excess Porewater Pressures (kPa)

	E1	E2	E3	W1	W2	W3
Measured	≥150*	≥190*	≥40*	≈10	≈20	≈20
Predicted	148	196	103	0**	0**	0**

*Maximum values not registered. Data gap between time 8:27 and 8:29
**No significant values computed.

The excess porewater pressures versus time computed at the locations of piezometers E1, E2 and E3 are presented in Fig. 7.17 and a comparison between the measured excess porewater pressure versus time and computed at the location of piezometer E1 are presented in Fig. 7.18.

It may be seen from the results presented in the above table and figures that the maximum residual excess porewater pressures computed from the analysis for the locations of piezometers E1 and E2 are in good agreement with the field measurements, which indicate that liquefaction was developed at these two locations.

The results also indicate that the prediction of the time to liquefaction, at the location of piezometer E1, is not correct. The computed time is 8:21 while the recorded time was 8:26. This fact is not unexpected because as described earlier the liquefaction resistance curves used in the analysis do not take into account the effects of the initial static bias, the effects of drainage and the effects of the previous dynamic ice loading events that took place at the Amauligak I-65 site during the time period March 7-8, 1986. In addition, the analyses were carried out using the idealized ice loading function presented earlier in Fig. 7.1 which is somewhat different from the actual ice loading of April 12, 1986 presented in Fig. 7.2.

The results also indicate that the predictions of the residual porewater pressure for the location of piezometer E3 is substantially higher than the maximum measured value before the data gap took place. This can also be explained by the above considerations.

Regarding the piezometers W1, W2 and W3 no significant residual porewater pressure values were computed from the analysis which is in agreement with the low values measured at those locations (see Table 7.1).

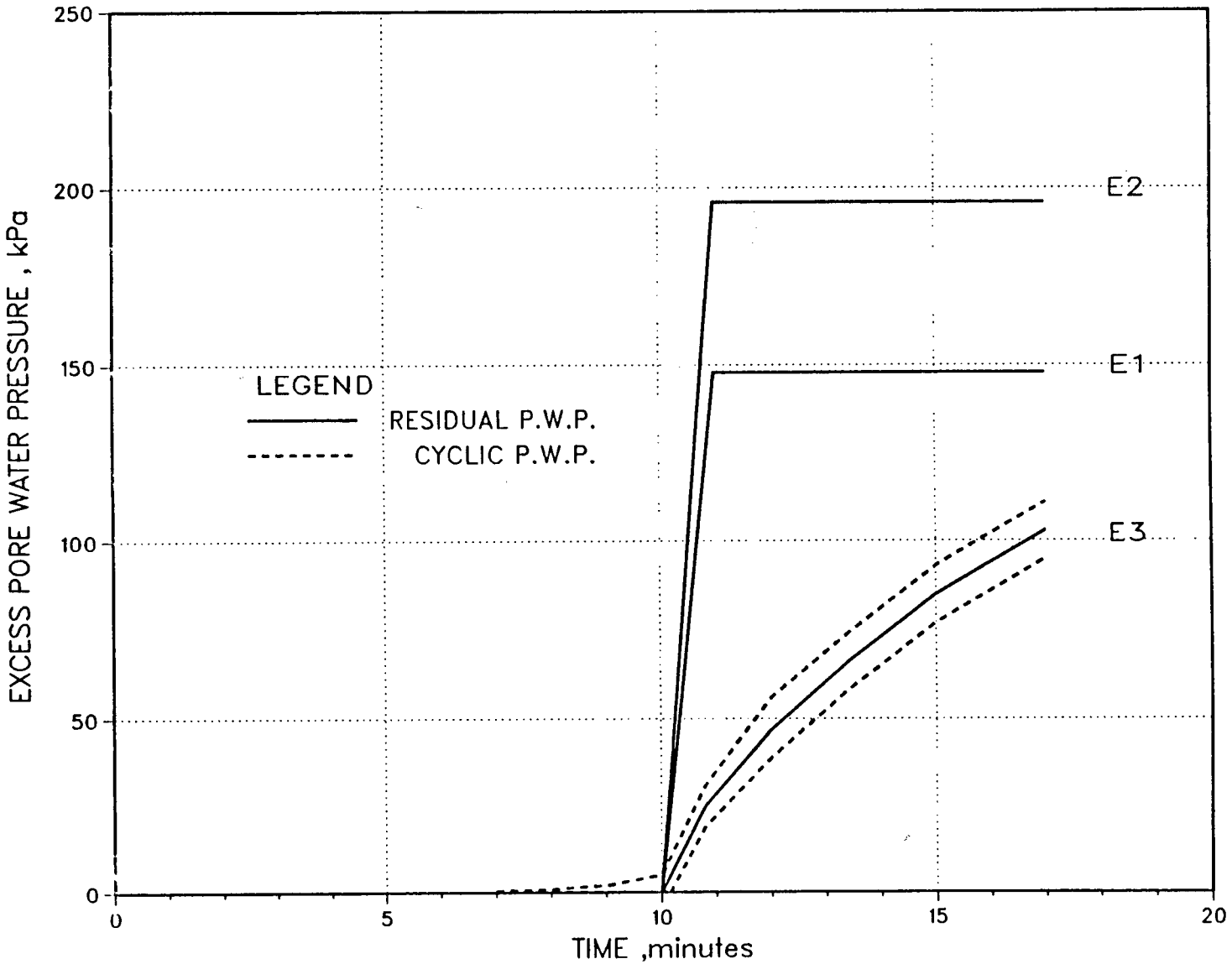

Figure 7.17 Excess porewater pressure values versus time computed at the locations of pieszometers E1, E2 and E3

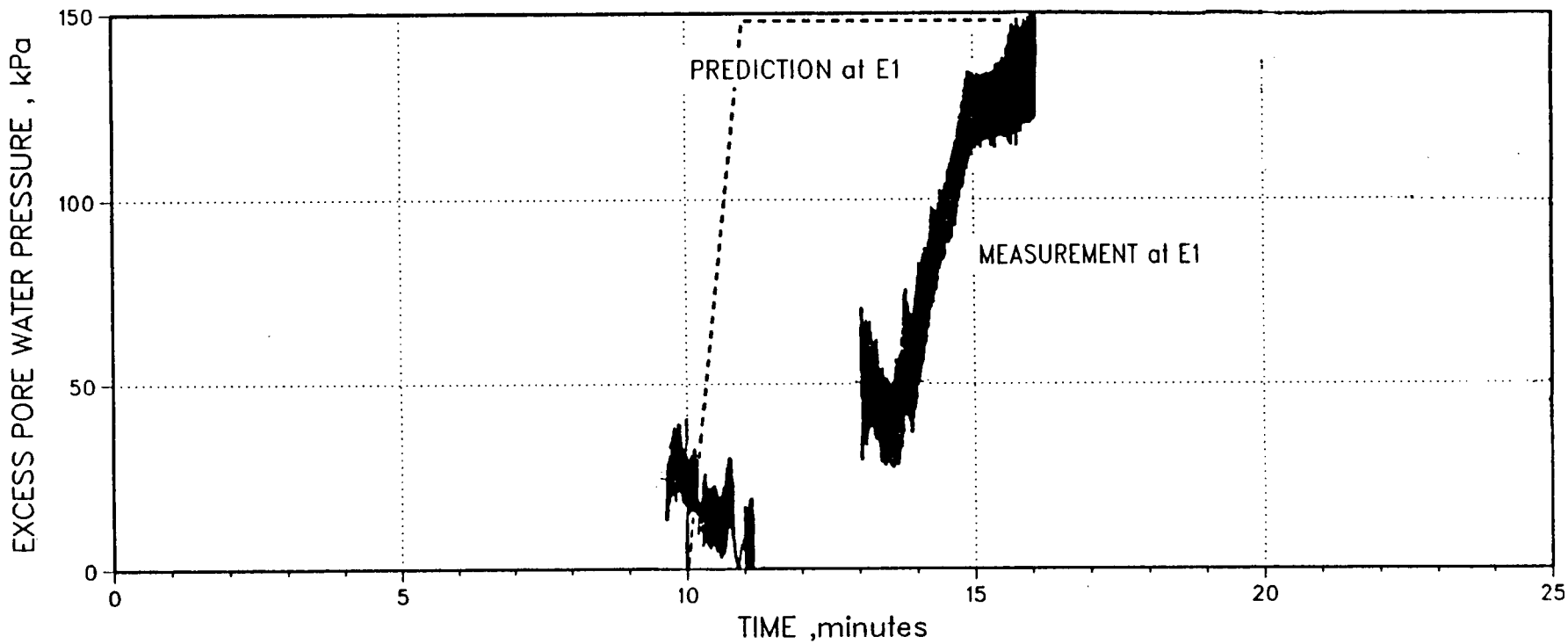

Figure 7.18 Comparison between the excess porewater pressure values versus time, measured and computed at the location of piezometer El

Based on the results shown above it is concluded that the procedures followed in the analysis to compute the residual porewater pressures are adequate. However, future analysis should be carried out with the actual ice loading and taking into account the effects of the initial static bias, drainage and previous dynamic loading since they can be very important for the evaluation of the exact time to liquefaction.

7.4.3.3 Acceleration Assessment

The procedures followed in the analysis to evaluate the accelerations developed by the ice loading function shown in Fig. 7.1, are described in this section.

The 3-D response of the caisson to series of cyclic ice loading pulses was determined by computing the static response to one-half cycle of load/unload. The amplitude of the displacements so computed were assumed to be the dynamic values corresponding to a dynamic amplification factor of 1. In addition, assuming that the response to cyclic loading of a particular frequency was harmonic, the peak acceleration at time t, A(t), was computed by the following equation:

$$A(t) = X(t) \cdot \omega(t)^2 \qquad (7.3)$$

where:

$X(t)$ = the amplitude of the static displacement at time t correspondent to one-half cycle of load/unload

$\omega(t)$ = the angular frequency at time t

The procedures followed in the analysis to evaluate the function X(t) are described in detail in Appendix 7.4 (section 7.4.3).

The above procedures were followed for the evaluation of the accelerations. The results obtained are presented below together with available field measurements.

The field accelerations developed during the ice load event of 12 April 1986 were monitored with the accelerometers located as shown in Fig. 7.19. However, the available field data is restricted to the accelerations measured, with accelerometer no. TM706 located on the loaded wall, and with accelerometer No. 841 located at centre line on the top of the core.

The magnitudes and time of maximum acceleration, measured, and predicted by the 3-D analysis following the procedures described earlier are presented in Table 7.2.

Table 7.2

Magnitude and Time of Maximum Acceleration

	TM-706		ACC-841	
	%g	Time	%g	Time
Measured	≥10.5	≥8:25:36	≥5	8:22:30
Predicted	17.0	8:23:00	6.0	8:23:00

A comparison between the accelerations versus time, measured at the location of ACC-841, and computed at this location are presented in Fig. 7.20 and the measured and computed accelerations correspondent to the location of TM-706 are presented in Fig. 7.21.

It may be seen from the results presented in the above table and figures that the predictions of the accelerations for the location of ACC-841 underestimate the field measurements around the time 8:20 but agree

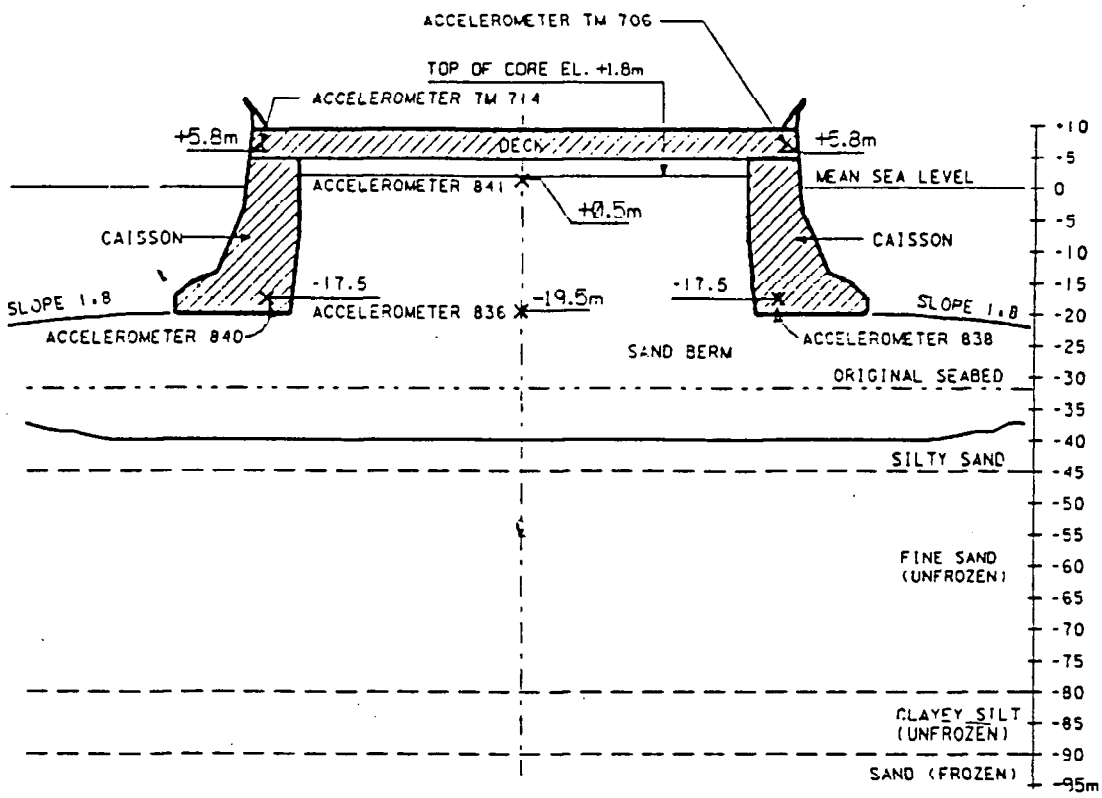

SECTION A-A

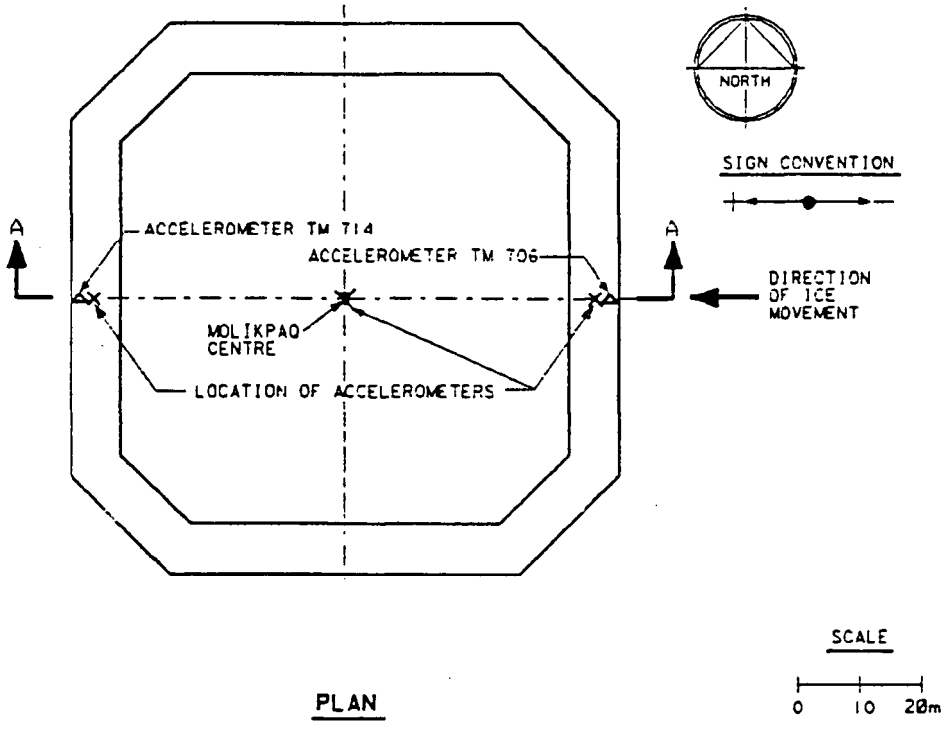

PLAN

Figure 7.19 Location of accelerometers

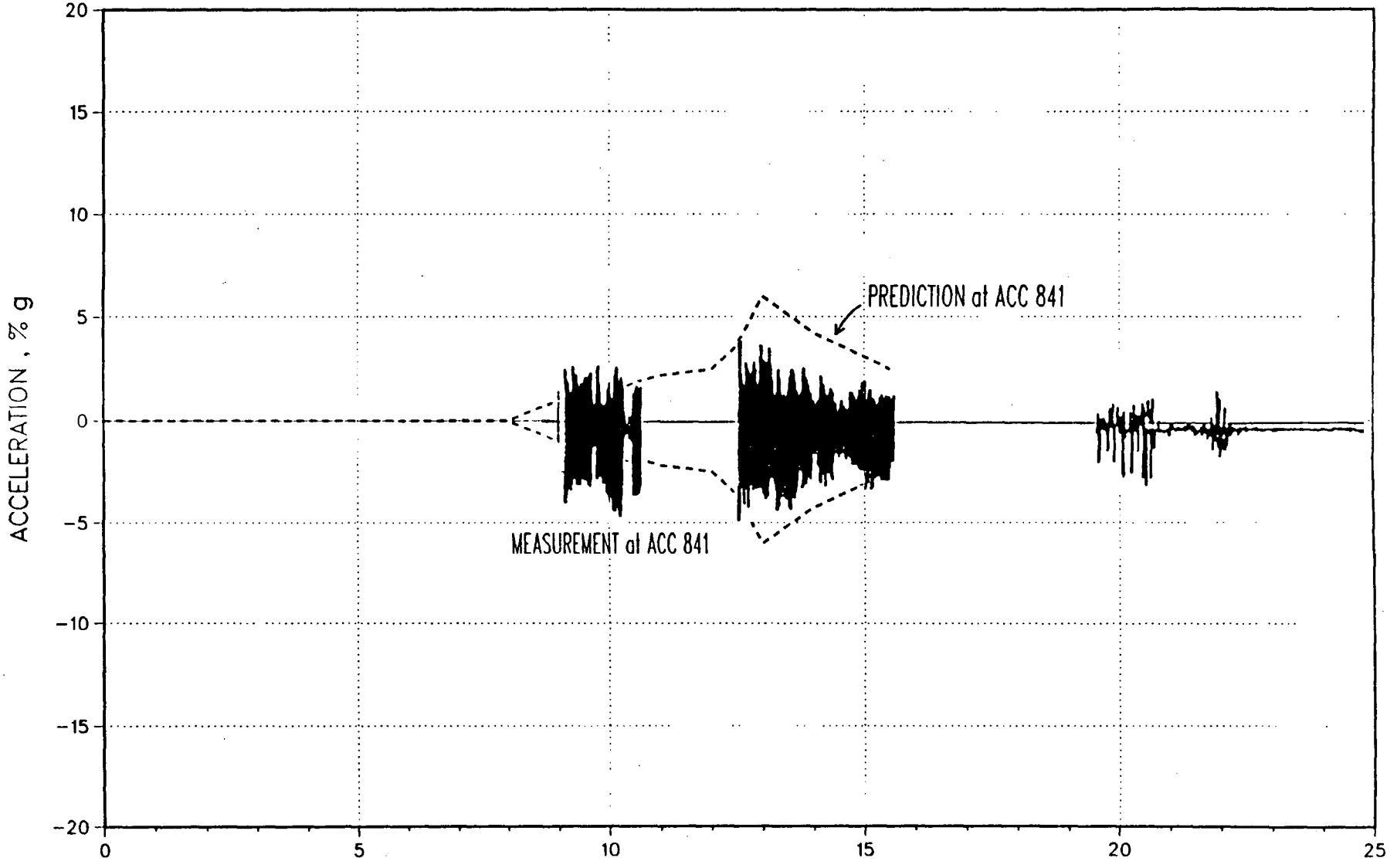

Figure 7.20 Comparison between the acceleration values versus time, measured and computed at the location of accelerometer no. 841

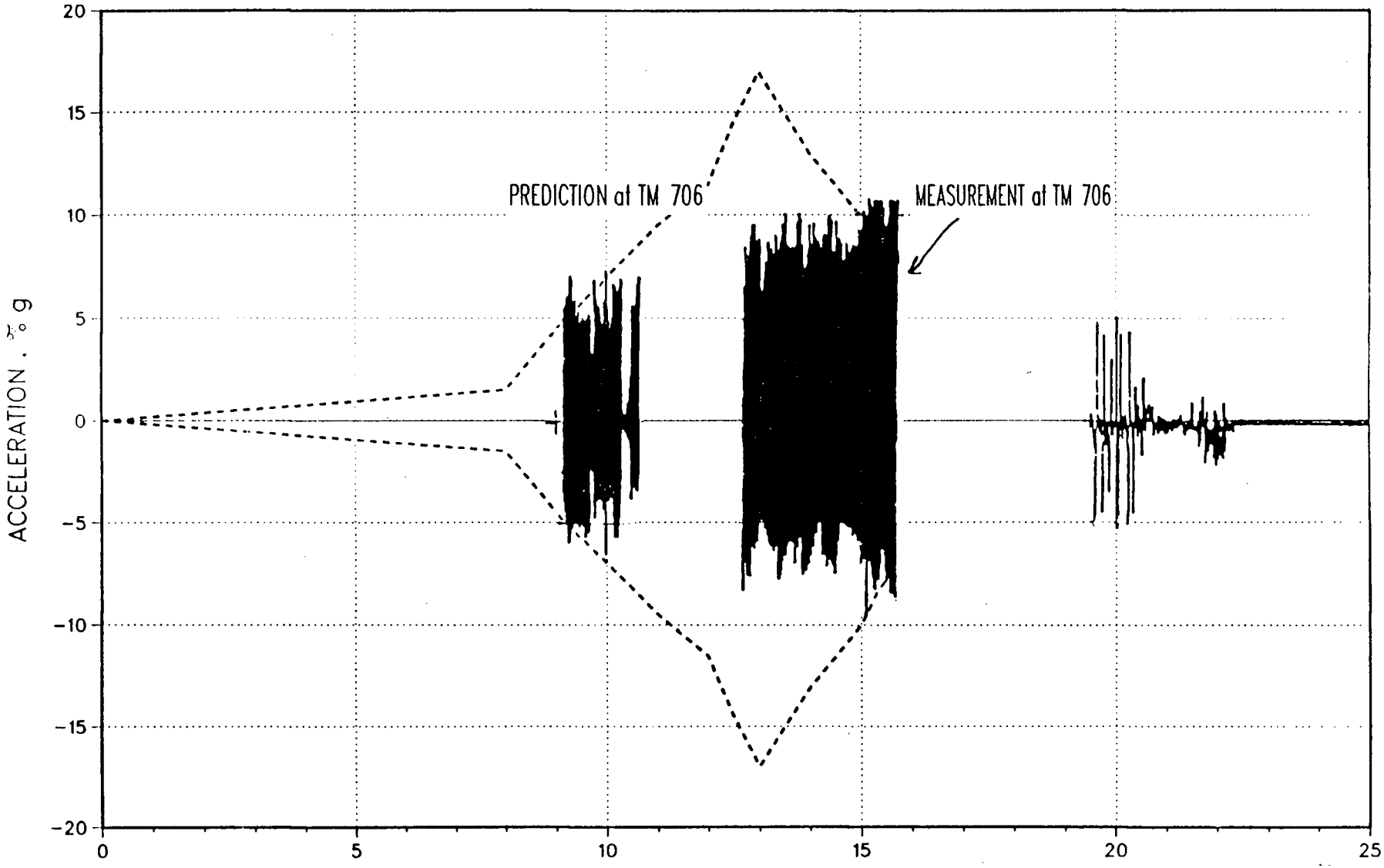

Figure 7.21 Comparison between the acceleration values versus time, measured and computed at the location of tiltmeter no. 706

quite well with both the maximum acceleration value recorded and the time of its occurrence.

On the other hand the predictions of the accelerations for the location of TM-706 agree quite well with the field measurements around time 8:20, but both the maximum acceleration recorded and its time of occurrence are not well predicted by the analysis. This is not unexpected because the computed values of the accelerations were based on the assumption that the response of the Molikpaq to cyclic loading was harmonic which is an extremely crude assumption. In addition an idealized loading function was used in the analysis.

7.4.4 3-Dimensional Analysis for the Settlement Assessment

After the ice loading phase was completed the east face of the caisson was unloaded to zero ice load and the settlement assessment carried out as follows.

The cyclic shear stresses and strains from the ice loading event induce plastic volumetric strains which cause a rise in porewater pressure and subsequently settlement of the sand core.

Because testing of the sand core material from which such plastic volumetric strains could be evaluated was not performed, estimates of such strains were made based on the work developed by Tokimatsu and Seed (1987) and Byrne (1990), as is described below.

The procedures followed were subdivided into two parts. In the first, an assessment of the volumetric strains associated with earthquakes of magnitude = 7.5 (or 15 cycles) was made based on the work reported by Tokimatsu and Seed. In the second part an assessment of the volumetric strains associated with a larger number of cycles than 15 was made based on the work developed by Byrne.

- Assessment of Plastic Volumetric Strains Associated with 15 Cycles of Load

A chart showing the expected volumetric strains as a function of both cyclic stress ratio and $(N_1)_{60}$ value was developed by Tokimatsu and Seed and is presented in Fig. 7.22. Their values are based on laboratory tests and field experience during earthquakes.

The material of the core has a density corresponding to a $(N_1)_{60}$ value in the range of 8 to 12 as is shown in Fig. 7.23 and hence from Fig. 7.22, the likely volumetric strains associated with 15 cycles of load, if liquefaction is triggered, would be in the range $2^{1/2}$ to 3%. If liquefaction is not triggered, the cyclic shear strains and the volumetric strains are likely to be small and may be neglected.

- Assessment of Volumetric Strains Associated with a Larger Number of Cycles than 15

As described earlier, 400 equivalent cycles of load of magnitude 118 MN were assessed for the time period starting at 8:10 and finishing at 8:27(see Fig. 7.1). As shown in the figure a data gap took place between 8:27 and approximately 8:29 and therefore the total number of equivalent cycles, N, is unknown but is expected to have been > 400.

Based on the work developed by Byrne (1990) the ratio between the volumetric strains associated with 400 cycles and 15 cycles, $\epsilon_{v_{400}}/\epsilon_{v_{15}}$, is equal to 2.6. Therefore, using the ϵ_v values of $2^{1/2}$ to 3% obtained from Fig. 7.22 the volumetric strains due to 400 cycles are 6.5% to 8.0%. Because N is expected to have been > 400 a value of ϵ_v = 8% was considered in the analysis.

To evaluate the settlement associated with the above volumetric srains, these strains were assigned as potential strains to the liquefied

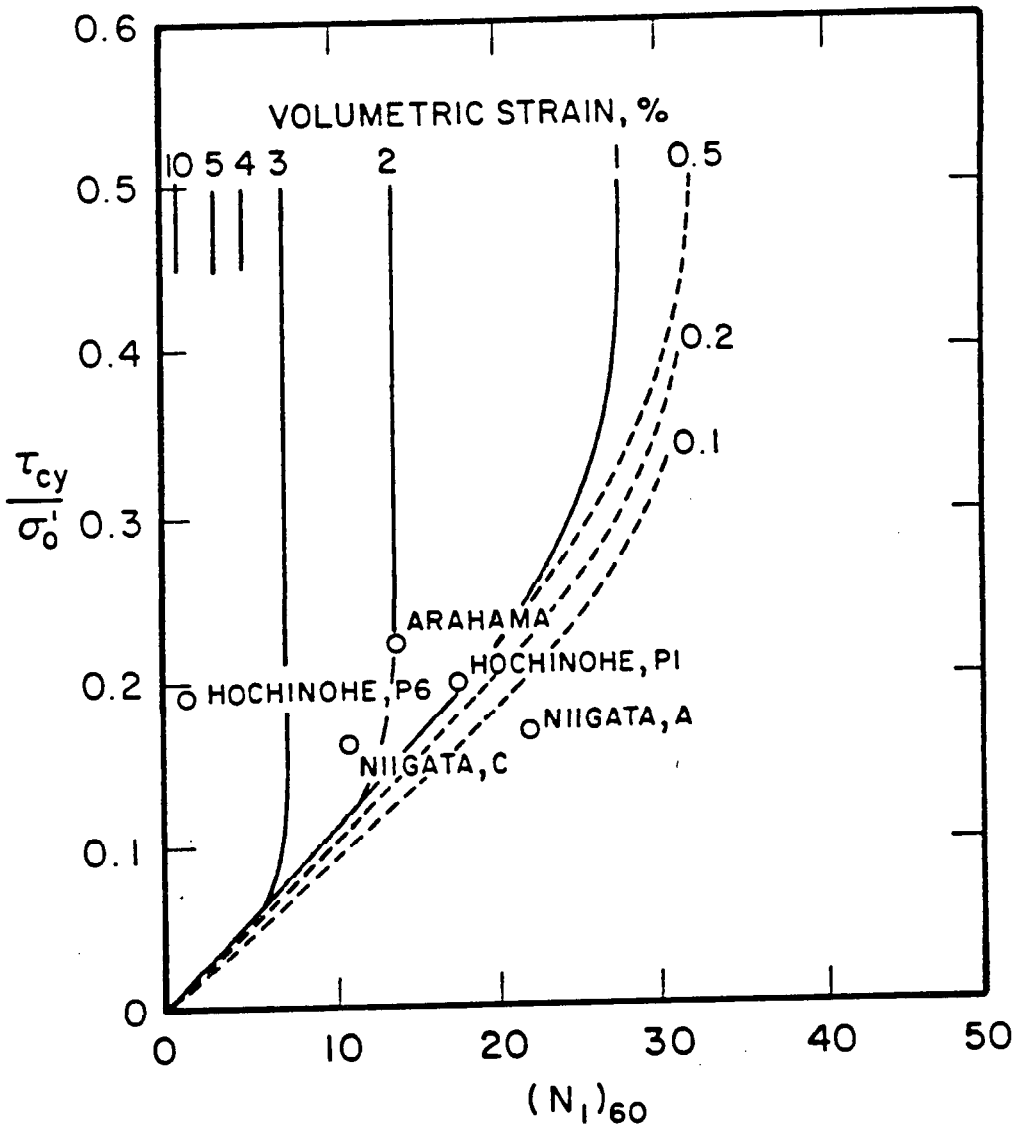

Figure 7.22 Volumetric strains induced by cyclic stresses and liquefaction (after Tokimatsu and Seed, 1987)

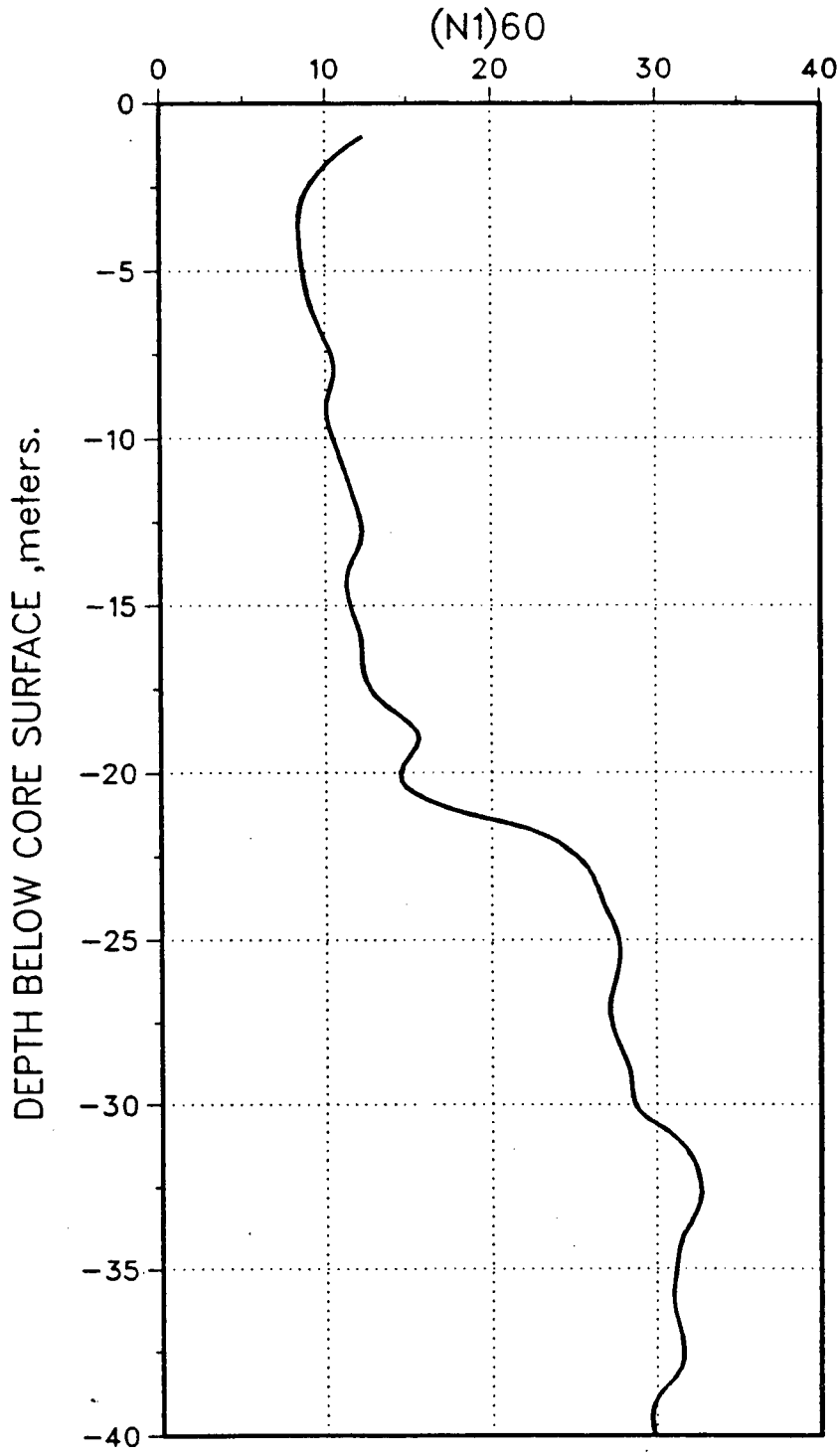

Figure 7.23 Relationship between $(N_1)_{60}$ and depth

elements and finite element analysis were carried out to obtain a compatible distribution of the volume strain and the settlement. The moduli and load vector used in the above analysis are described in Appendix 7.5.

The settlement results obtained following the above procedures are discussed below together with the field measurements.

The settlement measurements of the top of the core surface along its E-W centreline are presented in Fig. 7.24 together with the settlement results computed from the analysis based on a volumetric strain value, ϵ_v = 8%.

It may be seen that both the trend and the magnitude of the predictions agree quite well with the field observations.

Because the settlement areal extent is closely associated with the liquefied soil zone extent, it is concluded that the zone of liquefaction that occurred during the ice loading event of 12 April 1986 was adequately identified by the analysis procedure carried out herein.

In addition, inclinometer observations were also carried out to assess the residual deformations of the sand fills of the Molikpaq structure. These observations were carried out in the inclinometer located as shown in Fig. 7.25.

The displacement profile measured in the inclinometer located adjacent to the west wall of the caisson and the corresponding computed displacements from the analysis are presented in Fig. 7.26.

It may be seen that the predictions underestimate the field measurements. This could be associated with the fact that a Poisson's ratio value of ν = 0.0 was used in the analysis (see Appendix 7.5).

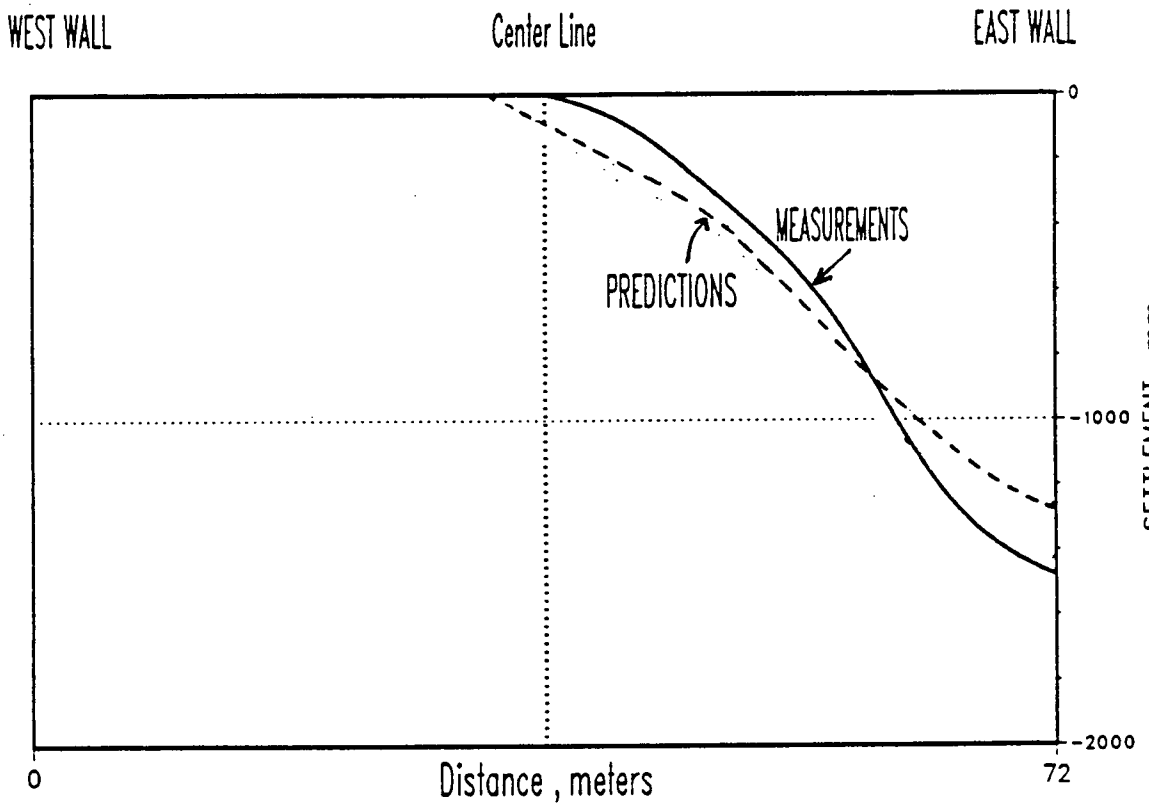

Figure 7.24 Comparison between the settlement, measurements and predictions of the top of the core surface

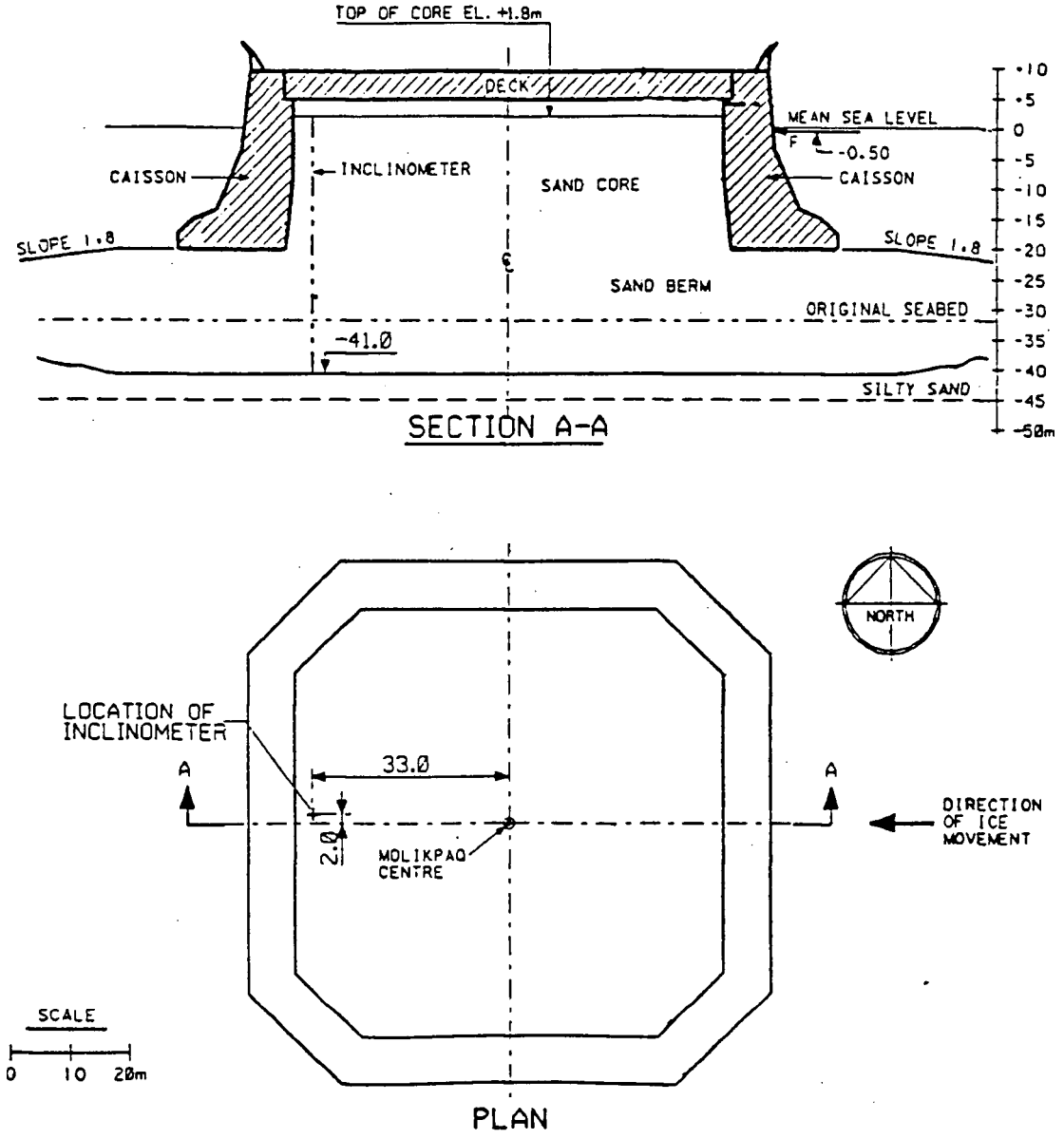

Figure 7.25 Location of the inclinometer used to measure the residual horizontal displacements

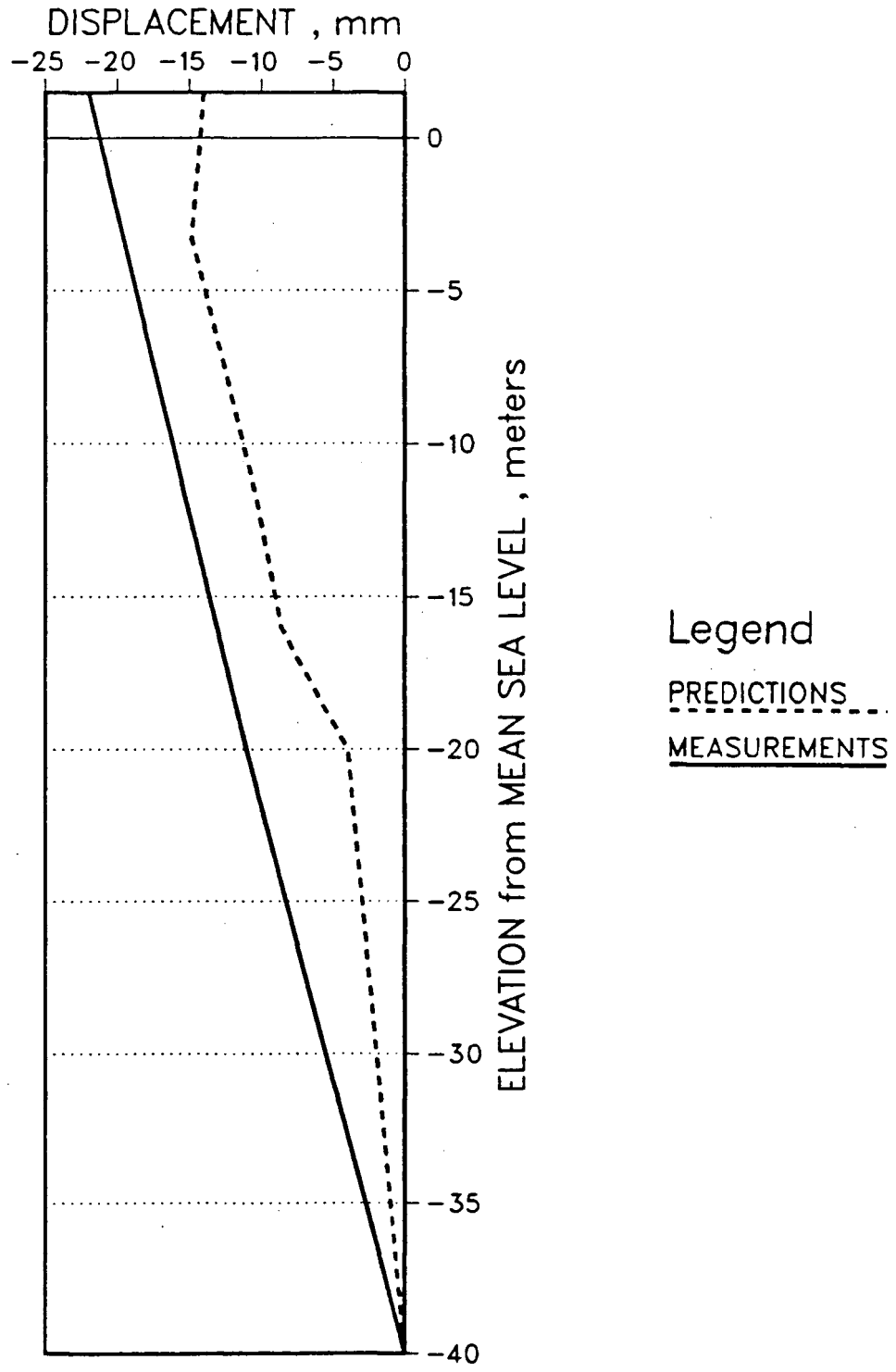

Figure 7.26 Comparison between the residual horizontal displacements, measured and computed at the location of the west side inclinometer

7.5 2-D Finite Element Analysis of the Dynamic Ice Load Event of April 12, 1986

To study the influence on the results of some key parameters, several 2-D analyses were carried out.

A brief description of the key parameters studied is presented below. The details of the analysis are described in Appendix 7.6 and the main conclusions are presented afterwards.

7.5.1 Description of the Key Parameters Studied in the 2-D Analysis

(a) Influence of the Interface Element Type and the Value of the Angle of Friction, δ

The interface between the steel structure and the sand fills was modelled in the 3-D analysis by a standard solid isoparametric brick element characterized by an angle of friction, $\delta = 20°$.

To study the influence of the interface element type in the results, 2-D analyses were carried out using both the standard isoparametric element and the "thin" interface element that was described in Chapter 4. For both cases a value of the angle of friction $\delta = 20°$ was considered (see Apendix 7.6).

To study the influence of δ in the results, additional 2-D analyses were carried out using the "thin" element with values of $\delta = 0$ and $\delta = \phi$. The main conclusions from the above studies are presented later in section 7.5.2.

(b) Influence of the Stress Redistribution Method

The procedures followed in the 3-D analysis to redistribute the shear stresses of the liquefied soil elements to the adjacent soil and structural elements was described earlier. This stress redistribution method is con-

sidered to be an adequate method, but not the only method. An alternative method to the above was also considered in the 2-D analysis and consisted briefly on the following.

Once a soil element is identified as having liquefied its shear strength is assigned a low value corresponding with its residual strength, s_u. The amount of shear stress, $\Delta\tau$ that exceeds s_u is redistributed to the adjacent stiffer elements using the load shedding procedures developed by Byrne and Janzen (1984) and described earlier in Chapter 2.

To study the influence of the two different methods of stress-redistribution, in the results, 2-D analyses were carried out using both methods as is described in Appendix 7.6. The main conclusions of this study are presented later in section 7.5.2.

(c) Influence of the Constitutive Law

The 3-D analysis of the Molikpaq were carried out following a combination of an elastic and hyperbolic stress-strain laws as described in section 7.3.3. To study the influence of the stress-strain law in the outcome of the results, 2-D analysis were also carried out in Appendix 7.6 using the modified SMP model which was developed and presented earlier in Chapter 2.

Ideally, the above items would have been studied with a 3-D analysis, but either due to the computer time required or due to the shortage of computer memory space, the influence of the above had to be studied with 2-D analysis. The main conclusions from the 2-D analysis are presented below:

7.5.2 Conclusions from the 2-D Analysis

a) The same initial response of the Molikpaq loaded wall movement was computed by the analysis carried out using the "Thin" interface element and the "Standard" soil element for the same $\delta = 20°$. However at ice load levels of 400 MN the displacements obtained with the "Thin" element are shown to be about 85% of that computed by the "Standard" element.

b) The same response of the Molikpaq loaded wall was computed by the analysis when using the "thin" interface element with $\delta = 20°$ or $\delta = \phi$. For the case $\delta = 0°$ however, the displacements of the loaded wall are shown to be about 10% larger than those computed by the above analysis.

c) The same initial response of the Molikpaq loaded wall was computed by the analysis carried out using the modified SMP model and the hyperbolic model. However, at ice load levels of 400 MN, the displacements computed by the modified SMP model are shown to be about 82% of that computed by the hyperbolic model. This difference is related with the Mohr-Coulomb failure criteria that is used in the hyperbolic model and also because this model does not compute increases in mean normal stress, $\Delta\sigma_m$ due to increases in shear stress $\Delta\tau_{zx}$.

d) Similar responses of the Molikpaq back wall movements were computed from all analyses except for the movements computed by the analyses where the shear stresses of the liquefied soil elements were redistributed following the "load shedding" method. This method computed larger movements for the back wall than that computed from the stress redistribution method used in the 3-D analysis.

e) Essentially the same 2-D liquefaction areal extent is computed from all analyses and coincides with the 3-D liquefaction assessment for the location of the E-W cross-section.

7.6 Summary and Conclusions

An analysis procedure for a caisson-retained island type structure was described and used to predict the response of Gulf's Molikpaq structure to the ice load event of April 12, 1986.

The liquefaction assessments from the 3-D analysis indicate that the computed liquefaction areal extent is in good agreement with the field liquefaction assessment based on porewater measurements and settlement observations.

The results obtained from the 3-D analysis also indicate that the overall predictions of porewater pressure and accelerations agree well with the field measurements except for the time to liquefaction and the magnitude and time of occurrence of the maximum accelerations. These discrepancies are attributed to the idealized ice loading function used in the analysis and to the influence of the initial static bias, drainage and previous loading history which were not considered in the analysis.

In addition, several 2-D analyses, which considered different types of interface elements ("thin" and "standard" elements) and constitutive models (modified SMP and hyperbolic models) indicate that the computed liquefaction areal extent is practically insensitive to the above parameters and in good agreement with that computed by the 3-D analysis.

Based on the above it is concluded that both the procedures followed to obtain soil parameters and the analysis procedures followed in the 3-D analysis are adequate procedures for design purposes, and that the influence of the above 3 factors must be considered in future analysis.

CHAPTER 8

SUMMARY AND CONCLUSIONS

A procedure to analyze the response of large offshore drilling platforms to the high ice loading conditions of the Beaufort Sea has been presented in this thesis. These platforms comprise a large steel box infilled with a sand core for stability against high ice loading. One such structure was subjected to very severe ice loading, and being the response monitored, it allows a case study against which the proposed procedures were checked.

To analyze the behaviour of these highly complex soil-structure interaction systems a 3-D F.E. computer program with soil, interface and structural elements was developed in this thesis. The stress-strain relations and the evaluation of the stress-strain parameters from in situ testing as well as interface elements were considered the key aspects of the analysis and were considered in detail. These aspects together with the analysis of the Molikpaq structure are summarized in this chapter.

8.1 3-D Constitutive Law for Sands

The 2-D hyperbolic model developed by Duncan and Chang (1970) and Duncan et al. (1980) was expanded to 3-D and implemented into F.E. formulation. This model does not account for the dilation characteristics of the sand material and to account for this an additional dilatant parameter based on Byrne and Eldridge (1982) was expanded to 3-D and also implemented into F.E. formulation. However, preliminary analysis of simple shear tests on Ottawa sand indicate that the predictions obtained by the hyperbolic

model (with and without dilatant parameters) considerably underestimate the failure shear stresses measured in those tests.

Based on the above, and because the simple shear stress path is the path most closely followed in the sand fills of the Molikpaq due to the horizontal ice loading on this structure, a review of the existing 3-D stress strain models was carried out in chapter 2 to select the most appropriate one. Special emphasis was focussed on the 3-D yield criterion, and stress-dilatancy theory of the models.

From the review, presented in Chapter 2, the 3-D model developed by Matsuoka (1974,1983) following the concept of the Spatial Mobilized Plane (SMP) was selected. This model was modified by the writer to make it more practical, and, take into account the rotation of principal axes during the simple shear test. The model so developed is called the modified SMP model.

Particular attention was addressed in this thesis to the development of procedures to evaluate soil parameters for use in the modified SMP. In all, eleven soil parameters (4 elastic and 7 plastic) are required. It was shown that these soil parameters can be obtained from the following sources:

(a) Laboratory tests (Chapter 3);

(b) Pressuremeter tests (Chapter 5); and

(c) Laboratory and cone penetration tests (Chapter 6).

The performance of the modified SMP model was evaluated by comparisons with laboratory measurements, pressuremeter chamber test measurements, and in situ measurements obtained from field tests.

The laboratory data selected for the comparisons was obtained from simple shear test data on Leighton-Buzzard sand, simple shear, and true-

triaxial test data on Ottawa sand. In addition comparisons were also made against triaxial test data on Erksak 320/1 sand.

From the comparisons between the predictions and the reported data the following is concluded:

- Both the 3-D and 2-D plane strain formulations of the proposed model can reproduced well the reported simple shear test data on Leighton-Buzzard sand. This indicates that: (i) the model takes into account he gradual rotation of the axes of principal stresses and strains that occur during that test; and (ii) the 2-D formulation which is derived from the 3-D formulation by applying the appropriate boundary conditions give a good prediction of the intermediate principal stress σ_2.

- The overall good predictions of the triaxial tests on Erksak 320/1 sand and both the simple shear and true-triaxial on Ottawa sand with the exception of the circular path test further indicate that the proposed model is able to predict the behaviour of sand with reasonable accuracy for the stress-paths of practical importance for the Molikpaq structure.

- Because the circular path test is not representative of the stress paths that occur in the sand fills of the Molikpaq structure during either the construction or ice loading phases, the reasons of the poor predictions of this test by the modified SMP model were not investigated herein.

To further validate the modified SMP model, F.E. predictions of pressuremeter chamber tests on Leighton-Buzzard sand were carried out as described in Chapter 5. The parameters for the model were determined from the simple shear test data on Leighton-Buzzard sand (Chapter 3), the same sand used in the pressuremeter chamber tests.

From the comparisons between the pressuremeter chamber test measurements and the F.E. predictions the following conclusions are made:

• The results indicate generally good agreement between computed and observed pressure-deflection relations at the face of the pressuremeter provided the actual boundary conditions of the chamber tests are modelled. The measured response is a little softer at the initial stages of loading. This may be due to disturbance.

• The computed displacement patterns in the chamber tests are sensitive to the vertical stress σ_z applied at the base of the chamber and indicate that plane strain conditions did not prevail in the chamber tests.

8.2 Evaluation of Stress-Strain Parameters of Soil from Laboratory and/or In Situ Testing

Particular attention was addressed in this thesis to the development of procedures to evaluate soil parameters for use in the modified SMP model and hyperbolic model. The current methods of soil parameters evaluation were reviewed, some expanded and applied in this thesis. It was shown that the soil parameters for use in these two models can be obtained from the following three sources:

i) Laboratory tests (Chapter 3);

ii) Pressuremeter tests (Chapter 5); and

iii) Laboratory and cone penetration tests (Chapter 6).

8.2.1 Evaluation of Soil Parameters from Laboratory Tests

It was shown in Chapter 3 that the laboratory data obtained from any test, including the standard triaxial test, that measures the three principal stresses and strains can be used to evaluate soil parameters for use in the modified SMP model. The procedures used to evaluate the shear

(elastic and plastic) and failure parameters follow closely those developed by Duncan et al. (1980) to evaluate the E moduli and failure parameters used in the hyperbolic model. The procedures used to evaluate the elastic bulk parameters follow those developed by Byrne and Eldridge (1982) to evaluate the bulk moduli used in the hyperbolic model and the procedures used to evaluate the flow rule parameters of the model follow those developed by Matsuoka (1983).

8.2.2 Evaluation of Soil Parameters from the Pressuremeter Test

The current methods to infer soil parameters from the unloading and first time loading pressuremeter test data were reviewed, expanded and applied in this thesis. A summary of the work carried out is presented below:

- A procedure for analyzing the unloading response of the pressuremeter was presented in Chapter 5. The analysis considers the effects of change in the average stress $(\sigma'_r+\sigma'_\theta)/2$, the stress ratio σ'_r/σ'_θ, and shear induced volume change on the maximum modulus. Results of the analysis are presented in a chart which allows the in situ, $G_{max,o}$ to be computed from the equivalent elastic shear modulus G* taking into account both the level of pressuremeter loading and unloading.

The predicted G_{max} values from pressuremeter chamber and field tests using the proposed chart were compared with values obtained from resonant column and crosshole seismic test and are found to be in good agreement provided factors are included to account for disturbance and anisotropic effects.

- The proposed chart was also used in Chapter 6 to evaluate G_{max} values from the SBP tests carried out at the Amauligak I-65 site. These

values were shown to be in good agreement with the G_{max} values obtained from the cone penetration test (CPT) using empirical correlations.

- A procedure for analyzing the first time loading response of the pressuremeter has been developed by Manassero (1989). His method was applied to the finite element generated pressuremeter response for plane strain conditions with the outer boundary at infinity. An excellent agreement was obtained between the stress-strain and volume changes, predicted by Manassero's method, and computed by the modified SMP model.

- Soil parameters for use in the modified SMP model can be determined from pressuremeter test data using Manassero's method provided that: (i) elastic parameters for the model are estimated first from the unloading response of the pressuremeter using the proposed $G^*/G_{max,o}$ chart; and (ii) that Manassero's method is expanded to take into account the intermediate principal stress, σ_2.

- From a practical point of view (i.e. to interpret in situ self-boring pressuremeter tests) the method proposed by Manassero needs further validation to assess the influence of initial disturbance that might occur at the beginning of these tests.

8.2.3 Evaluation of Soil Parameters from Laboratory and In Situ Testing

The stress-strain parameters for Erksak 320/1 sand used in the analysis of the Molikpaq structure at the Amauligak I-65 site were evaluated following the procedures described in Chapter 6.

The soil parameters were estimated on the basis of both in situ test and laboratory data. The in situ test data consisted of cone penetration test (CPT) data, self-boring pressuremeter (SBP) data, and direct shear measurements of shear wave velocity. The laboratory data used in the assessment consisted of monotonic drained triaxial tests.

The following three types of soil parameters were evaluated from the above data:

a) Moduli. These were subdivided as (1) repeated loading moduli, and, (2) first time loading moduli.

b) Failure Parameters.

c) Liquefaction resistance curves.

8.2.3.1 Summary of the Procedures Followed to Evaluate the Moduli Used in the Analysis

One of the key parameters used in the procedures to define the different soil types and moduli used in the analysis was the in situ void ratio, e_c. This parameter was evaluated from the in situ state parameter, ψ, which was obtained from the CPT cone bearing, q_c, following the procedures developed by Been et al. (1986). Soil moduli such as the Young's modulus, E, the shear modulus, G, and bulk modulus, B, and the plastic shear parameter, G_p, are highly dependent on the consolidated void ratio, e_c. Therefore once the in situ void ratio, e_c was known, the in situ moduli and G_p could be estimated by combining the in situ void ratio, e_c, with the existing laboratory data.

Another key parameter used in the analysis was the in situ maximum shear modulus, G_{max}. This modulus was determined in Chapter 6 from empirical correlations between G_{max} and void ratio (Hardin and Drnevich, 1972), G_{max} and cone bearing q_c (Robertson and Campanella, 1984), and G_{max} and $K_{2_{max}}$ (Seed and Idriss, 1970). The unloading SBP data obtained at the Amauligak I-65 site was also used to evaluate G_{max} using the G^*/G_{max} chart developed in Chapter 5. In addition the G_{max} values determined by Golder Associates (1986,1987) at the TARSIUT I-45 site from SBP tests and shear

wave velocities measurements were also used to assess the in situ maximum shear modulus, G_{max}. The various method gave rise to considerable scatter obtained in the plot of G_{max} versus depth, and an average G_{max} was used in the analysis.

8.2.3.2 Summary of the Procedures Followed to Evaluate the Failure Parameters Used in the Analysis

To evaluate the failure parameters ϕ_1 and $\Delta\phi$, the relationship between failure friction angle, ϕ_F, and state parameter, ψ, developed by Golder Associates (1986) was used together with the corresponding in situ effective mean normal stress, σ'_m, and the procedures developed by Duncan et al., (1980). The failure parameters $(\tau_{SMP}/\sigma_{SMP})_1$ and $\Delta(\tau_{SMP}/\sigma_{SMP})$ were evaluated in turn from the ϕ_1 and $\Delta\phi$ parameters through linear relationships developed based on laboratory data.

8.2.3.3 Summary of the Procedures Followed to Evaluate the Liquefaction Resistance Curves or Erksak 320/1 Sand

The liquefaction resistance curves for Erksak 320/1 sand were evaluated based on the cone penetration resistance, q_c, of this sand fills and the chart developed by Seed and DeAlba (1986). This chart shows the relationship between the modified cone tip resistance, $(q_c)_1$, and the cyclic stress ratio, τ_{eq}/σ'_{vo}, causing liquefaction. This chart is valid for earthquakes of magnitude 7.5 or 15 significant cycles of loading. Because during the April 12, 1986 ice load event the Molikpaq was subject to a substantially larger number of cycles than 15, it was necessary to develop a relationship between the shear stress, τ_N, to cause liquefaction in N cycles, and τ_{15}, which caused liquefaction in 15 cycles. Such a correlation was developed by Been (1988) based on both published data and data obtained by Golder Associates (1984).

Because test data was not available to determine the possible increase in liquefaction resistance of the sand core of the Molikpaq due to: (a) initial effects of the static bias developed by the ice loading; (b) past history of cyclic loading; and (c) drainage conditions developed by the water pumps, the liquefaction resistance curves used in the analysis did not consider the above factors and therefore represent a lower bound to liquefaction resistance.

8.3 Interface Elements

To model the contact between the Molikpaq steel structure and its sand fills, an interface element following the concept of Desai's "thin" element was developed and implemented into F.E. formulation (Chapter 4). Both formulations include the implementation of load shedding techniques for interface elements that failed in tension or shear. Procedures to evaluate soil parameters for use with the "thin" element were also developed and follow those developed by Clough and Duncan (1971) combined with the procedures recommended by Desai.

The performance of the "thin" element was assessed by comparing its F.E. results with the closed form solutions of a soil-pipe system developed by Burns and Richards (1964). The F.E. results show that an excellent agreement with the closed form solutions was obtained when the "thin" element is used in both the 2-D and 3-D F.E. analysis.

In addition, both the "thin" element and the "standard" soil element (using the hyperbolic and modified SMP models) predictions were compared with earth pressure measurements on a 10 m retaining wall field test. These F.E. studies were necessary to check the procedures followed in the construction analyses of the Molikpaq, since there were no earth pressure measurements during the core construction phase of this structure.

From the comparisons between the field measurements and the F.E. predictions the following conclusions are made:

- All the combination of element types and constitutive model types give results that are in fair agreement with the field measurements for both the at-rest condition and active condition.

- The field measurements carried out by Matsuo et al. (1978) and the F.E. predictions carried out by the writer, are in good agreement with the results of tests performed by Terzaghi (1934) and with the analytical work carried out by Clough and Duncan (1971). The field measurements show that the coefficient of earth pressure at rest, K_0 varies from a maximum K_0 = .74 at 1.0 m depth to a minimum K_0 = .28 at 5.0 m depth. If the wall is allowed to rotate away from the backfill than the coefficient of earth pressure, K decrases considerably to an average $(IK)_{av}$ = .11 which corresponds to a movement of the top of the wall of 8.4 cm or .84% of the wall height.

- From this particular case study it seems that the need for a "thin" interface type of element is not completely justified if "standard" solid elements with stress-strain models, such as the hyperbolic model (Duncan et al., 1980), or the modified SMP model, both expanded with load shedding capabilities, are used in the analysis.

8.4 Summary of the Analysis Procedure and the Results Obtained from the Analysis

The following 3-D assessments of the Molikpaq response to different load conditions were carried out by:

- Static assessment during the construction phase of the berm and core;

- Static assessment during the ice loading phase of the event of March 25, 1986;
- Pseudo-static assessment during the high ice loading phases of the event of April 12, 1986;
- Static assessment of the settlement phase after the ice loading event of April 12, 1986.

The above 3-D analyses were carried out using the hyperbolic model because the 3-D formulation of the modified SMP model, could not be used since the required computer memory exceeded the existing UBC computer capacity of 1 megaword.

To study the influence on the results of some key parameters (interface element type, constitutive law, stress redistribution) several 2-D analyses were carried out using both the hyperbolic and the modified SMP models.

A summary of the procedures followed in the analysis carried out and of the results obtained is presented next.

a) Construction Phase of the Berm and Core

The construction of the berm and core was simulated in the 3-D analysis by placing the fill in one single layer. Although the ideal approach is to "analytically construct" the fill in layers, that procedure was not followed due to the large band width of the system of equations. The stresses so obtained were compared with the stresses obtained from 2-D plane strain construction analysis where the sand fills were built in 7 layers. It was found that the stresses obtained from both 2-D and 3-D analyses were in reasonable agreement.

b) 3-D Analysis of the Static Ice Load Event of March 25, 1986

Prior to the dynamic ice load event of April 12, 1986, the Molikpaq structure was subject to several other ice load events. Because the event of March 25, 1986 was the best documented ice event, several 3-D analyses were carried out to predict the available field measurements and therefore calibrate the soil-structure parameters for use subsequently in the 3-D analysis of the dynamic ice load event of April 12, 1986. From the comparisons between the F.E. predictions and measurements, the following is concluded:

- The 3-D deflected shape of the caisson is adequately modelled by the analysis except for the NE corner, where the results indicate movements in the opposite direction from the measurements.
- The measured deformation profile, by the in-place inclinometer, in the core and berm is well modelled by the analysis and both show a remarkable difference between the shear behaviour of the core and the shear behaviour of the berm.

c) 3-D Analysis of the Dynamic Ice Load Event of April 12, 1986

On April 12, 1986 the Molikpaq structure was subject to severe dynamic ice loads. To analyse this event a 3-D finite element dynamic computer program with an appropriate stress-strain law is required. To date, however, such a program does not exist.

Adequate 2-D finite element dynamic computer programs do exist, such as the program RICEL developed by Yogendrakumar and Finn (1987). This program was used in 2-D dynamic and pseudo-dynamic analysis of the Molikpaq's response to the above ice load event by Finn et al. (1988), who showed that the Molikpaq's system damping was very large and consequently

no significant dynamic amplifications developed. Hence, the response of the structure can be studied from pseudo-dynamic or pseudo-static analysis which do not consider inertia forces.

Based on the above, the 3-D dynamic response of the caisson to a series of cyclic ice loading pulses was determined by computing the static response to one-half cycle of load/unload. The amplitude of displacement and the cyclic stress ratios so computed were assumed to be the dynamic values corresponding to a dynamic amplification factor of 1.

The 3-D analysis of the response of the Molikpaq to the ice loading event of April 12, 1986 were subdivided in Chapter 7 into four separate assessments: liquefaction, porewater pressure rise, accelerations, and settlement.

- The liquefaction assessment was carried out by comparing the cyclic stress ratio, $\Delta\tau_{zx}/\sigma'_{vo}$, correspondent to one-half cycle of load/unload, mobilized in each soil element, with the cyclic resistance ratio, τ_{av}/σ'_{vo}. These comparisons were carried out at different stages of loading (i.e. for different numbers of cycles) and the liquefaction assessment updated until the end of the ice loading.
- The pore pressure rise assessment was carried out following the pore pressure model developed by Seed et al. (1976).
- The acceleration assessment was carried out assuming that the response of the Molikpaq structure to cyclic loading was harmonic.
- The settlement assessment was carried out based on the work developed by Tokimatsu and Seed (1987) and Byrne (1990).

From the comparisons between the F.E. predictions and the measured data at the Amauligak I-65 site the following is concluded.

- The liquefaction assessments from the 3-D analysis indicate that the computed liquefaction areal extent is in good agreement with the field liquefaction assessment based on porewater measurements and settlement observations.

- Both the trend and the magnitude of the predictions of settlement agree quite well with the field observations.

- The residual displacement profile measured by the inplace inclinometer located adjacent to the west wall of the caisson was underestimated by the F.E. predictions. This could be associated with the fact that a Poisson's ratio value of $\nu = 0.0$ was used in the analysis of settlement.

- The maximum residual excess porewater pressures computed from the analysis for the locations of the piezometers E_1 and E_2 (adjacent to the loaded wall) are in good agreement with the field measurements, which indicate that liquefaction was developed at these two locations. However the results indicate that the prediction of the time to liquefaction, at the location of piezometer E_1, is not correct. This could be due to the fact that the liquefaction resistance curves used in the analysis do not take into account the effects of the initial static bias, drainage, and previous dynamic ice loading events at the site. In addition, the analyses were carried out using an idealized ice loading function which is somewhat different from the actual ice loading of April 12, 1986.

- The results also indicate that the predictions of the residual porewater pressure for the location of piezometer E_3 is substantially higher than the maximum measured value. This can also be explained by the above considerations.

• The predictions of the accelerations measured at the centre of the top of the core by the accelerometer ACC-841 underestimate the field measurements during the initial phase, but agree quite well with both the maximum acceleration value recorded and the time of its occurrence. On the other hand the predictions of the accelerations measured at the top of the loaded wall by the accelerometer TM-706 agree quite well with the field measurements during the initial phase but both the maximum acceleration recorded and its time of occurrence are not well predicted by the analysis. These differences are not unexpected because the computed values of the accelerations were based on the assumption that the response of the Molikpaq to cyclic loading was harmonic which is an extremely crude assumption. In addition an idealized loading function was used in the analysis.

• The results obtained from the several 2-D analysis, which considered different types of interface elements ("thin" and "standard" elements) and constitutive models (modified SMP and hyperbolic models) indicate that the computed liquefaction areal extent is practically insensitive to the above parameters and in good agreement with both the 3-D analysis and field observations.

Based on the above, it is concluded that both the procedures followed to obtain soil parameters from laboratory and in situ testing and the procedures followed in the analysis have been validated.

REFERENCES

CHAPTER 1

Bellotti, R., Ghionna, V., Jamiolkowswki, M., Robertson, P.K. and Petterson, R.W. (1989) "Interpretation of Moduli from Self-Boring Pressuremeter Tests in Sand", Geotechnique, Vol. 39, No. 2, 269-292.

Bruce, J. and Harrington, A.G. (1982) "Design Aspects of a Mobile Artic Caisson", Proc. 14th Annual Offshore Technology Conf., OTC 4333, Houston.

Byrne, P.M. and Eldridge, T.L. (1982) "A Three Parameter Dilatant Elastic Stress-Strain Model for Sand", Int. Symposium on Numerical Models in Geomechanics, Switzerland, pp. 73-79.

Desai, C.S., Zaman, M.M., Lightner, J.G. and Siriwardane, H.J. (1984) "Thin-Layer Element for Interfaces and Joints", Int. Journal for Numerical and Analytical Methods in Geomechanics, Vol. 8, pp. 19-43.

Finn, W.D., Anderson, D.L., Byrne, P.M. and Stuckert, B. (1988) "Analysis of the Response of Molikpaq to the Ice Loading Event of April 12, 1986", Department of Civil Engineering, University of British Columbia, Vancouver, B.C.

Fitzpatrick, J. and Stenning, D.G. (1983) "Design and Construction of Tarsiut Island in the Canadian Beaufort Sea", Proc. 15th Annual Offshore Technology Conf., OTC 4517, Houston, Vol. 2, pp. 51-60.

Jefferies, M.G., Stewart, H.R., Thomson, R.A.A. and Rogers, B.T. (1985) "Molikpaq Deployment at Tarsiut P-45", Proc. ASCE Spec. Conf. on Artic Offshore, San Francisco.

Jefferies, M.G. and Wright, W.H. (1988) "Dynamic Response of Molikpaq to Ice-Structure Interaction", Proc. 7th Int. Conf. on Offshore Mechanics and Artic Engineering.

Jefferies, M.G., Rogers, B.T., Stewart, H.R., Shinde, S., James, D. and Williams-Fitzpatrick, S. (1988) "Island Construction in the Canadian Beaufort Sea". Proc. Conf. on Hydraulic Fill Structures, ASCE, Fort Collins, Colorado.

Manassero, M. (1989) "Stress-Strain Relationship for Drained Self-Boring Pressuremeter Tests in Sand", Geotechnique, Vol. 39, No. 2, 293-307.

Matsuoka, H. (1983) "Deformation and Strength of Granular Materials Based on the Theory of 'Compounded Mobilized Plane' (CMP) and 'Spatial Mobilized Plane' (SMP)", Advances in the Mechanics and the Flow of Granular Materials, Vol. II, Trans Tech Publications.

Matsuoka, H. (1974) "Stress-Strain Relationships of Sands Based on the Mobilized Plane", Soils and Foundations, Vol. 14, No. 2.

McCreath, D.R., Hodge, W.E. and Harrington, A.G. (1982) "Geotechnical Design Considerations for the Gulf Mobile Artic Caisson", 2nd Canadian Conference on Marine Geotechnical Engineering, Halifax.

Seed, H.B. and De Alba (1986) "Use of SPT and CPT Tests for Evaluating the Liquefaction Resistance of Sands", Proc. In Situ 86, ASCE Specialty Conf. on "Use of In Situ Tests in Geotechnical Engineering", Blacksburg, Virginia.

Stewart, H.R. and Brakel, J. (1986) "Molikpaq Berm Construction at Amauligak I-65", World Dredging Conference, Brighton, U.K.

Yogendrakumar, M. and Finn, W.D. (1987) "RICEL: Program for Determining Response to Ice Loading of Offshore Structures", Department of Civil Engineering, University of British Columbia, Vancouver, B.C.

REFERENCES

CHAPTER 2

Arthur, J.R.F., Dunstan, T., Al-Ani, Q.J.L. and Assadi, A. (1977) "Plastic Deformation and Failure in Granular Media", Geotechnique 27, No. 1, pp. 53-74.

Bathe, K.J., Wilson, E.L. an Iding, R.H. (1974) "A Structural Analyis Program for Static and Dynamic Response of Nonlinear Systems", Report No. UC SESM 74-3, Structural Engineering Laboratory, University of California, Berkeley, California.

Bishop, A.W. (1966) "The Strength of Soils as Engineering Materials", Geotechnique 16, No. 2, pp. 91-130.

Byrne, P.M. and Janzen, W. (1984) "INCOIL: A Computer Program for Nonlinear Analysis of Stress and Deformations in Oil Sand Masses", Soil Mechanics Series No. 80, Dept. of Civil Engineering, University of British Columbia, Vancouver.

Byrne, P.M. and Eldridge, T.L. (1982) "A Three Parameter Dilatant Elastic Stress-Strain Model for Sand", Int. Symposium on Numerical Models in Geomechanics, Switzerland, pp. 73-79.

Duncan, J.M. and Chang, C.-Y. (1970) "Nonlinear Analysis of Stress and Strain in Soils", Journal of the Soil Mechanics and Foundations Division, ASCE, Vol. 96, No. SM5, September 1970, pp. 1629-1653.

Duncan, J.M., Byrne, P.M., Wong, K.S. and Mabry, P. (1980) "Strength, Stress-Strain and Bulk Modulus Parameters for Finite-Element Analysis of Stresses and Movements in Soil Masses", Report No. UCB/GT/80-01, Dept. of Civil Engineering, University of California, Berkeley, California.

Kondner, R.L. (1963) "Hyperbolic Stress-Strain Response: Cohesive Soils", Journal of the Soil Mechanics and Foundation Division, ASCE, Vol. 89, No. SM1, pp. 115-143.

Kondner, R.L. and Zelasko, J.S. (1963) "A Hyperbolic Stress-Strain Formulation of Sands", Proc. of the 2nd Pan American Conference on Soil Mechanics and Foundation Engineering, Vol. 1, Brasil, p. 289.

Lade, P.V. (1972) "The Stress-Strain and Strength Characteristics of Cohesionless Soils", Ph.D. Thesis, University of California, Berkeley.

Lade, P.V. and Duncan, J.M. (1975) "Elastoplastic Stress-Strain Theory for Cohesionless Soil", Proc. ASCE, Vol. 101, No. GT10, pp. 1037-1053.

Matsuoka, H. (1974) "Stress Strain Relationships of Sands Based on the Mobilized Plane", Soil and Found., Vol. 14, No. 2, 47-61.

Matsuoka, H. and Nakai, T. (1974) "Stress-Deformation and Strength Characteristics of Soil Under Three Different Principal Stresses", Proc. JSCE, No. 232, 59-70.

Matsuoka, H. and Nakai, T. (1985) "Relationship Among Tresca, Mises, Mohr-Coulomb an Matsuoka-Nakai Failure Criteria", Soil and Found., Vol. 25, No. 4, 123-128.

Matsuoka, H. (1983) "Deformation and Strength of Granular Materials Based on the Theory of 'Compounded Mobilized Plane' (CMP) and 'Spatial Mobilized Plane' (SMP)", Advances in the Mech. and the Flow of Granular Materials, Trans. Tech. Publications, 813-836.

Matsuoka, H. and Sakakibara, K. (1987) "A Constitutive Model for Sands and Clays Evaluating Principal Stress Rotation", Soils and Foundations, Vol. 27, No. 4, pp. 73-88.

Murayama, S. (1964) "A Theoretical Consideration on a Behaviour of Sand", Proc. IUTAM, Symposium on Rheology and Soil Mechanics, Grenoble, pp. 146-159.

Murayama, S. and Matsuoka, H. (1973) "A Microscopic Study on Shearing Mechanism of Soils", Proc. 8th Int. Conf. SMFE, Vol 1, Part 2, 293-298.

Roscoe, K.H. (1970) "The Influence of Strains in Soil Mechanics", Tenth Rankine Lecture, Géotechnique 20, No. 2, pp. 129-170.

Rowe, P.W. (1962) "The Stress-Dilatancy Relation for Static Equilibrium of an Assembly of Particles in Contact", Proc. Royal Society, Series A, London, Vol. 269, pp. 500-527.

Rowe, P.W. (1971) "Theoretical Meaning and Observed Values of Deformation Parameters for Soil, Stress-Strain Behaviour of Soils", Proc., Roscoe Memorial Symposium, Cambridge University, pp. 143-194.

Saada, A. and Bianchani, G.S. (1987) Proc. of International Workshop on "Constitutive Equations for Granular Noncohesive Soils", Case Western Reserve University, Cleveland, Ohio (published by Balkema).

Sayao, A.S.F.J. (1989) "Behaviour of Sand Under General Stress Paths in the Hollow Cylinder Torsional Device", Ph.D. Thesis, University of British Columbia, Vancouver, B.C.

Stroud, M.A. (1971) "The Behaviour of Sand at Low Stress Levels in the Simple Shear Apparatus", Ph.D. Thesis, Cambridge University.

Symes, M.J., Hight, D.W. and Gens, A. (1982) "Investigating Anisotropy and the Effects of Principal Stress Rotation and of the Intermediate Principal Stress Using a Hollow Cylinder Apparatus", IUTAM Conf. on Deformation and Failure of Granular Materials.

Symes, M.J., Gens, A. and Hight, D.W. (1984) "Undrained Anisotropy and Principal Stress Rotation in Saturated Sand", Geotechnique 34, No. 1, pp. 11-27.

Symes, M.J. and Hight, D.W. (1988) "Drained Principal Stress Rotation in Saturated Sand", Geotechnique 38, No. 1, pp. 59-81.

Vaid, Y.P., Byrne, P.M. and Hughes, J.M.O. (1981) "Dilation Angle and Liquefaction Potential", Int. Conf. on Recent Avances in Geot. Earthquake Engineering and Soil Dynamics, St. Louis, pp. 161-166.

Wood, D.M., Drescher, A. and Budhu, M. (1979) "On the Determination of Stress State in the Simple Shear Apparatus", Geotechnical Testing Journal, Vol. 2, No. 4.

Wroth, C.P. (1984) "The Interpretation of In Situ Soil Tests", Rankine Lecture, Imperial College, London, OUEL Report No. 1541/84. SM 051/84.

Yong, R.K. and Ko, H.Y. (1980), Proc. of the Workshop on "Limit Equilibrium, Plasticity, and Generalized Stress-strain in Geotechnical Engineering", McGill University, published by ASCE.

Zienkiewicz, O.C., Valliappan, S. an King, I.P. (1968) "Stress Analysis of Rock as a 'No Tension Material'", Geotechnique 18, pp. 56-66.

REFERENCES

CHAPTER 3

Andrawes, K.Z. (1964) "The Behaviour of Particulate Materials in the 'At Rest' State", M.Sc. Thesis, University of Manchester.

Bryne, P.M., Cheung, H. and Yan. L. (1987) "Soil Parameters for Deformation Analysis of Sand Masses", Can. Geot. J., Vol. 24, No. 3, pp. 366-376.

Byrne, P.M. and Eldridge, T.L. (1982) "A Three Parameter Dilatant Elastic Stress-Strain Model for Sand", Int. Symposium on Numerical Models in Geomechanics, Switzerland, pp. 73-79.

Carter, J.P. and Yeung, S.K. (1985) "Analysis of Cylindrical Cavity Expansion in a Strain Weakening Material", Research Report No. R505, The University of Sydney, Sydney, Australia.

Duncan, J.M., Byrne, P.M., Wong, K.S. and Mabry, P. (1980) "Strength, Stress-Strain and Bulk Modulus Parameters for Finite-Element Analysis of Stresses and Movements in Soil Masses", Report No. UCB/GT/80-01, Dept. of Civil Engineering, University of California, Berkeley, California.

Finn, W.D. Liam, and Vaid, Y.P. (1977) "Liquefaction Potential from Drained Constant Volume Cyclic Simple Shear Tests", Proceedings, 6th World Conference on Earthquake Engineering, New Delhi.

Jambu, N. (1963) "Soil Compressibility as Determined by Oedometer and Triaxial Tests", European Conference on Soil Mechanics and Foundation Engineering, Wissbaden, Germany, Vol. 1, pp. 19-25.

Kolbuszewski, J. (1965) "San Particles and Their Density", Lecture delivered at Materials Science Colub's Symp., London.

Matsuoka, H. (1983) "Deformation and Strength of Granular Materials Based on the Theory of 'Compounded Mobilized Plane' (CMP) and 'Spatial Mobilized Plane' (SMP)", Advances in the Mech. and the Flow of Granular Materials, Trans. Tech. Publications, 813-836.

Negussey, D. (1984) "An Experimental Study on the Small Strain Response of Sand", Ph.D. Thesis, University of British Columbia, Vancouver, B.C.

Roscoe, K.H. "An Apparatus for the Application of Simple Shear to Soil Samples", Proceedings, 3rd Int. Conf. on Soil Mechanics, Zurich, Vol. 1, pp. 186-191.

Stroud, M.A. (1971) "The Behaviour of Sand at Low Stress Levels in the Simple Shear Apparatus", Ph.D. Thesis, Cambridge University.

Vaid, Y.P., Byrne, P.M. and Hughes, J.M.O. (1981) "Dilation Angle and Liquefaction Potential", Int. Conf. on Recent Avances in Geot. Earthquake Engineering and Soil Dynamics, St. Louis, pp. 161-166.

Yong, R.K. and Ko, H.Y. (1980), Proc. of the Workshop on "Limit Equilibrium, Plasticity, and Generalized Stress-strain in Geotechnical Engineering", McGill University, published by ASCE.

REFERENCES

CHAPTER 4

Anderson, H.W. and J.S. Dodd (1966). "Finite Element Method Applied to Rock Mechanics", Proc. 1st Congress, Int. Soc. for Rock Mechanics, Lisbon, Portugal.

Burns, J.W. and Richards, R.M. (1964). Attenuation of Stresses for Buried Cylinders", Proc. Symposium on Soil-Structure Interaction, University of Arizona, Tucson, Arizona.

Byrne, P.M., Cheung, H. and Yan, L. (1987). "Soil Parameters for Deformation Analysis of Sand Masses", Can. Geot. J., Vol. 24, No. 3, pp. 366-376.

Byrne, P.M. and Janzen, W. (1984). "Incoil: A Computer Program for Nonlinear Analysis of Stress and Deformations in Oil Sand Masses", Soil Mechanics Series No. 80, Dept. of Civil Engineering, University of British Columbia.

Clough, W.G. and Duncan, J.M. (1971). "Finite Element Analysis of Retaining Wall", Journal of the Soil Mechanics and Foundations Division, ASCE, Vol. 97, SM12, pp. 1657.

Cook, R.D., Malkus, D.S. and Plesha, M.E. (1989). "Concepts and Applications of Finite Element Analysis". University of Wisconsin-Madison, Published by John Wiley & Sons, (3rd edition).

Desai, C.S. (1981) "Behaviour of Interfaces Between Structural and Geological Media", Proc. Int. Conf. on Recent Advances in Geotechnical Earthquake Engineering and Soil Dynamics, University of Missouri-Rolla, Rolla, Missouri.

Desai, C.S., Zaman, M.M., Lightner, J.G and Siriwardane, H.J. (1984). "Thin Layer Element for Interfaces and Joints", Int. Journal for Numerical and Analytical Methods in Geomechanics, Vol. 8, pp. 19-43.

Duncan, J.M., Byrne, P.M., Wong, K.S. and Mabry, P. (1980). "Strength, Stress-Strain and Bulk Modulus Parameters for Finite Element Analyses of Stresses and Movements in Soil Masses", Report No. UCB/GT/80-81, Department of Civil Engineering, University of California, Berkeley.

Duncan, J.M. and Chang, C.-Y. (1970). "Nonlinear Analysis of Stress and Strain in Soils", Journal of the Soil Mechanics and Foundations Division, ASCE, Vol. 96, No. SM5.

Goodman, R.E., Taylor, R.L. and Brekke, T.L. (1968) - "A Model for the Mechanics of Jointed Rock", J. Soil Mech. Found. Div., ASCE, 94, SM3.

Matsuo, M., Kenmochi, S. and Yagi, H. (1978). "Experimental Study on Earth Pressure of Retaining Wall by Field Tests", Soil and Foundations, Vol. 18, No. 3, pp. 27.

Nogo, D. and Scordelis, A.C. (1967). "Finite Element Analysis of Reinforced Concrete Beams", ACI Journal, 64.3.

Potyundy, J.G. (1961). "Skin Friction Between Various Soils and Construction Materials", Geotechnique, 11, 4, pp. 339.

Terzaghi, K. (1934). "Large Retaining Wall Tests. I. Pressure of Dry Sand", Engineering News Record, Vol. III, pp. 136-140.

Yoshimi, Y. and Kishida, T. (1981). "A Ring Torsion Apparatus for Evaluating Friction Between Soil and Metal Surfaces", Geotechnical Testing Journal, GTJODT, Vol. 4, No. 4, pp. 145.

REFERENCES

CHAPTER 5

Bolton, M.D. (1986). "The Strength and Dilatancy of Sands", Geotechnique 36, No. 1, pp. 65-78.

Bellotti, R., Ghionna, V., Jamiolkowski, M., Robertson, P.K. and Petterson, R.W. (1989). "Interpretation of Moduli from Self-Boring Pressuremeter Tests in Sand", Geotechnique, Vol. 39, No. 2, 269-292.

Byrne, P.M., Salgado, F.M. and Howie, J.A. (1990). "Relationship Between the Unload Shear Modulus from Pressuremeter Tests and the Maximum Shear Modulus for Sand", Proc. of the Third International Symposium on Pressuremeters, British Geotechnical Society, Oxford University.

Byrne, P.M., Cheung, H. and Yan, L. (1987). "Soil Parmeters for Deformation Analysis of Sand Masses", Can. Geot. J., Vol. 24, No. 3, 366-376.

Gibson, R.E. and Anderson, W.F. (1961) "In Situ Measurements of Soil Properties with the Pressuremeter", Civ. Eng. Pub. WKS Rev. 56, No. 658, May, 615-618.

Hardin, B.O. and Black, W.L. (1966) "Sand Stiffness Under Various Triaxial Stresses", J. Soil Mech. and Found. Div., ASCE, Vol. 92, No. SM2, 27-42.

Hardin, B.O. (1978) "The Nature of Stress-Strain Behaviour of Soils", Proc., ASCE, Geo. Eng. Div. Specialty Conf. Earth. Eng. and Soil Dyn., Pasadena, California, Vol. 1, 3-90.

Hughes, J.M.O., Wroth, C.P. and Windle, D. (1977) "Pressuremeter Tests in Sands", Geotechnique, Vol. XXVII, No. 4, 455.

Jewell, R.J., Fahey, M. and Wroth, C.P. (1980) "Laboratory Studies of the Pressuremeter Test in Sand", Geotechnique 30, No. 4, 507-531.

Knox, D.P. (1982) "Effect of State of Stress on Velocity of Low Amplitude Shear Wave Propagating Along Principal Stress Direction in Dry Sand", Ph.D. Thesis, Texas University.

Ladanyi, B. (1963) "Evaluation of Pressuremeter Tests in Granular Soils", 2nd Pan American Conf., Soil Mech. Found. Eng. 1, 3-20.

Lee, S.H.H. (1986) "Investigation on Low Amplitude Shear Wave Velocity in Anisotropic Materials", Ph.D. Thesis, Texas Universty.

Manassero, M. (1989) "Stress-Strain Relationship for Drained Self-Boring Pressuremeter Tests in Sands", Geotechnique 39, No. 2, 293-307.

Negussey, D. (1984) "An Experimental Study of the Small Strain Response of Sand", Ph.D. Thesis, University of British Columbia.

Robertson, P.K. (1982) "In Situ Testing of Soil with Emphasis on its Application to Liquefaction Assessment", Ph.D. Thesis, University of British Columbia.

Robertson, P.K. and Hughes, J.M.O. (1986) "Determination of Properties of Sand from Self-Boring pressuremeter Test", Proc. 2nd Int. Symp. on the Pressuremeter and its Marine Applications, Austin, Texas, American Society for Testing and Materials, 283-302.

Rowe, P.W. (1971) "Theoretical Meaning and Observed Values of Deformation Parameters for Soils, Stress-strain Behaviour of Soils", Proc. Roscoe Memorial Symp., Cambridge University, 143-194.

Stokoe, K.H. and Ni, F.H. (1985) "Effects of Stress State and Strain Amplitude on Shear Modulus of Dry Sand", Proc. 2nd Symp. Interaction of Non-nuclear Munitions with Structures, Panama City Beach, 407-412.

Stroud, M.A. (1971) "Sand at Low Stress Levels in the Simple Shear Apparatus", Ph.D. Thesis, University of Cambridge.

Vesic, A.S. (1972) "Expansion of Cavities in Infinite Soil Mass", J. Soil Mech. and Found. Div., ASCE, Vol. 98, No. SM3, 265-290.

Yan, L. and Byrne, P.M. (1989) "Simulation of Downhole and Crosshole Seismic Tests on Sand Using the Hydraulic Gradient Similitude Method", Soil Mech. Series No. 132, Dept. of Civil Engineering, University of British Columbia, Vancouver, Canada, October.

Yu, P. and Richart, F.E. (1984) "Stress Ratio Effects on Shear Modulus of Dry Sands", J. Geot. Eng., Vol. 110, No. 3, March, 331-345.

REFERENCES

CHAPTER 6

Been, K. and Jefferies, M.G. (1985). "A State Parmeter for Sands", Geotechnique 35, No. 2, 99-112.

Been, K., Jefferies, M.G., Crooks, J.H.A. and Rothenburg, L. (1987). "The Cone Penetration Test in Sands. Part 2: General Inference of State". Geotechnique 37, No. 3, 285-299.

Bjerrum, L. (1973). "Geotechnical Problems Involved in Foundations of Structures in the North Sea". Geotehcnique 23, No. 3, 319-358.

Byrne, P.M. and Eldridge, T.L. (1982). "A Three Parameter Dilatant Elastic Stress-Strain Model for Sand". International Symposium on Numerical Models in Geomechanics, Switzerland, 73-79.

Castro, G. (1969). "Liquefaction of Sand". Ph.D. Thesis, Division of Engineering and Applied Physics, Harvard University.

Duncan, J.M., Byrne, P.M., Wong, K.S. and Mabry, P. (1980). "Strength, Stress-Strain and Bulk Modulus Parameters for Finite Element Analysis of Stresses and Movemnets in Soil Masses". Report No. UCB/GT/80-81, Department of Civil Engineering, University of California, Berkeley, California.

Finn, W.D. Liam, Bransby, P.L., and Pickering, D.J. (1970). "Effect of Strain History on Liquefaction of Sand". Journal of the Soil Mechanics and Foundations Division, ASCE, Vol. 96, No. SM6, 1917-1934.

Garga, V.K. and McKay, L.D. (1984). "Cyclic Triaxial Strength of Mine Tailings". Journal of Geotechnical Engineering Division, ASCE, Vol. 110, GT8, 1091-1105.

Golder Associates (1986a). "Laboratory Testing on Sand Samples from Molikpaq Core at Amauligak I-65 Delineation Well". Report submitted to Gulf Canada Resources Ltd.

Golder Associates (1986b). "Fig. 4.23 in Contract Briefing Document. Supplied by Atlantic Geoscience Centre.

Golder Associates (1987). "Laboratory Testing of Molikpaq Core Sand Under Repated Loading". Report submitted to Gulf Canada Resources Ltd.

Hardin, B.O. and Drenvich, V.P. (1972). "Shear Modulus and Damping in Soils: Design Equations and Curves". Journal of the Soil Mechanics and Foundations Division, ASCE, Vol. 98, No. SM7, 667-692.

Jefferies M.G. and Livinstone, W.R. (1985). "Molikpaq at Amauligak I-65 Post-Construction Assessment", Gulf Canada Resources Ltd., Frontier Development Division.

Jefferies, M.G., Stewart, H.R., Thomson, R..A. and Rogers, B.T. (1985). "Molikpaq Deployment at Tarsiut P-45". Proc. ASCE Spec. Conf. on Artic Offshore, San Francisco.

Jefferies, M.G. and Wright, W.H. (1988). "Dynamic Response of 'Molikpaq' to Ice-Structure Interaction". Proceedings of the 7th International Conference on Offshore Mechanics and Arctic Engineering.

Jefferies, M.G., Rogers, B.T., Stewart, H.R., Shinde, S., James, D. and Williams-Fitzpatrick, S. (1988). "Island Construction in the Canadian Beaufort Sea". Proc. Conf. on Hydraulic Fill Structures, ASCE, Fort Collins Colorado.

Liao, S.S.C. and Whittman, R.V. (1986). "Overburden Correction Factors for SPT in Sand". Journal of Geotechnical Engineering, ASCE, Vol. 112, No. 3, 373-377.

MacKay, J.R. (1972). "Offshore Permafrost and Ground Ice, Southern Beaufort Sea, Canada". Canadian Journal of Earth Sciences, Vol. 9, No. 11, pp. 1550.

Negussey, D. (1987). Private Communication.

Robertson, P.K. and Campanella, R.G. (1983). "Interpretation of Cone Penetration Tests - Part I (Sand)". Canadian Geotechnical Journal, Vol. 20, No. 4.

Seed, H.B. and Lee, K.L. (1966). "Liquefaction of Saturated Sands During Cyclic Loading". Journal of the Soil Mechanics and Foundations Division, ASCE, Vol. 92, No. SM6, 105-134.

Seed, H.B. and Idriss, I.M. (1970). "Soil Moduli and Damping Factors for Dynamic Response Analyses". Report No. EERC 70-10, Earthquake Engineering Research Center, University of California, Berkeley, California.

Seed, H.B., Martin, P.P. and Lysmer, J. (1976). "Pore-water Pressure Changes During Soil Liquefaction". Journal of Geotechnical Eng. Div., ASCE, Vol. 102, GT34, 323-346.

Seed, H.B. (1979). "Soil Liquefaction and Cyclic Mobility Evaluation for Level Ground During Earthquake". Journal of the Soil Mechanics and Foundations Division, ASCE, Vol. 105, Nol. GT2, 201-255.

Seed, H.B., Idriss, I.M. and Arango, I. (1983). "Evaluation of Liquefaction Potential Using Field Performance Data". Journal of Geotechnical Engineering Division, ASCE, Vol. 109, No. 3, 458-482.

Seed, H.B. and De Alba, P. (1986). "Use of SPT and CPT Tests for Evaluating the Liquefaction Resistance of Sands". Proceedings, In Situ 86, ASCE Specialty Conference on 'Use of In Situ Tests in Geotechnical Engineering', Blacksburg, Virginia.

Seed, R.B. and Lee, S.R. (1988). "Penetration and Liquefaction Resistances: Prior Seismic History Effects". Journal of Geotechnical Engineering, ASCE, Vol. 114, No. 6, 691-697.

Shibata, T., Yukitomo, H. and Miyoshi, M. (1972). "Liquefaction Process of Sand During Cyclic Loading". Soil and Foundations, Vol. 12, No. 1, 1-16.

Tokimatsu, K.A.M. and Seed, H.B. (1987). "Evaluation of Settlement in Sands Due to Earthquake Shaking". Journal of Geotechnical Engineering, ASCE, Vol. 113, No. 8, 861-878.

Thurber Consultants Ltd. (1985). "Self-Boring Pressuremeter Testing of Molikpaq Sand Core at Amauligak I-65". Report submitted to Gulf Canada Resources Ltd.

Vaid, Y.P. and Chern, J.C. (1983). "Effect of Static Shear on Resistance to Liquefaction". Soil and Foundations, Vol. 23, No. 1, 47-60.

Vaid, Y.P. and Finn, W.D. Liam (1979). "Static Shear on Liquefaction Potential". Journal of the Geotechnical Engineering Division, ASCE, Vol. 105, GT10, 1233-1248.

REFERENCES

CHAPTER 7

Byrne, P.M. (1990). "Volume Change and Pore Pressure Rise in Sands Due to Cyclic Loading". Soil Mechanics Series No. __, Dept. of Civil Engineering, University of British Columbia, Vancouver.

Byrne, P.M. and Janzen, W. (1984). "INCOIL: A Computer Program for Nonlinear Analysis of Stress and Deformations in Oil Sand Masses". Soil Mechanics Series No. 80, Dept. of Civil Engineering, University of British Columbia, Vancouver.

Duncan, J.M., Byrne, P.M., Wong, K.S. and Mabry, P. (1980). "Strength, Stress-Strain and Bulk Modulus Parameters for Finite-Element Analysis of Stresses and Movements in Soil Masses", Report No. UCB/GT/80-01, Dept. of Civil Engineering, University of California, Berkeley, California.

Jefferies, M.G. (1987). Private Communication.

Jefferies, M.G. and Wright, W.H. (1988). "Dynamic Response of 'Molikpaq' to Ice-Structure Interaction". Proceedings of the 7th International Conference on Offshore Mechanics and Arctic Engineering.

Kulhawy, F.H., Duncan, J.M. and Seed, R.B. (1969). "Finite Element Analysis of Stresses and Movements in Embankments During Construction", Geotechnical Engineering Research Report No. TE-69-4, Department of Civil Engineering, University of California, Berkeley, November 1969.

Seed, H.B. and DeAlba, P. (1986). "Use of SPT and CPT Tests for Evaluating the Liquefaction Resistance of Sands". Proceedings, In Situ 86, ASCE Specialty Conference on "Use of In Situ Tests in Geotechnical Engineering", Blacksburg, Virginia.

Seed, H.B. and Idriss, I.M. (1982). "Ground Motions and Soil Liquefaction During Earthquakes". Earthquake Engineering Research Institute, Berkeley, California.

Seed, H.B., Martin, P.P. and Lysmer, J. (1976). "Porewater Pressure Changes During Soil Liquefaction". Journal of Geotechnical Engineering Division, ASCE, Vol. 102, GT4, 323-346.

Seed, H.B., Seed, R.B., Harder, L.F. and Jong, H.L. (1988). "Re-evaluation of the Slide in the Lower San Fernando Dam in the Earthquake of February 9, 1971". Report No. UCB/EERC-88-04, Earthquake Engineering Research Center, University of California, Berkeley, California.

Tokimatsu, K.A.M. and Seed, H.B. (1987). "Evaluation of Settlement in Sands Due to Earthquake Shaking". Journal of Geotechnical Engineering, ASCE, Vol. 113, No. 8. 861-878.

CHAPTER 2

APPENDIX INDEX

2.1 Evaluation of the friction angle ϕ_{13} for b-values varying from 0.0 to 1.0.

2.2 Relationship between principal stresses and, the normal and shear stress on the SMP. Extrapolation of these relationships to the increments of plastic strain space.

2.3 Fundamental relationship between cartesian stresses and principal stresses. Extrapolation of these relations to the increments of plastic strain space.

2.4 Development of $\Delta(\tau_{smp}/\sigma_{smp})$ in terms of $\Delta\sigma_1$, $\Delta\sigma_2$, $\Delta\sigma_3$.

2.5 Relations between increments of principal stress and increments of cartesian stress in the 3-Dimensional stress space

2.6 Evaluation of the plastic constitutive matrix $\{C^p\}$ of the SMP model.

- 2.6.1 3-Dimensional
- 2.6.2 2-Dimensional
- 2.6.3 Axisymmetric

2.7 Load shedding formulation to use with the modified SMP model.

2.8 Discussion of the assumptions regarding the direction of the increments of principal strain, based on data derived from hollow cylinder tests.

CHAPTER 2

APPENDIX FIGURES INDEX

APPENDIX 2 - LIST OF FIGURES (Cont'd)

APPENDIX 2.1

EVALUATION OF FRICTION ANGLE ϕ_{13} FOR VARYING b-VALUES

APPENDIX 2.1

Evaluation of Friction Angle ϕ_{13} for Varying b-Values

Matsuoka-Nakai failure criterion is expressed by the following equation (see main text eq. (2.29),

$$\frac{\tau_{SMP}}{\sigma_{SMP}} = \frac{2}{3}\left(\tan^2\phi_{m12} + \tan^2\phi_{m23} + \tan^2\phi_{m13}\right)^{1/2} \qquad (2.1.1)$$

This equation can also be written as:

$$\frac{\tau_{SMP}}{\sigma_{SMP}} = \frac{2}{3}\left(\frac{(\sin\phi_{m12})^2}{(\cos\phi_{m12})^2} + \frac{(\sin\phi_{m23})^2}{(\cos\phi_{m23})^2} + \frac{(\sin\phi_{m13})^2}{(\cos\phi_{m13})^2}\right)^{1/2} \qquad (2.1.2)$$

since

$$(\sin\phi_{m12})^2 = \left(\frac{\sigma_1-\sigma_2}{\sigma_1+\sigma_2}\right)^2$$

and

$$(\cos\phi_{m12})^2 = 1 - (\sin\phi_{m12})^2$$

then

$$(\cos\phi_{m12})^2 = \frac{(\sigma_1+\sigma_2)^2 - (\sigma_1-\sigma_2)^2}{(\sigma_1+\sigma_2)^2}$$

or

$$(\cos\phi_{m12})^2 = \frac{4\sigma_1\sigma_2}{(\sigma_1+\sigma_2)^2}$$

therefore

$$\left(\frac{\sin\phi_{m12}}{\cos\phi_{m12}}\right)^2 = \frac{(\sigma_1-\sigma_2)^2}{4\sigma_1\sigma_2} \tag{2.1.3}$$

and

$$\left(\frac{\sin\phi_{m23}}{\cos\phi_{m23}}\right)^2 = \frac{(\sigma_2-\sigma_3)^2}{4\sigma_2\sigma_3} \tag{2.1.4}$$

and

$$\left(\frac{\sin\phi_{m13}}{\cos\phi_{m13}}\right)^2 = \frac{(\sigma_1-\sigma_3)^2}{4\sigma_1\sigma_3} \tag{2.1.5}$$

Substituting eqs. (2.1.3) to (2.1.4) into eq. (2.1.2) the following eqution is obtained

$$\frac{\tau_{SMP}}{\sigma_{SMP}} = \frac{2}{3}\left(\frac{(\sigma_1-\sigma_2)^2}{4\sigma_1\sigma_2} + \frac{(\sigma_2-\sigma_3)^2}{4\sigma_2\sigma_3} + \frac{(\sigma_1-\sigma_3)^2}{4\sigma_1\sigma_3}\right)^{1/2} \tag{2.1.6}$$

In order to perform a study of the influence of the b-value on the value of the friction angle ϕ the above eq. (2.1.6) will be expressed as a function of the following quantities:

$$b = \frac{\sigma_2-\sigma_3}{\sigma_1-\sigma_3} \tag{2.1.7}$$

and

$$a = \frac{\sigma_1-\sigma_3}{\sigma_1+\sigma_3} \tag{2.1.8}$$

from (2.1.7)

$$\sigma_2 = b(\sigma_1-\sigma_3) + \sigma_3 \tag{2.1.9}$$

substituting eq. (2.1.9) into eq. (2.1.6) the following is obtained:

$$\frac{\tau_{SMP}}{\sigma_{SMP}} = \frac{2}{3}\left(\frac{(\sigma_1-\sigma_3)^2}{4\sigma_1\sigma_3} + \frac{b^2(\sigma_1-\sigma_3)^2}{4(b\sigma_1\sigma_3+\sigma_3^2-b\sigma_3)^2} + \frac{(1-b)^2(\sigma_1-\sigma_3)^2}{4(b\sigma_1^2+\sigma_1\sigma_3-b\sigma_1\sigma_3)}\right)^{1/2}$$

$$= \frac{2}{3}\left(\frac{(\sigma_1-\sigma_3)^2}{4\sigma_1\sigma_3}\left[\left(1 + \frac{b^2}{\frac{b\sigma_1\sigma_3}{\sigma_1\sigma_3} + \frac{\sigma_3^2}{\sigma_1\sigma_3} - \frac{b\sigma_3^2}{\sigma_1\sigma_3}}\right) + \left(\frac{(1-b)^2}{\frac{b\sigma_1^2}{\sigma_1\sigma_3} + \frac{\sigma_1\sigma_3}{\sigma_1\sigma_3} - b\frac{\sigma_1\sigma_3}{\sigma_1\sigma_3}}\right)\right)\right)^{1/2}$$

$$= \frac{2}{3}\left(\tan\phi_{m13}^2\left[1 + \frac{b^2}{b + \frac{\sigma_3}{\sigma_1} - b\frac{\sigma_3}{\sigma_1}} + \frac{(1-b)^2}{b\frac{\sigma_1}{\sigma_3} + 1 - b}\right)\right)^{1/2}$$

or

$$\frac{\tau_{SMP}}{\sigma_{SMP}} = \frac{2}{3}\tan\phi_{m13}\left(\frac{\sigma_1(b+b^2) + \sigma_3(2-3b+b^2)}{b\sigma_1+\sigma_3(1-b)}\right)^{1/2} \qquad (2.1.10)$$

from eq. 2.1.8.

$$\sigma_1 = \sigma_3\frac{(1+a)}{(1-a)} \qquad (2.1.11)$$

substituting eq. (2.1.11) into eq. (2.1.10) the following is obtained:

$$\frac{\tau_{SMP}}{\sigma_{SMP}} = \frac{2}{3}\tan\phi_{m13}\left(\frac{\sigma_3\frac{(1+a)}{(1-a)}(b+b^2) + \sigma_3(2-3b+b^2)}{b\,\sigma_3\frac{(1+a)}{(1-a)} + \sigma_3(1-b)}\right)^{1/2} =$$

$$\boxed{\frac{\tau_{SMP}}{\sigma_{SMP}} = \frac{2}{3}\tan\phi_{m13}\left(\frac{(1+a)(b+b^2)+(1-a)(2-3b+b^2)}{b(1+a)+(1-a)(1-b)}\right)^{1/2}} \qquad (2.1.12)$$

Entering in the above equation values of b=0 (or b=1), which correspond to the triaxial stress path compression (or extension) then:

$$\frac{\tau_{SMP}}{\sigma_{SMP}} = \frac{2\sqrt{3}}{3} \tan\phi_{m13} = K \qquad (2.1.13)$$

To note that the same value is obtained from eq. (2.1.1) by entering the triaxial stress path condition, i.e., $\phi_{m12} = \phi_{m13}$ and $\phi_{m23} = 0$ and therefore eq. 2.1.12 is considered to be verified.

Now from eq. (2.1.12) the value of $\tan\phi_{m13}$ is obtained:

$$\tan\phi_{m13} = \left(\frac{\tau_{SMP}}{\sigma_{SMP}}\right) \frac{3}{2} \frac{b(1+a)+(1-a)(1-b)}{(1+a)(b+b^2)+(1-a)(2-3b+b^2)}$$

since the value of $\left(\frac{\tau_{SMP}}{\sigma_{SMP}}\right)$ is assumed to be a constant, by Matsuoka-Nakai, when the sand reaches failure, then:

$$\tan\phi_{F13} = K_F \frac{3}{2} \left(\frac{b(1+a)+(1-a)(1-b)}{(1+a)(b+b^2)+(1-a)(2-3b+b^2)}\right)^{1/2} \qquad (2.1.14)$$

where:

K_F = constant value regardless of the stress path, and given by eq. (2.1.13).

Since the above eq. (2.1.14) is only valid when b=0 or b=1, for values of $b \neq 0$ and $b \neq 1$, then this equation is rewritten as:

$$\tan\phi^{*}_{F13} = K_F \frac{3}{2} \left(\frac{b(1+a)+(1-a)(1-b)}{(1+a)(b+b^2)+(1-a)(2-3b+b^2)}\right)^{1/2} \qquad (2.1.15)$$

where:

$$\phi^{*}_{F13} = \phi_{F13} \qquad \text{for } b=0 \text{ or } b=1$$
$$\phi^{*}_{F13} \neq \phi_{F13} \qquad \text{for } 0 < b < 1$$

i.e., ϕ^{*}_{F13} is the failure friction angle, defined by σ_1 and σ_3, for any general stress path.

APPENDIX 2.2

RELATIONSHIP BETWEEN PRINCIPAL STRESSES AND THE NORMAL AND SHEAR STRESS ON THE SMP. EXTRAPOLATION OF THESE RELATIONS TO THE INCREMENTS OF PLASTIC STRAIN SPACE

APPENDIX 2.2

Relationship Between Principal Stresses and the Normal and Shear Stress on the SMP. Extrapolation of These Relations to the Increments of Plastic Strain Space

The state of stress on a soil element can be characterized by its principal stresses σ_i (i = 1,2,3) or by the normal stress, σ_{SMP} and shear stress, τ_{SMP} defined on the Spatial Mobilized Plane of the element. A relationship between these stresses, which is based on equilibrium of stresses in direction i, was developed by Matsuoka (1983) and is given by the following equation:

$$(\sigma_i - \sigma_{SMP})a_i - \tau_{SMP}b_i = 0 \qquad (2.2.1)$$

where

b_i = direction cosines of the shear stress direction

a_i = direction cosines of the normal stress direction (see main text eq. (2.24))

From eq. (2.2.1) b_i is obtained as follows:

$$b_i = \frac{\sigma_i - \sigma_{SMP}}{\tau_{SMP}} a_i \qquad (2.2.2)$$

To obtain $\Delta\epsilon_i^p$ as a function of $\Delta\epsilon_{SMP}^p$ and $\Delta\gamma_{SMP}^p$, Matsuoka (1983) assumes that the direction cosines of the normal component of the increment of plastic strain are the same as the direction cosines, a_i of the normal stress, σ_{SMP}, in the SMP, and that the direction cosines of the shear

component of the increment of plastic strain are equal to the direction cosines, b_i of the shear stress on the SMP. Based on these two assumptions Matsuoka developed the following equation:

$$(\Delta\epsilon_i^p - \Delta\epsilon_{SMP}^p)a_i + \frac{\Delta\gamma_{SMP}^p}{2} b_i = 0 \qquad (2.2.3)$$

This equation is similar to eq. (2.2.1) developed for the stresses. From eq. (2.2.3), $\Delta\epsilon_i^p$ is obtained as follows:

$$\Delta\epsilon_i^p = \Delta\epsilon_{SMP}^p + (b_i/a_i)\ (\Delta\gamma_{SMP}^p/2) \qquad (2.2.4)$$

APPENDIX 2.3

FUNDAMENTAL RELATIONSHIP BETWEEN CARTESIAN STRESSES AND PRINCIPAL STRESSES. EXTRAPOLATION OF THESE RELATIONS TO THE INCREMENTS OF PLASTIC STRAIN SPACE

APPENDIX 2.3

Fundamental Relationship Between Cartesian Stresses and Principal Stresses. Extrapolation of these Relations to the Increments of Plastic Strain Space

- Fundamental relationship between Cartesian stresses and principal stresses: Extrapolation of these relations to the increments of plastic strain space

The state of stress on a soil element can be defined using a Cartesian coordinate system (x,y,z) or a principal coordinate system (1,2,3) . The relationship between the stresses defined in these two coordinate systems is obtained from equilibrium of stresses in the x,y,z directions and are given by the following equation:

$$\begin{bmatrix} \sigma_x & \tau_{xy} & \tau_{xz} \\ \tau_{yx} & \sigma_y & \tau_{yz} \\ \tau_{zx} & \tau_{zy} & \sigma_z \end{bmatrix} = \begin{bmatrix} \ell_1 & \ell_2 & \ell_3 \\ m_1 & m_2 & m_3 \\ n_1 & n_2 & n_3 \end{bmatrix} \begin{bmatrix} \sigma_1 & 0 & 0 \\ 0 & \sigma_2 & 0 \\ 0 & 0 & \sigma_3 \end{bmatrix} \begin{bmatrix} \ell_1 & m_1 & n_1 \\ \ell_2 & m_2 & n_2 \\ \ell_3 & m_3 & n_3 \end{bmatrix} \quad (2.3.1)$$

where

ℓ_i, m_i, n_i are the direction cosines of the principal stresses $\sigma_i (i=1,2,3)$

i.e.

$$\ell_i = \cos(i,x) \quad m_i = \cos(i,y) \quad \text{and} \quad n_i = \cos(i,z)$$

Developing the multiplication of matrices the following equations are obtained:

$$\sigma_x = \sum_{i=1,3} \sigma_i \ell_i^2$$

$$\sigma_y = \sum_{i=1,3} \sigma_i m_i^2$$

$$\sigma_z = \sum_{i=1,3} \sigma_i n_i^2 \qquad (2.3.2)$$

$$\tau_{xy} = \sum_{i=1,3} \sigma_i \ell_i m_i$$

$$\tau_{yz} = \sum_{i=1,3} \sigma_i m_i n_i$$

$$\tau_{zx} = \sum_{i=1,3} \sigma_i n_i \ell_i$$

Assuming that the increments of plastic principal strain and the stresses have the same direction, than the relationships shown in Eq. (2.3.2) can be extrapolated for the increments of plastic strain as follows:

$$\Delta\epsilon_x^p = \sum_{i=1,3} \Delta\epsilon_i^p \, \ell_i^2$$

$$\Delta\epsilon_y^p = \sum_{i=1,3} \Delta\epsilon_i^p \, m_i^2$$

$$\Delta\epsilon_z^p = \sum_{i=1,3} \Delta\epsilon_i^p \, n_i^2$$

$$\frac{\Delta\gamma_{xy}^p}{2} = \sum_{i=1,3} \Delta\epsilon_i^p \, \ell_i m_i \qquad (2.3.3)$$

$$\frac{\Delta\gamma_{yz}^p}{2} = \sum_{i=1,3} \Delta\epsilon_i^p \, m_i n_i$$

$$\frac{\Delta\gamma_{zy}^p}{2} = \sum_{i=1,3} \Delta\epsilon_i^p \, n_i \ell_i$$

APPENDIX 2.4

DEVELOPMENT OF $\Delta(\sigma_{SMP}/\sigma_{SMP})$ IN TERMS OF $\Delta\sigma_1$, $\Delta\sigma_2$, AND $\Delta\sigma_3$

APPENDIX 2.4

Development of $\Delta(\tau_{SMP}/\sigma_{SMP})$ in terms of $\Delta\sigma_1$, $\Delta\sigma_2$, and $\Delta\sigma_3$

To evaluate the increment of the stress ratio on the SMP, $\Delta(\tau_{SMP}/\sigma_{SMP})$, in terms of the increments of principal stress, $\Delta\sigma_i$ (i = 1,2,3), eq. (2.50) from the main text is differentiated as follows:

$$\Delta(\tau_{SMP}/\sigma_{SMP}) = \frac{\Delta\tau_{SMP}\sigma_{SMP} - \tau_{SMP}\Delta\sigma_{SMP}}{(\sigma_{SMP})^2} \qquad (2.4.1)$$

Therefore the terms $\Delta\tau_{SMP}$ and $\Delta\sigma_{SMP}$ need to be evaluated.

2.2.1 Evaluation of $\Delta\tau_{SMP}$

τ_{SMP} is given by (see main text, eq. (2.26))

$$\tau_{SMP} = [(\sigma_1-\sigma_2)^2a_1^2a_2^2 + (\sigma_2-\sigma_3)^2a_2^2a_3^2 + (\sigma_3-\sigma_1)^2a_3^2a_1^2]^{1/2} \qquad (2.4.2)$$

Designating the term inside the square brackets by A then

$$\tau_{SMP} = [A]^{1/2} \qquad (2.4.3)$$

Differentiating eq. (2.4.3) the following is obtained

$$\Delta\tau_{SMP} = \frac{1}{2} A^{-1/2} \Delta(A)$$

or

$$\Delta\tau_{SMP} = \frac{\Delta(A)}{2\tau_{SMP}} \tag{2.4.4}$$

• Evaluation of $\Delta(A)$

As described,

$$A = (\sigma_1-\sigma_2)^2a_1^2a_2^2 + (\sigma_2-\sigma_3)^2a_2^2a_3^2 + (\sigma_3-\sigma_1)^2a_3^2a_1^2 \tag{2.4.5}$$

differentiating with respect to σ_i and a_i (i = 1,2,3)

$$\begin{aligned}\Delta(A) = {} & 2(\sigma_1-\sigma_2)a_1^2a_2^2(\Delta\sigma_2-\Delta\sigma_3) + (\sigma_1-\sigma_2)^2 2a_1a_2^2\Delta a_1 + (\sigma_1-\sigma_2)^2 2a_1^2a_2\Delta a_2 \\ & + 2(\sigma_2-\sigma_3)a_2^2a_3^2(\Delta\sigma_2-\Delta\sigma_3) + (\sigma_2-\sigma_3)^2 2a_2a_3^2\Delta a_2 + (\sigma_2-\sigma_3)^2 2a_2^2a_3\Delta a_3 \\ & + 2(\sigma_3-\sigma_3)a_3^2a_1^2(\Delta\sigma_3-\Delta\sigma_1) + (\sigma_3-\sigma_1)^2 2a_3a_1^2\Delta a_3 + (\sigma_3-\sigma_1)^2 2a_3^2a_1\Delta a_1\end{aligned}$$

rearranging the above terms the following is obtained:

$$\begin{aligned}\Delta(A) = {} & \Delta\sigma_1(DS1) + \Delta\sigma_2(DS2) + \Delta\sigma_3(DS3) + \Delta a_1(DA1) \\ & + \Delta a_2(DA2) + \Delta a_3(DA3)\end{aligned} \tag{2.4.6}$$

where

$$DS1 = 2(\sigma_1-\sigma_2)a_1^2a_2^2 - 2(\sigma_3-\sigma_1)a_3^2a_1^2$$

$$DS2 = -2(\sigma_1-\sigma_2)a_1^2a_2^2 + 2(\sigma_2-\sigma_3)a_2^2a_3^2$$

$$DS3 = -2(\sigma_2-\sigma_3)a_2^2a_3^2 + 2(\sigma_3-\sigma_1)a_3^2a_1^2$$

and

$$DA1 = 2(\sigma_1-\sigma_2)^2a_1a_2^2 + 2(\sigma_3-\sigma_1)^2a_1a_3^2$$

$$DA2 = 2(\sigma_1-\sigma_2)^2a_1^2a_2 + 2(\sigma_2-\sigma_3)^2a_2a_3^2$$

$$DA3 = 2(\sigma_2-\sigma_3)^2a_2^2a_3 + 2(\sigma_3-\sigma_1)^2a_1^2a_3$$

in order to have $\Delta(A)$ as a function of $\Delta\sigma_i$ only, the terms Δa_i shown in eq. (2.4.6) will be evaluated as follows:

• Evaluation of Δa_1

From eq. (2.24) of the main text

$$a_1 = \left(\frac{\sigma_1\sigma_2\sigma_3}{\sigma_1^2\sigma_2+\sigma_1\sigma_2\sigma_3+\sigma_3\sigma_1^2}\right)^{1/2} \tag{2.4.7}$$

Designating the term inside the square brackets by A_1, than

$$a_1 = [A_1]^{1/2}$$

Differentiating

$$\Delta a_1 = \Delta(A_1)/2a_1 \tag{2.4.8}$$

- Evaluation of $\Delta(A_1)$

As described

$$A_1 = \frac{\sigma_1\sigma_2\sigma_3}{\sigma_1^2\sigma_2+\sigma_1\sigma_2\sigma_3\ \sigma_3\sigma_1^2} \tag{2.4.9}$$

Designating the numerator by A_1T and the denominator by A_1B, than

$$A_1 = A_1T/A_1B$$

Differentiating

$$\Delta(A_1) = \frac{\Delta(A_1T)A_1B - A_1T\Delta(A_1B)}{(A_1B)^2} \tag{2.4.10}$$

- Evaluation of $\Delta(A_1T)$ and $\Delta(A_1B)$

As described

$$A_1T = \sigma_1\sigma_2\sigma_3$$

Differentiating

$$\Delta(A_1T) = \Delta\sigma_1\sigma_2\sigma_3 + \Delta\sigma_2\sigma_1\sigma_3 + \Delta\sigma_3\sigma_1\sigma_2 \qquad (2.4.11)$$

and

$$A_1B = \sigma_1^2\sigma_2 + \sigma_1\sigma_2\sigma_3 + \sigma_3\sigma_1^2$$

Differentiating

$$\Delta(A_1B) = 2\sigma_1\sigma_2\Delta\sigma_1 + \sigma_1^2\Delta\sigma_2 + \Delta\sigma_1\sigma_2\sigma_3 + \Delta\sigma_2\sigma_1\sigma_3 + \Delta\sigma_3\sigma_1\sigma_2 + \Delta\sigma_3\sigma_1^2 + 2\sigma_3\sigma_1\Delta\sigma_1 \qquad (2.4.12)$$

Substituting $\Delta(A_1T)$ from eq. (2.4.11) and $\Delta(A_1B)$ from eq. (2.4.12) into eq. (2.4.10) the following is obtained:

$$\Delta(A_1) = \{\Delta\sigma_1(A_1B)\sigma_2\sigma_3 + \Delta\sigma_2(A_1B)\sigma_1\sigma_3 + \Delta\sigma_3(A_1B)\sigma_1\sigma_2) - [\Delta\sigma_1(A_1T)(2\sigma_1\sigma_2+\sigma_2\sigma_3+2\sigma_1\sigma_3)) + \Delta\sigma_2((A_1T)(\sigma_1^2+\sigma_1\sigma_3)) + \Delta\sigma_3((A_1T)(\sigma_1\sigma_2+\sigma_1^2))]\}/(A_1B)^2$$

rearranging in terms of $\Delta\sigma_1$, $\Delta\sigma_2$, $\Delta\sigma_3$

$$\Delta(A_1) = \Delta\sigma_1(A_{11}) + \Delta\sigma_2(A_{12}) + \Delta\sigma_3(A_{13}) \qquad (2.4.13)$$

where

$$A_{11} = [(A_1B)\sigma_2\sigma_3 - (A_1T)(2\sigma_1\sigma_2 + \sigma_2\sigma_3 + 2\sigma_1\sigma_3)]/(A_1B)^2 \qquad (2.4.14)$$

$$A_{12} = [(A_1B)\sigma_1\sigma_3 - (A_1T)(\sigma_1^2 + \sigma_1\sigma_3)]/(A_1B)^2 \qquad (2.4.15)$$

and

$$A_{13} = [(A_1B)\sigma_1\sigma_2 - (A_1T)(\sigma_1\sigma_2 + \sigma_1^2)]/(A_1B)^2 \qquad (2.4.16)$$

Substituting eq. (2.4.13) into eq. (2.4.8) the following is obtained:

$$\boxed{\Delta a_1 = (A_{11}/2a_1)\Delta\sigma_1 + (A_{12}/2a_1)\Delta\sigma_2 + (A_{13}/2a_1)\Delta\sigma_3} \qquad (2.4.17)$$

• Evaluation of Δa_2

From eq. (2.24) of the main text

$$a_2 = \left[\frac{\sigma_1\sigma_2\sigma_3}{\sigma_1\sigma_2^2 + \sigma_2^2\sigma_3 + \sigma_1\sigma_2\sigma_3}\right]^{1/2} \qquad (2.4.18)$$

Designating the term inside the square brackets by A_2, than

$$a_2 = [A_2]^{1/2}$$

Differentiating

$$\Delta a_2 = \Delta(A_2)/2a_2 \qquad (2.4.19)$$

- Evaluation of $\Delta(A_2)$

As described

$$A_2 = \frac{\sigma_1\sigma_2\sigma_3}{\sigma_1\sigma_2^2 + \sigma_2^2\sigma_3 + \sigma_1\sigma_2\sigma_3}$$

Designating the numerator by A_2T and the denominator by A_2B, than

$$A_2 = A_2T/A_2B$$

Differentiating

$$\Delta(A_2) = \frac{\Delta(A_2T)A_2B - A_2T\Delta(A_2B)}{(A_2B)^2} \qquad (2.4.20$$

- Evaluation of $\Delta(A_2T)$ and $\Delta(A_2B)$

As described

$$A_2T = \sigma_1\sigma_2\sigma_3$$

Differentiating

$$\Delta(A_2T) = \Delta\sigma_1\sigma_2\sigma_3 + \Delta\sigma_2\sigma_1\sigma_3 + \Delta\sigma_3\sigma_1\sigma_2 \qquad (2.4.21)$$

and

$$A_2B = \sigma_1\sigma_2^2 + \sigma_2^2\sigma_3 + \sigma_1\sigma_2\sigma_3$$

Differentiating

$$\Delta(A_2B) = \Delta\sigma_1\sigma_2^2 + 2\Delta\sigma_2\sigma_1\sigma_2 + \Delta\sigma_3\sigma_2^2 + 2\Delta\sigma_2\sigma_2\sigma_3 + \Delta\sigma_1\sigma_2\sigma_3$$
$$+ \Delta\sigma_2\sigma_1\sigma_3 + \Delta\sigma_3\sigma_1\sigma_2 = \Delta\sigma_1(\sigma_2^2+\sigma_2\sigma_3) +$$
$$+ \Delta\sigma_2(2\sigma_1\sigma_2+2\sigma_2\sigma_3+\sigma_1\sigma_3) + \Delta\sigma_3(\sigma_2^2+\sigma_1\sigma_2) \qquad (2.4.22)$$

Substituting $\Delta(A_2T)$ from eq. (2.4.21) and $\Delta(A_2B)$ from eq. (2.4.22) into eq. (2.4.20) the following is obtained:

$$\Delta(A_2) = \Delta\sigma_1(A_{21}) + \Delta\sigma_2(A_{22}) + \Delta\sigma_3(A_{23}) \qquad (2.4.23)$$

where:

$$A_{21} = [(A_2B)(\sigma_2\sigma_3)-(A_2T)(\sigma_2^2+\sigma_2\sigma_3)]/(A_2B)^2 \qquad (2.4.24)$$

$$A_{22} = [(A_2B)(\sigma_1\sigma_3) - (A_2T)(2\sigma_1\sigma_2 + 2\sigma_2\sigma_3 + \sigma_1\sigma_3)]/(A_2B)^2 \qquad (2.4.25)$$

and

$$A_{23} = [(A_2B)(\sigma_1\sigma_2) - (A_2T)(\sigma_2^2 + \sigma_1\sigma_2)]/(A_2B)^2 \qquad (2.4.26)$$

Substituting eq. (2.4.23) into eq. (2.4.19) the following is obtained:

$$\boxed{\Delta a_2 = (A_{21}/2a_2)\Delta\sigma_1 + (A_{22}/2a_2)\Delta\sigma_2 + (A_{23}/2a_2)\Delta\sigma_3} \qquad (2.4.27)$$

• Evaluation of Δa_3

From eq. (2.24) of the main text

$$a_3 = \left[\frac{\sigma_1\sigma_2\sigma_3}{\sigma_1\sigma_2\sigma_3 + \sigma_2\sigma_3^2 + \sigma_1\sigma_3^2}\right]^{1/2} \qquad (2.4.28)$$

Designating the term inside the square brackets by A_3, than:

$$a_3 = [A_3]^{1/2}$$

Differentiating

$$\Delta a_3 = \Delta(A_3)/2a_3 \qquad (2.4.29)$$

as described above

$$A_3 = \frac{\sigma_1\sigma_2\sigma_3}{\sigma_1\sigma_2\sigma_3 + \sigma_2\sigma_3^2 + \sigma_1\sigma_3^2}$$

Designating the numerator by A_3T and the numerator by A_3B, than

$$A_3 = A_3T/A_3B$$

Differentiating

$$\Delta(A_3) = \frac{\Delta(A_3T)A_3B - A_3T\Delta(A_3B)}{(A_3B)^2} \qquad \Delta(2.4.30)$$

- Evaluation of $\Delta(A_3T)$ and $\Delta(A_3B)$

$$\Delta(A_3T) = \Delta(A_1T) = \Delta\sigma_1\sigma_2\sigma_3 + \Delta\sigma_2\sigma_1\sigma_3 + \Delta\sigma_3\sigma_1\sigma_2 \qquad (2.4.31)$$

and

$$A_3B = \sigma_1\sigma_2\sigma_3 + \sigma_2\sigma_3^2 + \sigma_1\sigma_3^2$$

Differentiating

$$\begin{aligned}\Delta(A_3B) &= \Delta\sigma_1\sigma_2\sigma_3 + \Delta\sigma_2\sigma_1\sigma_3 + \Delta\sigma_3\sigma_1\sigma_2 + \Delta\sigma_2\sigma_3^2 + 2\Delta\sigma_3\sigma_2\sigma_3 + \Delta\sigma_1\sigma_3^2 \\ &\quad + \Delta\sigma_1\sigma_3^2 + 2\Delta\sigma_3\sigma_1\sigma_3 \\ &= \Delta\sigma_1(\sigma_2\sigma_3+\sigma_3^2) + \Delta\sigma_2(\sigma_1\sigma_3+\sigma_3^2) + \Delta\sigma_3(\sigma_1\sigma_2+2\sigma_2\sigma_3+2\sigma_1\sigma_3)\end{aligned} \qquad (2.4.32)$$

Substituting $\Delta(A_3T)$ from eq. (2.4.31) and $\Delta(A_3B)$ from eq. (2.4.32) into eq. (2.4.30) the following is obtained:

$$\Delta(A_3) = \Delta\sigma_1(A_{31}) + \Delta\sigma_2(A_{32}) + \Delta\sigma_3(A_{33}) \tag{2.4.33}$$

where:

$$A_{31} = [(A_3B)(\sigma_2\sigma_3) - A_3T(\sigma_2\sigma_3 + \sigma_3^2)]/(A_3B)^2 \tag{2.4.34}$$

$$A_{32} = [(A_3B)(\sigma_1\sigma_3) - A_3T(\sigma_1\sigma_3 + \sigma_3^2)]/(A_3B)^2 \tag{2.4.35}$$

and

$$A_{33} = [(A_3B)(\sigma_1\sigma_2) - A_3T(\sigma_1\sigma_2 + 2\sigma_2\sigma_3 + 2\sigma_1\sigma 3)]/(A_3B)^2 \tag{2.4.36}$$

Substituting eq. (2.4.33) into eq. (2.4.29) the following is obtained:

$$\boxed{\Delta a_3 = (A_{31}/2a_3)\Delta\sigma_1 + (A_{32}/2a_3)\Delta\sigma_2 + (A_{33}/2a_3)\Delta\sigma_3} \tag{2.4.37}$$

Substituting the values of Δa_1 from eq. (2.4.17), Δa_2 from eq. (2.4.27) and Δa_3 from eq. (2.4.37) into eq. (2.4.6) the following is obtained:

$$\Delta(A) = \Delta\sigma_1[DS_1 + \frac{A_{11}}{2a_1}DA_1 + \frac{A_{21}}{2a_2}DA_2 + \frac{A_{31}}{2a_3}DA_3]$$

$$+ \Delta\sigma_2[DS_2 + \frac{A_{12}}{2a_1}DA_1 + \frac{A_{22}}{2a_2}DA_2 + \frac{A_{32}}{2a_3}DA_3]$$

$$+ \Delta\sigma_3[DS_3 + \frac{A_{13}}{2a_1}DA_1 + \frac{A_{23}}{2a_2}DA_2 + \frac{A_{33}}{2a_3}DA_3]$$

designating the terms in brackets by TM1, TM2 and TM3, respectively, the following is obtained:

$$\Delta(A) = \Delta\sigma_1[TM1] + \Delta\sigma_2[TM2] + \Delta\sigma_3[TM3] \qquad (2.4.38)$$

Substituting the value of $\Delta(A)$ from eq. (2.4.38) into eq. (2.4.4) the value of $\Delta\tau_{SMP}$ is obtained:

$$\boxed{\Delta\tau_{SMP} = \Delta\sigma_1 \left[\frac{TM1}{2\tau_{SMP}}\right] + \Delta\sigma_2 \left[\frac{TM2}{2\tau_{SMP}}\right] + \Delta\sigma_3 \left[\frac{TM3}{2\tau_{SMP}}\right]} \qquad (2.4.39)$$

2.1.2 Evaluation of $\Delta\sigma_{SMP}$

σ_{SMP} is given by (see main text, eq. (2.25))

$$\sigma_{SMP} = \sigma_1 a_1^2 + \sigma_2 a_2^2 + \sigma_3 a_3^2 \qquad (2.4.40)$$

Differentiating

$$\Delta\sigma_{SMP} = \Delta\sigma_1 a_1^2 + 2a_1\sigma_1\Delta a_1 + \Delta\sigma_2 a_2^2 + 2a_2\sigma_2\Delta a_2 + \Delta\sigma_3 a_3^2 + 2a_3\sigma_3\Delta a_3 \qquad (2.4.41)$$

Substituting the values of Δa_1 from eq. (2.4.17), Δa_2 from eq. (2.4.27) and Δa_3 from eq. (2.4.37) into eq. (2.4.41), the following is obtained:

$$\boxed{\Delta\sigma_{SMP} = \Delta\sigma_1(SIGMO1) + \Delta\sigma_2(SIGMO2) + \Delta\sigma_3(SIGMO3)} \qquad (2.4.42)$$

where:

$$SIGMO1 = (a_1^2 + \sigma_1 A_{11} + \sigma_2 A_{21} + \sigma_3 A_{31})$$

$$SIGMO2 = (a_2^2 + \sigma_1 A_{12} + \sigma_2 A_{22} + \sigma_3 A_{32})$$

$$SIGMO3 = (a_3^2 + \sigma_1 A_{13} + \sigma_2 A_{23} + \sigma_3 A_{33})$$

Substituting the values of $\Delta\tau_{smp}$ from eq. (2.4.39) and $\Delta\sigma_{smp}$ from eq. (2.4.42) into eq. (2.4.1) the following is obtained:

$$\Delta\left(\frac{\tau_{SMP}}{\sigma_{SMP}}\right) = \left[\begin{array}{l}\left(\Delta\sigma_1\left(\frac{TM1}{2\tau_{SMP}}\right) + \Delta\sigma_2\left(\frac{TM2}{2\tau_{SMP}}\right) + \Delta\sigma_3\left(\frac{TM3}{2\tau_{SMP}}\right)\right]\sigma_{SMP}\right) - \\ - \left[\Delta\sigma_1(SIGMO1) + \Delta\sigma_2(SIGMO2) + \Delta\sigma_3(SIGMO3)\right]\tau_{SMP}\end{array}\right] \cdot 1/(\sigma_{SMP})^2$$

or rearranging

$$\boxed{\Delta\left(\frac{\tau_{SMP}}{\sigma_{SMP}}\right) = \Delta\sigma_1[TSMOB1] + \Delta\sigma_2[TSMOB2] + \Delta\sigma_3[TSMOB3]} \qquad (2.4.43)$$

where:

$$TSMOB1 = \left[\frac{TM1}{2\tau_{SMP}}\sigma_{SMP} - (SIGMO1)\tau_{SMP}\right]/(\sigma_{SMP})^2$$

$$TSMOB2 = \left[\frac{TM2}{2\tau_{SMP}}\sigma_{SMP} - (SIGMO2)\tau_{SMP}\right]/(\sigma_{SMP})^2$$

$$TSMOB3 = \left[\frac{TM3}{2\tau_{SMP}}\sigma_{SMP} - (SIGMO3)\tau_{SMP}\right]/(\sigma_{SMP})^2$$

APPENDIX 2.5

RELATIONS BETWEEN INCREMENTS OF PRINCIPAL STRESS AND INCREMENTS OF CARTESIAN STRESS IN 3-DIMENSIONAL STRESS SPACE

APPENDIX 2.5

Relations Between Increments of Principal Stress and Increments of Cartesian Stress in 3-Dimensional Stress Space

2.5.1 Relation Between Principal Stresses and Cartesian Stresses

In Fig. 2.5.1 it is shown the plane ABC defined in the 3-Dimensional cartesian stress system x,y,z. Assuming that the direction, i, perpendicular to the plane is a principal direction, than the normal stress to the plane, σ_i is a principal stress and the plane ABC, on which there is no shear stress, is a principal plane.

A relationship between the principal stress, σ_i and the cartesian stresses σ_x, σ_y, σ_z, τ_{xy}, τ_{yz} and τ_{zx} can be developed based on force equilibrium in the x,y and z directions and given by the following equations:

$$\begin{cases} (\sigma_x-\sigma_i)\cos(i,x) + \tau_{xy}\cos(i,y) + \tau_{xz}\cos(i,z) = 0 \\ \tau_{yx}\cos(i,x) + (\sigma_y-\sigma_i)\cos(i,y) + \tau_{yz}\cos(i,z) = 0 \\ \tau_{zx}\cos(i,x) + \tau_{zy}\cos(i,y) + (\sigma_z-\sigma_i)\cos(i,z) = 0 \end{cases} \qquad (2.5.1)$$

where cos(i,x), cos(i,y) and cos(i,z) are the direction cosines of direction i (i = 1,2,3) in respect to directions x,y and z, respectively.

From the known relation for direction cosines, a fourth equation is obtained

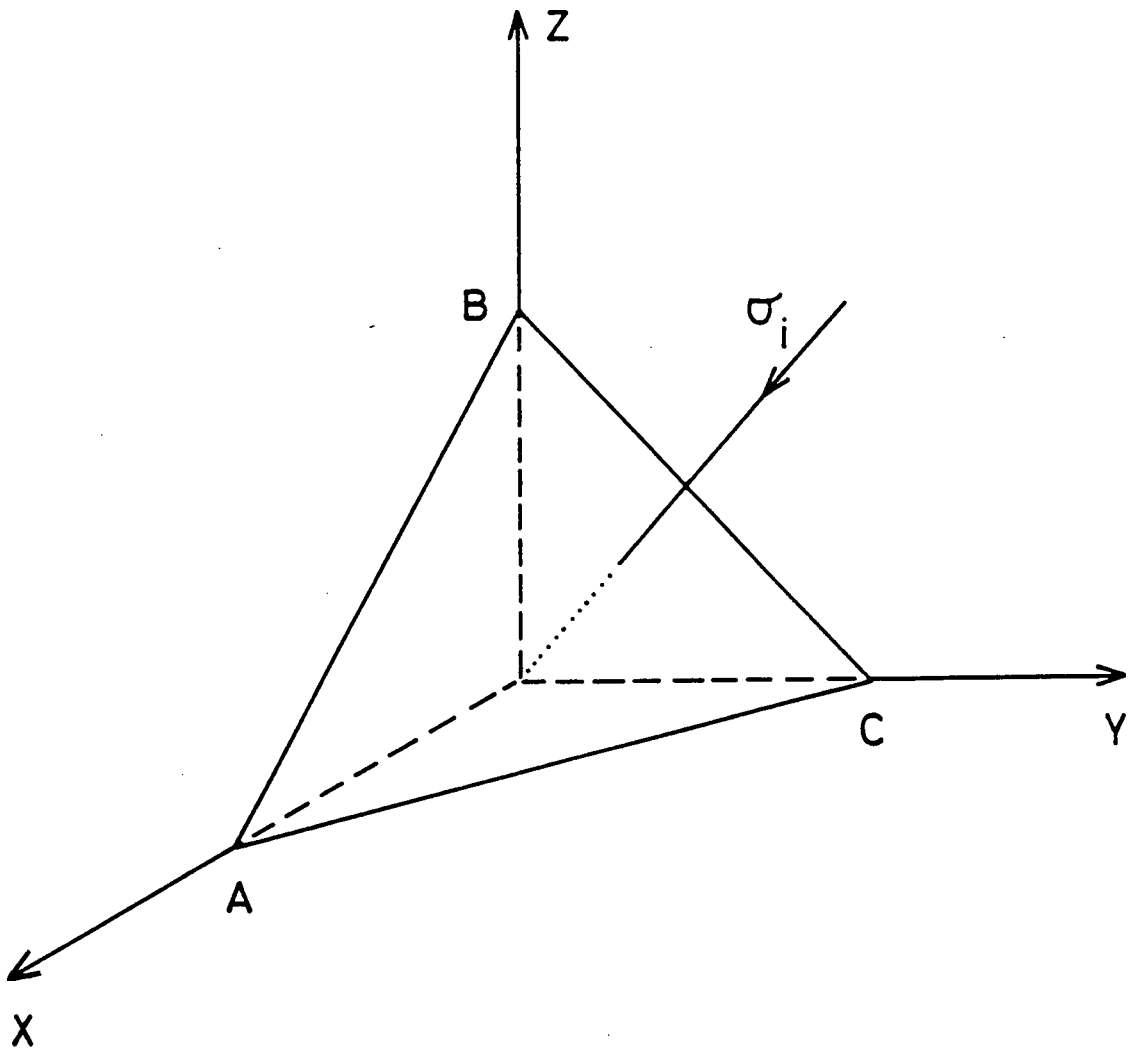

Figure 2.5.1 Sketch of a Principal Plane

$$\cos^2(i,x) + \cos^2(i,y) + \cos^2(i,z) = 1 \qquad (2.5.2)$$

2.5.2 Relations Between Increments of Principal Stress, Increments of the Rotation of Principal Directions and Increments of Cartesian Stress

Differentiating eqs. (2.5.1) and (2.5.2) the following is obtained:

$$\begin{bmatrix} (\Delta\sigma_x-\Delta\sigma_i)\cos(i,x) - (\sigma_x-\sigma_i)\sin(i,x)\Delta(i,x) + \Delta\tau_{xy}\cos(i,y) - \\ \quad - \tau_{xy}\sin(i,y)\Delta(i,y) + \Delta\tau_{xz}\cos(i,z) - \tau_{xz}\sin(i,z)\Delta(i,z) = 0 \\ \\ \Delta\tau_{yx}\cos(i,x) - \tau_{yx}\sin(i,x)\Delta(i,x) + (\Delta\sigma_y-\Delta\sigma_i)\cos(i,y) - \\ \quad - (\sigma_y-\sigma_i)\sin(i,y)\Delta(i,y) + \Delta\tau_{yz}\cos(i,z) - \tau_{yz}\sin(i,z)\Delta(i,z) = 0 \\ \\ \Delta\tau_{zx}\cos(i,x) - \tau_{zx}\sin(i,x)\Delta(i,x) + \Delta\tau_{zy}\cos(i,y) - \tau_{zy}\sin(i,y)\Delta(i,y) + \\ \quad + (\Delta\sigma_z-\Delta\sigma_i)\cos(i,z) - (\sigma_z-\sigma_i)\sin(i,z)\Delta(i,z) = 0 \\ \\ \cos(i,x)\sin(i,x)\Delta(i,x) + \cos(i,y)\sin(i,y)\Delta(i,y) + \\ \quad + \cos(i,z)\sin(i,z)\Delta(i,z) = 0 \end{bmatrix}$$

(2.5.3)

The above equations constitute a system of 4 equations with the 4 unknowns: $\Delta\sigma_i$, $\Delta(i,x)$, $\Delta(i,y)$ and $\Delta(i,z)$. Since i = 1,2,3 than 3 systems of 4 equations with 4 unknowns are obtained and those will be solved as follows:

2.5.2.1 Relations between increment of principal stress, $\Delta\sigma_1$, with increments of cartesian stress

Substituting i=1 in eqs. (2.5.3) the following is obtained:

$$\left[\begin{array}{l}
\Delta\sigma_x\cos(1,x) - \Delta\sigma_1\cos(1,x) - (\sigma_x-\sigma_1)\sin(1,x)\Delta(1,x) + \Delta\tau_{xy}\cos(1,y) - \\
\qquad - \tau_{xy}\sin(1,x)\Delta(1,y) + \Delta\tau_{xz}\cos(1,z) - \tau_{xz}\sin(1,z)\Delta(1,z) = 0 \\
\\
\Delta\tau_{yx}\cos(1,x) - \tau_{yx}\sin(1,x)\Delta(1,x) + \Delta\sigma_y\cos(1,y) - \Delta\sigma_1\cos(1,y) - \\
\qquad - (\sigma_y-\sigma_1)\sin(1,y)\Delta(1,y) + \Delta\tau_{yz}\cos(1,z) - \tau_{yz}\sin(1,z)\Delta(1,z) = 0 \\
\\
\Delta\tau_{xz}\cos(1,x) - \tau_{zx}\sin(1,x)\Delta(1,x) + \Delta\tau_{zy}\cos(1,y) - \tau_{zy}\sin(1,y)\Delta(1,y) + \\
\qquad + \Delta\sigma_z\cos(1,z) - \Delta\sigma_1\cos(1,z) - (\sigma_z-\sigma_1)\sin(1,z)\Delta(1,z) = 0 \\
\\
\cos(1,x)\sin(1,x)\Delta(1,x) + \cos(1,y)\sin(1,y)\Delta(1,y) + \\
\qquad + \cos(1,z)\sin(1,z)\Delta(1,z) = 0
\end{array}\right]$$

To simplify the above equations take the following form:

$$A1l-\Delta\sigma_1\ell_1-\Delta(1,x)B1l+C1l-\Delta(1,y)D1l+E1l-\Delta(1,z)F1l = 0 \qquad (2.5.4)$$

$$A2l-\Delta(1,x)B2l+C2l-\Delta\sigma_1 m_1-\Delta(1,y)D2l+E2l-\Delta(1,z)F2l = 0 \qquad (2.5.5)$$

$$A3l-\Delta(1,x)B3l+C3l-\Delta(1,y)D3l+E3l-\Delta\sigma_1 n_1-\Delta(1,z)F3l = 0 \qquad (2.5.6)$$

$$A41\ \Delta(1,x)+B41\ \Delta(1,y)+C41\ \Delta(1,z) = 0 \qquad (2.5.7)$$

where:

$A11 = \Delta\sigma_x \cos(1,x)$ $\quad A21 = \Delta\tau_{yx}\cos(1,x)$ $\quad A31 = \Delta\tau_{zx}\cos(1,x)$

$B11 = (\sigma_x-\sigma_1)\sin(1,x)$ $\quad B21 = \tau_{yx}\sin(1,x)$ $\quad B31 = \tau_{zx}\sin(1,x)$

$C11 = \Delta\tau_{xy}\cos(1,y)$ $\quad C21 = \Delta\sigma_y\cos(1,y)$ $\quad C31 = \Delta\tau_{zy}\cos(1,y)$

$D11 = \tau_{xy}\sin(1,y)$ $\quad D21 = (\sigma_y-\sigma_1)\sin(1,y)$ $\quad D31 = \tau_{zy}\sin(1,y)$

$E11 = \Delta\tau_{xz}\cos(1,z)$ $\quad E21 = \Delta\tau_{yz}\cos(1,z)$ $\quad E31 = \Delta\sigma_z\cos(1,z)$

$F11 = \tau_{xz}\sin(1,z)$ $\quad F21 = \tau_{yz}\sin(1,z)$ $\quad F31 = (\sigma_z-\sigma_1)\sin(1,z)$

$A41 = \cos(1,x)\sin(1,x)$ $\qquad \ell_1 = \cos(1,x)$

$B41 = \cos(1,y)\sin(1,y)$ $\qquad m_1 = \cos(1,y)$

$C41 = \cos(1,z)\sin(1,z)$ $\qquad n_1 = \cos(1,z)$

Note: all the above equations are designated as (2.5.8)

- Evaluation of the System of Equations (2.5.4) to (2.5.7)

From eq. (2.5.6) $\Delta\sigma_1$ is obtained:

$$\Delta\sigma_1 = \frac{A31}{n_1} - \frac{B31}{n_1}\Delta(1,x) + \frac{C31}{n_1} - \frac{D31}{n_1}\Delta(1,y) + \frac{E31}{n_1} - \frac{F31}{n_1}\Delta(1,z) \qquad (2.5.9)$$

and from eq. (2.5.7)

$$\boxed{\Delta(1,x) = -\frac{B41}{A41}\Delta(1,y) - \frac{C41}{A41}\Delta(1,z)} \qquad (2.5.10)$$

Substituting eqs. (2.5.9) and (2.5.10) into Eq. (2.5.5) the following is obtained:

$$A21 + \frac{B41}{A41} B21\,\Delta(1,y) + \frac{C41}{A41} B21\,\Delta(1,z) + C21 - \frac{A31}{n_1} m_1$$

$$- \frac{B41}{A41}\frac{B31}{n_1} m_1\,\Delta(1,y) - \frac{C41}{A41}\frac{B31}{n_1} m_1\,\Delta(1,z) - \frac{C31}{n_1} m_1 + \frac{D31}{n_1} m_1\,\Delta(1,y)$$

$$- \frac{E31}{n_1} m_1 + \frac{F31}{n_1} m_1\,\Delta(1,z) - D21\,\Delta(1,y) + E21 - F21\,\Delta(1,z) = 0$$

collecting terms in the above equation:

$$\Delta(1,y)\left[\frac{B41}{A41} B21 - \frac{B41}{A41}\frac{B31}{n_1} m_1 + \frac{D31}{n_1} m_1 - D21\right]$$

$$+ \Delta(1,z)\left[\frac{C41}{A41} B21 - \frac{C41}{A41}\frac{B31}{n_1} m_1 + \frac{F31}{n_1} m_1 - F21\right]$$

$$+ A21 + C21 - \frac{A31}{n_1} m_1 - \frac{C31}{n_1} m_1 - \frac{E31}{n_1} m_1 + E21 = 0$$

Designating the terms inside the square brackets by [FM1] and [FJ1] the following is obtained

$$\Delta(1,y)[FM1] + \Delta(1,z)[FJ1] + A21 + C21 - \frac{A31}{n_1} m_1 - \frac{C31}{n_1} m_1 - \frac{E31}{n_1} m_1 + E21 = 0$$

and solving for $\Delta(1,y)$:

$$\boxed{\Delta(1,y) = - \frac{FJ1}{FM1} \Delta(1,z) - \frac{A21}{FM1} - \frac{C21}{FM1} - \frac{E21}{FM1} + \frac{A31}{FM1} \frac{m_1}{n1} + \frac{C31}{FM1} \frac{m_1}{n_1} + \frac{E31}{FM1} \frac{m_1}{n_1}}$$

(2.5.11)

Substituting now the values of $\Delta\sigma_1$ from eq. (2.5.9) and $\Delta(1,x)$ from eq. (2.5.10) into eq. (2.5.4) the following is obtained:

$$A11 - A31 \frac{\ell_1}{n_1} + B31 \frac{\ell_1}{n_1} \left(- \frac{B41}{A41} \Delta(1,y) - \frac{C41}{A41} \Delta(1,z)\right) - C31 \frac{\ell_1}{n_1}$$

$$+ D31 \frac{\ell_1}{n_1} \Delta(1,y) - E31 \frac{\ell_1}{n_1} + F31 \frac{\ell_1}{n_1} \Delta(1,z) + B11 \frac{B41}{A41} \Delta(1,y)$$

$$+ B11 \frac{C41}{A41} \Delta(1,z) + C11 - D11 \Delta(1,y) + E11 - F11 \Delta(1,z) = 0$$

Collecting terms the following is obtained:

$$\Delta(1,y) \left[-B31 \frac{B41}{A41} \frac{\ell_1}{n_1} + D31 \frac{\ell_1}{n_1} + B11 \frac{B41}{A41} - D11\right]$$

$$+ \Delta(1,z) \left(-B31 \frac{C41}{A41} \frac{\ell_1}{n_1} + F31 \frac{\ell_1}{n_1} + B11 \frac{C41}{A41} - F11\right)$$

$$+ A11 - A31 \frac{\ell_1}{n_1} - C31 \frac{\ell_1}{n_1} - E31 \frac{\ell_1}{n_1} + C11 + E11 = 0$$

designating the term inside the square bracket by FP1 and substituting the value of $\Delta(1,y)$ from eq. (2.5.11) the following is obtained:

$$-FP1\,\frac{FJ1}{FM1}\,\Delta(1,z) - \frac{FP1}{FM1}\,A21 - \frac{FP1}{FM1}\,C21 - \frac{FP1}{FM1}\,E21 + \frac{FP1}{FM1}\,A31\,\frac{m_1}{n_1} + \frac{FP1}{FM1}\,C31\frac{m_1}{n_1}$$

$$+ \frac{FP1}{FM1}\,E31\,\frac{m_1}{n_1} + \Delta(1,z)\,\left(-B31\,\frac{C41}{A41}\,\frac{\ell_1}{n_1} + F31\,\frac{\ell_1}{n_1} + B11\,\frac{C41}{A41} - F11\right)$$

$$+ A11 - A31\,\frac{\ell_1}{n_1} - C31\,\frac{\ell_1}{n_1} - E31\,\frac{\ell_1}{n_1} + C11 + E11 = 0$$

collecting terms:

$$\Delta(1,z)\,\left[-FP1\,\frac{FJ1}{FM1} - B31\,\frac{C41}{A41}\,\frac{\ell_1}{n_1} + F31\,\frac{\ell_1}{n_1} + B11\,\frac{C41}{A41} - F11\right]$$

$$+ A11 + C11 + E11 - \frac{FP1}{FM1}\,A21 - \frac{FP1}{FM1}\,C21 - \frac{FP1}{FM1}\,E21 + \left(\frac{FP1}{FM1}\,\frac{m_1}{n_1} - \frac{\ell_1}{n_1}\right)\,A31$$

$$+ \left(\frac{FP1}{FM1}\,\frac{m_1}{n_1} - \frac{\ell_1}{n_1}\right)\,C31 + \left(\frac{FP1}{FM1}\,\frac{m_1}{n_1} - \frac{\ell_1}{n_1}\right)\,E31 = 0$$

Designating the term inside the square brackets by FL1 and solving for $\Delta(1,z)$ the following equation is obtained:

$$\Delta(1,z) = A11(A1z) + C11(C1z) + E11(E1z) + A21(A2z) + C21(C2z) + E21(E2z) + A31(A3z) + C31(C3z) + E31(E3z) \qquad (2.5.12)$$

where:

$$A1z = C1z = E1z = -\frac{1}{FL1}$$

$$A2z = C2z = E2z = \frac{FP1}{FL1\ FM1}$$

and

$$A3z = C3z = E3z = -\left(\frac{FP1}{FM1}\frac{m_1}{n_1} - \frac{\ell_1}{n_1}\right)\frac{1}{FL1}$$

Substituting the value of $\Delta(1,z)$ from eq. (2.5.12) into eq. (2.5.11) the value of $\Delta(1,y)$ is obtained:

$$\Delta(1,y) = -A11(A1z)\frac{FJ1}{FM1} - C11(C1z)\frac{FJ1}{FM1} - E11(E1z)\frac{FJ1}{FM1} - A21(A2z)\frac{FJ1}{FM1}$$

$$- C21(C2z)\frac{FJ1}{FM1} - E21(E2z)\frac{FJ1}{FM1} - A31(A3z)\frac{FJ1}{FM1} - C31(C3z)\frac{FJ1}{FM1}$$

$$- E31(E3z)\frac{FJ1}{FM1} - \frac{A21}{FM1} - \frac{C21}{FM1} - \frac{E21}{FM1} + \frac{A31}{FM1}\frac{m_1}{n_1} + \frac{C31}{FM1}\frac{m_1}{n_1} + \frac{E31}{FM1}\frac{m_1}{n_1}$$

rearranging terms:

$$\boxed{\begin{aligned}\Delta(1,y) = {} & A11(A1y) + C11(C1y) + E11(E1y) + A21(A2y) + C21(C2y) \\ & + E21(E2y) + A31(A3y) + C31(C3y) + E31(E3y)\end{aligned}} \qquad (2.5.13)$$

where:

$$A1y = -A1z \frac{FJ1}{FM1}$$

$$C1y = -C1z \frac{FJ1}{FM1}$$

$$E1y = -E1z \frac{FJ1}{FM1}$$

$$A2y = -(A2z \frac{FJ1}{FM1} + \frac{1}{FM1})$$

$$C2y = -(C2z \frac{FJ1}{FM1} + \frac{1}{FM1})$$

$$E2y = -(E2z \frac{FJ1}{FM1} + \frac{1}{FM1})$$

and

$$A3y = -(A3z \frac{FJ1}{FM1} - \frac{1}{FM1} \frac{m_1}{n_1}) \qquad C3y = -(C3z \frac{FJ1}{FM1} - \frac{1}{FM1} \frac{m_1}{n_1})$$

$$E3y = -(E3z \frac{FJ1}{FM1} - \frac{1}{FM1} \frac{m_1}{n_1})$$

Substituting $\Delta(1z)$ from eq. (2.5.12) and $\Delta(1,y)$ from eq. (2.5.13) into eq. (2.5.10) $\Delta(1,x)$ is obtained as follows:

$$\Delta(1,x) = A11(A1x) + C11(C1x) + E11(E1x) + A21(A2x) + C21(C2x) + E21(E2x) + A31(A3x) + C31(C3x) + E31(E3x) \tag{2.5.14}$$

where:

$$A1x = -\frac{B41}{A41}(A1y) - \frac{C41}{A41}(A1z) \quad C1x = -\frac{B41}{A41}(C1y) - \frac{C41}{A41}(C1z) \quad E1x = -\frac{B41}{A41}(E1y) - \frac{C41}{A41}(E1z)$$

$$A2x = -\frac{B41}{A41}(A2y) - \frac{C41}{A41}(A2z) \quad C2x = -\frac{B41}{A41}(C2y) - \frac{C41}{A41}(C2z) \quad E2x = -\frac{B41}{A41}(E2y) - \frac{C41}{A41}(E2z)$$

$$A3x = -\frac{B41}{A41}(A3y) - \frac{C41}{A41}(A3z) \quad C3x = -\frac{B41}{A41}(C3y) - \frac{C41}{A41}(C3z) \quad E3x = -\frac{B41}{A41}(E3y) - \frac{C41}{A41}(E3z)$$

Substituting the values of $\Delta(1,z)$ from eq. (2.5.12), $\Delta(1,y)$ from eq. (2.5.13) and $\Delta(1,x)$ from eq. (2.5.14) into eq. (2.5.9) the value of $\Delta\sigma_1$ is obtained as follows:

$$\Delta\sigma_1 = \frac{A31}{n_1} - \frac{B31}{n_1} A11(A1x) - \frac{B31}{n_1} C11(C1x) - \frac{B31}{n_1} E11(E1x) - \frac{B31}{n_1} A21(A2x)$$

$$- \frac{B31}{n_1} C21(C2x) - \frac{B31}{n_1} E21(E2x) - \frac{B31}{n_1} A31(A3x) - \frac{B31}{n_1} C31(C3x)$$

$$- \frac{B31}{n_1} E31(E3x) + \frac{C31}{n_1} - \frac{D31}{n_1} A11(A1y) - \frac{D31}{n_1} C11(C1y)$$

$$- \frac{D31}{n_1} E11(E1y) - \frac{D31}{n_1} A21(A2y) - \frac{D31}{n_1} C21(C2y) - \frac{D31}{n_1} E21(E2y)$$

$$- \frac{D31}{n_1} A31(A3y) - \frac{D31}{n_1} C31(C3y) - \frac{D31}{n_1} E31(E3y) + \frac{E31}{n_1} - \frac{F31}{n_1} A11(A1z)$$

$$- \frac{F31}{n_1} C11(C1z) - \frac{F31}{n_1} E11(E1z) - \frac{F31}{n_1} A21(A2z) - \frac{F31}{n_1} C21(C2z)$$

$$- \frac{F31}{n_1} E21(E2z) - \frac{F31}{n_1} A31(A3z) - \frac{F31}{n_1} C31(C3z) - \frac{F31}{n_1} E31(E3z)$$

collecting terms

$$\Delta\sigma_1 = A11(QA11) + C11(QC11) + E11(QE11) + A21(QA21) + C21(QC21)$$

$$+ E21(QE21) + A31(QA31) + C31(QC31) + E31(QE31)$$

where:

$$QA11 = -\frac{B31}{n_1}(A1x) - \frac{D31}{n_1}(A1y) - \frac{F31}{n_1}(A1z)$$

$$QC11 = -\frac{B31}{n_1}(C1x) - \frac{D31}{n_1}(C1y) - \frac{F31}{n_1}(C1z)$$

$$QE11 = -\frac{B31}{n_1}(E1x) - \frac{D31}{n_1}(E1y) - \frac{F31}{n_1}(E1z)$$

$$QA21 = -\frac{B31}{n_1}(A2x) - \frac{D31}{n_1}(A2y) - \frac{F31}{n_1}(A2z)$$

$$QC21 = -\frac{B31}{n_1}(C2x) - \frac{D31}{n_1}(C2y) - \frac{F31}{n_1}(C2z)$$

$$QE21 = -\frac{B31}{n_1}(E2x) - \frac{D31}{n_1}(E2y) - \frac{F31}{n_1}(E2z)$$

$$QA31 = -\frac{B31}{n_1}(A3x) - \frac{D31}{n_1}(A3y) - \frac{F31}{n_1}(A3z) + \frac{1}{n_1}$$

$$QC31 = -\frac{B31}{n_1}(C3x) - \frac{D31}{n_1}(C3y) - \frac{F31}{n_1}(C3z) + \frac{1}{n_1}$$

$$QE31 = -\frac{B31}{n_1}(E3x) - \frac{D31}{n_1}(E3y) - \frac{F31}{n_1}(E3z) + \frac{1}{n_1}$$

Since from eqs. (2.5.8)

$$A11 = \ell_1 \Delta\sigma_x, \quad C11 = m_1 \Delta\tau_{yx}, \quad E11 = n_1 \Delta\tau_{xz}$$
$$A21 = \ell_1 \Delta\tau_{xy}, \quad C21 = m_1 \Delta\sigma_y, \quad E21 = n_1 \Delta\tau_{yz}$$
$$A31 = \ell_1 \Delta\tau_{zx}, \quad C31 = m_1 \Delta\tau_{zy}, \quad E31 = n_1 \Delta\sigma_z$$

and assuming that $\Delta\tau_{xy} = \Delta\tau_{yx}$, $\Delta\tau_{yz} = \Delta\tau_{zy}$ and $\Delta\tau_{xz} = \Delta\tau_{zx}$, then

$$\Delta\sigma_1 = \Delta\sigma_x(Qx1) + \Delta\sigma_y(Qy1) + \Delta\sigma_z(Qz1) + \Delta\tau_{xy}(Qxy1) + \Delta\tau_{yz}(Qyz1) + \Delta\tau_{zx}(Qzx1) \qquad (2.5.15)$$

where:

$$Qx1 = \ell_1(QA11)$$
$$Qy1 = m_1(QC21)$$
$$Qz1 = n_1(QE31)$$
$$Qxy1 = \ell_1(QA21) + m_1(QC11)$$
$$Qyz1 = m_1(QC31) + n_1(QE21)$$
$$Qzx1 = \ell_1(QA31) + n_1(QE11)$$

2.5.2.2 Relations Between Increment of Principal Stress, $\Delta\sigma_3$ with Increments of Cartesian Stress

The procedures followed to obtain $\Delta\sigma_3$ in terms of increments of cartesian stress are the same as the procedures followed for $\Delta\sigma_1$ and consist on the following.

Substituting i = 3 in eq. (2.5.3) the following equations are obtained:

$$A13 - \Delta\sigma_3 \ell_3 - \Delta(3,x)B13 + C13 - \Delta(3,y)D13 + E13 - \Delta(3,z)F13 = 0 \quad (2.5.4a)$$

$$A23 - \Delta(3,x)B23 + C23 - \Delta\sigma_3 m_3 - \Delta(3,y)D23 + E23 - \Delta(3,z)F23 = 0 \quad (2.5.5a)$$

$$A33 - \Delta(3,x)B33 + C33 - \Delta(3,y)D33 + E33 - \Delta\sigma_3 n_3 - \Delta(3,z)F23 = 0 \quad (2.5.6a)$$

$$A43\ \Delta(3,x) + B43\ \Delta(3,y) + C43\ \Delta(3,z) = 0 \quad (2.5.7a)$$

where:

$A13 = \Delta\sigma_x \cos(3,x)$ $\quad A23 = \Delta\tau_{yx}\cos(3,x)$ $\quad A33 = \Delta\tau_{zx}\cos(3,x)$

$B13 = (\sigma_x - \sigma_3)\sin(1,x)$ $\quad B23 = \tau_{yx}\sin(3,x)$ $\quad B33 = \tau_{zx}\sin(3,x)$

$C13 = \Delta\tau_{xy}\cos(3,y)$ $\quad C23 = \Delta\sigma_y\cos(3,y)$ $\quad C33 = \Delta\tau_{zy}\cos(3,y)$

$D13 = \tau_{xy}\sin(3,y)$ $\quad D23 = (\sigma_y - \sigma_3)\sin(3,y)$ $\quad D33 = \tau_{zy}\sin(3,y)$

$E13 = \Delta\tau_{xz}\cos(3,z)$ $\quad E23 = \Delta\tau_{yz}\cos(3,z)$ $\quad E33 = \Delta\sigma_z\cos(3,z)$

$F13 = \tau_{xz}\sin(3,z)$ $\quad F23 = \tau_{yz}\sin(3,z)$ $\quad F33 = (\sigma_z - \sigma_3)\sin(3,z)$

$A43 = \cos(3,x)\sin(3,x)$ $\quad \ell_3 = \cos(3,x)$

$B43 = \cos(3,y)\sin(3,y)$ $\quad m_3 = \cos(3,y)$

$C43 = \cos(3,z)\sin(3,z)$ $\quad n_3 = \cos(3,z)$

Note: all the above equations are designated as (2.5.8a).

- Evaluation of the System of Equations (2.4.4a) to (2.4.7a)

From Eq. (2.5.4a)

$$\boxed{\Delta\sigma_3 = \frac{A13}{\ell_3} - \frac{B13}{\ell_3}\,\Delta(3,x) + \frac{C13}{\ell_3} - \frac{D13}{\ell_3}\,\Delta(3,x) + \frac{E13}{\ell_3} - \frac{F13}{\ell_3}\,\Delta(3,z)} \qquad (2.5.9a)$$

and from eq. (2.5.7a)

$$\boxed{\Delta(3,x) = -\frac{B43}{A43}\,\Delta(3,x) - \frac{C43}{A43}\,\Delta(3,z)} \qquad (2.5.10a)$$

Substituting eqs. (2.5.9a) and (2.5.10a) into eq. (2.5.5a) the following is obtained:

$$A23 + \frac{B23\ B43}{A43}\,\Delta(3,y) + \frac{B23\ C43}{A43}\,\Delta(3,z) + C23 - A13\,\frac{m_3}{\ell_3}$$

$$+ B13\,\frac{m_3}{\ell_3}\left(-\frac{B43}{A43}\,\Delta(3,y) - \frac{C43}{A43}\,\Delta(3,z)\right) - C13\,\frac{m_3}{\ell_3} + D13\,\frac{m_3}{\ell_3}\,\Delta(3,y)$$

$$- E13\,\frac{m_3}{\ell_3} + F13\,\frac{m_3}{\ell_3}\,\Delta(3,z) - D23\,\Delta(3,y) + E23 - F23\,\Delta(3,z) = 0$$

Collecting terms in the above equation:

$$\Delta(3,y)\ \left[\frac{B23\ B43}{A43} - \frac{B13\ B43}{A43}\frac{m_3}{\ell_3} + D13\frac{m_3}{\ell_3} - D23\right] + \Delta(3,z)\ \left[\frac{B23\ C43}{A43}\right.$$

$$\left. - \frac{B13\ C43}{A43}\frac{m_3}{\ell_3} + F13\frac{m_3}{\ell_3} - F23\right] + A23 + C23 + E23 - A13\frac{m_3}{\ell_3}$$

$$- C13\frac{m_3}{\ell_3} - E13\frac{m_3}{\ell_3} = 0$$

Designating the terms inside the square brackets by FM3 and FJ3 the following is obtained:

$$\Delta(3,y)[FM3] + \Delta(3,z)[FJ3] + A23 + C23 + E23 - A13\frac{m_3}{\ell_3} - C13\frac{m_3}{\ell_3} = 0$$

and solving for $\Delta(3,y)$:

$$\boxed{\Delta(3,y) = -\frac{FJ3}{FM3}\Delta(3,z) - \frac{A23}{FM3} - \frac{C23}{FM3} - \frac{E23}{FM3} + \frac{A13}{FM3}\frac{m_3}{\ell_3} + \frac{C13}{FM3}\frac{m_3}{\ell_3} + \frac{E13}{FM3}\frac{m_3}{\ell_3}}$$

(2.5.11a)

Substituting the values of $\Delta\sigma_3$ from eq. (2.5.9a) and $\Delta(3,x)$ from eq. (2.5.10a) into eq. (2.5.6a) the following is obtained:

$$A33 + \frac{B33\ B43}{A43}\Delta(3,y) + \frac{B33\ C43}{A43}\Delta(3,z) + C33 - D33\ \Delta(3,y) + E33$$

$$- A13\frac{n_3}{\ell_3} - B13\frac{n_3}{\ell_3}\frac{B43}{A43}\Delta(3,y) - \frac{B13\ C43}{A43}\frac{n_3}{\ell_3}\Delta(3,z) - C13\frac{n_3}{\ell_3}$$

$$+ D13\frac{n_3}{\ell_3}\Delta(3,y) - E13\frac{n_3}{\ell_3} + F13\frac{n_3}{\ell_3}\Delta(3,z) - F33\ \Delta(3,z) = 0$$

Collecting terms the following is obtained

$$\Delta(3,y)\ \left[\frac{B33\ B43}{A43} - D33 - \frac{B13\ B43}{A43}\ \frac{n_3}{\ell_3} + D13\ \frac{n_3}{\ell_3}\right] + \Delta(3,z)\ \left(\frac{B33\ C43}{A43}\right.$$

$$\left. - \frac{B13\ C43}{A43}\ \frac{n_3}{\ell_3} + F13\ \frac{n_3}{\ell_3} - F33\right) + A33 + C33 + E33 - A13\ \frac{n_3}{\ell_3}$$

$$- C13\ \frac{n_3}{\ell_3} - E13\ \frac{n_3}{\ell_3} = 0$$

Designating the term inside the square bracket by FP3 and substituting the value of $\Delta(3,y)$ from eq. (2.5.11a) the following is obtained:

$$- \frac{FP3\ FJ3}{FM3}\ \Delta(3,z) - \frac{FP3}{FM3}\ A23 - \frac{FP3}{FM3}\ C23 - \frac{FP3}{FM3}\ E23 + \frac{FP3}{FM3}\ \frac{m_3}{\ell_3}\ A13$$

$$+ \frac{FP3}{FM3}\ \frac{m_3}{\ell_3}\ C13 + \frac{FP3}{FM3}\ \frac{m_3}{\ell_3}\ E13 + \Delta(3,z)\ \left(\frac{B33\ C43}{A43} - \frac{B13\ C43}{A43}\ \frac{n_3}{\ell_3}\right.$$

$$\left. + F13\ \frac{n_3}{\ell_3} - F33\right) + A33 + C33 + E33 - A13\ \frac{n_3}{\ell_3} - C13\ \frac{n_3}{\ell_3} - E13\ \frac{n_3}{\ell_3} = 0$$

Collecting terms:

$$\Delta(3,z)\ \left[- \frac{FP3\ FJ3}{FM3} + \frac{B33\ C43}{A43} - \frac{B13\ C43}{A43}\ \frac{n_3}{\ell_3} + F13\ \frac{n_3}{\ell_3} - F33\right] + A33$$

$$+ C33 + E33 + A23\ \left(- \frac{FP3}{FM3}\right) + C23\ \left(- \frac{FP3}{FM3}\right) + E23\ \left(- \frac{FP3}{FM3}\right)$$

$$+ A13\ \left(\frac{FP3}{FM3}\ \frac{m_3}{\ell_3} - \frac{n_3}{\ell_3}\right) + C13\ \left(\frac{FP3}{FM3}\ \frac{m_3}{\ell_3} - \frac{n_3}{\ell_3}\right) + E13\ \left(\frac{FP3}{FM3}\ \frac{m_3}{\ell_3} - \frac{n_3}{\ell_3}\right) = 0$$

Designating the term inside the square bracket by FL3 and solving for $\Delta(3,z)$ the following is obtained:

$$\Delta(3,z) = A13(A13z) + C13(C13z) + E13(E13z) + A23(A23z) + C23(C23z) + E23(E23z) + A33(A33z) + C33(C33z) + E33(E33z)$$

(2.5.12a)

where:

$$A13z = C13z = E13z = -\left(\frac{FP3}{FM3}\frac{m_3}{\ell_3} - \frac{n_3}{\ell_3}\right)\frac{1}{FL3}$$

$$A23z = C23z = E23z = \frac{FP3}{FM3}\frac{1}{FL3}$$

$$A33z + C33z + E33z = -\frac{1}{FL3}$$

Substituting the value of $\Delta(3,z)$ from eq. (2.5.12a) into eq. (2.5.11a) the value of $\Delta(3,y)$ is obtained:

$$\Delta(3,y) = -\frac{FJ3}{FM3}A13(A13z) - \frac{FJ3}{FM3}C13(C13z) - \frac{FJ3}{FM3}E13(E13z) - \frac{FJ3}{FM3}A23(A23z) - \frac{FJ3}{FM3}C23(C23z) - \frac{FJ3}{FM3}E23(E23z) - \frac{FJ3}{FM3}A33(A33z) - \frac{FJ3}{FM3}C33(C33z) - \frac{FJ3}{FM3}E33(E33z) - \frac{A23}{FM3} - \frac{C23}{FM3} - \frac{E23}{FM3} + \frac{A13}{FM3}\frac{m_3}{\ell_3} + \frac{C13}{FM3}\frac{m_3}{\ell_3} + \frac{E13}{FM3}\frac{m_3}{\ell_3}$$

rearranging terms:

$$\Delta(3,y) = A13(A13y) + C13(C13y) + E13(E13y) + A23(A23y) + C23(C23y) + E23(E23y) + A33(A33y) + C33(C33y) + E33(E33y)$$

(2.5.13a)

where:

$$A13y = C13y = E13y = -\frac{FJ3}{FM3}(A13z) + \frac{1}{FM3}\frac{m_3}{\ell_3}$$

$$A23y + C23y + E23y = -\frac{FJ3}{FM3}(A23z) - \frac{1}{FM3}$$

$$A33y = C33y = E33y = -\frac{FJ3}{FM3}(A33z)$$

Substituting $\Delta(3,z)$ from eq. (2.5.12a) and $\Delta(3,y)$ from eq. (2.5.13a) into eq. (2.5.10a), $\Delta(3,x)$ is obtained as follows:

$$\Delta(3,x) = A13(A13x) + C13(C13x) + E13(C13x) + A23(A23x) + C23(C23x) + E23(E23x) + A33(A33x) + C33(C33x) + E33(E33x)$$

(2.5.14a)

where:

$$A13x = -\frac{B43}{A43}(A13y) - \frac{C43}{A43}(A13z) \quad C13x = -\frac{B43}{A43}(C13y) - \frac{C43}{A43}(C13z) \quad E13x = -\frac{B43}{A43}(E13y) - \frac{C43}{A43}(E13z)$$

$$A23x = -\frac{B43}{A43}(A23y) - \frac{C43}{A43}(A23z) \quad C23x = -\frac{B43}{A43}(C23y) - \frac{C43}{A43}(C23z) \quad E23x = -\frac{B43}{A43}(E23y) - \frac{C43}{A43}(E23z)$$

$$A33x = -\frac{B43}{A43}(A33y) - \frac{C43}{A43}(A33z) \quad C33x = -\frac{B43}{A43}(C33y) - \frac{C43}{A43}(C33z) \quad E33x = -\frac{B43}{A43}(E33y) - \frac{C43}{A43}(E33z)$$

Substituting the values of $\Delta(3,z)$ from eq. (2.5.12a), $\Delta(3,y)$ from eq. (2.5.13a) and $\Delta(3,x)$ from eq. (2.5.14a) into eq. (2.5.9a) the value of $\Delta\sigma_3$ is obtained as follows:

$$\Delta\sigma_3 = A13(QA13) + C13(QC13) + E13(QE13) + A23(QA23) + C23(QC23) + E23(QE23) + A33(QA33) + C33(QC33) + E33(QE33)$$

where:

$$QA13 = -\frac{B13}{\ell_3}(A13x) - \frac{D13}{\ell_3}(A13y) - \frac{F13}{\ell_3}(A13z) + \frac{1}{\ell_3}$$

$$QC13 = -\frac{B13}{\ell_3}(C13x) - \frac{D13}{\ell_3}(C13y) - \frac{F13}{\ell_3}(C13z) + \frac{1}{\ell_3}$$

$$QE13 = -\frac{B13}{\ell_3}(E13x) - \frac{D13}{\ell_3}(E13y) - \frac{F13}{\ell_3}(E13z) + \frac{1}{\ell_3}$$

$$QA23 = -\frac{B13}{\ell_3}(A23x) - \frac{D13}{\ell_3}(A23y) - \frac{F13}{\ell_3}(A23z)$$

$$QC23 = -\frac{B13}{\ell_3}(C23x) - \frac{D13}{\ell_3}(C23y) - \frac{F13}{\ell_3}(C23z)$$

$$QE23 = -\frac{B13}{\ell_3}(E23x) - \frac{D13}{\ell_3}(E23y) - \frac{F13}{\ell_3}(E23z)$$

$$QA33 = -\frac{B13}{\ell_3}(A33x) - \frac{D13}{\ell_3}(A33y) - \frac{F13}{\ell_3}(A33z)$$

$$QC33 = -\frac{B13}{\ell_3}(C33x) - \frac{D13}{\ell_3}(C33y) - \frac{F13}{\ell_3}(C33z)$$

$$QE33 = -\frac{B13}{\ell_3}(E33x) - \frac{D13}{\ell_3}(E33y) - \frac{F13}{\ell_3}(E33z)$$

Since from eqs. (2.5.8a)

$$A13 = \ell_3 \Delta\sigma_x \quad , \quad C13 = m_3 \Delta\tau_{yx} \quad , \quad E13 = n_3 \Delta\tau_{zx}$$

$$A23 = \ell_3 \Delta\tau_{xy} \quad , \quad C23 = m_3 \Delta\sigma_y \quad , \quad E23 = n_3 \Delta\tau_{yz}$$

$$A33 = \ell_3 \Delta\tau_{zx} \quad , \quad C33 = m_3 \Delta\tau_{zy} \quad , \quad E33 = n_3 \Delta\sigma_z$$

and assuming that $\Delta\tau_{xy} = \Delta\tau_{yx}$, $\Delta\tau_{yz} = \Delta\tau_{zy}$ and $\Delta\tau_{xz} = \Delta\tau_{zx}$, then

$$\Delta\sigma 3 = \Delta\sigma_x(Qx3) + \Delta\sigma_y(Qy3) + \Delta\sigma_z(Qz3) + \Delta\tau_{xy}(Qxy3) + \Delta\tau_{yz}(Qyz3) + \Delta\tau_{zx}(Qzx3) \qquad (2.5.15a)$$

where:

$$Qx3 = \ell_3(QA13)$$

$$Qy3 = m_3(QC23)$$

$$Qz3 = n_3(QE33)$$

$$Qxy3 = \ell_3(QA23) + m_3(QC13)$$

$$Qyz3 = m_3(QC33) + n_3(QE23)$$

$$Qzx3 = \ell_3(QA33) + n_3(QE13)$$

2.5.2.3 Relations Between Increment of the Principal Stress, $\Delta\sigma_2$ with Increments of Cartesian Stress

Substituting i = 2 in eqs. (2.5.3) the following equations are obtained:

$$A12 - \Delta\sigma_2 \ell_2 - \Delta(2,x)B12 + C12 - \Delta(2,y)D12 + E12 - \Delta(2,z)F12 = 0 \quad (2.5.4b)$$

$$A22 - \Delta(2,x)B22 + C22 - \Delta\sigma_2 m_2\ \Delta(2,y)D22 + E22 - \Delta(2,z)F22 = 0 \quad (2.5.5b)$$

$$A32 - \Delta(2,x)B32 + C32 - \Delta(2,y)D32 + E32 - \Delta\sigma_2 n_2 - \Delta(2,z)F32 = 0 \quad (2.5.6b)$$

$$A42\ \Delta(2,x) + B42\ \Delta(2,y) + C42\ \Delta(2,z) = 0 \quad (2.5.7b)$$

where:

$A12 = \Delta\sigma_x \ell_2$ $\quad A22 = \Delta\tau_{yx} \ell_2$ $\quad A32 = \Delta\tau_{zx} \ell_2$

$B12 = (\sigma_x - \sigma_2)\sin(2,x)$ $\quad B22 = \tau_{yx}\sin(2,x)$ $\quad B32 = \tau_{zx}\sin(2,x)$

$C12 = \Delta\tau_{xy} m_2$ $\quad C22 = \Delta\sigma_y m_2$ $\quad C32 = \Delta\tau_{zy} m_2$

$D12 = \tau_{xy}\sin(2,y)$ $\quad D22 = (\sigma_y - \sigma_2)\sin(2,y)$ $\quad D32 = \tau_{zy}\sin(2,y)$

$E12 = \Delta\tau_{xz} n_2$ $\quad E22 = \Delta\tau_{yz} n_2$ $\quad E32 = \Delta\sigma_z n_2$

$F12 = \tau_{xz}\sin(2,z)$ $\quad F22 = \tau_{yz}\sin(2,z)$ $\quad F32 = (\sigma_z - \sigma_2)\sin(2,z)$

$A42 = \ell_2 \sin(2,x)$ $\quad \ell_2 = \cos(2,x)$

$B42 = m_2 \sin(2,y)$ $\quad m_2 = \cos(2,y)$

$C42 = n_2 \sin(2,z)$ $\quad n_2 = \cos(2,z)$

Note: all the above equations are designated as (2.5.8b).

- Evaluation of the System of equations (2.5.4b) to (2.5.7b)

From eq. (2.5.5b) $\Delta\sigma_2$ is obtained:

$$\Delta\sigma_2 = \frac{A22}{m_2} - \frac{B22}{m_2}\ \Delta(2,x) - \frac{D22}{m_2}\Delta(2,y) + \frac{E22}{m_2} - \frac{F22}{m_2}\Delta(2,z) + \frac{C22}{m_2} \tag{2.5.9b}$$

and from eq. (2.5.7b)

$$\Delta(2,x) = -\frac{B42}{A42}\Delta(2,y) - \frac{C42}{A42}\Delta(2,z) \tag{2.5.10b}$$

Substituting eqs. (2.5.9b) and (2.5.10b) into eq. (2.5.6b) the following is obtained:

$$A32 + \frac{B32\ B42}{A42}\Delta(2,y) + \frac{B32\ C42}{A42}\Delta(2,z) + C32 - \Delta(2,y)D32 + E32 - A22\frac{n_2}{m_2}$$

$$- \frac{n_2}{m_2}\frac{B22\ B42}{A42}\Delta(2,y) - \frac{n_2}{m_2}\frac{B22\ C42}{A42}\Delta(2,z) + \frac{n_2}{m_2}D22\ \Delta(2,y)$$

$$- \frac{n_2}{m_2}E22 + \frac{n_2}{m_2}F22\ \Delta(2,z) - \frac{n_2}{m_2}C22 - F32\ \Delta(2,z) = 0$$

collecting terms in the above equation:

$$\Delta(2,y)\ \left[\frac{B32\ B42}{A42} - D32 - \frac{n_2}{m_2}\frac{B22\ B42}{A42} + \frac{n_2}{m_2} D22\right] + \Delta(2,z)\ \left[\frac{B32\ C42}{A42}\right.$$

$$\left. - \frac{n_2}{m_2}\frac{B22\ C42}{A42} + \frac{n_2}{m_2} F22 - F32\right] - A22\frac{n_2}{m_2} - C22\frac{n_2}{m_2} - E22\frac{n_2}{m_2}$$

$$+ A32 + C32 + E32 = 0$$

Designating the terms inside the square brackets by FM2 and FJ2 the following is obtained:

$$\Delta(2,y)[FM2] + \Delta(2,z)[FJ2] - A22\frac{n_2}{m_2} - C22\frac{n_2}{m_2} - E22\frac{n_2}{m_2}$$

$$+ A32 + C32 + E32 = 0$$

solving for $\Delta(2,y)$

$$\boxed{\Delta(2,y) = -\frac{FJ2}{FM2}\Delta(2,z) + \frac{A22}{FM2}\frac{n_2}{m_2} + \frac{C22}{FM2}\frac{n_2}{m_2} + \frac{E22}{FM2}\frac{n_2}{m_2} - \frac{A32}{FM2} - \frac{C32}{FM2} - \frac{E32}{FM2}}$$

(2.5.11b)

Substituting now the values of $\Delta\sigma_2$ from eq. (2.5.9b) and $\Delta(2,x)$ from eq. (2.5.10b) into eq. (2.5.4b) the following is obtained:

$$A12 - A22\frac{\ell_2}{m_2} + B22\frac{\ell_2}{m_2}\Delta(2,x) + D22\frac{\ell_2}{m_2}\frac{B22\ C42}{A42}\Delta(2,z) + D22\frac{\ell_2}{m_2}\Delta(2,y)$$

$$- E22\frac{\ell_2}{m_2} + F22\frac{\ell_2}{m_2}\Delta(2,z) - C22\frac{\ell_2}{m_2} + \frac{B12\ B42}{A42}\Delta(2,y) + \frac{B12\ C42}{A42}\Delta(2,z)$$

$$+ C12 - \Delta(2,y)D12 + E12 - \Delta(2,z)F12 = 0$$

collecting terms the following is obtained:

$$\Delta(2,y)\ \left[-\frac{\ell_2}{m_2}\ \frac{B22\ B42}{A42} + D22\ \frac{\ell_2}{m_2} + \frac{B12\ B42}{A42} - D12\right] + \Delta(2,z)$$

$$\left(-\frac{\ell_2}{m_2}\ \frac{B22\ C42}{A42} + F22\ \frac{\ell_2}{m_2} + \frac{B12\ C42}{A42} - F12\right) + A12 + C12 + E12$$

$$- A22\ \frac{\ell_2}{m_2} - C22\ \frac{\ell_2}{m_2} - E22\ \frac{\ell_2}{m_2} = 0$$

Designating the term inside the square bracket by FP2 and substituting the value of $\Delta(2,y)$ from eq. (2.5.11b) the following is obtained:

$$\Delta(2,z)\ \left[-\ FP2\ \frac{FJ2}{FM2} - \frac{\ell_2}{m_2}\ \frac{B22\ C42}{A42} + F22\ \frac{\ell_2}{m_2} + \frac{B12\ C42}{A42} - F12\right]$$

$$+ \frac{FP2}{FM2}\ A22\ \frac{n_2}{m_2} + \frac{FP2}{FM2}\ C22\ \frac{n_2}{m_2} + \frac{FP2}{FM2}\ E22\ \frac{n_2}{m_2} - \frac{FP2}{FM2}\ A32 - \frac{FP2}{FM2}\ C32$$

$$- \frac{FP2}{FM2}\ E32 + A12 + C12 + E12 - A22\ \frac{\ell_2}{m_2} - C22\ \frac{\ell_2}{m_2} - E22\ \frac{\ell_2}{m_2} = 0$$

Designating the term in brackets by FL2 and rearranging:

$$\Delta(2,z)\ [FL2] + A12 + C12 + E12 + A22\ \left(\frac{FP2}{FM2}\ \frac{n_2}{m_2} - \frac{\ell_2}{m_2}\right) + C22\ \left(\frac{FP2}{FM2}\ \frac{n_2}{m_2} - \frac{\ell_2}{m_2}\right)$$

$$+ E22\ \left(\frac{FP2}{FM2}\ \frac{n_2}{m_2} - \frac{\ell_2}{m_2}\right) - \frac{FP2}{FM2}\ A32 - \frac{FP2}{FM2}\ C32 - \frac{FP2}{FM2}\ E32 = 0$$

solving for $\Delta(2,z)$:

$$\Delta(2,z) = A12(A12z) + C12(C12z) + E12(E12z) + A22(A22z) + C22(C22z) + E22(E22z) + A32(A32z) + C32(C32z) + E32(E32z) \tag{2.5.12b}$$

where:

$$A12z = C12z = E12z = -\frac{1}{FL2}$$

$$A22z = C22z = E22z = -\left(\frac{FP2}{FM2}\frac{n_2}{m_2} - \frac{\ell_2}{m_2}\right)\frac{1}{FL2}$$

$$A32z = C32z = E32z = \frac{FP2}{FM2\ FL2}$$

Substituting the value of $\Delta(2,z)$ from above into eq. (2.5.11b) the value of $\Delta(2,y)$ is obtained as follows:

$$\Delta(2,y) = -\left(\frac{FJ2}{FM2}(A12z)\right)A12 - \left(\frac{FJ2}{FM2}(C12z)\right)C12 - \left(\frac{FJ2}{FM2}(E12z)\right)E12$$

$$+ \left(\frac{1}{FM2}\frac{n_2}{m_2} - \frac{FJ2}{FM2}(A22z)\right)A22 + \left(\frac{1}{FM2}\frac{n_2}{m_2} - \frac{FJ2}{FM2}(C22z)\right)C22$$

$$+ \left(\frac{1}{FM2}\frac{n_2}{m_2} - \frac{FJ2}{FM2}(E22z)\right)E22 - \left(\frac{1}{FM2} + \frac{FJ2}{FM2}(A32z)\right)A32$$

$$- \left(\frac{1}{FM2} + \frac{FJ2}{FM2}(32z)\right)C32 - \left(\frac{1}{FM2} + \frac{FJ2}{FM2}(E32z)\right)E32$$

or

$$\Delta(2,y) + (A12y)A12 + (C12y)C12 + (E12y)E12 + (A22y)A22 + (C22y)C22 + (E22y)E22 + (A32y)A32 + (C32y)C32 + (E32y)E32 \tag{2.5.13b}$$

where:

$$A12y = C12y = E12y = - A12z \frac{FJ2}{FM2}$$

$$A22y = C22y = E22y = + \frac{1}{FM2}\frac{n_2}{m_2} - \frac{FJ2}{FM2} A22z$$

$$A32y = C32y = E32y = - \frac{1}{FM2} - \frac{FJ2}{FM2} A32z$$

Substituting $\Delta(2,z)$ from eq. (2.5.12b) and $\Delta(2.y)$ from eq. (2.5.13b) into eq. (2.5.10b) $\Delta(2,x)$ is obtained:

$$\Delta(2,x) + A12(A12x) + C12(C12x) + E12(E12x) + A22(A22x) + C22(C22x) + E22(E22x) + A32(A32x) + C32(C32x) + E32(E32x) \tag{2.5.14b}$$

where:

$$A12x = -\frac{B42}{A42}(A12y) - \frac{C42}{A42}(A12z) \quad C12x = -\frac{B42}{A42}(C12y) - \frac{C42}{A42}(C12z) \quad E12x = -\frac{B42}{A42}(E12y) - \frac{C42}{A42}(E12z)$$

$$A22x = -\frac{B42}{A42}(A22y) - \frac{C42}{A42}(A22z) \quad C22x = -\frac{B42}{A42}(C22y) - \frac{C42}{A42}(C22z) \quad E22x = -\frac{B42}{A42}(E22y) - \frac{C42}{A42}(E22z)$$

$$A32x = -\frac{B42}{A42}(A32y) - \frac{C42}{A42}(A32z) \quad C32x = -\frac{B42}{A42}(C32y) - \frac{C42}{A42}(C32z) \quad E32x = -\frac{B42}{A42}(E32y) - \frac{C42}{A42}(E32z)$$

Substituting the values of $\Delta(2,z)$ from eq. (2.5.12b), $\Delta(2,y)$ from eq., (2.5.13b) and $\Delta(2,x)$ from eq. (2.5.14b) into eq. (2.5.9b) the value of $\Delta\sigma_2$ is obtained as follows:

$$\Delta\sigma_2 = \frac{A22}{m_2} - \frac{B22\ A12}{m_2}(A12x) - \frac{B22\ C12}{m_2}(C12x) - \frac{B22\ E12}{m_2}(E12x)$$

$$- \frac{B22\ A22}{m_2}(A22x) - \frac{B22\ C22}{m_2}(C22x) - \frac{B22\ E22}{m_2}(E22x) - \frac{B22\ A32}{m_2}(A32x)$$

$$- \frac{B22\ C32}{m_2}(C32x) - \frac{B22\ E32}{m_2}(E32x) - \frac{D22\ A12}{m_2}(A12y) - \frac{D22\ C12}{m_2}(C12y)$$

$$- \frac{D22\ E12}{m_2}(E12y) - \frac{D22\ A22}{m_2}(A22y) - \frac{D22\ C22}{m_2}(C22y) - \frac{D22\ E22}{m_2}(E22y)$$

$$- \frac{D22\ A32}{m_2}(A32y) - \frac{D22\ C32}{m_2}(C32y) - \frac{D22\ E32}{m_2}(E32y) + \frac{E22}{m_2}$$

$$- \frac{F22\ A12}{m_2}(A12z) - \frac{F22\ C12}{m_2}(C12z) - \frac{F22\ E12}{m_2}(E12z) - \frac{F22\ A22}{m_2}(A22z)$$

$$- \frac{F22\ C22}{m_2}(C22z) - \frac{F22\ E22}{m_2}(E22z) - \frac{F22\ A32}{m_2}(A32z) - \frac{F22\ C32}{m_2}(C32z)$$

$$- \frac{F22\ E32}{m_2}(E32z) + \frac{C22}{m_2}$$

collecting terms

$$\Delta\sigma_2 = A12(QA12) + C12(QC12) + E12(QE12) + A22(QA22) + C22(QC22)$$
$$+ E22(QE22) + A32(QA32) + C32(QC32) + E32(QE32)$$

where:

$$QA12 = -\frac{B22}{m_2}(A12x) - \frac{D22}{m_2}(A12y) - \frac{F22}{m_2}(A12z)$$

$$QC12 = -\frac{B22}{m_2}(C12x) - \frac{D22}{m_2}(C12y) - \frac{F22}{m_2}(C12z)$$

$$QE12 = -\frac{B22}{m_2}(E12x) - \frac{D22}{m_2}(E12y) - \frac{F22}{m_2}(E12z)$$

$$QA22 = -\frac{B22}{m_2}(A22x) - \frac{D22}{m_2}(A22y) - \frac{F22}{m_2}(A22z) + \frac{1}{m_2}$$

$$QC22 = -\frac{B22}{m_2}(C22x) - \frac{D22}{m_2}(C22y) - \frac{F22}{m_2}(C22z) + \frac{1}{m_2}$$

$$QE22 = -\frac{B22}{m_2}(E22x) - \frac{D22}{m_2}(E22y) - \frac{F22}{m_2}(E22z) + \frac{1}{m_2}$$

$$QA32 = -\frac{B22}{m_2}(A32x) - \frac{D22}{m_2}(A32y) - \frac{F22}{m_2}(A32z)$$

$$QC32 = -\frac{B22}{m_2}(C32x) - \frac{D22}{m_2}(C32y) - \frac{F22}{m_2}(C32z)$$

$$QE32 = -\frac{B22}{m_2}(E32x) - \frac{D22}{m_2}(E32y) - \frac{F22}{m_2}(E32z)$$

Since from eqs. (2.5.8b)

$$A12 = \Delta\sigma_x \ell_2 \qquad C12 = \Delta\tau_{yx} m_2 \qquad E12 = \Delta\tau_{xz} n_2$$

$$A22 = \Delta\tau_{xy} \ell_2 \qquad C22 = \Delta\sigma_y m_2 \qquad E22 = \Delta\tau_{yz} n_2$$

$$A32 = \Delta\tau_{zx} \ell_2 \qquad C32 = \Delta\tau_{zy} m_2 \qquad E32 = \Delta\sigma_z n_2$$

and assuming that $\Delta\tau_{xy} = \Delta\tau_{yx}$; $\Delta\tau_{yz} = \Delta\tau_{zy}$; and $\Delta\tau_{xz} = \Delta\tau_{zx}$ then

$$\Delta\sigma_2 = \Delta\sigma_x(Qx2) + \Delta\sigma_y(Qy2) + \Delta\sigma_z(Qz2) + \Delta\tau_{xy}(Qxy2) + \Delta\tau_{yz}(Qyz2) + \Delta\tau_{zx}(Qzx2) \qquad (2.5.15b)$$

where:

$Qx2 = \ell_2(QA12)$

$Qy2 = m_2(QC22)$

$Qz2 = n_2(QE32)$

$Qxy2 = \ell_2(QA22)+m_2(QC12)$

$Qyz2 = m_2(QC32)+n_2(QE22)$

$Qzx2 = \ell_2(QA32)+n_2(QE12)$

APPENDIX 2.6

EVALUATION OF THE PLASTIC CONSTITUTIVE MATRIX $\{C^P\}$ OF THE SMP MODEL

2.6.1 3-DIMENSIONAL FORMULATION

2.6.2 2-DIMENSIONAL FORMULATION

2.6.3 AXISYMMETRIC FORMULATION

APPENDIX 2.6

Evaluation of the Plastic Constitutive Matrix $\{C^p\}$ of the SMP Model

2.6.1 3-Dimensional Formulation

Evaluation of the Plastic Constitutive Matrix $\{C^p\}$ of the SMP Model

Substituting eq. (2.55) into eq. (2.49) (see main text), the relationship between increments of plastic Cartesian strain $\{\Delta\epsilon^p\}$ and increment of Cartesian stress $\{\Delta\sigma\}$ are obtained and given by:

$$\begin{bmatrix} \Delta\epsilon_x^p \\ \Delta\epsilon_y^p \\ \Delta\epsilon_z^p \\ \Delta\gamma_{xy}^p \\ \Delta\gamma_{yz}^p \\ \Delta\gamma_{zx}^p \end{bmatrix} = \begin{bmatrix} CP(1,1) & CP(1,2) & CP(1,3) & CP(1,4) & CP(1,5) & CP(1,6) \\ CP(2,1) & CP(2,2) & CP(2,3) & CP(2,4) & CP(2,5) & CP(2,6) \\ CP(3,1) & CP(3,2) & CP(3,3) & CP(3,4) & CP(3,5) & CP(3,6) \\ CP(4,1) & CP(4,2) & CP(4,3) & CP(4,4) & CP(4,5) & CP(4,6) \\ CP(5,1) & CP(5,2) & CP(5,3) & CP(5,4) & CP(5,5) & CP(5,6) \\ CP(6,1) & CP(6,2) & CP(6,3) & CP(6,4) & CP(6,5) & CP(6,6) \end{bmatrix} \begin{bmatrix} \Delta\sigma_x \\ \Delta\sigma_y \\ \Delta\sigma_z \\ \Delta\tau_{xy} \\ \Delta\tau_{yz} \\ \Delta\tau_{zx} \end{bmatrix} \tag{2.6.1}$$

where:

$$CP(1,1) = \left(\sum_{i=1,3} M_i \ell_i^2\right) TMX/G_p \qquad CP(1,4) = \left(\sum_{i=1,3} M_i \ell_i^2\right) TMXY/G_p$$

$$CP(1,2) = \left(\sum_{i=1,3} M_i \ell_i^2\right) TMY/G_p \qquad CP(1,5) = \left(\sum_{i=1,3} M_i \ell_i^2\right) TMYZ/G_p$$

$$CP(1,3) = \left(\sum_{i=1,3} M_i \ell_i^2\right) TMZ/G_p \qquad CP(1,6) = \left(\sum_{i=1,3} M_i \ell_i^2\right) TMZX/G_p \tag{2.6.2}$$

Since for rows 2 to 6 a similar structure to the above is obtained, only the first and last term of each row is given below

$$\begin{bmatrix} CP(2,1) = \left(\sum_{i=1,3} M_i m_i^2\right) TMX/G_p \\ \vdots \\ CP(2,6) = \left(\sum_{i=1,3} M_i m_i^2\right) TMZX/G_p \end{bmatrix} \qquad (2.6.3)$$

$$\begin{bmatrix} CP(3,1) = \left(\sum_{i=1,3} M_i n_i^2\right) TMX/G_p \\ \vdots \\ CP(3,6) = \left(\sum_{i=1,3} M_i n_i^2\right) TMZX/G_p \end{bmatrix} \qquad (2.6.4)$$

$$\begin{bmatrix} CP(4,1) = 2\left(\sum_{i=1,3} M_i \ell_i m_i\right) TMX/G_p \\ \vdots \\ CP(4,6) = 2\left(\sum_{i=1,3} M_i \ell_i m_i\right) TMZX/G_p \end{bmatrix} \qquad (2.6.5)$$

$$\begin{bmatrix} CP(5,1) = 2\left(\sum_{i=1,3} M_i m_i n_i\right) TMX/G_p \\ \vdots \\ CP(5,6) = 2\left(\sum_{i=1,3} M_i m_i n_i\right) TMZY/G_p \end{bmatrix} \qquad (2.6.6)$$

$$\begin{bmatrix} CP(6,1) = 2\left(\sum_{i=1,3} M_i n_i \ell_i\right) TMX/G_p \\ \vdots \\ CP(6,6) = 2\left(\sum_{i=1,3} M_i n_i \ell_i\right) TMZX/G_p \end{bmatrix} \qquad (2.6.7)$$

2.6.2 2-Dimensional Formulation

2-D FE analysis are, in general, carried out more often in practice that 3-D FE analysis because the 3-D analysis require more time to define and input the relevant data (nodes and soil elements) and also because a great deal more computer time is required to numerically solve the problem

at hand. Therefore it is considered useful to adapt the 3-D formulation that has been described in the previous sections to 2-D. This simply requires imposing the necessary plain strain boundary conditions, and this way the 3-D characteristics will not be lost because the 2-D formulation will still be able to consider the influence of the intermediate principal stress, σ_2, as will be described next.

The stress-strain relationship given in Eq. (2.6.1) is rewritten below.

$$\begin{bmatrix} \Delta\epsilon_x^p \\ \Delta\epsilon_y^p \\ \Delta\epsilon_z^p \\ \Delta\gamma_{xy}^p \\ \Delta\gamma_{yz}^p \\ \Delta\gamma_{zx}^p \end{bmatrix} = \begin{bmatrix} C11 & C12 & C13 & C14 & C15 & C16 \\ C21 & C22 & C23 & C24 & C25 & C26 \\ C31 & C32 & C33 & C34 & C35 & C36 \\ C41 & C42 & C43 & C44 & C45 & C46 \\ C51 & C52 & C53 & C54 & C55 & C56 \\ C61 & C62 & C63 & C64 & C65 & C66 \end{bmatrix} \begin{bmatrix} \Delta\sigma_x \\ \Delta\sigma_y \\ \Delta\sigma_z \\ \Delta\tau_{xy} \\ \Delta\tau_{yz} \\ \Delta\tau_{zx} \end{bmatrix} \qquad (2.6.8)$$

where the C_{ij} terms were described in eq. (2.6.2) to (2.6.7).

Assuming that the 2-D Cartesian coordinate system is defined by the x-axis (horizontal) and z-axis vertical, then all the terms associated with xy or yz, i.e.$\Delta\gamma_{xy}$, $\Delta\gamma_{yz}$, $\Delta\tau_{xy}$ and $\Delta\tau_{yz}$ can be deleted since there is no contribution from these terms in the 2-D plane strain analysis. Therefore, eq. (2.6.8) will take the following form:

$$\begin{bmatrix} \Delta\epsilon_x \\ \Delta\epsilon_y \\ \Delta\epsilon_z \\ \Delta\gamma_{zx} \end{bmatrix} = \begin{bmatrix} C11 & C12 & C13 & C16 \\ C21 & C22 & C23 & C26 \\ C31 & C32 & C33 & C36 \\ C61 & C62 & C63 & C66 \end{bmatrix} \begin{bmatrix} \Delta\sigma_x \\ \Delta\sigma_y \\ \Delta\sigma_z \\ \Delta\tau_{zx} \end{bmatrix} \qquad (2.6.9)$$

By renumbering the above terms the following is obtained:

$$\begin{bmatrix} \Delta\epsilon_x \\ \Delta\epsilon_y \\ \Delta\epsilon_z \\ \Delta\gamma_{zx} \end{bmatrix} = \begin{bmatrix} C11 & C12 & C13 & C14 \\ C21 & C22 & C23 & C24 \\ C31 & C32 & C33 & C34 \\ C41 & C42 & C43 & C44 \end{bmatrix} \begin{bmatrix} \Delta\sigma_x \\ \Delta\sigma_y \\ \Delta\sigma_z \\ \Delta\tau_{zx} \end{bmatrix} \tag{2.6.10}$$

Since in 2-D plain strain analysis, $\Delta\epsilon_y = 0$, then from above, the following equation is obtained:

$$\Delta\epsilon_y = C21\ \Delta\sigma_x + C22\ \Delta\sigma_y + C23\ \Delta\sigma_z + C24\ \Delta\tau_{zx} = 0 \tag{2.6.11}$$

and solving for $\Delta\sigma_y$:

$$\Delta\sigma_y = -\frac{C21}{C22}\Delta\sigma_x - \frac{C23}{C22}\Delta\sigma_z - \frac{C24}{C22}\Delta\tau_{zx} \tag{2.6.12}$$

From eqs. (2.6.10) the following equations are also obtained:

$$\begin{aligned} \Delta\epsilon_x &= C11\ \Delta\sigma_x + C12\ \Delta\sigma_y + C13\ \Delta\sigma_z + C14\ \Delta\tau_{zx} \\ \Delta\epsilon_z &= C31\ \Delta\sigma_x + C32\ \Delta\sigma_y + C33\ \Delta\sigma_z + C34\ \Delta\tau_{zx} \\ \Delta\gamma_{zx} &= C41\ \Delta\sigma_x + C42\ \Delta\sigma_y + C43\ \Delta\sigma_z + C44\ \Delta\tau_{zx} \end{aligned} \tag{2.6.13}$$

Substituting the value of $\Delta\sigma_y$ from eq. (2.6.12) into eq. (2.6.13) and rearranging the following equations are obtained:

$$\Delta\epsilon_x = (C11 - \frac{C12\ C21}{C22})\Delta\sigma_x + (C13 - \frac{C12\ C23}{C22})\Delta\sigma_z + (C14 - \frac{C12\ C24}{C22})\Delta\tau_{zx}$$

$$\Delta\epsilon_z = (C31 - \frac{C32\ C21}{C22})\Delta\sigma_x + (C33 - \frac{C32\ C23}{C22})\Delta\sigma_z + (C34 - \frac{C32\ C24}{C22})\Delta\tau_{zx}$$

$$\Delta\gamma_{zx} = (C41 - \frac{C24\ C21}{C22})\Delta\sigma_x + (C43 - \frac{C24\ C23}{C22})\Delta\sigma_z + (C44 - \frac{C24\ C24}{C22})\Delta\tau_{zx} \qquad (2.6.14)$$

or in a general format

$$\begin{bmatrix} \Delta\epsilon_x \\ \Delta\sigma_z \\ \Delta\gamma_{zx} \end{bmatrix} = \begin{bmatrix} C11^* & C12^* & C13^* \\ C21^* & C22^* & C23^* \\ C31^* & C32^* & C33^* \end{bmatrix} \begin{bmatrix} \Delta\sigma_x \\ \Delta\sigma_z \\ \Delta\tau_{zx} \end{bmatrix} \qquad (2.6.15)$$

where the C^*_{ij} terms are given by the corresponding terms in brackets shown in eq. (2.6.14).

The above eq. (2.6.15) together with eq. (2.6.12) constitute the complete 2-D F.E. formulation of the modified SMP model. This means that during the 2-D F.E. analysis the value of the intermediate principal stress $\sigma_y(\sigma_2)$ is updated at all load steps with eq. (2.6.12) and with this value the 3-D formulation earlier described is used in its full extent for the 2-D F.E. analysis. This way the 3-D effects of the intermediate principal stress are taken into account in the 2-D FE analysis. Predictions of laboratory simple shear results that include predictions of σ_2 are presented in Chapter 3 to show the validity of the above formulation.

2.6.3 Axisymmetric Formulation

The axisymmetric formulation is also useful to implement into a F.E. code, since it allows to solve 3-D problems that are axisymmetric in nature. A good example is the pressuremeter test, which will be considered in some detail later in this thesis. The elasto-plastic stress strain relation used for the axisymmetric F.E. analysis are obtained from eq. (2.6.8) by imposing the necessary axisymmetric boundary conditions, which consist of deleting the terms $\Delta\gamma_{xz}$,$\Delta\gamma_{yz}$, $\Delta\tau_{xy}$ and $\Delta\tau_{yz}$ from eq. (2.87) and by changing the x coordinate to the r coordinate (radial), the y coordinate to the θ coordinate (circumferencial) and keeping the z coordinate (vertical) the same. Performing these changes the following equations are obtained:

$$\begin{bmatrix} \Delta\epsilon_R \\ \Delta\epsilon_\theta \\ \Delta\epsilon_z \\ \Delta\gamma_{zR} \end{bmatrix} \begin{bmatrix} C11 & C12 & C13 & C16 \\ C21 & C22 & C23 & C26 \\ C31 & C32 & C33 & C36 \\ C41 & C42 & C43 & C46 \end{bmatrix} \begin{bmatrix} \Delta\sigma_R \\ \Delta\sigma_\theta \\ \Delta\sigma_z \\ \Delta\tau_{zR} \end{bmatrix} \qquad (2.6.16)$$

and by renumbering the above terms the following equations are obtained:

$$\begin{bmatrix} \Delta\epsilon_R \\ \Delta\epsilon_\theta \\ \Delta\epsilon_z \\ \Delta\gamma_{zR} \end{bmatrix} \begin{bmatrix} C11 & C12 & C13 & C14 \\ C21 & C22 & C23 & C24 \\ C31 & C32 & C33 & C34 \\ C41 & C42 & C43 & C44 \end{bmatrix} \begin{bmatrix} \Delta\sigma_R \\ \Delta\sigma_\theta \\ \Delta\sigma_z \\ \Delta\tau_{zR} \end{bmatrix} \qquad (2.6.17)$$

APPENDIX 2.7

LOAD SHEDDING FORMULATION TO USE WITH THE MODIFIED SMP MODEL

APPENDIX 2.7

Load Shedding Formulation to Use with the Modified SMP Model

The load shedding procedures described in the main text were implemented in the modified SMP formulation to account for soil elements that failed in shear and in tension, and consist of the following.

• Load Shedding for Elements Failed in Shear

A sketch of the Matsuoka-Nakai failure criterion in the 3-D stress space shown in Fig. 2.7.1. Let us assume that the stress conditions of a soil element at a given load step is given by the stress point A. If, for instance, the subsequent load increment is too large the stress conditions of the soil element will shift from the stress point A to the stress point B which corresponds to a stress condition outside the failure envelope and therefore violating the failure criterion which is represented by the stress point F. The magnitude of the violation, which is represented in the figure by $\overline{BF}$, is given by the following equation:

$$\overline{BF} = \Delta\left(\frac{\tau_{smp}}{\sigma_{smp}}\right)_{LS} = \left(\frac{\tau_{smp}}{\sigma_{smp}}\right)_{B} - \left(\frac{\tau_{smp}}{\sigma_{smp}}\right)_{F} \qquad (2.7.1)$$

where

$(\tau_{smp}/\sigma_{smp})_B$ = stress ratio at B

$(\tau_{smp}/\sigma_{smp})_F$ = failure stress ratio

$\Delta(\tau_{smp}/\sigma_{smp})_{LS}$ = stress ratio increment to be "shedded" to the surrounding soil or structural elements.

Substituting Eq. (2.51) from the main text into eq. (2.7.1) the following equation is obtained:

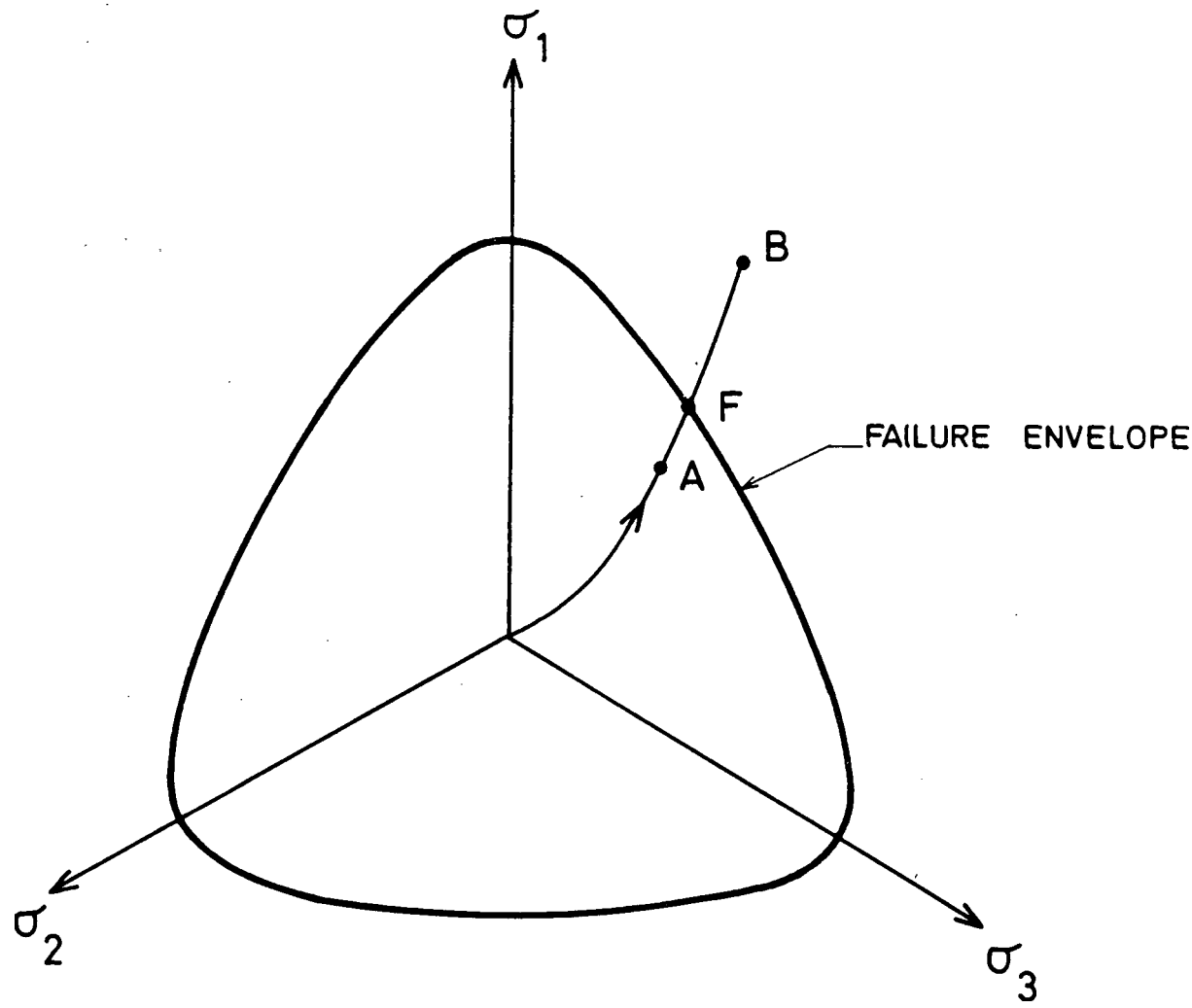

Figure 2.7.1 Matsuoka-Nakai Failure Criterion

$$\Delta\left(\frac{\tau_{SMP}}{\sigma_{SMP}}\right)_{LS} = (TSMOB1)\Delta\sigma_{1LS} + (TSMOB2)\Delta\sigma_{2LS} + (TSMOB_3)\Delta\sigma_{3LS}$$

$$= \left(\frac{\tau_{SMP}}{\sigma_{SMP}}\right)_B - \left(\frac{\tau_{SMP}}{\sigma_{SMP}}\right)_F \qquad (2.7.2)$$

where

$\Delta\sigma_{1LS}$, $\Delta\sigma_{2LS}$ and $\Delta\sigma_{3LS}$ are the increments of principal stress to be shedded to the surrounding soil or structural elements

In order to evaluate the $\Delta\sigma_{i_{LS}}$ values (i = 1,2,3), 2 more equations are required, and for that the following assumptions are made:

a) The mean normal stress remains constant during load shedding, which implies that

$$\Delta\sigma_{1LS} + \Delta\sigma_{2LS} + \Delta\sigma_{3LS} = 0 \qquad (2.7.3)$$

b) The b-value = $(\sigma_2-\sigma_3)/(\sigma_1-\sigma_3)$ of the soil element at stress point F is equal to the b-value that the soil element had at stress point A. (This requires that the b-value for every soil element be stored for the current and previous load step.)

$$(\text{b-value})_F = \frac{((\sigma_2-\Delta\sigma_{2LS}) - (\sigma_3-\Delta\sigma_{3LS}))}{((\sigma_1-\Delta\sigma_{1LS}) - (\sigma_3-\Delta\sigma_{3LS}))} = (\text{b-value})_A \qquad (2.7.4)$$

where the σ_i (i = 1,2,3) are the principal stresses at point B.

Now that a system of 3 equations with 3 unknowns has been established it is a question to solve the system for $\Delta\sigma_{1LS}$, $\Delta\sigma_{2LS}$ and $\Delta\sigma_{3LS}$.

• Evaluation of the Increments of Principal Stress $(\Delta\sigma_i)_{LS}$

To simplify, the terms $(\Delta\sigma_i)_{LS}$ will, from now on, be referred to as $\Delta\sigma$. From eq. (2.7.4) the following is obtained.

$$\sigma_1 b - b\Delta\sigma_1 - \sigma_3 b + b\Delta\sigma_3 = \sigma_2 - \Delta\sigma_2 - \sigma_3 + \Delta\sigma_3$$

$$b\Delta\sigma_1 = \sigma_1 b + \sigma_3 b - b\Delta\sigma_3 + \sigma_2 - \Delta\sigma_2 - \sigma_3 + \Delta\sigma_3$$

$$\Delta\sigma_1 = \left[\frac{b\sigma_1-\sigma_2-b\sigma_3+\sigma_3}{b}\right] + \left[\frac{1}{b}\right]\Delta\sigma_2 + \left[\frac{b-1}{b}\right]\Delta\sigma_3$$

or

$$\boxed{\Delta\sigma_1 = (TS11) + \Delta\sigma_2(TS12) + \Delta\sigma_3(TS13)} \qquad (2.7.5)$$

where:

$$TS11 = \left(\frac{b\sigma_1-\sigma_2-b\sigma_3+\sigma_3}{b}\right)$$

$$TS12 = \frac{1}{b}$$

$$TS13 = \frac{b-1}{b}$$

Substituting into (2.7.3)

$$TS11 + \Delta\sigma_2(TS12) + \Delta\sigma_3(TS13) + \Delta\sigma_2 + \Delta\sigma_3 = 0$$

collecting terms

$$\Delta\sigma_2\ [TS12 + 1] = -TS11 - \Delta\sigma_3[1 + TS13]$$

Solving for $\Delta\sigma_2$

$$\Delta\sigma_2 = \left(\frac{-TS11}{TS12+1}\right) - \Delta\sigma_3\ \left(\frac{1+TS13}{TS12+1}\right)$$

or

$$\boxed{\Delta\sigma_2 = (TS22) - \Delta\sigma_3(TS23)} \qquad (2.7.6)$$

where:

$$TS22 = \frac{-TS11}{TS12+1}$$

$$TS23 = \frac{1+TS13}{TS12+1}$$

Substituting the values of $\Delta\sigma_1$ from eq. (2.7.5) and $\Delta\sigma_2$ from eq. (2.7.6) into eq. (2.7.2) the following is obtained:

$$(TSMOB1)\ [TSS11 + (TS22 - \Delta\sigma_3(TS23))(TS12) + \Delta\sigma_3 TS13]$$

$$+ (TSMOB2)[TS22 - \Delta\sigma_3(TS23)] + (TSMOB3)\ \Delta\sigma_3 = \Delta\left(\frac{\tau_{SMP}}{\sigma_{SMP}}\right)_{LS}$$

Solving:

$$\text{TSMOB1 TSS11} + \text{TSMOB1 TS22 TS12} - \text{TSMOB1 TS23 TS12}\ \Delta\sigma_3$$

$$+ \text{TSMOB1 TS13}\ \Delta\sigma_3 + \text{TSMOB2 TS22} - \text{TSMOB2 TS23}\ \Delta\sigma_3$$

$$+ \text{TSMOB3}\ \Delta\sigma_3 = \Delta\left(\frac{\tau_{smp}}{\sigma_{smp}}\right)_{LS}$$

assembling:

$$\Delta\sigma_3\ [(-\text{TSMOB1})(\text{TS23})(\text{TS12}) + (\text{TSMOB1})(\text{TS13}) - (\text{TSMOB2})(\text{TS23})$$

$$+ \text{TSMOB3}] + [(\text{TSMOB1})(\text{TS11}) + (\text{TSMOB1})(\text{TS22})(\text{TS12})$$

$$+ (\text{TSMOB2})(\text{TS22})] = \Delta\left(\frac{\tau_{SMP}}{\sigma_{SMP}}\right)_{LS}$$

Designating the terms inside the brackets by TS33 and TS31 than

$$\Delta\sigma_3[\text{TS33}] + [\text{TS31}] = \Delta\left(\frac{\tau_{SMP}}{\sigma_{SMP}}\right)_{LS}$$

and solving for $\Delta\sigma_3$

$$\boxed{\Delta\sigma_3 = \Delta\left(\frac{\tau_{SMP}}{\sigma_{SMP}}\right)_{LS}/(\text{TS33}) - \frac{(\text{TS31})}{(\text{TS33})}} \qquad (2.7.7)$$

To summarize the increments of principal stresses to be shedded are $\Delta\sigma_{1_{LS}}$ (given by Eq. (2.7.5)), $\Delta\sigma_{2_{LS}}$ (given by eq. (2.7.6)) and $\Delta\sigma_{3_{LS}}$ (given by eq. (2.7.7)).

The next step is to obtain the increments of Cartesian stress $\{\Delta\sigma\}_{LS}$ that are equivalent to the increments of principal stress $\Delta\sigma_{i_{LS}}$ evaluated above, and that is done the following way.

The new principal stresses at point F (see Fig. 2.7.1), $(\sigma_i)_F$, are obtained from the principal stresses at point B, $(\sigma_i)_B$ following the equations:

$$
\begin{aligned}
(\sigma_1)_F &= (\sigma_1)_B - \Delta\sigma_{1LS} \\
(\sigma_2)_F &= (\sigma_2)_B - \Delta\sigma_{2LS} \\
(\sigma_3)_F &= (\sigma_3)_B - \Delta\sigma_{3LS}
\end{aligned}
\tag{2.7.8}
$$

now assuming that the direction cosines of the principal stresses at point F are the same as the direction cosines of the principal stresses at point B, then using eq. (2.3.1) from Appendix 2.3, which relates cartesian stresses with principal stresses the new Cartesian stresses at point F, $\{\sigma\}_F$, are obtained as it is described below:

$$
\begin{bmatrix}
(\sigma_x)_F & (\tau_{xy})_F & (\tau_{xz})_F \\
(\tau_{yx})_F & (\sigma_y)_F & (\tau_{yz})_F \\
(\tau_{zx})_F & (\tau_{zy})_F & (\sigma_z)_F
\end{bmatrix}
=
\begin{bmatrix}
\ell_1 & \ell_2 & \ell_3 \\
m_1 & m_2 & m_3 \\
n_1 & n_2 & n_3
\end{bmatrix}
\begin{bmatrix}
(\sigma_1)_F & 0 & 0 \\
0 & (\sigma_2)_F & 0 \\
0 & 0 & (\sigma_3)_F
\end{bmatrix}
\begin{bmatrix}
\ell_1 & m_2 & n_3 \\
\ell_1 & m_2 & n_3 \\
\ell_1 & m_2 & n_3
\end{bmatrix}
$$

Finally the increments of cartesian shear stress to be shedded are evaluated following the equations below:

$$
\begin{aligned}
\Delta\sigma_{x_{LS}} &= (\sigma_x)_B - (\sigma_x)_F \\
\Delta\sigma_{y_{LS}} &= (\sigma_y)_B - (\sigma_y)_F \\
\Delta\sigma_{z_{LS}} &= (\sigma_z)_B - (\sigma_z)_F \\
\Delta\tau_{xy_{LS}} &= (\tau_{xy})_B - (\tau_{xy})_F \\
\Delta\tau_{yz_{LS}} &= (\tau_{yz})_B - (\tau_{yz})_F \\
\Delta\tau_{zx_{LS}} &= (\tau_{zx})_B - (\tau_{zx})_F
\end{aligned}
\qquad (2.7.9)
$$

To finish the stress redistribution, the stresses of the soil element that failed are defaulted to the stress values of point F, the G_p of the soil element is defaulted to a low prescribed value (G_p = Pa/100) and the increments of cartesian stress to be shedded, $\{\Delta\sigma\}_{LS}$, are transformed into a load vector, $\{f\}_{LS}$, which is applied at the nodes of the soil element that failed in shear and will develop equivalent stresses $\{\Delta\sigma\}_{eq}$ ($\Delta\sigma_{eq} = \Delta\sigma_{LS}$) on the surrounding soil or structural elements. This way, stress equilibrium will be maintained within the soil mass. To develop the load vector $\{f\}_{LS}$ the following equation is used:

$$\{f\}_{LS} = \{\Delta\sigma\}_{LS}\,[B]^T \text{ volume} \qquad (2.7.10)$$

where

$[B]^T$ is the transpose of the strain-displacement matrix of the failed element

volume = volume of the soil element.

This equation is derived as follows:

Within any soil element considered in a finite element formulation, the principle of virtual work requires, for equilibrium, that the work done by the virtual displacements $\{\bar{\delta}\}$ to be equal to the work done by the increment of internal strains as it is shown by the following equation:

$$\{\bar{\delta}\}^T\{f\} = \int\{\Delta\epsilon\}^T\{\Delta\sigma\}dv \qquad (2.7.11)$$

where:

$\{f\}$ = the force increment at the element nodes

$\{\Delta\sigma\}$ = the increment of stresses within the element

v = element volume

and

$\Delta\epsilon$ = the increment of strains within the element

Since this incremental strain vector, $\{\Delta\epsilon\}$ can be related with the incremental nodal displacement vector, $\{\delta\}$, using the following equation:

$$\{\Delta\epsilon\} = [B]\ \{\delta\} \qquad (2.7.12)$$

where:

$[B]$ = the strain-displacement matrix of the element

than substituting eq. (2.7.12) into eq. (2.7.11) the following is obtained:

$$\{\bar{\delta}\}^T\{f\} = \int\{\delta\}^T[B]^T\{\Delta\sigma\}dv$$

Since [B] is constant, then

$$\{\bar{\delta}\}^T\{f\} = \{\bar{\delta}\}^T[B]^T\{\Delta\sigma\} \text{ volume}$$

or

$$\boxed{\{f\} = [B]^T \{\Delta\sigma\} \text{ volume}} \qquad (2.7.13)$$

• Load Shedding for Elements in Tension

The load shedding procedures for the soil elements that failed in tension are rather simple and consist of the following.

Physically, a soil-element fails in tension whenever $\sigma_i \leq 0$, i.e. either $\sigma_3 \leq 0$ or σ_2 and $\sigma_3 \leq 0$ or σ_1, σ_2, and $\sigma_3 \leq 0$. To void excessive interactions, however, the following tension failure bound is used instead.

If $(-\sigma_i) \leq (-\frac{Pa}{K})$ the soil element is considered to have failed in tension, where a K = 100 has been used with success.

The increments of principal stress to be shedded are easily evaluated using the following equation:

$$\Delta\sigma_{i_{LS}} = \text{abs}(-\sigma_i) \qquad (2.7.14)$$

and from this stage, the procedures described earlier for the elements that failed in shear are applied for the elements that failed in tension, i.e. using eqs. (2.7.8) through (2.7.10).

APPENDIX 2.8

DISCUSSION OF THE ASSUMPTIONS REGARDING THE DIRECTION OF THE INCREMENTS OF PRINCIPAL STRAINS BASED ON HOLLOW CYLINDER TESTS

APPENDIX 2.8

Discussion of the Assumptions Regarding the Direction of the Increments of Principal Strains Based on Hollow Cylinder Tests

The hollow cylinder apparatus was developed mainly because it allows the independent control of the magnitude and direction of the three principal stresses. This allows to investigate the effects that the initial anisotropy, and/or the stress ratio σ_1/σ_3, and/or b-valve, and/or mean normal stress, have on the sand behaviour. From the work of Symes et al. (1982,1984,1988) and Sayao (1989), only the aspects related with Assumptions Nos. 3 and 4 will be considered here.

2.8.1 Hollow Cylinder Tests Carried out by Symes et al. on Ham River Sand

The hollow cylinder tests carried out by Symes et al. were divided in the following categories:

a) Initial anisotropy tests,

b) Continuous rotation tests,

c) Shear after rotation tests, and

d) Combined rotation and shear tests,

and therefore this order will be followed next in the discussion.

- Initial Anisotropy Tests

To study the effects of the initial anisotropy, the angle ψ that σ_1 makes with the vertical was kept constant through the test together with a constant b-value and constant mean normal stress. Several tests with different initial ψ angles were performed on Ham River sand by Symes et al. and these are listed below:

1) Dry tests on dense sand, test C_1, C_2 and C_3 (1982).

2) Undrained tests on medium-loose sand, tests A_0, A_2 and A_4 (1984).

3) Drained tests on medium-loose sand, tests L_0, L_2 and L_4 (1988).

All the above tests were performed with a b-valve = .5 and a constant effective mean normal stress, σ'_m = 200 kPa.

The results of the $C_{(s)}$, $A_{(s)}$ and $L_{(s)}$ tests are shown in the Figs. 2.8.1, 2.8.2 and 2.8.3, respectively. In each of the above figures, three plots are presented: (a) the stress path followed in terms of the shear stress, $\tau = (\sigma_1-\sigma_3)/2$ versus ψ; (b) the stress-strain relationship in terms of τ versus octahedral shear strain, γ_{oct}; and (c) the variation of the angle of the increments of strain ξ with τ. From the test results shown, a list of facts will be given first and conclusions derived from these will be given last.

Facts:

1) From the dry tests on dense sand ($\psi \neq 90°$) the angle ξ diverges from the angle ψ from 0 to 8° at the start of the test and from 4 to 6° at the end of the test. For the test $\psi = 90°$ there is no divergency, because this is a triaxial extension stress path.

2) From the undrained tests on medium-loose sand ($\psi \neq 0°$) the angles ξ diverge from the angle ψ from 15° to 18° at the start of the test. This divergency decreases rapidly while shear increases and at peak and after peak, the divergency between ξ and ψ vary from 0° to 5°. For the test $\psi = 0°$ there is no divergence because this is a triaxial compressive stress path.

3) From the drained tests on medium loose sand ($\psi \neq 0°$) the angle ξ diverges from the angle ψ from -3° to 17° at the start of the test.

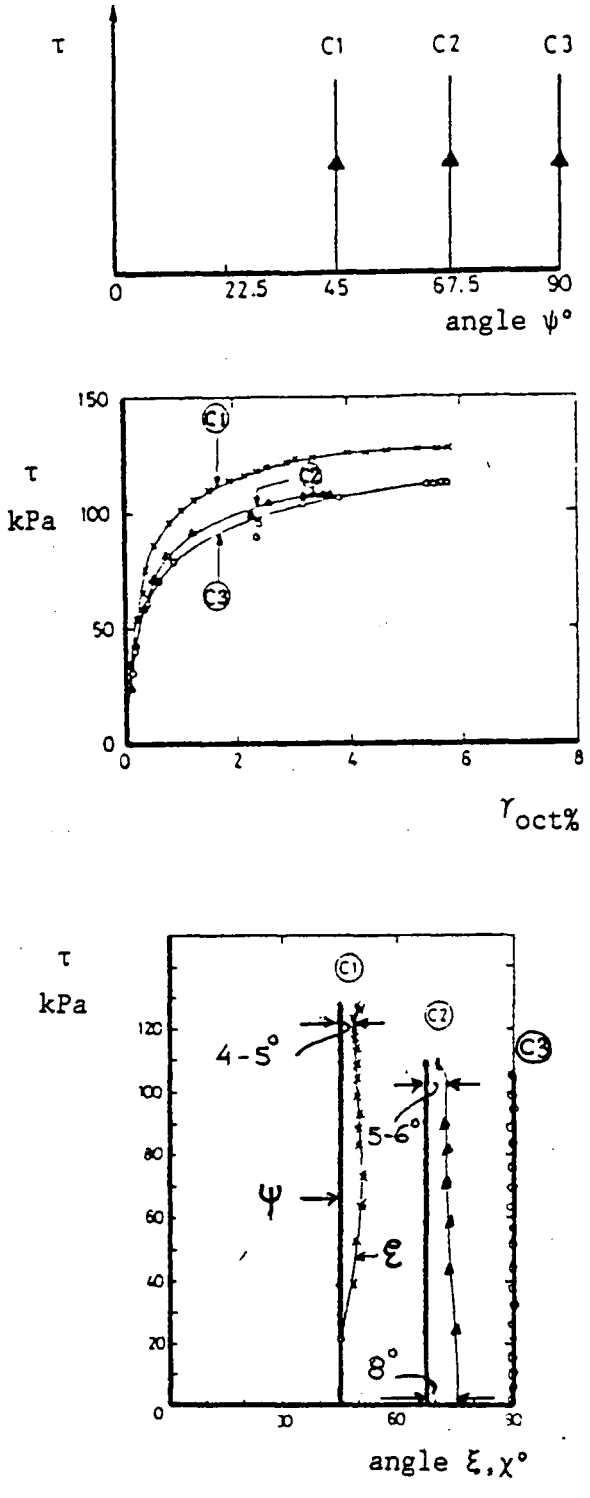

Figure 2.8.1 Initial Anisotropy Hollow Cylinder Drained Tests. Dense Ham River Sand (after Symes et al., 1982)

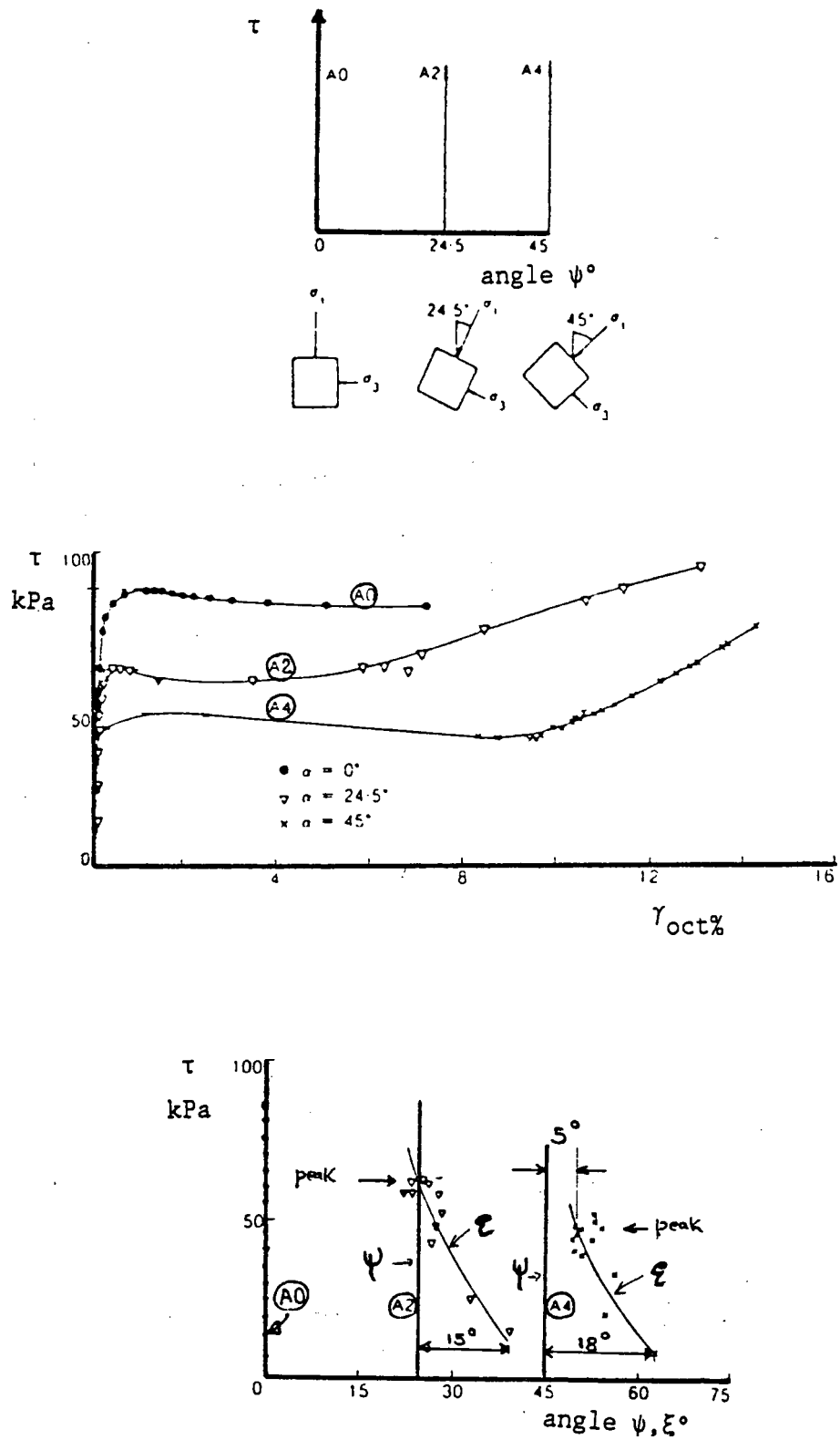

Figure 2.8.2 Initial Anisotropy Hollow Cylinder Undrained Tests. Medium Loose Ham River Sand (after Symes et al., 1984)

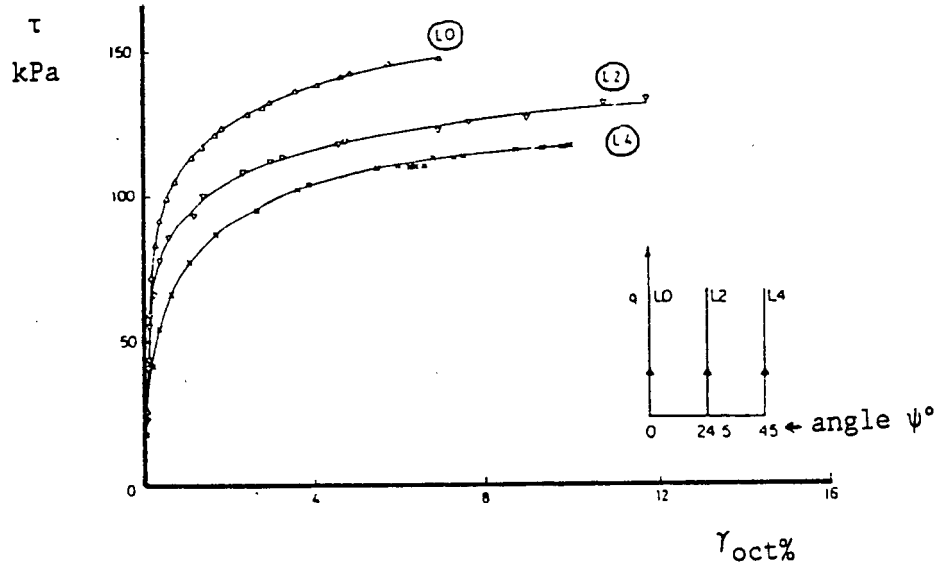

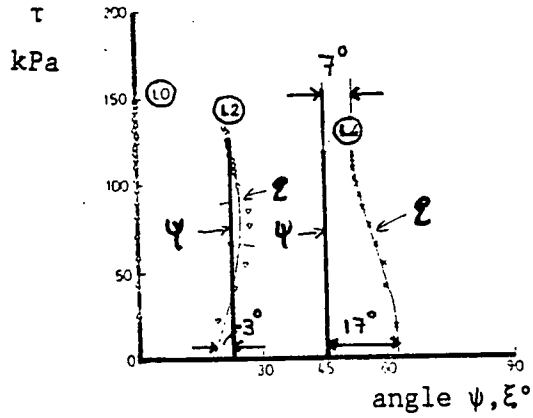

Figure 2.8.3 Initial Anisotropy Hollow Cylinder Drained Tests. Medium Loose Ham River Sand (after Symes et al., 1988)

Again this divergency decreases with shear and at the end of the test the divergency between ξ and ψ varies from 0° to 7°. For the test ψ = 0° there is no divergency.

Conclusions: Based on the above facts it is concluded that Assumption #4 regarding the direction of the increments of strain is a valid assumption since at the end of the above Initial Anisotropy tests the deviation between ξ and ψ varies from 0° to 7°.

• Continuous Rotation Tests

These tests are characterized by increasing or decreasing the angle ψ while the b-value, the stress ratio σ_1/σ_3, the mean normal stress and the deviatoric stress are kept constant. For the tests carried out by Symes et al. a b = .5 and σ'_m = 200 kPa were used. The value of τ varied from test to test as it is listed below:

1) Dry test on dense sand (1982)

   Test M: τ = 110 kPa and ψ varied from 0 to 67.5°

2) Undrained tests on medium-loose sand (1984)

   Test R1: τ = 40 kPa and ψ varied from 0 to 45°

   Test R2: τ = 40 kPa and ψ varied from 45 to 0°

3) Drained tests on medium-loose sand (1988)

   Test LR1: τ = 43 kPa and ψ varied from 0 to 45°

   Test LR3: τ = 89 kPa and ψ varied from 0 to 45°

   Test LR2: τ = 43 kPa and ψ varied from 45 to 0°

   Test LR4: τ = 89 kPa and ψ varied from 45 to 0°.

The results of these seven tests are shown in the following 7 figures (Figs. 2.8.4 to 2.8.10) by the order listed above and in each figure three

plots are presented: (a) τ versus ψ; (b) τ versus γ_{oct}; and (c) ψ versus ξ, and χ (when available). Before any factual conclusions are made, some of the comments by Symes et al. (1988) will be outlined herein, and those are: "when the angle ψ increases there is an increase in γ_{oct} and therefore these test paths should be related with a "loading" path. When the angle ψ decreases there is a decrease in γ_{oct} and therefore these test paths should be related with an "unloading" path". Perhaps the above terms "loading" and "unloading" should be substituted by "strain loading" and "strain unloading" since there is no change in the τ terms, or perhaps the variation of the stress ratio on the mobilized plane τ_{smp}/σ_{smp} with ψ should be evaluated to see if there is any physical variation on the 3-D state of shear stresses while ψ varies during the tests. What is important, however, is that the reader should keep in mind that there are "strain loading" paths and "strain unloading" paths. From the test results the following is inferred:

(1) From the dry test on dense sand (Fig. 2.8.4) which is a "strain loading" test, the divergency between ξ and ψ is about 20° at the start of the rotation and γ_{oct} = .3%. This divergence decreases rapidly when ψ varies from 5° to 67.5° and γ_{oct} increases from .3% to 6%. At the end of the test the divergency between ξ and ψ is about 5°.

From the results of this test it is concluded that Assumption #4 has been validated.

(2) From the undrained test on medium-loose sand, R1 (Fig. 2.8.5), which is a "strain loading" test, it may be seen that the mobilized γ_{oct} are very small (< 0.15%).

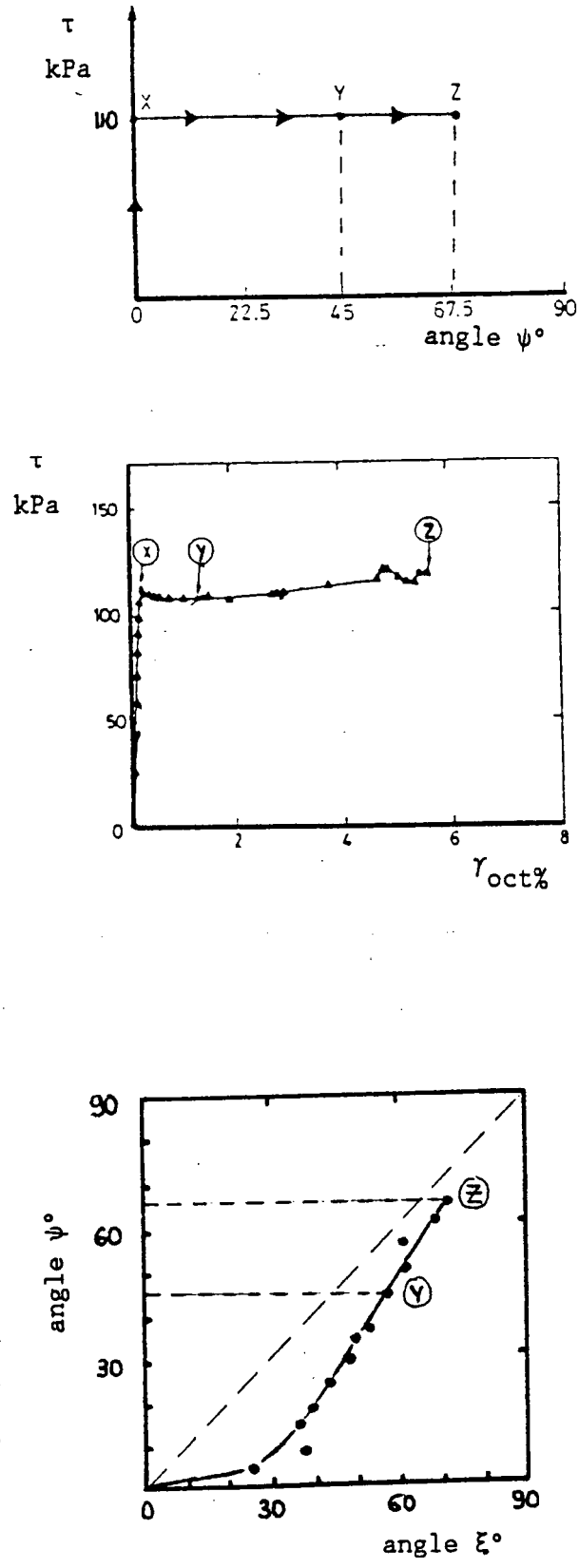

Figure 2.8.4 Continuous Rotation Hollow Cylinder Drained Test. Medium Dense Ham River Sand (after Symes et al., 1982)

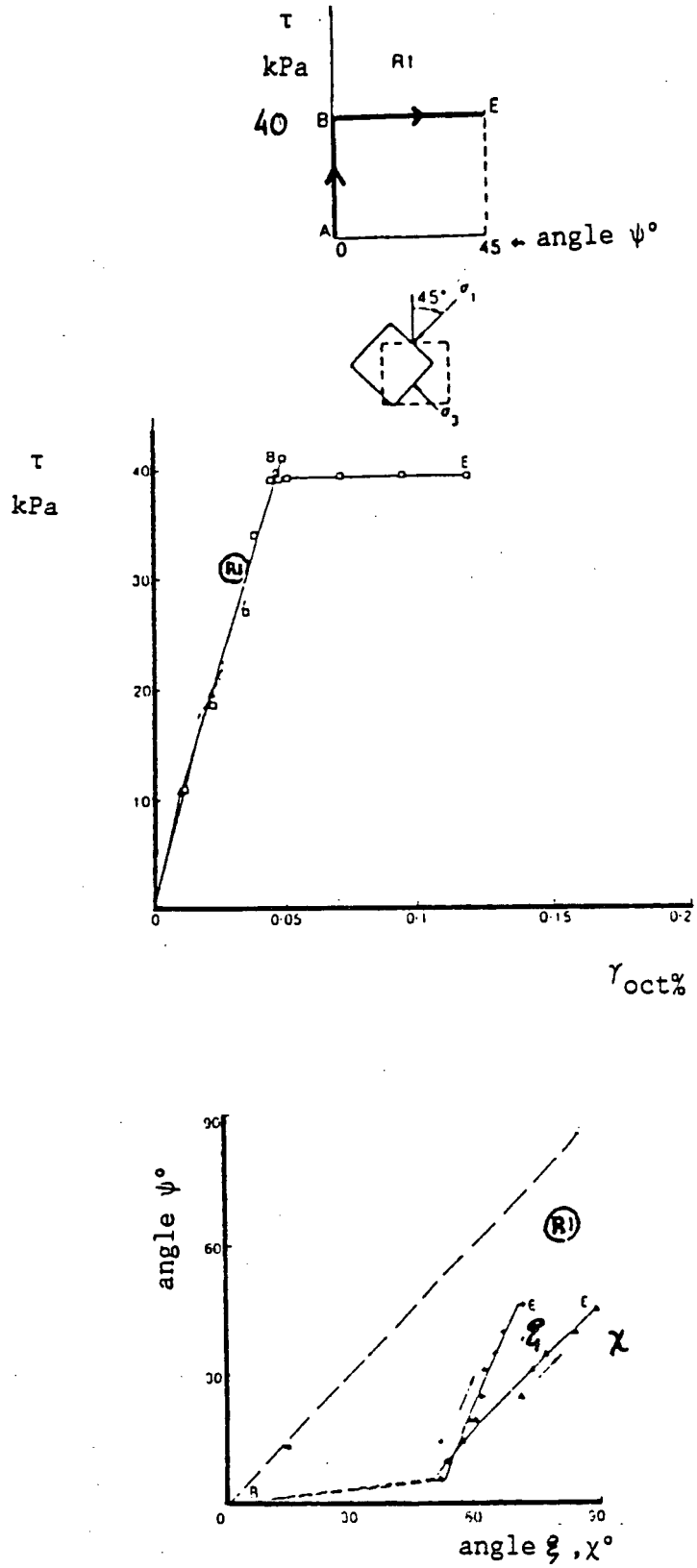

Figure 2.8.5 Continuous Rotation Hollow Cylinder Undrained Test. Test R1: Medium Losse Ham River Sand (after Symes et al., 1984)

As the test results show there is no significant divergency between the angles χ and ξ for the initial stages of the test ($0° < \psi < 15°$) which can be associated with an elastic phase of the test. However, when $15° < \psi \leq 45°$ the angle ξ starts converging towards the angle ψ and diverging from the angle χ. This stage of the test can be associated with the begining of the plastic phase of the test.

From the undrained test on medium loose sand, R2 (Fig. 2.8.6), which is a "strain unloading test", it may be seen from the laboratory results that the angles χ and ξ show a divergency of about 14° through the test, being the divergency between ξ and ψ about 30° The mobilized γ_{oct} during the stage of rotation are small and about .05%. The above facts can be associated with an elastic behaviour of the sand during unloading.

(3) From the drained tests on medium-loose sand the following facts are collected:

Test LR1 (Fig. 2.8.7) is a strain loading test carried out at a low stress level (q = 43 kPa). The mobilized γ_{oct} are small and less than .2%. Again as test R1 the angles χ and ξ almost coincide for the initial stages of the test ($0 < \psi < 25°$) which can be associated with an elastic phase of the test. However, when $25° < \psi < 45°$ the angle ξ starts converging towards ψ and diverging from the angle χ. This stage of the test can be associated with the beginning of the plastic phase.

Test LR3 (Fig. 2.8.8) is, as well, a strain loading test but the shear stress level is higher (τ = 89 kPa) than the shear stress level of test LR1 (τ = 43 kPa). Therefore the mobilized γ_{oct} are as well higher than in the other test and in the order of 2%. The response of the angles ξ and χ reflect the above fact. It may be seen that the angle ξ lies closer to ψ

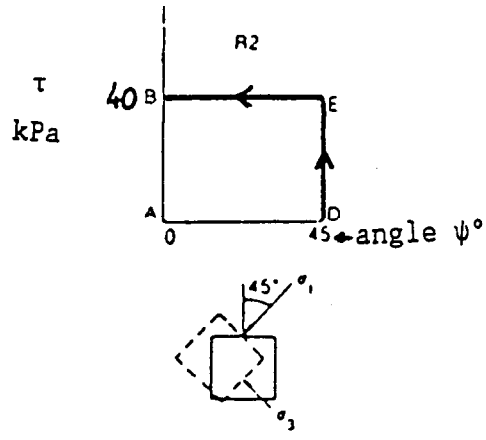

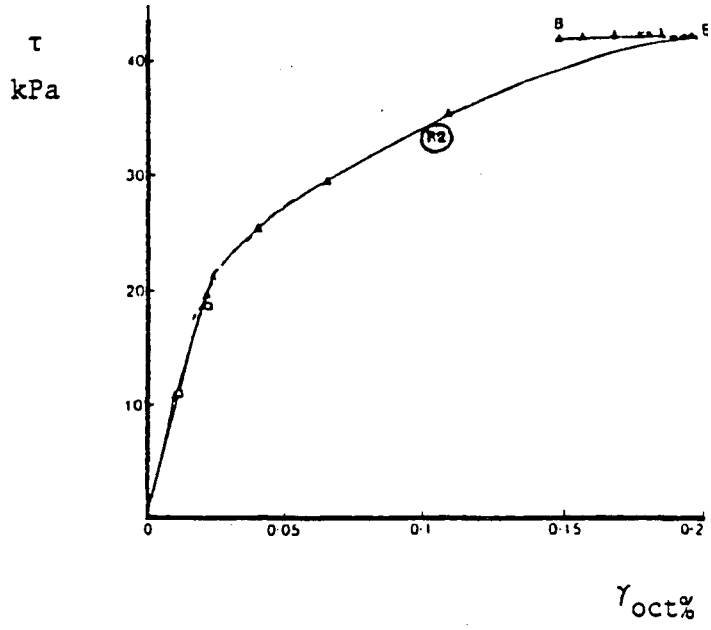

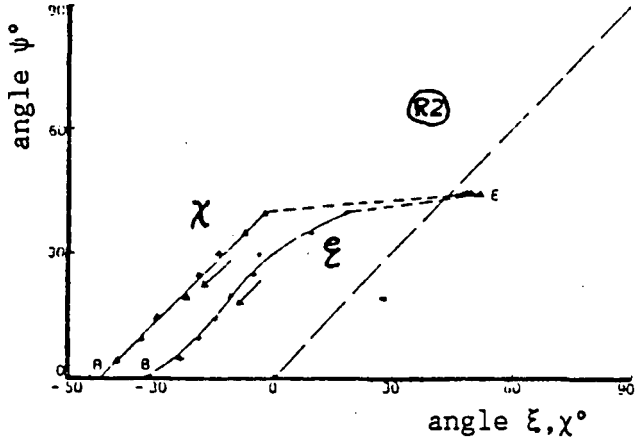

Figure 2.8.6 Continuous Rotation Hollow Cylinder Uncrained Test. Test R2: Medium Loose Ham River Sand (after Symes et al., 1984)

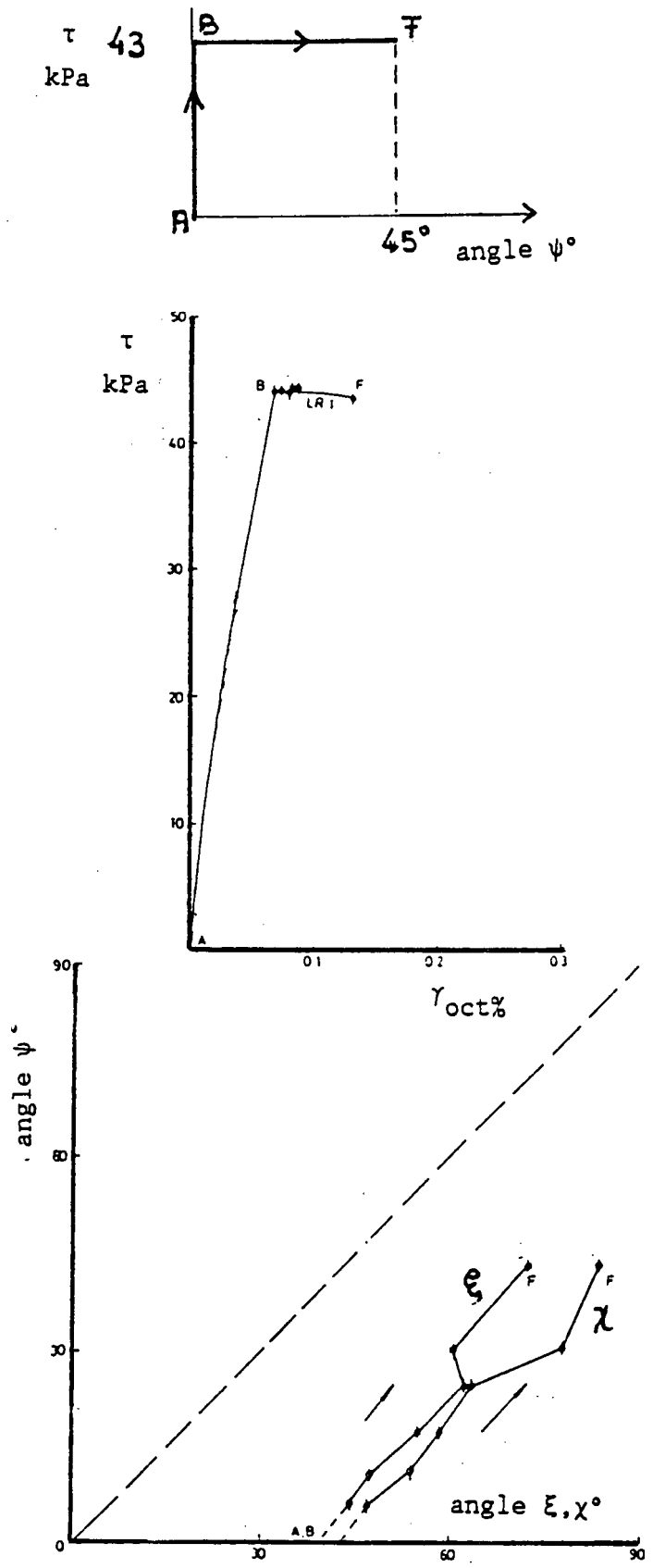

Figure 2.8.7 "Continuous Rotation" Hollow Cylinder Drained Test. Test LR1: Medium Loose Ham River Sand (after Symes et al., 1988)

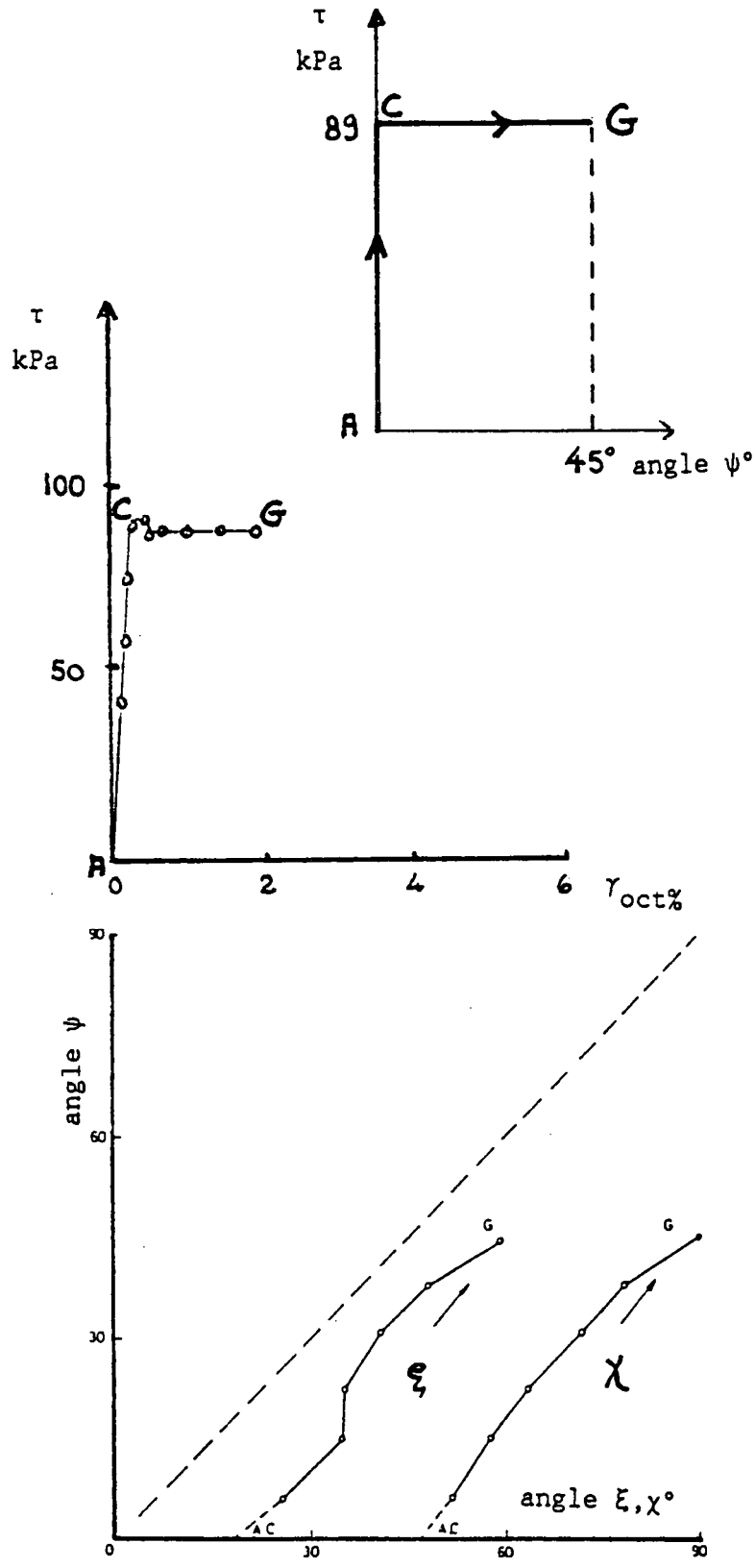

Figure 2.8.8 "Continuous Rotation" Hollow Cylinder Drained Test. Test LR3: Medium Loose Ham River Sand (after Symes et al., 1988)

than to χ, diverging from the former from 10 to 15° (at large strains) and reflecting that at higher stress levels the behaviour of the sand is essentially plastic.

Tests LR2 and LR4 (see Fig. 2.8.9 and 2.8.10) are "strain unloading tests" carried out at q = 43 kPa and q = 89 kPa. It may be seen that the response of the angles χ and ξ is identical (to the observed during the other strain unloading test (test R2) and show that regardless of the stress level during strain reversal the behaviour is essentially elastic.

• Shear After Rotation Tests

For the case of the continuous rotation tests carried out in medium loose sand, tests R1, R2 (undrained) and tests LR1, LR2, LR3 and LR4 (drained), once the rotation phase was terminated, these tests were extended with an additional shear phase where the deviatoric stress, τ, was increased until failure was developed. The results of the undrained tests are presented in Fig. 2.8.11 and the results of the drained tests are presented in Fig. 2.8.12. Again in each figure three plots: (a) τ versus ψ; (b) τ versus γ_{oct}; and (c) τ versus ξ are presented.

The results show that for all tests the initial divergency between ξ and ψ decreases rapidly with increasing shear. At the end of the tests the divergency between ξ and ψ is zero for test R2, LR1, LR2, LR4 and 5° for test R1. Test LR3 is the only exception where the results show that the angle ξ deviates from ψ during the last part of the test.

• Combine Rotation and Shear Test

To study the combined effects of rotation and shear the drained test LR5 was carried out by Symes et al. (1988) on medium loose sand, where the

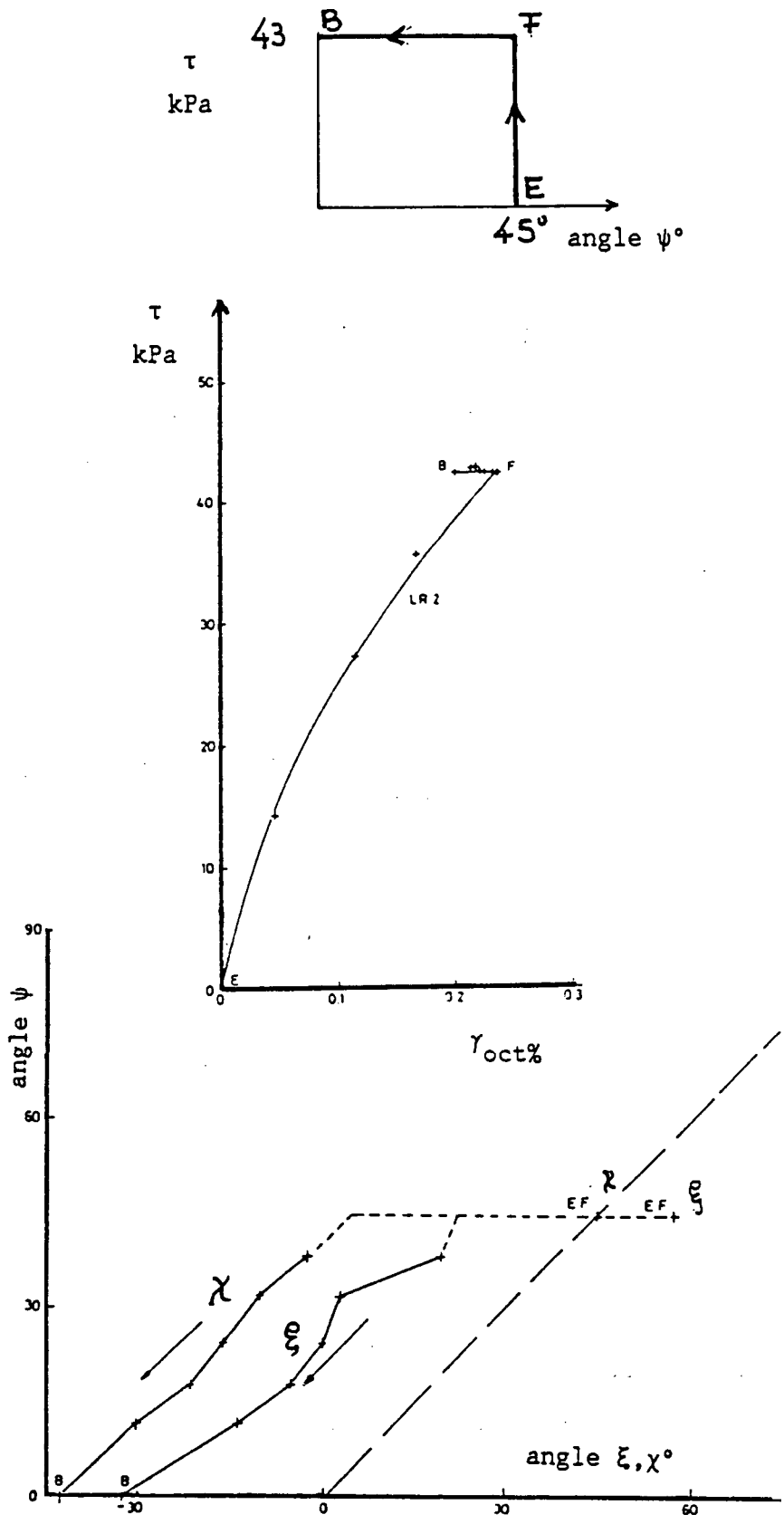

Figure 2.8.9 "Continuous Rotation" Hollow Cylinder Drained Test. Test LR2: Medium Loose Ham River Sand (after Symes et al., 1988)

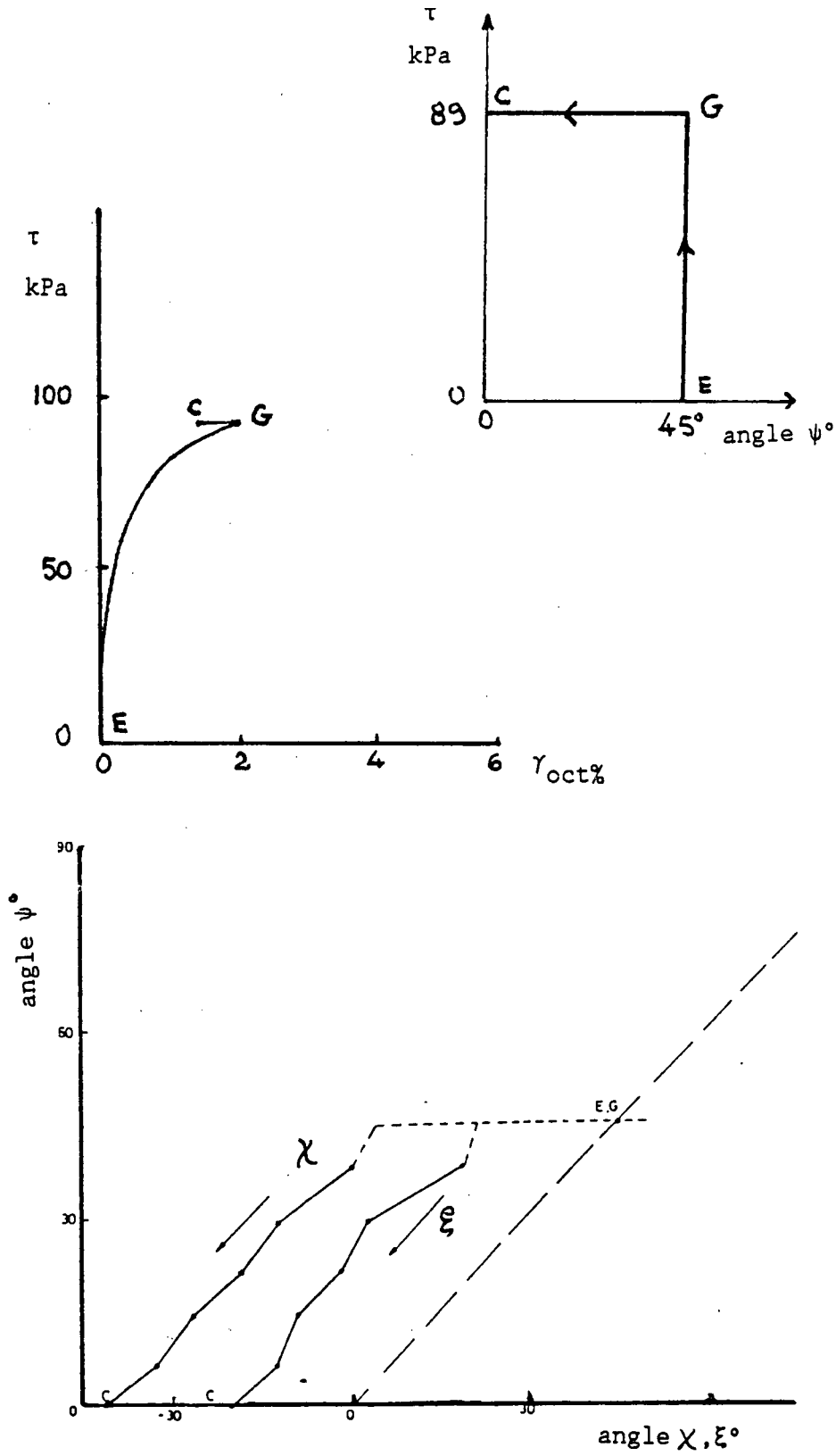

Figure 2.8.10 "Continuous Rotation" Hollow Cylinder Drained Test. Test LR4: Medium Loose Ham River Sand (after Symes et al., 1988)

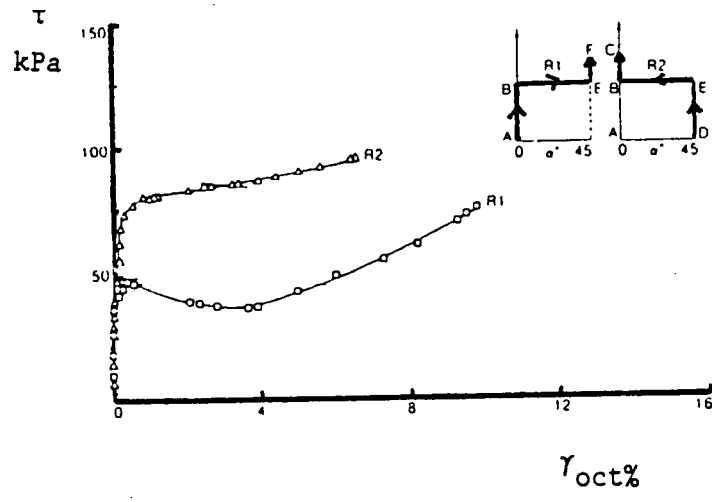

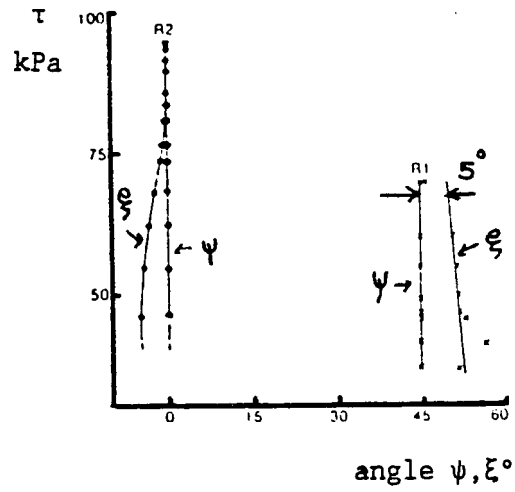

Figure 2.8.11 "Shear After Rotation" Hollow Cylinder Undrained Test. Medium Loose Ham River Sand (after Symes et al., 1984)

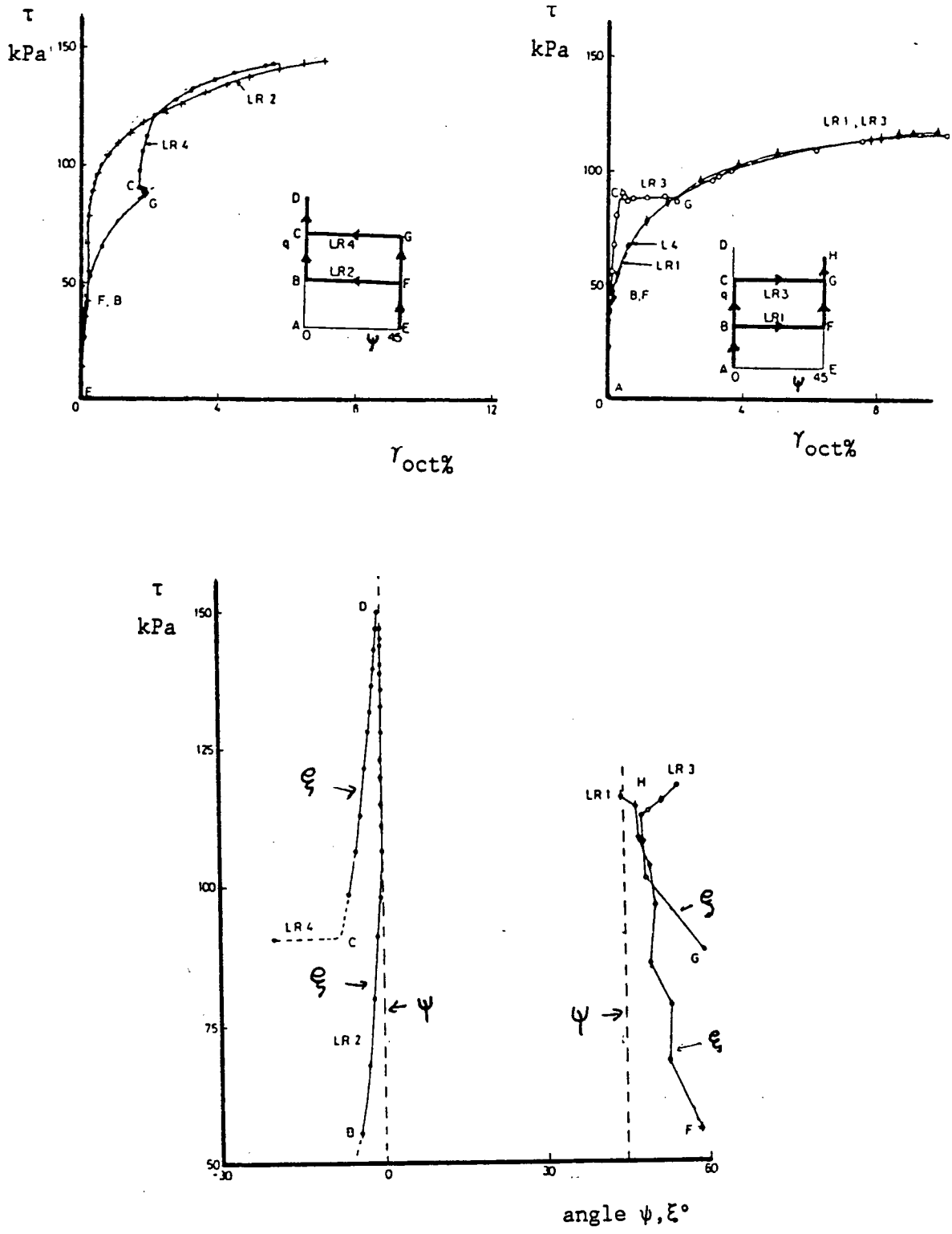

Figure 2.8.12 "Shear After Rotation" Hollow Cylinder Drained Test. Medium Loose Ham River Sand (after Symes et al., 1988)

sand sample initially confined to 200 kPa was sheared to τ = 90 kPa while ψ was constant and equal to 0°. From this point the angle ψ varied from 0° to 45° while the magnitude of τ was simultaneously increased. In Fig. 2.8.13 it is presented the test path (τ versus ψ) and the results τ versus γ_{oct} and τ versus ψ, ξ and χ. It may be seen that while both τ and ψ increase the initial deviation of ψ and ξ of 10° decrease to almost zero when failure is developed.

2.8.2 Hollow Cylinder Tests Carried out by Sayao (1989) on Ottawa Sand

These tests were carried out on Ottawa sand with D_r ranging from 20% to 36% and were divided in the following categories:

a) Initial anisotropy tests

b) Proportional loading tests

c) Continuous variation in b-value tests.

Because the results from these tests are well documented by Sayao (1989) these will not be discussed in detail here. A summary of these tests together with a summary of the tests carried out by Symes et al. is presented below.

2.8.3 Summary

For the "continuous rotation tests" carried out by Symes et al. and Sayao, with increasing or decreasing values of ψ but with constant values of stress ratio σ_1/σ_3, b-value, and mean normal stress, σ_m it is concluded that the deviations between the angle ψ (σ_1) and the angle ξ ($\Delta\epsilon_1$) can be quite significant. The same conclusions apply for the "continuous variation in b-value tests" carried out, by Sayao, with increasing or decreasing

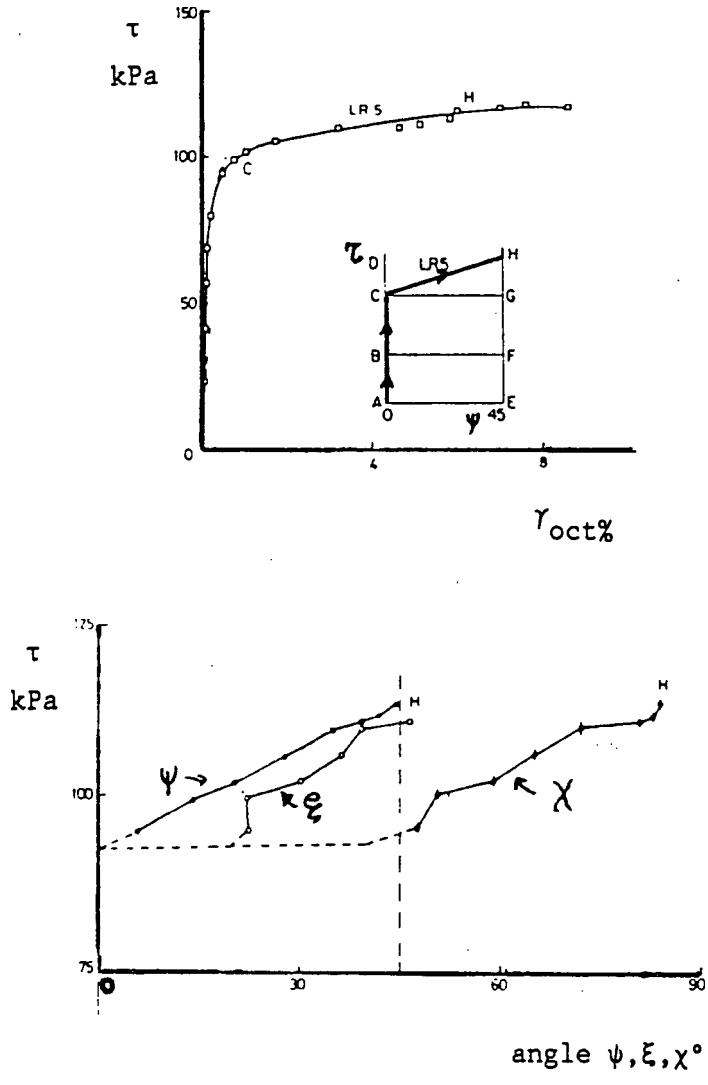

Figure 2.8.13 "Combined Rotation and Shear" Hollow Cylinder Drained Test. Medium Loose Ham River Sand (after Symes et al., 1988)

b-value but with constant values of ψ, σ_1/σ_3, and σ_m. This indicates that Assumption #4 is not valid for these two types of tests. However Assumption #4 is shown to be valid for the hollow cylinder tests where a stress path to failure was followed (except for the early stages of the tests) such as the "initial anisotropic tests" carried out by Symes et al. and Sayao, with increasing σ_1/σ_3 but with constant values of ψ, b-value and σ_m. The same conclusions apply for the "proportional loading tests" carried out by Sayao with increasing σ_m but constant σ_1/σ_3, ψ, and b-value.

CHAPTER 3

APPENDIX INDEX

APPENDIX 3

APPENDIX FIGURES INDEX

APPENDIX 3 - LIST OF FIGURES (Cont'd)

APPENDIX 3.1

PROCEDURES FOR THE EVALUATION OF SOIL PARAMETERS FOR USE IN THE MODIFIED SMP MODEL FROM THE STANDARD TRIAXIAL TEST

APPENDIX 3.1

PROCEDURES FOR THE EVALUATION OF SOIL PARAMETERS FOR USE IN THE MODIFIED SMP MODEL FROM THE STANDARD TRIAXIAL TEST

The soil parameters required for the modified SMP model can be divided in two main groups:

i) Elastic parameters

ii) Plastic parameters.

Therefore these groups will be dealt with separately.

3.1.1 Evaluation of the Elastic Parameters

As described earlier two elastic parameters were selected to define the $\{C^e\}$ term of the constitutive matrix $\{C^{ep}\}$. One is the shear modulus, G, and the other the bulk modulus, B. Since these two moduli will be used to model the unloading reloading characteristics of the sand they will be referred to as G_e (or G_{max}) and B_e (or B_{ur}) respectively. These two moduli will be considered to be dependent on the mean normal stress (σ_m) and therefore nonlinear-elastic.

- Evaluation of G_e From the Standard Triaxial Test

In practice the laboratory test used to evaluate G_e (or G_{max}) is the resonant column test, however a brief review of the methods to evaluate G_{max} by Byrne et al. (1987) and Negussey (1984) on loading, unloading and reloading on Ottawa sand, using the standard triaxial test, indicate that the G value obtained from triaxial unloading is in agreement with the G_{max}

obtained from the resonant column tests. Therefore the unloading data from standard triaxial tests can be used to evaluate G_e.

The variation of G_e with σ_m is represented by the following equation, which is similar to the equation proposed by Janbu (1963):

$$G_e = KG_e \, Pa \, (\sigma_m/Pa)^n \qquad (3.1.1)$$

where:

KG_e = elastic shear modulus number

n = elastic shear modulus exponent

To evaluate the above two parameters the procedures described by Duncan et al. (1980) are followed here after being adapted to the elastic shear modulus G_e. A brief description is presented below.

Plots of the shear strain-shear stress ratio, (γ/τ), versus γ are developed from the unload data of the standard triaxial test. The shear strain and shear stress are obtained by the following equations:

$$\gamma = \epsilon_1 - \epsilon_3 \qquad (3.1.2)$$

$$\tau = (\sigma_1 - \sigma_3)/2 \qquad (3.1.3)$$

where:

ϵ_1, σ_1 are the major principal strain and stress, respectively.

ϵ_3, σ_3 are the minor principal strain and stress, respectively.

In principle the data from three unload tests carried out at three different initial (prior to unloading) mean normal stresses, $(\sigma_m)_i$ is required. From these plots three values of $(G_e)_i$ are evaluated as is shown by the sketch presented in Fig. 3.1.1(a).

To obntain KG_e and n a log-log plot of $(G_e)_i/Pa)$ versus $(\sigma_m)_i/Pa)$ is developed as is shown in pg. 74, Fig. 3.1.1(b). KG_e is the $(G_e)_i$ correspondent to $(\sigma_m)_i$ = 1 atmosphere and n is the slope of the line.

• Evaluation of B_e

As for G_e the bulk modulus, B_e is considered to be dependent on teh mean normal stress, σ_m, and expressed by the following equation:

$$B_e = KB_e Pa\ (\sigma_m/Pa)^m \qquad (3.1.4)$$

where:

KB_e = elastic bulk modulus number

m = elastic bulk modulus exponent

To obtain KB_e and m the procedures proposed by Byrne and Eldridge (1982) are followed herein. Based on data from conventional triaxial isotropic consolidation tests, Byrne and Eldridge show that the volumetric strain, ϵ_v, due to consolidation can be related to the mean normal stress, σ_m, in the following manner:

$$\epsilon_v = a(\sigma_m)^{1-m} \qquad (3.1.5)$$

where:

a = soil parameter

Using the data from an unload isotropic consolidation test and plotting the above relation on a log-log stress strain plot, Fig. 3.1.1(c) is obtained. From this figure, m, a, and KB_e are evaluated as follows:

(1-m) is the slope of the line, the soil parameter a, is the intercept and KB_e is given by the following equation developed by Byrne and Eldridge:

$$KB_e = \frac{1}{a(1-m)(Pa)^{1-m}} \qquad (3.1.6)$$

In summary, to characterize the elastic behaviour of sand two pairs of soil parameters are needed: (KB_e,m) and (KG_e,n) and can be obtained respectively from the isotropic consolidation phase and shear phase of the standard triaxial test.

3.1.2 Evaluation of the Plastic Parameters

The plastic soil parameters for the modified SMP model can be divided into three main groups:

i) Hardening parameters KG_p and np to define the plastic shear modulus parameter G_p;

ii) Flow rule parameters μ and λ; and

iii) Failure parameters $(\tau_{SMP}/\sigma_{SMP})_F$ and R_F.

Therefore these groups will be dealt with separately.

3.1.2.1 Evaluation of the Plastic Shear Modulus Parameter, G_p

As discussed earlier the hardening rule used in the modified SMP model is assumed to be described by a hyperbolic relationship between the stress

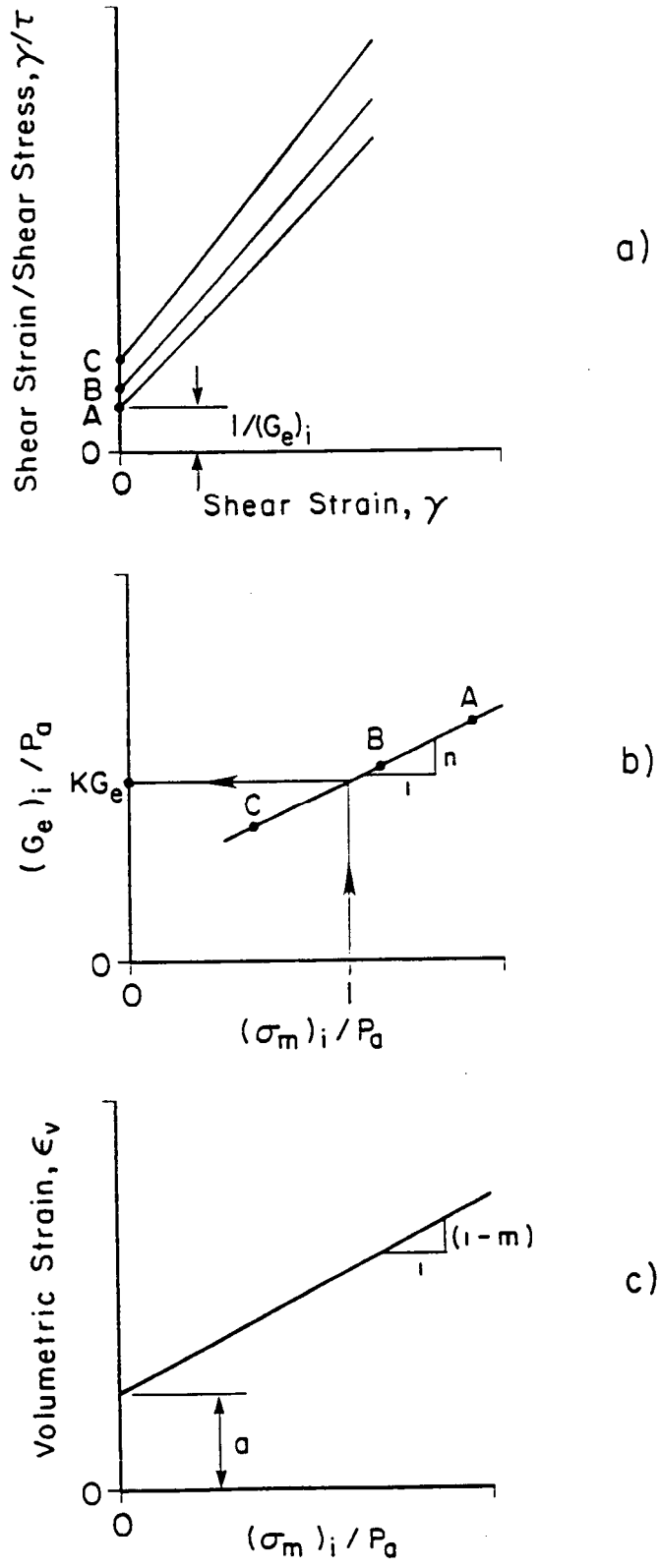

Figure 3.1.1 Sketches Showing the Procedures to Evaluate the Following Elastic Parameters. (a) $(G_e)_i$. (b) KG_e and n. (c) 'a' and (1-m).

ratio, $(\tau_{SMP}/\sigma_{SMP})$, and the plastic shear strain, γ^p_{SMP}. This relationship is given by the following equation (see eq. (2.34)):

$$\Delta\gamma^p_{SMP} = 1/G_p \; \Delta(\tau_{SMP}/\sigma_{SMP}) \qquad (3.1.7)$$

Therefore, to obtain the plastic shear modulus parameter, G_p, iot is necessary to derive values of $(\tau_{SMP}/\sigma_{SMP})$ and γ^p_{SMP} from laboratory test data.

• Evaluation of $(\tau_{SMP}/\sigma_{SMP})$

The stress ratio is evaluated using the following equation (see eq. (2.50)):

$$(\frac{\tau_{SMP}}{\sigma_{SMP}}) = (\frac{(\sigma_1-\sigma_2)^2a_1^2a_2^2+(\sigma_2-\sigma_3)^2a_2^2a_2^2+(\sigma_3-\sigma_1)^2a_2^2a_1^2}{\sigma_1a_1^2+\sigma_2a_2^2+\sigma_3a_3^2})^{1/2} \qquad (3.1.8)$$

where:

a_i = direction cosines of the normal to the SMP and given by the following equation (see eq. (2.24)):

$$a_i = (\frac{\sigma_1\sigma_2\sigma_3}{\sigma_i(\sigma_1\sigma_2+\sigma_2\sigma_3+\sigma_3\sigma_1)})^{1/2} \qquad (3.1.9)$$

For the case of the triaxial compression test $(\sigma_2=\sigma_3)$ eq. (3.1.8) takes the following form as shown by Matsuoka (1983):

$$(\tau_{SMP}/\sigma_{SMP}) = \sqrt{2}/3 \; (\sigma_1/\sigma_3)^{1/2}-(\sigma_3/\sigma_1)^{1/2} \qquad (3.1.10)$$

• Evaluation of γ^p_{SMP}

Fir the increments of elastic principal strain, Δe^e_i are evaluated using the equation:

$$\Delta\epsilon^e_i = [C^e]\Delta\sigma_i \tag{3.1.11}$$

where:

$[C^e]$ = Hooke's constitutive relation, which is developed based on the elastic moduli B_e and G_e obtained in section 3.1.1.

$\Delta\sigma_i$ = increments of principal stress which were recorded during the laboratory test.

Next the increments of plastic principal strain, $\Delta\epsilon^p_i$, are evaluated using the following equation:

$$\Delta\epsilon^p_i = \Delta\epsilon_i - \Delta\epsilon^e_i \tag{3.1.12}$$

where:

$\Delta\epsilon_i$ = increments of principal strain which were recorded during the laboratory test.

Finally, γ^p_{SMP} is obtained using the following equation:

$$\gamma^p_{SMP} = \sum_k \Delta\gamma^p_{SMP} \tag{3.1.13}$$

where:

k = total number of stress increments carried out during the test.

$\Delta\gamma^p_{SMP}$ = increment of plastic shear strain on the SMP and obtained using the following equation (see main text eq. (2.28)):

$$\Delta\gamma^p_{SMP} = ((\Delta\epsilon^p_1 - \Delta\epsilon^p_2)^2 a_1^2 a_2^2 + (\Delta\epsilon^p_2 - \Delta\epsilon^p_2)^2 a_2^2 a_3^2 + (\Delta\epsilon^p_3 - \Delta\epsilon^p_1)^2 a_3^2 a z_1^2)^{1/2} \quad (3.1.14)$$

For the case of the triaxial compression test ($\sigma_2=\sigma_3$, $\Delta\epsilon^p_2=\Delta\epsilon^p_3$) eq. (3.1.14) takes the following form as shown by Matsuoka (1983):

$$\Delta\gamma^p_{SMP} = 2\sqrt{2}\ (\sigma_1\sigma_3)^{1/2}\ (\Delta\epsilon^p_1-\Delta\epsilon^p_3)/(2\sigma_1+\sigma_3) \quad (3.1.15)$$

Since the proposed hardening relationship is assumed to be hyperbolic, the procedures developed by Duncan et al. (1980) to ev aluate the tangent Young's modulus, E_t, for the hyperbolic model were adapted to the modified SMP model and the tangent shear plastic parameter, G_p, is iven by the following equation (see main text eq. (2.12)):

$$G_p = G_{pi}\ (1 - R_F\ SRL)^2 \quad (3.1.16)$$

where:

G_{pi} = the initial tangent value or the initial slope of the hyperbolic stress ratio - strain curve.

R_F = a parameter that relates the asymptotic value of the stress ratio, $(\tau_{SMP}/\sigma_{SMP})_{ult}$ with the failure stress ratio $(\tau_{SMP}/\sigma_{SMP})_F$ by the following equation (see main text eq. (2.36)):

$$(\tau_{SMP}/\sigma_{SMP})_F = R_F\ (\tau_{SMP}/\sigma_{SMP})_{ult} \tag{3.1.17}$$

where:

SRL = the stress ratio level which relates the mobilized stress ratio, $(\tau_{SMP}/\sigma_{SMP})$, with the failure stress ratio by the following equation (see main text eq. (2.37)):

$$SRL = (\tau_{SMP}/\sigma_{SMP})/(\tau_{SMP}/\sigma_{SMP})_F \tag{3.1.18}$$

To obtain $(G_p)_i$ and $(\tau_{SMP}/\sigma_{SMP})_{ult}$ plots of $(\gamma^p_{SMP}/(\tau_{SMP}/\sigma_{SMP}))$ versus γ^p_{SMP} are developed as is shown in Fig. 3.1.2(a). From this figure, values of $(G_p)_i$ and $(\tau_{SMP}/\sigma_{SMP})_{ult}$ are obtained as shown.

As described, the initial shear parameter, $(G_p)_i$, is considered to be dependent on the normal stress, σ_{SMP}, on the SMP and given by the following equation (see main text eq. (2.35)):

$$(G_p)_i = KG_p\ (\sigma_{SMP}/Pa)^{np} \tag{3.1.19}$$

where:

KG_p = is the plastic shear parameter

np = is the plastic shear exponent

To obtain KG_p and np, plots of log $((G_p)_i)$ versus log $((\sigma_{SMP})_i/Pa)$ are developed as shown in Fig. 3.1.2(b). KG_p is the $(G_p)_i$ correspondent to $(\sigma_{SMP})_i$ = 1 atmosphere and np is the slope of the line.

3.1.2.2 Evaluation of the Flow Rule Parameters, μ and λ

The equation that expresses the flow rule on the SMP is given by the following equation (see main text eq. (2.40)):

$$(\tau_{SMP}/\sigma_{SMP}) = \lambda(-\Delta\epsilon^p_{SMP}/\Delta\gamma^p_{SMP}) + \mu \qquad (3.1.20)$$

To develop the above relationship from the standard triaxial test data the values of $(\tau_{SMP}/\sigma_{SMP})$ and $\Delta\gamma^p_{SMP}$ are obtained from eqs. (3.1.10) and (3.1.14) respectively and the value of $\Delta\epsilon^p_{SMP}$ is obtained from the following equation (see main text eq. (2.27)):

$$\Delta\epsilon^p_{SMP} = \Delta\epsilon^p_1 a_1^2 + \Delta\epsilon^p_2 a_2^2 + \Delta\epsilon^p_3 a_3^2 \qquad (3.1.21)$$

For the case of the triaxial compression test ($\Delta\epsilon^p_2 = \Delta\epsilon^p_3$) eq. (3.1.21) takes the following form:

$$\Delta\epsilon^p_{SMP} = (2\sigma_1\ \Delta\epsilon^p_3 + \sigma_3\Delta\epsilon^p_1)/(2\sigma_1 + \sigma_3) \qquad (3.1.22)$$

A sketch of the SMP flow rule is shown in Fig. 3.1.2(c) from which the values of λ and μ are obtained as shown.

3.1.2.3 Evaluation of the Failure Parameters $(\tau_{SMP}/\sigma_{SMP})_f$ and $\Delta(\tau_{SMP}/\sigma_{SMP})$

The failure stress ratio on the SMP is given by the following equation (see main text eq. (2.31)):

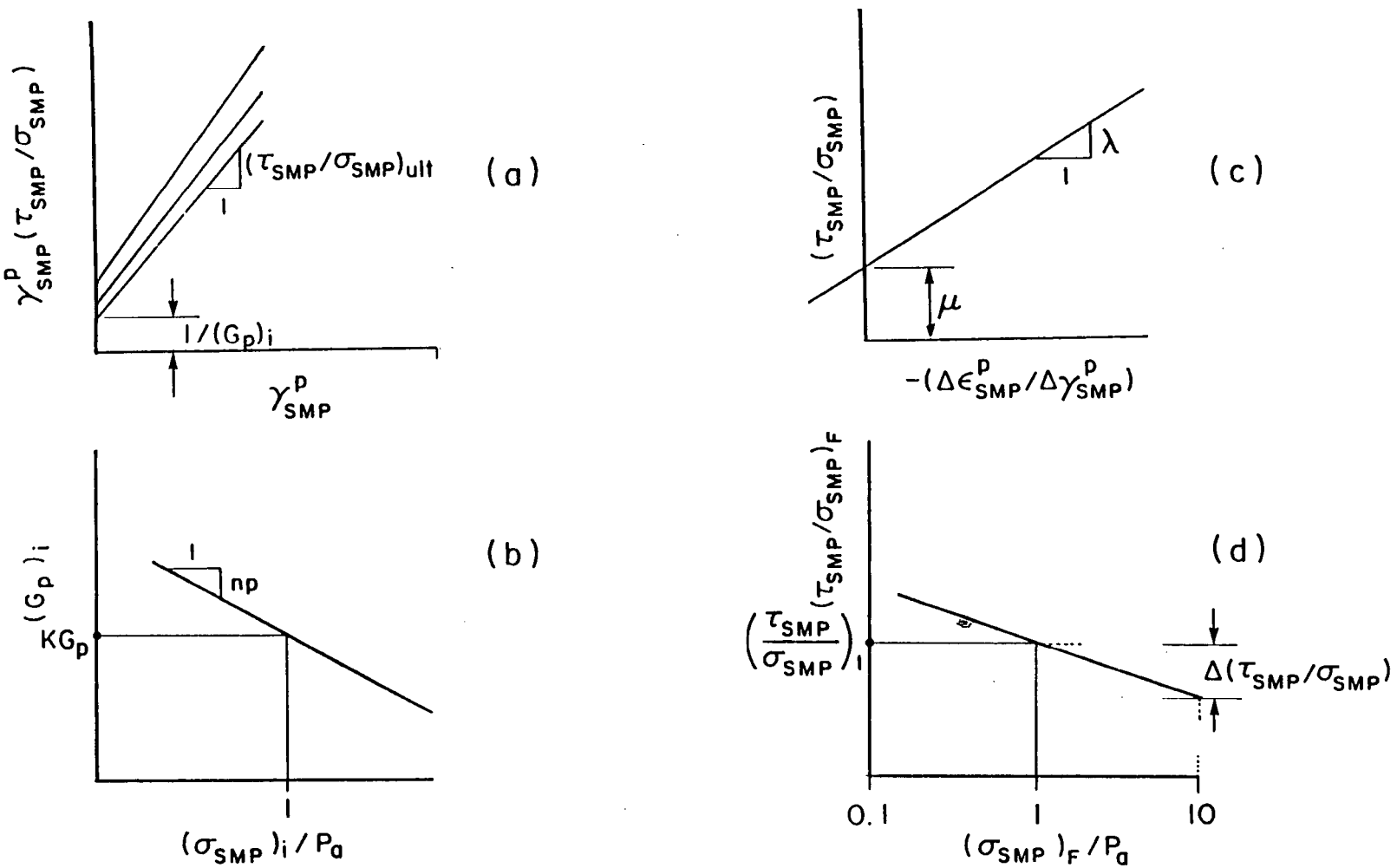

Figure 3.1.2 Sketches Showing the Procedures to Evaluate the Following Plastic Parameters. (a) $(G_p)_i$. (b) KG_p and np. (c) μ and λ. (d) $(\tau_{SMP}/\sigma_{SMP})_i$ and $\Delta(\tau_{SMP}/\sigma_{SMP})$

$$(\tau_{SMP}/\sigma_{SMP})_F = (\tau_{SMP}/\sigma_{SMP})_1 - \Delta(\tau_{SMP}/\sigma_{SMP})\log_{10}((\sigma_{SMP})_F/Pa) \quad (3.1.23)$$

where:

$(\tau_{SMP}/\sigma_{SMP})_1$ = the failure stress ratio at 1 atmosphere

$\Delta(\tau_{SMP}/\sigma_{SMP})$ = the decrease in one log cycle of $(\tau_{SMP}/\sigma_{SMP})_F$

$(\sigma_{SMP})_F$ = the mobilized normal stress on the SMP at failure.

Plotting $(\tau_{SMP}/\sigma_{SMP})_F$ versus $\log_{10}((\sigma_{SMP})_F/Pa)$, the above failure parameters are obtained as is shown in Fig. 3.1.2(d).

Finally the failure ratio parameter, R_F, is evaluated from eq. (3.1.17):

$$R_F = (\tau_{SMP}/\sigma_{SMP})_F/(\tau_{SMP}/\sigma_{SMP})_{ult} \quad (3.1.24)$$

where $(\tau_{SMP}/\sigma_{SMP})_F$ is evaluated from eq. (3.1.8) and $(\tau_{SMP}/\sigma_{SMP})_{ult}$ is evaluated as shown in Fig. 3.1.2(a).

3.1.3 Summary of the Required Soil Parameters for Use in the Modified SMP Model

In all, 11 parameters are used in the modified SMP model. These parameters are summarized below in Table 3.1.1.

Table 3.1.1

Summary of Soil Parameters for Use in the Modified SMP Model

Type		Parameter	Description
Elastic		KG_e	Elastic shear modulus number
		n	Elastic shear modulus exponent
		KB_e	Elastic bulk modulus number
		m	Elastic bulk modulus exonent
Plastic	Hardening Rule	KG_p	Plastic shear number
		np	Plastic shear exponent
	Flow Rule	μ	Flow rule intercept
		λ	Flow rule slope
	Failure	$(\tau_{SMP}/\sigma_{SMP})_i$	Failure stress ratio at 1 atmosphere
		$\Delta(\tau_{SMP}/\sigma_{SMP})$	Decrease in one log cycle of $(\tau_{SMP}/\sigma_{SMP})_F$
		R_F	Failure ratio

APPENDIX 3.2

EVALUATION OF THE SOIL PARAMETERS FOR LEIGHTON-BUZZARD SAND (e_o = .53) FOR USE IN THE MODIFIED SMP MODEL

APPENDIX 3.2

EVALUATION OF THE SOIL PARAMETERS FOR LEIGHTON-BUZZARD SAND (e_0 = .53) FOR USE IN THE MODIFIED SMP MODEL

- Elastic Parameters, B_e and G_e

The elastic bulk modulus, B_e, was evaluated based on triaxial test data obtained on Leighton-Buzzard sand (e_0 = .53) by Kolbuszewski (1965) and on Silver sand (e_0 = .55) by Andrawes (1964). These data were retrieved from the work published by Stroud (1971). The elastic shear modulus, G_e was evaluated based on triaxial test data obtained on Silver sand (e_0 = .55) by Andrawes (1964). The Silver sand is also a coarse rounded sand and was considered by Stroud to have similar elastic properties as the Leighton-Buzzard sand. The variation of B_e and G_e with mean normal stress, σ_m is shown in Fig. 3.2.1 where the log-log plots of B_e/pa and G_e/pa versus σ_m/pa are presented. From this figure, the following equations for B_e and G_e were evaluated:

$$B = 580 \text{ Pa } (\sigma_m/Pa)^{.60}$$

$$G = 620 \text{ Pa } (\sigma_m/Pa)^{.63}$$

i.e.: $KB_e = 650$, $m = .60$, and $KG_e = 620$, $n = .63$.

- Plastic Parameteres

The evaluation of the plastic parameters G_p, μ, λ, $(\tau_{SMP}/\sigma_{SMP})_1$, $\Delta(\tau_{SMP}/\sigma_{SMP})$ and R_F is described below.

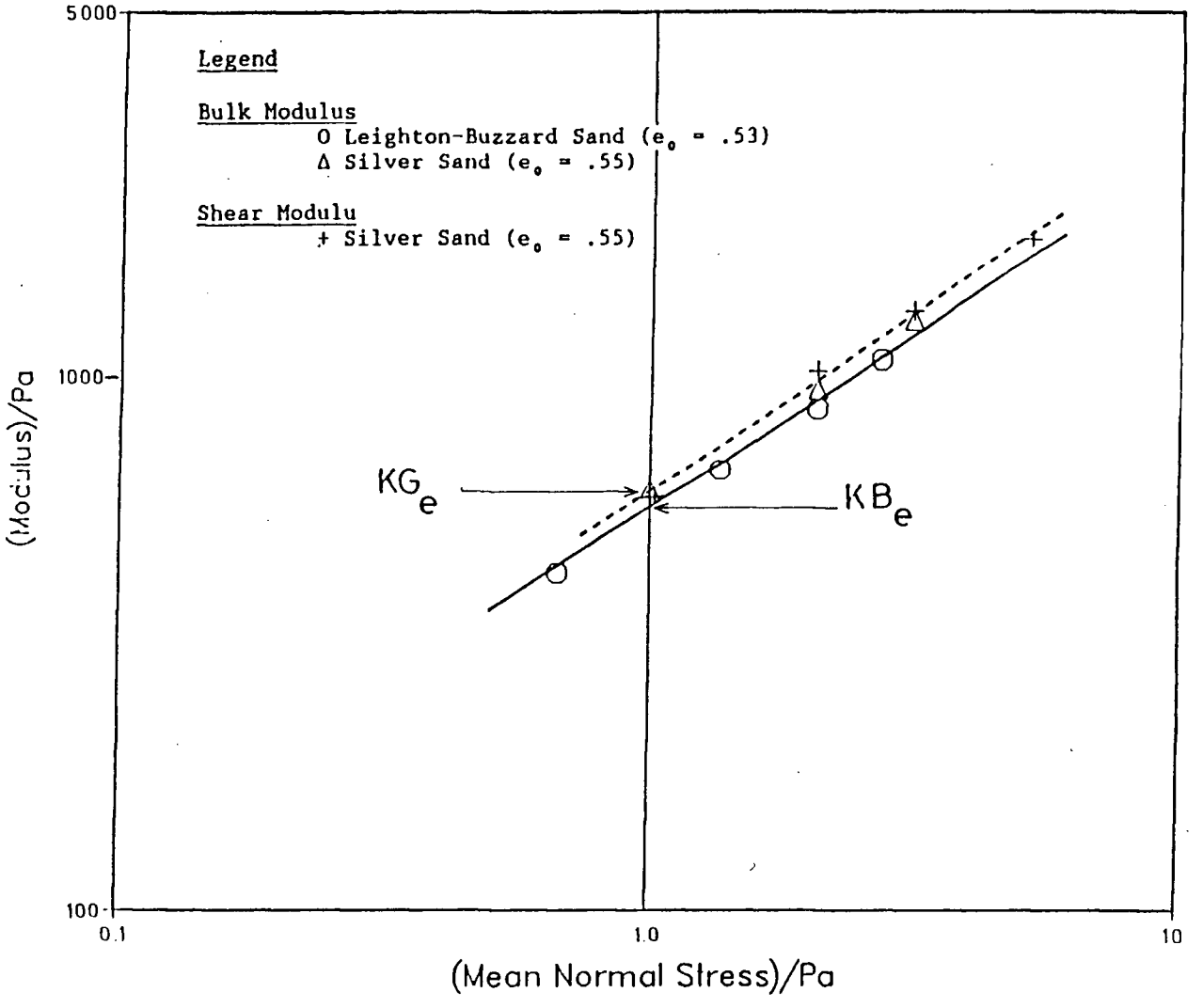

Figure 3.2.1 Variation of B_e and G_e with Mean Normal Stress

• Plastic Shear Modulus Parameter, G_p

The procedures to evaluate the plastic shear modulus parameter, G_p as a function of σ_{SMP} from simple shear data are exactly the same as that outlined in the main text (section 3.1) from the triaxial data once the values of the principal stresses σ_1, σ_2, and σ_3, and the values of the increments of plastic strain $\Delta\epsilon_1^p$, $\Delta\epsilon_2^p$, and $\Delta\epsilon_3^p$ are known from each test. Based on the laboratory data published by Stroud (1971) the above quantities were obtained as presented in Appendix 3.3, and in turn the values of the stress ratio $(\tau_{SMP}/\sigma_{SMP})$ and the plastic shear strain γ_{SMP}^p evaluated. Based on these two quantities, Figs. 3.2.2 and 3.2.3 were developed. The plot of $\gamma_{SMP}^p/(\tau_{SMP}/\sigma_{SMP})$ versus γ_{SMP}^p is shown in Fig. 3.2.2 and the log-log plot of $(G_p)_i$ versus $(\sigma_{SMP})_i/Pa)$ is shown in Fig. 3.2.3. From this figure, the value of G_p is obtained and is given by:

$$G_p = 335\ (\sigma_m/pa)^{-.48}$$

i.e., $KG_p = 335$ np $= -.48$.

• Flow Rule Parameters μ and λ

Manipulating Stroud's data and following the procedures described earlier in Appendix 3.1, the plot of τ_{SMP}/σ_{SMP} versus $-\Delta\epsilon_{SMP}^p/\Delta\gamma_{SMP}^p$ is presented in Fig. 3.2.4. From this figure, the following flow rule parameters are evaluated:

$$\mu = .20$$

$$\lambda = 1.20$$

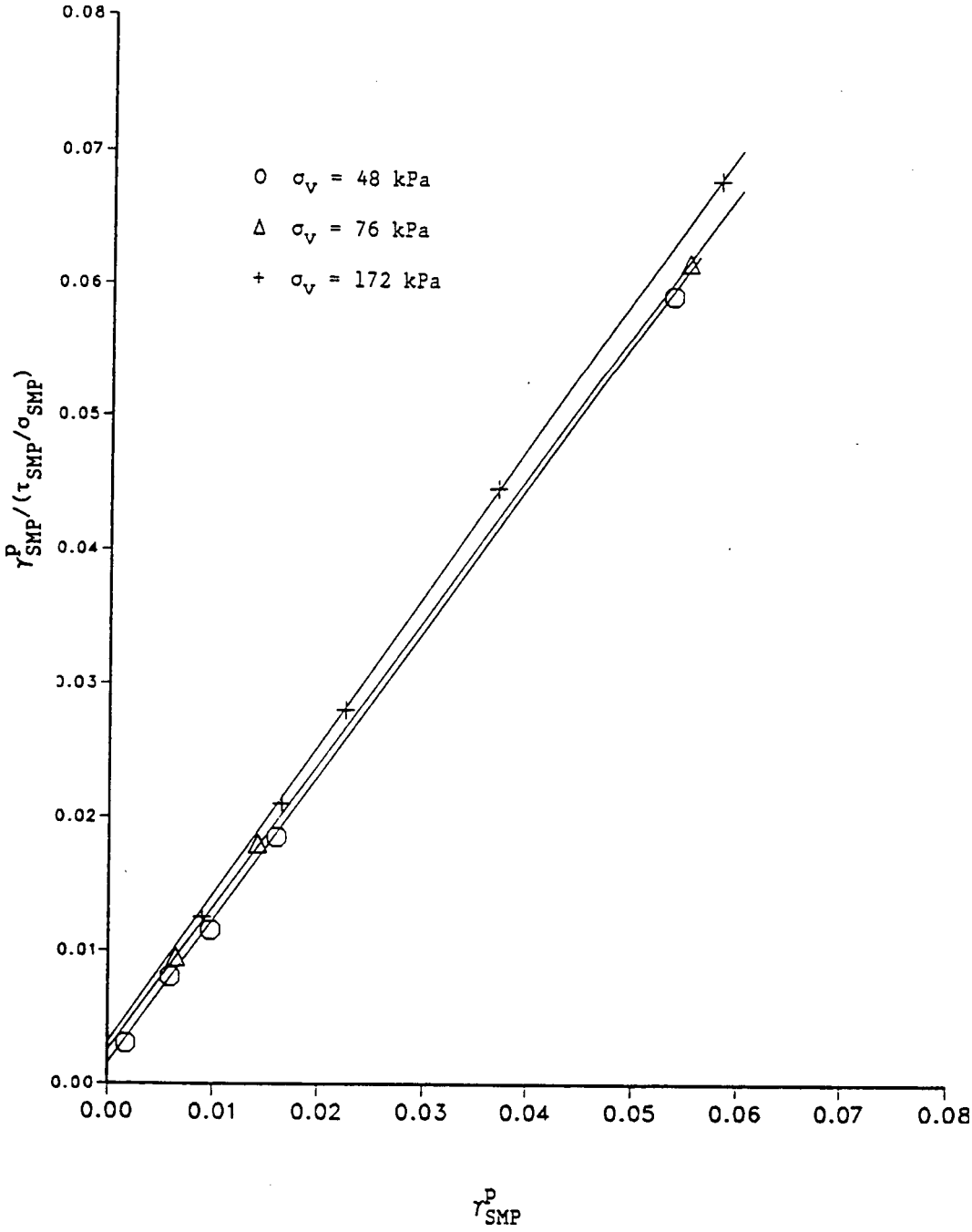

Figure 3.2.2 Plot of $(\gamma^p_{SMP}/(\tau_{SMP}/\sigma_{SMP}))$ versus γ^p_{SMP}

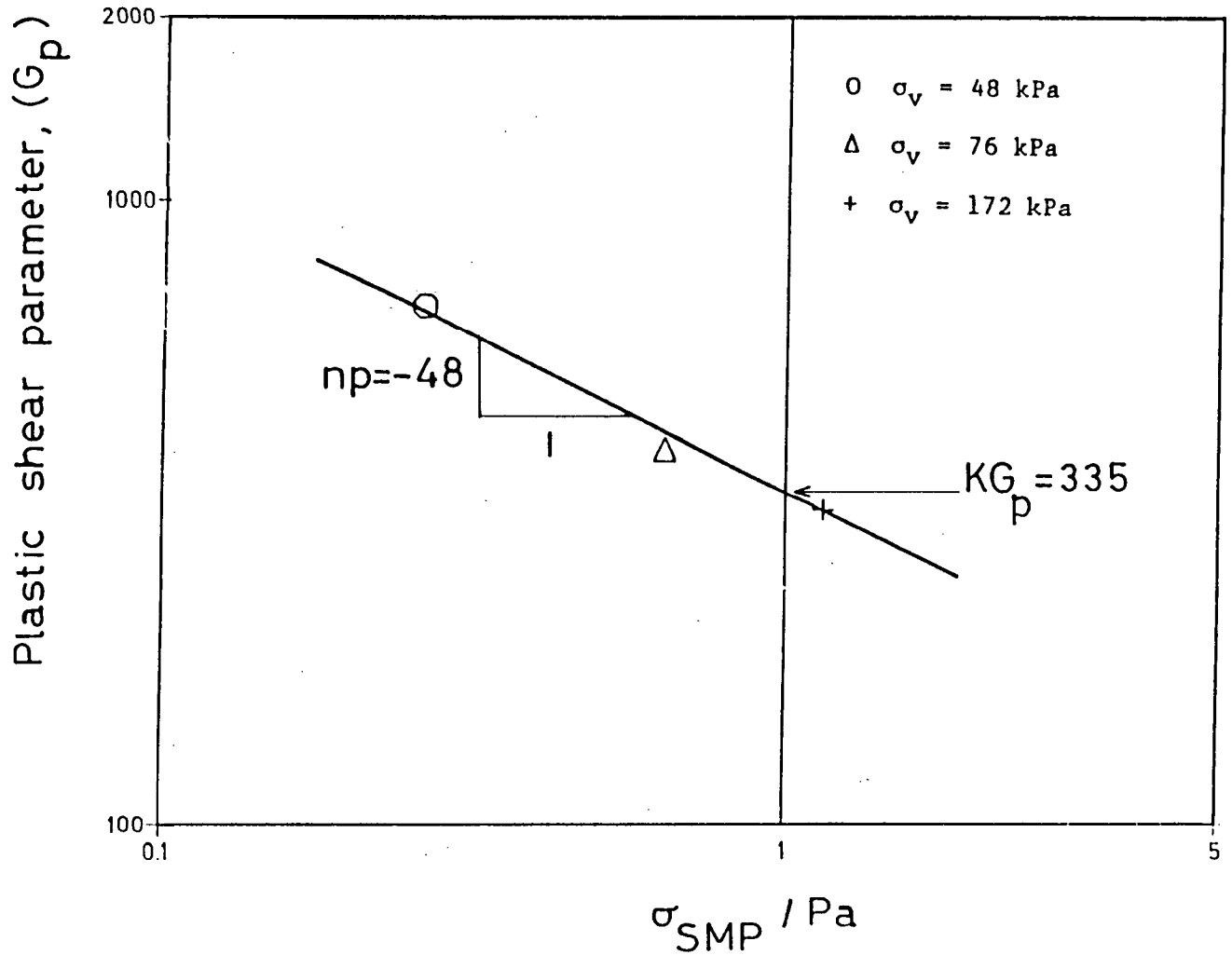

Figure 3.2.3 Plot of $(G_p)_i$ versus (σ_{SMP}/Pa)

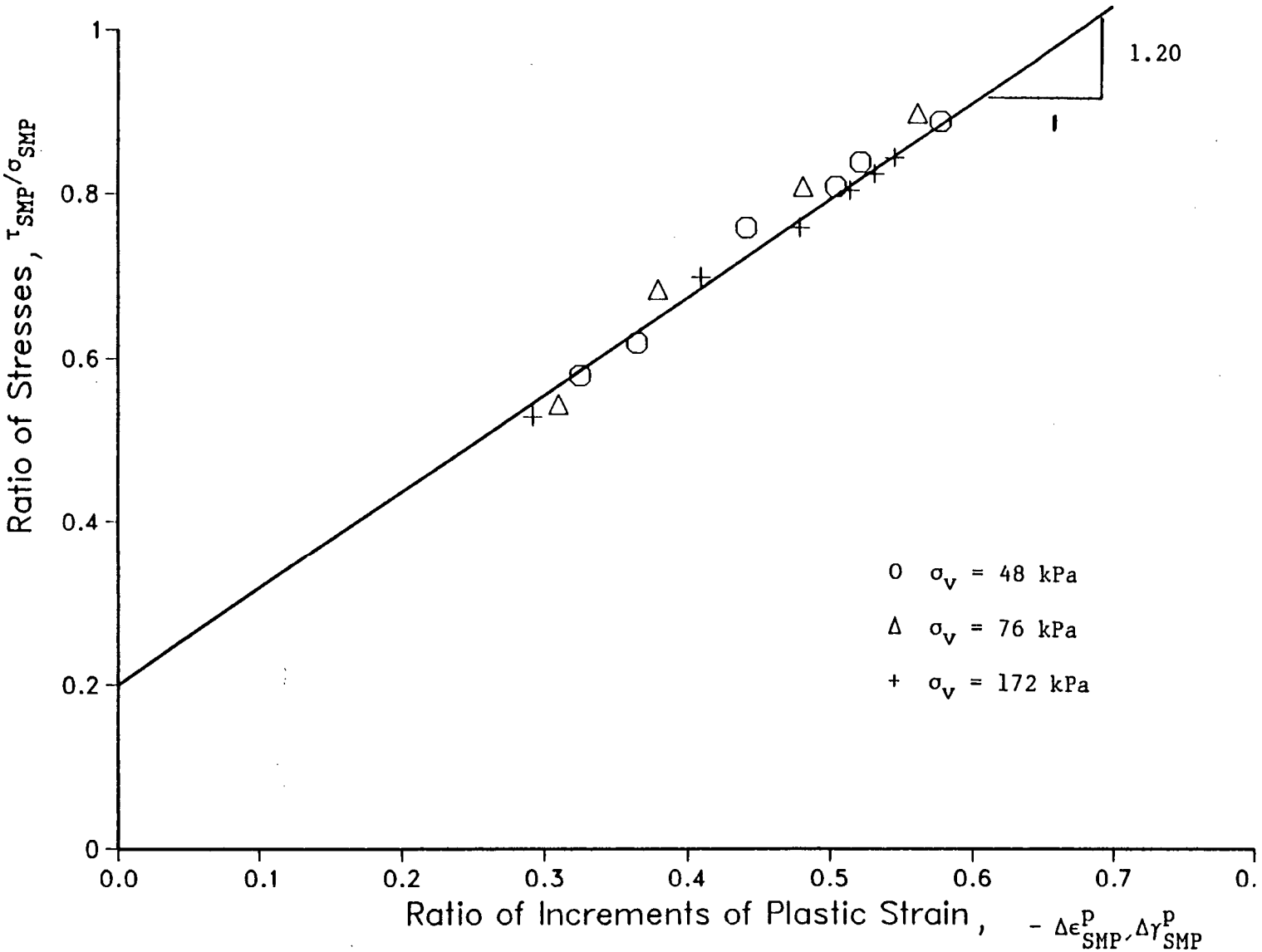

Figure 3.2.4 Flow Rule Plot for Leighton-Buzzard Sand

• Failure Parameters $(\tau_{SMP}/\sigma_{SMP})_1$, $\Delta(\tau_{SMP}/\sigma_{SMP})$ and R_F

The values of $(\tau_{SMP}/\sigma_{SMP})_F$ versus $(\sigma_{SMP})_F/pa$ are presented in a semi-log plot in Fig. 3.2.5 and from this figure $(\tau_{SMP}/\sigma_{SMP})_F$ is given by the following equation,

$$(\tau_{SMP}/\sigma_{SMP})_F = .862 - .08 \log_{10} (\sigma_{SMP}/Pa)$$

i.e.

$$(\tau_{SMP}/\sigma_{SMP})_1 = .862$$

and

$$\Delta(\tau_{SMP}/\sigma_{SMP}) = .08.$$

The failure parameter R_F was obtained using the $(\tau_{SMP}/\sigma_{SMP})_{ult}$ values obtained from Fig. 3.2.2 together with the $(\tau_{SMP}/\sigma_{SMP})_F$ values obtained above. From those values, a $(R_F)_{av} = .957$ was obtained.

A summary of the soil parameters for Leighton-Buzzard sand ($e_0 = .53$) is presented in Table 3.2.1.

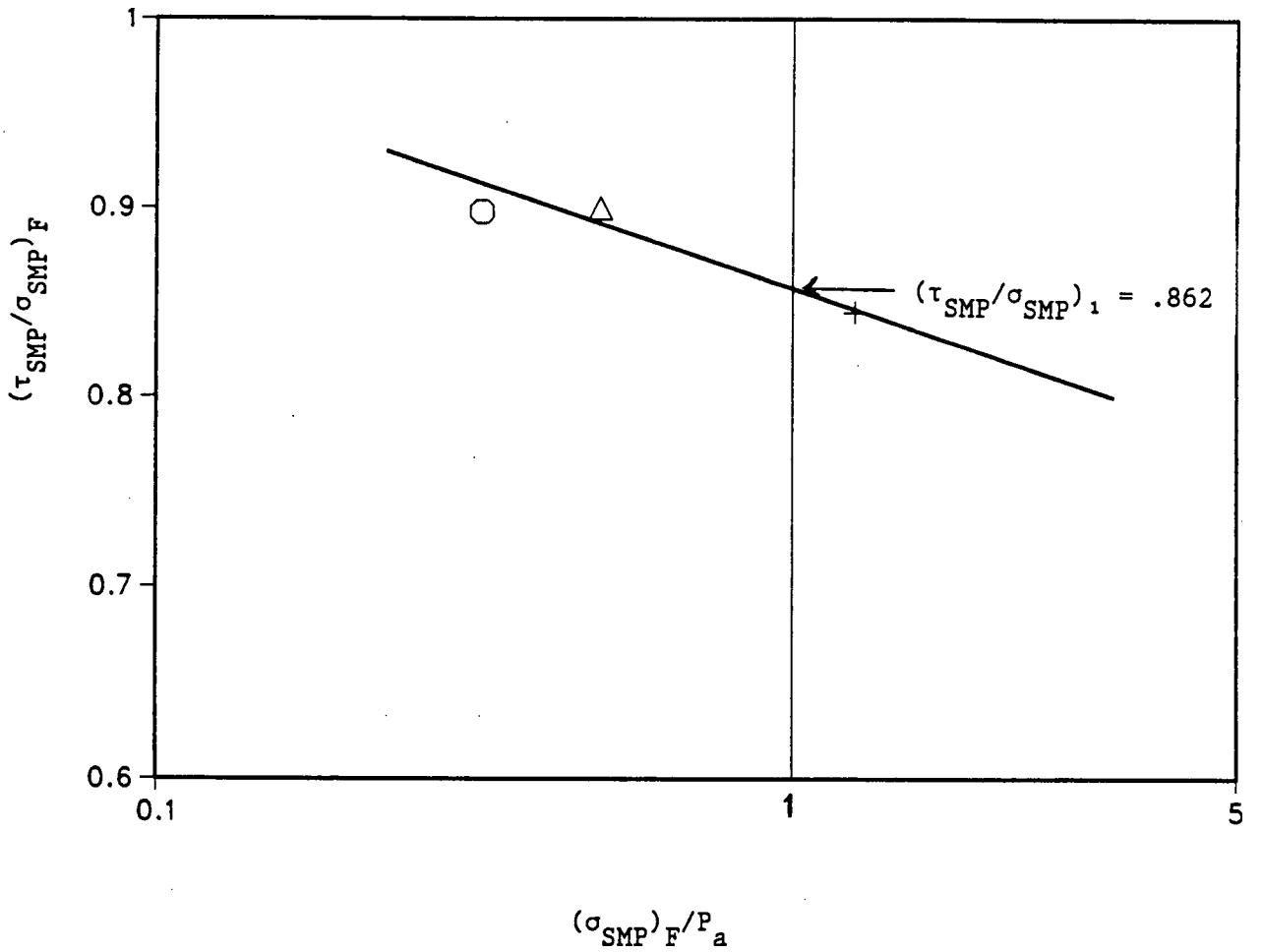

Figure 3.2.5 Plot of $(\tau_{SMP}/\sigma_{SMP})_F$ versus (σ_{SMP}/Pa)

Table 3.2.1

Soil Parameters for Leighton-Buzzard Sand (e_o=.53) for use in the SMP Modified Model

Elastic Parameters		KG_e = 620 n = 0.63 KB_e = 580 m = 0.60
Plastic Parameters	Plastic Shear Modulus Parameters	KG_p = 335 np = -.48
	Flow Rule Parameters	μ = .20 λ = 1.20
	Failure Parameters	$(\frac{\tau_{smp}}{\sigma_{smp}})_{1 \text{ atm.}}$ = .862 $\Delta(\frac{\tau_{smp}}{\sigma_{smp}})$ = .08 $(R_F)_{av}$ = .957

APPENDIX 3.3

A) EVALUATION OF σ_1, σ_2, σ_3 and $\Delta\epsilon_1^p$, $\Delta\epsilon_2^p$, $\Delta\epsilon_3^p$ FROM SIMPLE SHEAR DATA ON LEIGHTON-BUZZARD SAND (Stroud, 1971)

B) EVALUATION OF THE MOBILIZED σ_x: (shown in Fig. 3.5 of the Main Text)

APPENDIX 3.3

A) Evaluation of σ_1, σ_2, σ_3 and $\Delta\epsilon_1^p$, $\Delta\epsilon_2^p$, $\Delta\epsilon_3^p$ from Simple Shear Data on Leighton-Buzzard Sand (Stroud, 1971)

From the laboratory test data reported by Stroud (1971) (simple shear tests with constant vertical stress) on Leighton-Buzzard sand, the following figures were retrieved:

- Fig. 3.3.1 - plot of t versus s

where:

$t = (\sigma_1-\sigma_3)/2$

$s = (\sigma_1+\sigma_3)/2$

and

σ_1,σ_3 = major and minor principal stresses

- Fig. 3.3.2 - plot of (t/s) versus γ

where:

$\gamma = (\epsilon_1-\epsilon_3)$

and

ϵ_1,ϵ_3 = major and minor principal strains

- Fig. 3.3.3 - plot of $(\Delta v/\Delta\gamma)$ versus γ (t/s)

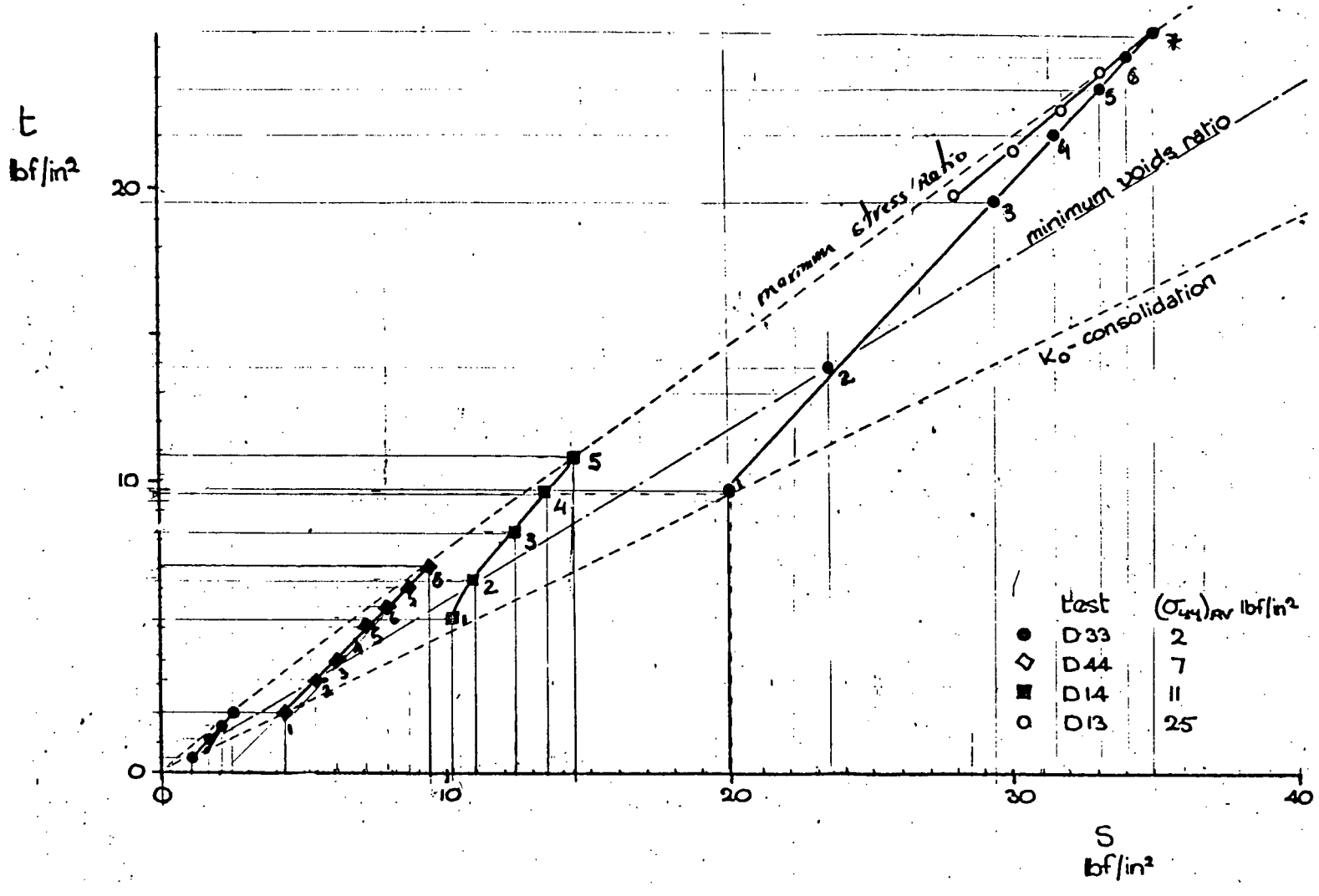

Figure 3.3.1 Plot of t versus s (after Stroud, 1971)

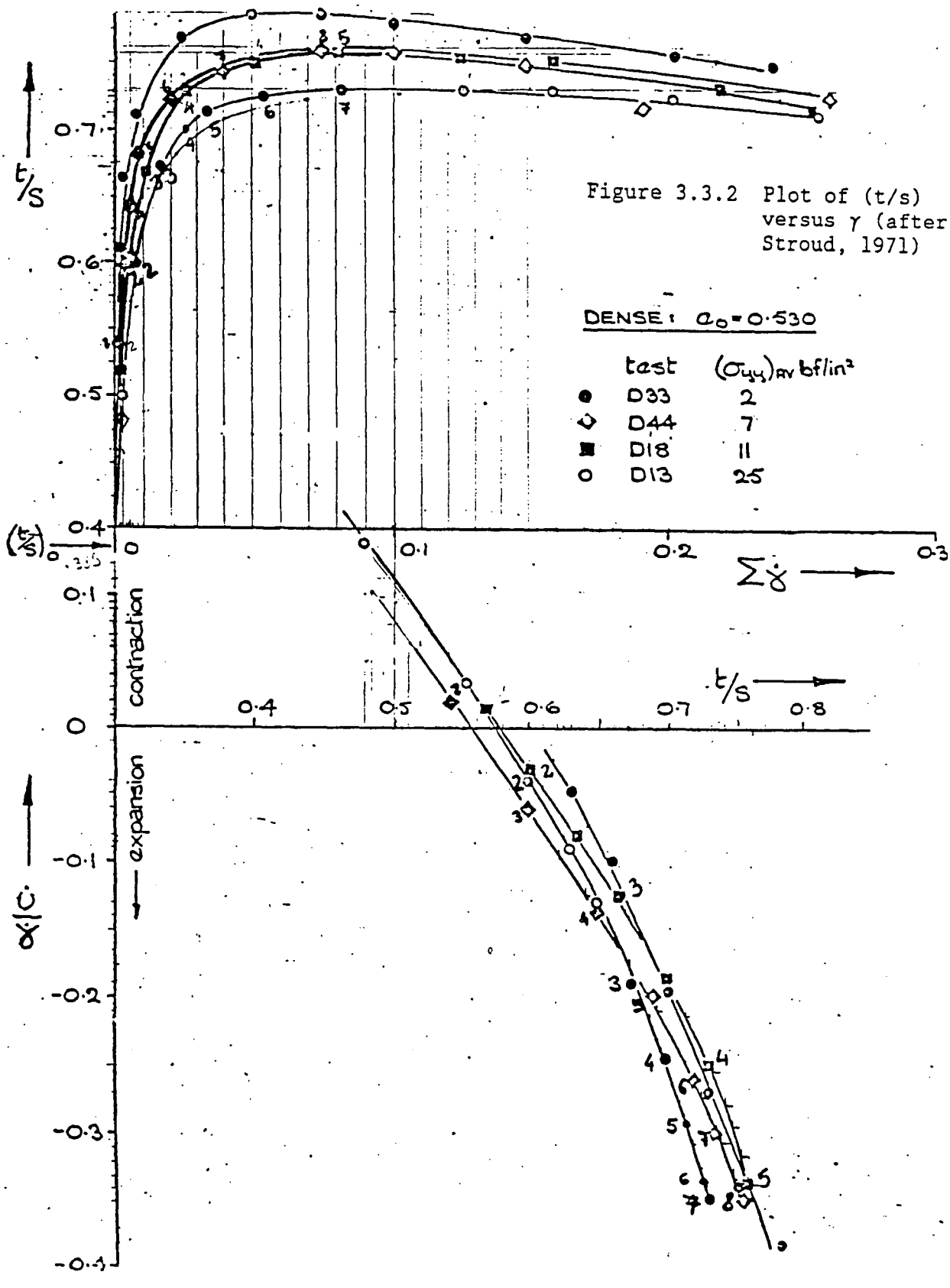

Figure 3.3.2 Plot of (t/s) versus γ (after Stroud, 1971)

Figure 3.3.3 Plot of ($\Delta V/\Delta\gamma$) versus γ (after Stroud, 1971)

where:

$\Delta v = \Delta\epsilon_1 + \Delta\epsilon_3$

$\Delta\gamma = \Delta\epsilon_1 - \Delta\epsilon_3$

and

$\Delta\epsilon_1, \Delta\epsilon_3$ = major and minor increments of principal strain

- Fig. 3.3.4 - plot of (σ_2/s) versus γ

where:

σ_2 = intermediate principal stress

From the data shown in the above 4 figures the following tables were developed:

- Table 3.3.1 for test D44 (σ_v = 48 kPa);
- Table 3.3.2 for test D14 (σ_v = 76 kPa);

and

- Table 3.3.3 for test D13 (σ_v = 172 kPa).

These tables were developed in the following manner:

a) From Fig. 3.3.1 values of s and t were obtained for each data point.

b) With the above s and t values the ratio (t/S) is obtained. Entering this (t/s) value in Fig. 3.3.2 the corresponding shear strain γ is evaluated.

c) Entering this γ value in Fig. 3.3.4 the value of σ_2/s is obtained and in turn that of σ_2.

d) The values of σ_1 and σ_3 are obtained as follows:

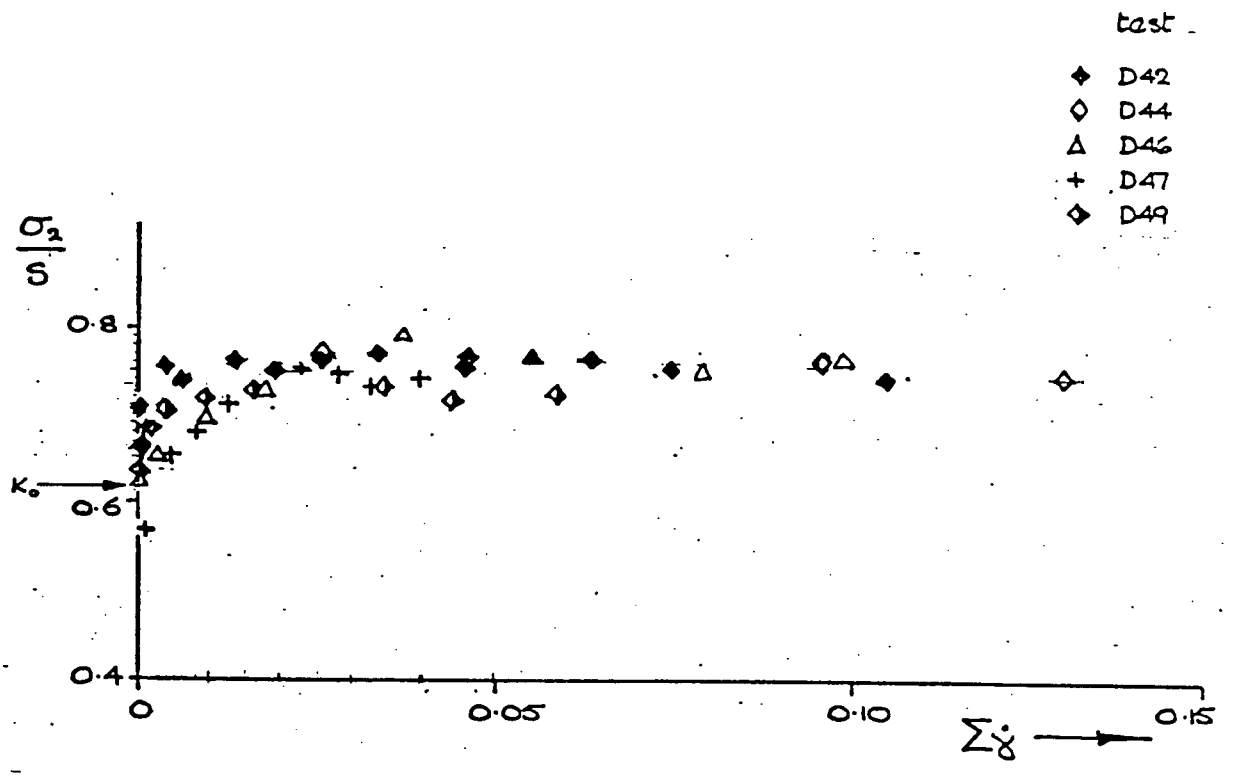

Figure 3.3.4 Plot of (σ_2/s) versus γ (after Stroud, 1971)

Table 3.3.1

Reduction of Data From Simple Shear Results

σ_v = 48.27 kPa

s (kPa)	t (kPa)	t/s	γ	σ_2/s	$(t/s)_{av}$	$\Delta v/\Delta\gamma$	$\Delta\gamma$	Δv
34.9	13.4	.385	0.0	.615				
					.420	N/A	0.00140	N/A
30.0?	13.8	.46	0.00140	.675				
					.525	.040	0.00140	+.000560
37.0	22.0	.59	0.00280	.690				
					.605	-.070	0.00137	-.000096
42.0	26.0	.62	0.00417	.700				
					.655	-.150	0.00623	-.000935
49.0	34.0	.69	0.01040	.720				
					.700	-.234	0.00490	-.001147
54.0	39.0	.71	0.01530	.730				
					.720	-.270	0.00900	-.002430
59.0	43.0	.73	0.02430	.740				
					.745	-.350	0.05070	-.017740
64.8	49.3	.76	0.07500	.740				

Table 3.3.2

Reduction of Data From Simple Shear Results

σ_v = 75.8 kPa

s (kPa)	t (kPa)	t/s	γ	σ_2/s	$(t/s)_{av}$	$\Delta v/\Delta\gamma$	$\Delta\gamma$	Δv
54.8	21.1	.385	0.0	.615				
					.448	N/A	.0028	N/A
70.3	36	.51	.0028	.690				
					.555	.020	.0025	.00005
76	46	.60	.0053	.710				
					.635	-.085	.0072	-.00061
85	56	.67	.0125	.725				
					.695	-.190	.0111	-.0021
93	67	.72	.0236	.740				
					.740	-.280	.0564	-.0158
99.3	74.8	.75	.0080	.740				

Table 3.3.3

Reduction of Data From Simple Shear Results

σ_v = 172 kPa

s (kPa)	t (kPa)	t/s	γ	σ_2/s	$(t/s)_{av}$	$\Delta v/\Delta\gamma$	$\Delta\gamma$	Δv
124.5	47.9	.385	0.0	.615				
					.440	N/A	0.0028	N/A
138	67	.49	0.0028	.690				
					.545	0.045	0.0048	+.000216
161	96	.60	0.0076	.715				
					.635	-0.114	0.0083	-.000946
201	135	.67	0.0159	.735				
					.685	- .235	0.0105	-.002470
216	152	.70	0.0264	.740				
					.705	- .298	0.0083	-.002470
228	163	.71	0.0347	.740				
					.720	- .330	0.0195	-.006430
234	170	.73	0.0542	.740				
					.730	- .350	0.0258	-.009030
241	176	.73	0.0816	.740				

$$\sigma_1 = s + t \; ; \quad \sigma_3 = s - t \tag{3.3.1}$$

e) From the values of every two consecutive rows, in the tables, the following quantities are obtained:

$$\Delta\gamma = \gamma_{row(i+1)} - \gamma_{row(i)} \tag{3.3.2}$$

$$\begin{aligned} \Delta\sigma_1 &= \sigma_{1\,row(i+1)} - \sigma_{1\,row(i)} \\ \Delta\sigma_2 &= \sigma_{2\,row(i+1)} - \sigma_{2\,row(i)} \\ \Delta\sigma_3 &= \sigma_{3\,row(i+1)} - \sigma_{3\,row(i)} \end{aligned} \tag{3.3.3}$$

$$(t/s)_{av} = [(t/s)_{row(i+1)} + (t/s)_{row(i)}]/2 \tag{3.3.4}$$

f) Entering the value of $(t/s)_{av}$ in Fig. 3.3.3 the corresponding value of $(\Delta v/\Delta\gamma)$ is obtained.

g) Using the value of $\Delta\gamma$ from eq. (3.3.2) and the value of $(\Delta v/\Delta\gamma)$ obtained above the value of Δv is evaluated.

h) The values of $\Delta\epsilon_1$ and $\Delta\epsilon_3$ are evaluated as follows:

$$\begin{aligned} \Delta\epsilon_1 &= (\Delta v + \Delta\gamma)/2 \\ \Delta\epsilon_3 &= (\Delta v - \Delta\gamma)/2 \end{aligned} \tag{3.3.5}$$

and $\Delta\epsilon_2 = 0$ from boundary conditions

i) The mean normal stress, σ_m is evaluated using the values of $\sigma_i (i=1,2,3)$ obtained above in (c) and (d) together with the following equation:

$$\sigma_m = \frac{1}{3}(\sigma_1 + \sigma_2 + \sigma_3) \tag{3.3.6}$$

j) Using the values of KG_e, n and KB_e and m obtained in Appendix 3.2, the moduli G_e and B_e are obtained using the following equations,

$$G_e = 620 \text{ pa } (\sigma_m/pa)^{.63} \tag{3.3.7}$$

$$B_e = 580 \text{ pa } (\sigma_m/pa)^{.60} \tag{3.3.8}$$

where σ_m is the value obtained above in (i).

k) Using the relationship between Poisson's ratio, ν, and G and B, the Poisson's ratio is obtained as follows:

$$\nu = (3B_e-2G_e)/(6B_e+2G_e) \tag{3.3.9}$$

and in turn the Young's modulus, E obtained using the equation

$$E_e = 2(1+\nu)\ G_e \tag{3.3.10}$$

ℓ) The increments of elastic strain $\Delta\epsilon_1^e$, $\Delta\epsilon_2^e$, $\Delta\epsilon_3^e$ are then obtained using Hooke's Law:

$$\begin{aligned}
\Delta\epsilon_1^e &= \frac{1}{E_e}\ (\Delta\sigma_1 - \nu(\Delta\sigma_2 + \Delta\sigma_3) \\
\Delta\epsilon_2^e &= \frac{1}{E_e}\ (\Delta\sigma_2 - \nu(\Delta\sigma_1 + \Delta\sigma_3) \qquad (3.3.11) \\
\Delta\epsilon_3^e &= \frac{1}{E_e}\ (\Delta\sigma_3 - \nu(\Delta\sigma_1 + \Delta\sigma_2)
\end{aligned}$$

m) Assuming that the increments of strain are composed of increments of elastic strain, $\Delta\epsilon^e$, and increments of plastic strain $\Delta\epsilon^p$, i.e.

$$\Delta\epsilon_i = \Delta\epsilon_i^e + \Delta\epsilon_i^p \qquad (i = 1,2,3) \tag{3.3.12}$$

than the values of $\Delta\epsilon_i^p$ are evaluated from the values of $\Delta\epsilon_i$ (given by eq. (3.3.5)) and the values of $\Delta\epsilon_i^e$ (given by eq. (3.3.11)), i.e.

$$\Delta\epsilon_1^p = \Delta\epsilon_1 - \Delta e_1^e$$

$$\Delta\epsilon_3^p = \Delta\epsilon_3 - \Delta\epsilon_3^e$$

and since $\Delta\epsilon_2 = 0$

$$\Delta\epsilon_2^p = -\Delta\epsilon_2^e$$

B) Evaluation of the Mobilized σ_x During Shear (Shown in Fig. 3.5 of the Main Text)

For the tests carried out with constant vertical stress (i.e. σ_z = const.) the following equality is observed:

$$\sigma_1 + \sigma_3 = \sigma_z + \sigma_x$$

or

$$\sigma_x = \sigma_1 + \sigma_3 - \sigma_z \tag{3.3.13}$$

entering the values of σ_1 and σ_3 from eq. (3.3.1) and the value of σ_z correspondent to each test into eq. (3.3.13) the values of σ_x were evaluated.

APPENDIX 3.4

EVALUATION OF THE SOIL PARAMETERS FOR OTTAWA SAND (D_r = 87%). FOR USE IN THE MODIFIED SMP MODEL

APPENDIX 3.4

EVALUATION OF THE SOIL PARAMETERS FOR OTTAWA SAND (D_r = 87%). FOR USE IN THE MODIFIED SMP MODEL

The stress paths used to generate the data base for modelling are shown in Fig. 3.4.1 together with the description of each test.

3.4.1 Evaluation of Elastic Parameters

- Evaluation of G_e

To obtain KG_e and n, plots of (γ/τ) versus γ were developed from the unload data of the conventional triaxial compression tests CTC-5 and CTC-10 (5 and 10 mean the initial, prior to shear, confining pressure in psi). As it is shown in Fig. 3.4.2 three values of $(G_e)_i$ were evaluated. One from the only unload cycle of test CTC-5 and two values of $(G_e)_i$ from the 2 unload cycles of test CTC-10. The mean normal stresses prior to the unloading for each unload cycle is also presented in the figure. To obtain KG_e a log-log plot of $((G_e)_i/p_a)$ versus (σ_m (prior to unload)/p_a) was developed and it is presented in Fig. 3.4.3, and from this figure values of KG_e = 1640 and n = 0.49 were obtained. Therefore the G_e for Ottawa sand (D_r = 87%) is given by the following equation:

$$G_e = 1640\ p_a\ \left(\frac{\sigma_m}{p_a}\right)^{.49} \qquad (3.4.1)$$

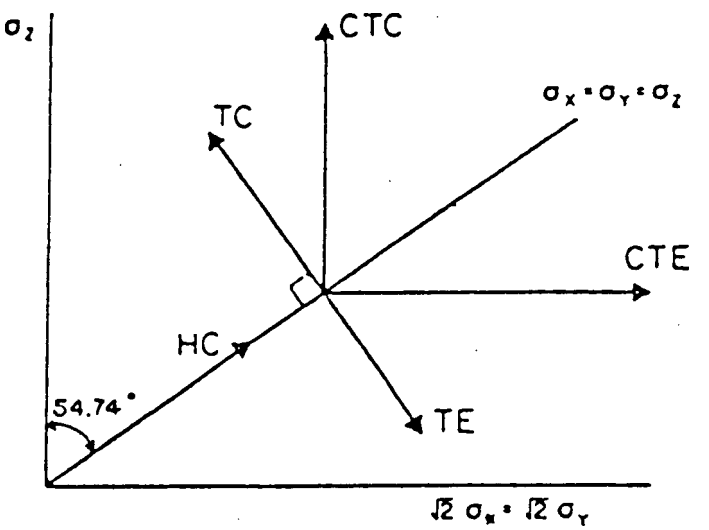

Figure 3.4.1 Stress Paths Used to Generate the Data Base

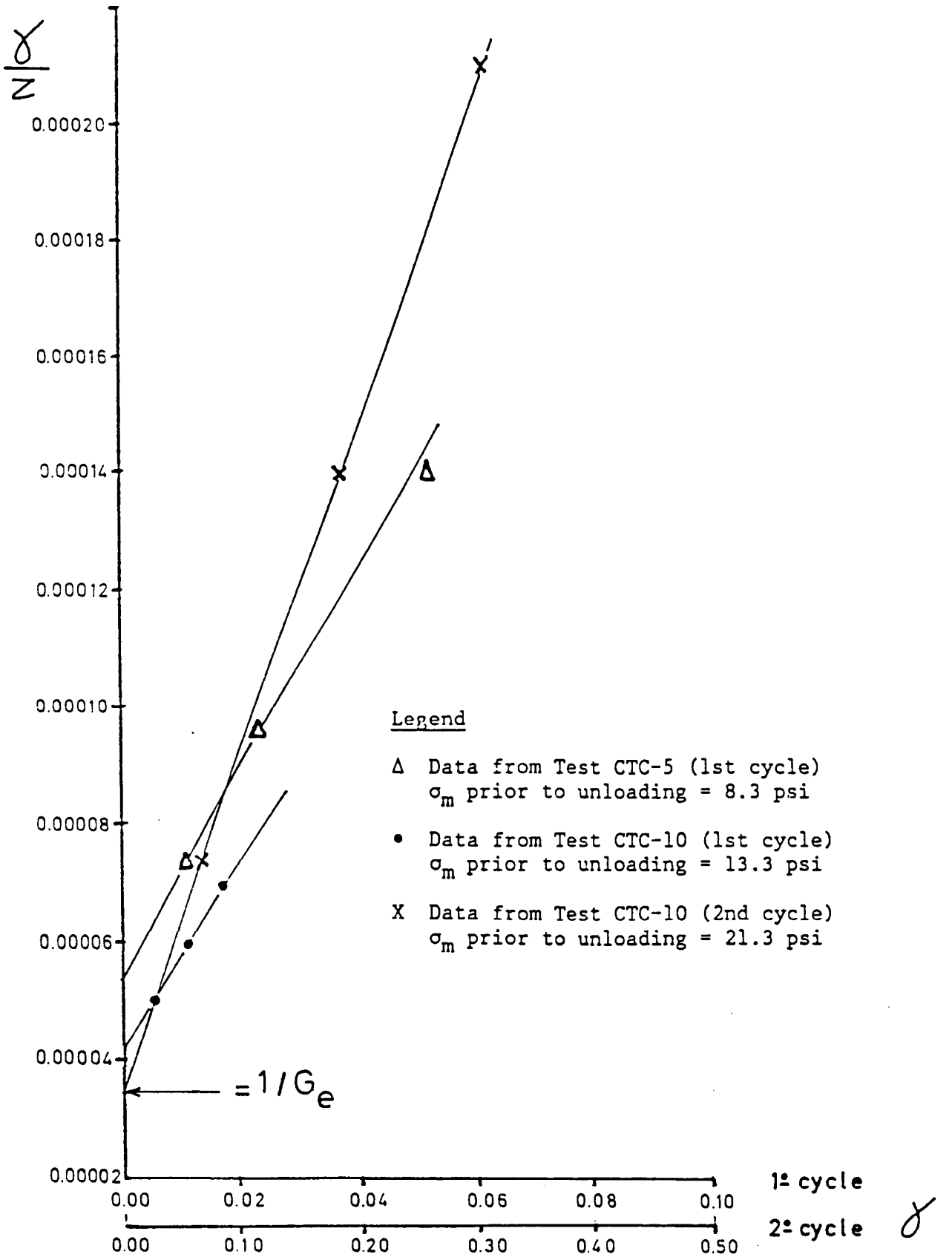

Figure 3.4.2 Plot of (γ/τ) versus γ obtained from the Unload CTC Data

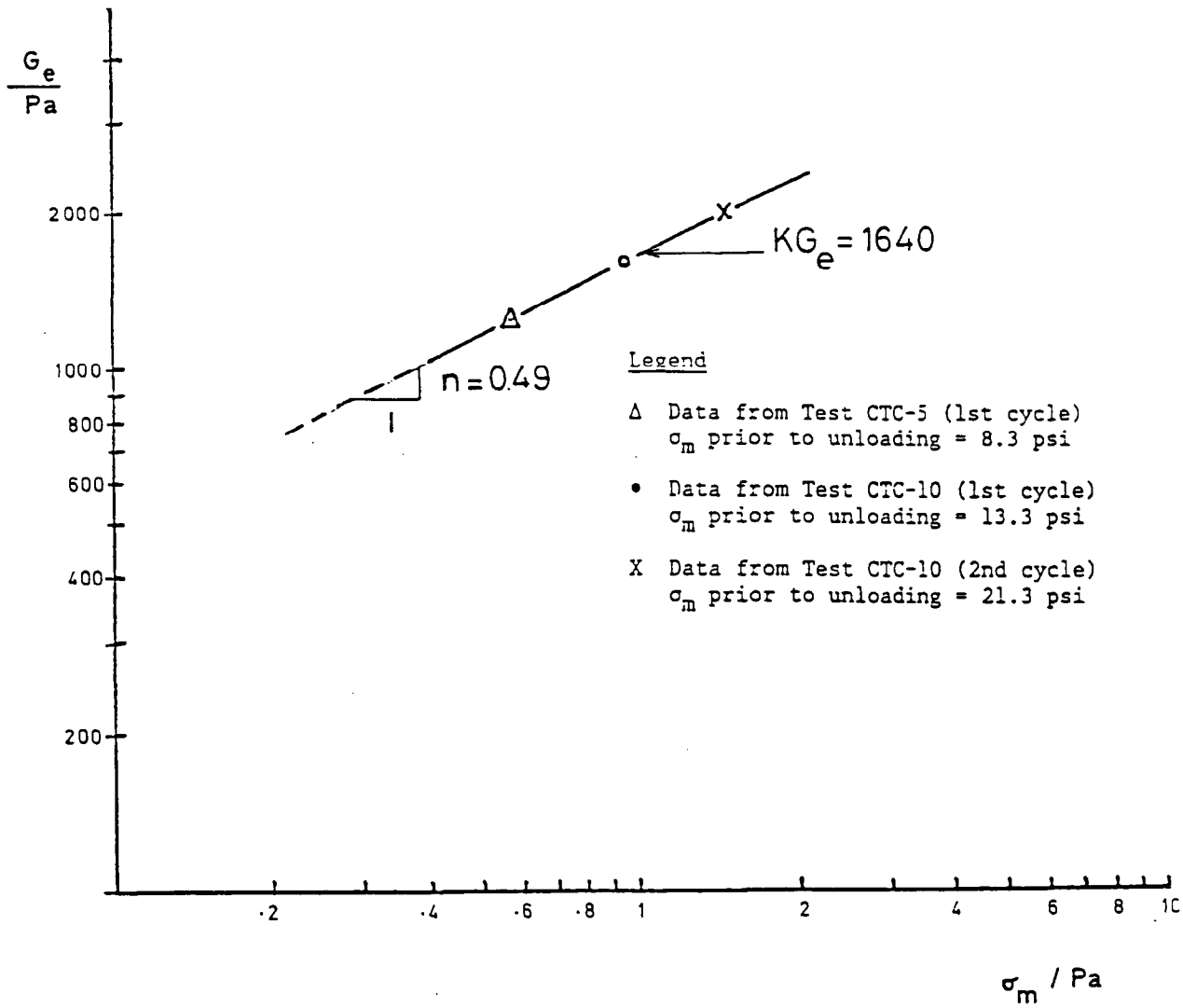

Figure 3.4.3 Plot of (G_e/Pa) versus (σ_m/Pa)

• Evaluation of B_e

To obtain the KB_e and m parameters the procedures proposed by Byrne and Eldridge (1982) are followed. Based on data from conventional triaxial isotropic consolidation tests, Byrne and Eldridge shown that the volumetric strain, ϵ_v, due to consolidation can be related to the mean normal stress, σ_m in the following manner:

$$\epsilon_v = a(\sigma_m)^{1-m} \tag{3.4.2}$$

where:

a = soil parameter

Using the unloading part of the data of test HC (hydrostatic compression) and plotting the above relation on a log-log stress strain plot, Fig. 3.4.4 is obtained. From this figure m and KB_e are evaluated as follows:

i) (1-m) is the slope of the average line through the laboratory data points

ii) $$KB_e = \frac{1}{a(1-m)(Pa)^{1-m}} \tag{3.4.3}$$

From this figure, a = 0.00007, m = .25 and KB_e = 2578 are obtained. Substituting these values in Eq. (3.4.3), B_e is obtained by:

$$\boxed{B_e = 2578\ Pa\ (\sigma_m/Pa)^{.25}} \tag{3.4.4}$$

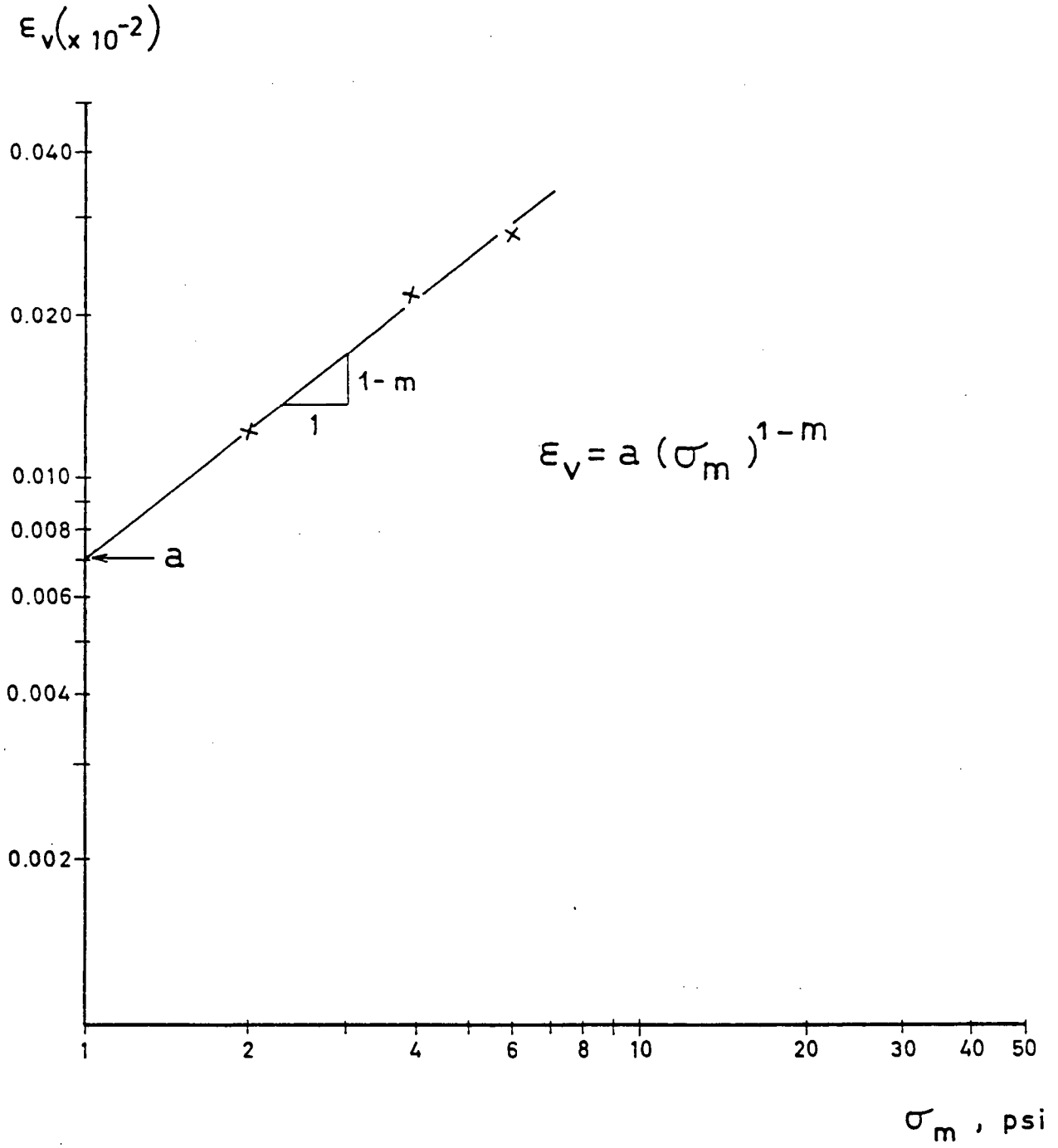

Figure 3.4.4 Plot of ϵ_v versus σ_m

3.4.2 Evaluation of Plastic Parameters

• Evaluation of the Plastic Shear Modulus Parameter, G_p

Using the laboratory data of tests CTC and CTE and following the procedures outlined in Appendix 3.1 (section 3.1.2.1), plots of $(\tau_{SMP}/\sigma_{SMP})$ versus γ^p_{SMP} were obtained as shown in Fig. 3.4.5.

To obtain $(G_p)_i$ and $(\tau_{SMP}/\sigma_{SMP})_{ult}$, plots of $\gamma^p_{SMP}/(\tau_{SMP}/\sigma_{SMP})$ versus γ^p_{SMP} were developed from the CTC and CTE laboratory data and are shown in Fig. 3.4.6. From this figure the values of $(G_p)_i$ and $(\tau_{SMP}/\sigma_{SMP})_{ult}$ were obtained as shown.

To obtain KG_p and np, plots of $(G_p)_i$ versus $((\sigma_{SMP})_i/Pa)$ in a log-log plot were developed as shown in Fig. 3.4.7. In this figure the values of $(G_p)_i$ and $(\sigma_{smp})_i/pa$ obtained from all the triaxial tests of the workshop Data base are shown. Since the lab data does not follow a single line an average line is considered and shown as a dashed line, and from it a KG_p = 190 and a np = -.50 are obtained. Therefore the shear parameter $(G_p)_i$ for Ottawa sand (D_r = 87%) is given by the following equation

$$(G_p)_i = 190\ (\sigma_{SMP}/Pa)^{-.50} \qquad (3.4.5)$$

• Evaluation of the Flow Rule Parameters μ and λ

The equation that expresses the flow rule on the SMP was given earlier in Chapter 3 (eq. (3.21)) and is reproduced below

$$(\tau_{SMP}/\sigma_{SMP}) = \lambda(-\Delta\epsilon^p_{SMP}/\Delta\gamma^p_{SMP}) + \mu$$

Following the procedures outlined in section 3.1.2.2 of Appendix 3.1 with the Data base of the workshop, the flow rule relationship shown in Fig. 3.4.8 was obtained.

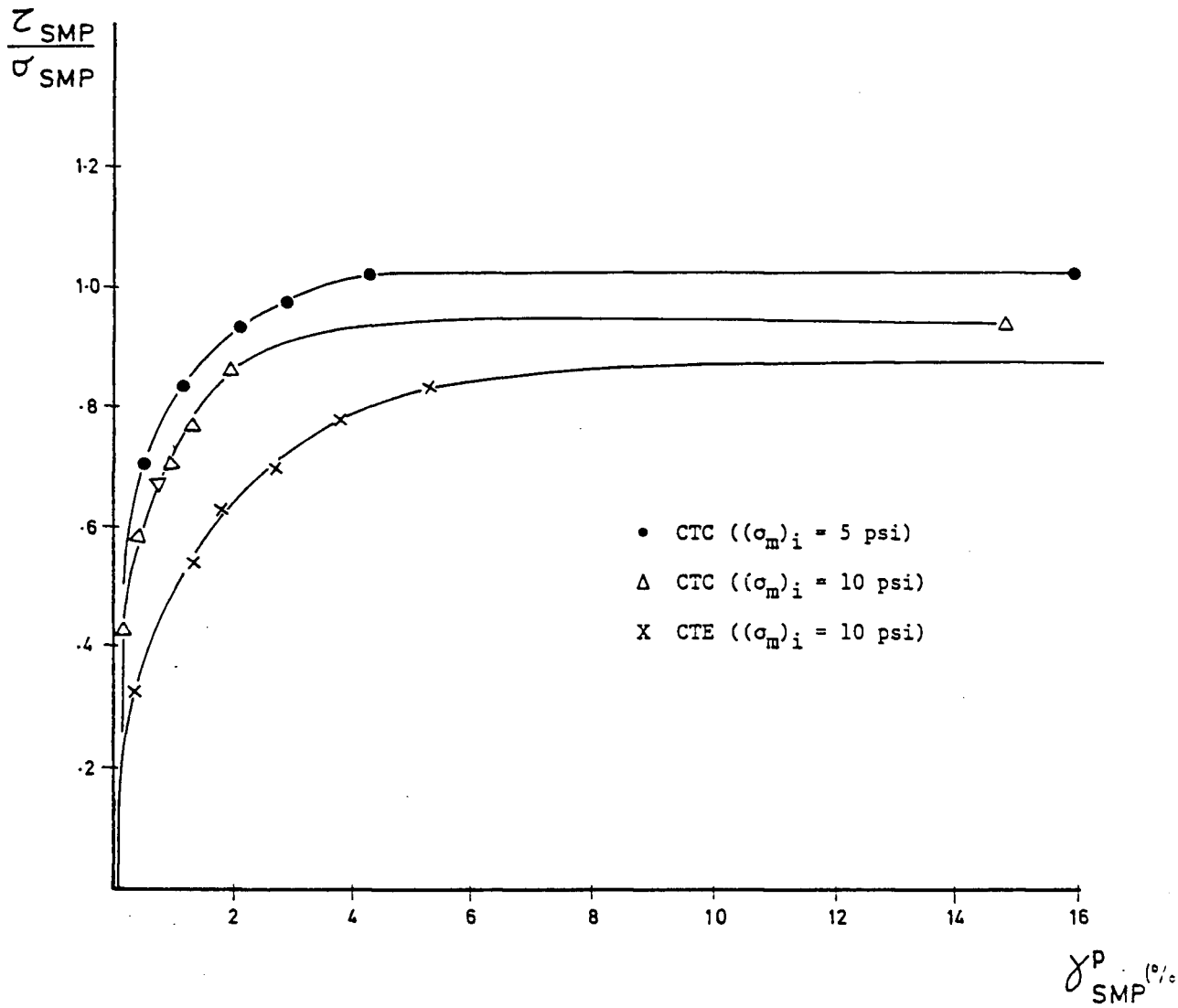

Figure 3.4.5 Plot of $(\tau_{SMP}/\sigma_{SMP})$ versus γ^{p}_{SMP}

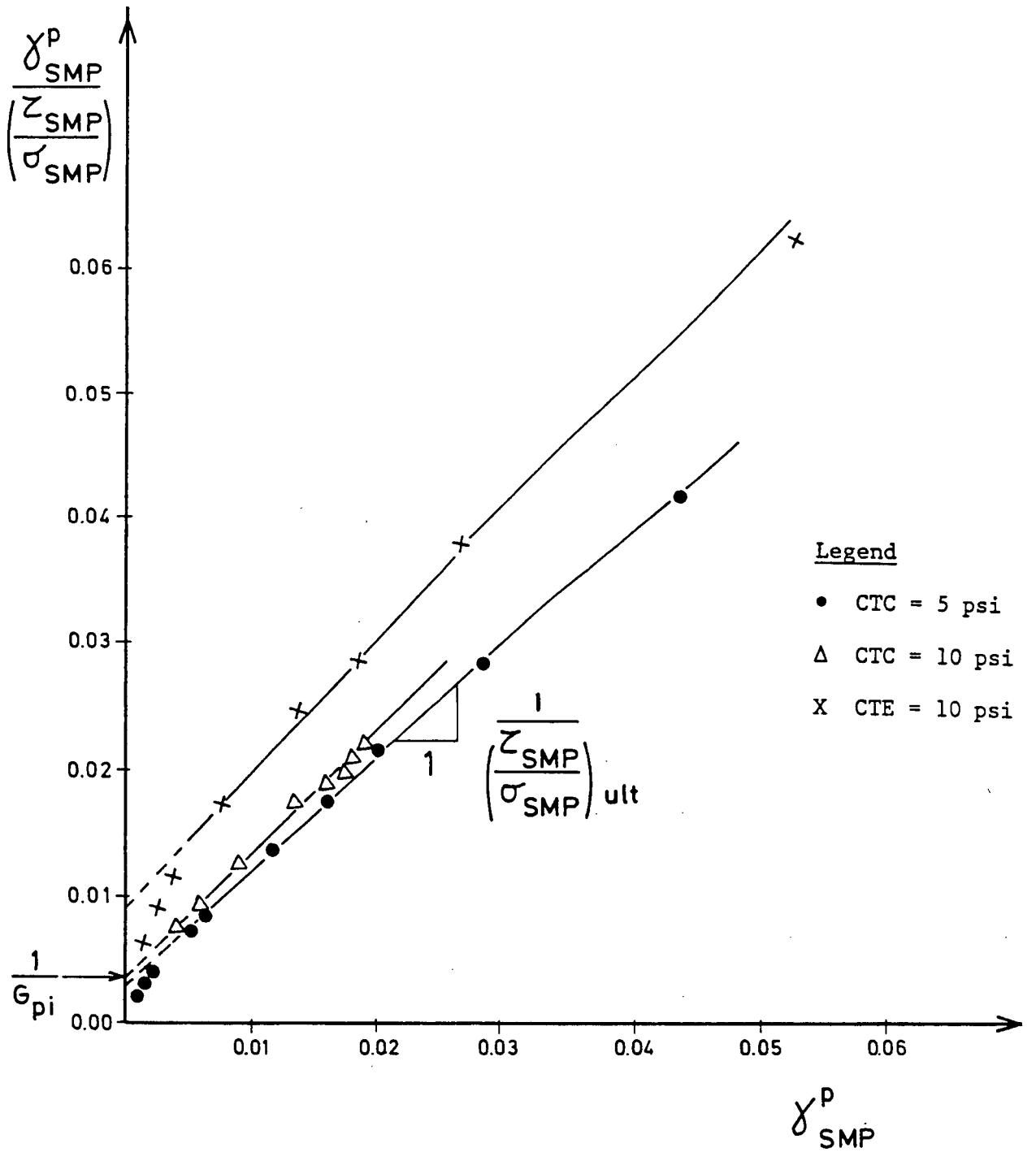

Figure 3.4.6 Plot of $(\gamma^p_{SMP}/(\tau_{SMP}/\sigma_{SMP}))$ versus γ^p_{SMP}

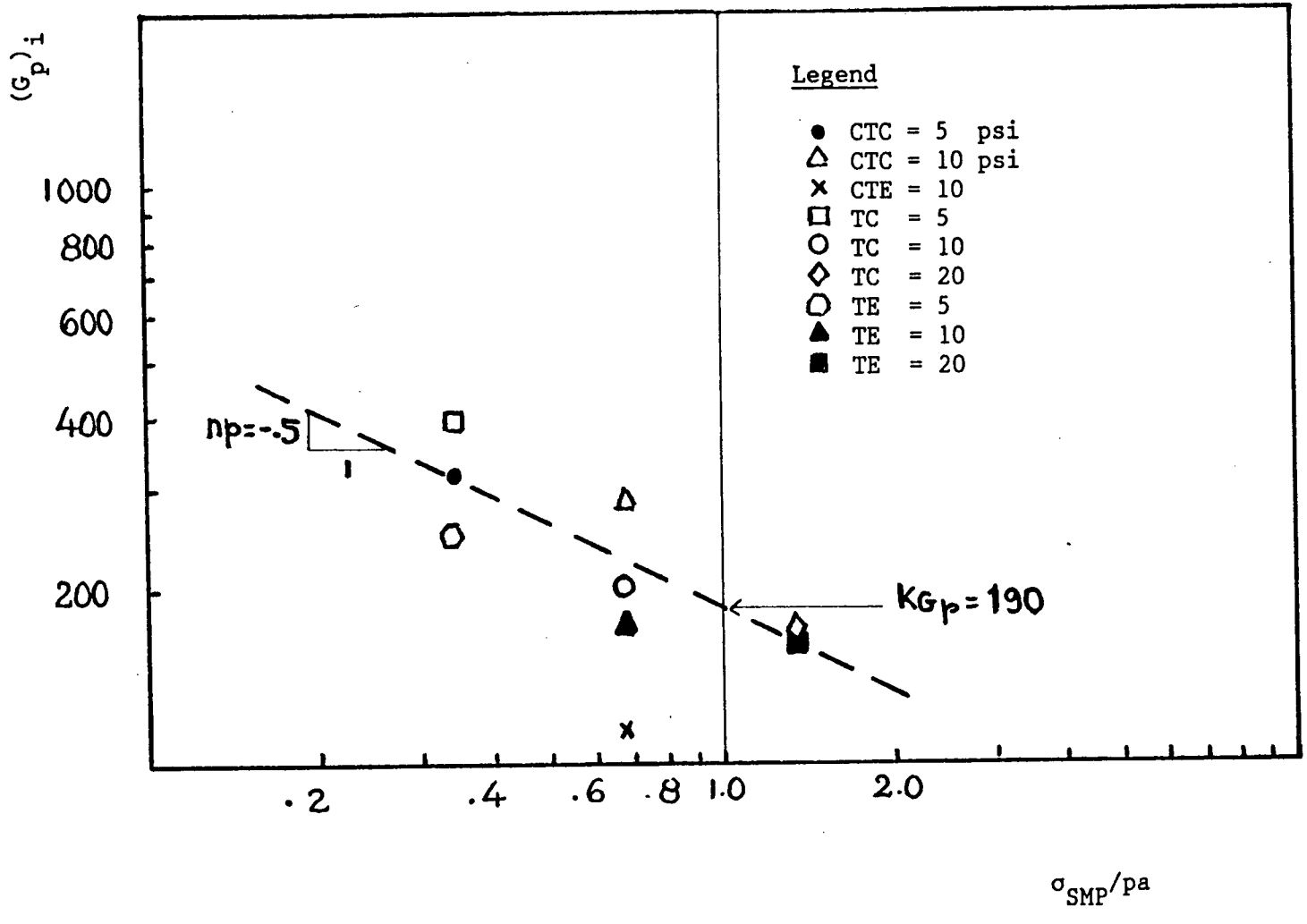

Figure 3.4.7 Plot of $(G_p)_i$ versus $(\sigma_{SMP})_i/Pa$

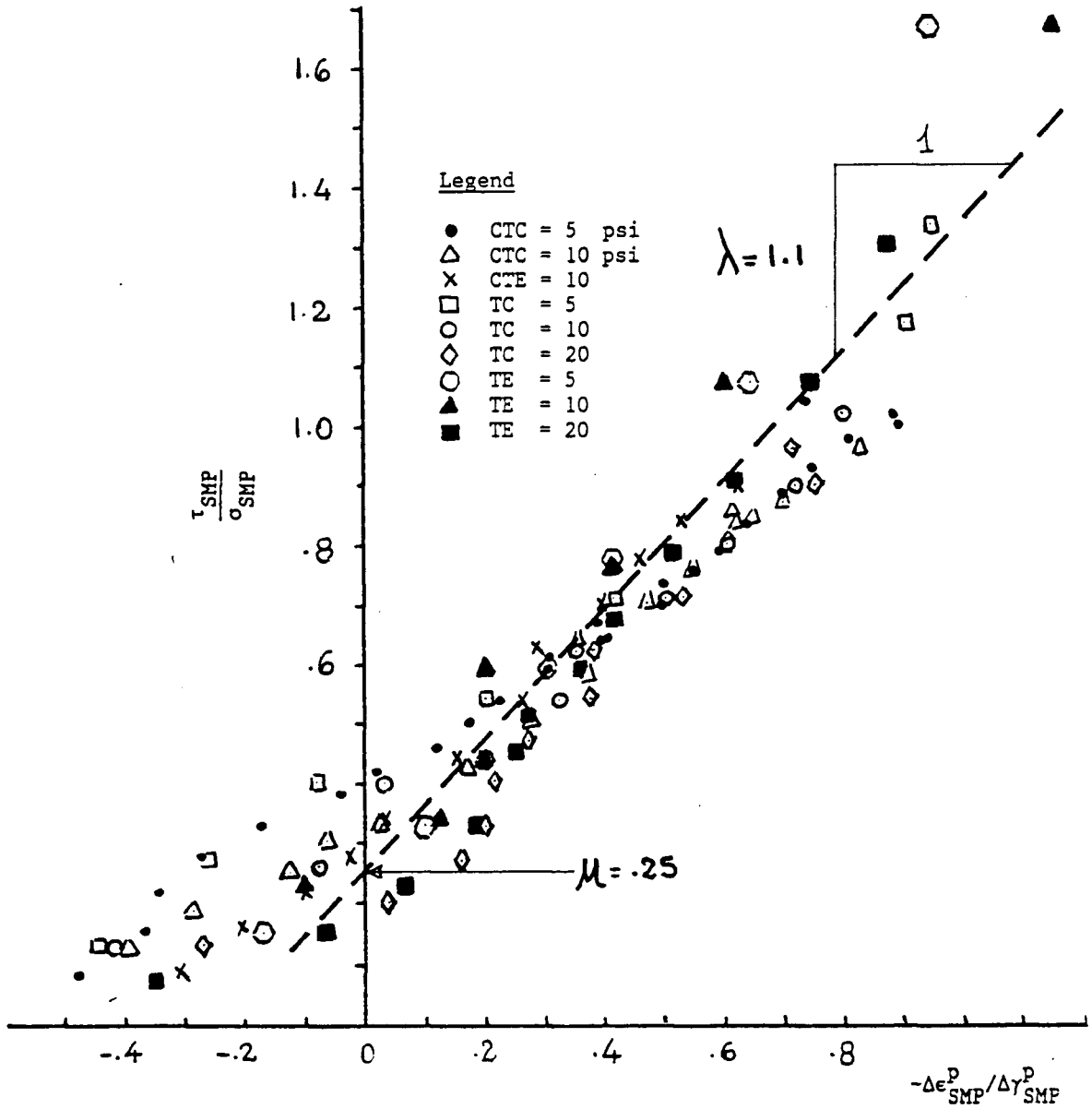

Figure 3.4.8 Flow Rule Plot for Ottawa Sand

from this figure values of μ = .25 and λ = 1.1 were evaluated from the dashed line which represents the average of all data points.

3.4.4 Evaluation of the Failure Parameters

Following the procedures outlined in section 3.1.2.3 of Appendix 3.1 the stress ratio at failure for all the Data base tests were plotted against $\log_{10}((\sigma_{SMP})_F/Pa)$ where $(\sigma_{SMP})_F$ is the mobilized normal stress on the SMP at failure. This relationship is shown in Fig. 3.4.9. Considering the dashed lined as being representative of the average laboratory data points shown in Fig. 3.4.9, values of $(\tau_{SMP}/\sigma_{SMP})_l$ = .935 and $\Delta(\tau_{SMP}/\sigma_{SMP})$ = .62 were obtained and constitute the failure parameters of the modified SMP model.

Finally to obtain the parameter R_F the ratios between $(\tau_{SMP}/\sigma_{SMP})_F$ and $(\tau_{SMP}/\sigma_{SMP})_{ult}$ were evaluated for all the tests and an average value $(R_F)_{av}$ = .97 was obtained.

A summary of all soil parmeters for Ottawa sand is presented in the following Table 3.4.1.

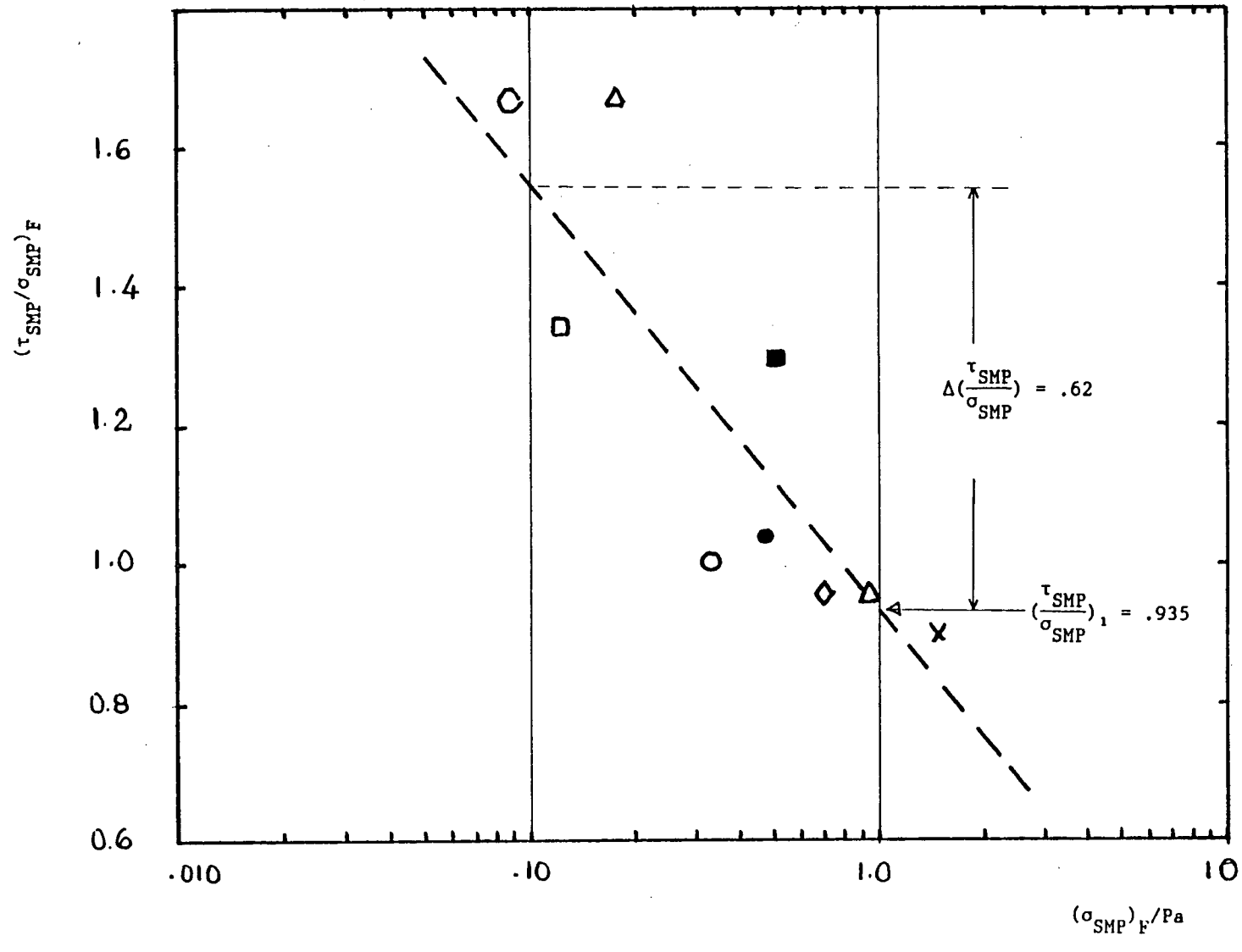

Figure 3.4.9 Plot of $(\tau_{SMP}/\sigma_{SMP})_F$ versus $(\sigma_{SMP})_F/Pa$

Table 3.4.1

Soil Parameters for Ottawa Sand (D_r = 87%) for Use in the SMP Modified Model

KG_e = 1640 n = 0.49 KB_e = 2578 m = 0.25	Elastic Parameters	
KG_p = 190 np = -.50	Plastic Shear Modulus Parameters	Plastic Parameters
μ = .25 λ = 1.10	Flow Rule Parameters	
$(\frac{\tau_{SMP}}{\sigma_{SMP}})_1$ = .935 $\Delta(\frac{\tau_{SMP}}{\sigma_{SMP}})$ = .62 $(R_F)_{av}$ = .97	Failure Parameters	

APPENDIX 3.5

STRAIN SOFTENING FORMULATION FOR USE IN THE MODIFIED SMP MODEL

APPENDIX 3.5

Strain Softening Formulation for use in the Modified SMP Model

To analytically study the effects of strain softening, a formulation taking these effects into account was implemented in the modified SMP model and follows similar procedures as that outlined by Carter and Yeung (1985).

A sketch of the relationship between the stress ratio on the SMP, τ_{SMP}/σ_{SMP}, and the plastic shear strain on the plane, γ^p_{SMP}, for a strain softening material, is shown in Fig. 3.5.1. From point 0 to point F the material is hardening until the mobilized stress ratio reaches the value $(\tau_{SMP}/\sigma_{SMP})_F$. From point F onf the sand starts to exhibit softening, and that is taken into account as follows:

a) After peak failure the plastic shear modulus, G_p, is obtained using the following equation:

$$G_p = (G_p)_{sof} = \frac{(\tau_{SMP}/\sigma_{SMP})_R - (\tau_{SMP}/\sigma_{SMP})_F}{(\Delta\gamma^p_{SMP})_{sof}} \qquad (3.5.1)$$

where:

$(\tau_{SMP}/\sigma_{SMP})_R$ = residual stress ratio of the sand

$(\tau_{SMP}/\sigma_{SMP})_F$ = peak failure stress ratio of the sand

$(\Delta\gamma^p_{SMP})_{sof}$ = increment of plastic strain characterizing the degree of softening and given by the equation:

$$(\Delta\gamma^p_{SMP})_{sof} = (\gamma^p_{SMP})_F - (\gamma^p_{SMP})_R \qquad (3.5.2)$$

where:

$(\gamma^{p}_{SMP})_R$ = residual plastic shear strain correspondent to point R

$(\gamma^{p}_{SMP})_F$ = plastic shear strain at peak failure, correspondent to point F

It may be seen from eq. (3.5.1) that $(G_p)_{sof}$, will be negative since $(\tau_{SMP}/\sigma_{SMP})_R \leq (\tau_{SMP}/\sigma_{SMP})_F$ and that will develop the desired strain softening characteristics of the sand.

b) Since the sand is softening from point F to point R the new failure stress ratio at a point A, $(\tau_{SMP}/\sigma_{SMP})_A$ located between F and R will be obtained using the following equation:

$$\left(\frac{\tau_{SMP}}{\sigma_{SMP}}\right)_A = \left(\frac{\tau_{SMP}}{\sigma_{SMP}}\right)_F - \left[\left(\frac{\tau_{SMP}}{\sigma_{SMP}}\right)_F - \left(\frac{\tau_{SMP}}{\sigma_{SMP}}\right)_R\right] \frac{(\gamma^{p}_{SMP})_A}{(\gamma^{R}_{SMP})_R} \qquad (3.5.3)$$

where:

$(\gamma^{p}_{SMP})_A$ = mobilized plastic shear strain at point A.

c) When the residual plastic shear strain, $(\gamma^{p}_{SMP})_R$ is reached, G_p will be defaulted to a prescribed low value and $(\tau_{SMP}/\sigma_{SMP})_F = (\tau_{SMP}/\sigma_{SMP})_R$. At the same time the parameter λ of the SMP flow rule is defaulted to $\simeq\infty$ in order that no more volumetric strains take place.

To summarize only two additional soil parameters are required to take into account the strain softening behaviour of sand and consist of:

- $(\tau_{SMP}/\sigma_{SMP})_R$ = the residual stress ratio on the SMP, and

- $(\gamma^p_{SMP})_R$ = the plastic residual shear strain on the SMP.

For Ottawa sand these two parameters were assessed with the value $(\tau_{SMP}/\sigma_{SMP})_R = .61$, i.e. the equivalent to $\phi_{cr} = 33°$ and $(\gamma^p_{SMP})_R = .50$ which was obtained by trial and error.

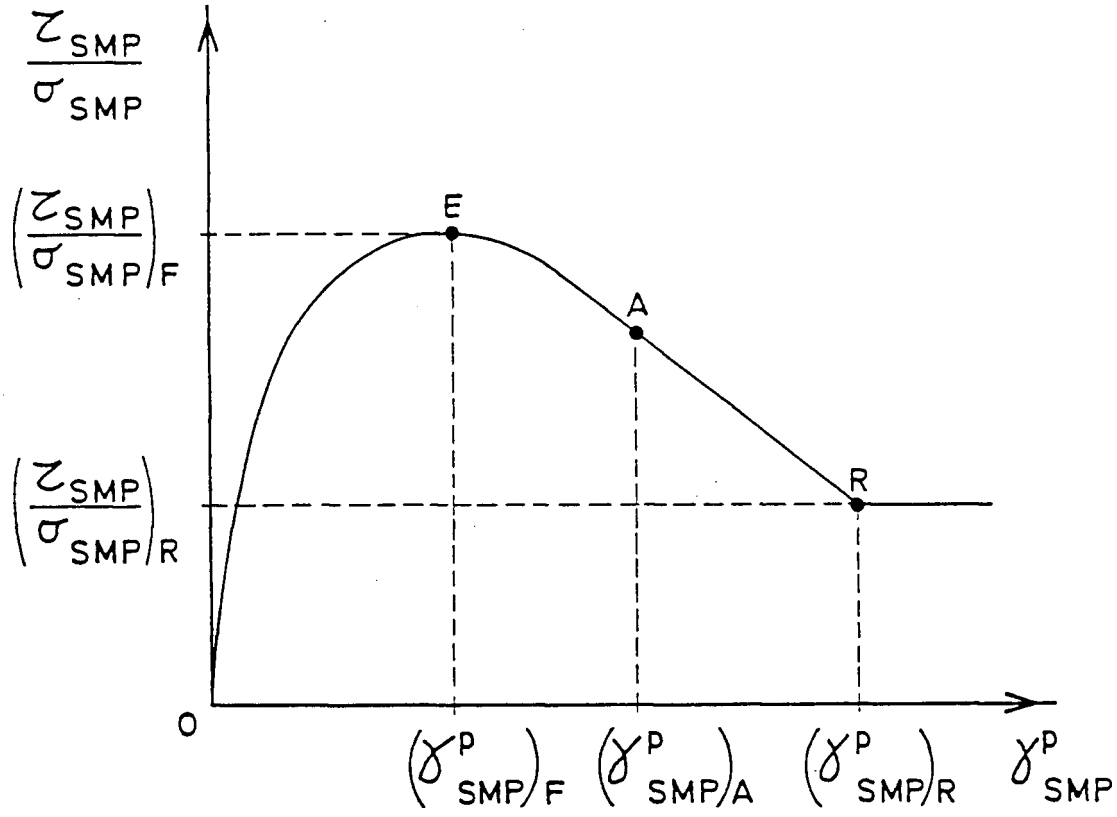

Figure 3.5.1 Strain Softening Behaviour on the SMP.

CHAPTER 4

APPENDIX INDEX

CHAPTER 4

APPENDIX FIGURES INDEX

APPENDIX 4.1

IMPLEMENTATION OF THE "THIN" INTERFACE ELEMENT INTO THE FINITE ELEMENT FORMULATION

APPENDIX 4.1

IMPLEMENTATION OF THE "THIN" INTERFACE ELEMENT INTO THE FINITE ELEMENT FORMULATION

The implementation of this interface element into 3-D and 2-D F.E. formulations is described below:

4.1.1 3-D Formulation

(a) Transformation of stresses

Let us consider the 3-D "thin" interface element, shown in the main text Fig. 4.1(b), defined in its local coordinate system (n,s,t). This coordinate system is related with the global coordinate system (x,y,z) by the direction cosines ℓ_i, m_i and n_i (i = 1,2,3) as is shown in Table 4.1.1.

Table 4.1.1

Table of Direction Cossines Between Axes of the Local and Global Coordinate Systems (3-D)

	x	y	z
s	ℓ_1	m_1	n_1
t	ℓ_2	m_2	n_2
n	ℓ_3	m_3	n_3

At the beginning of every load step the cartesian stresses $\{\sigma\}$, which are defined in the global coordinate system (x,y,z) are transformed into the stresses $\{\sigma^*\}$, which are defined in the local coordinate sytem (n,s,t).

Such transformation of stresses is obtained using the equations published by Cook et al. (1989) which are reproduced below:

$$\{\sigma^*\} = [T_\sigma]\ \{\sigma\} \tag{4.1.1}$$

where:

$[T_\sigma]$ = stress transformation matrix, which is given by:

$$[T_\sigma] = \begin{bmatrix} T_Q & 2T_R \\ \frac{1}{2}T_S & T_T \end{bmatrix} \tag{4.1.2}$$

and

$$[T_Q] = \begin{bmatrix} \ell_1^2 & m_1^2 & n_1^2 \\ \ell_2^2 & m_2^2 & n_2^2 \\ \ell_3^2 & m_3^2 & n_3^2 \end{bmatrix} \tag{4.1.3}$$

$$[T_R] = \begin{bmatrix} \ell_1 m_1 & m_1 n_1 & n_1 \ell_1 \\ \ell_2 m_2 & m_2 n_2 & n_2 \ell_2 \\ \ell_3 m_3 & m_3 n_3 & n_3 \ell_3 \end{bmatrix} \tag{4.1.4}$$

$$[T_S] = \begin{bmatrix} 2\ell_1\ell_2 & 2m_1m_2 & 2n_1n_2 \\ 2\ell_2\ell_3 & 2m_2m_3 & 2n_2n_3 \\ 2\ell_3\ell_1 & 2m_3m_1 & 2n_3n_1 \end{bmatrix} \tag{4.1.5}$$

$$[T_T] = \begin{bmatrix} (\ell_1 m_2 + \ell_2 m_1)(m_1 n_2 + m_2 n_1)(n_1 \ell_2 + n_2 \ell_1) \\ (\ell_2 m_3 + \ell_3 m_2)(m_2 n_3 + m_3 n_2)(n_2 \ell_3 + n_3 \ell_2) \\ (\ell_3 m_1 + \ell_1 m_3)(m_3 n_1 + m_1 n_3)(n_3 \ell_1 + n_1 \ell_3) \end{bmatrix} \qquad (4.1.6)$$

Once the $\{\sigma^*\}$ stresses are obtained, only the normal stress on the interface plane, σ_N and the shear stresses on this plane, τ_s and τ_t are considered to evaluate the normal modulus E_N and shear modulus G_t as will be described next. The other stresses are neglected as recommended by Desai (1984) since they represent coupling effects that are difficult to determine from laboratory tests.

(b) Constitutive Matrix

Now that the stresses are evaluated in the local coordinate system of the element, (n,s,t), its constitutive matrix [D*] can be evaluated as well in this system and that is done as recommended by Desai (1984). The [D*] matrix is composed of two components, a normal component D_N^* and a shear component D_S^*, as is described below:

$$[D^*] = \begin{bmatrix} [D_N^*] & 0 \\ 0 & [D_S^*] \end{bmatrix} = \begin{bmatrix} \begin{bmatrix} D_1^* & D_2^* & D_2^* \\ D_2^* & D_1^* & D_2^* \\ D_2^* & D_2^* & D_1^* \end{bmatrix} & \begin{matrix} 0 & 0 & 0 \\ 0 & 0 & 0 \\ 0 & 0 & 0 \end{matrix} \\ \begin{matrix} 0 & 0 & 0 \\ 0 & 0 & 0 \\ 0 & 0 & 0 \end{matrix} & \begin{bmatrix} D_3^* & 0 & 0 \\ 0 & D_4^* & 0 \\ 0 & 0 & D_5^* \end{bmatrix} \end{bmatrix} \qquad (4.1.7)$$

where:

$$D_1^* = \frac{E(1-\upsilon)}{(1+\upsilon)(1-2\upsilon)} = E_N$$

$$D_2^* = \frac{E\upsilon}{(1+\upsilon)(1-2\upsilon)} \cong 0$$

$D_3^* = D_4^* = D_5^* = G_t$ (assumes an isotropic shear behaviour on the interface plane)

Desai is not too clear on the role of Poisson's ratio, υ, in the above formulation. To be consistant with the E_N definition, the writer attributed low values for υ such as .1 except for the closed form solution example that will be presented.

As described in the main text in Section 4.3, the E_N and G_t moduli are independent of each other and are controlled by the local stresses. The E_N modulus is controlled only by σ_N and the G_t modulus is controlled by the shear stresses τ_s and τ_t. When $\sigma_N > 0$ the normal modulus, E_N, is given by eq. (4.7) (main text). If $\sigma_N \leq 0$ then E_N is defaulted to a small value. When $|\tau_s|$ and $|\tau_t|$ are less than τ_f the shear modulus, G_t, is given by eq. (4.5) (main text), and assuming that the shear behaviour of the interface is isotropic in the shear directions, s and t, the G_t modulus will be defaulted to a small value whenever $|\tau_s|$ or $|\tau_t|$ are greater than τ_f. Based on the writer's experience, defaulted values for E_N and G_t in the range of Pa/100 to Pa/1000 give reasonable results.

Now that the constitutive matrix [D*] is defined in the local coordinate system of each element, this matrix needs to be transformed into the constitutive matrix [D] defined in the global coordinate system. That is done following the equation published by Cook (19__):

$$[D] = [T_E]^T [D^*] [T_E] \tag{4.1.8}$$

where:

$$[T_E] = \begin{bmatrix} T_Q & T_R \\ T_S & T_T \end{bmatrix} \tag{4.1.9}$$

where T_Q, T_R, T_S and T_T are given by eq(s). 4.1.3 to 4.1.6 respectively.

Finally the stiffness matrix [K] of each interface is obtained as any other standard solid element using the following equation:

$$[K] = \int_V [B]^T [D][B] \, dV \tag{4.1.10}$$

where [B] is the strain-displacement matrix of the element and V is the element volume.

4.1.2 2-D Formulation (Plane Strain)

Let us consider the 2-D "thin" interface element, shown in the main text Fig. 4.1(a), and defined in its local coordinate system (n,s). Defining β as the angle between the axis z and n the relationship between the local and global coordinate systems is given by the direction cossines presented in Table 4.2.

Table 4.1.2

Table of Direction Cossines Between Axis of the Local and Global Coordinate Systems (2-D)

	x	z
s	$\ell_1 = \cos\beta$	$n_1 = \sin\beta$
n	$\ell_3 = -\sin\beta$	$n_3 = \cos\beta$

As for the case of the 3-D formulation the cartesian stresses $\{\sigma\}$ are transformed into the local stresses $\{\sigma^*\}$ following eq. (4.1.1) which is reproduced below:

$$\{\sigma^*\} = [T_\sigma]\ \{\sigma\}$$

For the case of the 2-D formulation, the stresses transformation matrix, $[T_\sigma]$ is given by:

$$[T_\sigma] = \begin{bmatrix} c^2 & s^2 & 2cs \\ s^2 & c^2 & -2cs \\ -cs & cs & c^2-s^2 \end{bmatrix} \qquad (4.1.11)$$

where:

$c = \cos\beta$

$s = \sin\beta$

and the local constitutive matrix D* is given by

$$[D^*] = \begin{bmatrix} [D_N^*] & 0 \\ 0 & [D_S^*] \end{bmatrix} = \begin{bmatrix} \begin{bmatrix} D_1^* & D_2^* \\ D_2^* & D_1^* \end{bmatrix} & 0 \\ 0 & [D_3^*] \end{bmatrix} \qquad (4.1.12)$$

where the terms D_1^*, D_2^* and D_3^* are described as in eq. (4.14).

As for the case of th 3-D formulation the constitutive matrix [D*] is transformed into the global constitutive matrix [D] following eq. (4.1.8) which is reproduced below:

$$[D] = [T_E]^T\ [D^*]\ [T_E]$$

For the case of the 2-D formulation, the matrix $[T_E]$ is given by:

$$[T_E] = \begin{bmatrix} c^2 & s^2 & cs \\ s^2 & c^2 & -cs \\ -2cs & 2cs & c^2-s^2 \end{bmatrix} \qquad (4.1.13)$$

and the stiffness matrix [K] of each interface is obtained as follows:

$$[K] = \int_A [B]^T [D] [B] \, dA \qquad (4.1.14)$$

where A is the area of the element.

4.1.3 Load Shedding Formulation

The importance of redistributing the stresses of the standard soil elments that violate the failure criterion through shear or tension was emphasized earlier in Chapter 2 (section 2.7). The case of the interface elements is no different than any standard soil element. Therefore the load shedding technique described in Chapter 2 was adapted to the "thin" interface element's formulation and that is presented in Appendix 4.2.

APPENDIX 4.2

LOAD SHEDDING FORMULATION FOR INTERFACE ELEMENTS

APPENDIX 4.2

LOAD SHEDDING FORMULATION FOR INTERFACE ELEMENTS

4.2.1 Load Shedding for Elements in Tension

Physically an interface element fails in tension whenever the normal stress, $\sigma_N \leq 0$. To avoid excessive iterations, however, the following tension failure bound is used instead:

If $(-\sigma_N) \leq -Pa/K$ the interface element is considered to have failed in tension, where a K = 100 has been used with success.

The overshooting tensile normal stress to be load shedded is evaluated following the equation:

$$\{\Delta\sigma^*\}_{LS} = \text{abs}(-\sigma_N) \tag{4.2.1}$$

and the current normal stress is corrected using the equation

$$(\sigma_N)_{\text{corrected}} = (\sigma_N)_{\text{current}} + \{\Delta\sigma^*\}_{LS} \tag{4.2.2}$$

At the same time the load shedding force vector, $\{f\}_{LS}$ is developed following the next two equations. The first equation transforms the local $\{\Delta\sigma^*\}_{LS}$ stresses into the global $\{\Delta\sigma^*\}_{LS}$ stresses as follows:

$$\{\Delta\sigma\}_{LS} = [T_\sigma]^{-1} \{\Delta\sigma^*\}_{LS} \tag{4.2.3}$$

where $[T_\sigma]^{-1}$ is the inverse matrix of $[T_\sigma]$ which is given by eq. (4.1.2) (Appendix 4.1) for the 3-D formulation or eq. (4.1.11) for the 2-D formulation. The second equation evaluates the load shedding force vector $\{f\}_{LS}$ as follows:

- 3-D formulation $\{f\}_{LS} = \{\Delta\sigma\}_{LS}\ [B]^T$ volume

- 2-D Formulation $\{f\}_{LS} = \{\Delta\sigma\}_{LS}\ [B]^T$ Area (4.2.4)

The basis for eq(s). 4.2.4 have been already discussed in Appendix 2.5.

This force vector, $\{f\}_{LS}$, is applied at the nodes that define the interface element in question and that will develop equivalent stresses, $\{\Delta\sigma\}_{eq} = \{\Delta\sigma\}_{LS}$, on the adjacent soil or structural elements because the element that failed in tension has now a low defaulted E_N value. The above procedures, which maintain stress equilibrium, will be repeated until convergency is obtained within the same load step.

4.2.2 Load Shedding for Elements in Shear Failure

Physically an interface element fails in shear whenever the absolute value of the mobilized shear stress, $|\tau_m|$ is greater or equal than the resistant shear failure stress, τ_f. To avoid excessive iterations the following shear failure bond is used instead:

If abs $\left| \frac{\tau_m}{\tau_f} \right| \geq (1.0 + CONV)$ the interface element is considered to have failed in shear, where a CONV = 0.05 has been used with success.

The overshooting shear stress to be load shedded is evaluated following the equation:

$$\{\Delta\sigma^*\}_{LS} = \Delta\tau = \tau_f - abs|\tau_m| \qquad (4.2.5)$$

and from this stage on the same procedures described earlier for the interface elements that failed in tension are followed.

APPENDIX 4.3

EXTENSION OF MATSUOKA-NAKAI FAILURE CRITERION TO GRANULAR SOILS WITH COHESION AND FRICTION

APPENDIX 4.3

EXTENSION OF MATSUOKA-NAKAI FAILURE CRITERION TO GRANULAR SOILS WITH COHESION AND FRICTION

The fills used in the Molikpaq consist essentially of sand as will be described later in this thesis. However, fills commonly comprise silty sand soils which have limiting resistances characterized by a cohesion, C, and an internal friction angle, ϕ. This is the case of the backfill used in the retaining wall field study carried out by Matsuo et al. (1978) (see main text section, 4.6.2). Therefore the modified SMP model was expanded to take into account the extra cohesion term as is described below.

It is assumed that the factor of safety, FS, of a silty sand matrix is composed of two terms, the Factor of Safety due to cohesion, (FSC), and the Factor of Safety due to Friction, (FSϕ). It is further assumed that the Total Factor of Safety, (TFS), is given by the following equation:

$$TFS = FSC + FS\phi \tag{4.3.1}$$

By definition

$$FS = \frac{\text{Resistant Shear}}{\text{Mobilized Shear}} \tag{4.3.2}$$

Using this equation the FSϕ term is defined as:

$$FS\phi = \frac{(\tau_{SMP}/\sigma_{SMP})_F}{(\tau_{SMP}/\sigma_{SMP})_m} \tag{4.3.3}$$

Comparing Eq. (4.3.3) with Eq. (2.77) of the main text it is concluded that:

$$FS\phi = 1/SRL \tag{4.3.4}$$

where SRL = stress ratio level.

To define the FSC term, a similar approach is followed, but von Mises failure criterion is used instead:

$$FSC = \frac{(\tau_{oct})_F}{(\tau_{oct})_m} \tag{4.3.5}$$

where:

$$\tau_{oct} = \frac{2}{3}\left[((\sigma_1-\sigma_2)/2)^2 + ((\sigma_2-\sigma_3)/2)^2 + ((\sigma_3-\sigma_1)/2)^2\right]^{1/2} \tag{4.3.6}$$

$(\tau_{oct})_F$ = octahedral failure shear stress

$(\tau_{oct})_m$ = octahedral mobilized shear stress

By analogy with eq. (4.3.4) the FSC term can be given by the following equation:

$$FSC = 1/CL \tag{4.3.7}$$

where:

CL = the cohesion level = $(\tau_{oct})_m/(\tau_{oct})_F$

Substituting eq(s). (4.3.4) and (4.3.7) into eq. (4.3.1) the following equation is obtained:

$$TFS = 1/CL + 1/SRL \tag{4.3.8}$$

and inverting this equation the total stress level, TSL, is obtained:

$$TSL = (TFS)^{-1} = \frac{1}{1/CL + 1/SRL} \qquad (4.3.9)$$

The meaning of this equation is that the Matsuoka-Nakai failure envelope instead of starting from the origin of the principal stress coordinate system starts from a circle with a radius = τ_{oct}. The failure envelopes for sands with and without cohesion in 2-D and 3-D stress spaces are schematized in Fig. 4.3.1.

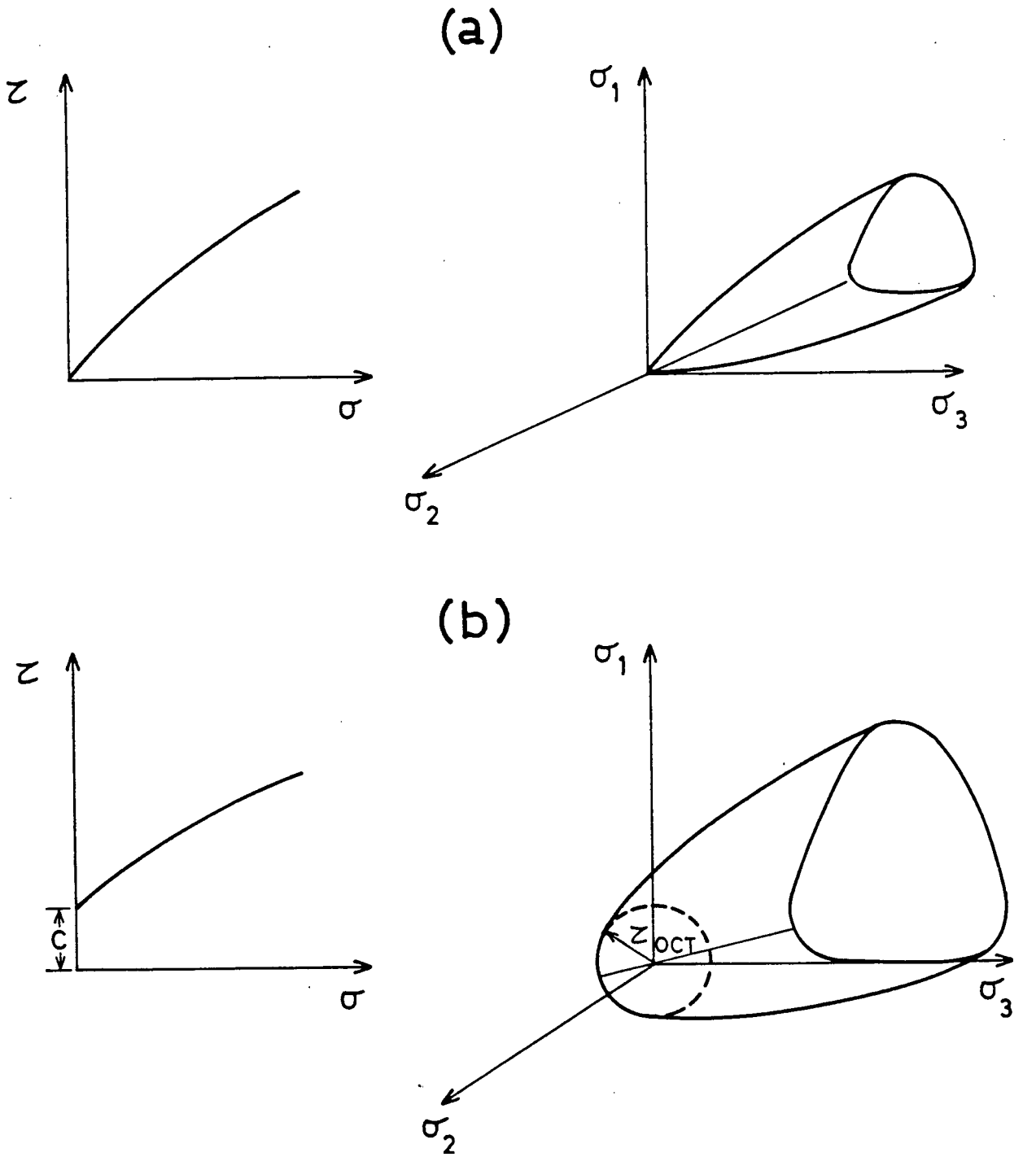

Figure 4.3.1 Sketches of failure envelopes for granular material: (a) With friction and no cohesion; (b) With friction and cohesion

CHAPTER 5

APPENDIX INDEX

CHAPTER 5

APPENDIX FIGURES INDEX

APPENDIX 5.1

BRIEF DESCRIPTION OF THE METHOD DEVELOPED BY MANASSERO (1989)

APPENDIX 5.1

BRIEF DESCRIPTION OF THE METHOD DEVELOPED BY MANASSERO (1989)

Manassero's method (1989) like other researchers assumes that the pressuremeter cavity expansion takes place under plane strain boundary conditions, that elastic strains are neglected and that Rowe's stress dilatancy theory is valid. However his method allows to infer the complete plane strain nonlinear nature of the stress and volume change of sand from the pressuremeter test data. This method is briefly described below.

Combining the equilibium and compatibility equations (correspondent to the axisymmetric plane strain conditions) with Rowe's stress dilatancy equation Manassero obtains the following equation for a soil element adjacent to the pressuremeter face (see Appendix 5.2):

$$(\Delta\sigma_r)_{face}/\Delta\epsilon_{\theta face} = -((\sigma_r)_{face}(1 + (1/K)((\Delta\epsilon_r)_{face}/(\Delta\epsilon_\theta)_{face})) /((\epsilon_r)_{face}-(\epsilon_\theta)_{face}) \quad (5.1.1)$$

where:

$(\Delta\sigma_r)_{face}$ = increment of radial stress =

$$= (\sigma_r)_{face}(i) - (\sigma_r)_{face}(i-1) \quad (5.1.2)$$

K = Rowe's constant = $(1+\sin\phi_{cv})/(1-\sin\phi_{cv})$

ϕ_{cv} = the friction angle of sand at constant volume

$(\Delta\epsilon_r)_{face}$ = increment of radial strain =

$$= (\epsilon_r)_{face}(i) - (\epsilon_r)_{face}(i-1) \quad (5.1.3)$$

$(\Delta\epsilon_\theta)_{face}$ = increment of circumferential strain =

$$= (\epsilon_\theta)_{face}(i) - (\epsilon_\theta)_{face}(i-1) \quad (5.1.4)$$

i = 1,n = the increment number

Manipulating eq. (5.1.1), Manassero (1989) shows that $(\epsilon_r)_{face}(i)$ can be obtained as follows:

$$(\epsilon_r)_{face}(i) = M1 + M2 + M3 + M4 \qquad (5.1.5)$$

where M1, M2, M3, and M4 are terms that are functions of $(\sigma_r)_{face}(i)$, $(\sigma_r)_{face}(i-1)$, $(\epsilon_\theta)_{face}(i)$, $(\epsilon_\theta)_{face}(i-1)$ and $(\epsilon_r)_{face}(i-1)$, see Appendix 5.2.

Because when i=1, $(\sigma_r)_{face}(i-1) = (\sigma_r)_{face}(o) = \sigma_o$ = the lift-off pressure and $(\epsilon_r)_{face}(o) = (\epsilon_\theta)_{face}(o) = 0$, eq. 5.1.5 allows the step by step computation of the unknown values of $(\epsilon_r)_{face}(i)$ for i=2 to n where n is the number of the last measurement data point. Once $(\epsilon_r)_{face}(i)$, $(\epsilon_\theta)_{face}(i)$ and $(\sigma_r)_{face}(i)$ are known, then $(\Delta\epsilon_r)_{face}$ and $(\Delta\epsilon_\theta)_{face}$ can be computed using eqs. 5.1.3 and 5.1.4, respectively, and in turn $(\sigma_\theta)_{face}(i)$ evaluated using Rowe's stress dilatancy eq., i.e.:

$$(\sigma_\theta)_{face}(i) = -((\sigma_r)_{face}(i)/K)((\Delta\epsilon_r)_{face}/(\Delta\epsilon_\theta)_{face}) \qquad (5.1.6)$$

To compute the mobilized plane strain friction angle, ϕ_m^{ps}, at the pressuremeter face the following equation is used:

$$\phi_m^{ps}(i) = \sin^{-1}\left(((\sigma_r)_{face}(i) - (\sigma_\theta)_{face}(i))/((\sigma_r)_{face}(i) + (\sigma_\theta)_{face}(i))\right) \qquad (5.1.7)$$

and once these are evaluated, for i = 1 to n, the maximum mobilized friction angle or peak friction angle ϕ_p^{ps} can be easily obtained.

APPENDIX 5.2

DEVELOPMENT OF MANASSERO'S (1989) INCREMENTAL EQUATION

APPENDIX 5.2

DEVELOPMENT OF MANASSERO'S (1989) INCREMENTAL EQUATION

- From Rowe's stress dilatancy theory

$$\sigma_1/\sigma_3 = -K\ \Delta\epsilon_3/\Delta\epsilon_1 \qquad (5.2.1)$$

where:

σ_1, σ_3 = the major and minor principal stresses

$K = (1+\sin\phi_{cv})/(1-\sin\phi_{cv})$

ϕ_{cv} = the friction angle of sand at constant volume

$\Delta\epsilon_1, \Delta\epsilon_3$ = the increments of major and minor principal strains

Using the axisymmetric formulation eq. (5.2.1) takes the following form (within the plastic region)

$$\sigma_r/\sigma_\theta = -K\ \Delta\epsilon_\theta/\Delta\epsilon_r \qquad (5.2.2)$$

where the subscripts r and θ mean radial and circumferential, respectively.

- From the equilibrium equation

$$\Delta\sigma_r/\Delta r = (\sigma_\theta - \sigma_r)/r \qquad (5.2.3)$$

where:

r = radial distance

• From the compatibility equation

$$\Delta\epsilon_\theta/\Delta r = (\epsilon_r-\epsilon_\theta)/r \qquad (5.2.4)$$

Combining eqs. (5.2.3) and (5.2.4) the following equation is obtained

$$(\sigma_\theta-\sigma_r)/\Delta\sigma_r = (\epsilon_r-\epsilon_\theta)/\Delta\epsilon_\theta \qquad (5.2.5)$$

From eq. 5.2.2, σ_θ is given by

$$\sigma_\theta = -(\sigma_r/K)(\Delta\epsilon_r/\Delta\epsilon_\theta) \qquad (5.2.6)$$

Substituting σ_θ into eq. (5.2.5) and rearranging the following is obtained

$$(\Delta\sigma_r/\Delta\epsilon_\theta) = -\frac{\sigma_r(1+(1/K)(\Delta\epsilon_r/\Delta\epsilon_\theta))}{(\epsilon_r - \epsilon_\theta)} \qquad (5.2.7)$$

to solve the above equation Manassero followed the numerical technique described below

$$\begin{aligned}\Delta\sigma_r &= \sigma_r(i) - \sigma_r(i-1)\\ \Delta\epsilon_\theta &= \epsilon_\theta(i) - \epsilon_\theta(i-1)\\ \Delta\epsilon_r &= \epsilon_r(i) - \epsilon_r(i-1)\end{aligned} \qquad (5.2.8)$$

where

i = 1 to n is the number of the measurement data point (see Fig. 5.2.1).

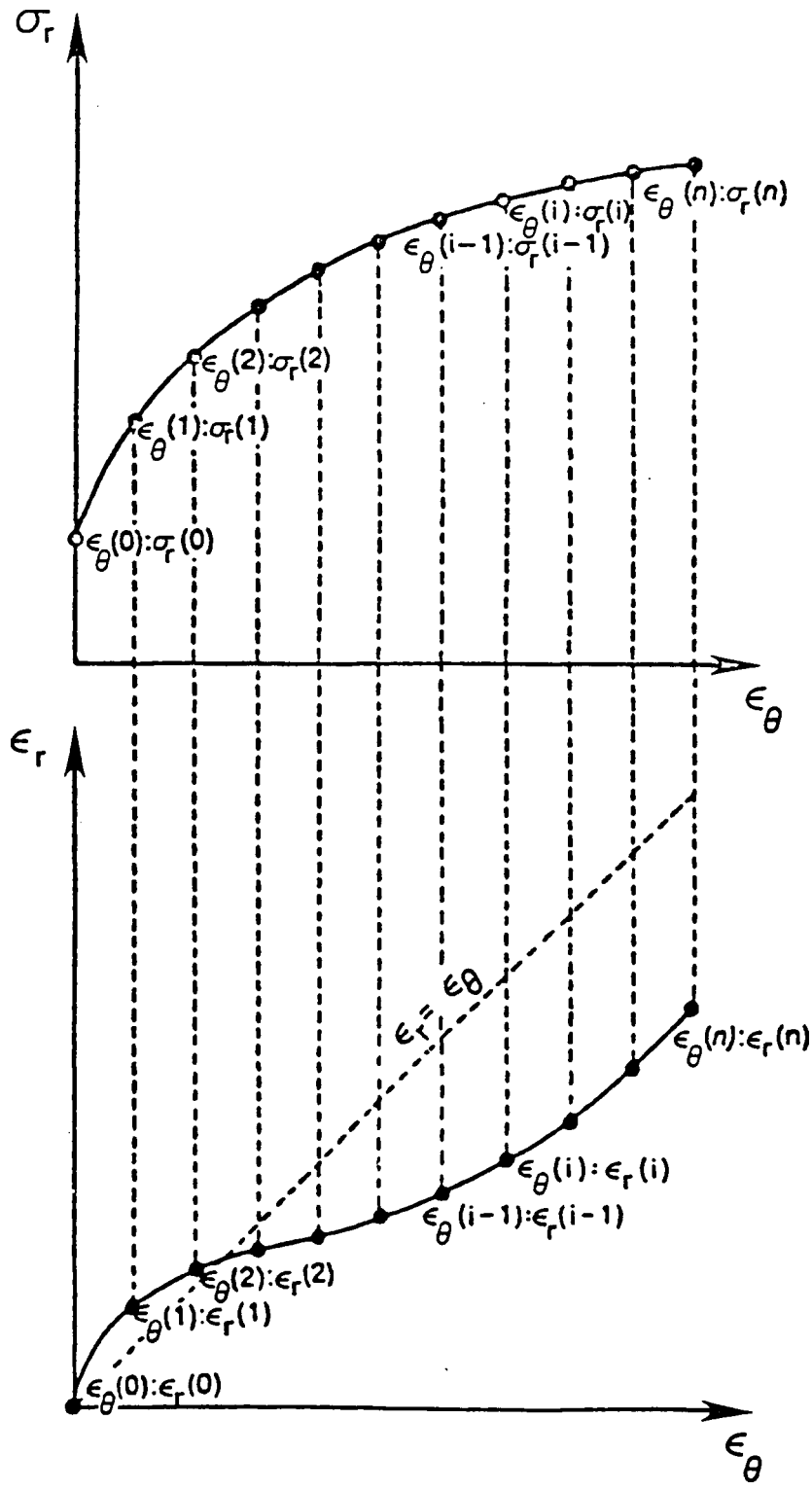

Figure 5.2.1 Use of pressuremeter curve for numerical analysis (after Manassero, 1989)

Substituting eq. (5.2.8) into eq. (5.2.7) and rearranging Manassero obtained the following equation.

$$\epsilon_r(i) = M1 + M2 + M3 + M4 \tag{5.2.9}$$

where:

$$M1 = \frac{\sigma_r(i)(\epsilon_\theta(i-1) + (1/K)\epsilon_r(i-1)}{2(\sigma_r(i)(1+(1/K)) - \sigma_r(i-1)} \tag{5.2.10}$$

$$M2 = \frac{-\sigma_r(i-1)\epsilon_\theta(i)}{2(\sigma_r(i)(1+(1/K) - \sigma_r(i-1)} \tag{5.2.11}$$

$$M3 = \frac{\sigma_r(i)(\epsilon_\theta(i-1) - \epsilon_r(i-1))}{2(1/K)\ \sigma_r(i-1)} \tag{5.2.12}$$

$$M4 = \frac{\sigma_r(i-1)(\epsilon_r(i-1)(1+(1/K) - \epsilon_\theta(i))}{2(1/K)\sigma_r(i-1)} \tag{5.2.13}$$

APPENDIX 5.3

ASSESSMENT OF THE PEAK FRICTION ANGLE, ϕ_p, AND THE ANGLE OF DILATION, ν, FOR LEIGHTON-BUZZARD SAND (e_o = .53) BASED ON THE SIMPLE SHEAR DATA REPORTED BY STROUD (1971) AND BUDHU (1979)

APPENDIX 5.3

ASSESSMENT OF THE PEAK FRICTION ANGLE, ϕ_p, AND THE ANGLE OF DILATION, ν, FOR LEIGHTON-BUZZARD SAND (e_o = .53) BASED ON THE SIMPLE SHEAR DATA REPORTED BY STROUD (1971) AND BUDHU (1979)

It is a well known fact that for sands the peak angle $\phi_p = \sin^{-1}((\sigma_1-\sigma_3)/(\sigma_1+\sigma_3))$ is stress path dependent. Several detailed investigations on the variation of ϕ_p with b-value have been reported and are shown schematically in Fig. 5.3.1. It may be seen that this variation is not unique. Arthur (1977) shows that for Leighton-Buzzard sand the variation of ϕ_p with b-value is as presented in Fig. 5.3.2.

Based on the above, it was considered important to assess the expected mobilized b-value during the pressuremeter test path. Manipulating data from the F.E. analysis a plot of b-value versus shear strain, $\gamma = \epsilon_1-\epsilon_3$, was obtained for the soil element adjacent to the pressuremeter face and is presented in Fig. 5.3.3. The variation of b-value with γ obtained from simple shear data reported by Stroud (1971) is also shown in the figure. It may be seen that the computed b-values at failure for the pressuremeter stress path agree extremely with those obtained from the simple shear test data. The data also show that the b-value at failure is independent of the K_o used in the analysis.

From the above it is concluded that a failure surface based on simple shear test data can be used to assess the plane strain peak friction angle ϕ_p^{ps} correspondent to the pressuremeter test stress path conditions.

Based on simple shear test data reported by Stroud (1971) and Budhu (1979) the failure surface (plane strain conditions) for Leighton-Buzzard sand was obtained and is presented in Fig. 5.3.4. The computed stress

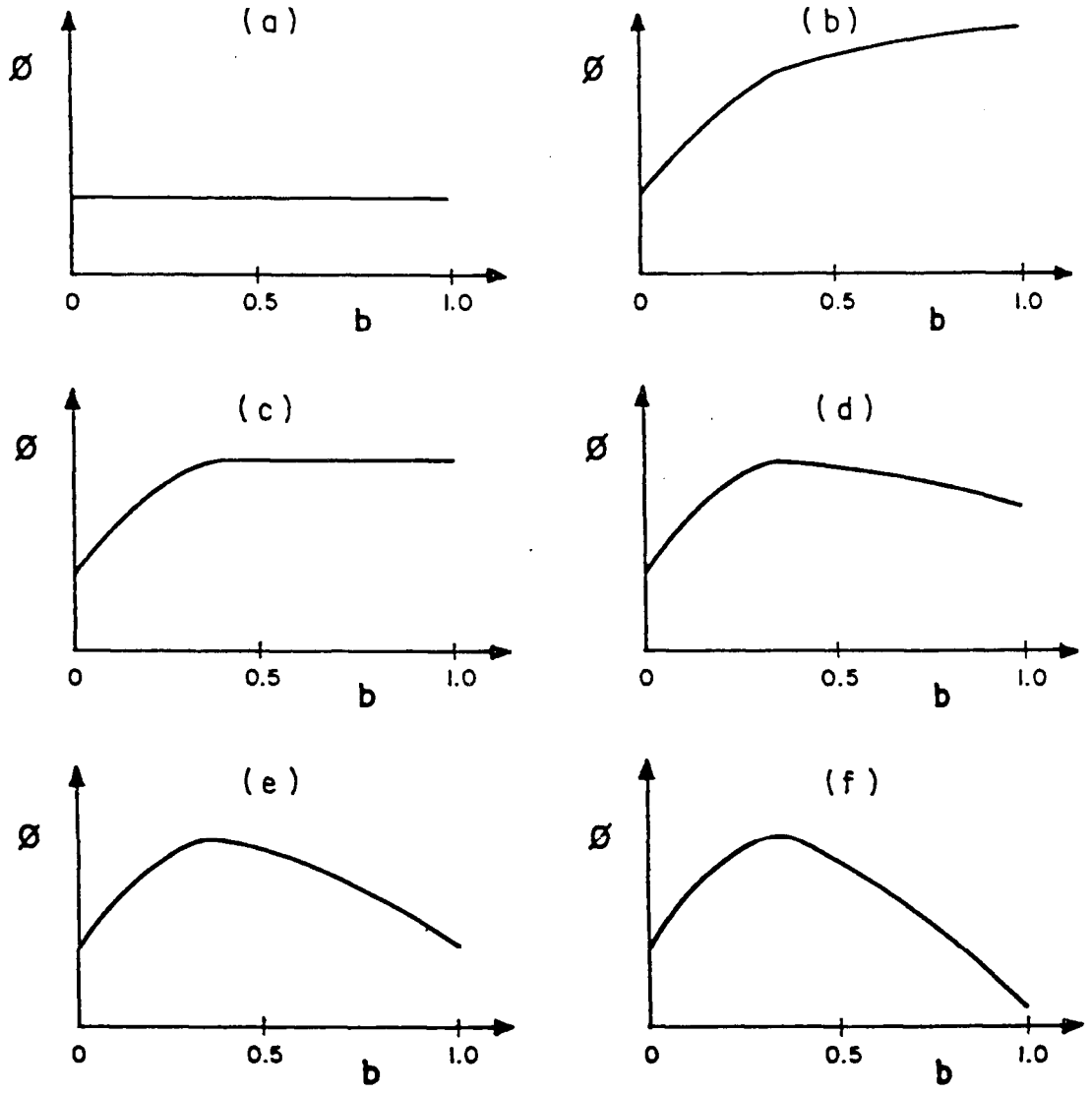

Curve	Reference	Relat. Density
(a)	Bishop (1966)	Loose
(b)	Lade & Duncan (1973) Reades & Green (1976)	Loose Loose to Dense
(c)	Green (1971) Lade & Duncan (1973)	Loose to Dense Dense
(d)	Ergun (1981) Haruyama (1981)	Dense Loose
(e)	Sutherland & Mesdary (1969) Ramamurthy & Rowat (1973)	Loose to Dense Dense
(f)	Shankariah & Ramamurthy(1980)	Medium to Dense

Figure 5.3.1 Reported variation of ϕ_p with b-value for sands (data collected by Sayao, 1989)

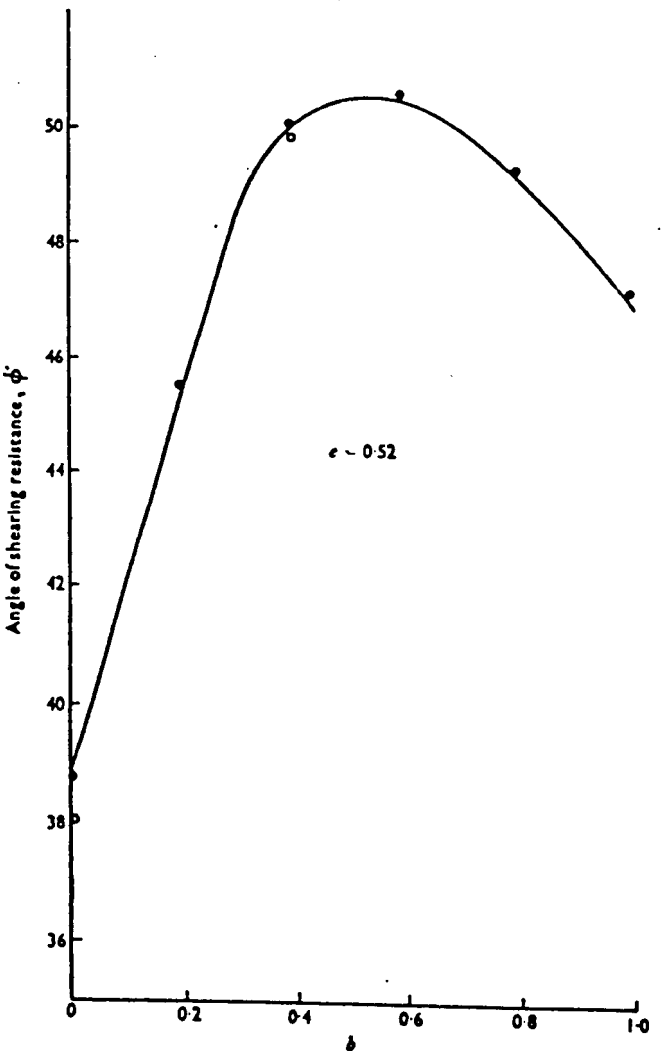

Figure 5.3.2 Reported variation of ϕ_D with b-value for Leighton-Buzzard sand (after Arthur, 1977)

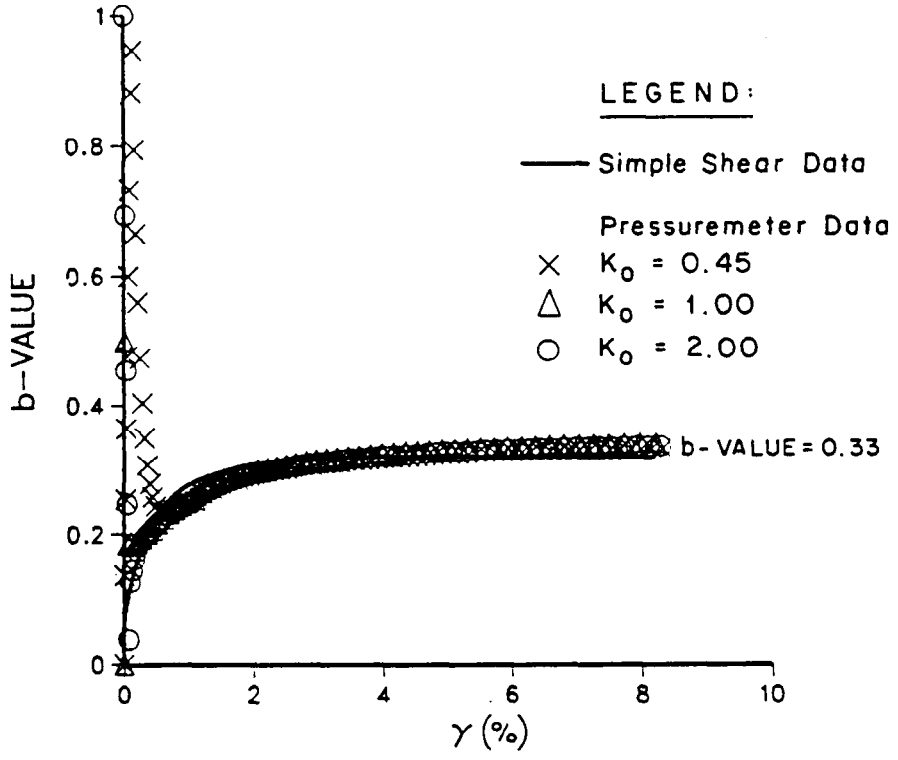

Figure 5.3.3 Variation of b-value with shear strain (based on measured simple shear test data and computed pressuremeter test data

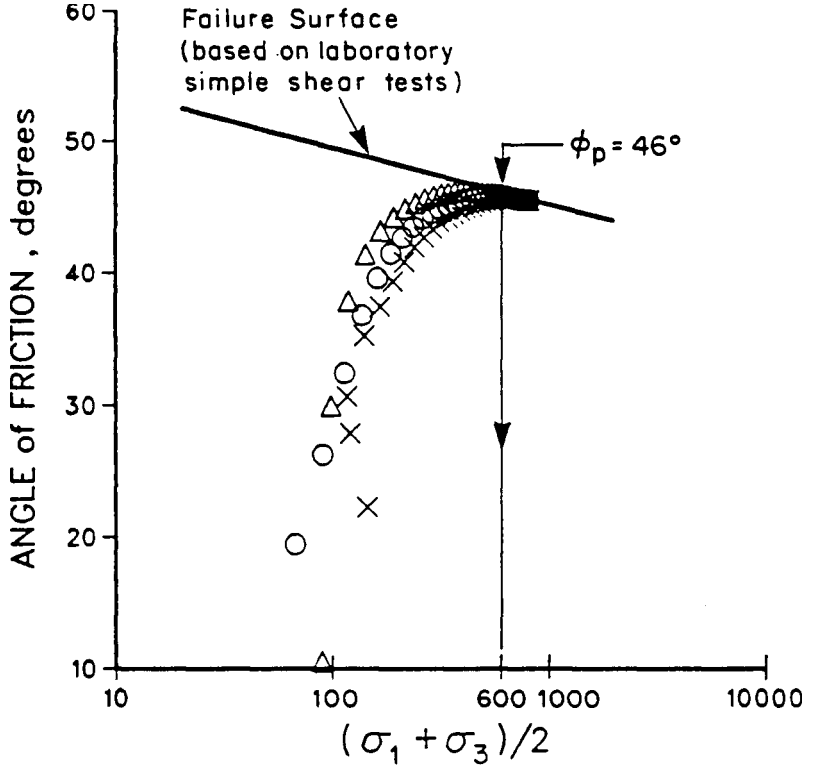

Figure 5.3.4 Failure surface for Leighton-Buzzard sand (b-value = 0.33)

paths mobilized at the face of the pressuremeter correspondent to $K_o(s)$ = .45, 1.0 and 2.0 are also shown in the figure. It may be seen that values of ϕ_p^{ps} = 46.4 (K_o = 1.0); ϕ_p^{ps} = 46.0 (K_o = 2.0) and ϕ_p^{ps} = 45.6 (K_o = .45) were computed from the analysis. Based on the above, an average value of ϕ_p^{ps} = 46 and an average value of σ_m = 600 kPa (at failure) are obtained.

To assess the expected dilation angle, ν, for the pressuremeter test stress conditions, the simple shear data reported by Stroud (1971) and Budhu (1979) was also used here and the variation of ν with mean normal stress, σ_m, inferred from these tests is presented in Fig. 5.3.5. Using the average value of σ_m = 600 kPa, a value of ν = 15° is obtained.

Based on the above, it is concluded that a value of ϕ_p^{ps} = 46° and ν = 15° are representative of the strength and dilation characteristics of Leighton-Buizzard sand (correspondent to an average value of σ_m = 600 kPa) for the pressuremeter test stress conditions analyzed in the main text.

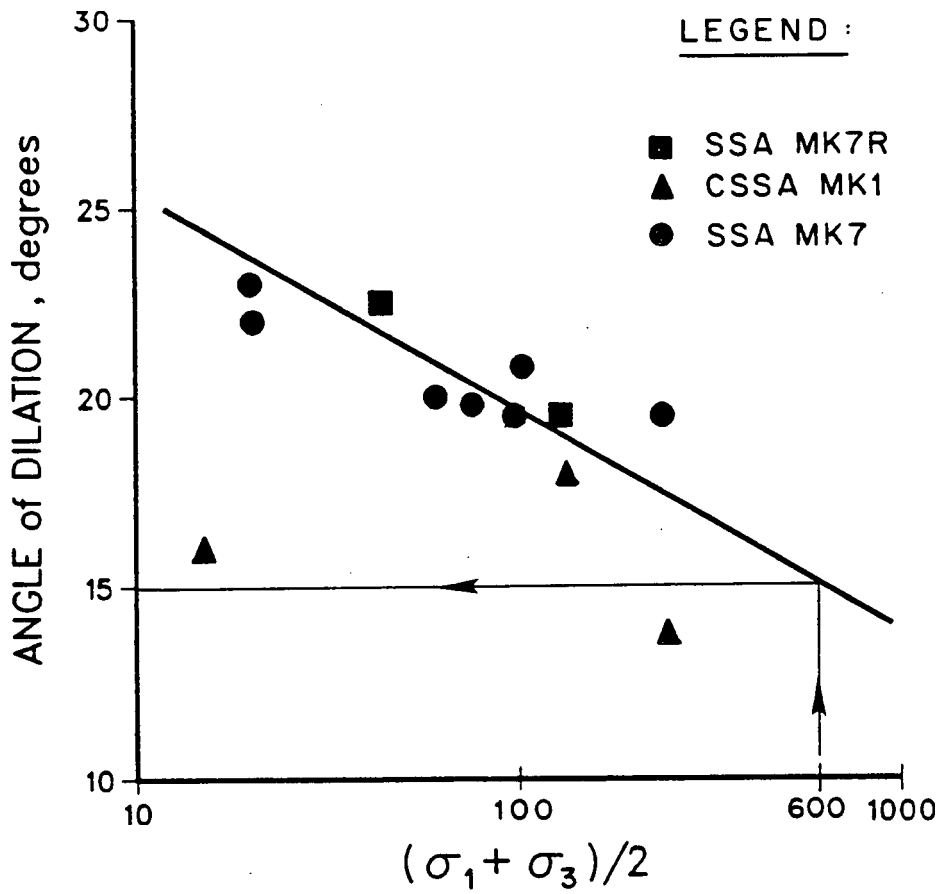

Figure 5.3.5 Variation of the dilation angle ν with mean normal stress

APPENDIX 5.4

RELATIONSHIP BETWEEN KG_e and G_{HH}

APPENDIX 5.4

RELATIONSHIP BETWEEN KG_e and G_{HH}

The elasic tangent shear modulus G_t is defined in the modified SMP model as follows:

$$G_t = KG_e\ Pa\ \left(\frac{\sigma_1+\sigma_2+\sigma_3}{3Pa}\right)^n \qquad (5.4.1)$$

Using the pressuremeter initial lift-off conditions this equation takes the form

$$G_t = KG_e\ Pa\ \left(\frac{\sigma_{vo}+\sigma_{ro}+\sigma_{\theta o}}{3Pa}\right)^n$$

where:

σ_{vo} = the initial vertical stress

σ_{ro} = the initial radial stress

$\sigma_{\theta o}$ = the initial circumferential stress

Since $\sigma_{ro} = \sigma_{\theta o} = K_o\ \sigma_{vo}$, then

$$G_t = KG_e\ Pa\ \left(\frac{\sigma_{vo}(1+2K_o)}{3Pa}\right)^n \qquad (5.4.2)$$

The maximum shear modulus for horizontal loading G_{HH} is evaluated by the following equation:

$$G_{HH} = \frac{G^*}{\alpha_P}\ \alpha_D \text{ (see eq. 5.24, main text)}$$

Assuming that G_{HH} can be expressed as

$$G_{HH} = KG_e \, Pa \, \left(\frac{\sigma_{vo} K_o}{Pa}\right)^n \qquad (5.4.3)$$

Dividing eq. (5.4.2) by eq. (5.4.3) the following relationship is obtained

$$G_t = ((1+2K_o)/3K_o)^n \, G_{HH} \qquad (5.4.4)$$

Assuming that n = 0.5, common value for sands and substituting eq. (5.4.4) into eq. (5.4.2) the following equation is obtained

$$KG_e = \left(\frac{Pa}{\sigma_{v_0} K_o}\right)^{0.5} G_{HH} \qquad (5.4.5)$$

APPENDIX 5.5

EVALUATION OF SOIL PARAMETERS FROM PRESSUREMETER TEST DATA, FOR USE IN THE MODIFIED SMP MODEL

APPENDIX 5.5

EVALUATION OF SOIL PARAMETERS FROM PRESSUREMETER TEST DATA, FOR USE IN THE MODIFIED SMP MODEL

As described in the main text Manassero's method was applied together with eq. (5.33) to the finite element generated response for plane strain conditions with the outer boundary at infinity for Leighton-Buzzard sand (K_o = .45). The predicted values at the face of the pressurementer of $(\sigma_v)_{face}$, $(\sigma_\theta)_{face}$, and $(\epsilon_r)_{face}$, by the above method and equation, together with the input values of $(\sigma_r)_{face}$ and $(\epsilon_\theta)_{face}$ were shown in Fig. 5.20(a) and (b) of the main text. These set of data will be used next to evaluate plastic soil parameters for use in the modified SMP model.

The elastic soil parameters, KG_e, n, KB_e and m are assumed here to be known and equal to the elastic parameters used in the F.E. analysis because pressuremeter test data from unload reload loops in Leighton-Buzzard sand for plane strain boundary conditions with outer boundary at infinity are not known. Therefore values of KG_e = 620, n = .60, KB_e = 580 and m = .63 (see Table 5.1 of main text) will be used for the computations that follow.

The plastic soil parameters used in the modified SMP model consist of the following (see main text chapters 2, 3, and 5):

- Hardening Parameters — KG_p and np
- Flow Rule Parameters — μ and λ
- Failure Parameters — $(\tau_{smp}/\sigma_{smp})_i$, $\Delta(\tau_{smp}/\sigma_{smp})$ and R_F

To evaluate these parameters, the procedures described in Chapter 3 together with the above elastic parameters and the set of data shown in Fig. 5.20 of the main text, were used here as follows:

- Evaluation of Hardening Parameters, KG_p and np

The above parameters KG_p and np are used to define the initial shear parameter, G_{pi}, by the following equation (see eq. 3.20, Chapter 3)

$$G_{pi} = KG_p \ (\sigma_{SMP}/Pa)^{np} \tag{5.5.1}$$

and this parameter is used to define the tangent shear plastic parameter, G_p, by the following equation (see eq. 3.16, chapter 3)

$$G_p = G_{pi} \ (1 - R_F \ SRL)^2 \tag{5.5.2}$$

where:

R_F = the failure ratio = $(\tau_{SMP}/\sigma_{SMP})_F/(\tau_{SMP}/\sigma_{SMP})_{ult}$ (5.5.3)

and

SRL = the stress ratio level

The above quantities have been defined in chapter 3.

To evaluate G_{pi} and $(\tau_{SMP}/\sigma_{SMP})_{ult}$ a relationship between $(\gamma^p_{SMP}/(\tau_{SMP}/\sigma_{SMP})$ and γ^p_{SMP} was obtained using the data shown in Fig. 5.20 and is presented in Fig. 5.5.1. It may be seen that for shear strains γ^p_{SMP} > 0.1 the above relationship plot in a straight line with an intercept a = .0032 and a slope b = 1.205. Since $G_{pi} = (a)^{-1}$ and $(\tau_{SMP}/\sigma_{SMP})_{ult} = (b)^{-1}$ (see chapter 3) then the following values are obtained

$$G_{pi} = 312$$

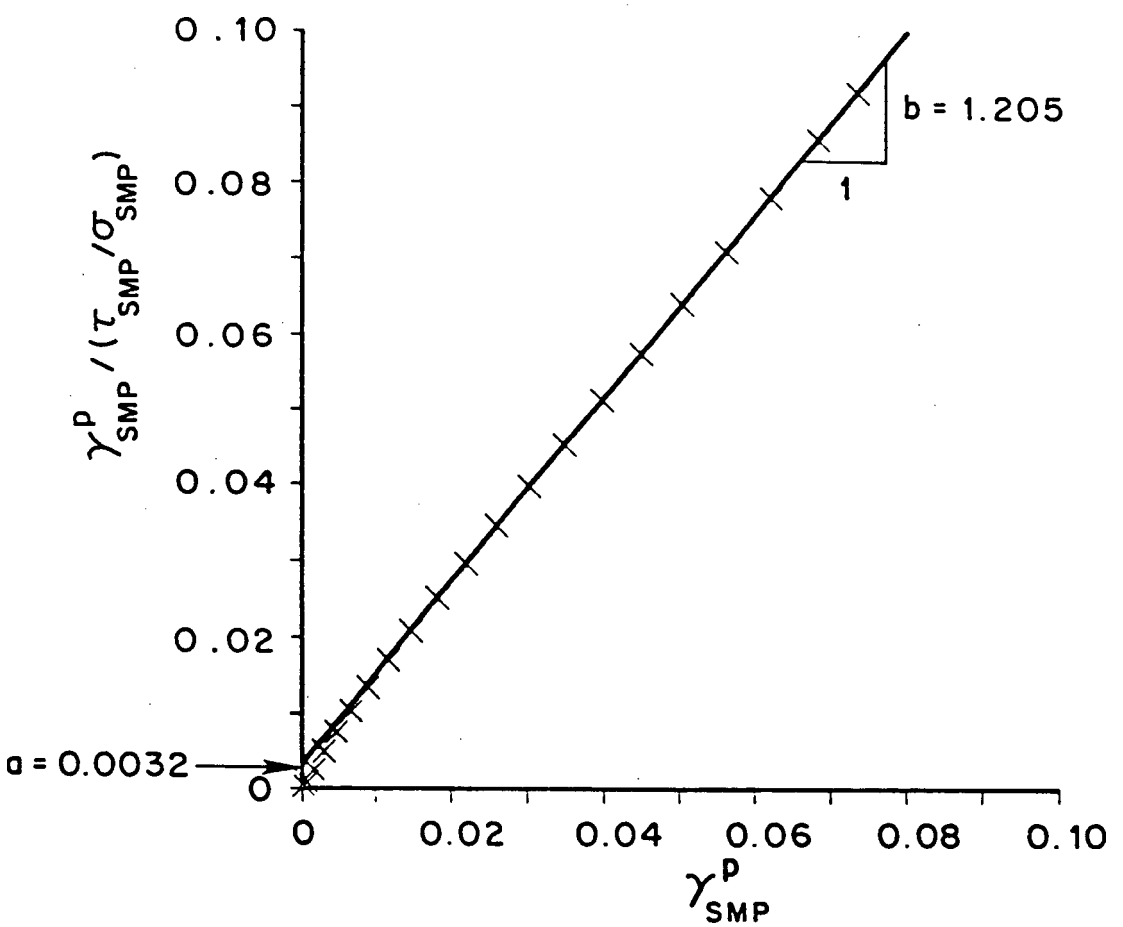

Figure 5.5.1 Evaluation of G_{p_i} and $(\tau_{SMP}/\sigma_{SMP})_{ult}$

and

$$(\tau_{SMP}/\sigma_{SMP})_{ult} = .830 \qquad (5.5.4)$$

To evaluate KG_p equation (5.5.1) is used below, i.e.

$$KG_p = G_{pi} \ (\sigma_{SMP}/Pa)^{-np}$$

Since σ_{SMP} = 110 kPa is the initial normal stress on the SMP (for K_o = .45) and assuming that np = -0.5, common value for sand (based on the writer's experience), then it follows that KG_p = 325.

- Evaluation of Flow Rule Parameters

To evaluate the flow rule parameters μ and λ, a relationship between $(\tau_{SMP}/\sigma_{SMP})$ and $(-\Delta\epsilon^p_{SMP}/\Delta\gamma^p_{SMP})$ was obtained and is presented in Fig. 5.5.2. The solid line shown in the figure represents the flow rule obtained earlier (chapter 3) from the simple shear data reported by Stroud (1971). It may be seen that the solid line almost coincides with the average of the data points (dashed line) predicted by the present study. This line has an intercept μ = .195 and a slope λ = 1.22, which are the flow rule parameters required. It should be noted that these same parameters can be obtained from laboratory testing on remolded (or disturbed) samples of sand and therefore its evaluation can be verified at a later stage.

- Evaluation of Failure Parameters

The failure parameters used in the modified SMP model are listed below:

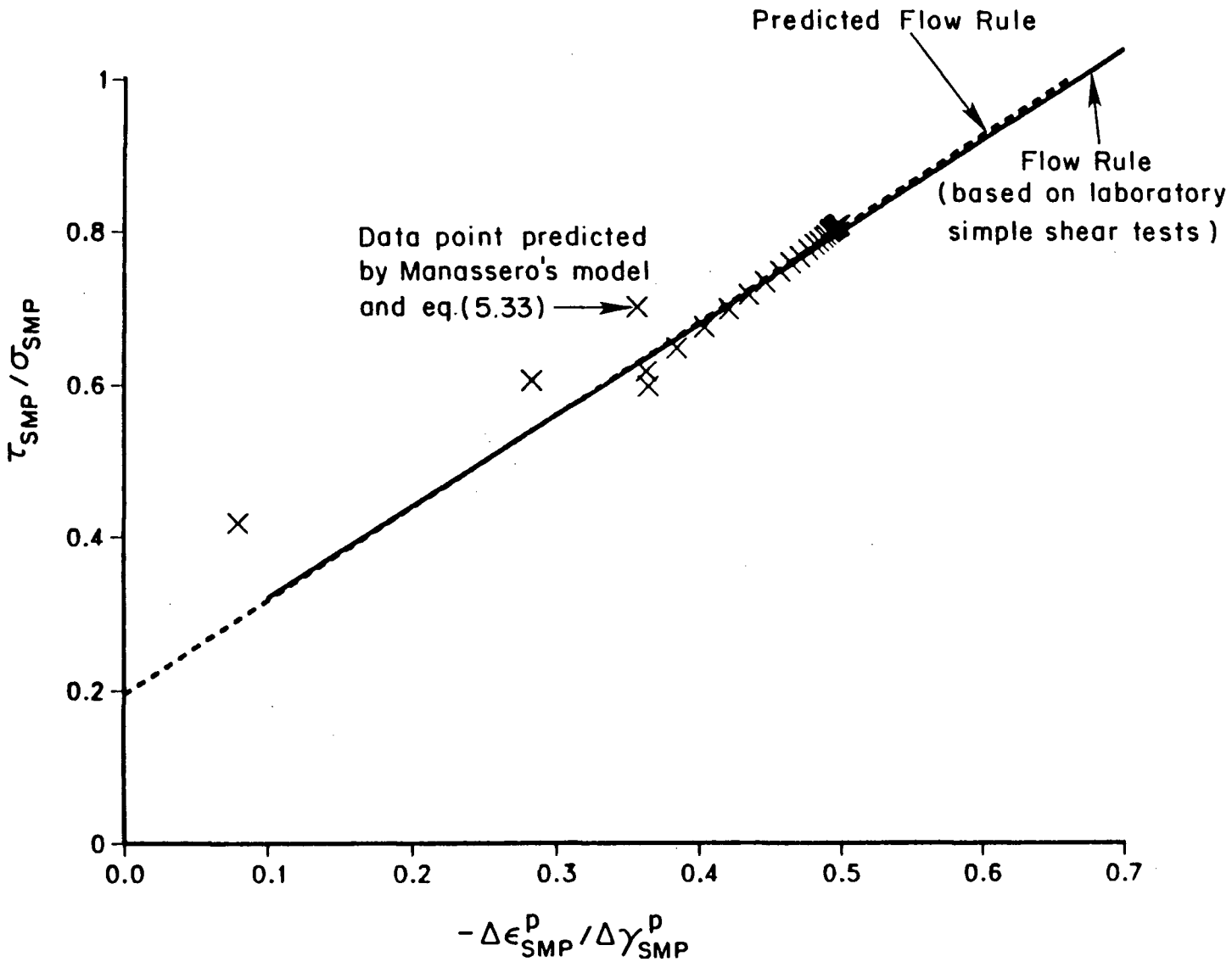

Figure 5.5.2 Evaluation of flow rule parameters

R_F = the failure ratio (see eq. (5.5.3))

$(\tau_{SMP}/\sigma_{SMP})_1$ = the failure stress ratio at 1 atmosphere

$\Delta(\tau_{SMP}/\sigma_{SMP})$ = the decrease in failure stress ratio for a 10 fold increase in σ_{SMP}

• Evaluation of R_F

Manipulating the data a relationship between the mobilized stress ratio $(\tau_{SMP}/\sigma_{SMP})_{mob}$ and $\log_{10}(\sigma_{SMP}/pa)$ was obtained and is presented in Fig. 5.5.3. The solid line shown in the figure represents the failure surface obtained earlier (chapter 3) from the simple shear data reported by Stroud (1971). It may be seen that a peak failure stress ratio $(\tau_{SMP}/\sigma_{SMP})_F$ = .81 is computed from the figure. Entering this value in eq. (5.5.3) together with $(\tau_{SMP}/\sigma_{SMP})_{ult}$ = .83 (see eq. (5.5.4)) a value for R_F = .976 is obtained.

• Evaluation of $(\tau_{SMP}/\sigma_{SMP})_1$ and $\Delta(\tau_{SMP}/\sigma_{SMP})$

The following two approaches will be used to evaluate $(\tau_{SMP}/\sigma_{SMP})_1$ and $\Delta(\tau_{SMP}/\sigma_{SMP})$:

(a) using the data shown in Fig. 5.5.3; and

(b) using data published by Bolton (1986).

The reason for the two approaches is explained below.

Using the analytical data shown in Fig. 5.5.3 a failure surface can be defined by point P (which corresponds to the peak stress ratio) and point L (the last data point). This surface is represented in the figure by the dashed line. Using this line values of $(\tau_{SMP}/\sigma_{SMP})_1$ = .854 and $\Delta(\tau_{SMP}/\sigma_{SMP})$ = .076 are obtained. However, because points P and L are too close, it might turn out difficult to infer a failure line from real pressuremeter data. One of course could expand the pressuremeter with

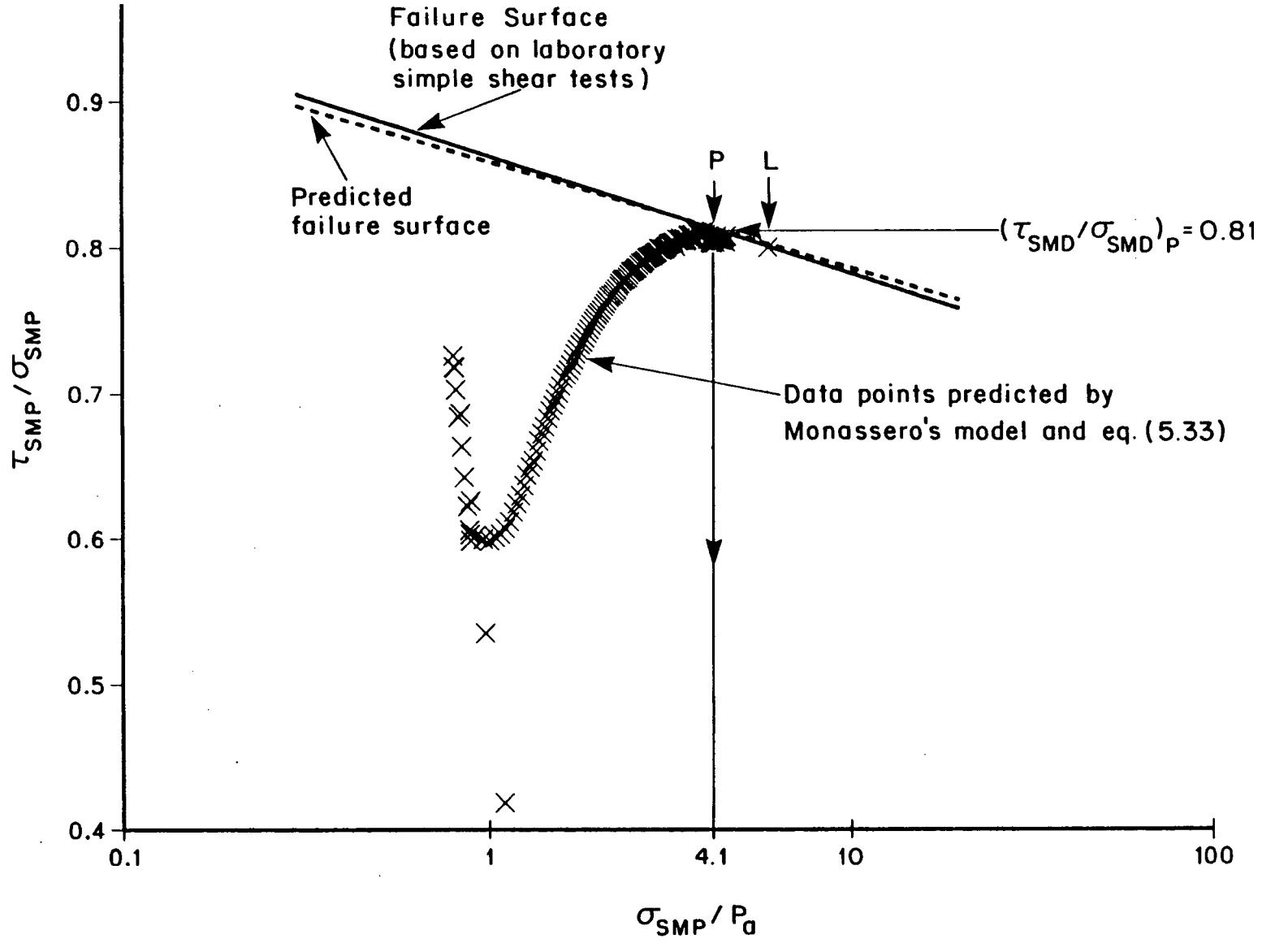

Figure 5.5.3 Evaluation of $(\tau_{SMP}/\sigma_{SMP})_F$

stresses larger than that shown in the figure until the failure line becomes more evident. However, because the circumferential strain computed for point L, as a value of $(\epsilon_\theta)_{face}$ = 30% the above approach cannot be followed in practice since $(\epsilon_\theta)_{face}$ = 30% is about the maximum value that can be mobilized with the existing SBP devices.

Based on the above, it was decided to use the procedures and test data reported by Bolton (1986) to evaluate values for $(\tau_{SMP}/\sigma_{SMP})_1$ and $\Delta(\tau_{SMP}/\sigma_{SMP})$. This alternative approach is described next.

The following relationship between the peak friction angle, ϕ_p, and the friction angle at constant volume, ϕ_{cv} was developed by Bolton (1986)

$$\phi_p - \phi_{cv} = 0.8\ \nu_{max} = KI_r \qquad (5.5.5)$$

where:

ν_{max} = the maximum dilation angle

K = a constant

and

I_r = the relative dilatancy index, which is given by the following equation:

$$I_r = D_r\ (Q - \ln(P)) - 1 \qquad (5.5.6)$$

where:

D_r = the relative density

p = the mean normal stress =

= $(\sigma_1+\sigma_3)/2$

Q = constant

Substituting eq. (5.5.6) into eq. (5.5.5) the following is obtained:

$$\phi_p - \phi_{cv} = 0.8\ \nu_{max} = K\ (D_r(Q - \ln(P)) - 1) \qquad (5.5.7)$$

Therefore once D_r is estimated and the constants Q, K and ϕ_{cv} are established, values of ϕ_p for different levels of stress, p, can be evaluated.

• Estimation of D_r

Based on the laboratory sand data referenced in Table 5.5.1 (Bolton, 1986) developed a relationship between maximum dilatancy rate $(-\Delta\epsilon_v/\Delta\epsilon_1)_{max}$, and D_r for both triaxial and plane strain tests. This relationship is presented in Fig. 5.5.4 and plots as a straight line with a slope $K_1 = 1.0$ and an intercept $K_2 = .13$. Therefore once $(-\Delta\epsilon_v/\Delta\epsilon_1)_{max}$ is known, D_r can be evaluated as follows:

$$D_r = ((-\Delta\epsilon_v/\Delta\epsilon_1)_{max} + K_2)/K_1 \qquad (5.5.8)$$

substituting the values of K_1 and K_2 in the above equation, the following is obtained

$$D_r = (-\Delta\epsilon_v/\Delta\epsilon_1)_{max} + .13 \qquad (5.5.9)$$

A plot of $-\Delta\epsilon_v$ versus $\Delta\epsilon_1$ was developed from the values of $(\epsilon_\theta)_{face}$ and $(\epsilon_r)_{face}$ predicted by Manassero's model and is presented in Fig. 5.5.5. From this figure a value of $-(\Delta\epsilon_v/\Delta\epsilon_1)_{max} = .61$ is obtained which in turn leads to a value of $D_r = .74$. The values computed by the modified SMP

model are also shown in the figure. From these a value of $-(\Delta\epsilon_v/\Delta\epsilon_1)_{max}$ = .68 is obtained which leads to D_r = .81. Comparing these values with the actual D_r = .87 of the sand analyzed (Leighton-Buzzard sand, e_0 = .53) deviations of -6.9% (modified SMP model) and -15% (Manassero's model) are obtained.

Table 5.5.1
Sand Data

ID	Name	d_{60}: mm	d_{10}: mm	e_{min}	e_{max}	ϕ'_{crit}	Reference
A	Brasted river	0.29	0.12	0.47	0.79	32.6	Conforth (1964,1973)
B	Limassol marine	0.11	0.003	0.57	1.18	34.4	Cornforth (1973)
C	Mersey river	≈0.2	≈0.1	≈0.49	0.82	32.0	Rowe (1969) Rowe & Barden (1964)
D	Monterey #20	≈0.3	≈0.15	≈0.57	0.78	36.9	Marachi, Chan, Seed & Duncan (1969)
E	Monterey #0	≈0.5	≈0.3	≈0.57	0.86	37.0	Lade & Duncan (1969)
F	Ham river	0.25	0.16	0.59	0.92	33.0	Bishop & Green (1965)
G	Leighton-Buzzard 14/25	0.85	0.65	0.49	0.79	35.0	Stroud (1971)
H	Welland river	0.14	0.10	0.62	0.94	35.0	Barden et al. (1969)
I	Chattahoochee river	0.47	0.21	0.61	1.10	32.5	Vesic & Clough (1968)
J	Mol	0.21	0.14	0.56	0.89	32.5	Ladanyi (1960)
K	Berlin	0.25	0.11	0.46	0.75	33.0	De Beer (1965)
L	Guinea marine	0.41	0.16	0.52	0.90	33.0	Cornforth (1973)
M	Portland river	0.36	0.23	0.63	1.10	36.1	Cornforth (1973)
N	Glacial outwash sand	0.9	0.15	0.41	0.84	37.0	Hirschfield & Poulos (1964)
P	Karlsruhe med. sand	0.38	0.20	0.54	0.82	34.0	Hettler (1981)
R	Sacramento river	0.22	0.15	0.61	1.03	33.3	Lee & Seed (1967)
S	Ottawa sand	0.76	0.65	0.49	≈0.8	30.0	Lee & Seed (1967)

- Evaluation of Constant Q

To evaluate Q, eq. (5.5.6) will be used next, together with the simple shear data reported by Stroud on Leighton-Buzzard sand.

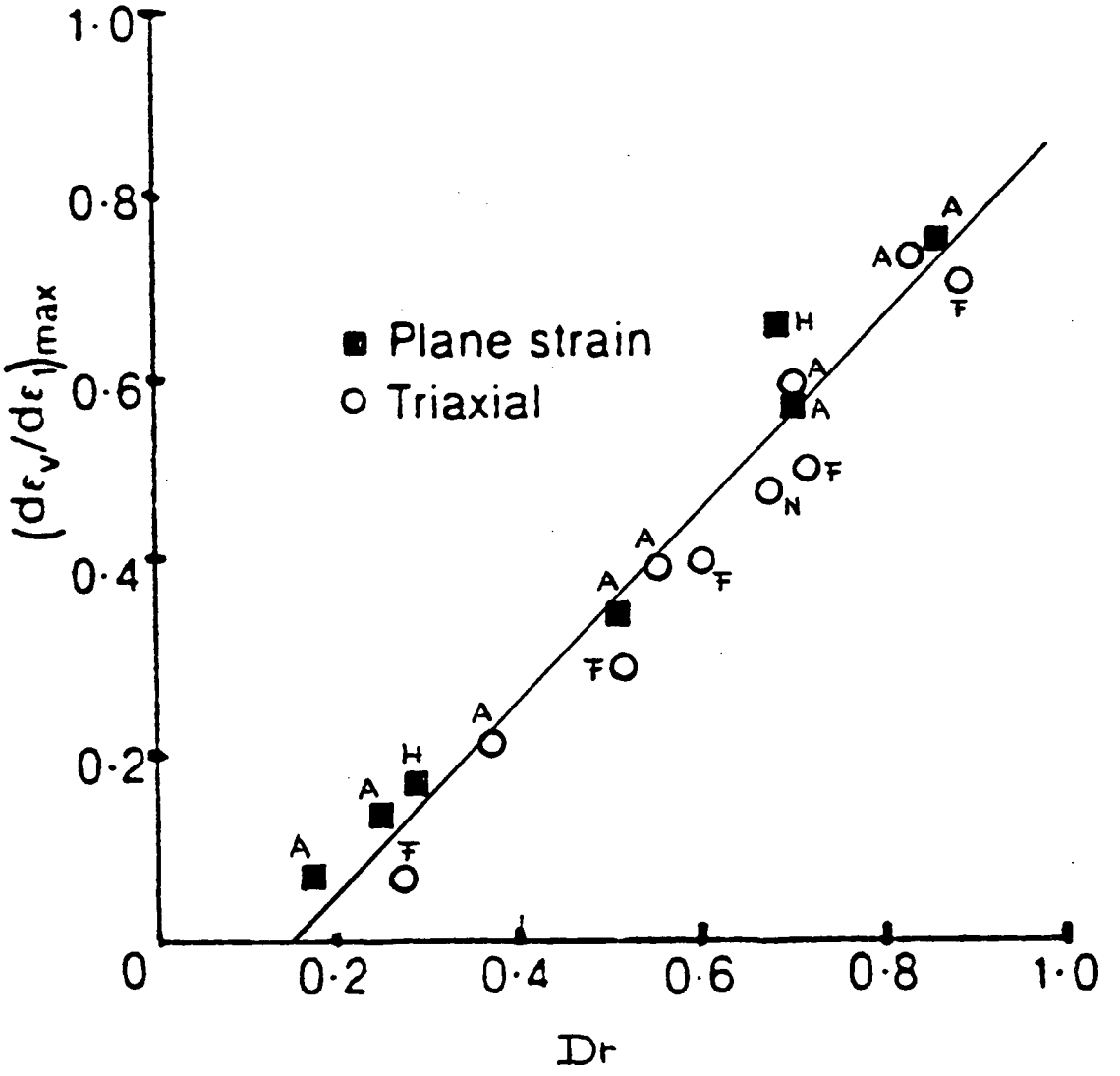

Figure 5.5.4 Relationship between $(\Delta\varepsilon_v/\Delta\varepsilon_1)_{max}$ and D_r (after Bolton (1986))

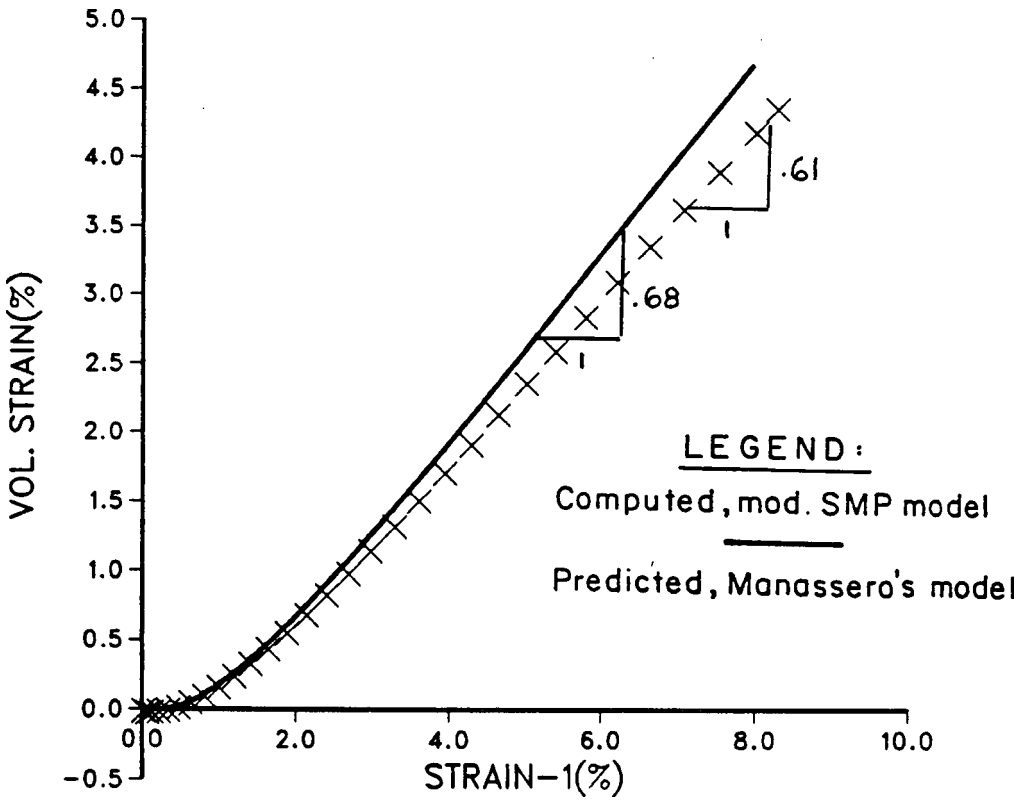

Figure 5.5.5 Variation of $\Delta\epsilon_v$ with $\Delta\epsilon_1$

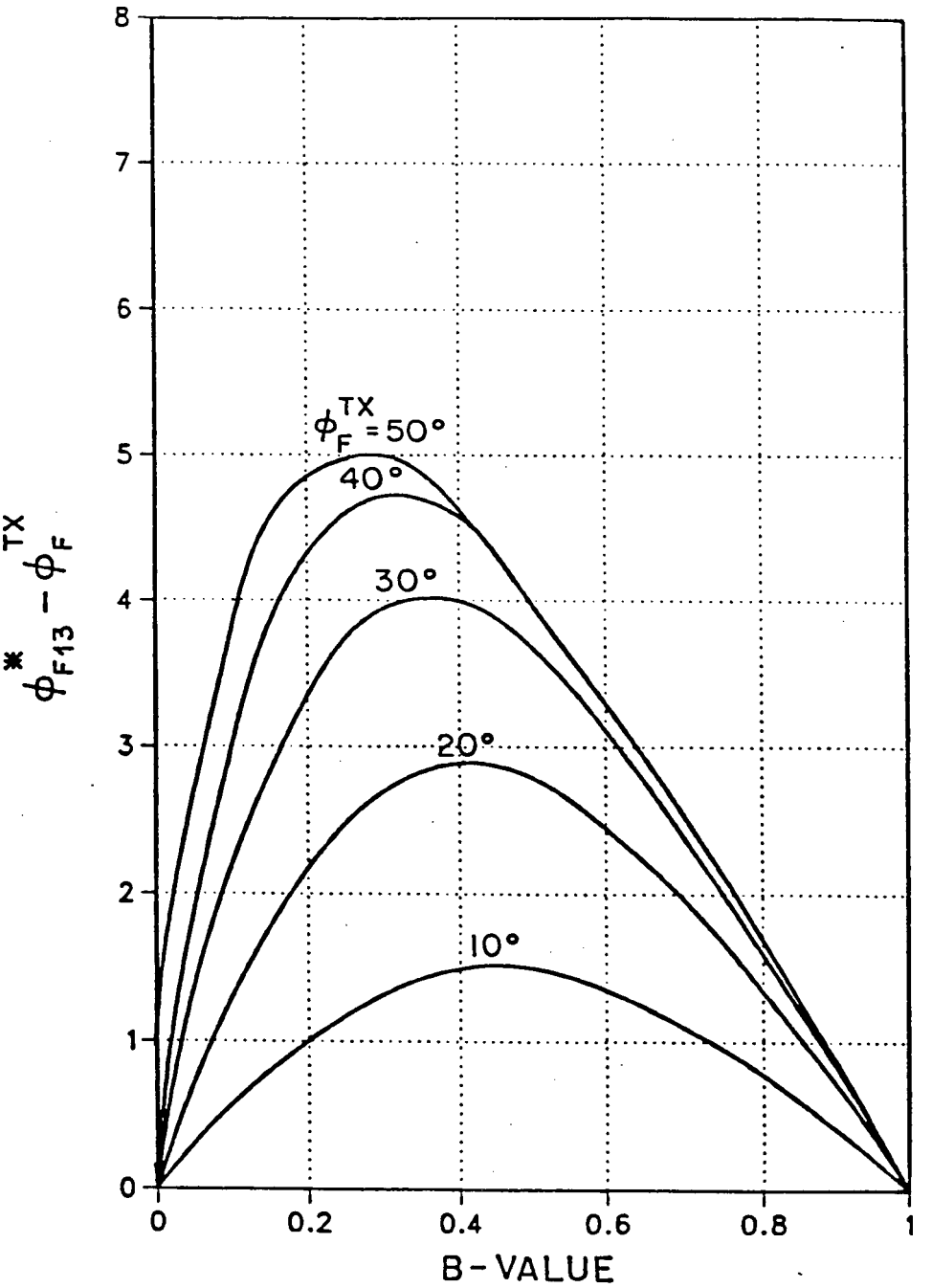

Figure 5.5.6 Variation of $(\phi_p^{13}-\phi_p^{tx})$ with b-value

From eq. (5.5.6) it follows that:

$$Q = (I_r + 1 + D_r \ln(P))/D_r \qquad (5.5.10)$$

and when $\phi_p = \phi_{cv}$ it follows that $I_r = 0$ (see eq. (5.5.5)), i.e. the value of Q can be obtained by the following equation:

$$Q = (1 + D_r \ln(P_{cv}))/D_r \qquad (5.5.11)$$

where:

p_{cv} = the mean normal stress required for $\phi_p = \phi_{cv}$.

Because the above equation is considered to be valid for any value of D_r (Bolton, 1986) it implies that Q can be evaluated from laboratory tests on remoulded samples of sand prepared at different D_r(s). Herein the simple shear data reported by Stroud (1971) on Leighton-Buzzard sand (D_r = .87) is used below for that effect.

Manipulating Stroud's data (shown in Fig. 5.3.4) and using $\phi_{cv} = 35°$ a value of P_{cv} = 230,000 kPa is evaluated. Entering this value of p_{cv} with D_r = .87 in eq. (5.5.11) a value of Q = 13.7 kPa is obtained. This Q value is considered to be representative of Leighton-Buzzard sand for plane strain conditions.

• Evaluation of Constant K

Substituting the values of $\phi_{cv} = 35°$, D_r = .74 (estimated value) and Q = 13.7 kPa into eq. (5.5.7) the following equations are obtained:

$$K = (\phi_p^{ps} - 35)/(.74(13.7 - \ln(P))-1) \qquad (5.5.12a)$$

or

$$K = (.8\ \nu_{max})/(.74(13.7 - \ln(P))-1) \qquad (5.5.12b)$$

Therefore, to evaluate K, values of ϕ_p^{ps} (or ν_{max}) and p are necessary. These values were computed earlier in the main text using Manassero's model (see section 5.3.2.1) and consist on the following: $\phi_p = 45.5°$; $\nu_p = 13°$; and p = 600 kPa. Entering these values in eqs. (5.5.12) the following is obtained:

$$K = 2.38 \quad \text{(from eq. (5.5.12a)}$$

or

$$K = 2.36 \quad \text{(from eq. (5.5.12b)}$$

Based on the above an average value of K = 2.37 will be used below.

- Evaluation of $(\tau_{SMP}/\sigma_{SMP})_i$ and $\Delta(\tau_{SMP}/\sigma_{SMP})$

Entering the above values of ϕ_{cv}, D_r, Q and K in eq. (5.5.7) the following equation is obtained:

$$\phi_p^{ps} = 35 + 2.37(.74(13.7 - \ln(P))-1) \qquad (5.5.13)$$

To evaluate the parameters $(\tau_{SMP}/\sigma_{SMP})_i$ and $\Delta(\tau_{SMP}/\sigma_{SMP})$ the above equation will be used here together with the following relationships:

- $p = 1.45\ \sigma_{SMP}$ (5.5.14)

- $(\tau_{SMP}/\sigma_{SMP}) = 2\sqrt{2}/3 \tan(\phi^{tx})$ (5.5.15)

- $\phi^{tx} = \phi^{ps} - 4.8°$ (5.5.16)

where:

ϕ^{tx} = the angle of friction for triaxial conditions

The relationship $p = 1.45\ \sigma_{SMP}$ was obtained from the data generated by the F.E. pressuremeter analysis (plane strain infinite outer boundary conditions). The relationship $(\tau_{SMP}/\sigma_{SMP}) = 2\sqrt{2}/3 \tan(\phi^{tx})$ was obtained from the equation defining the stress ratio on the SMP (see eq. (2.29), main text) after applying it the correspondent triaxial boundary conditions and the relationship $\phi^{tx} = \phi^{ps} - 4.8°$ was obtained based on the data presented in Fig. 5.5.6 which was developed earlier in Chapter 2 (section 2.4.2.1), together with a b-value = .33 which was computed earlier in Appendix 5.1.

Manipulating eqs. (5.5.13) to (5.5.16) the following equation is obtained:

$$(\tau_{SMP}/\sigma_{SMP}) = 2\sqrt{2}/3\tan(30+2.37(.74(13.7-\ln(1.45\sigma_{SMP})-1))) \quad (5.5.17)$$

Entering a value of σ_{SMP} = Pa = 101.33 kPa in the above equation a value of $(\tau_{SMP}/\sigma_{SMP})_1$ = .876 is obtained, and entering a value of σ_{SMP} = (10 • Pa) = 10,133 kPa a value of $(\tau_{SMP}/\sigma_{SMP})_{10}$ = .760 is obtained. Since $\Delta(\tau_{SMP}/\sigma_{SMP}) = (\tau_{SMP}/\sigma_{SMP})_1 - (\tau_{SMP}/\sigma_{SMP})_{10}$ it follows that $\Delta(\tau_{SMP}/\sigma_{SMP})$ = .116.

Comparing these two values with the actual values used in the F.E. analysis: $(\tau_{SMP}/\sigma_{SMP})_1 = .862$ and $\Delta(\tau_{SMP}/\sigma_{SMP}) = 0.8$ deviations of 1.62% and 45.0% are computed respectively.

The above indicates that a good prediction of the value $(\tau_{SMP}/\sigma_{SMP})_1$ was obtained. However, the predicted value for $\Delta(\tau_{SMP}/\sigma_{SMP})$ is high. Nevertheless if the stress ratio correspondent to $\sigma_{SMP} = (10 \cdot Pa)$ is computed using both the F.E. parameters and the backpredicted parameters the following values are obtained:

$$(\tau_{SMP}/\sigma_{SMP})_{10} = .862-.08 = .782 \quad \text{(F.E. parameters)}$$

$$(\tau_{SMP}/\sigma_{SMP})_{10} = .876 - .116 = .760 \quad \text{(backpredicted)}$$

i.e., a deviation of -2.8% between these two values is obtained indicating that for stress levels of σ_{SMP} in the range of $(1 \cdot Pa)$ to $(10 \cdot PA)$ the deviations for the failure stress ratio are in the range of +1.62% to -2.8%. Based on this fact the failure parameters $(\tau_{SMP}/\sigma_{SMP})_1$ and $\Delta(\tau_{SMP}/\sigma_{SMP})$ assessed above are considered to be acceptable for analyses purposes.

CHAPTER 6

APPENDIX INDEX

CHAPTER 6

APPENDIX FIGURES INDEX

APPENDIX 6.1

K_o ASSESSMENT

APPENDIX 6.1

K_o ASSESSMENT

The earth pressure coefficient, K, is a parameter that is important to assess with some degree of accuracy since its effects are two-fold:

a) Affects the evaluation of the two mean normal stresses, σ_m and σ'_m which in turn affect the evaluation of the in situ state parameter, ψ, and in situ void ratio, e_c. Presented in Fig. 6.1.1 are three different assessments of e_c for K_o = .4, .7 and 1.0. It may be seen that the void ratios in the core can range from .68 to .73 depending upon if K_o = .4 or 1.0. To see its influence, for example in the evaluation of maximum shear modulus, G_{max} the equation proposed by Hardin and Drnevick (1972) can be used:

$$G_{max} = 320 \frac{(2.973 - e_c)^2}{1 + e_c} \; pa \; (\frac{\sigma'_m}{pa})^{.5} \qquad (6.1.1)$$

and the following values are obtained:

$$e_c = .68 \rightarrow G_{max} = 94{,}000 \text{ kPa}$$
$$e_c = .73 \rightarrow G_{max} = 78{,}300 \text{ kPa}$$

i.e., for a decrease of void ratio from .73 to .68 G_{max} increases by 17%.

b) The earth pressure coefficient, K, which is mobilized during the deployment of the Molikpaq sand fills also affects the mobilized

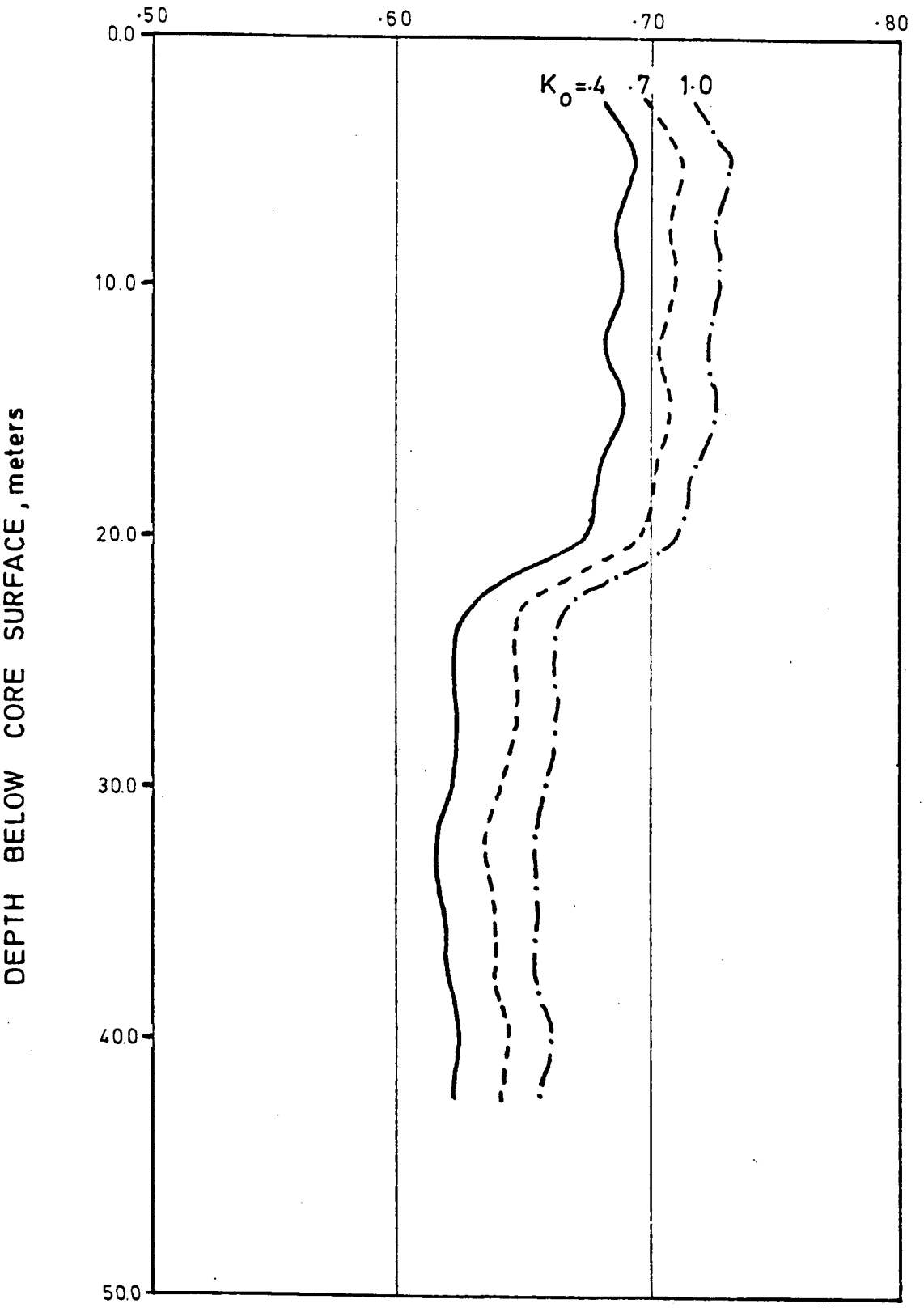

Fig. 6.1.1 Variation of Void Ratio, e_c, with Depth as a Function of K_o.

stress level (MSL) = $((\sigma_1-\sigma_3)_{mobilized}/(\sigma_1-\sigma_3)_{failure})$ prior to the ice loading. The maximum magnitude of this pre-ice loading shear stress level, $(MSL)_{max}$, is an important parameter. Upon ice loading, MSL first drops in value due to the increased horizontal normal stress and therefore, in this phase of loading the sand fills wil behave with unloading characteristics. At higher levels of ice loading MSL increases again and when MSL $\geq (MSL)_{max}$ then the and fills will behave with first loading characteristics.

Based on the above, a F.E. study was carried out to evaluate the probable value of K after the construction of the core fills. This study consisted of the following.

The deployment or construction of the upper 20 meters of the core was simulated by "analytically constructing" it with 17 layers and following the procedures outlined by Byrne and Duncan (1979). The F.E. mesh and the boundary conditions used in the analysis are shown in Fig. 6.1.2. Plane strain conditions with zero lateral outward movement were assumed since this condition will develop higher horizontal stresses, than the horizontal stresses developed if the horizontal boundary was free to move. The above have been verified experimentally by the retaining wall field test study carried out by Matsuo et al. (1978) which was described earlier in Chapter 4 (section 4.7.2).

Three F.E. studies were carried out: Two of them using the hyperbolic model and the modified SMP model for a condition of initial K_0 = 1.0 and the third using the modified SMP model for a condition of initial K_0 = .7.

In the analysis, all the 20 metres of the soil were assumed to be composed of the same soil type, and the properties of this soil type were

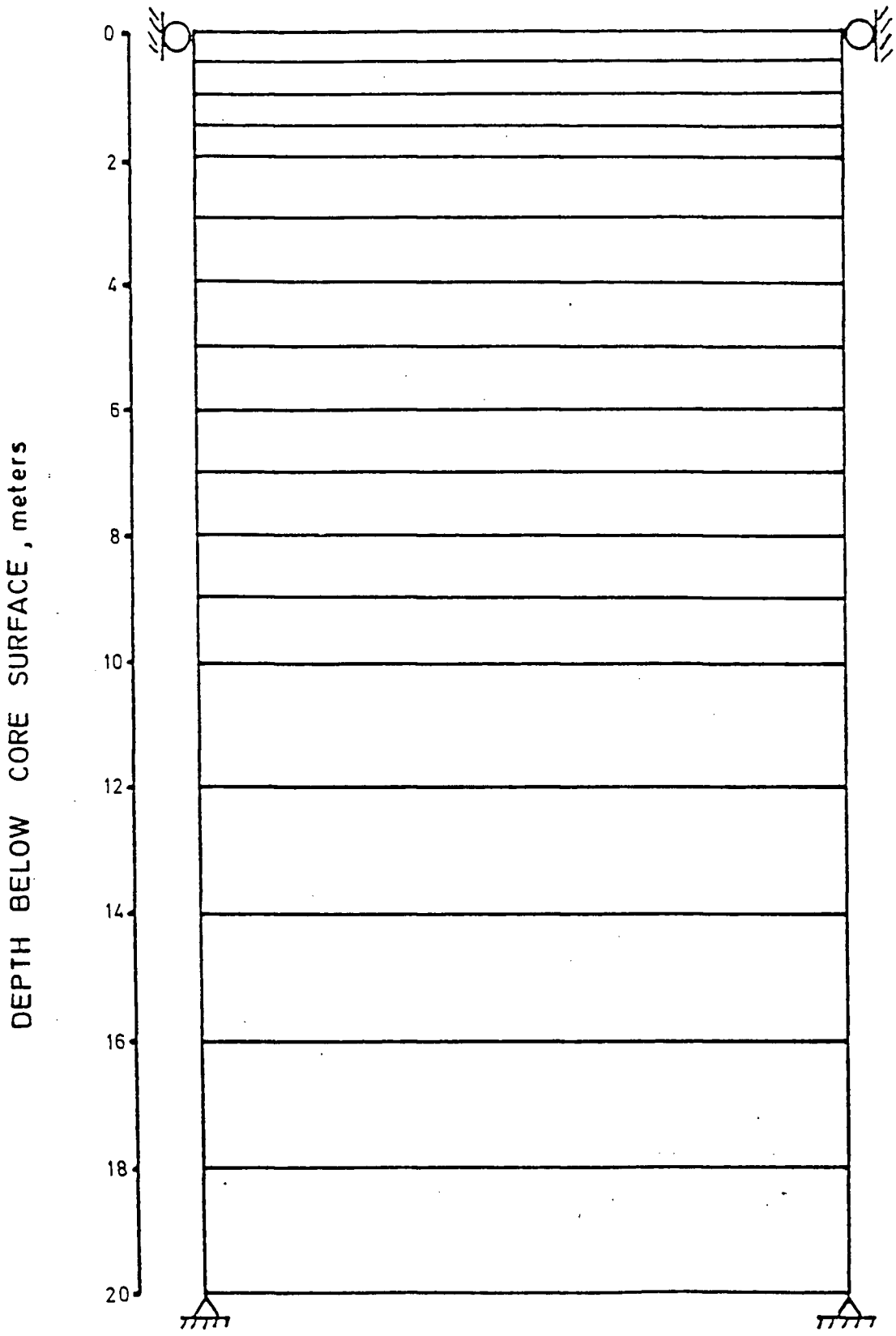

Fig. 6.1.2. Finite Element Mesh Used to Simulate Core Construction.

assumed to be equal to the soil properties that were derived from the drained triaxial test No. 02 (e_c = .717) which was carried out by Golder's Associates (1986) on Erksak 320/1 Sand. The soil properties for the two models are given in Table 6.1.1 and were obtained as it is described in the main text (section 6.3.1 and 6.3.2).

The results obtained for the condition of initial (K_o = 1.0, using the hyperbolic model and the modified SMP model are presented in Fig. 6.1.3.

Table 6.1.1

a) Hyperbolic Soil Parameters for Erksak 320/1 Sand (Triaxial Test #2)

KE	n	KB	m	R_F	ϕ_1	$\Delta\phi$	K_o
960	.50	250	.38	.80	35.5	2.8	1.0

b) Modified SMP Soil Parameters for Erksak 320/1 Sand (Triaxial Test #2)

KG_{max}	n	KB_{ur}	m	KG_p	np	R_F	$(\frac{\tau_{SMP}}{\sigma_{SMP}})_1$	$\Delta(\frac{\tau_{SMP}}{\sigma_{SMP}})$	λ	μ	K_o
710	.50	.610	.38	620	-.56	.94	.68	.072	.97	.25	1.0 & .70

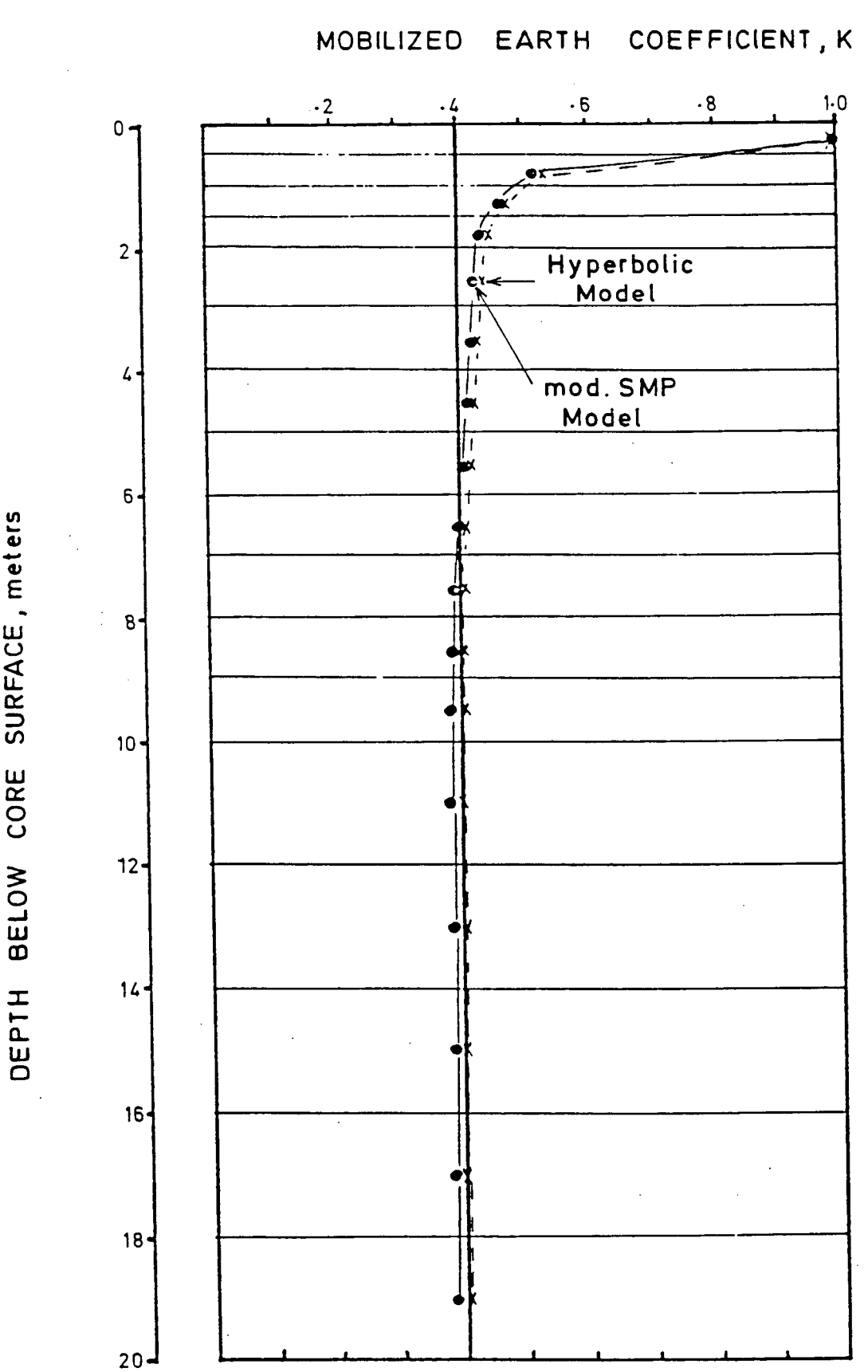

Fig. 6.1.3. Assessment of the Mobilized Earth Coefficient After Core Construction, Using the Hyperbolic and the Modified SMP Models (K_o=1.0)

It may be seen from the figure, that both models give results that are in very good agreement with each other. The results indicate that, although an initial K_0 = 1.0 was used, the mobilized earth coefficient, K at the end of the construction, decreases from 1.0 to .4 in the upper 4 meters of the core and remain with a value of .40 for the bottom 16 meters.

To study the effect of starting with different initial K_0's a third study was performed with the modified SMP model and using a K_0 = .70. The results obtained using K_0 = 1.0 and K_0 = .70 are presented in Fig. 6.1.4. Again the trend obtained is very similar. This time the mobilized K decreases from .70 to .40 in the upper 4 meters of the core and the same results as before are obtained for the lower 16 meters.

The above study indicates that a K_0 = .40 is an appropriate value to be used in the Molikpaq analysis. it should be noted that the soil parameters used were derived from a drained triaxial test on Erksak 320/1 sand with a e_c = .717. It turns out, that the void ratio assessments for the berm and core fills range from .620 to .685, if a K_0 = .40 is used. To check if, the soil properties correspond to a soil type of e_c = .62 have any influence on the outcome of the mobilized K, the analysis simulating the construction of the core were repeated using soil parameters correspondent to e_c = .62. Similar results were obtained and therefore a K_0 = .40 is considered to be appropriate.

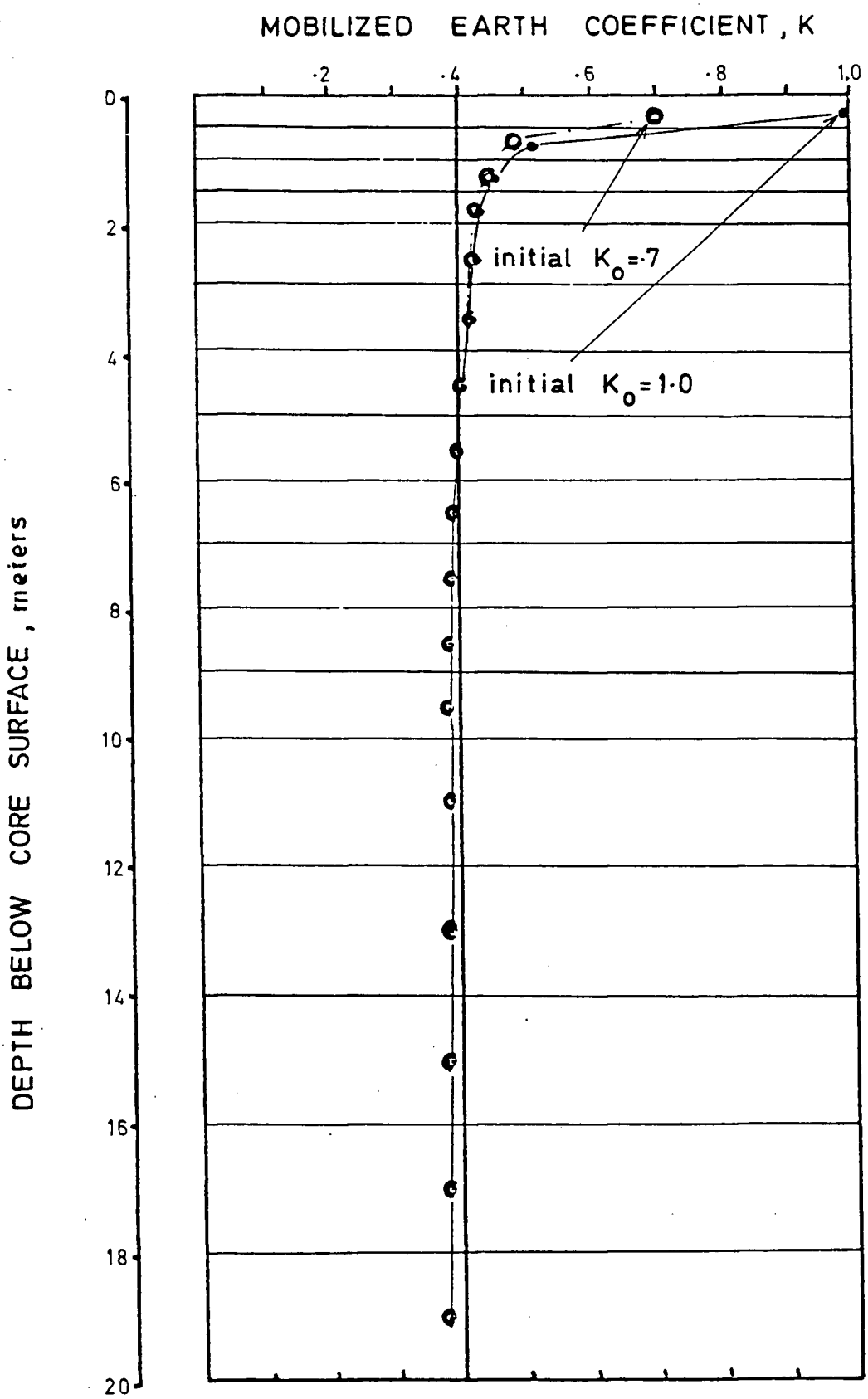

Fig. 6.1.4 Assessment of the Mobilized Earth Coefficient During Construction using the modified SMP Model for the Conditions of K_0 = 1.0 and K_0 = .70.

APPENDIX 6.2

ASSESSMENT OF SOIL PARAMETERS FOR ERKSAK 320/1 SAND BASED ON THE DRAINED TRIAXIAL TEST DATA REPORTED BY GOLDER ASSOCIATES (1986)

APPENDIX 6.2

Assessment of Soil Parameters for Erksak 320/1 Sand Based on the Drained Triaxial Tests Data Reported by Golder Associates (1986)

A) Evaluation of KE, n and R_F

The transformed hyperbolic plots of tests 01, 02 are presented in Fig. 6.2.1 and that of tests 61, 62 and 63 in Fig. 6.2.2. As shown in Fig. 6.2.1, the vertical axis for test 01 is expressed by $\epsilon_1/(\sigma_1-2\nu\sigma_3)$ instead of the standard $\epsilon_1/(\sigma_1-\sigma_3)$ because test 01 is a constant mean normal stress triaxial test. A poisson's ratio ν = .2 was assumed for the calculation.

From these figures and from the laboratory data shown in Fig. 6.24 (see main text) the values shown in Table 6.2.1 were obtained following the procedures outlined by Duncan et al. (1980). Values of KE and n correspondent to each test are tabulated in Table 6.2.2 and were obtained from the log-log plot of E_i/pa versus σ_{m_i}/pa shown in Fig. 6.2.3.

Table 6.2.1

Hyperbolic Parameters I

Test	E_i/pa	σ_{m_i}/pa	$\sigma_{d_{ult}}$	$\sigma_{d_{peak}}$	R_F
01	1096	2.46	425	340	0.800
02	1410	2.46	730	652	0.800
61	1316	0.99	550	498	.905
62	2990	3.95	1608	1400	.870
63	2055	3.95	1605	1330	.830

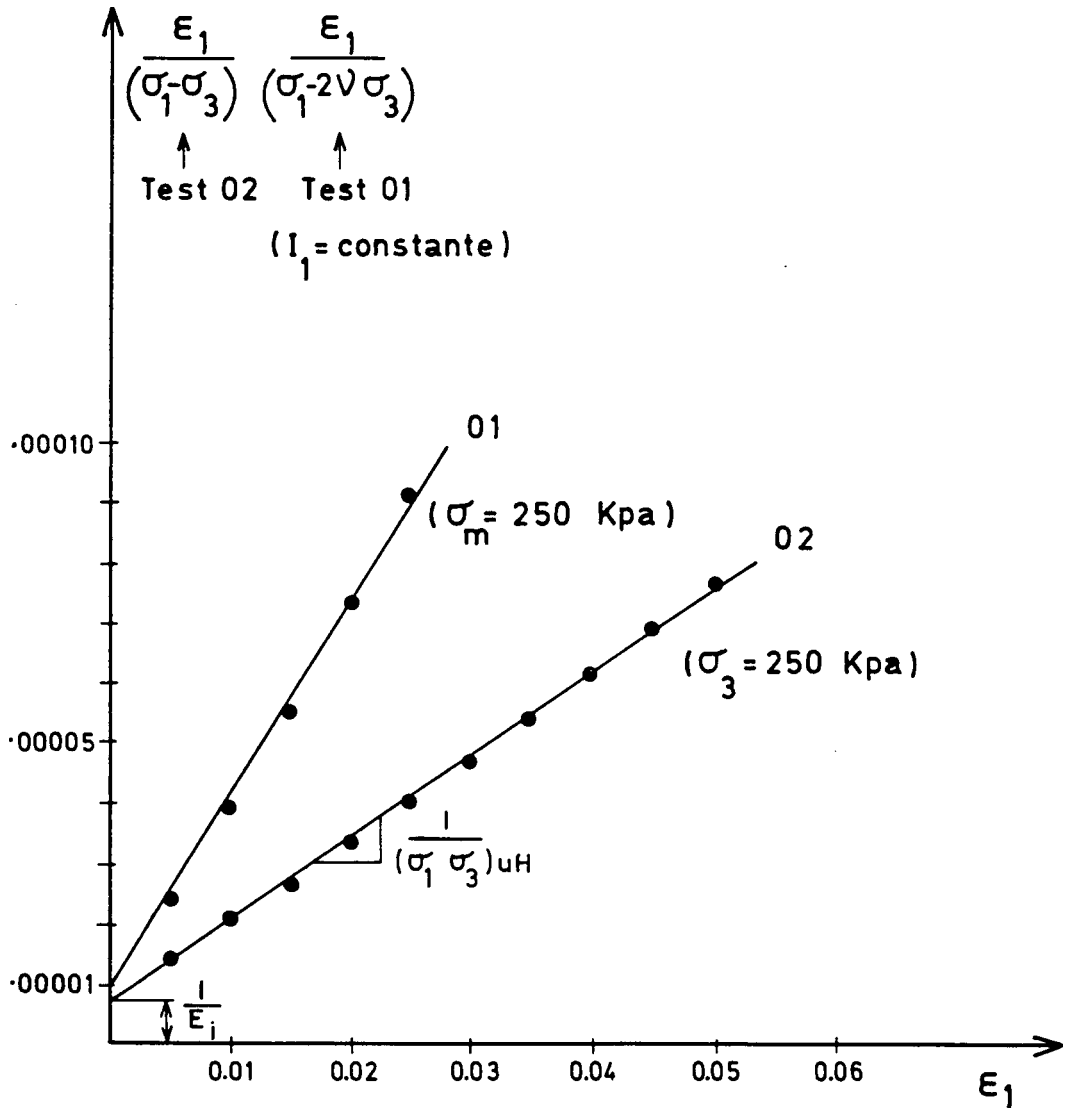

Figure 6.2.1 Transformed plot test o1 and o2

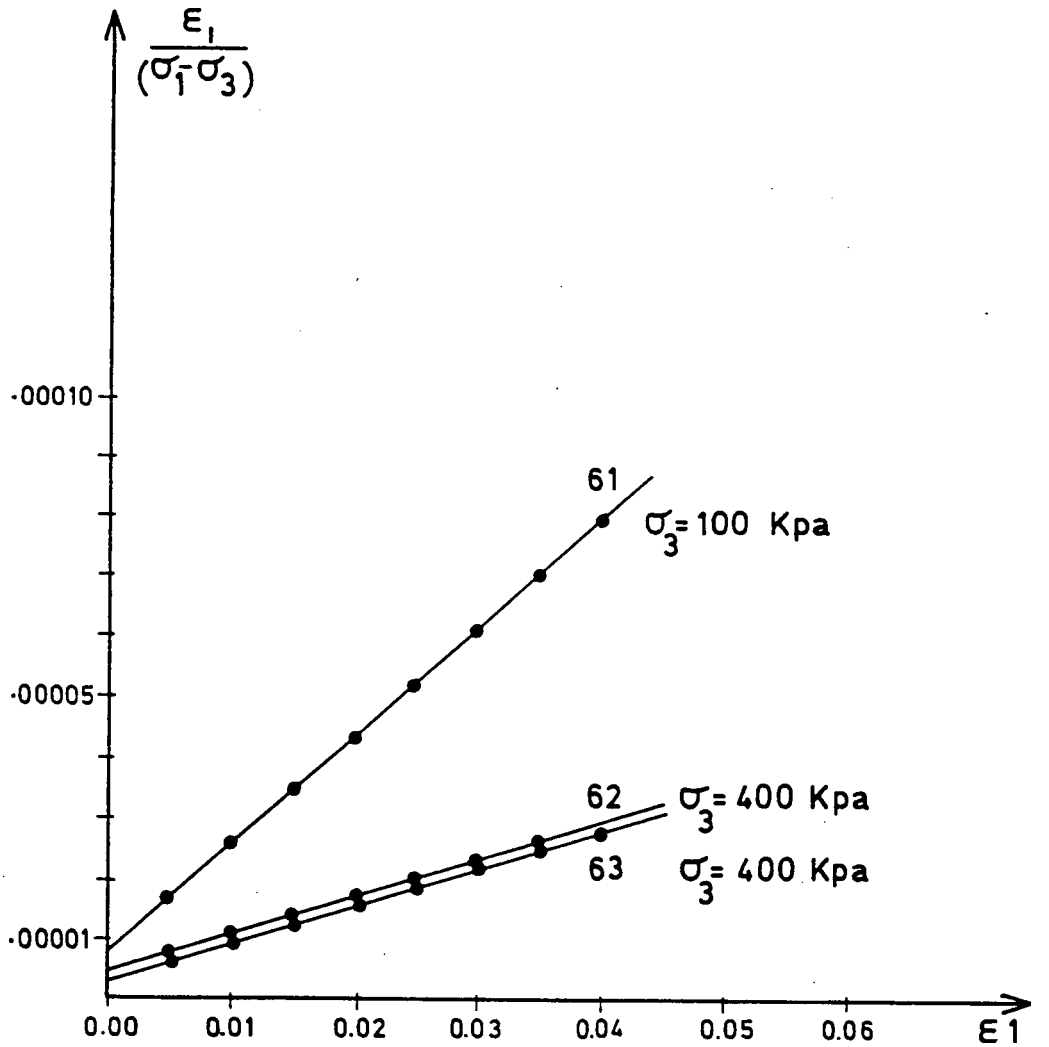

Fig. 6.2.2 Transformed plot
test 61,62,63

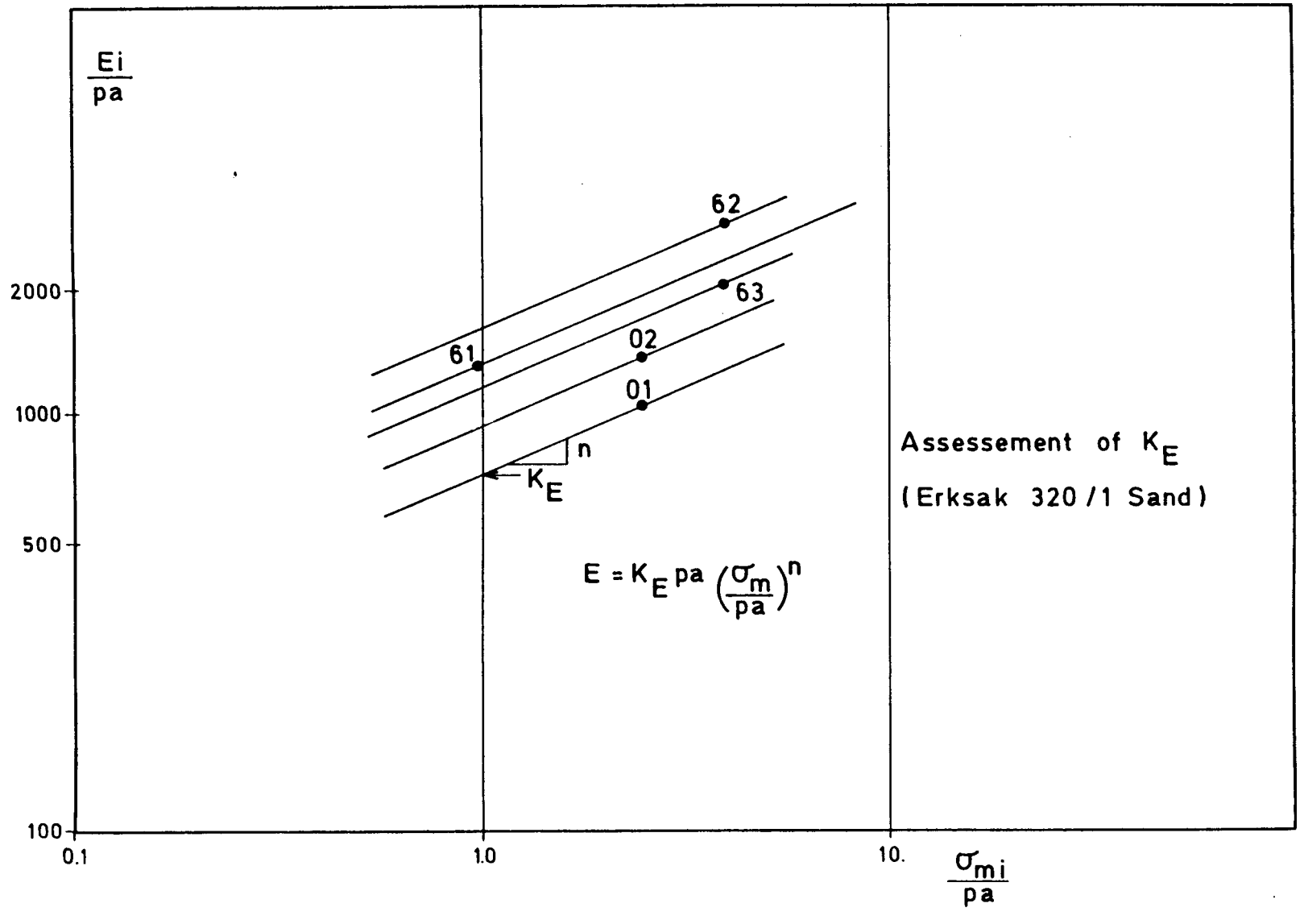

Fig. 6.2.3 Assessment of K_E for Erksak 320/1 Sand

Table 6.2.2

Hyperbolic Parameters II

Test	K_E	n
01	720	.5
02	960	.5
61	1320	.5
62	1650	.5
63	1160	.5

B) Evaluation of K_B and m

To evaluate the parameters K_B and m from the drained isotropic triaxial consolidation tests the procedures outlined by Byrne and Eldridge (1982) were followed, after a small modification was introduced to the method, which consists on the following: Byrne and Eldridge relate the volumetric strain due to consolidation with mean normal stress following the equation:

$$\epsilon_v = a(\sigma_m)^{1-m} \qquad (6.2.1)$$

where a and (1-m) are parameters as defined in Fig. 6.2.4.

Based on the above equation and the equation defining the tangent bulk modulus, B_t, which is

$$B_t = K_B \, Pa \, (\sigma_m/Pa)^m \qquad (6.2.2)$$

those researchers obtain

$$K_B = \frac{1}{a(1-m)(Pa)^{1-m}} \qquad (6.2.3)$$

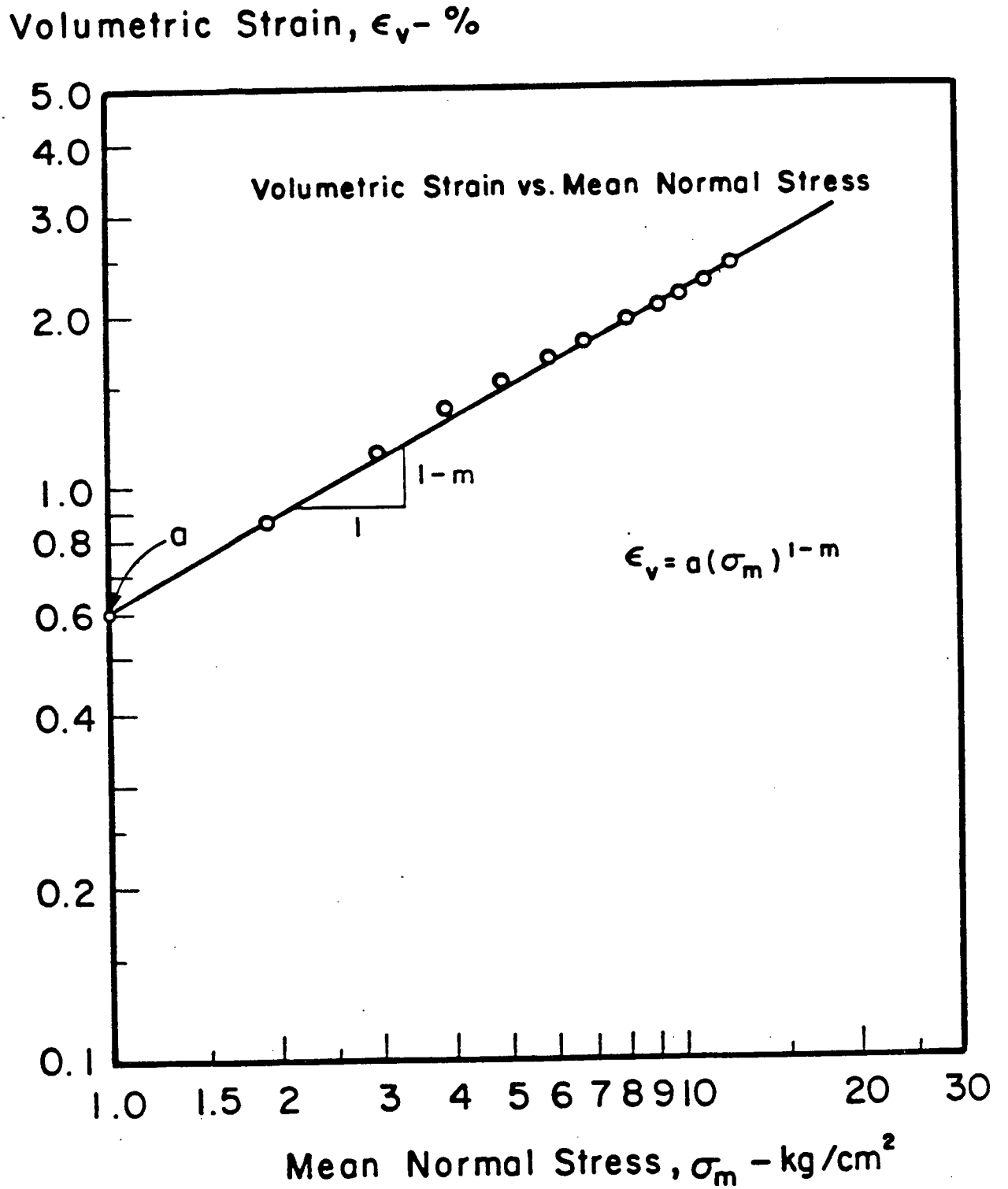

Fig. 6.2.4. Isotropic Consolidation of Sand.

Since, however, equation (6.2.3) is atmospheric pressure dependent, it was decided to relate the volumetric strain to the mean normal stress using the following equation:

$$\epsilon_v = a \left(\frac{\sigma_m}{Pa}\right)^{1-m} \tag{6.2.4}$$

differentiating with respect to σ_m

$$\frac{\Delta\epsilon_v}{\Delta\sigma_m} = \frac{1}{B_t} = a \frac{1}{(Pa)^{1-m}} (1-m)\sigma_m^{-m}$$

or

$$B_t = \frac{(Pa)^{1-m}}{a(1-m)} \sigma^m \tag{6.2.5}$$

Since B_t is given also by 6.2.2. then

$$B_t = K_B\, Pa \left(\frac{\sigma_m}{Pa}\right)^m = \frac{(Pa)^{1-m}}{a(1-m)} \sigma^m$$

or

$$K_B = \frac{1}{a(1-m)} \tag{6.2.6}$$

Based on the data from the isotropic triaxial consolidation test plots of log ϵ_v-log (σ_m/pa) were obtained and are shown in Fig. 6.2.5. From this figure the following values shown in Table 6.2.3 were evaluated.

C) Evaluation of KG_p, n_p, R_F

Following the procedures outlined in Chapter 2 the transformed plots of $\gamma^p_{SMP}/(\tau_{SMP}/\sigma_{SMP})$ versus γ^p_{SMP} for the tests 01, 02, 61, 62, and 63 were

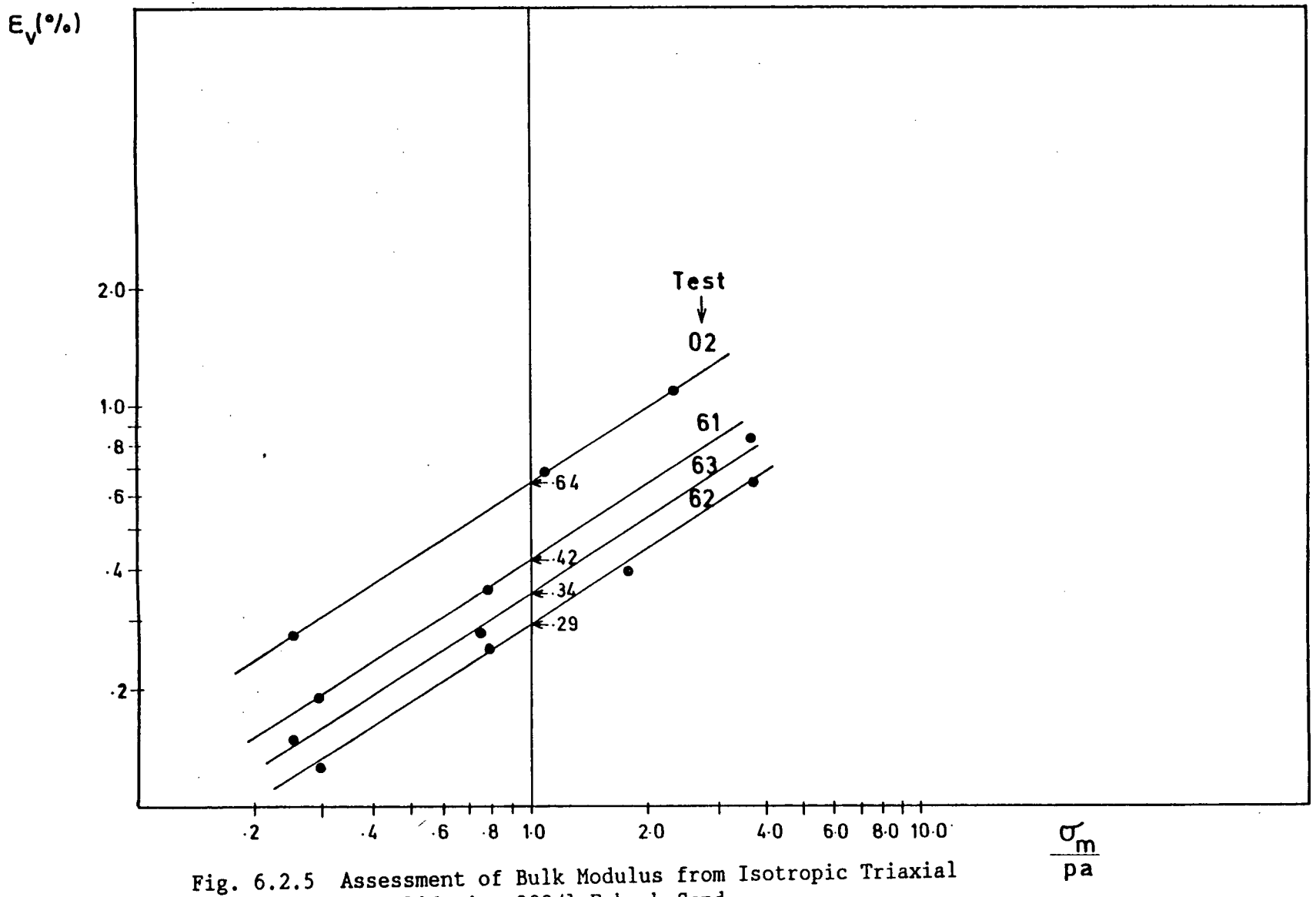

Fig. 6.2.5 Assessment of Bulk Modulus from Isotropic Triaxial Consolidation 320/1 Erksak Sand

Table 6.2.3

Hyperbolic Parameters III

Test	m	a	KB
01	N/A	N/A	N/A
02	.38	.0064	250
61	.36	.0042	378
62	.40	.0029	573
63	.38	.0034	474

Note: For Test 01 there was not enough laboratory data to evaluate K_B.

evaluated and are presented in Fig. 6.2.6 (for test 01 and 02) and in Fig. 6.2.7 for the other tests.

From these figures and from the laboratory data shown in Fig. 6.24 (see main text) the values shown in Table 6.2.4 were obtained.

Table 6.2.4

Modified SMP Parameters-I

Test	G_p	$(\sigma_m)_i/pa$	$(\tau_{SMP}/\sigma_{SMP})_{ult}$	$(\tau_{SMP}/\sigma_{SMP})_F$	R_F
01	330	2.46	.663	.630	.95
02	360	2.46	.686	.645	.94
61	910	0.99	.960	.960	1.00
62	435	3.95	.826	.777	.94
63	360	3.95	.802	.754	.94

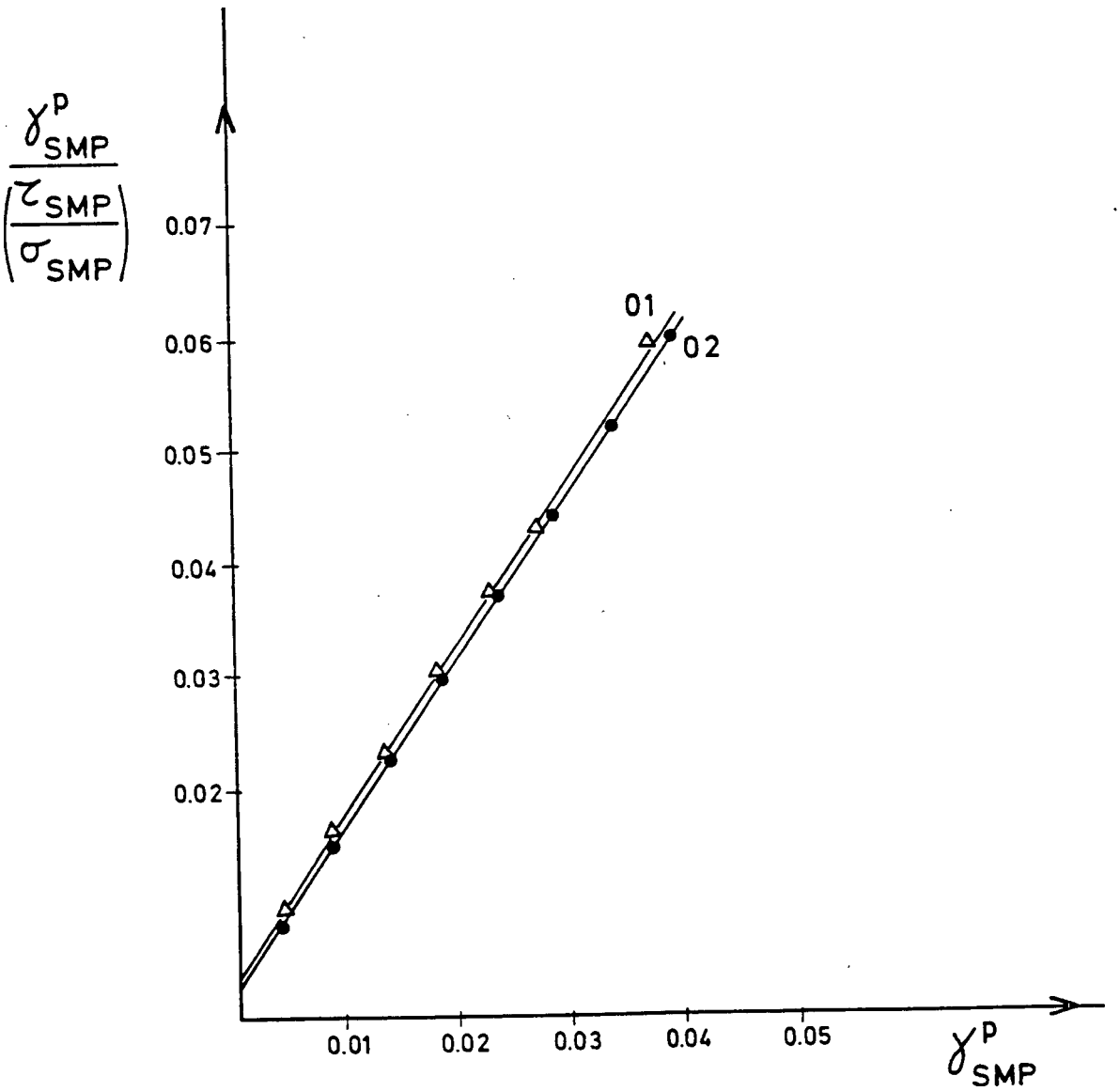

6.2.6 Transformed Modified SMP Plots (Tests No. 1 and 2)

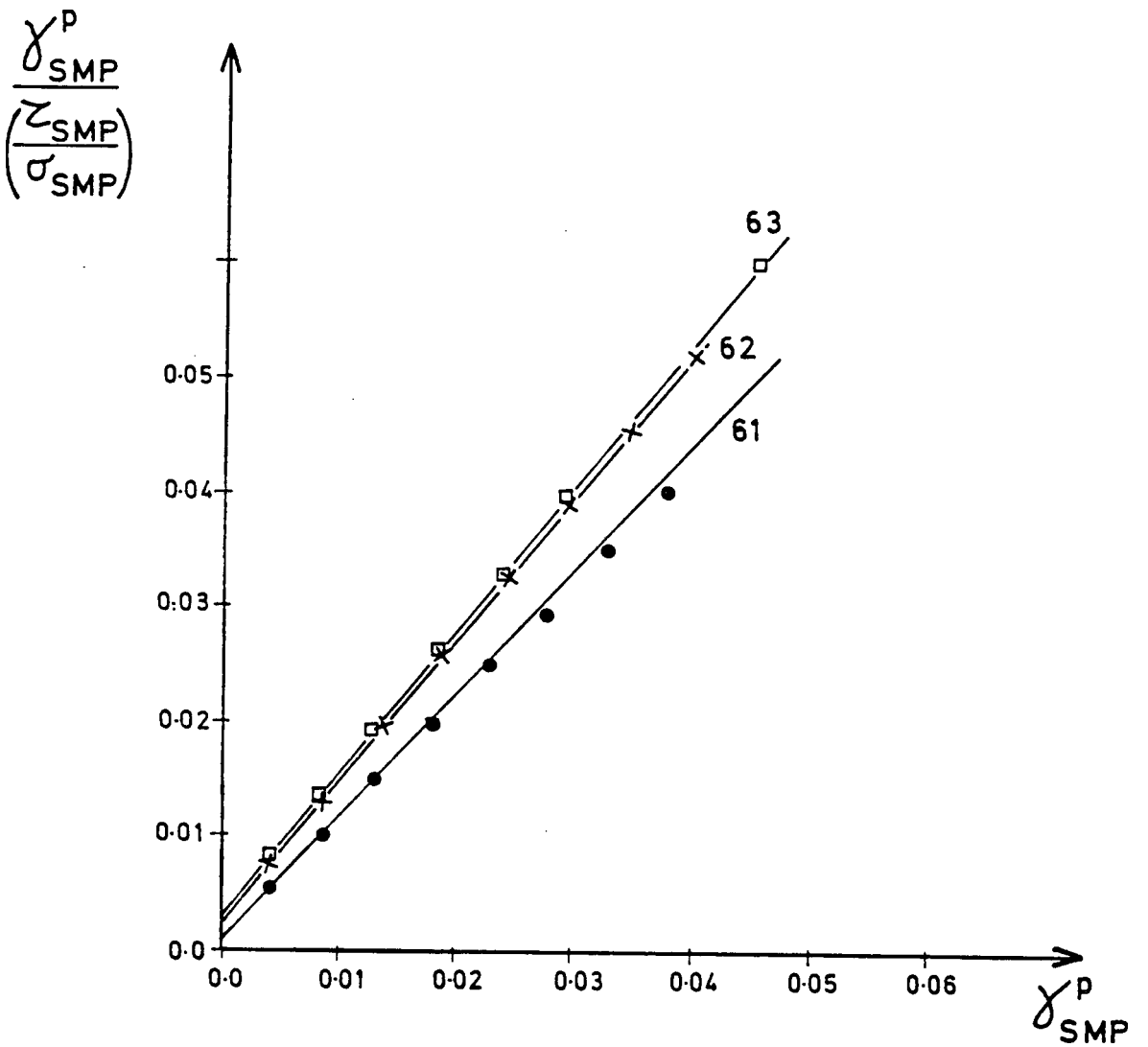

6.2.7 Transformed Modified SMP Plots (Tests No. 61, 62, and 63)

Using the G_{p_i} and (σ_{m_i}/pa) values, a log-log plot of these quantities was obtained and presented in Fig. 6.2.8. From this figure the values of KG_p and n_p were evaluated and are presented in Table 6.2.5.

Table 6.2.5

Modified SMP Parameters-II

Test	K_{G_p}	n_p
01	575	-.56
02	620	-.56
61	910	-.56
62	980	-.56
63	840	-.56

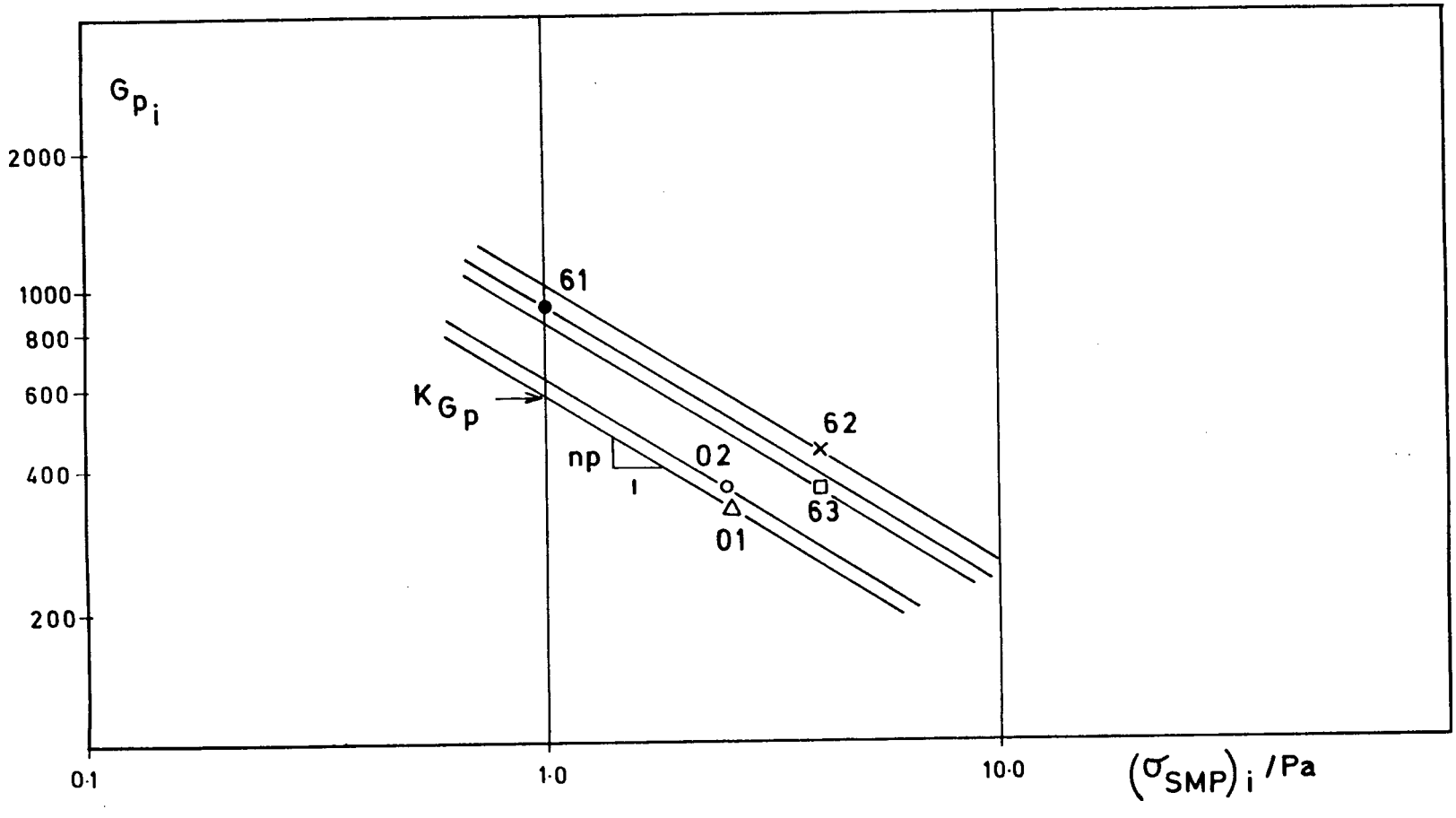

Fig. 6.2.8 Log-log Plot of G_{p_i} versus $(\sigma_{SMP})_i$/Pa)

CHAPTER 7

APPENDIX INDEX

CHAPTER 7

APPENDIX FIGURES INDEX

APPENDIX 7 - LIST OF FIGURES (Cont'd)

APPENDIX 7.1

EVALUATION OF THE NUMBER OF EQUIVALENT CYCLES OF THE GIVEN ICE LOADING FUNCTION

APPENDIX 7.1

Evaluation of the Number of Equivalent Cycles of the Given Ice Loading Function

The given ice loading function is presented in Fig. 7.1.1. To simplify this ice loading function was treated as a load with uniform cycles of a magnitude = 236 MN, which is the magnitude of the cycles within the steady portion of the load from time 8:21:45 to 8:26:00. The procedures followed are presented below.

- Evaluation of the Number of "Equivalent Cycles" for the Time Interval 8:17:51 to 8:21:45

During this time interval the load presents a variable but increasing magnitude (see Fig. 7.1.1). To obtain the number of "equivalent cycles" of magnitude = 236 MN for this time interval the following procedures were followed:

a) The total number of cycles, from 8:17:51 to 8:21:45 is 290. This time interval was subdivided into 10 time intervals of 29 cycles each.

b) The liquefaction resistance curves to liquefaction which were obtained as described in Chapter 6 are reproduced in Fig. 7.1.2. From this figure, the stress ratio to resist liquefaction correspondent to 29 cycles is (τ_{eq}/σ'_{vo}) = .122. (The curve correspondent to layer no. 4 and 5 was used for that effect.)

c) For each of the 10 time intervals evaluated in (a) the correspondent Δ(ice load) was assessed at the average time of each interval. For instance for the 1st time interval, Δ(ice load) = 46 MN.

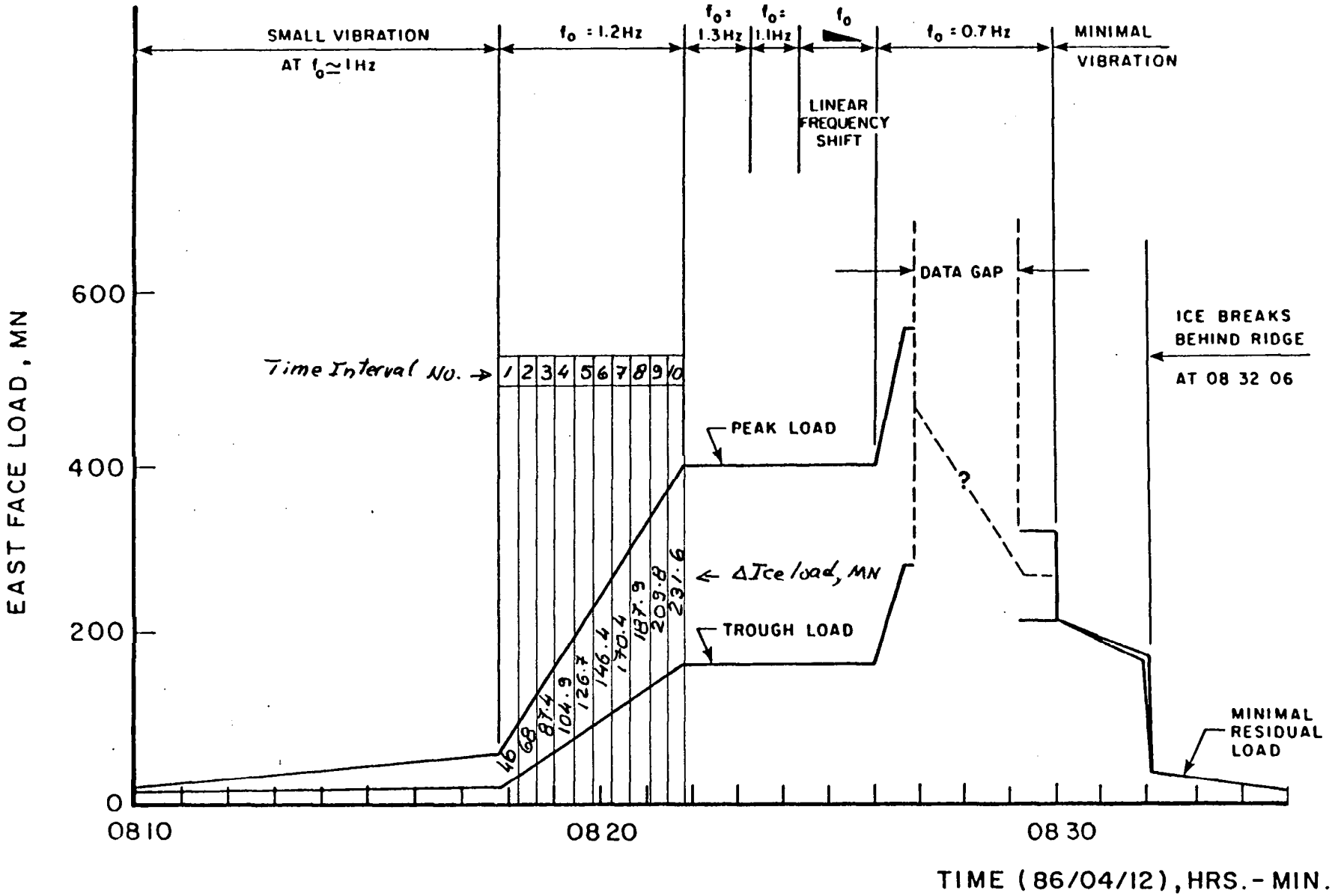

Figure 7.1.1 Ice loading function used in the analysis

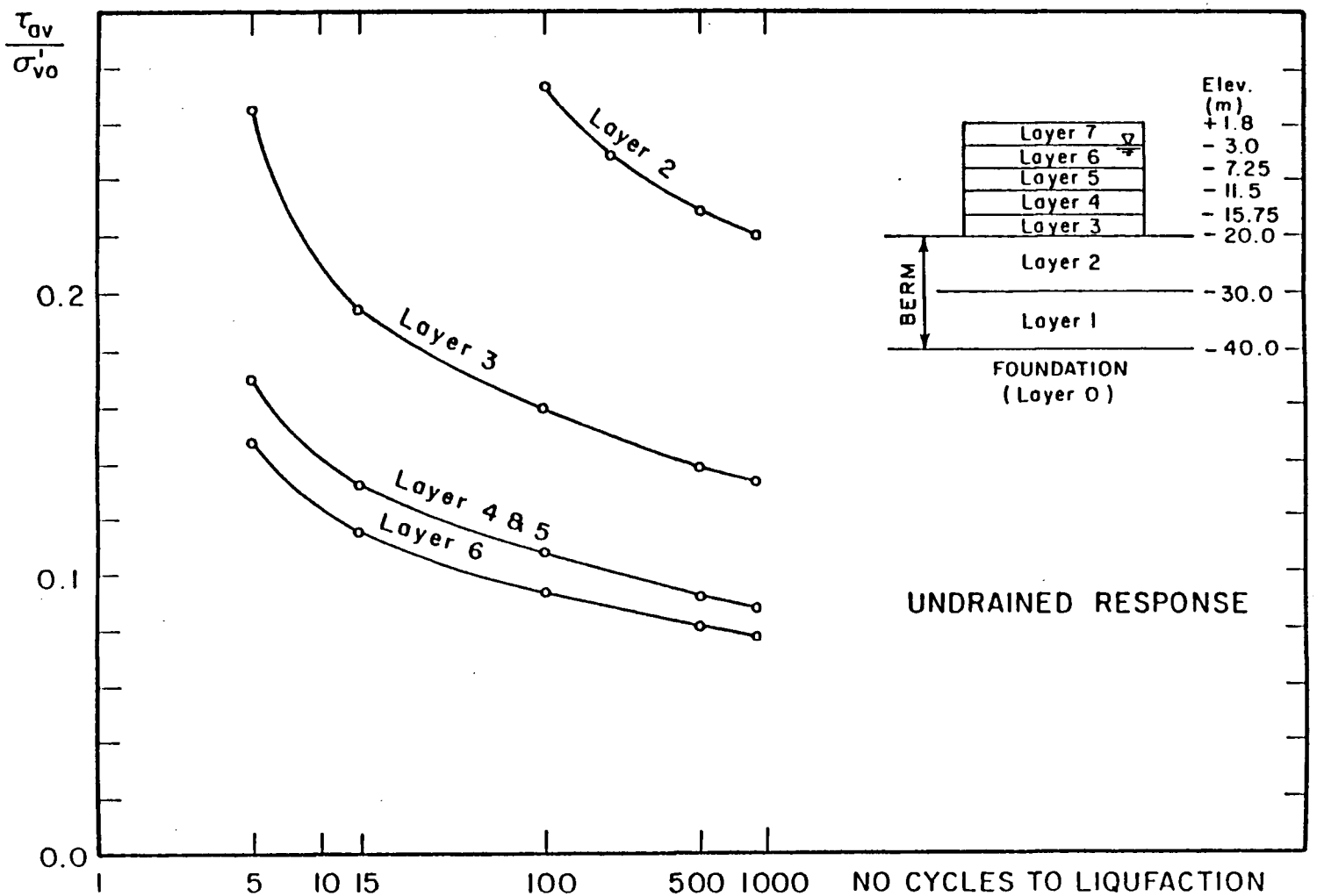

Fig. 7.1.2 Liquefaction resistance curves used in the analysis

d) Assuming that the stress ratio to resist liquefaction evaluated in (b) τ_{eq}/σ'_{vo} = .122 corresponds to 29 cycles of magnitude = 236 MN than the stress ratio to resist liquefaction correspondent to 29 cycles of magnitude = 46 MN is obtained following the procedures proposed by Seed and Idriss (1982) used for scalling the liquefaction resistance curves correspondent to earthquakes of magnitude = 7.5 to other earthquake magnitudes. The equation used is as follows:

$$(\tau_{eq}/\sigma'_{vo})_{46} = \frac{(\tau_{eq}/\sigma''_{vo})_{236}}{(46/236)} = .63 \qquad (7.1.1)$$

e) Using the same liquefaction resistance curve the number of cycles correspondent to (τ_{eq}/σ'_{vo}) = .63 is evaluated as being ≤ 1.

The steps described from (c) to (e) were repeated for all the 10 time intervals and Table 7.1.1 developed.

Table 7.1.1

Assessment of Equivalent Number of Cycles From Time 8:17:51 to 8:21:48

Increment No.	Δ(ice load) MN	$(\frac{\Delta(\text{ice load})}{236})$	$(\tau/\sigma'_{vo})_{equiv.}$	Number of Equiv. Cycles
1	46.0	.194	.630	1
2	68.0	.287	.430	1
3	87.4	.370	.330	1
4	104.9	.440	.280	1
5	126.7	.537	.227	2
6	146.4	.620	.196	3
7	170.4	.722	.169	5
8	187.9	.796	.159	7
9	209.8	.880	.139	12
10	231.6	.980	.124	25
			Total	≈ 60

It may be seen that the 290 cycles of variable magnitude were assessed as being equivalent to approximately 60 cycles of magnitude = 236 MN.

- Evaluation of the Number of Equivalent Cycles for the Time Interval 8:21:45 to 8:26:00

During this time interval the ice loading function is uniform with a constant magnitude = 236 MN. Taking into account the natural frequencies shown in Fig. 7.1.1 the number of cycles for this time interval is assessed as being = 250.

- Evaluation of the Number of Equivalent Cycles for the Time Interval 8:26:00 to 8:27:00

An average Δ(ice load) = 255 MN is assessed for this interval. Although the number of cycles for this interval is 40 cycles the number of equivalent cycles of magnitude = 236 MN is 90, which was evaluated following the same procedure described above.

Therefore, based on the above calculations a total number of 400 cycles of magnitude = 236 MN occurred from time 8:17:51 to 8:27:00.

APPENDIX 7.2

2-DIMENSIONAL STRUCTURAL MODELS

APPENDIX 7.2

2-DIMENSIONAL STRUCTURAL MODELS

The 2-D structural models of the Molikpaq's steel caisson were developed by D.L. Anderson (see Chapter 7, Section 7.1) and the procedures followed for its development consisted briefly on the following.

During the construction of the sand core, the 2-D structural model must be able to simulate the 3-D restraining effects of the caisson. For this construction phase the simple 2-D structural model presented in Fig. 7.2.1 was developed and consists essentially on a rigid front and back members connected by a beam at a height H above the berm. The properties of the beam and the height, H were selected to ensure that the displacements of the front and back members were similar to those at equivalent sections of a 3-D model under equivalent loading.

During the ice loading phase the 2-D structural model must be able to transfer the ice load to the sand core and also to the berm along the caisson sides. To develop an appropriate 2-D structural model, finite element analysis were carried out using the (2-D) F.E. mesh presented in Fig. 7.2.2 which is the replica of the cross-section of the 3-D F.E. mesh along the E-W direction (ice load direction), i.e. the same number elements were used with the same material properties, as the 3-D cross-section. To achieve the same results as that obtained from the 3-D analysis the complex 2-D beam system presented in Fig. 7.2.3 was developed by D.L. Anderson.

In this model, beams 1, 2 and 3 are located at the same elevation and are straight. Beam 3 is shown bent in the figure only for clarity of illustration. The joint common to beams 1 and 2 is assumed to have only

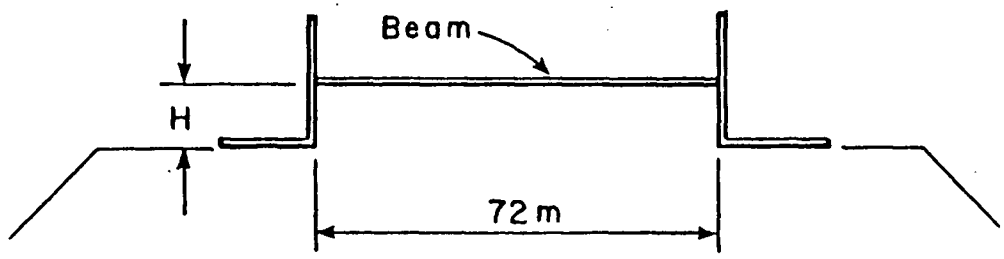

PROPERTIES FOR 2-D STRUCTURAL MODEL CONSTRUCTION PHASE		
A = 0.042 m^2/m	I = 82 m^4/m	E = 200,000 MPa
Location, H = 13.5 m		

Figure 7.2.1 Properties of the structural model used in the 2-D construction analysis

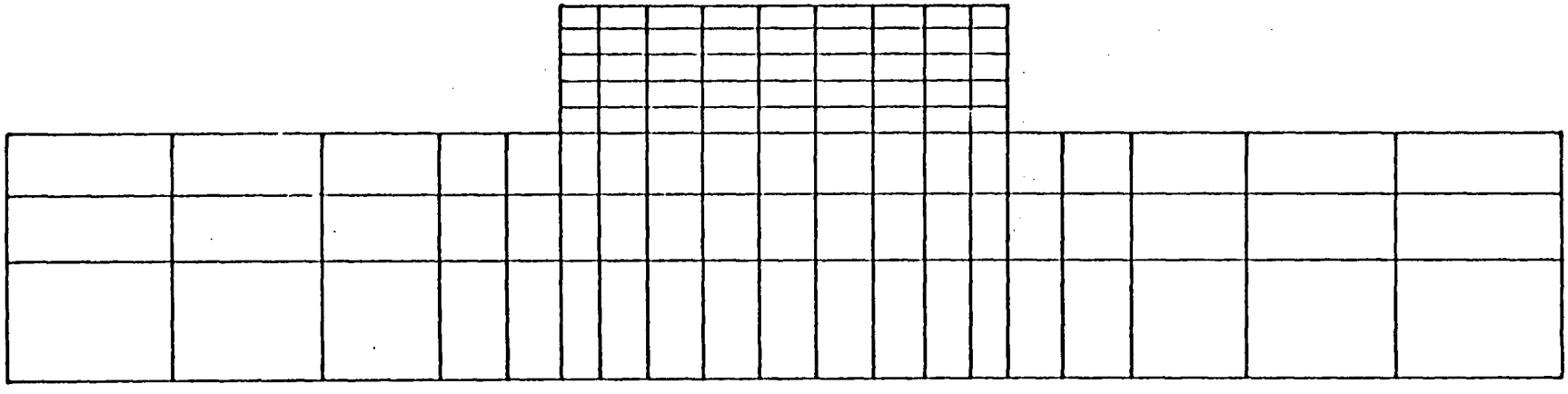

Figure 7.2.2 Finite element mesh used in the 2-D analysis

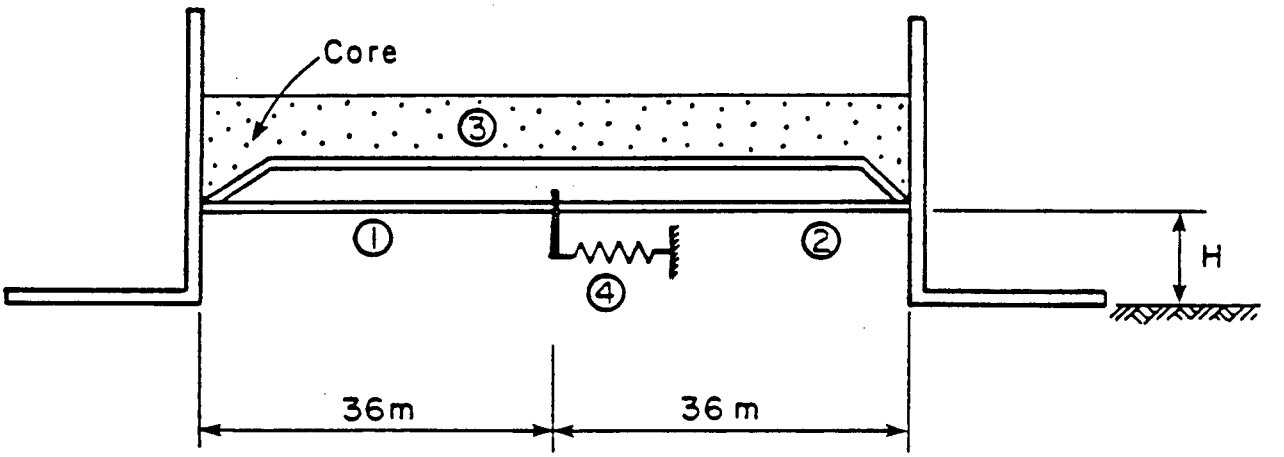

Member	A m^2/m	I m^4/m	Height H m
1 and 2	.0063	0.50	12.4
3	-.001	0.0	12.4
Spring 4 Axial stiffness = 330,000 kN/mm @ 330(1.18) MN load = 190,000 kN/mm @ 550(1.18) MN load			

Figure 7.2.3 Properties of the structural model used in the 2-D ice loading analysis

horizontal movement, and spring 4 is attached to this joint and aligned horizontally. Beam 1 transfers load from the loaded face to the berm, whose stiffness is modelled by spring 4. Beam 2 transfers load from the berm to the back side of the caisson, and because of symmetry was assumed to have the same propeties as beam 1. Beam 3 is included because it was observed that if the berm is rigid, application of the ice load causes a negative or inward displacement of the back face when the caisson is empty, hence a negative area is assigned to beam 3.

The properties of the beams are also given in Fig. 7.2.3. The area of beam 1 was determined from a 3-D analysis that included the soil in the berm and core. The area of beam 3 and the moment of inertia (I) of beam 1 were estimating by propriating the results from an earlier simpler 3-D structural analysis of the caisson only. The location of the beams, given by the height H, was based on the results reported by Sandwell Swan Wooster Inc. (1986) and essentially agrees with the results from the simpler 3-D structural analysis.

The axial stiffness of spring 4 was calculated to range from 330,000 to 190,000 kN/m/m as the total ice load increased from 330 MN to 550 MN. The reduced stiffness with increasing load is an indication of the nonlinear response of the berm material at higher load levels.

The 2-D results obtained following the procedures described above were in very good agreement with their 3-D counterparts as it will be shown later in Appendix 7.4.

APPENDIX 7.3

EVALUATION OF THE 3-D LOAD VECTOR USED IN THE ANALYSIS

APPENDIX 7.3

Evaluation of the 3-D Load Vector Used in the Analysis

The ice load of the April 12, 1986 event was treated in the analysis as a rectangular pressure as it is shown in Fig. 7.3.1(a). To evaluate the force vector shown in the figure the following procedures were followed.

A plan view of the forces and pressures involved are shown in Fig. 7.2.1(b). From equilibrium in the direction of the ice force

$$Q = P \cdot L \qquad (7.3.1)$$

where:

Q = ice force

P = pressure

L = length of the caisson face

= $2(L_a + L_b + L_c)$(see Fig. 7.3.1(b))

Values of L_a = 10.92 m, L_b = 7.5 m and L_c = 7.2 m were considered in the analysis.

From eq. (7.3.1) the value of the pressure P is evaluated

$$P = Q/51.24 \qquad (7.3.2)$$

To develop this pressure P on the face of the caisson the following force vectors were obtained:

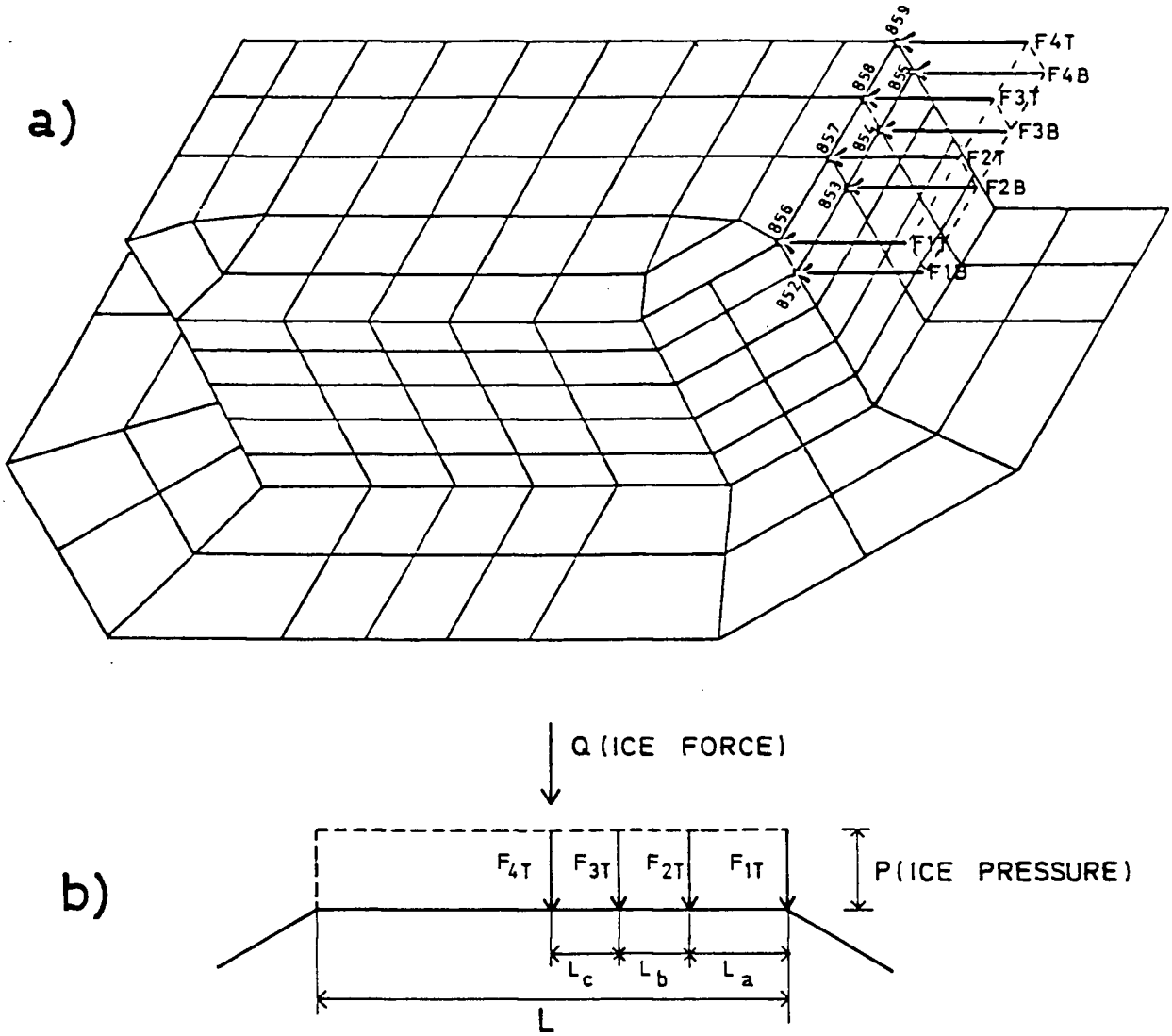

Figure 7.3.1 Ice load vector used in the analysis (a) 3-Dimensional view, (b) plan view.

$$F_{1T} = F_{1B} = \frac{L_a \cdot P}{4} = 2.73\ P$$

$$F_{2T} = F_{2B} = \frac{L_a \cdot P}{4} + \frac{L_b \cdot P}{4} = 4.605\ P \qquad (7.3.3)$$

$$F_{3T} = F_{3B} = \frac{L_b \cdot P}{4} + \frac{L_c \cdot P}{4} = 3.675$$

$$F_{4T} = F_{4B} = \frac{L_c \cdot P}{4} = 1.8\ P$$

APPENDIX 7.4

PROCEDURES FOLLOWED IN THE 3-D ANALYSIS OF THE DYNAMIC ICE LOAD EVENT OF APRIL 12, 1986

APPENDIX 7.4

PROCEDURES FOLLOWED IN THE 3-D ANALYSIS OF THE DYNAMIC ICE LOAD EVENT OF APRIL 12, 1986

The 3-D dynamic assessment of the response of the Molikpaq to the ice loading was subdivided into three separate assessments: (a) liquefaction assessment; (b) porewater pressure rise assessment; and (c) acceleration assessment.

The procedures followed are described below.

7.4.1 Procedures for the Liquefaction Assessment

The 3-D response of the caisson to series of cyclic loading pulses was determined by computing the static resonse to one-half cycle of load/unload. The amplitude of displacement and the cyclic stress ratios so computed were assumed to be the dynamic values corresponding to a dynamic amplification factor of 1. This is in close agreement with the findings of the 2-D dynamic analysis carried out by Finn adn Yogendraumar (see Section 7.1 of this chapter). With the above in mind, the procedures followed during the dynamic ice loading phases are presented below together with the displacements versus ice load obtained from the analysis at four selected locations (see Fig. 7.4.1).

1) The east face of the caisson was loaded to 397 MN using one increment of 110 MN and 5 increments of 57.4 MN. The soil elements were considered to be drained during this phase.

2) Next the east face of the caison was unloaded back to 279 MN, in one load increment (see Fig. 7.4.1). This is equivalent to half of the cyclic load for this cyclic loading stage (see main text Fig. 7.1). During unloading, the unload/reload moduli were used.

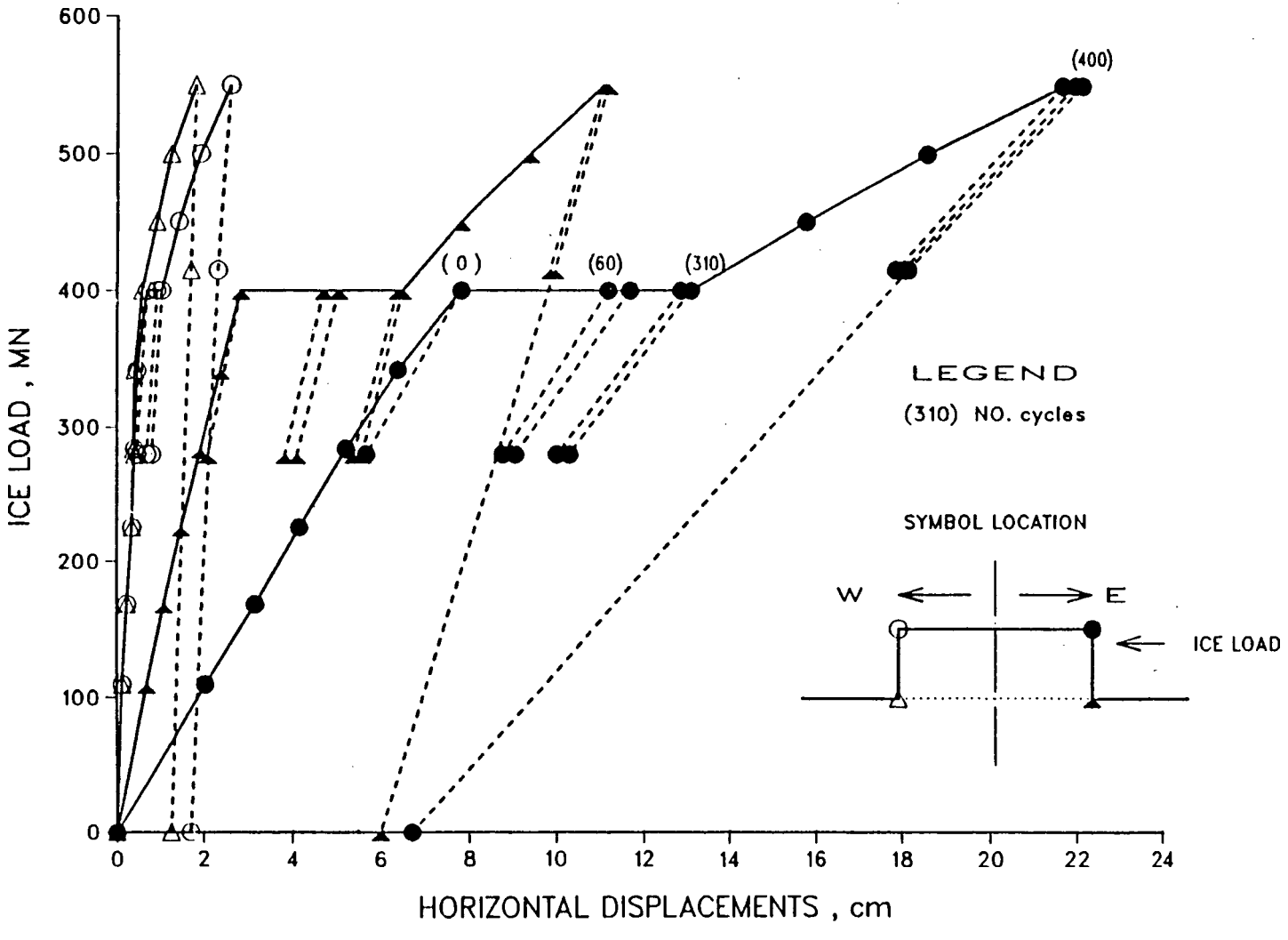

Figure 7.4.1 Displacements versus ice load obtained from the 3-D analysis of the 12 April, 1986 ice load event

3) The elements that would liquefy during the initial equivalent 60 cycles of loading (from time 8:17:51 to 8:21:45) were determinjed by comparing the cyclic stress ratio $\Delta\tau_{zx}/\sigma'_{vo}$ with the cyclic resistance, τ_{av}/σ'_{vo}, for 60 cycles obtained from Fig. 7.14 (main text) The cyclic stress ratio is evaluated in the analysis by the following equation:

$$\frac{\Delta\tau_{zx}}{\sigma'_{vo}} = \frac{\tau_{zx_{397}} - \tau_{zx_{279}}}{\sigma'_{z_{279}}} \qquad (7.4.1)$$

The numbers 279 and 397 indicate the ice load levels in MN.

4) The Young's modulus and bulk modulus of the liquefied elements were now assigned their default values. The east face of the caisson was loaded again from 0 to 397 MN and the static analysis repeated.

5) Steps 2 to 4 were repeated to determine the effects of an additional 250 cycles of loading from time 8:21:48 to 8:26:00 on the elements which did not liquefy in the first 60 cycles. This step was repeated until no further elements liquefied. It may be seen from Fig. 7.4.1 that it took 5 of such "static load cycles" from 0 to 397 MN for that to happen.

6) The east face was loaded from zero to 555 MN and then unloaded to 417f MN which is equivalent to half the cyclic laod of this loading stage. Elements which had been predicted to liquefy up to time 8:26:00 were assigned a very low value of Young's modulus and bulk modulus.

7) The procedure described in step 5 was then repeated to determine the effect of an additional 90 ycles of laod (from time 8:26:00 to 8:26:38). It may be seen that, at this ice load level only 3 "static load cycles" from 0 to 550 MN were carried out to assess the genera-

tion of more liquefied elements, but no significant generation took place.

The 3-D liquefaction areal extent obtained following the above procedures is presented in teh main text in Figs. 7.14(a) to (d).

7.4.2 Pore Pressure Rise Assessment

During cyclic loading two kinds of porewater pressure are generated in saturated sands. One is cyclic in nature and the other is residual.

The procedures followed to assess the soil elements that liquefy (i.e. the soil elements in which the ratio between the generated residual porewater pressure and effective overburden pressure, $u_g/\sigma'_{vo} = 1$) were described in the previous section.

The procedures followed to evaluate the residual pore pressure rise (i.e. to evaluate ratios $u_g/\sigma'_{vo} < 1$) and the cyclic porewater pressure, ΔU_{cy}, are presented in this section.

The models to evaluate the above porewater pressures were described earlier in Chapter 6 and are summarized below.

- Evaluation of Residual Pore Pressures

The following equation proposed by Seed et al. (1976) was used in the analysis to predict the gradual increase in residual porewater pressures:

$$u_g/\sigma'_{vo} = (2/\pi)\sin^{-1}(N/N_\ell)^{0.71} \qquad (7.4.2)$$

where:

N = the number of cycles

N_ℓ = the number of cycles to cause liquefaction

To evaluate the number of cycles, N, the relationship between the number of equivalent cycles of amplitude 118 MN versus time was obtained as described in Appendix 7.1 and is presented in Fig. 7.4.2. From this figure, N was evaluated at any desired time.

To evaluate the number of cycles to cause liquefaction, N_ℓ, the liquefaction resistance curves presented in Fig. 7.14 (main text) were used together with the cyclic stress ratio, $\Delta\tau_{zx}/\sigma'_{vo}$, which was computed as described in section (7.4.1).

The ratio (N/N_ℓ) was then computed and in turn u_g/σ'_{vo} evaluated using eq. (7.4.2).

The effective overburden pressure, σ'_{vo}, was computed using the unit weights shown in Fig. 7.6 (main text) and with this value the increase in residual porewater pressure, u_g, was finally evaluated.

• Evaluation of Cyclic Porewater Pressures

The following equation developed earlier in Chapter 6 was used herein to compute the cyclic porewater pressure, ΔU_{cy}:

$$\Delta U_{cy} = \Delta\sigma_m - 0.7\ \Delta\tau_{oct} \qquad (7.4.3)$$

where:

$\Delta\sigma_m$ = cyclic variation in total mean normal stress during a half cycle of load

$\Delta\tau_{oct}$ = cyclic variation in octahedral shear stress during the half cycle

The above procedures were followed for the evaluation of the porewater pressures. The results obtained are presented in the main text together with available field measurements.

7.4.3 Procedures for the Acceleration Assessment

The procedures followed in the analysis to evaluate the accelerations developed by the ice loading function shown in Fig. 7.1 (main text) are described in this section.

Assuming that the resonse to cyclic loading of a particular frequency was harmonic, the peak acceleration at time t, A(t), is given by the following equation:

$$A(t) = X(t) \cdot \omega(t)^2 \qquad (7.4.4)$$

where:

$X(t)$ = the amplitude of the displacement at time t

$\omega(t)$ = the angular frequency at time t

In the analysis, X(t) was computed using the following equation:

$$X(t) = X_{SL} \cdot SDF(t) \qquad (7.4.5)$$

where X_{SL} represents the amplitude of the displacement correspondent to the steady ice load time interval (see Fig. 7.1), and is given by the following equation:

$$X_{SL} = X_{397} - X_{279} \qquad (7.4.6)$$

where:

X_{397} = displacement obtained at peak cycle (ice load level = 397 MN)

X_{279} = displacement obtained at half cycle (ice load level = 279 MN)

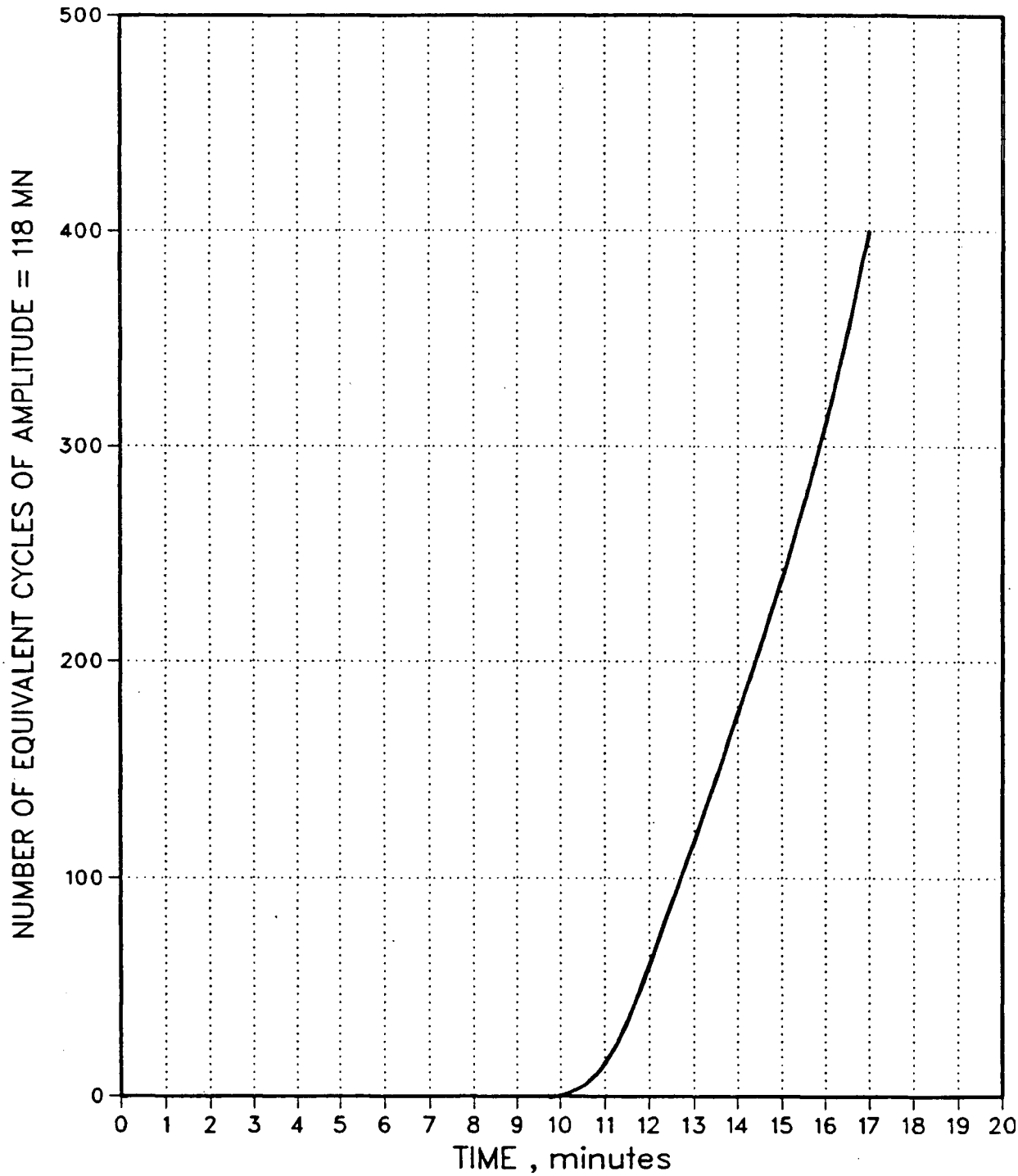

Figure 7.4.2 Relationship between number of equivalent load cycles of amplitude 118 MN and time

In eq. (7.4.6), the term SDF(t) represents a scaling displacement factor which is a function of time and is given by the following equation:

$$\text{SDF(g)} \frac{\Delta \text{ ice load (t)}}{(\Delta \text{ ice load})_{SL}} \tag{7.4.7}$$

where:

Δ ice load (t) = the amplitude of the cyclic laod at time t

$(\Delta \text{ ice load})_{SL}$ = the amplitude of the cyclic laoding during the steady loading time interval = 379-279 = 118 MN

The values of the scaling displacement factor, SDF, versus time were evaluated from the ice loading function presented in Fig. 7.1 (main text), and are presented in Fig. 7.4.3. It may be seen that during the steady part of the loading function, SDF(t) = 1.

The values of the angular frequency $\omega(t)$ were computed from the values of the natural frequency $f_o(t)$ shown in Fig. 7.4.3. The relationship between $\omega(t)$ and $f_o(t)$ by definition is as follows:

$$\omega(t) = 2\pi f_o(t) \tag{7.4.8}$$

The above procedures were followed for the evaluation of the accelerations. The results obtained are presented in the main text together with available field measurements.

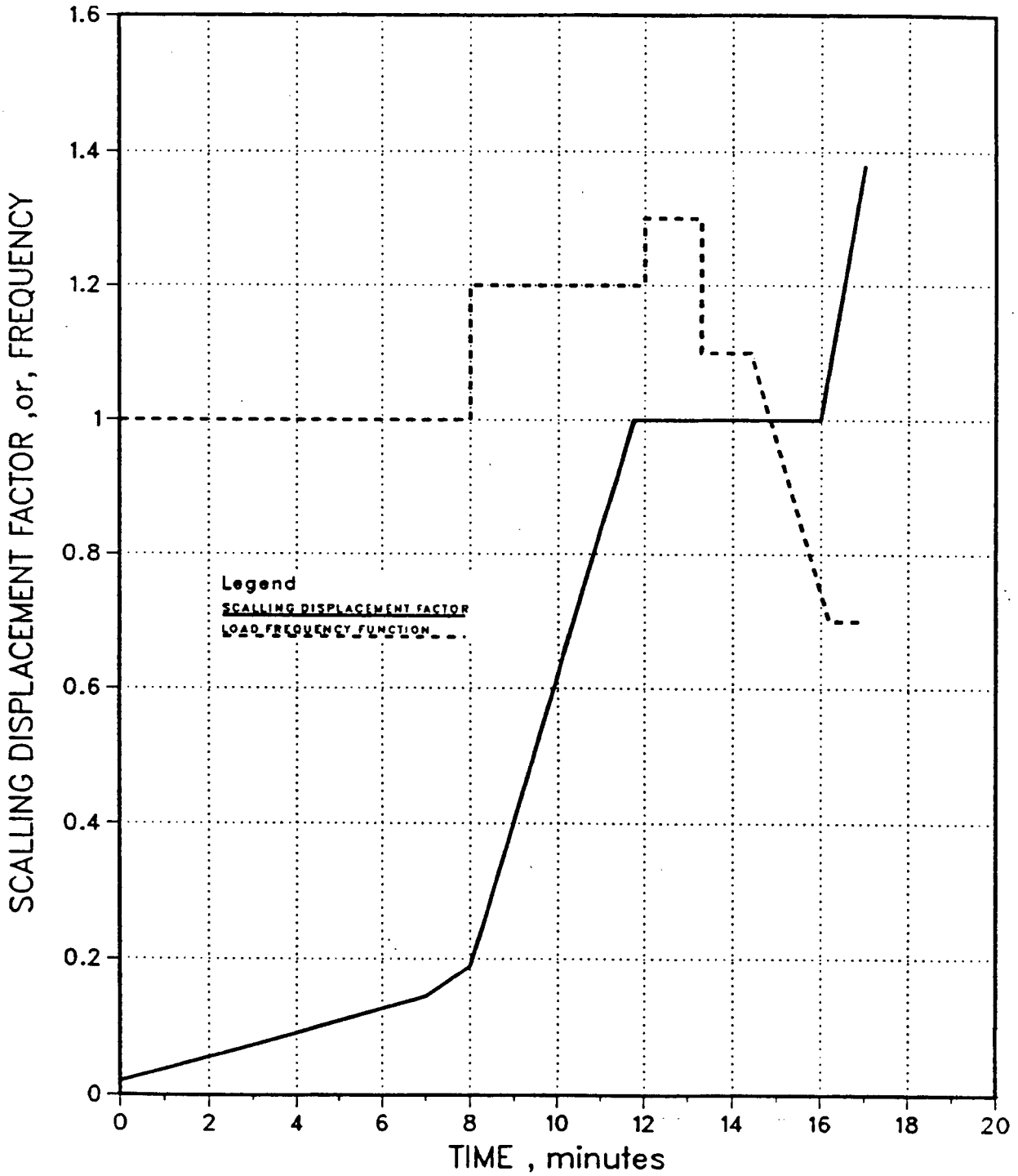

Figure 7.4.3 Relationships between scaling displacement factor, ice load frequency function, and time

APPENDIX 7.5

EVALUATION OF THE MODULI AND LOAD VECTOR USED IN THE SETTLEMENT ANALYSIS

APPENDIX 7.5

Evaluation of the Moduli and Load Vector Used in the Settlement Analysis

- Evaluation of the Moduli

At a depth of 10 m below the core surface the excess porewater pressure is given by the following equation:

$$\Delta U = z\ \gamma' \qquad (7.5.1)$$

where:

γ' = effective unit weight of the soil.

Considering $\gamma' \cong 10$ kPa and the water level at 5.0 m then,

$$\Delta U = 150 \text{ kPa}$$

Assuming that the volume changes are due to changes in the vertical direction only and that the Poisson's ratio, $\upsilon = 0$ then

$$\Delta\epsilon_z = \Delta\epsilon_v = \frac{\Delta U}{E} \qquad (7.5.2)$$

where:

$\Delta\epsilon_z$ = vertical srain

$\Delta\epsilon_v$ = volumetric strain

E = Young's modulus

from above

$$E = \Delta U/\Delta \epsilon_v \qquad (7.5.3)$$

assuming that $\Delta \epsilon_v = .08$ (8%) and $\Delta U = 150$ kPa, then

$$E = 1875 \text{ kPa}$$

Since the bulk modulus is related with the Young's modulus by following equation

$$B = \frac{E}{3(1-2\nu)} \qquad (7.5.4)$$

and since a $\nu=0$ is considered above then,

$$B = E/3 = 625 \text{ kPa}$$

Since in the analysis E and B are given by

$$E = K_E \text{ Pa } (\sigma'_m/\text{Pa})^n (1-R_F SL)^2 \qquad (7.5.5)$$

and

$$B = K_B \text{ Pa } (\sigma'_m/\text{Pa})^m \qquad (7.5.6)$$

assuming that $n = m = R_F = 0$ than from the above equations it follows that

$$K_E = 18.5 \quad \text{and} \quad K_B = 6$$

• Evaluation of the Load Vector

To predict the settlement due to the dissipation of the excess pore pressure ΔU in each liquefied element, a force vector $\{f\}$ was applied to the nodes of each liquefied element, developing a pressure $-\Delta U$.

The equation used to evaluate the force vector $\{f\}$ is as follows:

$$\{f\} = [B]^T \{-\Delta U\} \text{ volume} \qquad (7.5.7)$$

The basis for this equation has been described in Appendix 2.5.

APPENDIX 7.6

2-DIMENSIONAL FINITE ELEMENT ANALYSIS OF THE DYNAMIC ICE LOAD EVENT OF APRIL 12, 1986

APPENDIX 7.6

2-Dimensional Finite Element Analysis of the Dynamic Ice Load Event of April 12, 1986

7.6.1 Introduction

Several two-dimensional (2-D) plane strain analysis of the Molikpaq resopnse to the ice loading event of April 12, 1986 were carried out here to study the following aspects (see chapter 7, Section 7.4.3.1).

- Influence of the interface element type and the value of the angle of friction, δ.
- Influence of the stress redistribution method.
- Influence of the constitutive law.

Before the above studies were carried out, however, it was considered important to verify first the 2-D structural model developed in Appendix 7.2. This is presented next.

7.6.2 Verification of the Structural Model Used in the 2-D Ice Loading Analysis of the Molikpaq Structure

To verify the 2-D structural model 2-D analysis were carried out here following the exact same procedures as that followed earlier in the 3-D analysis. The 2-D finite element mesh and structural model used were discussed and presented earlier in Appendix 7.2.

Comparisons between the results obtained from the 2-D and 3-D analysis consisted of displacements, and the liquefaction soil zone developed during the ice loading, because these are considered to be the most representative of the dynamic ice loading effects on the Molikpaq structure.

In addition, the maximum ice load level used in the 2-D analysis was restricted to 397 MN, because this was the maximum ice load level developed during the ice load steady period, during which the majority of the ice dynamic action took place as was shown earlier in Chapter 7.

The displacements versus ice load obtained from the 2-D analysis, for the dynamic stages of zero dynamic cycles (pre-liquefaction) and 310 dynamic cycles (liquefaction is considered) are presented in Fig. 7.6.1 together with the correspondent results obtained from the 3-D analysis.

It may be seen that the results obtained from the 2-D and 3-D analysis agree very well except for the displacements obtained at the bottom of the loaded wall where the 2-D displacements are shown to be softer before liquefaction but stiffer after liquefaction. Nevertheless these differences did not have any effect on the number of soil elements to liquefy as is shown in Fig. 7.6.2, where the 2-D liquefaction assessement is presented.

By comparing this liquefaction zone with the 3-D liquefaction zone obtained earlier at the E-W cross-section (see main text Fig. 7.15) it is concluded that a coincidence was obtained.

Based on the above results the 2-D structural model shown in Fig. 7.2.3 (Appendix 7.2) is considered to be appropriate for use in the several 2-D parametric studies that are presented next.

7.6.3 Study of the Influence of the Interface Element Type, and of the Angle of the Friction δ Used in the Analysis

The analysis carried out to study the influence of the above two factors in the outcome of the results are presented below.

- Study of the Influence of the Interface Element Type

The following two sets of analyses were carried out to study the

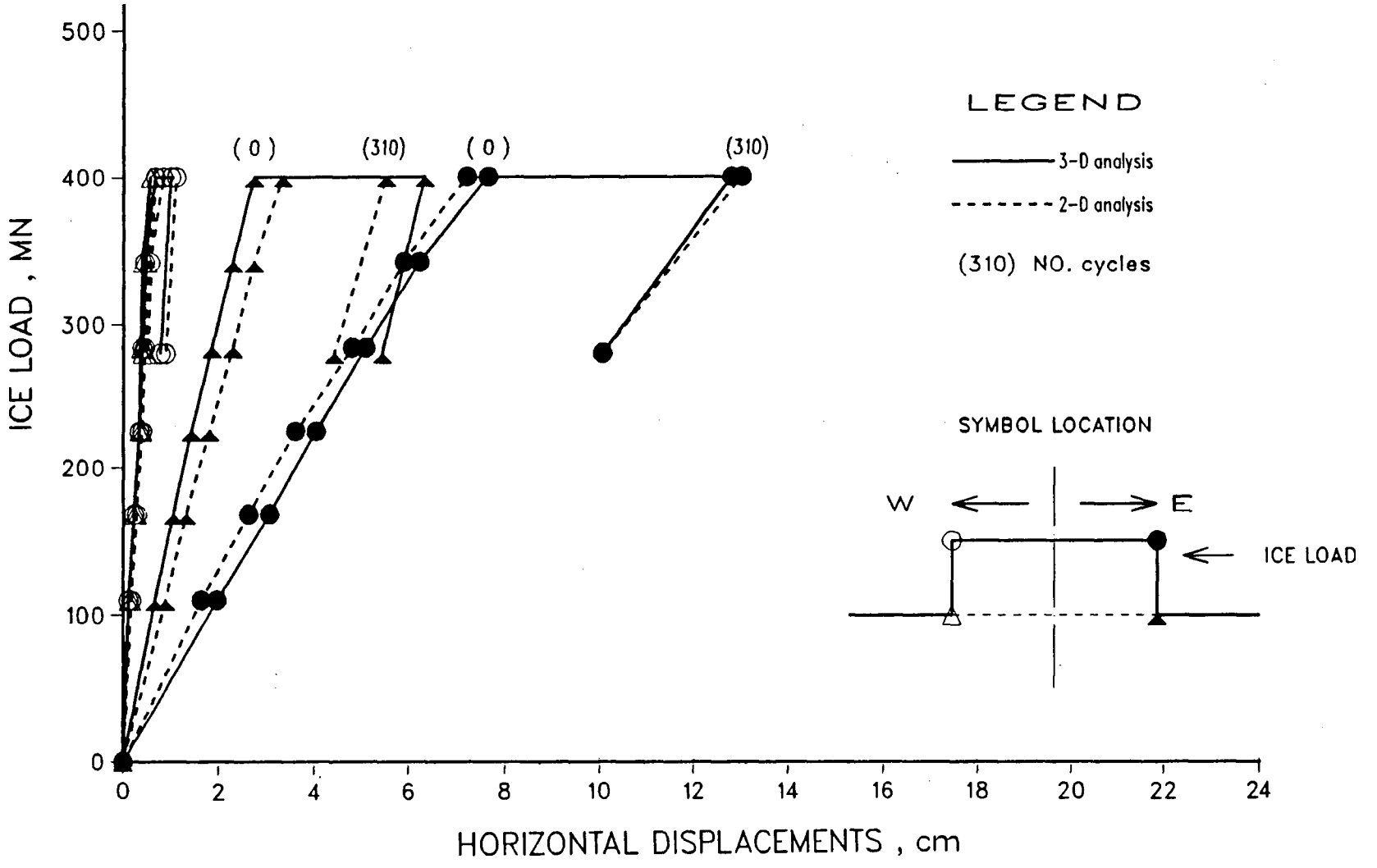

Figure 7.6.1 Displacements versus ice load obtained from 2-D and 3-D finite element analysis of the ice loading phases

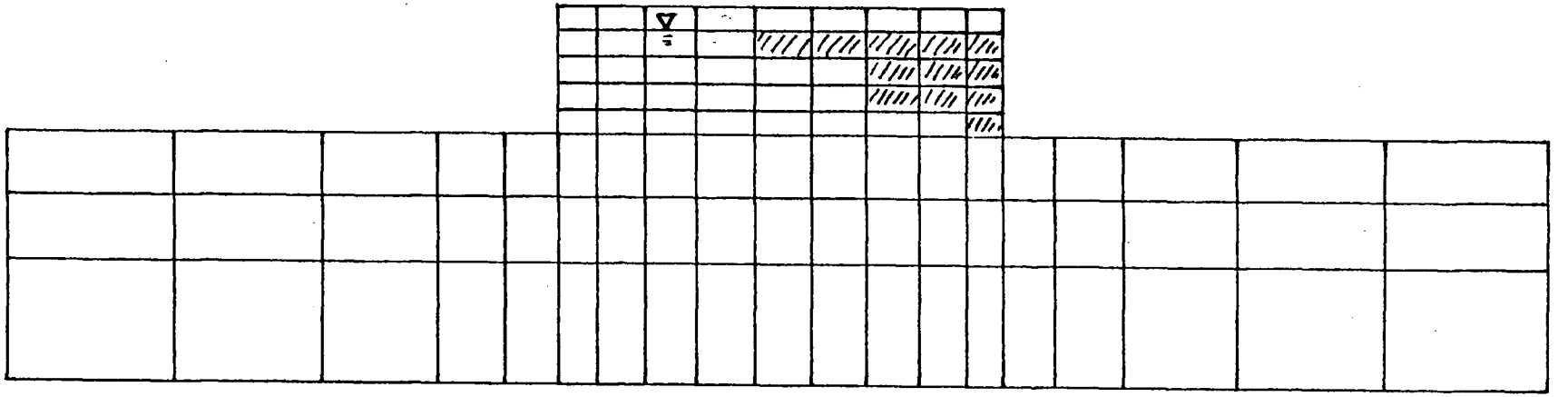

Figure 7.6.2 Liquefaction assessment obtained from 2-D analysis following the same procedures as that followed in the 3-D analysis

influence of the element type used to simulate the behaviour of the "interface" between the sand fills and the Molikpaq steel structure.

The first set of analyses correspond to the 2-D analysis described in the previous section. These analyses were carried out with the "interface" represented by the "standard" isoparametric solid element. The second set of analyses were carried out with the "interface" represented by the "thin" element. This element was described in detail in Chapter 4 and uses an uncoupled elastic-perfect plastic stress-strain law where the two moduli used to described its behaviour, normal modulus, E_N and shear modulus, G, are independent of each other. The values of E_N and G used in the analysis correspond to the unload/reload moduli of the adjacent soil elements to the "interface" (see Fig. 7.6; Chapter 7).

The results obtained from the two analysis, using a value of $\delta = 20°$ are presented in Fig. 7.6.3.

It may be seen that the same initial response of the Molikpaq loaded wall movement was computed by the analysis carried out using the "thin" interface element and the "standard" soil element. However at ice load levels of approximately 400 MN the displacements obtained with the "thin" element are shown to be about 85% of the computed by the "standard" soil element. This fact is not unexpected because the "thin" element uses an anisotropic constitutive law as opposed to the isotropic constitutive law used in the "standard" element.

Regarding the number of soil elements to liquefy, the same liquefaction distribution was obtained from both analysis. This indicates that, although different displacements were obtained from the two analyses, the stress distribution remained the same.

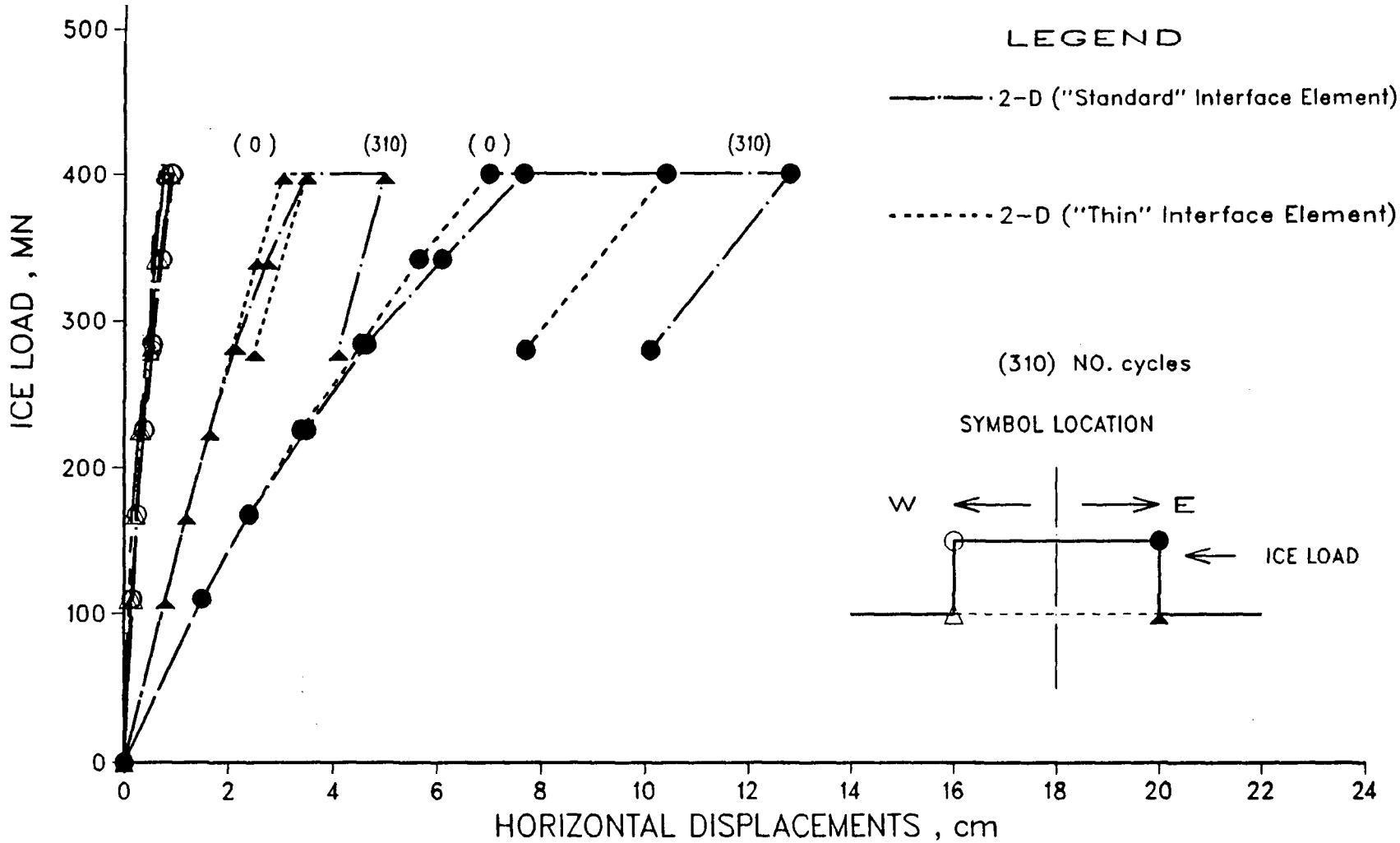

Figure 7.6.3 Displacements versus ice load. Study of the influence of the interface element type used in the analysis

• Study of the Influence of the Angle of Friction, δ

Two additional set of analyses were carried out, using values of $\delta = 0$ and $\delta = \phi$, to supplement the previous analysis which were carried out using a value of $\delta = 20°$. Both analyses were carried out using the "thin" element to characterize the "interface", and the values of ϕ used in the analysis correspond to the ϕ angle of the adjacent soil elements to the "interface" (see Fig. 7.6; Chapter 7).

The results obtained from the analyses for the cases of $\delta = 0$, $\delta = 20°$ and $\delta = \phi$ are presented in Fig. 7.6.4.

It may be seen that the results obtained from the analyses carried out with $\delta = 20°$ and $\delta = \phi$ are essentially the same. On the other hand, the displacements correspondent to the case $\delta = 0°$ are slightly (110%) higher than the displacements correspondent to $\delta = 20°$ or $\delta = \phi$, and approach the displacement values obtained earlier from the analysis that were carried out using the "interface" represented by standard soil elements (see Fig. 7.6.3).

Regarding the number of soil elements to liquefy the same liquefaction distribution was obtained from all the analysis.

Based on the above results it is concluded that if the 3-D analysis had been carried out using the "thin" element with a value of $\delta = 0°$ (worse condition) the displacements would not change much from the displacements computed earlier using the "standard" element and furthermore the 3-D liquefaction assessment shown earlier in Chapter 7 would remain the same.

7.6.4 Study of the Influence of the Method Used to Redistribute the Shear Stress of the Liquefied Soil Elements

As described in Chapter 7 (section 7.5) an alternative method to redistribute the shear stresses of the liquefied soil elements to the

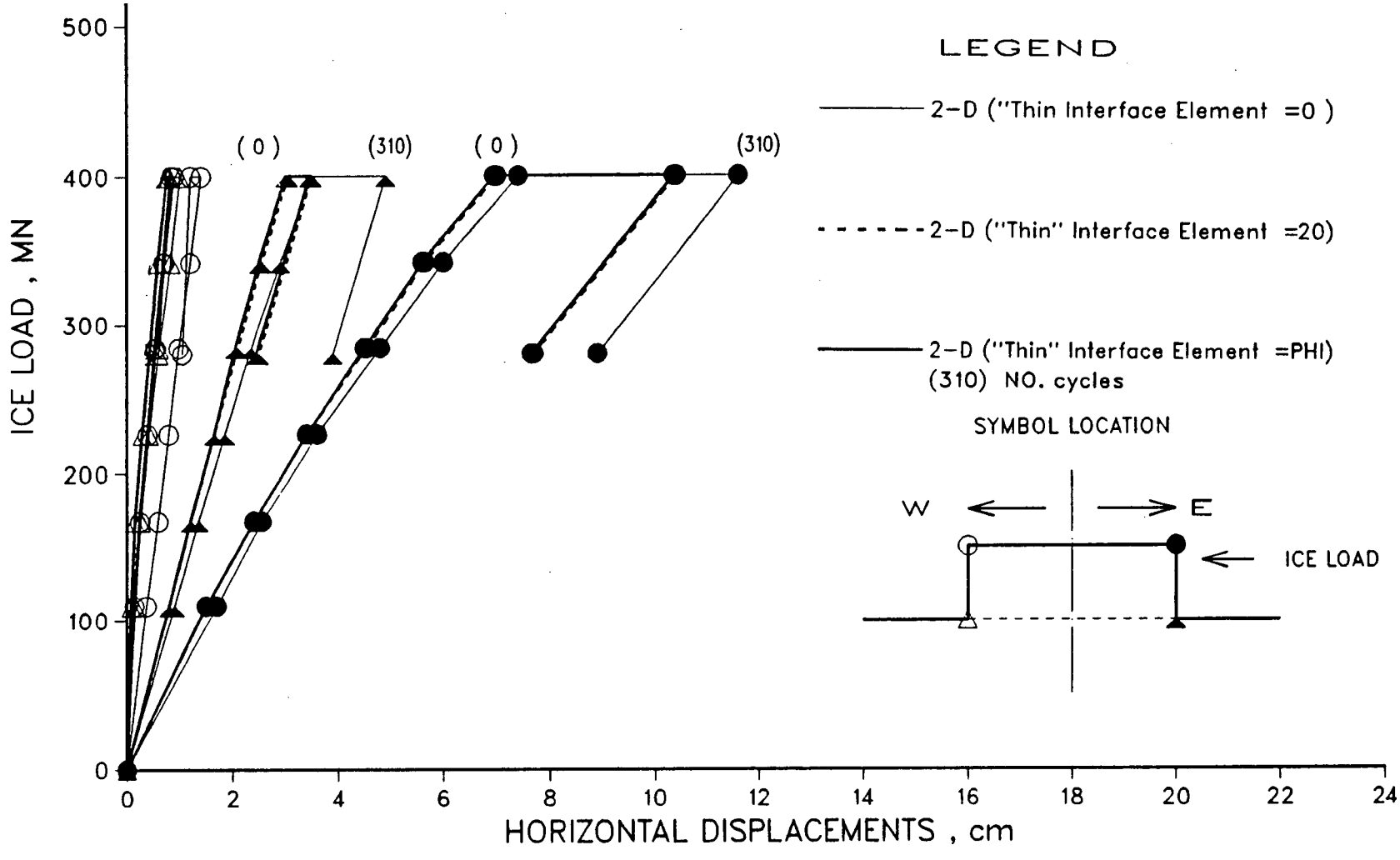

Figure 7.6.4 Displacements versus ice load. Study of the influence of the angle of friction, δ, used in the analysis

adjacent elements was also considered in the 2-D analysis. The method follows the load shedding technique developed by Byrne and Janzen (1984) and consists of the following.

The assessment of the soil elements to liquefy is carried out in the exact same way as described previously in Chapter 7. However, once these elements are identified, the shear strength of these elements is defaulted to a residual shear strength value, s_u. Next, and within the same load step, the load shedding technique developed by Byrne and Janzen (1984) is triggered following the procedures described in Chapter 2 and the shear stresses, $\Delta\tau$, exceeding the residual strength, s_u of the liquefied soil elements are redistributed to the adjacent soil and structural elements.

To assess the residual strength, s_u assigned to the liquefied soil elements the relationship, presented in Fig. 7.6.5, between $(N_1)_{60}$ and s_u developed by Seed et al. (1988), was followed herein.

Plots of the average $(N_1)_{60}$ values, $((N_1)_{60})_{av}$ versus depth, correspondent to the soil layers used in the finite element analysis are presented in Fig. 7.6.6. The procedures followed to compute the $(N_1)_{60}$ values were described earlier in Chapter 6.

Combining the $((N_1)_{60})_{av}$ values from Fig. 7.6.6 with the relationship between $(N_1)_{60}$ and s_u shown in Fig. 7.6.5, a lower bound profile for the shear strength, s_{uL}, and a higher bound profile for the shear strength, s_{uH}, were obtained and are included in Fig. 7.6.6.

Two sets of 2-D analysis were carried out following the above procedures. One correspondent to the residual shear strength, s_{uL} and the other to the residual shear strength, s_{uH}. Both analyses were carried out using the "interface" represented by the "thin" element with a value of δ = 20°.

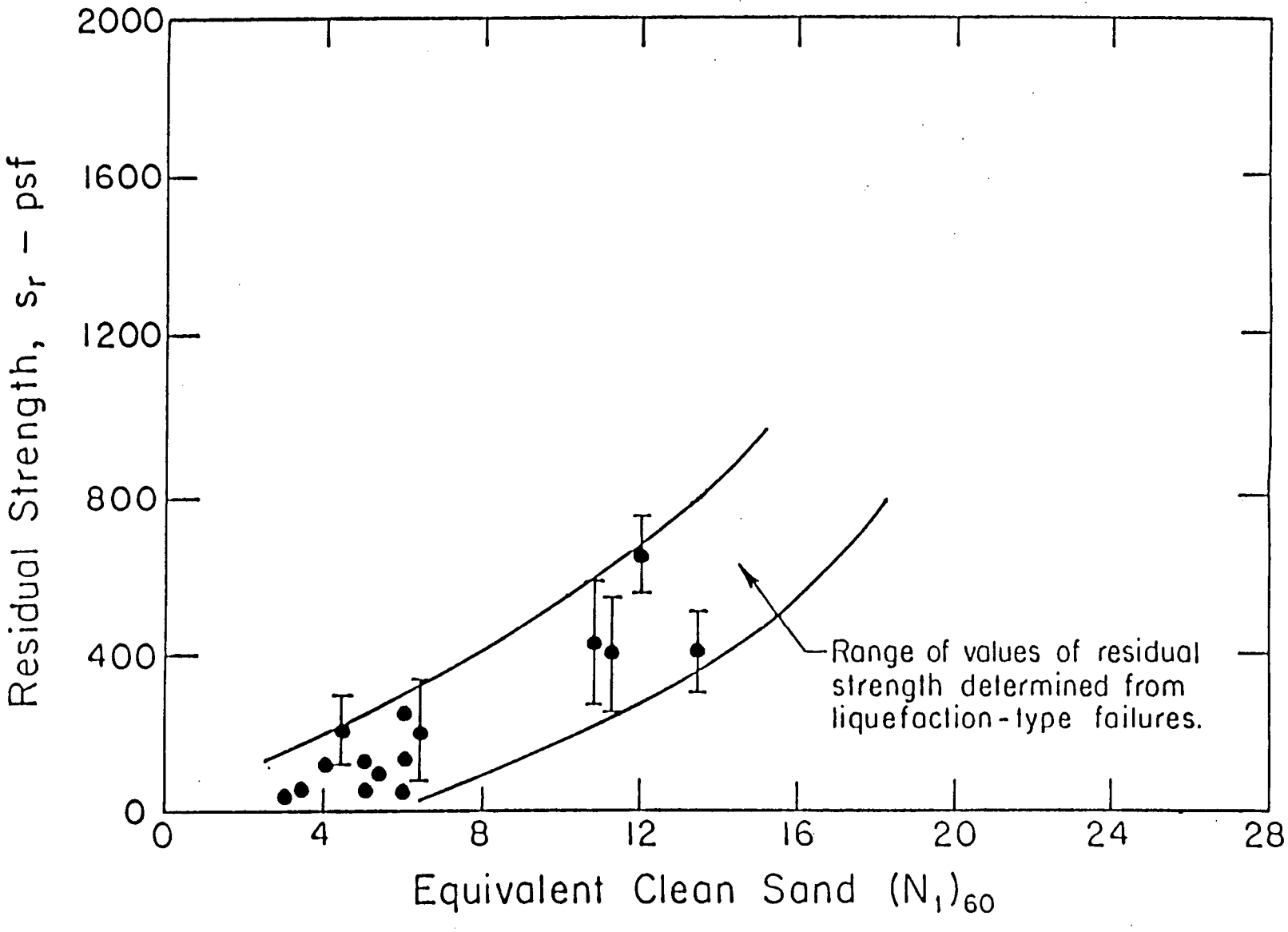

Figure 7.6.5 Relationship between residual shear strength, s_u and $(N_1)_{60}$ (after Seed et al, 1988)

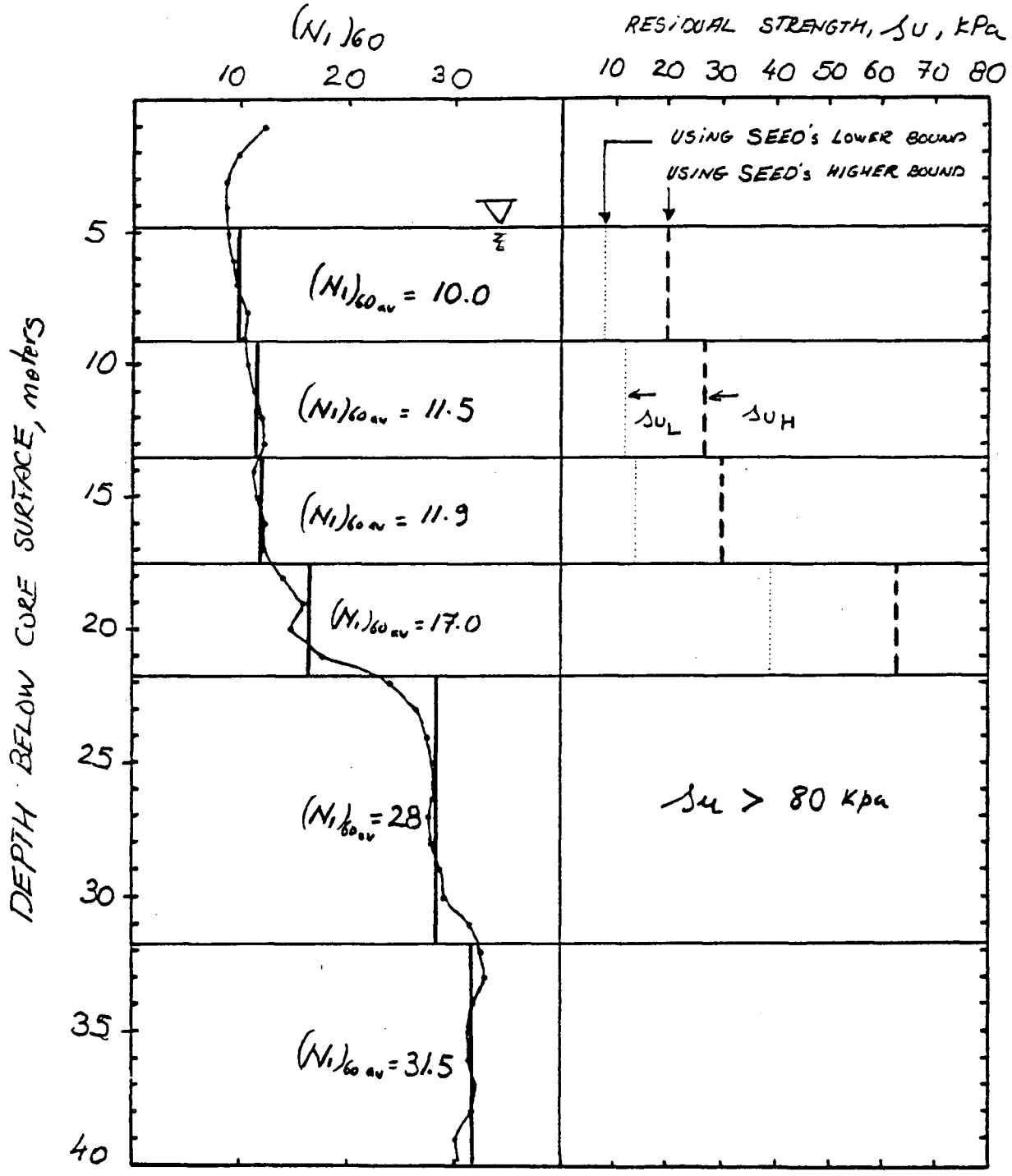

Figure 7.6.6 $((N_1)_{60})_{av}$ and residual shear strength, s_u versus depth

The results obtained from the two analyses are presented in Fig. 7.6.7 together with the results obtained earlier from the 2-D analyses which were carried out using the same "thin" element but using the stress redistribution method that was followed earlier in the 3-D analysis.

To simplify the discussion of results presented below, the stress redistribution method followed in the 3-D analyses is referred here as method 1 and the "residual strength + load shedding" method as method 2.

It may be seen that the two sets of displacements obtained from the analyses following method 2 are quite similar, although larger displacements were computed when $s_u = s_{uL}$.

It may also be seen that the results obtained from the analysis following method 1 show an opposite trend to the trend computed from the analysis following method 2, i.e. the results obtained from method 1 show that the ratio between the displacements computed at the locations of the loaded wall and the back wall, $d\ell/db$, is quite higher than the $d\ell/db$ ratio computed from the results obtained following method 2.

Despite the displacement differences noted above the liquefaction distributions computed from the analysis following method 1 and 2 were essentially the same, except for one soil element located in the top row of the submerged core.

Based on the above results it is concluded that if method 2 had been used in the 3-D analysis, instead of method 1, the 3-D liquefaction assessment would remain essentially the same as the computed earlier in Chapter 7.

7.6.5 Study of the Influence of the Stress-Strain Law Used in the Analysis

The 3-D analyses of the Molikpaq were carried out following a combination of elastic and hyperbolic laws as described earlier in Chapter 7.

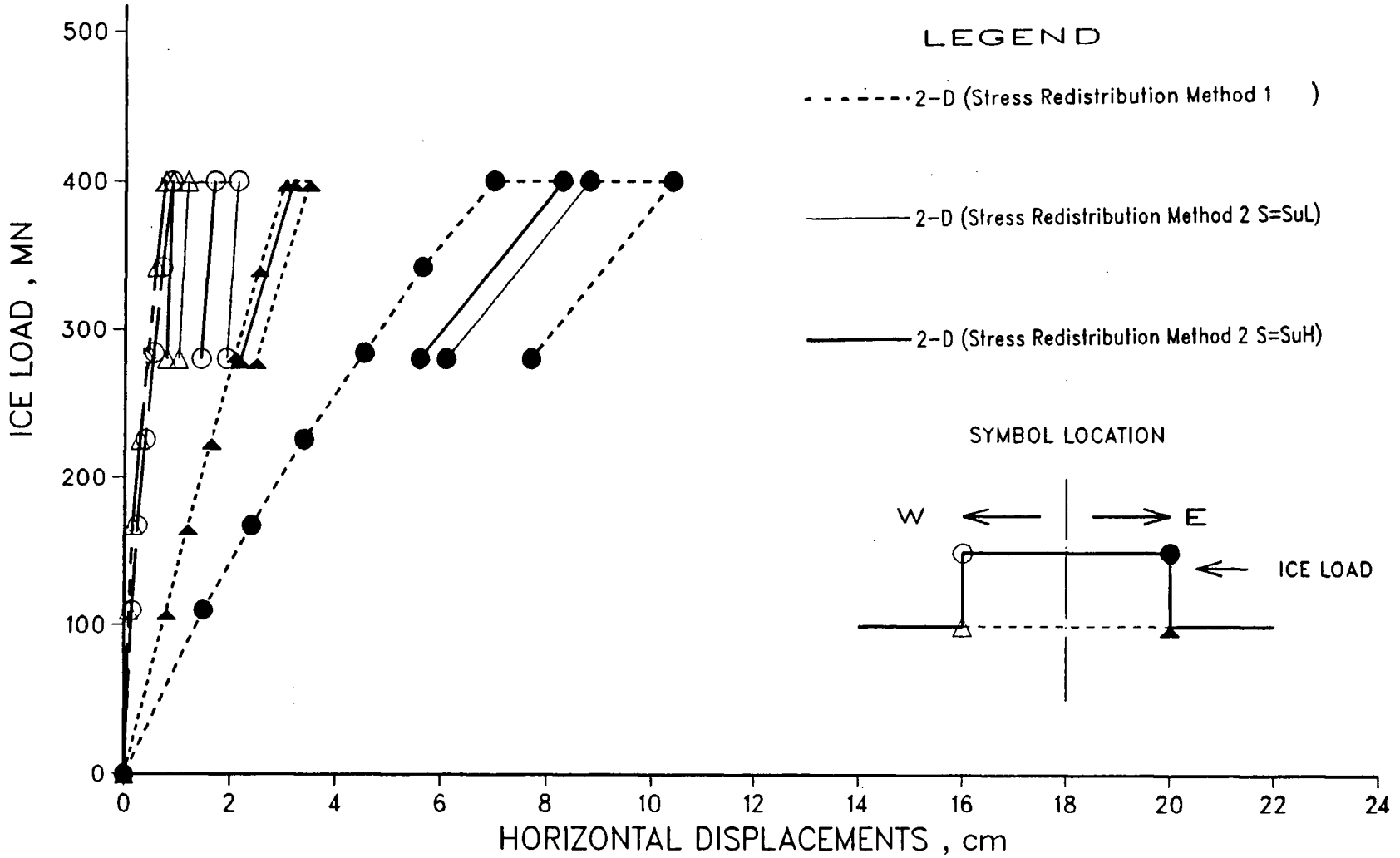

Figure 7.6.7 Displacements versus ice load. Study of the influence of the stress redistribution method followed in the analysis

To study the influence of the stress-strain law in the outcome of the results, two additional sets of 2-D analyses were carried out. One using the constitutive laws described above and the other using the modified SMP constitutive law developed earlier in Chapter 2.

Except for the constitutive law, both analyses were carried out following the same procedures. These are listed below.

a) The "interface" between the steel structure and the sand fills was simulated by the "thin" type of element.

b) The shear stresses, $\Delta\tau$, of the liquefied soil elements were redistributed using method 2, i.e. following the "residual shear strength + load shedding" approach described in the previous section. The lower bound profile for the residual shear strength, $s_{u\ell}$, shown in Fig. 7.6.6 was used in the analysis.

The soil parameters used in the modified SMP model are presented in Fig. 7.6.8 and were evaluated as described earlier in Chapter 6. The soil parameters used in the other model were presented earlier in Chapter 7 (Fig. 7.6).

The results obtained from the 2-D analyses are shown in Fig. 7.6.9 and a discussion of these is presented below.

It may be seen that up to an ice load level of about 200 MN the displacements computed by the two models are essentially the same. This indicates that the response of the sand fills to that ice load level was essentially elastic because the same elastic parameters were used in both models when MSL < $(MSL)_{max}$.

When the ice load increased from 200 to 397 MN, however, the displacements computed, by both models, at the loaded wall locations are quite different, but about the same at the back wall location. This indicates that the modified SMP model computed a stiffer response for the sand

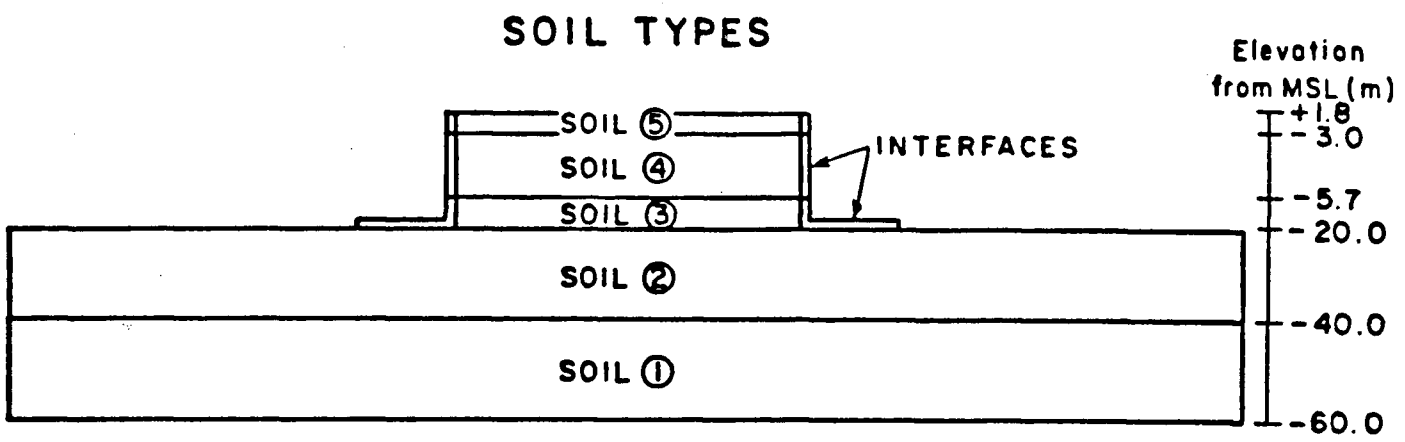

				Elastic Parameters				Plastic Parameters						
								Hardening Parameter		Flow Rule Param.		Yield Parameters		
Soil Type No.	Avg. Void Ratio $(e_c)_{av}$	γ kN/m	K_o	KG_{max}	n	KB_{ur}	m	KG_p	np	μ	λ	$(\frac{\tau_{SMP}}{\sigma_{SMP}})_1$	$\Delta(\frac{\tau_{SMP}}{\sigma_{SMP}})$	R_F
5	.685	15.6	.40	670	.50	750	.38	645	-.56	.25	.97	.685	.070	.94
4	.685	9.7	.40	670	.50	750	.38	645	-.56	.25	.97	.685	.070	.94
3	.660	9.7	.40	790	.50	850	.38	685	-.56	.25	.97	.715	.105	.94
2	.620	9.7	.40	1120	.50	1030	.38	760	-.56	.25	.97	.815	.180	.94
1	.680	9.7	.40	880	.50	750	.38	650	-.56	.25	.97	.710	.095	.94

Figure 7.6.8 Soil parameters and soil types used in the analysis carried out with the modified SMP model

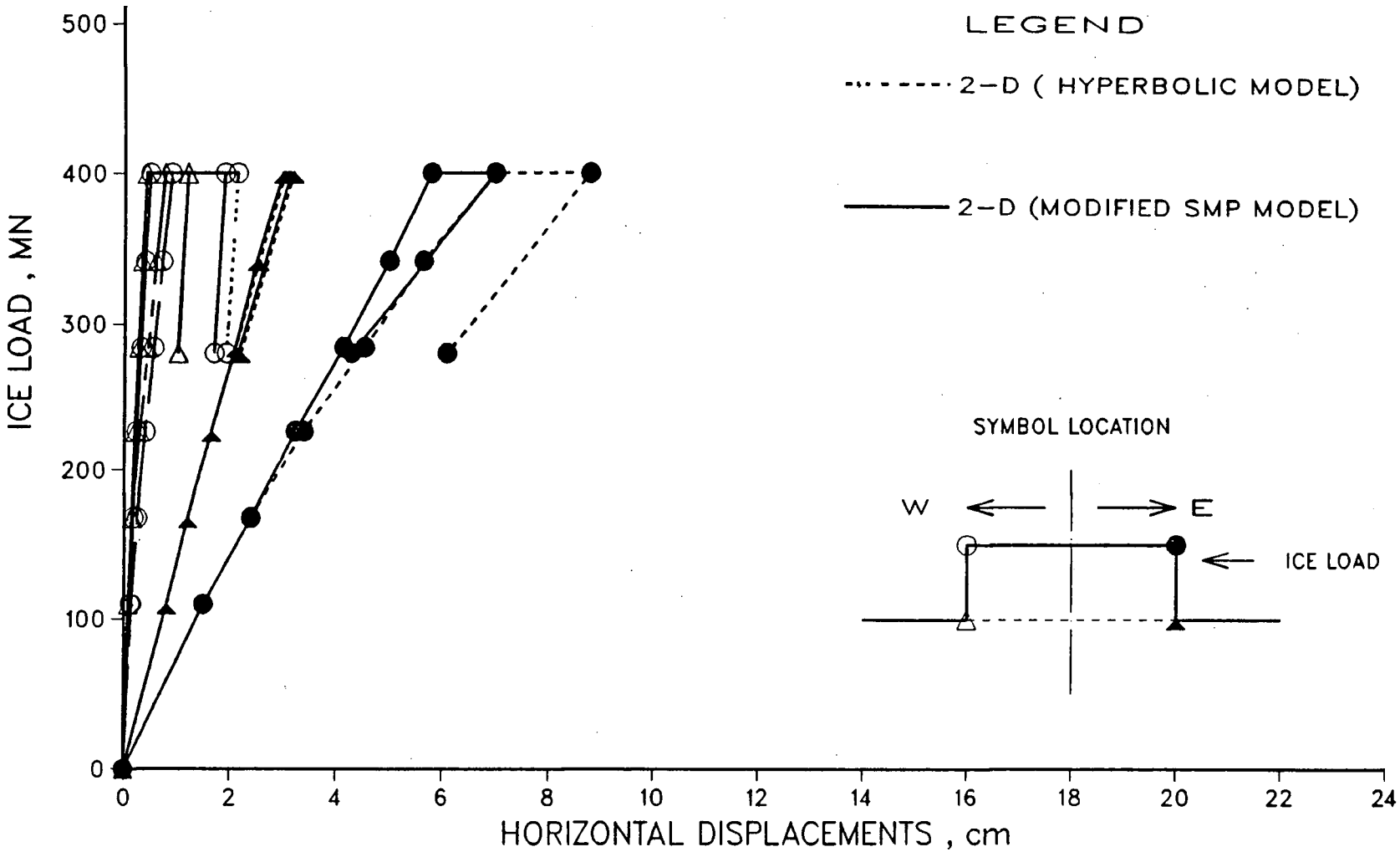

Figure 7.6.9 Displacements versus ice load. Study of the influence of the stress-strain law used in the analysis

adjacent to the loaded wall, than the computed by the hyperbolic model. The same trend was computed after triggering liquefaction. The results show that the displacements computed by the modified SMP model are about 82% of that computed by the hyperbolic model.

The above results are not surprising because the hyperbolic model uses a yield criterion that underestimates the failure strength of sand subjected to stress paths that differ from the triaxial path. On the other hand, the yield criterion followed in the modified SMP model takes different stress paths into account, as shown earlier in Chapter 3. In addition, the dilatant and rotational (rotation of principal stress axis) characteristics of the sand fills were not modelled by the hyperbolic model but were modelled by the modified SMP model. It is felt that the above considerations explain the different displacement results computed, before and after liquefaction, by the two models.

The liquefaction assessment by the two models is presented in Fig. 7.6.10. It may be seen that the computed number of soil elements to liquefy by the modified SMP model is 10 while a number of 13 was computed by the hyperbolic model. Nevertheless, the two liquefaction distributions are quite similar and indicate that the distribution of the shear stress, τ_{zx} and effective vertical stress, σ'_z, computed by the two models are also similar because only these two stresses were used in the assessment of liquefaction as described in Chapter 7.

Based on the above, it is concluded that if the modified SMP model had been used in the 3-D analysis instead of the hyperbolic model, then:

a) The horizontal displacements correspondent to the elastic phase (MSL < $(MSL)_{max}$) would be essentially the same as that computed earlier in Chapter 7. However, the horizontal displacements correspondent to the

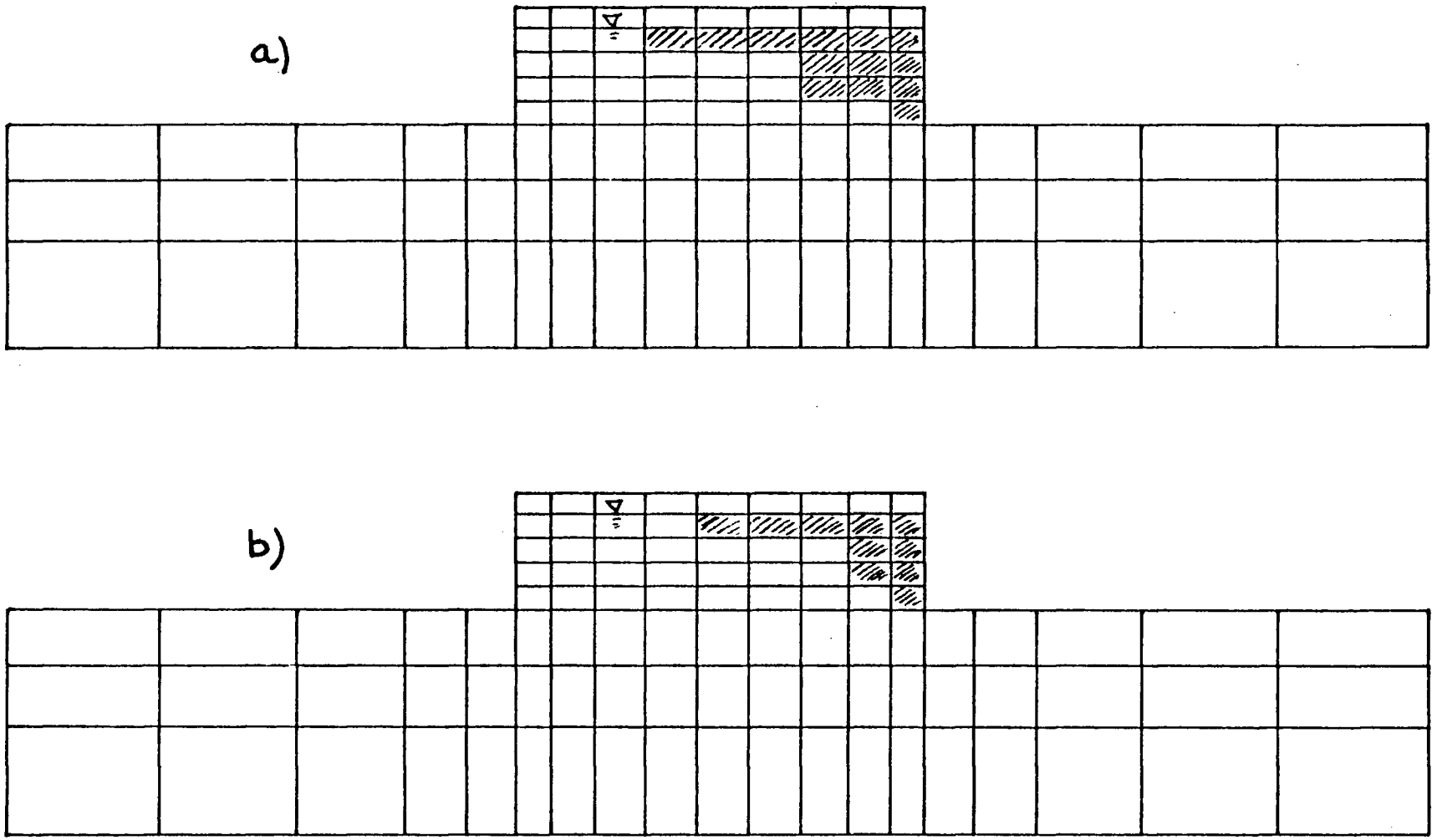

Figure 7.6.10 Liquefaction assessment obtained from 2-D analysis: (a) using the hyperbolic model; (b) using the modified SMP model.

plastic phases (MSL > $(MSL)_{max}$) would be smaller than that computed earlier for the loaded wall location, but about the same for the back wall location.

b) The 3-D liquefaction assessment would remain essentially the same as computed earlier in Chapter 7.

7.6.6 Conclusions

The main conclusions, derived from the results of the several 2-D analysis of the Molikpaq structure response to ice loading are summarized in Table 7.6.1 together with a brief description of each case studied.

It may be seen that the influence of the several parameters considered in the analysis on the horizontal displacements of the structure varied from case to case.

Stiffer responses of the Molikpaq loaded wall were computed by the analysis carried out using the "thin" interface element and the modified SMP model than that computed by the analysis carried out using the "standard" interface element and the hyperbolic model.

Similar responses of the Molikpaq back wall movements were computed from all analysis except for that computed by the analysis where the shear stresses of the liquefied soil elements were redistributed following the "residual strength + load shedding" method. This method computed larger displacements for the back wall than the computed from the stress redistribution method used in the 3-D analysis.

The results also indicate that the influence of the different parameters considered in the analysis, on the liquefaction distribution was of no significance.

Table 7.6.1
Summary of Conclusions

CASE STUDIED	DESCRIPTION	INFLUENCE ON THE RESULTS	
		HORIZONTAL DISPLACEMENTS	LIQUEFACTION ASSESSMENT
• INTERFACE TYPE (Sec. 7.6.3)	Behaviour of the interface between the Molikpaq steel structure and the sand fills. "Standard" soil elements, versus, Desai's "thin" element. Both analyses carried out with δ = 20°	• Larger displacements were computed at the loaded wall locations from the "standard" element analyses • Similar displacements were computed at the back wall locations from both analyses (see Fig. 7.6.3)	The same liquefaction distribution was computed from both analyses
• ANGLE OF FRICTION, δ (Sec. 7.6.3)	Three cases considered: δ=0°; δ=20°; and $\delta=\phi$. All analyses carried out using the "thin" element	• Larger displacements were computed at the loaded wall locations from the "δ=0°" analysis, & approach the displacements obtained from the "standard" element analysis (δ=20°) • Same displacements were computed at the loaded wall location from the "δ=20" and "$\delta=\phi$" analyses • Similar displacements were computed at the back wall locations from all analyses (see Fig. 7.6.4)	The same liquefaction distribution was computed from all analyses
• SHEAR STRESS REDISTRIBUTION METHOD (Sec. 7.6.4)	The shear stresses of the soil elements to liquefy at an ice load level, ILL are redistributed to the adjacent elements by: Method 1: defaulting the moduli of these elements to a small value and by reloading from ice load = 0 to ice load = ILL Method 2: using the "residual strength + load shedding" method.	• Larger displacements were computed at the loaded wall locations by the "method 1" analysis • Larger displacements were computed at the back wall locations by the "method 2" analysis	Similar liquefaction distributions were computed from both analyses
• CONSTITUTIVE MODEL (Sec. 7.6.5)	Hyperbolic model, versus, modified SMP model. Both analyses used the following: • Method 2 to redistribute the shear stresses of the liquefied elements • "Thin" element to simulate the interface between steel and sand (δ=20°)	• Larger displacements were computed at the loaded wall locations by the "hyperbolic" analysis • Similar displacements were computed at the back wall locations by both analyses (see Fig. 7.6.9)	Similar liquefaction distributions were computed from both analyses (see Fig. 7.6.10)